

MCLC S & T

SECTION B

Nonlinear Optics

Principles, Materials, Phenomena, and Devices

Editor: Takayoshi Kobayashi, University of Tokyo, Japan

Consultant Editors: M M Labes, A F Garito

East European and CIS Editor: Vladilen S Letokhov

North American Editor: Jerome D Swalen

West European Editor: François Kajzar

DISTRIBUTION STATEMENT A

Approved for public release

Distribution Unlimited

Proceedings of

**First International Conference on
Organic Nonlinear Optics
ICONO'1**

Val Thorens, France, 9-13 January, 1994

Coordinating Editor

**François Kajzar, Commissariat à l'Énergie Atomique,
Centre d'Études de Saclay, France**

ASTIC QUALITY INSPECTED 8



GORDON AND BREACH PUBLISHERS

MCLCS & T - Section B: NONLINEAR OPTICS

PRINCIPLES, MATERIALS, PHENOMENA, AND DEVICES

Editor

Takayoshi Kobayashi, Department of Physics, University of Tokyo, Hongo, Tokyo 113, Japan

Consultant Editors

M M Labes, Department of Chemistry, Temple University, Philadelphia, Pennsylvania 19122, USA

A F Garito, Department of Physics, University of Pennsylvania, Philadelphia, Pennsylvania 19104, USA

East European and CIS Editor: *Vladilen S Letokhov*, Institute of Spectroscopy, Troitzk, Russia

North American Editor: *Jerome D Swalen*, IBM Almaden Research Center, San Jose, California 95120-6095, USA

West European Editor: *François Kajzar*, DEIN/LPEM, CEN Saclay, Gif-sur-Yvette, 91191, France

Editorial Advisory Board

East Europe and CIS. *N I Koroteev*, Moscow State University, Moscow, Russia • *V V Ragul'skii*, Institute of Problems of Mechanics, Moscow, Russia • *V V Smirnov*, General Physics Institute, Moscow, Russia

North America. *Daniel S Chemla*, University of California, Berkeley, California, USA • *Stephen T Kowel*, University of Alabama, Huntsville, Alabama, USA • *RS Lytel*, Lockheed Palo Alto Research Laboratory, Palo Alto, California, USA • *Gerald R Meredith*, E I Dupont de Nemours and Co, Wilmington, Delaware, USA • *Nasser Peyghambarian*, University of Arizona, Tucson, Arizona, USA • *YR Shen*, University of California, Berkeley, California, USA • *Kenneth Singer*, Case Western Reserve University, Cleveland, Ohio, USA • *Eric W Van Stryland*, CREOL, University of Florida, Orlando, Florida, USA • *David J Williams*, Eastman Kodak Company, Rochester, New York, USA

West Europe. *David Bloor*, Durham University, Durham, UK • *Jean - Luc Brédas*, Université den Mons, Mons, Belgium • *David Cotter*, British Telecom Research Laboratories, Ipswich, UK • *Christos Flytzanis*, Laboratoire d'Optique Quantique du CNRS, Palaiseau, France • *Peter Günter*, Institute of Quantum Electronics, Zürich, Switzerland • *Yves Lévy*, Institut d'Optique, Orsay, France • *Gerd Marowsky*, Laser Laboratorium Göttingen e.V., Göttingen, Germany • *Arnold Migus*, École Polytechnique ENSTA, Palaiseau, France • *Jean-Paul Pocholle*, Thomson CSF, Orsay, France • *Joseph Zyss*, CNET, Bagneux, France

Japan. *Tadashi Itoh*, Tohoku University, Sendai • *Yuzo Ito*, Hitachi Ltd, Hitachi-shi • *Toshikuni Kaino*, NTT Optoelectronics Laboratory, Tokai • *Ken'ichi Kubodera*, NTT Interdisciplinary Research Laboratories, Tokyo • *Arao Nakamura*, Nagoya University, Nagoya • *Hachiro Nakanishi*, Tohoku University, Sendai • *Hiroki Nakatsuka*, University of Tsukuba, Tsukuba • *Hiroyuki Sasabe*, RIKEN, Wako • *Keisuke Sasaki*, Keio University, Yokohama • *Shinsuke Umegaki*, Keio University, Yokohama • *Masamichi Yamanishi*, Hiroshima University, Hiroshima

Aims and Scope

Nonlinear Optics publishes primary papers reporting original research, review articles, and rapid communications. The journal is divided into four main sections. 1. Principles — covering studies into the fundamental theoretical understanding of the origins and mechanisms of nonlinear optical processes, such as squeezing, phase conjugation, and optical bistability, and theoretical calculations of susceptibilities either by band theory or by quantum mechanical theory. 2. Materials — including work on the solid state physics of semiconductors and dielectrics, and organic and polymer compounds exhibiting nonlinear and electrooptical behaviour. 3. Phenomena — devoted to papers on: the discovery of new nonlinear optical phenomena; measurement of nonlinear optical processes; determination of nonlinear optical constants and figures of merit; observation of ultrafast and fast nonlinear optical processes; and the characterization of nonlinear optical materials by new measurement methods. 4. Device — featuring fundamental research articles on applications to devices, optical switches, optical bistable devices, phase conjugation, and optical logics. The journal recognizes the multidisciplinary nature of this field, and will include materials science and device implementation material, as well as the physicochemical aspects. The editors place great emphasis on the importance of the development of applications of nonlinear optical materials to practical devices.

Notes for contributors can be found at the back of the journal.

© 1995 by OPA (Overseas Publishers Association) Amsterdam BV. Published under license by Gordon and Breach Science Publishers SA, a member of the Gordon and Breach Publishing Group. All rights reserved.

Except as permitted under national laws or under the Photocopy License described below, no part of this publication may be reproduced or transmitted in any form or by any means, electronic or mechanical, photocopying or otherwise, or stored in a retrieval system of any nature, without the advance written permission of the Publisher.

Ordering Information

Four issues per volume. 1995 Volume(s): 11-15

Nonlinear Optics is Section B of the combined *Molecular Crystals Science and Technology*. Other journals offered in this collection will be Section A: *Molecular Crystals and Liquid Crystals*; Section C: *Molecular Materials*; and Section D: *Display and Imaging*. Please contact the publisher for details.

continued on inside back cover

REPORT DOCUMENTATION PAGE

Form Approved OMB No. 0704-0188

Public reporting burden for this collection of information is estimated to average 1 hour per response, including the time for reviewing instructions, searching existing data sources, gathering and maintaining the data needed, and completing and reviewing the collection of information. Send comments regarding this burden estimate or any other aspect of this collection of information, including suggestions for reducing this burden to Washington Headquarters Services, Directorate for Information Operations and Reports, 1215 Jefferson Davis Highway, Suite 1204, Arlington, VA 22202-4302, and to the Office of Management and Budget, Paperwork Reduction Project (0704-0188), Washington, DC 20503.

1. AGENCY USE ONLY (Leave blank)		2. REPORT DATE 1994	3. REPORT TYPE AND DATES COVERED Conference Proceedings	
4. TITLE AND SUBTITLE First International Conference on Organic Nonlinear Optics			5. FUNDING NUMBERS F6170894W0175	
6. AUTHOR(S) Conference Committee				
7. PERFORMING ORGANIZATION NAME(S) AND ADDRESS(ES) Dept. of Electronics & Nuclear Instrumentation Research Center in Saclay Gif-sur-Yvette Cedex 91191 France			8. PERFORMING ORGANIZATION REPORT NUMBER N/A	
9. SPONSORING/MONITORING AGENCY NAME(S) AND ADDRESS(ES) EOARD PSC 802 BOX 14 FPO 09499-0200			10. SPONSORING/MONITORING AGENCY REPORT NUMBER CSP 94-1001	
11. SUPPLEMENTARY NOTES				
12a. DISTRIBUTION/AVAILABILITY STATEMENT Approved for public release; distribution is unlimited.			12b. DISTRIBUTION CODE A	
13. ABSTRACT (Maximum 200 words) The Final Proceedings for International Conference on Organic Nonlinear Optics, 9 January 1994 - 13 January 1994				
14. SUBJECT TERMS Nil			15. NUMBER OF PAGES 470	
			16. PRICE CODE N/A	
17. SECURITY CLASSIFICATION OF REPORT UNCLASSIFIED	18. SECURITY CLASSIFICATION OF THIS PAGE UNCLASSIFIED	19. SECURITY CLASSIFICATION OF ABSTRACT UNCLASSIFIED	20. LIMITATION OF ABSTRACT UL	

NSN 7540-01-280-5500

Standard Form 298 (Rev. 2-89)
Prescribed by ANSI Std. Z39-18
298-102

Please refer to colour plates inserted at the back of this issue. The Publisher would like to inform that the figures for Colour Plate 1 and 2 have been reversed. Kindly refer to pages 411 and 412 for the correct placement of figures. The Publisher apologizes for any inconvenience caused.

ICONO'1

International Conference on Organic Nonlinear Optics

Val Thorens, January 9-13, 1994

Scientific Program Committee

- W. Blau, Trinity College, Dublin, Ireland
G. Bjorklund, IBM, Almaden Research Center, San Jose, USA
S. Ermer, Lockheed Missiles, Palo Alto, USA
A. F. Garito, University of Pennsylvania, Philadelphia, USA
P. Günter, Institute of Quantum Electronics, ETH Zurich, Switzerland
R. Lytel, AKZO USA, Redwood City, USA
H. Sasabe, RIKEN, Saitama, Japan
J. Zyss, Centre National d'Etudes des Télécommunications, Bagneux, France

Organizing Committee

- F. Kajzar (*chair*), Commissariat à l'Energie Atomique, CE Saclay, France
M. G. Kuzyk (*co-chair*), Washington State University, Pullman, USA
S. Miyata (*co-chair*), Tokyo University of Technology and Agriculture,
Tokyo, Japan

Local Organizing Committee

- F. Charra (*secretary*)
P.-A. Chollet (*treasurer*)
F. Kajzar (*chair*)
Commissariat à l'Energie Atomique,
CE Saclay, France

The papers listed below are to be found in Part I of this special issue Nonlinear Optics
Volume 10(1-4)

CONTENTS — Part II

Volume 10(1-4)

IV. Third Order Effects

J. R. HEFLIN, D. C. RODENBERGER, W. D. CHEN, R. F. SHI, Q. L. ZHOU and A. F. GARITO: Enhanced Third Order Nonlinear Optical Responses from Populated Electronic Excited States	1
CHRISTOPH BUBECK: Relations Between Structure and Third-Order Nonlinear Optical Properties of Conjugated Polymers	13
M. BLANCHARD-DESCE, J.-M. LEHN, M. BARZOUKAS, C. RUNSER, A. FORT, G. PUC CETTI, I. LEDOUX and J. ZYSS: Functionalized Polyenes and Carotenoids with Enhanced Nonlinear Optical Responses	23
P. N. PRASAD, M. E. ORCZYK, J. SWIATKIEWICZ, C.-K. PARK and C. F. ZHAO: Third-Order Nonlinear Optics of Organic Chromophores	37
G. BOURHILL, B. G. TIEMANN, J. W. PERRY and S. R. MARDER: Effect of Aromaticity on the Second Hyperpolarizability of Conjugated Donor-Acceptor Molecules	49
VÉRONIQUE DENTAN, PHILIPPE ROBIN and JEAN-PIERRE HUIGNARD: Nonlinear Optical Response of C_{60} Solutions at $\lambda = 1.60 \mu m$ in the Nanosecond Regime	61
W. SCHROF, J. R. WÜNSCH, A. ESSER, K. H. HAAS and H. NAARMANN: Nonlinear Optics of Conjugated Polyacetylene Thin Films Produced by Different Preparation Techniques	69
DAO VAN LAP, S. RENTSCH and H. NAARMANN: Femtosecond Time Resolved Measurement of the Nonlinear Refractive Index of Thiophene Oligomers in Solution	79
S. N. OLIVER, S. V. KERSHAW, A. E. UNDERHILL, C. A. S. HILL and A. CHARLTON: Nonlinear Optical Properties of Tetraaryl Substituted Metal Dithiolene Complexes in the Near Infra-Red	87

M. A. DÍAZ-GARCÍA, I. LEDOUX, F. FERNÁNDEZ-LÁZARO, A. SASTRE, T. TORRES, F. AGULLÓ-LÓPEZ and J. ZYSS: Third Harmonic Generation in New Crown Ether Substituted Metallotriazolehemiporphyrazines	101
MASARU MATSUOKA, ATSUSHI OSHIDA, AKIRA MIZOGUCHI, YASUHIRO HATTORI and AKIRA NISHIMURA: Molecular Design of Quinoid Dyes for 3rd Order NLO Materials	109
A. S. DHINDSA, A. UNDERHILL, S. OLIVER and S. KERSHAW: New $\chi^{(3)}$ Materials for Electro-Optic and All Optical Signal Processing Based on Metal Complexes	115
H. MATSUDA, E. VAN KEUREN, A. MASAKI, K. YASE, A. MITO, C. TAKAHASHI, H. KASAI, H. KAMATANI, S. OKADA and H. NAKANISHI: Nonlinear Optical Properties of J-Aggregated Merocyanine Dye Microcrystals in Polymer Matrices	123
T. BJØRNHOLM, T. GEISLER, J. C. PETERSEN, D. R. GREVE and N. C. SCHIØDT: The Third-Harmonic Generation in Gold and Nickel Bis-Dithiolene Complexes	129
S. BURBRIDGE, H. PAGE, A. DRURY, A. P. DAVEY, J. CALLAGHAN and W. BLAU: The Third Order Nonlinear Optical Response of a Soluble form of Polyizothionaphthene	139
CHARLES W. SPANGLER, MINGQIAN HE, PEIKANG LIU, ERIC G. NICKEL, JOYCE LAQUINDANUM and LARRY R. DALTON: The Design of New Organic Materials with Enhanced Nonlinear Optical Properties: Incorporation of Bipolaronic Charge States	147
J. HEIN, H. BERGNER, M. LENZNER and S. RENTSCH: Determination of Real and Imaginary Part of $\chi^{(3)}$ Values of Thiophene Oligomers by z-Scan Method	153
F. J. BARTOLI, J. R. LINDLE, J. S. SHIRK, S. R. FLOM, A. W. SNOW and M. E. BOYLE: Resonant Third-Order Optical Response in the Metallo-Phthalocyanines at 1064 nm.	161
A. DRURY, A. P. DAVEY, S. BURBRIDGE, H. PAGE and W. BLAU: The Synthesis of the Narrow-Gap, Nonlinear, Organic Polymer Poly(tertbutylisothianaphthene)	167
W. WERNCKE, M. PFEIFFER, T. JOHR, A. LAU, S. WOGGON, S. SCHRADER and H.-J. JÜPNER and W. FREYER: Determination of $\chi^{(3)}$ -Parameters of Solutions and of Thin Layers by Coherent Antistokes Raman Scattering (CARS)	173
S. R. FLOM, R. G. S. PONG, F. J. BARTOLI and Z. H. KAFABI: Nonlinear Optical Properties of Fullerenes and their Derivatives	183

BRIAN L. LAWRENCE, MYOUNGSIK CHA, WILLIAM E. TORRUELLAS, GEORGE I. STEGEMAN, SHAHAB ETEMAD and GREGORY BAKER: Z-Scan Measurement of Third and Fifth Order Nonlinearities in Single Crystal PTS at 1064 nm	193
--	-----

V. Nonlinear Spectroscopy and Basic Phenomena

T. KOBAYASHI: Mechanism of Optical Nonlinearity in Conjugated Polymers	207
E.TOKUNAGA, A. TERASAKI and T. KOBAYASHI: Femtosecond Phase Spectroscopy with a Frequency-Domain Interferometer	217
JAMES H. ANDREWS, JOHN D. V. KHAYDAROV, KENNETH D. SINGER, DIANA L. HULL and KATHY C. CHUANG: Spectral Dispersion of Third Harmonic Generation in Squaraines	227
P. VIDA KOVIC, J. ZYSS, D. KIM, W. TORRUELLAS and G. STEGEMAN: Large Effective $\chi^{(3)}$ by Cascading of $\chi^{(2)}$ in Crystal Cored Fibers	239
S. QUILLARD, G. LOUARN, K. BERRADA, S. LEFRANT, K. A. COPLIN, S. W. JESSEN and A. J. EPSTEIN: Resonance Raman Scattering and Photoinduced Infrared Absorption in Different Forms of Polyanilines and Substituted Polyanilines	253
IFOR D. W. SAMUEL, ISABELLE LEDOUX, CHRISTOPHE DHENAUT, JOSEPH ZYSS, HAROLD H. FOX, RICHARD R. SCHROCK and ROBERT J. SILBEY: Chainlength Dependence of Cubic Nonlinearities in Polyene Oligomers: Saturation and Scaling Law	263
PEETER KUKK, EDA REINOT and MARGUS RÄTSEP: Local-Field Effects and Preresonance Amplification of Coherent Anti-Stokes Raman Scattering in Thin Anthracene Monocrystals at Low Temperatures	273
J. M. NUNZI, F. CHARRA, N. PFEFFER, T. P. NGUYEN and V. H. TRAN: Picosecond Light-Induced Dichroism in Thin Films of Phenylene-Vinylene Oligomers	279

VI. Transport Properties and Electrooptic Effects

F. CHARRA: Nonlinear Optical Properties of Organic MIS Structures	287
T. A. PASMORE, J. D. HARPER, J. TALBOT and H. S. LACKRITZ: Monte Carlo Simulations of Charge Transport through Doped Polymer Thin Films for Second Order Nonlinear Optics	295

ARND KRÜGER, CAROLA KRYSCI, DANKWARD SCHMID and H. PETER TROMMSDORFF: Transport Dynamics of Singlet Guest Excitations in High-Concentration <i>p</i> -Terphenyl Crystals	303
--	-----

Z. STRYŁA, J. KOWALAK, M. LUDWICZAK, J. J. LANGER and A. RAJCHEL: Light Induced Conductivity in N-Methyl-1, 10-Phenantroline-TCNQ RIS	313
--	-----

VII. Device Development

VII. 1. Frequency Doubling

HEIHACHI SATO, HIDEHISA NOZAWA, YUJI AZUMAI and IWAO SEO: Demonstration of Enhanced Cerenkov-Radiative SHG with Chirped Nonlinear Optical Susceptibility in Organic Polymer Waveguide	319
---	-----

A. OTOMO, Ch. BOSSHARD, S. MITTLER-NEHER, G. I. STEGEMAN, M. KÜPFER, M. FLÖRSHEIMER, P. GÜNTER, W. H. G. HORSTHUIS and G. R. MÖHLMANN: Second-Harmonic Generation by Counterpropagating Beams in Organic Thin Films	331
--	-----

M. KÜPFER, M. FLÖRSHEIMER, Ch. BOSSHARD and P. GÜNTER: Phase-Matched Second-Harmonic Generation by Mode Conversion in a $\chi^{(2)}$ -Inverted Waveguide Structure	341
--	-----

J. L. COUTAZ, B. BLAU, J.-F. ROUX, R. REINISCH, F. KAJZAR, P. RAIMOND, P. ROBIN, E. CHASTAING and P. LE BARNY: Experimental Investigation of Second Harmonic Generation from Organic Waveguides Diffraction Gratings	347
---	-----

VII. 2. Electro-and All Optical Switching

R. REINISCH and G. VITRANT: Electromagnetic Analysis of Nonlinear Couplers: Application to Nonlinear m-Lines Techniques	357
--	-----

J. D. SWALEN and J. I. THACKARA: Electro-Optic Measurements of Poled Polymeric Films	371
---	-----

L. DALTON, C. XU, A. W. HARPER, R. GHOSN, B. WU, Z. LIANG, R. MONTGOMERY and A. K.-Y. JEN: Development and Application of Organic Electro-Optic Modulators	383
--	-----

M. G. KUZYK, D. J. WELKER and S. ZHOU: Photomechanical Effects in Polymer Optical Fibers	409
---	-----

G. F. LIPSCOMB, R. LYTEL and A. J. TICKNOR: Electro-Optic Polymer Waveguide Arrays in Digital Systems	421
--	-----

J. LIANG, R. LEVENSON, J. ZYSS, D. BOSC and F. FOLL: Design and Fabrication of Electro-Optic Polymer Waveguides	431
---	-----

VII. 3. Spatial Light Modulation

JEAN-CLAUDE DUBOIS: Polymers in New Electrooptic Components	439
---	-----

JEAN-MICHEL NUNZI and FABRICE CHARRA: Molecular Engineering of Organic Materials for Efficient Spatial Light Modulation	447
---	-----

DENIS FICHOU, JEAN-MICHEL NUNZI, FABRICE CHARRA and NICOLA PFEFFER: Transient Photochromism of Oligothiophenes and its Use to Design an Incoherent-to-Coherent Optical Converter	457
--	-----

CONTENTS — Part I

Volume 9(1–4)

I. Introduction

- F. KAJZAR and J. ZYSS: Organic Nonlinear Optics: Historical Survey and Present Trends 3

II. Theory of Organic Hyperpolarizabilities

- B. CHAMPAGNE and J. M. ANDRÉ: Towards the Calculation of Polarizabilities of Infinite Polymeric Chains. Uncoupled and Coupled Hartree-Fock Schemes 25
- D. BELJONNE, C. DEHU and J. L. BRÉDAS: Theoretical Investigation of the Third-Order Nonlinear Optical Properties of Oligothiophenes and Derivatives: Conjugation-Length and Frequency-Dispersion Analysis 37
- Th. NEIDLINGER, P. REINEKER, V. M. AGRANOVICH and V. I. YUDSON: Nonlinear Optics of Organic Multilayers with Fermi Resonances 49
- F. MEYERS, S. R. MARDER, J. W. PERRY, G. BOURHILL, S. GILMOUR, L.-T. CHENG, B. M. PIERCE and J. L. BRÉDAS: Electric-Field Modulated Nonlinear Optical Properties of Conjugated Organic Chromophores: Influence of the Nature of the Conjugated Bridge 59
- I. B. TALANINA, M. A. COLLINS and V. M. AGRANOVICH: Dynamics of Bright Polariton Solitons in the Presence of Damping 67
- M. DEL ZOPPO, C. CASTIGLIONI and G. ZERBI: A Novel Approach to Estimate N.L.O. Response in Organic Conjugated Molecules from Vibrational Spectra: Molecules with Large β Values 73
- V. M. AGRANOVICH: Optical Nonlinearities in Multilayer Organic Structures 87

III. Second Order Effects

III. 1. Molecule Synthesis and Material Processing

- Y. MATSUOKA, A. SUZUKI and A. J. IKUSHIMA: Design for Nonlinear Optical Host-Guest Systems 103

R. MASSE: Design of Non-Linear Optical Crystalline Materials Based on Three-Dimensional Short Hydrogen Bond Networks	113
J. F. NICOUD, C. SERBUTOVIEZ, Y. BARRANS, D. CHASSEAU, I. GAUTIER-LUNEAU, I. LEDOUX and J. ZYSS: New Organic Crystals for Quadratic Nonlinear Optics: Molecular Engineering, Crystallographic Studies and Nonlinear Optical Properties	127
G. KNÖPFLE, R. SCHLESSER, R. DUCRET and P. GÜNTER: Optical and Nonlinear Optical Properties of 4'-Dimethylamino-N-Methyl-4-Stilbazolium Tosylate (DAST) Crystals	143
M. AHLHEIM and F. LEHR: Synthesis of Novel Electrooptically Active Polymers	151
I. CABRERA, A. MAYER, D. LUPO, U. FALK, U. SCHEUNEMANN and W. HICKEL: Blue Transparent Langmuir Blodgett Films for Second Harmonic Generation	161
R. SCHLESSER, G. KNÖPFLE, K. SUTTER, Ch. BOSSHARD and P. GÜNTER: Electro-Optic and Photorefractive Properties of 4'-Nitrobenzylidene-3-Acetamino-4-Methoxyaniline (MNBA) Single Crystals	171
MAN SHING WONG, JEAN-FRANÇOIS NICOUD, CLAUDE RUNSER, ALAIN FORT and MARGUERITE BARZOUKAS: Novel Approach in Molecular Design for Quadratic Nonlinear Optics (NLO): Design, Syntheses and Characterizations of New Classes of Dipolar and Multi-Dipolar Molecules	181
J. LE MOIGNE, L. OSWALD, F. KAJZAR and A. THIERRY: Oriented Thin Films for Nonlinear Optics	187
C. RUNSER, A. FORT, M. BARZOUKAS, P. BOY, C. COMBELLAS, C. SUBA and A. THIEBAULT: Solvent Dependent Quadratic Hyperpolarizability of some zwitterions: Effect of the Conjugation Path	195
J. ULAŃSKI, P. WOJCIECHOWSKI and M. KRYSZEWSKI: Unconventional Anisotropic Polymer/Crystalline Phase Composites	203
SETH R. MARDER, BRUCE G. TIEMANN, ANDRIENNE C. FRIEDLI, EDWARD YANG and LAP-TAK CHENG: Large First Hyperpolarizabilities of Push-Pull Polyenes with Strong Acceptors	213

III. 2. Characterization Techniques

M. KIGUCHI, M. KATO, N. KUMEGAWA and Y. TANIGUCHI: Simple Evaluation for Second-Order Nonlinear Optical Materials in Powder Form	223
KOEN CLAYS, ERIC HENDRICKX and ANDRÉ PERSOONS: Nonlinear Optical Properties of Bacteriorhodopsin and Retinal Chromophores as Studied by Hyper-Rayleigh Scattering	231

M. STÄEHELIN and I. ZSCHOKKE-GRÄNACHER: Hyper-Rayleigh Scattering: A Versatile Tool for the Characterization of Molecular Hyperpolarizabilities	241
---	-----

SIEGFRIED BAUER, WEI REN, ŞÜKRÜ YILMAZ, WERNER WIRGES and REIMUND GERHARD-MULTHAUPT: Relaxation Processes in Poled Nonlinear Optical Polymers	251
---	-----

III. 3. Thermostable Polymers for Electro-Optic Modulation

SUSAN ERMER, DEXTER G. GIRTON, DORIS S. LEUNG, STEVEN M. LOVEJOY, JOHN F. VALLEY, TIM E. VAN ECK and LAP-TAK CHENG: An Electro-Optic Modulator Fabricated Using a Polyimide Doped with Thermally Stable Chromophores	259
--	-----

TATSUO WADA, YADONG ZHANG, LIMING WANG and HIROYUKI SASABE: Carbazole Oligomers for Nonlinear Optics	267
--	-----

GILLES TAPOLSKY, JEAN-PIERRE LECOMTE and RÉMI MEYRUEIX: Orientational Stability and Electro Optical Properties of Maleimide Based Crosslinkable Polymers at Elevated Temperature	275
--	-----

P. PRÊTRE, P. KAATZ, U. MEIER, P. GÜNTER, B. ZYSSET, M. STÄEHELIN, M. AHLHEIM and F. LEHR: Polyimide Side Chain Polymers for Nonlinear Optical Applications	283
---	-----

RÉMI MEYRUEIX, GILLES TAPOLSKY, Y. P. CHAN and JEAN PIERRE LECOMTE: Orientation of Chromophores with NLO Functionalized Polymers: a Comparison between Theory and Experiment	293
--	-----

III. 4. New Orientation Techniques

DIDIER RIEHL, FRÉDÉRIC CHAPUT, ARMEN ROUSTAMIAN, YVES LÉVY and JEAN-PIERRE BOILOT: Preparation and Photoinduced Optical Properties of Aromatic AZO Silica Gels	305
--	-----

J. A. DELAIRE, Y. ATASSI, R. LOUCIF. SAIB and K. NAKATANI: Photoinduced Electric Field Poling of NLO Chromophores in Polymer Films	317
--	-----

M. DUMONT, G. FROC and S. HOSOTTE: Alignement and Orientation of Chromophores by Optical Pumping	327
--	-----

CÉLINE FIORINI, FABRICE CHARRA, JEAN-MICHEL NUNZI and PAUL RAIMOND: Photoinduced Non Centrosymmetry in Azo-Dye Polymers	339
---	-----

Enhanced Third Order Nonlinear Optical Responses from Populated Electronic Excited States

J. R. HEFLIN¹, D. C. RODENBERGER², W. D. CHEN², R. F. SHI²,
Q. L. ZHOU² and A. F. GARITO²

¹*Department of Physics, Virginia Tech, Blacksburg, VA 24061-0435, USA*

²*Department of Physics, University of Pennsylvania, Philadelphia, PA 19104, USA*

Received 17 March 1994; accepted 21 March 1994

Third harmonic generation experiments in silicon naphthalocyanine and degenerate four-wave mixing (DFWM) measurements in diphenylhexatriene have demonstrated that $\chi^{(3)}(-\omega_4; \omega_1, \omega_2, \omega_3)$ of conjugated organic materials can be increased by several orders of magnitude when the molecules are optically pumped into a π -electron excited state. In the case of the DFWM experiment, the enhanced nonlinearity is fully nonresonant since there was no excited state absorption. A dynamical model of the temporal behavior of the DFWM signal has been developed in terms of the directly populated one-photon excited state and the energetically lower-lying two-photon state that is populated through internal conversion.

INTRODUCTION

Conjugated organic molecules and polymers are an important class of nonlinear optical materials because of their delocalized π -electron systems which give rise to large values of $\chi^{(2)}(-\omega_3; \omega_1, \omega_2)$ and $\chi^{(3)}(-\omega_4; \omega_1, \omega_2, \omega_3)$, with extremely fast response times, in wavelength regimes where there is minimal background absorption.^{1–5} We have previously presented theoretical results demonstrating that $\chi^{(3)}(-\omega_4; \omega_1, \omega_2, \omega_3)$ can be further increased for nonlinear optical processes originating from real population of electronic excited states in conjugated linear chains.⁶ Compared with the ground state, the calculated nonresonant molecular third order optical susceptibility $\gamma(-\omega_4; \omega_1, \omega_2, \omega_3)$ of π -conjugated linear chain molecules can be enhanced by orders of magnitude, and even change sign, when the first S_1 or second S_2 electronic excited state is optically pumped and then populated for times long enough to perform nonresonant measurements of $\gamma(-\omega_4; \omega_1, \omega_2, \omega_3)$ at frequencies different from the resonant pump frequency. The principal reasons for this enhancement are the larger optical transition moments $\mu_{nn'}$ and smaller excitation energies $\omega_{nn'}$ between excited states S_n and $S_{n'}$, especially for highly charge correlated virtual excitations, and a reduced degree of competition between virtual excitation processes that contribute with opposite signs to determine the magnitude, sign, and dispersion of $\gamma_{ijkl}(-\omega_4; \omega_1, \omega_2, \omega_3)$.⁷ The electron correlation microscopic origin of the ground state $\gamma_{ijkl}(-\omega_4; \omega_1, \omega_2, \omega_3)$ has been experimentally confirmed through a series of dc-induced second harmonic generation (DCSHG) and third harmonic generation (THG)

dispersion measurements of key conjugated linear chain structures.⁸ This paper presents experimental confirmation of the theoretically predicted enhancement of excited state nonlinear optical responses. The enhancement has been observed in two separate experiments: third harmonic generation from a macrocyclic conjugated disc and degenerate four-wave mixing (DFWM) from a linear polyene.

EXCITED STATE THIRD HARMONIC GENERATION MEASUREMENTS IN SILICON NAPHTHALOCYANINE

For the third harmonic generation (THG) experiments,⁹ the nonlinear optical medium, silicon naphthalocyanine (SiNc), exhibits characteristic large oscillator strength $Q(\lambda = 778 \text{ nm } (1.59 \text{ eV}))$ and B(Soret) ($\lambda = 335 \text{ nm } (3.70 \text{ eV})$) absorption bands due to widely separated $S_0(1^1A_{1g}) \rightarrow S_1(1^1E_u)$ and $S_0(1^1A_{1g}) \rightarrow S_2(2^1E_u)$ π -electron transitions, respectively. Importantly, we have previously demonstrated that SiNc exhibits absorption saturation of the $S_0 \rightarrow S_1$ transition with a decay time of several nanoseconds (ns).¹⁰ Separate THG measurements¹¹ over the near infrared region (1907–1064 nm) of the frequency dependent, isotropically averaged, S_0 ground state $\langle \gamma^{S_0}(-3\omega; \omega, \omega, \omega) \rangle$ of SiNc solutions show for 10 ns pulses of fundamental wavelength $\lambda = 1543 \text{ nm}$, well below the $S_0 \rightarrow S_1$ Q band, that $\langle \gamma^{S_0}(-3\omega; \omega, \omega, \omega) \rangle$ is relatively small, being less than the experimental uncertainty of $\pm 10 \times 10^{-36} \text{ esu}$. The created third harmonic at 514 nm lies in the transparency window between the $S_0 \rightarrow S_1$ and $S_0 \rightarrow S_2$ absorption bands.

The excited state THG measurements were performed on dilute solutions of SiNc dissolved in transparent dioxane ($C = 1 - 5 \times 10^{-4} \text{ mole liter}^{-1}$) using the Maker fringe method in a flow cell wedged configuration. The laser source was a 10 Hz, 30 ps pulse-width, modelocked Nd:YAG laser with 40 mJ/pulse output at a wavelength of 1064 nm. The nonresonant probe beam at 1543 nm and the pump beam at 770 nm (in the $S_0 \rightarrow S_1$ Q absorption band) were created, respectively, by focusing the 1064 nm laser output and its 532 nm second harmonic, generated in a KD*P doubling crystal, into two separate methane Raman cells. The 770 nm pump beam passes through a right-angle prism employed as a retroreflector and mounted on a one meter long translation stage that enables temporal delay of the two beams. The 1543 nm probe beam is beamsplit with one arm focused on a glass plate that serves as a reference to divide out power fluctuations and with the other focused on the sample cell. TH light at 514 nm is detected by PMTs in each arm after frequency selection by spike and bandpass filters.

The sample cell consists of two 5 cm long BK-7 glass windows mounted to form a wedge compartment with angle $\alpha = 0.0123 \text{ rad}$ and mean thickness 0.44 mm and is located on a computer-controlled, stepper motor driven translation stage where the translational axis is perpendicular to the direction of beam propagation.^{8,12} The 770 nm pump beam intersects the 1543 nm probe beam in the center of the cell at an angle of 7° , and the overlapping and focal point coincidence of the two beams are carefully adjusted.

The TH fringes were analyzed to obtain $\chi_S^{(3)}(-3\omega; \omega, \omega, \omega)$ of the sample according to the expression

$$\chi_S^{(3)} = \frac{n_{3\omega}^S + n_\omega^S}{l_c^S T_S (t_S^{(2)})^3} \left[T_{GL} \frac{l_c^G \chi_G^{(3)}}{n_{3\omega}^G + n_\omega^G} + \left(\frac{\bar{A}^S}{\bar{A}^R} \right)^{1/2} \left| T_{GR} \frac{l_c^G \chi_G^{(3)}}{n_{3\omega}^G + n_\omega^G} - T_R \frac{l_c^R \chi_R^{(3)}}{n_{3\omega}^R + n_\omega^R} (t_R^{(2)})^3 \right| \right] \quad (1)$$

where \bar{A}^S and \bar{A}^R are the mean fringe amplitudes of the sample and reference liquids, respectively, l_c is the coherence length, T_{AB} and t_A are transmission factors for the glass/liquid interfaces, and the subscript G refers to the BK-7 glass windows.⁸ For the reference liquid, pure dioxane, we obtain $\chi^{(3)}(-3\omega; \omega, \omega, \omega) = 0.702 \times 10^{-14}$ esu and $l_c = 19.6 \mu\text{m}$, and for the glass windows we use the values $\chi^{(3)}(-3\omega; \omega, \omega, \omega) = 0.600 \times 10^{-14}$ esu and $l_c = 13.03 \mu\text{m}$.⁸ The coherence length l_c remained constant and the TH intensity was cubic in fundamental intensity for all measured concentrations of SiNc both with and without the pump beam.

Although SiNc molecules occupying the ground state have negligible absorption at 1543 and 514 nm, we have directly measured weak excited state absorption (ESA) at both the fundamental and harmonic wavelengths. A modified configuration of the excited state THG measurements was used to characterize the ESA of SiNc. The linear fits of values of the excited state absorption coefficient α_{S_1} obtained as a function of SiNc concentration result in experimental values for the molecular ESA cross section $\sigma_{S_1} = \alpha_{S_1}/N_{S_1}$ of 3.2 ± 0.3 and $4.7 \pm 0.5 \times 10^{-17} \text{ cm}^2$ at 1543 and 532 nm, respectively. These values are in good agreement with independent measurements of the intensity dependent absorption of a single 532 nm beam through solutions of SiNc in toluene that obtained $\sigma_{S_1} = 3.9 \times 10^{-17} \text{ cm}^2$.¹² The effects of absorption on the Maker fringes are accounted for fully by using in Eq. (1) the corrected mean fringe amplitude \bar{A}_{corr}^S given by

$$\bar{A}_{\text{corr}}^S = \frac{2\bar{A}_{\text{meas}}^S}{e^{-3\alpha_{\omega}l} + e^{-\alpha_{3\omega}l}} \quad (2)$$

where \bar{A}_{meas}^S is the directly measured mean fringe amplitude and α_ω ($\alpha_{3\omega}$) is the linear absorption coefficient of the sample at the fundamental (third harmonic) wavelength.

In solution, the macroscopic susceptibility $\chi^{(3)}(-3\omega; \omega, \omega, \omega)$ derives from the weighted sum of the isotropically averaged molecular susceptibilities $\langle \gamma(-3\omega; \omega, \omega, \omega) \rangle$ of each component. For SiNc in dioxane where both the S_0 and S_1 states of SiNc may have real populations, $\chi^{(3)}(-3\omega; \omega, \omega, \omega)$ is given by

$$\chi^{(3)}(-3\omega; \omega, \omega, \omega) = (f^\omega)^3 f^{3\omega} [N_D \langle \gamma^D(-3\omega; \omega, \omega, \omega) \rangle + N_{S_0} \langle \gamma^{S_0}(-3\omega; \omega, \omega, \omega) \rangle + [N_{S_1} \langle \gamma^{S_1}(-3\omega; \omega, \omega, \omega) \rangle]] \quad (3)$$

where N_D , N_{S_0} , and N_{S_1} are the number densities of dioxane molecules and SiNc molecules occupying the S_0 and S_1 states, respectively, and we have assumed the local field factors f^ω are the same for each component. Figure 1 shows typical examples of TH fringes obtained both with and without the 770 nm pump beam resonantly exciting the $S_0 \rightarrow S_1$ transition at a fixed probe delay of 20 ps. At relatively low concentrations, optical pumping of S_1 leads to greater than 60% reduction in the TH fringe amplitude. In agreement with our previous nanosecond THG measurements of

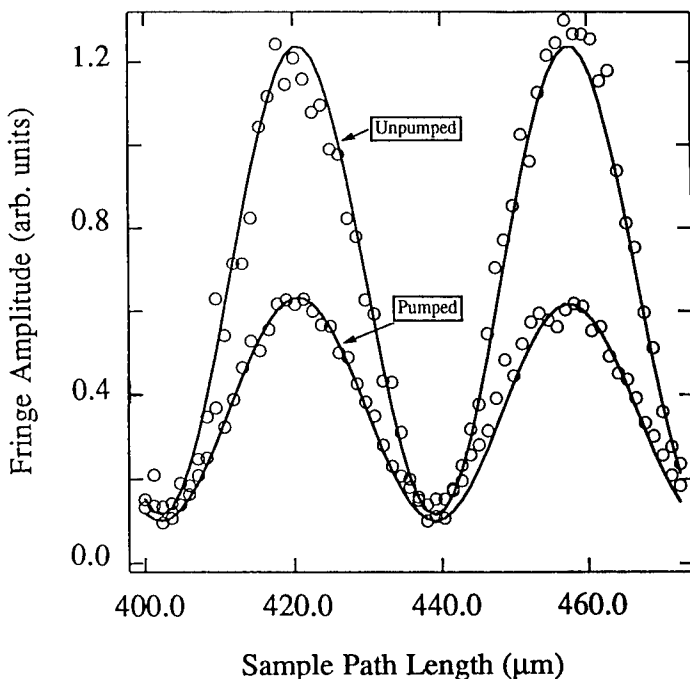


FIGURE 1 Third harmonic Maker fringes of SiNc in dioxane at 514 nm both with and without the 770 nm pump beam resonantly populating the S_1 state. The large decrease in fringe amplitude in the pumped configuration results from a very large, negative $\gamma^{S_1}(-3\omega; \omega, \omega, \omega)$.

$\langle \gamma^{S_0}(-3\omega; \omega, \omega, \omega) \rangle$,¹¹ the unpumped Maker fringes and $\chi^{(3)}(-3\omega; \omega, \omega, \omega)$ values are found to be independent of concentration, demonstrating that $\gamma^{S_0}(-3\omega; \omega, \omega, \omega)$ is so small that the term $N_{S_0} \langle \gamma^{S_0}(-3\omega; \omega, \omega, \omega) \rangle$ of Eq. (3) is negligible. Since $N_{S_1} = 0$ in the unpumped configuration, the unpumped TH fringe shown in Figure 1 originates purely from the dioxane term $N_D \langle \gamma^D(-3\omega; \omega, \omega, \omega) \rangle$.

The large decrease in TH fringe amplitude in Figure 1 when the S_1 state is optically pumped is due to a very large $\langle \gamma^{S_1}(-3\omega; \omega, \omega, \omega) \rangle$ that is of opposite sign to $\langle \gamma^D(-3\omega; \omega, \omega, \omega) \rangle$ leading to a reduction of $\chi^{(3)}(-3\omega; \omega, \omega, \omega)$ for the solution as a whole. Accordingly, in sharp contrast to the unpumped case, the pumped $\chi^{(3)}(-3\omega; \omega, \omega, \omega)$ values shown in Figure 2 are observed to decrease dramatically with concentration when SiNc is resonantly pumped at 770 nm and the S_1 state is populated. The linear fit in Figure 2 yields $\chi_{S_1}^{(3)}(-3\omega; \omega, \omega, \omega)/C = -1.55 \pm 0.09 \times 10^{-12}$ esu liter mole⁻¹ where $\chi_{S_1}^{(3)}(-3\omega; \omega, \omega, \omega) = \chi_{\text{pump}}^{(3)}(-3\omega; \omega, \omega, \omega) - \chi_{\text{no pump}}^{(3)}(-3\omega; \omega, \omega, \omega)$ is the contribution of the excited state to the overall $\chi^{(3)}(-3\omega; \omega, \omega, \omega)$ and C is the molar concentration. From the relation,

$$\chi_{S_1}^{(3)}(-3\omega; \omega, \omega, \omega) = \frac{N_0}{2} (f^\omega)^3 f^{3\omega} \langle \gamma^{S_1}(-3\omega; \omega, \omega, \omega) \rangle \quad (4)$$

where N_0 is the number density of SiNc molecules, $N_0/2$ is the excited state population of a two-level system for $I \gg I_s$, and $f^\omega = (n_\omega^2 + 2)/3$ is the Lorentz-Lorenz local field

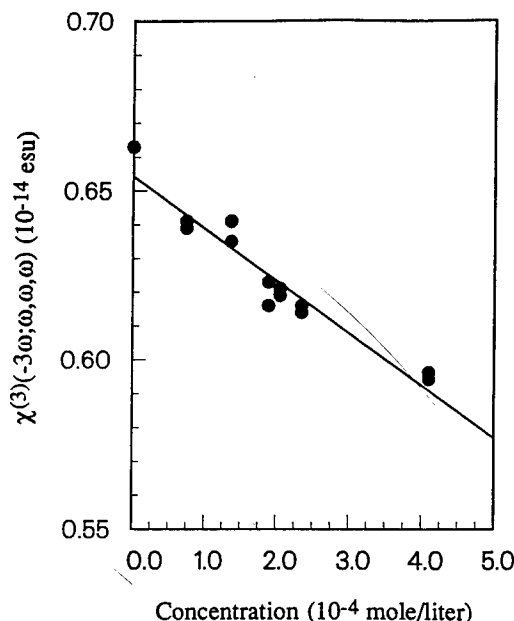


FIGURE 2 Concentration dependence of $\chi^{(3)}(-3\omega; \omega, \omega, \omega)$ for solutions of SiNc in dioxane in the pumped configuration. The linear fit yields $\langle \gamma^{S_1}(-3\omega; \omega, \omega, \omega) \rangle = -1640 \pm 100 \times 10^{-36}$ esu.

factor, we obtain $\langle \gamma^{S_1}(-3\omega; \omega, \omega, \omega) \rangle = -1640 \pm 100 \times 10^{-36}$ esu. Thus, the real population of the S_1 state by optical pumping increases $\langle \gamma(-3\omega; \omega, \omega, \omega) \rangle$ of SiNc by greater than two orders of magnitude. For comparison, the measured value of $\langle \gamma(-3\omega; \omega, \omega, \omega) \rangle$ for hexatriene, an $N = 6$ carbon site linear chain, is 1.2×10^{-36} esu at $\lambda = 1543$ nm while the values for β -carotene, an $N = 22$ site chain possessing a very large third order susceptibility, are 52×10^{-36} esu at the nonresonant wavelength $\lambda = 2148$ nm and 358×10^{-36} esu at the near-resonant wavelength $\lambda = 1543$ nm.⁸

EXCITED STATE DEGENERATE FOUR-WAVE MIXING IN DIPHENYLHEXATRIENE

Since the increased nonlinear optical susceptibility in the excited state THG measurements of SiNc was accompanied by an increased absorption, we studied excited state degenerate four-wave mixing (DFWM) in diphenylhexatriene (DPH) at $\lambda = 1064$ nm where there is no induced absorption upon excitation. DPH exhibits saturable absorption from the $S_0(1^1A_g)$ ground state to the $S_2(1^1B_u)$ excited state centered near 350 nm with an excited state lifetime of several nanoseconds [13, 14] and is transparent at wavelengths from 400 nm to greater than 2000 nm. Excitation to the S_2 state is known to additionally lead to population of the $S_1(2^1A_g)$ state, which lies at a slightly lower energy.¹³ For the moment, however, we will refer to the excited state population distribution simply as the S_2 state and will discuss the excited state dynamics in the

succeeding section. Fresh samples of DPH were dissolved in solutions of anhydrous dioxane in concentrations of $1\text{--}10 \times 10^{-3}$ molar and kept isolated from atmospheric contamination.

The DFWM experiment (Fig. 3) is carried out using two orthogonally polarized, 1064 nm probe beams and a 355 nm pump beam produced by a 30 ps pulsewidth, modelocked Nd:YAG laser.¹⁵ The three pulsed beams, for which the relative time delays can be variably adjusted, are focused in coincidence on a thin quartz cell flowed with the sample solutions. Coherent interference of the two probes in the sample produces a refractive index grating, and the diffracted intensity of each probe from this grating, proportional to the square of the third order optical susceptibility $\chi^{(3)}(-\omega; \omega, \omega, -\omega)$, is detected. In this DFWM arrangement, there are therefore only two incident beams, rather than three. The unique feature of our experimental configuration is that by introducing an intense optical pump beam tuned to the first electronic absorption band of the material, a large fraction of the molecules in the sample are made to occupy the first optical excited state.

An increase as large as a factor of 100 in the completely nonresonant 1064 nm DFWM signal from the highest DPH concentrations is observed when the 355 nm pump beam saturates the S_2 absorption as compared to when the pump beam is turned off. When no pump beam is present, the ground state molecular susceptibility $\gamma^{S_0}(-\omega; \omega, \omega, -\omega)$ of DPH and the dioxane solvent susceptibility $\gamma^D(-\omega; \omega, \omega, -\omega)$ contribute to the net observed macroscopic susceptibility,

$$\chi^{(3)}(-\omega; \omega, \omega, -\omega) = (f^\omega)^4 [N_D \gamma^D(-\omega; \omega, \omega, -\omega) + N_{S_0} \gamma^{S_0}(-\omega; \omega, \omega, -\omega)], \quad (5)$$

where N_{S_0} and N_D are the number densities of the ground state DPH and dioxane molecules respectively, and f^ω is the local field factor. When the pump beam is present, however, the corresponding macroscopic susceptibility is given by

$$\begin{aligned} \chi^{(3)}(-\omega; \omega, \omega, -\omega) = (f^\omega)^4 [N_D \gamma^D(-\omega; \omega, \omega, -\omega) + N_{S_0} \gamma^{S_0}(-\omega; \omega, \omega, -\omega) \\ + N_{S_2} \gamma^{S_2}(-\omega; \omega, \omega, -\omega)], \end{aligned} \quad (6)$$

where N_{S_2} and γ^{S_2} are the corresponding number density and molecular susceptibility for the S_2 state. The unpumped DFWM signal is observed to be independent of

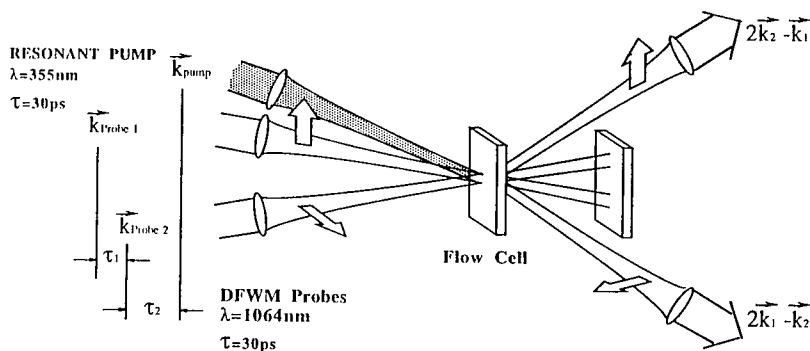


FIGURE 3 The forward scattering excited state DFWM experiment. The k_1 probe is vertically polarized, the k_2 probe is horizontally polarized, and the DFWM signal in the $2k_2 - k_1$ direction is detected.

concentration, demonstrating that the ground state $\gamma^{S_0}(-\omega; \omega, \omega, -\omega)$ for DPH is smaller than the experimental resolution of $\pm 50 \times 10^{-36}$ esu. The pumped DFWM signal, however, increases strongly with increased DPH concentration showing that the excited state $\gamma^{S_2}(-\omega; \omega, \omega, -\omega)$ is more than two orders of magnitude larger than $\gamma^{S_0}(-\omega; \omega, \omega, -\omega)$. The measured values of $\chi^{(3)}(-\omega; \omega, \omega, -\omega)$ are linearly dependent on the concentration of the solution, as expected, and yield a value for $\gamma^{S_2}(-\omega; \omega, \omega, -\omega)$ of $12,000 \pm 1700 \times 10^{-36}$ esu. Upon population of the excited state the $\gamma(-\omega; \omega, \omega, -\omega)$ of DPH at a nonresonant wavelength is greatly enhanced without introducing any optical loss.

In all measurements, the DFWM signal is non-zero only when the probe pulses temporally overlap in the sample (Fig. 4). As the relative delay between the two probe pulses is adjusted, the DFWM intensity follows the expected autocorrelation of the two 30 ps pulses. Additionally, the enhancement of the DFWM signal demonstrates a pump beam intensity dependence (Fig. 5) that is in excellent agreement with intensity saturation of the excited state population as found in separate saturable absorption measurements at 355 nm. Furthermore, we emphasize that we have performed separate transient absorption experiments at 1064 nm with excitation at 355 nm and found the excited state absorption to be negligible.

We have observed that the DFWM signal is independent of the polarization of the pump beam, indicating that there is no coherent coupling between the pump and probes. Thus, the sole purpose of the pump beam is to create the S_2 excited state population. The orthogonal probe polarizations assure that the experimental DFWM

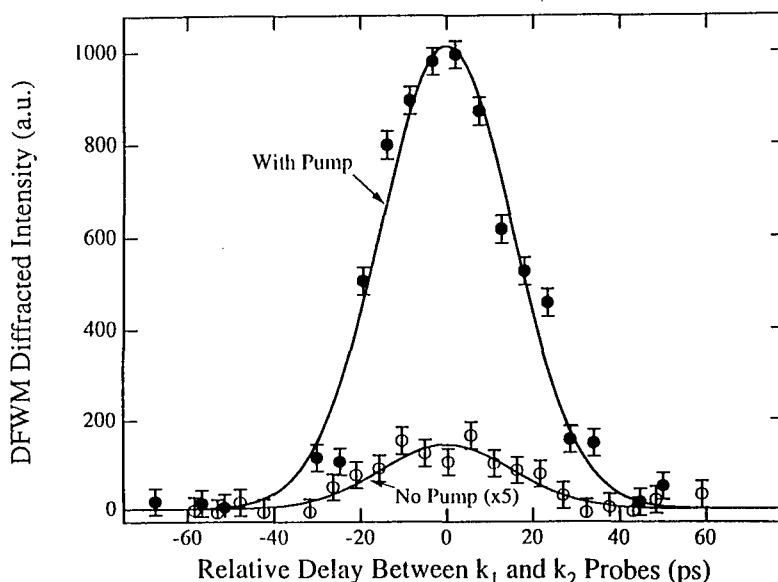


FIGURE 4 Typical DFWM signal of DPH in dioxane with pump on and pump off, as a function of the delay between the two 1064 nm probe beams. The pump delay is set so that the 355 nm pulse arrives 100 ps before the probe pulses in this data. The unpumped data has been multiplied by a factor of 5 for clarity.

signal is due entirely to the electronic third order susceptibility of the excited state, and not due to a thermal grating. Finally, the DFWM signal is in all cases observed to have the expected cubic dependence on the probe intensities. It is important to note that this experiment is distinct from the common resonant DFWM measurements where the wavelength of the DFWM probe beams is absorbed by the sample and results in excited state population gratings. In the present experiment, although the pump beam is resonant, the DFWM probe beams undergo no absorption loss.

DYNAMICS OF EXCITED STATE DFWM IN DPH

It has been well established that for conjugated linear polyenes such as DPH, the lowest two excited states are the S_2 (1^1B_u) and S_1 (2^1A_g) state, with S_1 generally lying below by a few tenths of an eV. Since a direct one-photon transition from the ground state S_0 (1^1A_g) to the S_1 state is forbidden, optical pumping initially populates only the S_2 state. Transitions then occur between the two excited states through internal conversion which leads to thermal equilibrium in the population of S_1 and S_2 .¹⁶ Equation (6) is then more accurately written as

$$\chi^{(3)}(-\omega; \omega, \omega, -\omega) = (f^\omega)^4 [N_D \gamma^D(-\omega; \omega, \omega, -\omega) + N_{S_0} \gamma^{S_0}(-\omega; \omega, \omega, -\omega) + N_{S_1} \gamma^{S_1}(-\omega; \omega, \omega, -\omega) + N_{S_2} \gamma^{S_2}(-\omega; \omega, \omega, -\omega)], \quad (7)$$

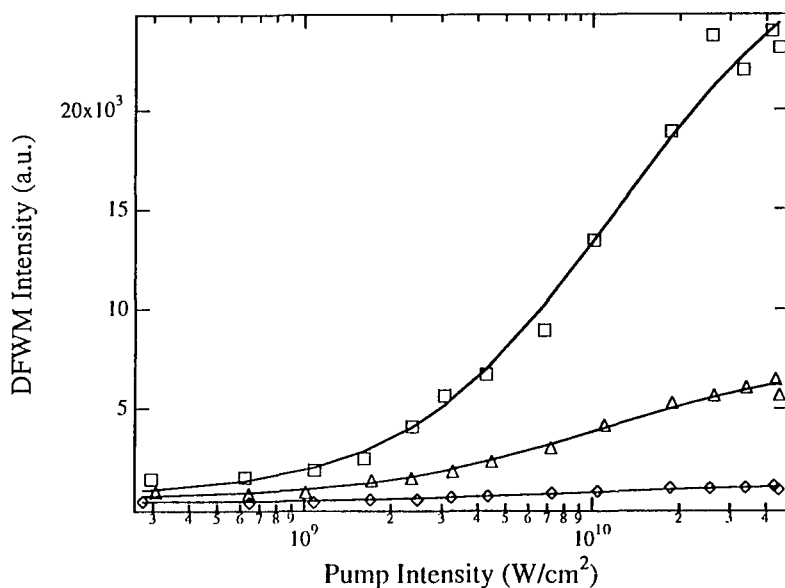


FIGURE 5 The excited state DFWM intensity as a function of 355 nm pump intensity for 1.6 (diamonds), 3.3 (triangles), and 6.5 (squares) mmolar concentrations of DPH in dioxane.

where N_{S_2} , N_{S_1} , and γ^{S_2} , γ^{S_1} are the corresponding number density and molecular susceptibility for the S_2 , and S_1 states and N_{S_2} and N_{S_1} have time dependences determined by the excited state dynamics.

Optical pumping initially populates only the S_2 state, transitions then occur between the S_1 and S_2 excited states through internal conversion which leads to thermal equilibrium in the population of each state. The contribution to $\chi^{(3)}(-\omega; \omega, \omega, -\omega)$ from the two excited states is strongly dependent on the energy gap between these two states. When the gap is considerably larger than the thermal energy, upon reaching thermal equilibrium after excitation, the population of S_2 is negligible compared to that of S_1 . The excited state contribution to $\chi^{(3)}(-\omega; \omega, \omega, -\omega)$ is therefore mostly due to S_1 . When the gap is small, thermal equilibrium maintains a finite S_2 population, and both states contribute. The behavior of the relaxation after the initial excitation depends on the relative magnitudes of $\gamma^{S_1}(-\omega; \omega, \omega, -\omega)$ and $\gamma^{S_2}(-\omega; \omega, \omega, -\omega)$, as shown in Figure 6.

The energy gap of DPH in dioxane is approximately 215 cm^{-1} , which is comparable to the thermal energy. Therefore both excited states contribute to the observed temporal DFWM intensity. With the relative DFWM probe delay equal to zero, the pump-probe delay was varied in the excited state DFWM experiment. As shown in Figure 7, the signal exhibits a fast rise time characteristic of the 30 ps pump and probe

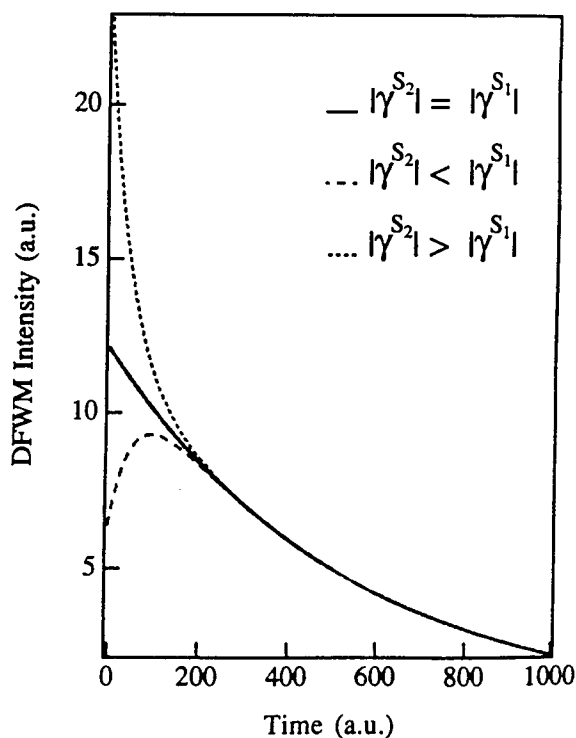


FIGURE 6 Temporal evolution of the DFWM intensity for various relative magnitudes of γ^{S_1} and γ^{S_2} . The energy gap between the excited states is taken as equal to the thermal energy here.

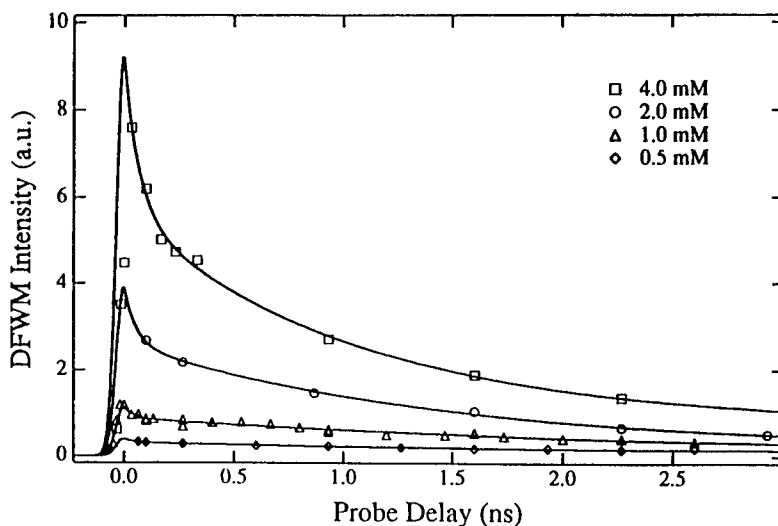


FIGURE 7 The pumped DFWM experimental intensities as a function of the delay time between the pump and the two probe pulses for several concentrations. The solid curves are fits using the excited state dynamical model. The slow decay component has a decay time of 8 ± 2 ns in agreement with separate decay measurements.

pulse widths, and two exponential decays. The first is a fast picosecond timescale decay τ_2 , corresponding to the relaxation from S_2 to S_1 , after initial excitation from S_0 to S_2 . The second is a slower nanosecond decay τ_1 , as the populations of S_1 and S_2 , in thermal equilibrium, recover to the ground state. The ground state contribution to $\chi^{(3)}(-\omega; \omega, \omega, -\omega)$ is negligible, and the signal with no pump excitation is due to the solvent $\gamma^D(-\omega; \omega, \omega, -\omega)$. The experimental data are seen to correspond to the condition $\gamma^{S_2} > \gamma^{S_1}$ of Figure 6. The excited state lifetime τ_1 of DPH in dilute solutions of dioxane measured by our excited state pump-probe DFWM experiment is 8 ± 2 ns as shown in Figure 7, in agreement with the lifetime determined by fluorescence decay studies of 7.8 ns.¹⁴

CONCLUSION

We have experimentally confirmed that the nonlinear optical responses of conjugated materials can be increased by orders of magnitude by real population of excited electronic states. The excited state enhancement mechanism for nonlinear optical responses demonstrated in this paper is generalizable to second order and other third order nonlinear optical processes and to other material structures, compositions, and phases. The experimental observations reported here as a demonstration of principle were carried out on molecules with small ground state $\gamma^{S_0}(-\omega_4; \omega_1, \omega_2, \omega_3)$. Furthermore, the measurements were made in solutions such that the relatively small number density of excited state molecules with large optical nonlinearity results in a much smaller $\chi^{(3)}(-\omega_4; \omega_1, \omega_2, \omega_3)$ than would be observed in a pure, single substance.

Studies are currently underway on pure polymer thin films where typical nonresonant ground state values of $\chi^{(3)}(-\omega_4; \omega_1, \omega_2, \omega_3)$ on the order of 10^{-11} to 10^{-10} esu are expected to be enhanced by several orders of magnitude, potentially leading to figures of merit sufficient for practical photonics devices.

ACKNOWLEDGEMENTS

This research was generously supported by the U.S. Air Force Office of Scientific Research, Advanced Research Projects Agency, and Pittsburgh Supercomputing Center.

REFERENCES

1. D. J. Williams, ed., *Nonlinear Optical Properties of Organic and Polymeric Materials* (American Chemical Society, Washington D.C., 1983).
2. J. Messier *et al.*, eds., *Nonlinear Optical Effects in Organic Polymers* (Kluwer Academic, Boston, 1989).
3. R. A. Hann and D. Bloor, eds., *Organic Materials for Nonlinear Optics* (Royal Society of Chemistry, 1989).
4. C. M. Bowden and J. W. Haus, eds., *Nonlinear Optical Properties of Materials*, *J. Opt. Soc. Am. B*, **6**, 562–853 (1989).
5. L. Y. Chiang, A. F. Garito and D. J. Sandman, eds., *Electrical, Optical and Magnetic Properties of Organic Solid State Materials* (Materials Research Society, Vol. 247, Pittsburgh, 1992).
6. Q. L. Zhou, J. R. Heflin, K. Y. Wong, O. Zamani-Khamiri and A. F. Garito, *Phys. Rev. A*, **43**, 1673–1676 (1991).
7. J. R. Heflin, K. Y. Wong, O. Zamani-Khamiri and A. F. Garito, *Phys. Rev. B*, **38**, 1573 (1988).
8. J. R. Heflin, Y. M. Cai and A. F. Garito, *J. Opt. Soc. Am. B*, **8**, 2132–2147 (1991).
9. J. R. Heflin, *et al.*, *Phys. Rev. A*, **45**, R4233 (1992).
10. J. W. Wu, J. R. Heflin, R. A. Norwood, K. Y. Wong, O. Zamani-Khamiri, A. F. Garito, P. Kalyanaraman and J. Sounik, *J. Opt. Soc. Am. B*, **6**, 707 (1989).
11. N. Q. Wang, Y. M. Cai, J. R. Heflin and A. F. Garito, *Mol. Cryst. Liq. Cryst.*, **189**, 39 (1990). The values for $\langle \gamma(-3\omega; \omega, \omega, \omega) \rangle$ reported in this paper use a reference standard value that is 8.0 times larger than the one employed in the present work. See reference 8 for details.
12. F. Kajzar and J. Messier, *Phys. Rev. A*, **32**, 2352 (1985); *Rev. Sci. Instrum.*, **58**, 2081 (1987); and references therein.
13. B. E. Kohler and T. A. Spiglanin, *J. Chem. Phys.*, **82**, 2939–2941 (1985).
14. E. D. Cehelnik, R. B. Cundall, J. R. Lockwood and T. F. Palmer, *J. Phys. Chem.*, **79**, 1369–1376 (1975).
15. D. C. Rodenberger, J. R. Heflin and A. F. Garito, *Nature*, **359**, 309 (1992).
16. C. Rulliere and A. Declemy, *Chem. Phys. Lett.*, **135**, 213–218 (1987).

Relations Between Structure and Third-Order Nonlinear Optical Properties of Conjugated Polymers

CHRISTOPH BUBECK

*Max-Planck-Institute for Polymer Research, Postfach 3148,
D-55021 Mainz, Germany*

Received 23 March 1994; accepted 25 March 1994

Studies of thin films of conjugated polymers and oligomers by third-harmonic generation with variable laser wavelengths are described. Resonance enhancements of the nonlinear optical susceptibilities $\chi^{(3)}$ are discussed and related to excitation states of conjugated polymers. A characteristic scaling behaviour of one-dimensional conjugated systems is found in masterplots, which relate third-order nonlinearities to linear optical properties of polymers and oligomers. Conjugated systems with one-dimensional π -electron delocalization are found to be superior to two-dimensional systems for large off-resonant third-order nonlinearities.

INTRODUCTION

Conjugated polymers have found much interest recently, because of perspectives to use their third-order nonlinearities in photonics.^{1–6} Many conjugated polymers have been studied by means of third-harmonic generation (THG) and described in reviews.^{7–9} A basic question is, which structural factors primarily determine the magnitude of the nonlinear optical susceptibility $\chi^{(3)}$. The strong influence of the π -electron delocalization length L_d was recognized early.^{10,11} However additional possible influences on $\chi^{(3)}$ exist, such as the dimensionality of the π -electron delocalization, or the question if compounds with heteroatoms like nitrogen or sulfur could lead to an increase of $\chi^{(3)}$.¹²

These questions will be studied here by means of a comparison of the different conjugated systems shown in Figure 1, which have been investigated by THG. This is a frequently used technique to measure the nonlinear optical susceptibility $\chi^{(3)}(-3\omega; \omega, \omega, \omega)$ of molecules or polymers. If performed properly, this technique is rather accurate and sensitive even to small $\chi^{(3)}$ values. Only electronic effects have influence on THG. Therefore thermal or stray light effects, which can be troublesome in measurements based on the intensity dependent refractive index, do not contribute to $\chi^{(3)}(-3\omega; \omega, \omega, \omega)$. Furthermore THG can be used as a spectroscopic technique, if the fundamental laser frequency ω is varied. This allows to detect multi-photon resonances with electronic states, which are not visible in the linear absorption spectrum. The aim of this paper is to summarize recent work and to show correlations between chemical structures, linear and nonlinear optical properties of conjugated π -electron systems.

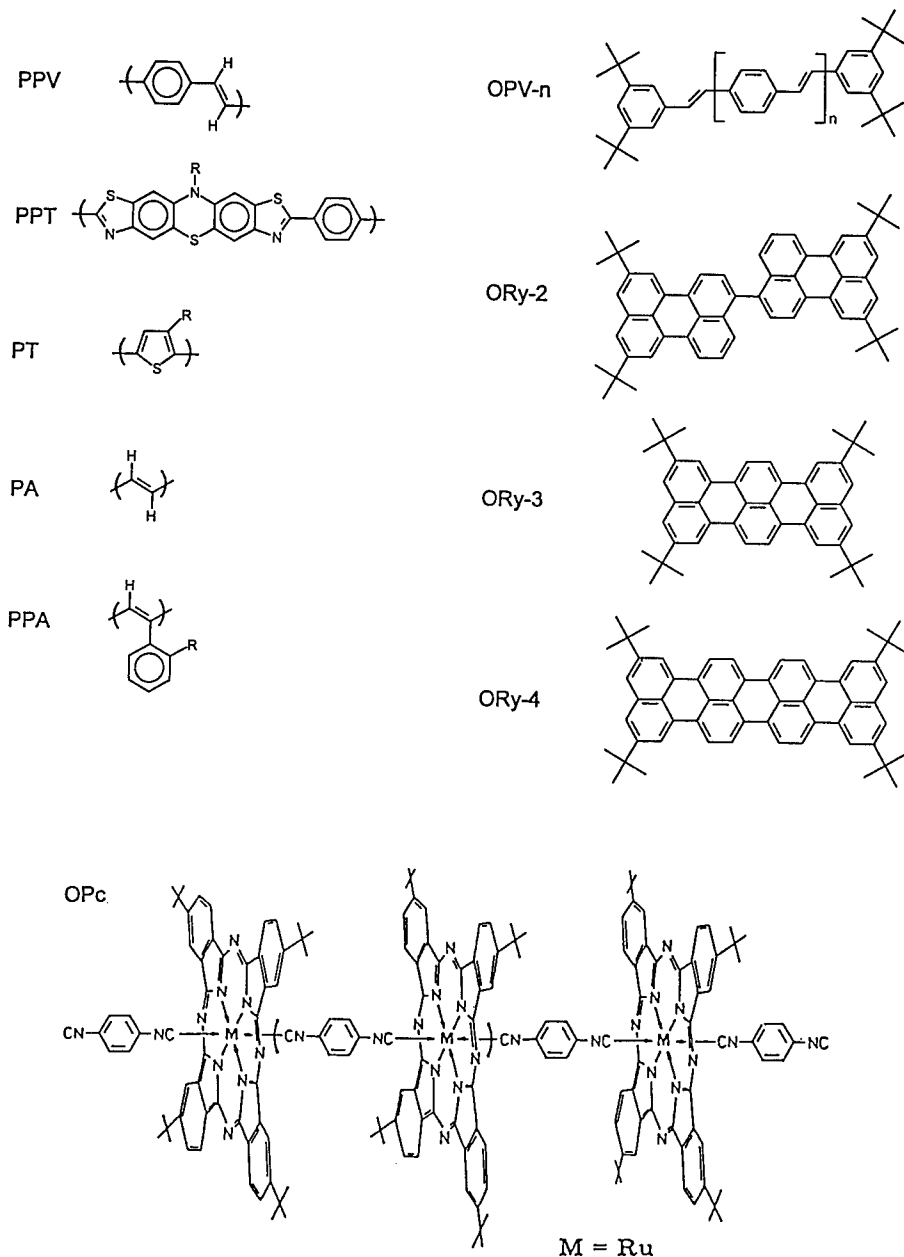


FIGURE 1 Chemical structures and abbreviations of some conjugated polymers and oligomers, which have been investigated by third harmonic generation: poly-p-phenylenevinylene (PPV),¹³⁻¹⁹ poly-phenothiazinobisthiazole (PPT),²⁰ polythiophene (PT),^{21,22} polyacetylene (PA),^{23,24} polyphenylacetylene (PPA),^{25,26} oligo-p-phenylenevinylene (OPV-n),¹⁹ oligorylene (ORy-n)^{27,28} and an oligomeric bridged phthalocyaninato ruthenium complex (OPc).²⁹

EXPERIMENTAL

The synthesis and the preparation of thin films of the compounds shown in Figure 1 are described in detail in References,¹³⁻²⁹ given in the caption to this Figure. Different techniques were used to prepare thin films on fused silica: spincoating of the completely soluble compounds PT, PPA and OPc; spincoating of precursor polymers followed by a thermal conversion to the conjugated polymers PPV and PPT; vacuum sublimation in case of the oligomers OPV-*n* and ORy-*n*. Uniform thin films with random orientation of the chromophores were obtained. The film thicknesses were measured with a Tencor Instruments α -step profiler. The typical film thicknesses for the THG experiments were in the range of 50–100 nm.

Absorption and reflection spectra of the thin films on fused silica were measured with a Perkin Elmer model Lambda 9 spectrophotometer. The refractive indices $n(\lambda)$ were obtained by a combined use of Kramers-Kronig analysis, prism coupling by means of the m-line technique³⁰ and a specially developed technique to calculate $n(\lambda)$ from the absorption and reflection spectra by solving the Fresnel equations by an iteration procedure without any fit parameter.³¹⁻³³

The basic experimental setup for the THG measurements was similar to earlier reports.^{25,26,34} An actively/passively modelocked Nd:YAG laser was used to generate picosecond pulses. They were amplified in a double pass amplifier. For THG investigations at variable wavelengths, they were transformed to the second harmonic with a KDP crystal. The second harmonic pulses of 2–3 mJ energy were used to pump an optical parametric generator/amplifier configuration (OPA) based on two LiIO₃ crystals.³⁵ The wavelength of the parametric signal could be tuned continuously from 700 to 1600 nm. The laser beam was focused on the sample mounted on a rotation stage. The Maker fringes were detected by a photomultiplier tube as a function of the angle of incidence. The evaluation of $\chi^{(3)}(-3\omega; \omega, \omega, \omega)$ was carried out using the formalism described earlier.²⁵ As reference, $\chi^{(3)}(-3\omega; \omega, \omega, \omega) = 3.11 \cdot 10^{-14}$ esu was used for fused silica.³⁶

THIRD-HARMONIC GENERATION SPECTROSCOPY

Third-harmonic generation experiments can be performed with variable laser frequencies ω (wavelengths λ_L) to determine the dispersion of $\chi^{(3)}(-3\omega; \omega, \omega, \omega)$. In studies of several conjugated polymers, two characteristic resonance maxima have been observed for example in polyacetylene (PA),^{23,24} polydiacetylines (PDA)^{37,38} and polythiophene (PT).²² The major maximum is usually observed at $\lambda_L = 3\lambda_{\text{max}}$, where λ_{max} is the wavelength of the linear absorption maximum. An additional weaker maximum has been found at $\lambda_L < 3\lambda_{\text{max}}$, which has no corresponding feature in the linear absorption spectrum. New results of THG investigations of thin films of PPV show, that PPV has also two resonance maxima of $\chi^{(3)}(-3\omega; \omega, \omega, \omega)$, which are observed at $\lambda_L = 1336$ nm (major maximum close to $3\lambda_{\text{max}}$, see Table 1) and at $\lambda_L = 1155$ nm (smaller maximum of $\chi^{(3)}(-3\omega; \omega, \omega, \omega)$).¹⁹ It seems that the appearance of two distinct resonances in the spectrum of $\chi^{(3)}(-3\omega; \omega, \omega, \omega)$ is a characteristic feature of conjugated polymers.

The THG spectra of conjugated polymers can be discussed with the energy level scheme shown in Figure 2, which is typical for one-dimensional semiconductors. It consists of a valence band (VB), conduction band (CB) and an exciton band (EB) located below CB. For very general reasons,³⁹ the one-dimensionality leads to a shift of oscillator strength from the VB-CB transition to the VB-EB transition. Therefore the conduction band edge is usually not visible in the linear absorption spectrum of one-dimensional semiconductors, which is dominated by the exciton absorption. In PDA the CB edge is located approximately 0.5 eV above the exciton band as can be concluded from photoconductivity and electroreflection experiments.⁴⁰⁻⁴² This model is widely accepted, at least for PDA. Presumably it can be applied also to other conjugated polymers.

The major maximum of $\chi^{(3)}(-3\omega; \omega, \omega, \omega)$, which is usually observed at $\lambda_L = 3\lambda_{\max}$, is ascribed to a three-photon resonance with states located at the top of the valence band and the exciton band (process 1 in Fig. 2). It dominates due to the large oscillator strength of the exciton absorption. The additional resonance at higher energies can have two possible origins as indicated by processes 2 and 3. Process 2 is a three-photon resonance with the continuum of states located at the bottom of the conduction band. Process 3 is a two-photon resonance with a two-photon state located energetically below EB. In contrast to short chain polyenes, where the location of two-photon states is well known and understood,^{43,44} there is still a debate whether the two-photon states in conjugated polymers are located below and/or above the exciton band. As sketched in Figure 2, processes 2 and 3 could be visible at the same laser wavelength λ_L . Therefore with THG alone, it is not possible to distinguish between

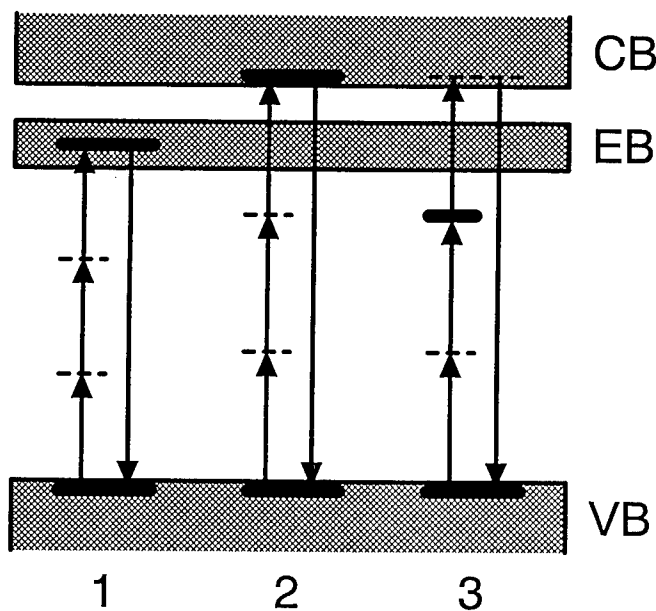


FIGURE 2 Model of energy states of conjugated polymers. The possible multi-photon resonances 1, 2 and 3 are explained in the text.

processes 2 and 3. Two-photon absorption spectroscopy or other nonlinear optical techniques could help to solve the interesting question, which are the essential states in conjugated polymers. This question is also discussed in several theoretical investigations,⁴⁵⁻⁵⁰ but a final, generally accepted view does not exist yet.

MAGNITUDE OF THIRD-ORDER NONLINEARITIES OF CONJUGATED POLYMERS

In a search for general structure-property relations, several conjugated π -electron systems must be compared. We have seen above, that large changes of $\chi^{(3)}(-3\omega; \omega, \omega, \omega)$ can occur, if ω is varied. Therefore it is necessary to choose representative $\chi^{(3)}$ data for a comparison of different materials. Three $\chi^{(3)}$ values are extracted from the wavelength dependent THG experiments at the following characteristic laser wavelengths: 1. the fundamental wavelength of the Nd:YAG laser at $\lambda_L = 1064$ nm, because most THG studies are performed at this wavelength, 2. $\lambda_L = 3\lambda_{\max}$ at the three photon resonance with the linear absorption maximum and 3. at a laser wavelength near to $\lambda_L = 3\lambda_0$. The cut-off wavelength λ_0 is determined by a linear extrapolation of the long wavelength flank of the main absorption band to zero absorption. The advantage of the choice of $\lambda_L = 3\lambda_{\max}$ and $\lambda_L = 3\lambda_0$ is, to obtain a means to compare the experimental data of different compounds studied in different laboratories. A selection of several linear and nonlinear optical data is shown in Table 1.

A general theory for extended chains of length $L > L_d$ with one-dimensional π -electron delocalization was developed by Flytzanis *et al.*^{51,52} It relates the linear and nonlinear optical properties to the delocalization length L_d according to

$$\chi^{(2n'-1)} \sim L_d^{4n'-2}, \quad (1)$$

where $n' = 1$ refers to $\chi^{(1)}$ and $n' = 2$ to $\chi^{(3)}$ respectively. The important consequence $\chi^{(3)} \sim L_d^6$ can be compared with experiments. If L_d is inversely proportional to E_0 , which is the optical energy gap^{51,52} and $E_0^{-1} \sim \lambda_{\max}$, it follows that the off-resonant $\chi^{(3)}$ values of one-dimensional conjugated polymers are expected to scale with λ_{\max}^6 , irrespectively of their chemical structure.

To examine whether such general relations exist, the $\chi^{(3)}$ -data of several conjugated π -electron systems are plotted in a double-logarithmic scale versus λ_{\max} . This masterplot is shown in Figure 3. The individual data points refer to THG experiments at $\lambda_L = 1064$ nm, which obviously can contain different resonance contributions. To visualize the resonance enhancements, the range of the dispersion of $\chi^{(3)}(-3\omega; \omega, \omega, \omega)$ obtained at variable laser wavelengths is symbolized by vertical bars between triangles facing up and down. The upper triangles correspond to $\chi^{(3)}$ at the three photon resonance with $\lambda_L = 3\lambda_{\max}$. The lower triangles represent low-resonant $\chi^{(3)}$ values obtained at a laser wavelength near to $\lambda_L = 3\lambda_0$.

The masterplots of Figure 3 show, that the conjugated systems with one-dimensional π -electron delocalization indeed show a general, systematic increase of $\chi^{(3)}$ with λ_{\max} .

TABLE 1

Spatial averages of $\chi^{(3)}$ and phase angles Φ , measured with THG at laser wavelengths λ_L . The structures of the compounds are given in Figure 1.

R		α_{\max} [10 ⁴ cm ⁻¹]	λ_{\max} [nm]	λ_L [nm]	$ \langle \chi^{(3)} \rangle $ [10 ⁻¹² esu]	Φ [°]	Ref.
PA		30	652	1064	100		[23]
				2070	5600		[24]
PPA-0	H	7.0	388	1064	2.7 ± 0.3	153 ± 5	[25]
PPA-1	H	7.07	330	1064	1.0 ± 0.5	131 ± 10	[26]
PPA-2	H	6.95	350	1064	2.5 ± 0.5	170 ± 10	[26]
PPA-3	CH ₃	6.78	414	1064	4.9 ± 0.2	200 ± 10	[26]
PPA-4	CH ₃	9.02	436	1064	9.3 ± 1.5	227 ± 10	[26]
PPA-5	C ₂ H ₅	6.24	429	1064	5.4 ± 0.8	218 ± 10	[26]
PPA-6	C ₂ H ₅	7.05	438	1064	7.1 ± 0.6	223 ± 10	[26]
PPA-7	C ₈ H ₁₇	8.70	462	1064	6.4 ± 1.0	240 ± 10	[26]
PPA-8	Si(CH ₃) ₃	6.14	515	1064	13.0 ± 2.0	280 ± 10	[26]
PT-1	C ₁₀ H ₂₁	9.7	455	1064	8.9 ± 1.5	239 ± 20	[21]
PT-2	C ₁₀ H ₂₁	9.5	485	1064	9.5 ± 1.5	276 ± 20	[21]
PT-3	C ₁₀ H ₂₁	10.6	505	1064	11.8 ± 1.5	295 ± 20	[21]
PPT	C ₁₂ H ₂₅	9.2	463	1064	21.3 ± 3	220 ± 20	[20]
PPV		34	458	1064	83.6 ± 7	227 ± 15	[19]
				1336	160 ± 17	115 ± 15	[19]
				1512	32.1 ± 7	43 ± 15	[19]
OPV-5		24	406	1064	17.2 ± 2	123 ± 15	[19]
				1222	36 ± 4	89 ± 15	[19]
				1485	8.1 ± 2	23 ± 15	[19]
OPV-4		21	394	1064	17 ± 2	101 ± 15	[19]
				1155	19.1 ± 2	95 ± 15	[19]
				1485	4 ± 1	10 ± 15	[19]
OPV-3		20	383	1064	16.1 ± 2	102 ± 15	[19]
				1155	15.2 ± 2	93 ± 15	[19]
				1440	3.2 ± 1	23 ± 15	[19]
ORy-2		12.0	457	1064	0.48	263	[27, 28]
ORy-3		14.5	574	1064	0.81	153	[27, 28]
ORy-4		15.0	689	1064	1.57	5	[27, 28]
OPc		15	656	1064	3.7 ± 1.5	155 ± 10	[29]

Because of different bulky substituents R, which do not contribute much to the nonlinearity (as in the case of alkyl chains) and very different morphologies, the polymers displayed in Figure 1 have a very different number of π -electrons per unit volume. This influences also the absorption coefficient α_{\max} at λ_{\max} of the thin films. In the normalized plot of $\chi^{(3)}/\alpha_{\max}$ against λ_{\max} shown in Figure 3b, it can be seen for example, that PPV has a $\chi^{(3)}$ value similar to the other conjugated polymers. This is not as obvious in Figure 3a. Because α_{\max} is proportional to $\chi^{(1)}$, the ratio $\chi^{(3)}/\alpha_{\max}$ should scale with L_d^4 according to relation (1). Clearly the limited range of available λ_{\max} values does not allow to deduce an accurate value of the exponent according to the power law in relation (1). This rather large uncertainty of the exponent can be estimated from Figure 3. The solid lines in parts (a) and (b) represent the exponents 6 and 4 respectively.

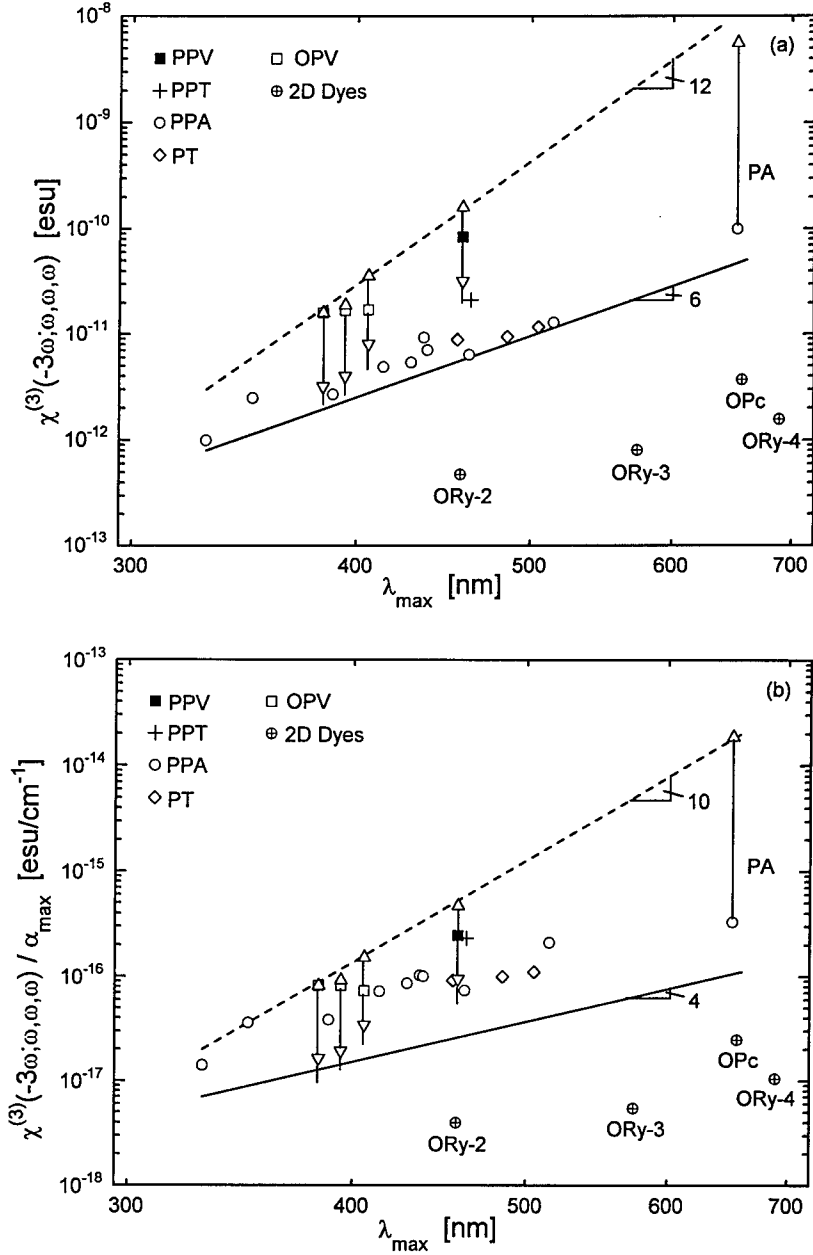


FIGURE 3 Masterplot of experimental data obtained by THG at the laser wavelength $\lambda_L = 1064$ nm (individual data points) and at variable λ_L (triangles pointing up: at $\lambda_L = 3 \lambda_{\max}$, triangles pointing down: low resonant values of $\chi^{(3)}$).

They represent relation (1) for the off-resonant $\chi^{(3)}$ values. The dashed lines, which tentatively connect the three-photon resonant $\chi^{(3)}$ data, would lead to much larger exponents.

For comparison with the THG data of one-dimensional conjugated systems, the results for the planar dyes ORy-n and OPc are also displayed in Figure 3. The dyes have an order of magnitude smaller $\chi^{(3)}$ values as the conjugated polymers with similar λ_{\max} . This is interpreted with the different dimensionality of the π -electron delocalization. The chemical structures of these dyes indicate, that their π -electron systems are delocalized in a second direction of space, in contrast to the conjugated polymers. The consequences are interpreted with the model of an electron in a one- and two-dimensional potential well.^{53,54} Because of additional degeneracies, the energy levels in the two-dimensional (2D) well are more closely arranged as in the one-dimensional (1D) well. With this argument, it can be qualitatively understood, that the 2D well of the same maximum lateral L as the 1D well should have a larger λ_{\max} value. Therefore the $\chi^{(3)}$ values of the 2D systems are much smaller as compared to the 1D systems, if they are compared at the same λ_{\max} . This underlines that the conjugated polymers with 1D π -electron delocalization are optimally suited to achieve large off-resonant $\chi^{(3)}$ values.

CONCLUSIONS

General relations between the linear and nonlinear optical properties of one-dimensional conjugated systems can be seen in a masterplot of experimental data of $\chi^{(3)}/\alpha_{\max}$ versus λ_{\max} . The electron delocalization length primarily determines $\chi^{(3)}(-3\omega; \omega, \omega, \omega)$. The oligomers OPV-n fit to the nonlinear optical properties of conjugated polymers. This indicates, that only short chain segments of the polymers are responsible for their optical properties and not their entire chain length. Materials with heteroatomic composition such as PT, PPT or OPc do not offer larger $\chi^{(3)}(-3\omega; \omega, \omega, \omega)$ values than pure hydrocarbon compounds like PPA or PPV. Conjugated systems with one-dimensional π -electron delocalization are found to be superior to two-dimensional systems for large off-resonant third-order nonlinearities. However the masterplot indicates that the off-resonant $\chi^{(3)}$ values of π -conjugated polymers are limited to approximately $\chi^{(3)} \leq 10^{-10}$ esu for systems with $\lambda_{\max} < 700$ nm.

ACKNOWLEDGEMENTS

The author wants to thank his former and present coworkers for their contributions and intensive interactions: Dr. D. Neher, Dr. R. Schwarz, Dr. A. Mathy, K. Ueberhofen, U. Baier and H. Menges. The fruitful cooperation and helpful discussions with Prof. G. Wegner, Prof. K. Müllen and their coworkers, who made available the polymers and oligomers, are gratefully acknowledged. Financial support to this work was given in part by the Bundesministerium für Forschung und Technologie and the Volkswagen-Stiftung.

REFERENCES

1. D. S. Chemla and J. Zyss (eds.), *Nonlinear Optical Properties of Organic Molecules and Crystals*, Vol. I and II, Academic Press, Orlando, 1987.
2. J. Messier, F. Kajzar, P. Prasad and D. Ulrich (Eds.), *Nonlinear Optical Effects in Organic Polymers*, NATO ASI E 162, Kluwer, Dordrecht, 1989.
3. J. L. Brédas and R. R. Chance (Eds.), *Conjugated Polymeric Materials: Opportunities in Electronics, Optoelectronics and Molecular Electronics*, NATO ASI E 182, Kluwer, Dordrecht, 1990.
4. J. Messier, F. Kajzar and P. Prasad (Eds.), *Organic Molecules for Nonlinear Optics and Photonics*, NATO ASI E 194, Kluwer, Dordrecht, 1991.
5. G. Zerbi (Ed.), *Organic Materials for Photonics*, North Holland, Amsterdam, 1993.
6. J. L. Brédas and R. Silbey (Eds.), *Conjugated Polymers*, Kluwer, Dordrecht, 1991.
7. F. Kajzar, J. Messier in Reference 6, p. 509.
8. H. S. Nalwa, *Adv. Mater.*, **5**, 341 (1993).
9. C. Bubeck in V. Degiorgio and C. Flytzanis (Eds.), *Nonlinear Optical Materials: Principles and Applications*, in press.
10. J. P. Hermann and J. Ducuing, *J. Appl. Phys.*, **45**, 5100 (1974).
11. K. C. Rustagi and J. Ducuing, *Opt. Commun.*, **10**, 258 (1974).
12. B. A. Reinhardt, M. R. Unroe, R. C. Evers, M. Zhao, M. Samoc, P. N. Prasad and M. Sinsky, *Chem. Mater.*, **3**, 864 (1991).
13. T. Kaino, K. Kubodera, S. Tomaru, T. Kurihara, S. Saito, T. Tsutsui and S. Tokito, *Electron. Lett.*, **23**, 1095 (1987).
14. D. D. C. Bradley and Y. Mori, *Jpn. J. Appl. Phys.*, **28**, 174 (1989).
15. C. Bubeck, A. Kaltbeitzel, R. W. Lenz, D. Neher, J. D. Stenger-Smith and G. Wegner, in Reference 2, p. 143.
16. T. Kurihara, Y. Mori, T. Kaino, H. Murata, N. Takada, T. Tsutsui and S. Saito, *Chem. Phys. Lett.*, **183**, 534 (1991).
17. R. O. Garay and R. W. Lenz, *Makromol. Chem. Suppl.*, **15**, 1 (1989).
18. R. O. Garay, U. Baier, C. Bubeck and K. Müllen, *Adv. Mater.*, **5**, 561 (1993).
19. A. Mathy, K. Ueberhofen, R. Schenk, H. Gregorius, R. Garay, K. Müllen and C. Bubeck, submitted for publication.
20. A. Kistenmacher, T. Soczka, U. Baier, K. Ueberhofen, C. Bubeck and K. Müllen, *Acta Polymerica*, **45**, 228 (1994).
21. D. Neher, A. Wolf, M. LeClerc, A. Kaltbeitzel, C. Bubeck and G. Wegner, *Synth. Met.*, **37**, 249 (1990).
22. W. E. Torruellas, D. Neher, R. Zanoni, G. I. Stegeman, F. Kajzar and M. LeClerc, *Chem. Phys. Lett.*, **175**, 11 (1990).
23. F. Kajzar, S. Etamad, G. L. Baker and J. Messier, *Synth. Met.*, **17**, 563 (1987).
24. W. S. Fann, S. Benson, J. M. J. Madey, S. Etamad, G. L. Baker and F. Kajzar, *Phys. Rev. Lett.*, **62**, 1492 (1989).
25. D. Neher, A. Wolf, C. Bubeck, G. Wegner, *Chem. Phys. Lett.*, **163**, 116 (1989).
26. D. Neher, A. Kaltbeitzel, A. Wolf, C. Bubeck, G. Wegner, *J. Phys. D: Applied Phys.*, **24**, 1193 (1991).
27. S. Schrader, K. H. Koch, A. Mathy, C. Bubeck, K. Müllen and G. Wegner, *Synth. Met.*, **41-43**, 3223 (1991).
28. S. Schrader, K. H. Koch, A. Mathy, C. Bubeck, K. Müllen and G. Wegner, *Progr. Colloid Polym. Sci.*, **85**, 143 (1991).
29. A. Grund, A. Kaltbeitzel, A. Mathy, R. Schwarz, C. Bubeck, P. Vermehren and M. Hanack, *J. Phys. Chem.*, **96**, 7450 (1992).
30. R. Ulrich and R. Torge, *Appl. Opt.*, **12**, 2901 (1973).
31. R. Schwarz, PhD-Thesis, University of Mainz, 1992.
32. R. Schwarz, W. A. Goedel, N. Somanathan, C. Bubeck, U. Scheunemann, W. Hickel and G. Wegner, *Springer Ser. Solid State Sci.*, **107**, 337 (1992).
33. K. Ueberhofen, R. Schwarz, C. Bubeck, to be published.
34. C. Bubeck in Reference 5, p. 215.
35. P. G. Kryukov, Y. A. Matveets, D. N. Nikogosyan, A. V. Sharkov, E. M. Gordeev and S. D. Fanchenko, *Sov. J. Quantum Electron.*, **7**, 127 (1977).
36. F. Kajzar and J. Messier, *Phys. Rev. A*, **32**, 2352 (1985).
37. F. Kajzar and J. Messier, *Thin Solid Films*, **132**, 11 (1985).
38. T. Kanetake, K. Ishikawa, T. Hasegawa, T. Koda, K. Takeda, M. Hasegawa, K. Kubodera and H. Kobayashi, *Appl. Phys. Lett.*, **54**, 2287 (1989).
39. H. Haug and S. W. Koch, *Quantum Theory of the Optical and Electrical Properties of Semiconductors*, World Scientific, Singapore, 1993, p. 199.
40. K. Lochner, H. Bässler, B. Tieke and G. Wegner, *Phys. Stat. Sol. (b)*, **88**, 653 (1978).
41. L. Sebastian and G. Weiser, *Chem. Phys.*, **62**, 447 (1981).
42. G. Weiser, *Phys. Rev. B*, **45**, 14076 (1992).
43. B. E. Kohler, *J. Chem. Phys.*, **93**, 5838 (1990).
44. B. E. Kohler, in Reference 6, p. 405.
45. S. Abe, M. Schreiber and W. -P. Su, *Chem. Phys. Lett.*, **192**, 425 (1992).
46. S. Abe, M. Schreiber, W. -P. Su and J. Yu, *Phys. Rev. B*, **45**, 9432 (1992).
47. T. Hasegawa, Y. Iwasa, H. Sunamura, T. Koda, Y. Tokura, H. Tachibana, M. Matsumoto and S. Abe, *Phys. Rev. Lett.*, **69**, 668 (1992).

48. Z. Shuai, J. L. Brédas, *Phys. Rev. B*, **44**, 5962 (1991).
49. S. N. Dixit, G. Guo and S. Mazumdar, *Phys. Rev. B*, **43**, 6781 (1991).
50. D. Guo, S. Mazumdar, G. I. Stegeman, M. Cha, D. Neher, S. Aramaki, W. Torruellas and R. Zanon, *Mat. Res. Soc. Symp. Proc.*, **247**, 151 (1992).
51. G. P. Agrawal, C. Cojan, C. Flytzanis, *Phys. Rev. B*, **17**, 776 (1978).
52. C. Flytzanis in Reference. 1, Vol. II, p. 121.
53. H. Kuhn, *J. Chem. Phys.*, **17**, 1198 (1949).

Functionalized Polyenes and Carotenoids with Enhanced Nonlinear Optical Responses

M. BLANCHARD-DESCE¹, J.-M. LEHN¹, M. BARZOUKAS², C. RUNSER²,
A. FORT², G. PUCETTI³, I. LEDOUX³ and J. ZYSS³

¹*Chimie des Interactions Moléculaires (UPR 285 of the CNRS),
Collège de France, 11 Place Marcelin Berthelot, 75005 Paris, France,*

²*IPCMS, Groupe d'Optique Nonlinéaire et d'Optoélectronique (UM 046 of
the CNRS), 5 rue de l'Université, 67084 Strasbourg Cedex, France,*

³*Département d'Electronique Quantique et Moléculaire,
Centre National d'Etudes des Télécommunications, 196 Avenue Henri Ravera,
92220 Bagneux, France*

Received 12 January 1994; accepted 11 February 1994

The functionalization of natural polyenes, the carotenoids, provides a straightforward strategy for the molecular engineering of polyenic chains of defined length. Within this framework, various α, ω -disubstituted polyenes and carotenoids of increasing size and bearing different donor and acceptor end groups have been synthesized in order to investigate the chain-length dependence of the quadratic (β) and cubic (γ) hyperpolarizabilities. β and γ measurements have been performed using the EFISH and THG techniques.

In each series of homologous push-pull carotenoids, lengthening the polyenic chain results in a substantial increase in β leading to very large static $\beta(0)$ values for the longest molecules (up to 30 Å).

For various series of functionalized carotenoids (either symmetrical bis-donor and bis-acceptor derivatives, or asymmetrical push-pull compounds), lengthening the polyenic chain also results in a sharp increase in γ . Very large γ values are found for long push-pull carotenoids and for extended symmetrical carotenoids functionalized with donor end groups (up to 40 Å).

The chain-length dependences of β and γ can be modeled by $\beta \propto n^{a_1}$ and $\gamma \propto n^{a_2}$ relationships where n is the number of conjugated double bonds in the polyenic chain. The exponents a_1 and a_2 are found to depend on the substitution pattern. No saturation effect is noticed within the molecular size range investigated.

INTRODUCTION

During the last few decades the interest in nonlinear optical materials has grown tremendously because of their potential applications in the area of integrated optics.¹ Due to their efficiency and chemical flexibility, organic derivatives have received considerable attention.^{2–7} Experimental studies have been conducted on a wide range of organic molecules and polymers, yielding guidelines for the design of compounds with large molecular optical nonlinearities.

It is now well established that molecules containing a donor-acceptor (or “push-pull”) substituted conjugated system exhibit large quadratic (β) hyperpolarizabilities. This is related to the occurrence of a low-lying charge-transfer excited state with a large oscillator strength.^{8–10} Although new original frameworks have emerged recently,^{11–14} the classical (donor-conjugated linker-acceptor) prototype molecular

structure is still relevant for the optimization of quadratic hyperpolarizabilities. In particular, early experimental studies carried out on benzene and stilbene derivatives have shown that extension of the conjugated path linking the electron-donating and electron-withdrawing substituents leads to a marked increase in β values.¹⁵⁻¹⁷

The guidelines for optimizing cubic hyperpolarizabilities are still a subject of debate and investigation but it has long been known that molecules with extended π -electron systems display high γ values.^{16,18-19}

In this context, the polyenic system is of particular interest. It allows for efficient electronic delocalization along the conjugated backbone. This is illustrated by the bathochromic effect induced by the lengthening of the polyenic chain, this phenomenon tending to level-off for long polyenes.²⁰⁻²² Polyenes of medium size (i.e., oligomers) are thus relevant candidates for the design of compounds with dramatically enhanced optical nonlinearities. In addition, different series of polyenic oligomers of defined and increasing length would provide an excellent base for systematic experimental studies of structure-property relationships leading to a better understanding of the parameters that govern optical nonlinearities.

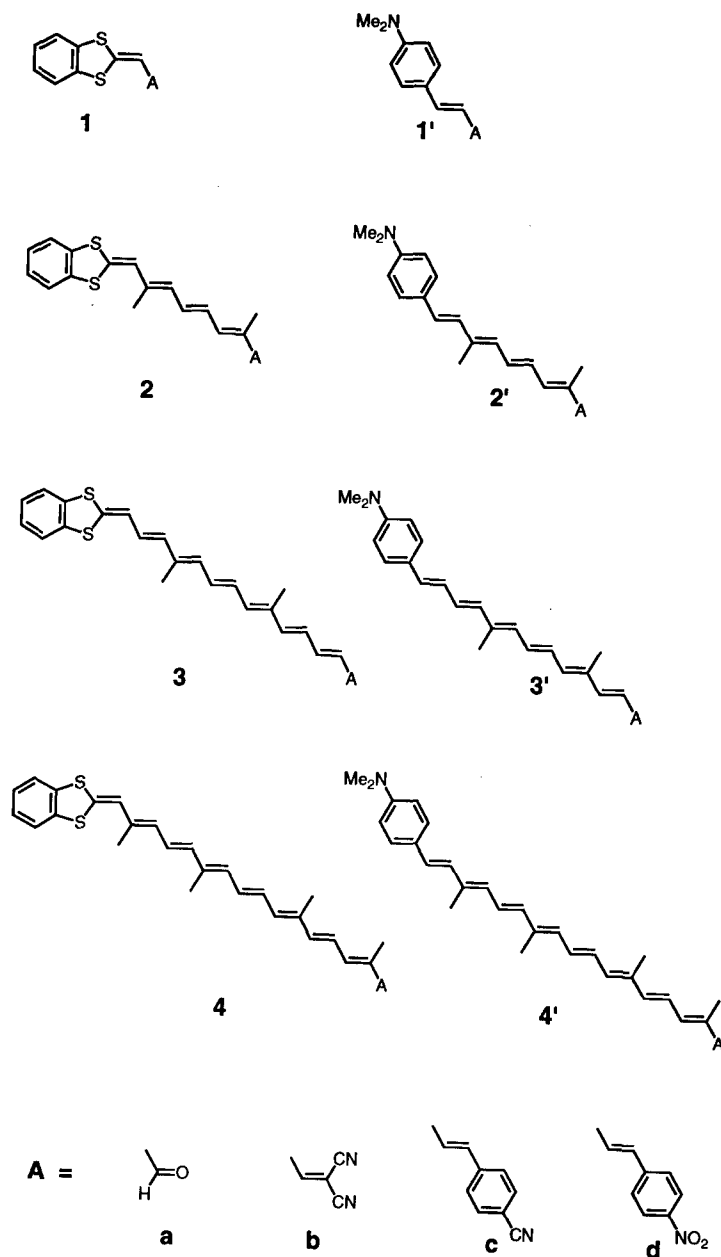
The modification and functionalization of natural conjugated polyenes, the carotenoids, provide an efficient route for the molecular engineering of polyenic oligomers of defined length.²³⁻³² Moreover, the presence of the characteristic methyl side groups on the conjugated skeleton of carotenoids confers better solubility and stability as compared to an unsubstituted polyenic chain.

PUSH-PULL CAROTENOIDS WITH ENHANCED QUADRATIC NONLINEAR OPTICAL SUSCEPTIBILITIES

A few years ago, semi-empirical calculations conducted on two series of push-pull polyenes predicted a rapid increase in β with the number n of double bonds, the effect per unit volume saturating beyond $n = 20$.³³ Moreover, the computed β values indicated that the polyenic system exhibits an efficiency greatly superior to that of the polyphenyl system. Recent experimental studies³⁴⁻³⁷ performed on several series of donor-acceptor polyenes of increasing but moderate length (up to $n = 4$ or $n = 5$) yielded superlinear dependences of β on the length. All these results taken together emphasize the relevance of longer donor-acceptor polyenes such as push-pull carotenoids in view of both the practical optimization of β and the investigation of the saturation phenomenon.

Within this framework, we have synthesized several series of push-pull polyenes and carotenoids of increasing length (up to 30 Å),^{24-25,28} in order to investigate the chain-length dependence of their quadratic hyperpolarizability (Scheme 1). Such molecules have been shown to display long-distance intramolecular charge transfer.³⁸ The series bear the benzodithia (compounds 1-4) or the dimethylaminophenyl (compounds 1'-4') donor moieties. Four distinct acceptor substituents have been used: formyl (derivatives a), dicyanovinyl (derivatives b), *p*-cyanophenyl (derivatives c) and *p*-nitrophenyl (derivatives d).

The variation of β was studied using the Electric-Field-Induced-Second-Harmonic (EFISH) generation technique.^{28,39} The EFISH experiment allows for the



SCHEME 1 Structural formulae of the series of push-pull polyenes and carotenoids investigated in this work.

determination of the mean microscopic hyperpolarizability γ_0 :

$$\gamma_0 = \gamma(-2\omega; \omega, \omega, 0) + \frac{\mu\beta(-2\omega; \omega, \omega)}{5kT}$$

The first term is the scalar part of the cubic hyperpolarisability tensor, whereas the second arises from the partial orientation of the permanent dipole moment μ in the static field. The orientational contribution is usually assumed to be, in first approximation, the predominant component in the case of polar charge-transfer molecules. Therefore, the product $\mu\beta(2\omega)$ —where $\beta(2\omega)$ (a short hand notation for $\beta(-2\omega; \omega, \omega)$) is the vector part of the hyperpolarisability tensor—is directly inferred. The results are collected in Table 1. Given along with the $\mu\beta(2\omega)$ values are the static values $\mu\beta(0)$ calculated by using the two-level model since $\beta(2\omega)$ can be significantly affected by dispersion enhancement.¹⁶

As a result of the quasi one-dimensional nature of the extended π -electron network for the long push-pull carotenoids, the β_{ijk} tensor is expected to be mainly one-dimensional along the charge-transfer molecular long axis, with the quadratic hyperpolarizability β and the dipole moment μ being nearly parallel.

Owing to the low solubility of the longest derivatives, the μ values were not measured. However, for the series 1a–4a, 1'a–4'a and 1'b–5'b, estimated values can be derived from the experimental or calculated values reported for shorter analogous compounds.^{35,40} In addition, from the μ values measured for various series of push-pull polyenes^{34–37,41} as well as from calculations,⁴⁰ the dipole moments of the push-pull carotenoids can be considered to be *relatively* unaffected by the conjugation length. The variations of $\mu\beta$ (or $\mu\beta(0)$) in each series of homologous compounds

TABLE 1

Experimental results of the EFISH experiments conducted at 1.34 μm or 1.907 μm (in order to avoid absorption of the second harmonic (2ω)). The maximum absorption wavelengths λ_1 and the $\mu\beta(2\omega)$ values were measured in chloroform. The experimental accuracy of the EFISH experiment is $\pm 20\%$. The static $\mu\beta(0)$ values are calculated by using the two-level model.¹⁶ The $\beta(0)$ values are obtained by dividing the $\mu\beta(0)$ values by the dipole moment magnitudes μ .

	ω μm	n^a	λ_1 nm	$\mu\beta(2\omega)$ 10^{-48} esu	$\mu\beta(0)$ 10^{-48} esu	μ^b D	$\beta(0)$ 10^{-30} esu
1a	1.34	1	372	30	20	5.8	3
2a	1.34	4	456	1200	570	6.5	90
3a	1.34	6	485	2700	1100	6.9	160
4a	1.34	8	500	7250	2800	7.1	390
1'a	1.34	1	384	320	200	5.6	35
2'a	1.34	4	450	2000	1000	6.5	150
3'a	1.34	6	474	4300	1900	6.8	275
4'a	1.34	8	498	8900	3400	7	490
1b	1.91	2	446	230	170		
2b	1.91	5	562	2850	1700		
1'b	1.91	2	489	1030	710	8.4	85
2'b	1.91	5	560	5500	3290	9.5	345
3'b	1.91	7	574	9400	5450	10	545
4'b	1.91	9	588	13400	7500	10.3	730
1c	1.34	2	410	250	140		
2c	1.34	5	465	1950	900		
1d	1.34	2	452	1000	480		
2d	1.34	5	488	2200	900		

^a n : number of conjugated double bonds in the polyenic chain.

^b For compounds 1a, 2a, 3a and 4a, μ values calculated from Ref. 40 are used. The dipole moment values given for compounds 2'a, 3'a, 4'a, 2'b, 3'b and 4'b are extrapolated from the μ values reported in Ref. 35 for smaller analogs (such as 1'a and 1'b).

of increasing size will therefore reflect, for the most part, the length dependence of β (or $\beta(0)$).

Effect of the Conjugation Length

As seen in Table 1, lengthening the polyenic chain induces a bathochromic shift of the charge-transfer absorption band and results in a significant increase in both $\mu\beta$ and $\mu\beta(0)$ values. This leads to exceptionally large quadratic optical nonlinearities for the longest molecules. The $\mu\beta(0)$ value for molecule 4'b is up to 16 times that of 4-dimethylamino-4'-nitrostilbene [DANS].⁴²

The enhancement of $\mu\beta(0)$ as a function of the number of double bonds n in the polyenic chain is shown in Figure 1 for the series 1a–4a and 1'a–4'a. The linear dependence of $\log(\beta(0))$ on $\log(n)$ observed for the series 1a–4a yields a $\mu\beta(0) \propto n^{2.35}$ relationship. For the series 1'a–4'a, a similar trend is noted, leading to a $\mu\beta(0) \propto n^{1.8}$ dependence but the value for molecule 1'a ($n = 1$) falls out of line. The non-alignment of the experimental point corresponding to $n = 1$ can also be derived from the set of computed data reported for two different series of push-pull polyenes.^{33,43}

A linear dependence of $\log(\mu\beta(0))$ on $\log(n)$ is also observed for the series 1'b–4'b as shown in Figure 1, leading to a $\mu\beta(0) \propto n^{1.6}$ dependence. In the case of series 1b–4b, molecule 2b proved very difficult to measure and compounds 3b and 4b did not yield reliable $\mu\beta(2\omega)$ values, owing to their very low solubility.

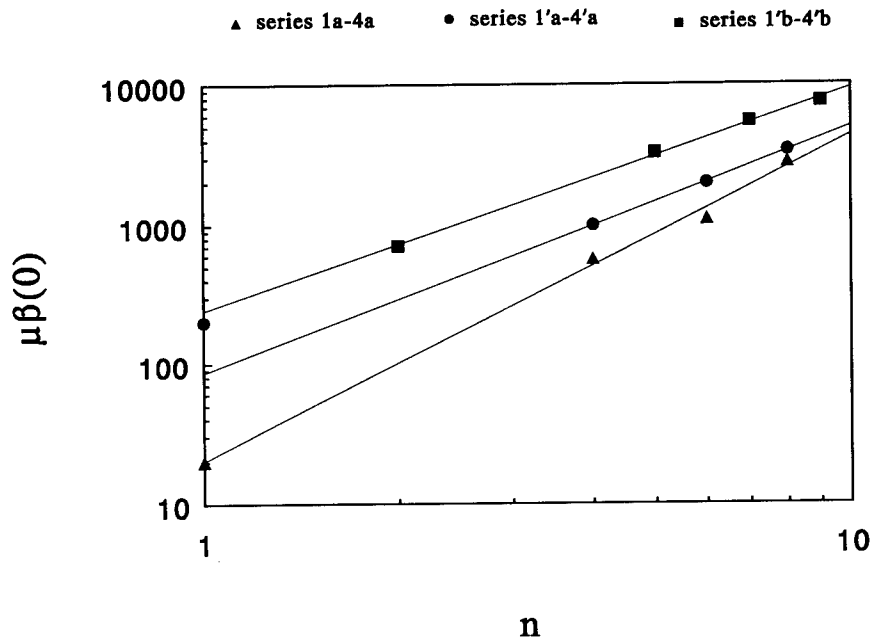


FIGURE 1 Plot of $\mu\beta(0)$ values versus the number n of double bonds in the polyenic chain for the series of push-pull carotenoids 1a–4a, 1'a–4'a and 1'b–4'b, using logarithmic scales. All $\mu\beta(0)$ values are expressed in 10^{-48} esu.

For the series 1a–4a and 1'a–4'a and 1'b–4'b, the chain-length dependence of $\beta(0)$ is shown in Figure 2. The linear dependencies of $\log(\beta(0))$ on $\log(n)$ yield $\beta(0) \propto n^a$ relationships, with a values of 2.25, 1.7 and 1.45 for the series 1a–4a and 2'a–4'a and 1'b–4'b respectively.

Effect of the End Groups on the Length Dependence

Before examining the effect of the end groups on the chain-length dependence, it should be observed that the magnitude of the exponent that describes the power law dependence of β depends on the definition of the conjugation length. This consideration arises from the fact that it is difficult to rigorously account for the end groups in the delocalization length. For instance, in most of the experimental studies reported in the literature for various series of push-pull diphenylpolyenes,^{17,34–35} the phenyl rings are arbitrary taken as equivalent to two double bonds in terms of effective conjugation length. However, examination of the experimental results reported for homologous push-pull stilbenes and styrenes,¹⁶ or polyenes and phenylpolyenes,^{35,37} shows that the relative contribution of the phenyl moiety to the conjugated path in terms of quadratic nonlinearity can be slightly superior, comparable or even inferior to one double bond. The influence of the phenyl rings can even be considered as detrimental as evidenced by comparison of homologous push-pull phenylpolyenes and diphenylpolyenes.³⁶ Finally, counting the phenyl ring as a given equivalent number of double

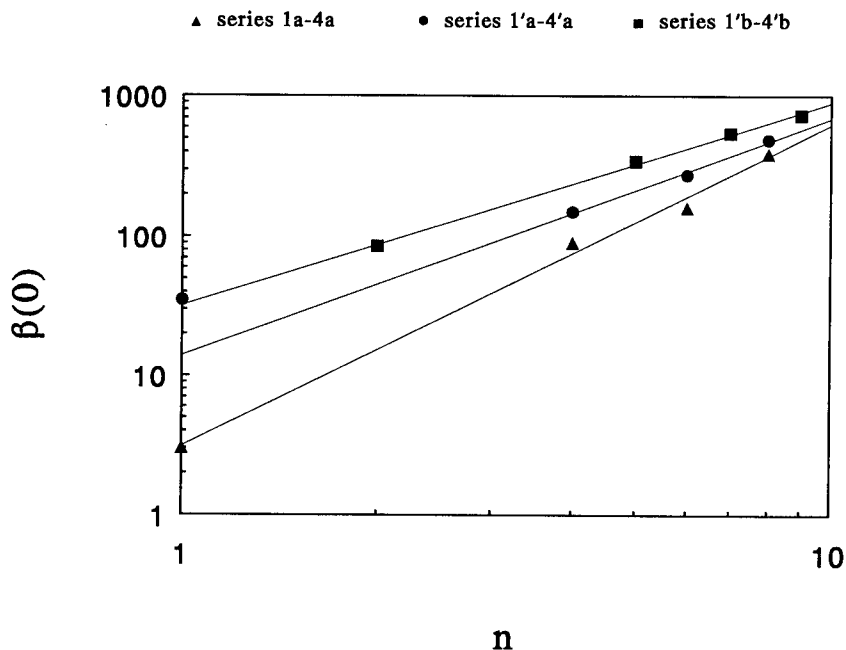


FIGURE 2 Plot of $\beta(0)$ values versus the number n of double bonds in the polyenic chain for the series 1a–4a, 1'a–4'a and 1'b–4'b using logarithmic scales. All $\beta(0)$ values are expressed in 10^{-30} esu.

bonds implicitly assumes that the relative contribution of the phenyl moiety to the conjugated path is a constant. This assumption seems questionable.

Ultimately, it appears that defining the delocalization length for the series of push-pull polyenes and carotenoids of increasing size is problematic. Therefore, we will discuss the influence of the end groups on the chain-length dependence by examining the increase in β as a function of n (number of double bonds in the polyenic chain), a structural parameter that does not include any contribution of the end groups to the conjugation path. However, we will try to compare compounds of similar size.

As seen in Figure 2 and evidenced by the respective exponent values obtained for the series 1a–4a (2.25) and 2'a–4'a (1.7), that exhibit an identical electron-withdrawing substituent but two different electron-donating groups, the rise in $\beta(0)$ is steeper for the series bearing the benzodithia donor end group. Although the benzodithia moiety leads to smaller β and $\mu\beta(0)$ values than the dimethylaminophenyl donor end group, the difference in nonlinear efficiency between benzodithia and dimethylaminophenyl derivatives of similar size decreases with increasing polyenic chain-length.

This is also illustrated by comparison of the series 1b–2b and 1'b–2'b bearing the same two donor end groups but a different, common acceptor moiety. The $\mu\beta(0)$ value for compound 1'b is 4 times larger than that of compound 1b but the enhancement factor between compounds 2b and 2'b is reduced by half. It follows that the difference in efficiency between the two donor groups lessens with increasing length. Similar behavior is noticed for the acceptor end groups. The rise in $\beta(0)$ is steeper for the series 2'a–4'a than for the series 1'b–4'b' as seen in Figure 2 and indicated by the corresponding a exponent values (1.7 and 1.45 respectively). Comparison of these two series, that display a common donor end group but two different acceptor end groups, reveals that the increase of $\beta(0)$ is steeper for the series bearing the weaker electron-acceptor since the formyl substituent (derivatives a) is a weak acceptor whereas the dicyanovinyl moiety is a powerful electron-withdrawing moiety (derivatives b).⁴⁴

Examination of series 1c–2c and 1d–2d calls for the same comment. The $\mu\beta(0)$ value for molecule 1d is 3.5 times larger than that of molecule 1c, in agreement with the strongest electron-withdrawing efficiency of the nitro substituent with respect to the cyano group. But compounds 2c and 2d show similar nonlinearities although the absorption of molecule 2d is red-shifted (Tab. 1). Therefore, the difference in nonlinear efficiency between the various acceptor derivatives also seems to decrease with increasing polyenic chain-length. This is corroborated by the analysis of the computed β values reported for two series of push-pull polyenes bearing a common donor but different acceptor end groups.³³ In this case again, the series bearing the weaker acceptor lead to steeper increase of β with conjugation length.^{28–29} Such a phenomenon has also been noticed for several series of push-pull diphenylpolyenes of moderate length.³⁵

FUNCTIONALIZED CAROTENOIDS WITH ENHANCED CUBIC NONLINEAR OPTICAL SUSCEPTIBILITIES

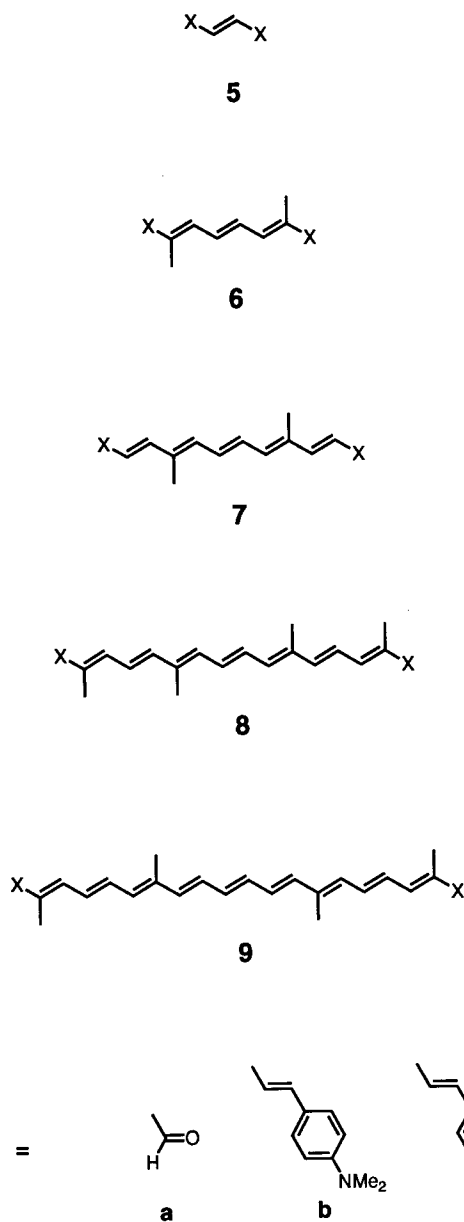
Polyenic molecules are among the compounds that exhibit the highest cubic optical nonlinearities. In particular, a number of natural carotenoids have been investigated,

leading to very large γ values.^{18–19,45–49} In the case of linear polyenes, the longitudinal component of γ is the dominant component of the third-order polarizability as a result of the one-dimensional nature of the extended π -electron system. In addition, various calculations have predicted a sharp enhancement of γ when increasing the number n of conjugated double bonds in the polyenic chain,^{50–61} leading to $\gamma \propto n^a$ relationships. However, there are some discrepancies regarding the exponent a , depending on the methodology and on the size range investigated. Successive scaling laws predicted values of a ranging from 5 to less than 2. Exponent values are expected to taper-off at large chain-length suggesting that γ/n approaches an asymptotic value for very long chains.^{54,55,62} An onset of saturation has been predicted around $n = 15$ –20 for linear polyenes.^{55,62} From such a behavior, one could derive an optimum dimension beyond which extending the conjugated chain would be needless. This point clearly calls for systematic experimental studies on the variation of γ for polyenes of defined and increasing length. In addition, an interesting point to investigate in order to optimize γ is the influence of electron-donating and electron-withdrawing substituents. It has been suggested that donor-acceptor substitution on polyenic chains would enhance γ through a breaking of the centrosymmetry.⁵⁵ It has also been shown that electron-donating substituents could significantly enhance the cubic hyperpolarizability of polarizable systems through increase of the electron density in the π -conjugated system.⁶³

Within this framework, functionalized carotenoids are again of particular interest. Both push-pull and bis-donor or bis-acceptor carotenoids (Scheme 2) were prepared and studied.^{64,65} The variation of γ for the symmetrical compounds was investigated using the EFISH technique. Since symmetry cancels the orientational contribution, the mean microscopic hyperpolarizability γ_0 obtained through EFISH measurements simplifies to $\gamma(-2\omega; \omega, \omega, 0)$ that will be noted γ^{SHG} later on. In the case of the asymmetrical push-pull compounds, γ measurements were performed using the third-harmonic generation (THG) technique that yields a purely cubic component $\gamma(-3\omega; \omega, \omega, \omega)$ that will be noted γ^{THG} later on. The results are summarized in Table 2.

Effect of the Conjugation Length

As seen in Table 2, the lengthening of the polyenic conjugation path induces a bathochromic shift of the main absorption band and results in a sharp increase in γ values in each series of homologous compounds. The enhancement of γ as a function of the number of double bonds n in the polyenic chain is shown in Figure 3 for the two series of push-pull carotenoids 1a–4a and 1'a–4'a. The logarithmic plots of the γ values versus n again show a linear dependence of $\log(\gamma)$ on $\log(n)$, although the value for molecule 1'a falls out of line as previously noticed for the β values. Thus, if one excludes the "anomalous" point corresponding to compound 1'a, $\gamma \propto n^a$ relationships may be established for the series 1a–4a and 1'a–4'a. The respective a values are 3.6 and 2.7. As evidenced in Figure 3, the benzodithia donor substituent is superior to the dimethylaminophenyl moiety in terms of the cubic nonlinearity. The benzodithia derivatives display larger absolute γ values than dimethylaminophenyl compounds of similar molecular size, and this difference becomes more pronounced with increasing polyenic chain length. An exceptionally large γ value is obtained for the longest benzodithia-formyl functionalized carotenoid (compound 4a.)



SCHEME 2 Structural formulae of the series of symmetrically-functionalized polyenes and carotenoids investigated in this work.

The series of bis-substituted carotenoids exhibit a similar behavior (Fig. 4). The linear dependences of $\log(\gamma)$ versus $\log(n)$ again yield $\gamma \propto n^a$ relationships. The lowest exponent corresponds to the bis-acceptor series 6a–8a ($a = 2.3$) and the highest one to the bis-donor family 5b–9b ($a = 3.0$). Thus, for symmetrically functionalized polyenes, a

TABLE 2

Experimental results of the EFISH and THG experiments conducted at 1.34 μm and 1.907 μm respectively (in order to avoid absorption of the second (2ω) or the third harmonic (3ω)). The maximum absorption wavelengths λ_1 and the γ values were determined in chloroform or acetone. The experimental accuracy of the EFISH and THG experiments ranges between ± 10 and $\pm 30\%$.

	ω μm	n^a	λ_1 nm	γ^{SHG} 10^{-36} esu	γ^{THG} 10^{-36} esu
1a ^b	1.91	1	372		30
2a ^b	1.91	4	456		4110
4a ^b	1.91	8	500		56600
1'a	1.91	1	384		200
2'a	1.91	4	450		1200
3'a	1.91	6	474		4000
4'a	1.91	8	498		7600
6a	1.34	3	328	170	
7a	1.34	5	392	500	
8a	1.34	7	446	1200	
5b ^c	1.91	3	410		252
5b	1.34	3	408	900	
6b	1.34	5	448	2700	
7b	1.34	7	476	12000	
9b	1.34	11	516	41300	
5c ^c	1.91	3	420		486
7c	1.34	7	490	3800	

^a n : number of conjugated double bonds in the polyenic chain.

^b from Ref. 65.

^c from Ref. 67.

steeper increase of γ is obtained when both the end groups are strong electron-donors. This behavior leads to very large values of γ for the longest bis-donor carotenoids and no saturation effect is noticed for the size range investigated (up to 40 Å).

Ultimately, $\gamma = kn^a$ relationships have been established for several series of functionalized carotenoids, yielding exponent values depending on the substitution pattern. However, one should keep in mind that the a values have been calculated on resonance-enhanced γ values. Therefore, one should be cautious in directly comparing the a values obtained for different series. A more rigorous comparison would necessitate the determination of the static $\gamma(0)$ values. Since the validity of the two-level model is highly questionable to account for the frequency dispersion of γ values, a reliable $\gamma(0)$ determination would require further frequency-dispersed nonlinear spectroscopic measurements.⁶⁵⁻⁶⁶

It should be mentioned that recent calculations conducted on disubstituted polyenes indicated a steeper increase of the static $\gamma(0)$ values for bis-donor with respect to bis-acceptor or donor-acceptor substitution.⁶¹

Effect of the End Groups

The influence of end groups on γ is clearly evidenced by direct comparison of the γ^{SHG} values of compounds 7b and 7c (Scheme 2). These molecules have identical conjugation paths, 7b bearing donor and 7c acceptor end groups. Although the absorption of

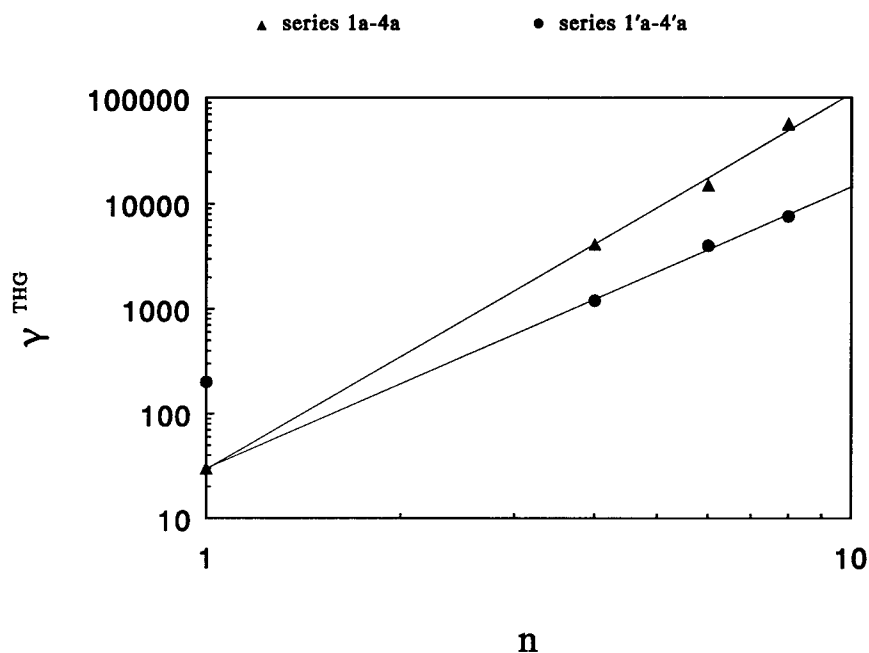


FIGURE 3 Plot of γ^{THG} values versus the number n of double bonds in the polyenic chain for the series of push-pull carotenoids 1a-4a and 1'a-4'a, using logarithmic scales. The THG experiments were conducted at $1.907\text{ }\mu\text{m}$ in chloroform (compounds 1a-4a) or in acetone (compounds 1'a-4'a). All γ values are expressed in 10^{-36} esu .

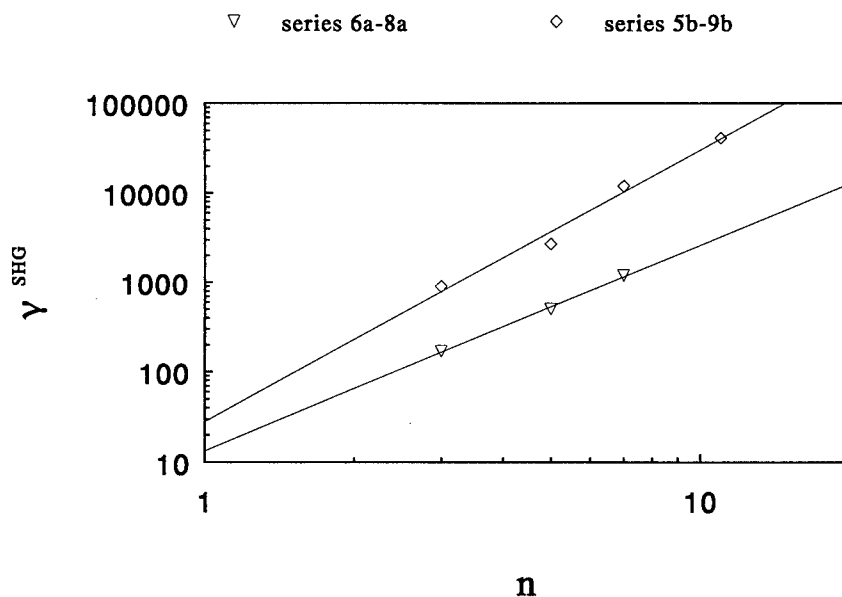


FIGURE 4 Plot of γ^{SHG} values versus the number n of double bonds in the polyenic chain for the series of symmetrically-functionalized carotenoids 6a-8a (bis-acceptor) and 5b-9b (bis-donor), using logarithmic scales. The EFISH experiments were performed at $1.34\text{ }\mu\text{m}$ in acetone. All γ values are expressed in 10^{-36} esu .

compound 7c is red-shifted, thus providing a more dispersion-enhanced nonlinear response, the γ^{SHG} value is 3 times higher for 7b than for 7c (Tab. 2). This suggests that the donor group is superior to the acceptor group in terms of cubic hyperpolarizability. However, examination of the experimental γ^{THG} values reported in the literature for 5b and 5c (*cf* Tab. 2) leads to the reverse trend.⁶⁷ This might indicate the existence of a critical length beyond which the bis-donor derivatives become more efficient than the bis-acceptors. Such a reversal of tendency is suggested by recent *ab initio* calculations.⁶¹ Only a reliable determination of frequency-independent $\gamma(0)$ values would allow to derive final conclusions from the available experimental results.

For this reason also, it is not possible to perform a quantitative comparison of the experimental γ^{THG} values measured for the push-pull carotenoids with the γ^{SHG} values determined for symmetric bis-substituted carotenoids of similar length.

CONCLUSION

The functionalization of carotenoids has proved to be an interesting strategy for the design of compounds with enhanced nonlinear optical responses as well as for the experimental investigation of the chain-length dependence of the quadratic and cubic hyperpolarizabilities.

For each series of homologous push-pull carotenoids, lengthening the polyenic conjugation path results in a substantial increase in the quadratic hyperpolarizability. This leads to very large static $\beta(0)$ values for the longest molecules. For various series of functionalized carotenoids (either symmetrical bis-donor and bis-acceptor derivatives, or asymmetrical donor-acceptor compounds), a sharp increase in the cubic hyperpolarizability is also observed with increasing polyenic chain-length. Exceptionally large γ values are found for long push-pull as well as bis-donor functionalized carotenoids.

The chain-length dependence of β and γ can be modeled by $\beta(0) \propto n^{a_1}$ relationships and $\gamma \propto n^{a_2}$ relationships with respect to the number n of conjugated double bonds in the polyenic chain, the exponents a_1 and a_2 depending on the end groups. However, a few points remain to be solved and require additional experimental studies. In particular, reliable determinations of frequency independent $\gamma(0)$ values, that require frequency-dispersed nonlinear spectroscopic measurements, are needed to clearly identify the different parameters underlying the mechanism of third-order polarizability. In addition, the accuracy of the EFISH methodology for the direct determination of the second-order polarizabilities appears questionable for long push-pull polyenes. In this case, the contribution of the cubic electronic component to the EFISH nonlinearity might be non-negligible as compared to the orientational contribution, since the cubic hyperpolarizability increases steeply with length. A combination of the EFISH and of the THG techniques (related by a valid dispersion model as described in Ref. 65) would help to discriminate between the two contributions of the over-all EFISH nonlinearity. The Hyper-Raleigh Scattering technique also appears to be an attractive alternative for the direct measurement of the quadratic hyperpolarizability.⁶⁸

No saturation was noticed within the molecular size range investigated (up to 30 or 40 Å). This result emphasizes the need for further experimental studies focussing on

longer and complementary molecules. In particular, the investigation of the possible influence of the end groups on the onset of saturation is of particular interest. Such studies call for the synthesis of longer analogs, that may be difficult due to the low solubility and stability of such compounds. Whereas the solubility can be easily increased by grafting alkyl chains,⁶⁹ the problem of chemical instability is inherent to very long polyenic compounds and limits the potential of such molecules for practical purposes.

ACKNOWLEDGEMENTS

The Centre National de la Recherche Scientifique (CNRS) is acknowledged for financial support and Hoffmann-La Roche AG, Basel (Switzerland) for generous gifts of the conjugated dialdehydes used in this work. We thank Valérie Alain for assistance in synthesizing some of the compounds and Thierry Bataille for performing the drawings of this paper.

REFERENCES

1. J. Zyss, *J. Mol. Electron.*, **1985**, **1**, 25.
2. *Nonlinear Optical Properties of Organic Molecules and Crystals*, eds. D. S. Chemla and J. Zyss (Academic Press, New York, 1987).
3. *Nonlinear Optical Properties of Polymers*, eds. A. J. Heeger, J. Orienstein and D. R. Ulrich, MRS Symp. Proc. 109 (Materials Research Society, Pittsburg, 1988).
4. *Nonlinear Optical and Electroactive Polymers*, eds. P. N. Prasad and D. R. Ulrich (Plenum, New York, 1988).
5. *Organic Materials for Nonlinear Optics*, eds. R. A. Hann and D. Bloor (Royal Society of Chemistry, London, 1989).
6. *Nonlinear Optical Effects in Organic Polymers*, eds. J. Messier, F. Kajzar, P. N. Prasad and D. R. Ulrich, NATO ASI Series (Kluwer, Dordrecht, 1989).
7. *Materials for Nonlinear Optics: Chemical Perspectives*, eds. S. R. Marder, J. E. Sohn and G. D. Stucky, ACS Symp. 455, (Washington, D.C., 1991).
8. J.-L. Oudar and D. S. Chemla, *J. Chem. Phys.*, **66**, 2664 (1977).
9. B. F. Levine, *Chem. Phys. Lett.*, **37**, 516 (1976).
10. S. J. Lalama and A. F. Garito, *Phys. Rev. A*, **75**, 3532 (1979).
11. I. Ledoux, J. Zyss, J. S. Siegel, J. Brienne and J.-M. Lehn, *Chem. Phys. Lett.*, **172**, 440 (1990).
12. W. Schuddeboom, B. Krijnen, J. W. Verhoeven, E. G. J. Staring, G. L. J. A. Rikken and H. Oevering, *Chem. Phys. Lett.*, **179**, 73 (1991).
13. J. Zyss, C. Dhenault, T. Chauvan and I. Ledoux, *Chem. Phys. Lett.*, **206**, 409 (1993).
14. W. M. Laidlaw, R. G. Denning, T. Verbiest, E. Chauchard and A. Persoons, *Nature*, **363**, 58 (1993).
15. J.-L. Oudar and H. Le Person, *Optics Commun.*, **15**, 258 (1975).
16. J.-L. Oudar, *J. Chem. Phys.*, **67**, 446 (1977).
17. A. Dulic, C. Flytzanis, C. L. Tang, D. Pépin, M. Fétizon and Y. Hoppilliard, *J. Chem. Phys.*, **74**, 1559 (1981).
18. J. P. Hermann, D. Richard and J. Ducuing, *Appl. Phys. Lett.*, **23**, 178 (1973).
19. J. P. Hermann and J. Ducuing, *J. Appl. Phys.*, **45**, 5100 (1974).
20. G. N. Lewis and M. Calvin, *Chem. Rev.*, **25**, 273 (1935).
21. J. Fabian and H. Hartmann, *Light Absorption of Organic Colorants*, Chap. 6, pp. 24–41 (Springer Verlag, Berlin, 1980).
22. S. Dänhe and R. Radeaglia, *Tetrahedron*, **27**, 3673 (1971).
23. T. S. Arrhenius, M. Blanchard-Desce, M. Dvolaitzky, J.-M. Lehn, and J. Malthête, *Proc. Natl. Acad. Sci., USA* **83**, 5355 (1986).
24. M. Blanchard-Desce, I. Ledoux, J.-M. Lehn, J. Malthête and J. Zyss, *J. Chem. Soc., Chem. Commun.*, 737 (1988).
25. M. Blanchard-Desce, J.-M. Lehn, I. Ledoux and J. Zyss in Ref. 5, p. 170.
26. a) J.-M. Lehn, *Angew. Chem. Int. Ed. Engl.*, **27**, 89 (1988); b) J.-M. Lehn, *Angew. Chem. Int. Ed. Engl.*, **29**, 1304 (1990).
27. H. Ikeda, Y. Kawabe, T. Sakai and K. Kawasaki, *Chem. Lett.*, 1285 (1989).
28. M. Barzoukas, M. Blanchard-Desce, D. Josse, J. M. Lehn and J. Zyss, *Chem. Phys.*, **133**, 323 (1989).

29. M. Barzoukas, M. Blanchard-Desce, D. Josse, J. M. Lehn and J. Zyss, *Materials for Nonlinear and Electro-Optics*, Inst. Phys. Conf. Ser. 103, ed. M. H. Lyons, p. 239 (IOP, Bristol, 1989).
30. J.-M. Lehn in Ref. 7, p. 436.
31. M. Blanchard-Desce, T. S. Arrhenius and J.-M. Lehn, *Bull. Soc. Chim. Fr.*, **130**, 266 (1993).
32. S. Gilmour, S. R. Marder, B. G. Tiemann and L.-T. Cheng, *J. Chem. Soc., Chem. Commun.*, 432 (1993).
33. J. O. Morley, V. J. Docherty and D. Pugh, *J. Chem. Soc., Perkin Trans. 2*, 1351 (1987).
34. R. A. Huijts and G. L. J. Hesselink, *Chem. Phys. Lett.*, **156**, 209 (1989).
35. L. T. Cheng, W. Tam, S. R. Marder, A. E. Stiegman, G. Rikken and C. W. Spangler, *J. Phys. Chem.*, **95**, 10643 (1991).
36. B. G. Tiemann, L.-T. Cheng and S. R. Marder, *J. Chem. Soc. Chem. Commun.*, 735 (1993).
37. S. R. Marder, C. B. Gorman, B. G. Tiemann and L.-T. Cheng, *J. Am. Chem. Soc.*, **115**, 3006 (1993).
38. A. Slama-Schwok, M. Blanchard-Desce and J.-M. Lehn, *J. Phys. Chem.*, **94**, 3894 (1990).
39. I. Ledoux and J. Zyss, *Chem. Phys.*, **73**, 203 (1982).
40. F. Meyers, J.-L. Bredas and J. Zyss, *J. Am. Chem. Soc.*, **114**, 2914 (1992).
41. M. H. Hutchinson and L. E. Sutton, *J. Chem. Soc.*, 4382 (1958).
42. M. Barzoukas, A. Fort, G. Klein, A. Boeglin, C. Serbutoviez, L. Oswald and J. F. Nicoud, *Chem. Phys.*, **164**, 395 (1992).
43. D. Li, M. A. Ratner and T. J. Marks, *J. Am. Chem. Soc.*, **110**, 1707 (1988).
44. H. E. Katz, K. D. Singer, J. E. Sohn, C. W. Dirk, L. A. King and H. M. Gordon, *J. Am. Chem. Soc.*, **109**, 6561 (1987).
45. J. B. Van Beek, F. Kajzar and A. C. Albrecht, *J. Chem. Phys.*, **95**, 6400 (1991).
46. J. R. Heflin, Y. M. Cai and A. F. Garito, *J. Opt. Soc. Am. B*, **8**, 2132 (1991).
47. S. Amarak, W. Toruellas, R. Zanon and G. I. Stegeman, *Optics Commun.*, **85**, 527 (1991).
48. J. B. Van Beek, F. Kajzar and A. C. Albrecht, *Chem. Phys.*, **161**, 229 (1992).
49. A. Esser, H. Fisch, K. H. Haas, E. Hädicke, J. Paust, W. Shrof and A. Tickin, *SPIE Proc.*, **1775**, 349 (1992).
50. K. L. Rustagi and J. Ducuing, *Optics Commun.*, **10**, 258 (1974).
51. E. Mc Intyre and H. F. Hameka, *J. Chem. Phys.*, **68**, 3481 (1978).
52. G. S. Agrawal, C. Cojan and C. Flytzanis, *Phys. Rev. B*, **17**, 776 (1978).
53. C. P. de Melo and R. Silbey, *Chem. Phys. Lett.*, **140**, 537 (1987).
54. G. J. Hurst, M. Dupuis and E. Clementi, *J. Chem. Phys.*, **89**, 385 (1988).
55. A. F. Garito, J. R. Heflin, K. Y. Wong and O. Zamani-Khamiri, in Ref. 5, p. 16.
56. P. Chopra, L. Carlucci, H. F. King and P. W. Prasad, *J. Phys. Chem.*, **93**, 7120 (1989).
57. B. M. Pierce, *J. Chem. Phys.*, **91**, 791 (1989).
58. Z. G. Soos and S. Ramasesha, *J. Chem. Phys.*, **90**, 1067 (1989).
59. B. M. Pierce, *SPIE Proc.*, **1560**, 148 (1991).
60. J. R. Tallent, R. R. Birge, C. W. Spangler and K. O. Havelka, *Molecular Electronics—Science and Technology*, AIP Conf. Proc. 262, ed. A. Aviram, p. 191 (AIP, New York, 1992).
61. F. Meyers and J.-L. Bredas, *Organic Materials for Nonlinear Optics III*, eds. R. A. Hann and D. Bloor (Royal Soc. chem., London, 1993), p. 1.
62. D. N. Beratan, J. N. Onuchic and J. W. Perry, *J. Phys. Chem.*, **91**, 2696 (1987).
63. P. N. Prasad and B. Reinhardt, *Chem. Mater.*, **2**, 660 (1990).
64. G. Puccetti, M. Blanchard-Desce, I. Ledoux, J.-M. Lehn and J. Zyss, *J. Phys. Chem.*, **97**, 9385 (1993).
65. J. Messier, F. Kajzar, C. Sentein, M. Barzoukas, J. Zyss, M. Blanchard-Desce and J.-M. Lehn, *Nonlinear Optics*, **2**, 53 (1992).
66. G. S. W. Craig, R. E. Cohen, R. R. Schrock, R. J. Silbey, G. Puccetti, I. Ledoux and J. Zyss, *J. Am. Chem. Soc.*, **115**, 860 (1993).
67. C. W. Spangler, K. O. Havelka, M. W. Becker, T. A. Kelleher and L.-T. Cheng, *SPIE Proc.*, **1560**, 139 (1991).
68. K. Clays and A. Persoons, *Phys. Rev. Lett.*, **66**, 2980 (1991).
69. M. Blanchard-Desce and J.-M. Lehn, work in progress.

Third-Order Nonlinear Optics of Organic Chromophores

P. N. PRASAD, M. E. ORCZYK, J. SWIATKIEWICZ, C.-K. PARK
and C. F. ZHAO

*Photonics Research Laboratory, State University of New York at Buffalo,
Buffalo, New York 14260*

Received 22 March 1994; accepted 25 March 1994

Possible strategies for optimization of third-order nonlinear optical response of organic chromophores are outlined and briefly discussed. The role of resonances and the usefulness of the new technique of phase tuned optically heterodyned Kerr gate in their investigations is described. In the experimental part, the $\chi^{(3)}$ resonant behavior of two model compounds, one of them being a representative of the newly synthesized group of phosphoylide chromophores, is investigated. The results of femtosecond phase tuned optically heterodyned OKG at the wavelength of 796 nm and DFWM at 602 nm are reported.

INTRODUCTION

Third-order nonlinear optics will play a major role in all-optical processing of information. The two important manifestations of the third-order effect are third-harmonic generation and intensity dependence of refractive index. From the point of view of optical information processing, the intensity dependence of refractive index is the useful manifestation which provides mechanism for optical switching and optical modulation. The relevant third-order susceptibility is $\chi^{(3)}(-\omega; \omega, -\omega, \omega)$ where all four interactive waves are of the same frequency. The relation between the optically induced refractive index change, Δn , and the nonlinear susceptibility can be written as:¹

$$\Delta n = n_2 I = \frac{12\pi\chi^{(3)}(-\omega; \omega, \omega, -\omega)}{cn_0^2} I. \quad (1)$$

However, near a resonance the optically induced refractive index change can have two contributions:² (i) the coherent four-photon parametric interaction described by the above pure electronic $\chi^{(3)}$ and (ii) the incoherent population dependent term due to the change in linear susceptibility, $\chi^{(1)}(-\omega; \omega)$, between the ground and the excited states ($\Delta\chi^{(1)} = \chi_e^{(1)} - \chi_g^{(1)}$). The first contribution describes virtual state interactions and is instantaneous. The second contribution is due to the population of a specific excited state. It is related to the population dynamics of this excited states and, therefore, is time-dependent. For ultrafast devices, it is desirable to optimize the materials and the operational optical frequency so that the incoherent contribution $\Delta\chi^{(1)}$ is minimized.

The three important classes of $\chi^{(3)}$ materials are: (i) semiconductors, and in particular multiple quantum wells,³ (ii) semiconductor-doped glasses⁴ and (iii) organic π -electron

systems.⁵ In the first two classes of materials the $\chi^{(3)}$ effect is due to the incoherent $\Delta\chi^{(1)}$ contribution while the organic π -electron systems have been shown to provide dominant coherent contribution i.e., $\chi^{(3)}(-\omega; \omega, -\omega, \omega)$ with time-response in femtoseconds (within the resolution of optical pulse width). This fast response, together with the ease of processing and flexibility of structural modification, makes organic and polymeric materials very attractive for all optical processing of information. However, in the use of organic and polymeric structures for $\chi^{(3)}$ devices two important issues are: (i) existing $\chi^{(3)}$ values still being at least two orders of magnitude smaller than those needed for most device concepts and (ii) complications arising from direct and sequential two-photon and higher order resonances.⁶

To address the first issue, we have focused on the study of structure-property relationship which involves synthesis and characterization of new types of structural units. For the second issue, we use femtosecond time-resolved Kerr gate studies. We recently developed⁷ femtosecond phase-tuned optically heterodyned Kerr gate method which has proved to be very useful for studying the roles of one-photon and two-photon resonances in determining the $\chi^{(3)}$ response. In this paper, we present recent results from Photonics Research Laboratory which deal with these two issues.

NEW CHROMOPHORES FOR $\chi^{(3)}$

Most effort for $\chi^{(3)}$ materials in the past have focused on pseudo-one-dimensional conjugated polymers in which the increase of effective conjugation provides an enhancement of molecular hyperpolarizability γ and hence $\chi^{(3)}$. This approach has two problems:¹ (i) the effective conjugation length is often limited by the presence of a physical or a chemical defect. Often the effective conjugation length is very small compared to the length of the polymer chain. Because of this reason, the improvement of achievable $\chi^{(3)}$ has only been modest. (ii) An increase of the effective conjugation length increases γ , but it also reduces the band gap ($\pi\pi^*$ HOMO-LUMO separation) and thus the optical transparency. It then becomes difficult to find a non-resonant optical region needed to achieve fastest speed and to avoid undesirable thermal effect.

New approaches are needed to explore avenues for enhancing $\chi^{(3)}$ by orders of magnitude. Through our systematic study of structure-property relationship, which has greatly benefited from our collaboration with the Polymer-Branch of Wright Laboratory, we have identified several structural features that enhance γ and $\chi^{(3)}$:

- (i) The presence of polarizable heavy atoms (S, I, etc.) enhances γ .
- (ii) The presence of atoms with d-orbital participation (S vs. O) enhances γ .
- (iii) Extension of π -conjugated structures in two dimensions (such as through benzimidazole N-linkage) enhances γ and also improves solubility.

Recently, we have designed and synthesized several new types of chromophores utilizing triarylphosphonium cyclopentadien which would incorporate the above structural features. The basic triarylphosphonium cyclopentadiene (phosphoylide) structural unit is shown in Figure 1.

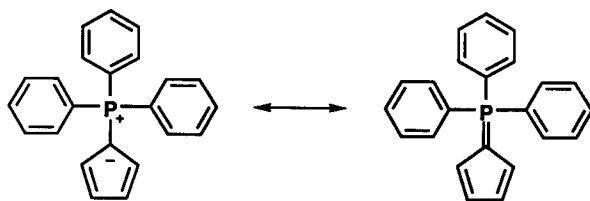


FIGURE 1

ROLE OF RESONANCES

Nonlinear optics is concerned with the interactions of optical fields with matter. Strong optical field can alter the properties of a medium in which it propagates. It is convenient to view this process as a nonlinear interaction which can affect propagation parameters, as phase, amplitude or frequency, of the field itself, as well as the propagation parameters of other optical fields present in the medium at the time of interaction or at the time delays allowing the light-induced excitation of the medium to persist. In the electric dipole approximation, neglecting magnetic dipole and higher order moments, this process can be described by a power expansion of the material's bulk polarization involving products of higher order nonlinear susceptibilities (hyperpolarizabilities $\chi^{(n)}$) and the field, E .^{1,2} In this approximation it is convenient to introduce the field-dependent effective susceptibility, χ_{eff} , given by:

$$\chi_{\text{eff}} = \chi^{(1)} + \chi^{(2)} \cdot E + \chi^{(3)} : EE + \dots \quad (2)$$

Since the refractive index relates to the optical susceptibility at the same optical frequency as $n^2 = 1 + 4\pi\chi_{\text{eff}}$, we can write a similar power expansion as (2) for n whereby

$$n = n_0 + n_1 E + n_2 EE + \dots \quad (3)$$

In this equation n_0 is the linear refractive index, n_1 and n_2 are nonlinear refractive indices (c.f., Equation (1)). Near an electronic resonance the susceptibility $\chi^{(3)}(-\omega; \omega, -\omega, \omega)$ and thereby the refractive index n of Equation (3) become complex, i.e., $n = n_{\text{Re}} + n_{\text{Im}}$. The imaginary part of n_0 describes the linear absorption (one-photon resonance). The imaginary part of n_2 and $\chi^{(3)}(-\omega; \omega, -\omega, \omega)$ has been considered to relate to two-photon absorption.² There has been relatively little thought devoted to the role of the imaginary part of n_1 (or r coefficient). In recent papers we presented a theoretical discussion and experimental results of electro-absorption and linear electro-optic effect to discuss the correlation between the imaginary part of n_1 and linear electro-absorption,⁸ as well as we discussed the influence of one-photon and two-photon resonances on the sign of the imaginary part of $\chi^{(3)}(-\omega; \omega, -\omega, \omega)$.⁹ In the case of two-photon absorption, one has intensity dependent enhanced absorption (or loss). Therefore, $n_{2,\text{Im}}$ or $\chi_{\text{Im}}^{(3)}(-\omega; \omega, -\omega, \omega)$, is positive. For one-photon absorption, one encounters a saturation at higher intensity. This is also intensity dependent absorption but with an opposite sign. Therefore, the sign $n_{2,\text{Im}}$ or $\chi_{\text{Im}}^{(3)}(-\omega; \omega, -\omega, \omega)$

will be negative at one photon resonance. The determination of the sign of the imaginary component of $\chi^{(3)}$ can thus be interpreted in terms of the dominance of one- or two-photon resonance.

Using a general definition of intensity dependence of the refractive index (or susceptibility), one can also define an effective $\chi^{(3)}$ which contains an excited state population term. Therefore, time-resolved studies of $\chi^{(3)}$ can provide valuable information on the excited state dynamics. The details of this theoretical description are provided elsewhere.^{10,11} Here we briefly review this approach. For simplicity, we consider here only the resonant behavior of a centrosymmetric (vanishing $\chi^{(2)}$) material for which the material susceptibility can be described as:

$$\chi = \chi_g^{(1)} + 3\chi_g^{(3)}:EE + \frac{N}{N_0}(\chi_e^{(1)} - \chi_g^{(1)}) + \dots \quad (4)$$

The frequency representation is dropped again for simplicity of notation with an understanding that, in the present context, the nonlinear susceptibility is $\chi^{(3)}(-\omega; \omega, -\omega, \omega)$. In Equation (4), $\chi_g^{(n)}$ stands for the n -th order susceptibility of the medium consisting of the molecules in their ground state, and $\chi_e^{(1)}$ is the linear susceptibility corresponding to excited state molecules, their density being N . N_0 is the total density of molecules. The temporal behavior of N depends on the kinetics of formation of excited species and their decay. The population contribution will depend on factors like the laser pulse parameters, the experimental geometry and kinetic properties of the excited species. In the case of two-photon generated species, the population, N , is proportional to I^2 . Therefore, the incoherent contribution derived from excited state population will have the same electric field dependence as a $\chi^{(5)}$ process.^{10,11} The time dependence of the effective $\chi^{(3)}$, therefore, through the incoherent term can provide valuable information on the dynamics of excited states.

The various types of resonances and excited state dynamics which may contribute to the incoherent nonlinearities and also yield a significant imaginary component are related to two-, three- or four-level systems which are coupled by a one-photon resonance, a direct two-photon resonance or a sequential two-photon absorption. These different resonances and their excited state dynamics will manifest differently in the time and intensity dependence of the real and the imaginary parts of $\chi^{(3)}$ as well as in the signs of $\text{Im}\{\chi^{(3)}\}$.⁹ For example, a direct two-photon resonance will yield a nonlinear incoherent response (time-delayed component) dependent on the fifth power of intensity.^{10,11} The imaginary part will be positive¹¹ and the transient absorption will show induced absorption with an instantaneous response.¹⁰

DETERMINATION OF THE COMPLEX THIRD-ORDER NONLINEARITIES

As discussed above, in order to develop a satisfactory understanding of the dynamics of excited states involved in determining the resonant third-order nonlinearity, one needs to study the spectral profile and the time dependence of both the magnitudes and signs (i.e., the phase of the nonlinearity) of the real and the imaginary parts of the complex $\chi^{(3)}$. It is important, thus, to gain straightforward information about the signs of the

probed nonlinearities. Below we describe briefly the newly developed phase-tuned optically heterodyned Kerr gate method,⁷ which was used in these studies. The method is equally suited for the study of solid, liquid (solutions) as well as thick or thin film samples. The details of the method are described elsewhere^{7,11} and here we limit ourselves only to presentation of some of its most important experimental considerations.

This method takes advantage of selective (i.e., optically phase tuned) enhancement of either the real or the imaginary component of the nonlinear response of the medium under study, followed by a polarization sensitive (optically heterodyned) detection. In the optical Kerr gate process the polarization state of the probe beam is analyzed.² In a classical homodyne version of the Kerr gate experiment an orthogonal polarization component in the probe beam is created through optically induced birefringence induced by the presence of the pumping beam. The measured intensity contains contributions from both the real and the imaginary parts of nonlinearity. Heterodyne detection, on the other hand, involves mixing of the OKG signal with a given fraction of a local oscillator signal, which may be the transmitted portion of the original probe itself. In this case the analyzer is rotated by some angle, ϕ , to admit a small contribution from the x component of the field which constitutes a local oscillator. In general, $\chi^{(3)}$ is complex; therefore the analyzed beam will contain components due to both the real and the imaginary parts of $\chi^{(3)}$. It can be shown¹¹ that the relevant component of the generated field due to the imaginary part of $\chi^{(3)}$ is in phase with the local oscillator whereas the component due to the real part of $\chi^{(3)}$ is $\pi/2$ out of phase. In the presented technique, the phase relation between the nonlinear response signal and the local oscillator beam is established by the presence or absence of a phase retardation element in the probe beam in front of the analyzer. For this purpose a properly oriented quarter-wave plate with one principal axis parallel to the probe beam polarization is optionally inserted in the signal path. The quarter-wave plate imposes a fixed $\pi/2$ phase bias between the local oscillator and the Kerr signal. In order to implement phase-sensitive (lock-in) detection one often modulates the pump beam intensity. Measuring at the chopping frequency, for small angles up to first order in ϕ we obtain the detected signal as:¹¹

$$I \propto \xi_{\text{Im}}(L)\phi + \text{const.}, \quad (5)$$

without $\pi/2$ phase bias, and

$$I \propto \xi_{\text{Re}}(L)\phi + \text{const.}, \quad (6)$$

with the $\pi/2$ phase bias imposed. In the former case the detection favors the imaginary component of the signal, ξ_{Im} while in the latter case the real component, ξ_{Re} is favored. From the experimental point of view, it is important to note here that the functions ξ_{Im} and ξ_{Re} are linearly dependent on, respectively, the imaginary part and the real part of the third-order susceptibility probed in a given experimental configuration. This important property allows us to access not only the magnitude but also the sign of the probed nonlinearity, in contrary to the methods employing homodyne detection which sense the signals dependent on the quadratures of investigated susceptibilities.

Performing the dependence of the OKG signal on the analyzer angle ϕ we obtain linear plots of the form $I = z_{\text{Im(Re)}}\phi + \text{const.}$, the coefficient z being proportional either to the imaginary component, $\xi_{\text{Im}}(L)$, or to the real component, $\xi_{\text{Re}}(L)$ of Equations (5)

and (6). Having the z -coefficients for the investigated sample, $z_{\text{Im(Re)}}^r$, and for the reference sample, $z_{\text{Im(Re)}}^s$, of known effective susceptibility, $\chi_r^{(3)}$, we can readily determine the real and the imaginary parts of the third-order susceptibility of the sample, $\chi_s^{(3)}$, according to:

$$(\chi_s^{(3)})_{\text{Re(Im)}} = \frac{z_{\text{Re(Im)}}^s}{z_{\text{Re(Im)}}^r} \frac{1}{R_2^s} (\chi_r^{(3)})_{\text{Re(Im)}}, \quad (7)$$

where R_2^s stands for the correction factor for the attenuation of the beams in the sample due to absorption. As we have shown above, phase-tuned optically-heterodyned Kerr gate technique allows one for a selective enhancement and separate determination of either the real or the imaginary part of the nonlinear response of the investigated medium. The use of sub-picosecond and femtosecond pulses additionally allows for a separation of the coherent instantaneous nonlinear optical response from the delayed incoherent signal.

EXPERIMENTAL

The measurements on the selected chromophores have been performed using the above discussed phase-tuned optically heterodyned Kerr gate technique and the inner reference method.¹ The laser system used for the latter technique consisted of a mode-locked Nd:YAG laser with a fiber optic pulse stretcher/compressor and a synchronously pumped dye laser followed by a three-stage dye amplifier pumped at 30 Hz repetition rate with a Q -switched Nd:YAG laser. The system delivers 400-fs pulses centered at 602 nm with the energy of approximately 0.4 mJ per pulse. The employed measurement setup was a standard folded boxcars DFWM configuration described earlier.¹⁰

For the phase-tuned optically heterodyned Kerr gate method we used a femtosecond Ti:sapphire laser system (Clark-MXR Inc., model CPA-1). Pulses of 170 fs duration and spectrum centered at 796 nm with 1 kHz repetition rate were used in the experiments. Only a small fraction (3.5 μ J per pulse) of the total output from the Ti:sapphire regenerative amplifier was used for the purpose of measurements, for which we implemented the setup shown in Figure 2. The laser beam is split into two portions at 20:1 ratio. The stronger beam is used as a pump beam, I_2 , and the weaker beam, after passing through a variable delay line, RR, is used as a probe beam, I_1 . The pump beam passes through a chopper working at a frequency of ~ 43 Hz to implement lock-in detection. Polarizers, P_1 and P_2 , are placed in the paths of the probe and the pump beams, respectively, before the sample. Both beams are polarized at 45° with respect to each other. Another polarizer, P_3 , is placed in the path of the signal beam after the sample in front of the detector, PD. A quarter-wave plate, QP, can be optionally inserted in front of the analyzer, P_3 , in order to provide a $\pi/2$ optical phase tuning between the two orthogonal components of the signal beam.

RESULTS AND DISCUSSION

Selected phosphoylides for the present studies were synthesized in our laboratory. Details of the synthetic approach will be described elsewhere. The structure of a

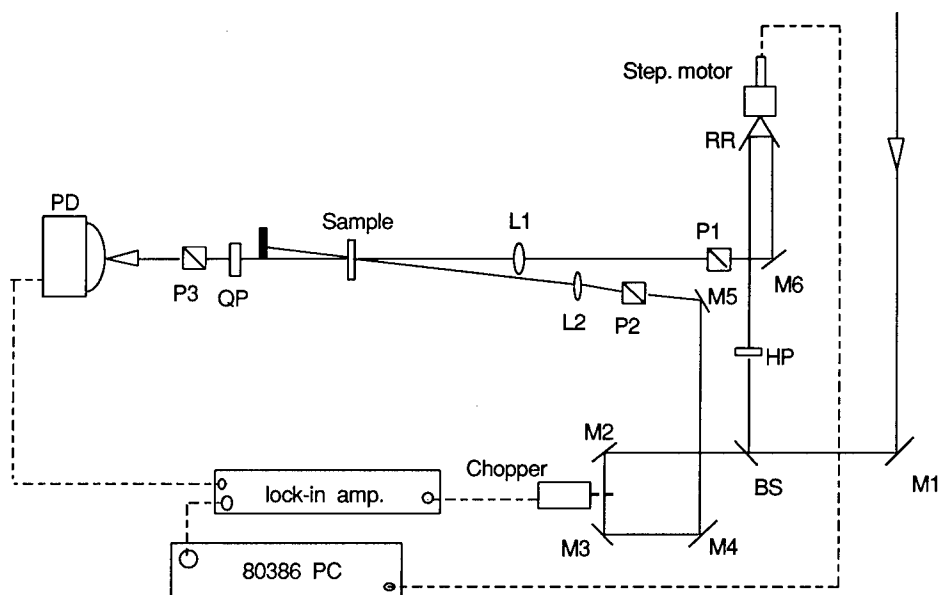


FIGURE 2 Experimental setup implemented for the phase-tuned optically heterodyned Kerr gate technique. M_1 – M_6 : mirrors; L_1 , L_2 : lenses; P_1 – P_3 : polarizers; QP: quarter-wave retardation plate; HP: half-wave retardation plate; BS: beamsplitter; PD: photodetector; RR: optical delay line.

representative phosphoylide, triphenylphosphonium cyclopentadienylene-2,5-bis(4-ethenylene pyridinium methyl iodide) hereafter referred to as TPCEPM, is shown in Figure 3. The linear absorption spectrum of dimethylsulfoxide (DMSO) solution of this chromophore is shown in Figure 4.

This compound was studied using the inner reference method implemented in a degenerate four-wave mixing geometry at the wavelength of 602 nm. The inner reference method, described in detail elsewhere,¹ is most suitably used in conjunction with DFWM or optical Kerr gate techniques. It relies on measuring the values of $\chi^{(3)}$ for a series of solutions containing the investigated molecules. For each concentration, the intensity of the signal is compared to that obtained for a reference sample (which can be the pure solvent itself) under identical conditions. An effective value of the third order susceptibility for the solution, equal to the modulus of the complex susceptibility, $|\chi_{\text{eff}}^{(3)}|$, responsible for the effect, is then calculated from the appropriate equations.¹ For solution measurements, the effective susceptibility determined for the solution sample contains contribution from both the solute and the solvent. Thus, having a set of $|\chi_{\text{eff}}^{(3)}|$ values collected for different concentrations of the solution, one can derive the real part, γ_{Re} , and the modulus, $|\gamma_{\text{Im}}|$, of the solute's molecular second hyperpolarizability. The method is relatively easy to implement, however it is important that the absorption corrections be taken into account precisely since their actual magnitude may in some cases critically affect determination of the sign of γ_{Re} . Using this method we derived for the TPCEPM chromophore $\gamma_{\text{Re}} = 8.1 \times 10^{-32}$ esu and $|\gamma_{\text{Im}}| = 22.3 \times 10^{-32}$ esu. The results are summarized in Table 1.

TABLE 1

Complex molecular second hyperpolarizabilities determined by the DFWM inner reference method at the wavelength of 602 nm.

Sample	λ_{\max} [nm]	ϵ [$L\text{ cm}^{-1}\text{ mol}^{-1}$] @ 602 nm	γ_{Re} [10^{-32} esu]	$ \gamma_{\text{Im}} $ [10^{-32} esu]
TPCEPM	550	5.3	8.1	22.3

Another chromophore, which incorporates some of the γ -enhancing features mentioned previously, chosen for the reported studies was 2,5-dimethoxyphenylene-1,4-bis(4-ethenylene pyridinium methyl iodide) hereafter referred to as DMPEPM. The chromophore structure is also shown in Figure 3. The linear absorption spectrum of DMSO solution of DMPEPM chromophore is shown in Figure 4. As one can see, the chromophore is virtually transparent at the wavelength of 796 nm. A two-photon absorption at $\lambda = 398\text{ nm}$ may be expected, on the other hand, to be an important mechanism of resonant enhancement of the optical susceptibility.

The angular dependencies of the phase-tuned optically heterodyned Kerr gate signal for the DMPEPM compound dissolved in DMSO are presented in Figure 5. The dependence for the real part of the nonlinearity for the DMSO solvent is also shown as a reference. It is worthy to note here that, since the third-order nonlinearity of DMSO at the wavelength of 796 nm has no imaginary component, the corresponding trace would have a zero slope (horizontal line) and so we do not show it in the Figure. The conclusion that can be drawn from these traces is that both the real and the imaginary part of γ for DMPEPM chromophore at $\lambda = 796\text{ nm}$ are positive. By taking the relevant slopes of the dependencies corresponding to the solution of DMPEPM and pure DMSO in Figure 5 and using $\chi^{(3)} = 4.9 \times 10^{-14}\text{ esu}$ (obtained from an independent experiment) as a non-resonant value for the nonlinear susceptibility of DMSO we can derive the values of the real and the imaginary parts of molecular second hyperpolarizability of the DMPEPM molecule. Straightforward calculations based on Equation (7) yield for DMPEPM $\gamma_{\text{Re}} = 1.6 \times 10^{-32}\text{ esu}$ and $\gamma_{\text{Im}} = 2.1 \times 10^{-32}\text{ esu}$, respectively.

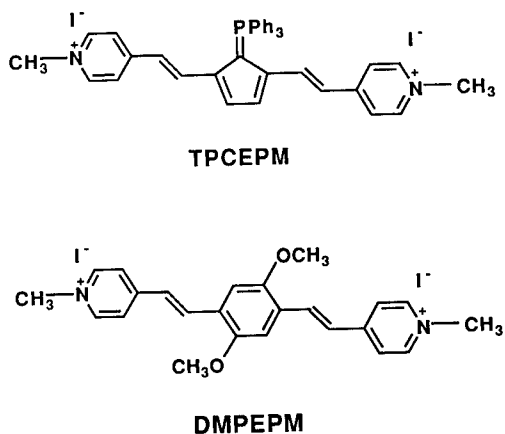


FIGURE 3

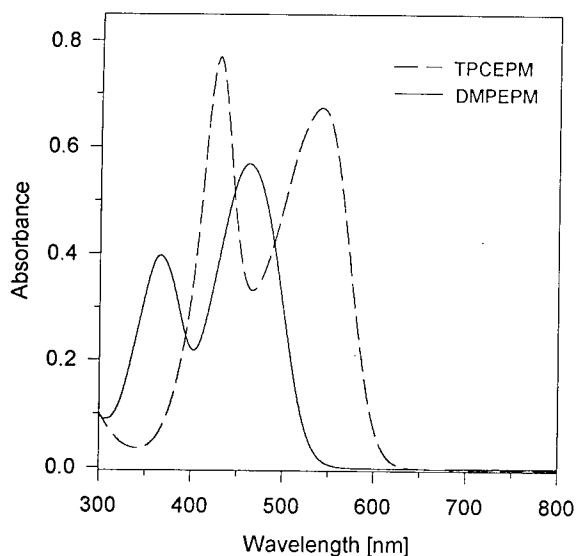


FIGURE 4 Linear absorption spectra of the TPCEPM (broken line) and the DMPEPM (solid line) chromophores in dimethylsulfoxide solution.

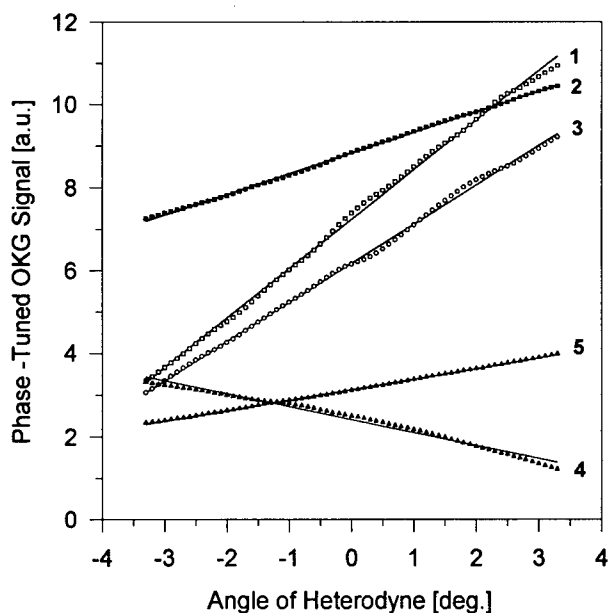


FIGURE 5 Angle-of-heterodyne dependencies of the phase-tuned optically heterodyned Kerr gate signal. (1) and (2): the real and the imaginary parts of the response from a solution of DMPEPM chromophore in DMSO, respectively; (3): the real part of the response from the pure DMSO solvent; (4) and (5): the real and the imaginary parts of the response from a solution of DTDCI dye in DMSO, respectively. The lines are linear least-square fits to the data points.

TABLE 2
Complex molecular second hyperpolarizabilities determined by the phase-tuned optically heterodyned Kerr gate method at the wavelength of 796 nm.

Sample	λ_{\max} [nm]	ϵ [$L \text{ cm}^{-1} \text{ mol}^{-1}$] (at 796 nm)	γ_{Re} [10^{-32} esu]	γ_{Im} [10^{-32} esu]
DMPEPM	475	27.6	+1.6	+2.1
DTDCI	653	32.6	-5.9	+2.2
DMSO		0	$+1.5 \times 10^{-4}$	0

As an illustration to the discussion of the signs of nonlinear susceptibilities, we show here for comparison angle-of-heterodyne traces for DTDCI laser dye. In this case we can see that the dependencies obtained for the real and the imaginary parts of the third-order nonlinearity are of opposite signs (and also opposite slopes); we obtain a positive sign for the imaginary part of nonlinearity and a negative one for the real part. The results of the discussed optically heterodyned phase-tuned Kerr gate investigations are summarized in Table 2.

In addition to optically heterodyned Kerr gate studies, we performed also complementary $\chi^{(3)}$ investigations of the DMPEPM chromophore using the inner reference method. In Figure 6 the concentration dependence of the effective susceptibility, $|\chi_{\text{eff}}^{(3)}|$, for a series of solutions of DMPEPM in DMSO is presented. The relation between the measured effective nonlinear susceptibility and the microscopic parameters is as

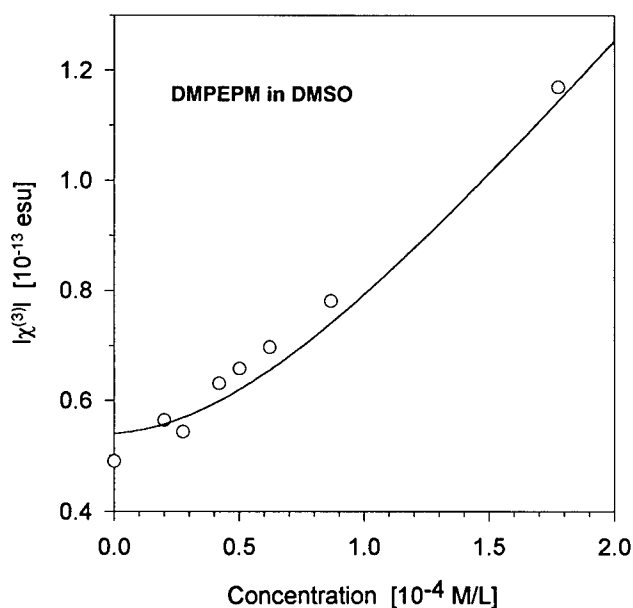


FIGURE 6 Concentration dependence of $|\chi_{\text{eff}}^{(3)}|$ measured in a DFWM experiment for a DMSO solution of DMPEPM chromophore.

follows: $|\chi_{\text{eff}}^{(3)}| = [(\chi_{\text{sol}}^{(3)} + L^4 N_x \gamma_{x,\text{Re}})^2 + (L^4 N_x \gamma_{x,\text{Im}})^2]^{1/2}$, where $\chi_{\text{sol}}^{(3)}$ is the real part of the solvent's third-order susceptibility (the imaginary part vanishes for a non-absorbing medium), N_x and γ_x stand for the density and the molecular second hyperpolarizability of the investigated specimen, respectively. L is the local field correction factor approximated by the Lorentz expression $L = (n^2 + 2)/3$, where n is the refractive index of the solution at the working wavelength. Shape of the dependence in Figure 6, where $|\chi_{\text{eff}}^{(3)}|$ monotonically increases with concentration of DMPEPM molecules in the solution, is typical of molecules with positive γ_{Re} . In the opposite case a characteristic local minimum, magnitude of which depends on the actual value of the negative γ_{Re} , appears at low concentrations. This becomes evident upon inspection of the above equation relating $|\chi_{\text{eff}}^{(3)}|$ with the concentration of the solution. For $\gamma_{x,\text{Re}} < 0$, the $\chi_{\text{sol}}^{(3)} + L^4 N_x \gamma_{x,\text{Re}}$ term decreases initially with increasing concentration of the investigated molecules, N_x , and, as its certain value brings the overall $\chi_{\text{eff}}^{(3)}$ to a local minimum or even to zero in the case of non-resonant media with $\gamma_{x,\text{Im}} = 0$.

In our recent paper⁹ we discussed the results of investigations of complex third-order nonlinear optical susceptibilities in relation to obtaining spectroscopic information on one- and two-photon resonances. We showed that near a one-photon resonance the saturation effect leads to a negative imaginary component of $\chi^{(3)}$ while near a two-photon resonance the sign of the imaginary component of $\chi^{(3)}$ is positive. The result obtained in this work corroborates with the previous studies since the positive sign of the imaginary part of nonlinearity of DMPEPM is indicative of its two-photon absorptive origin. Indeed, at higher fluencies of the Ti:sapphire beam ($\lambda = 796 \text{ nm}$) a broadband upconverted emission could be seen from the DMSO solution of DMPEPM.

ACKNOWLEDGEMENTS

This research was supported by the National Science Foundation, Grant No. DMR-90-22017, and by the U. S. Air Force Office of Scientific Research, Contract No. F-49620-93-C0017.

REFERENCES

1. P. N. Prasad and D. J. Williams, *Introduction to Nonlinear Optical Effects in Molecules and Polymers* (Wiley, New York, 1991).
2. M. D. Levenson, *Introduction to Nonlinear Laser Spectroscopy* (Academic Press, New York, 1982).
3. B. E. A. Saleh and M. C. Teich, *Fundamentals of Photonics* (Wiley-Interscience, New York, 1991).
4. L. C. Klein (Ed.), *Sol-Gel Technology for Thin Film, Fibers, Preforms, Electronics and Specialty Shapes* (Noyes Publications, Park Ridge, 1988).
5. D. S. Chemla and J. Zyss (Eds.), *Nonlinear Optical Properties of Organic Molecules and Crystals*, Vol. 2 (Academic Press, New York, 1987).
6. K. W. DeLong and G. I. Stegeman, *Appl. Phys. Lett.*, **57**, 2063 (1990).
7. M. E. Orczyk, M. Samoc, J. Swiatkiewicz, N. Manickam, M. Tomoia-Cotisel and P. N. Prasad, *Appl. Phys. Lett.*, **60**, 2837 (1992).
8. J. Bradshaw, M. E. Orczyk, J. Zieba and P. N. Prasad, *Nonlinear Optics* (1994), in press.
9. M. E. Orczyk, J. Swiatkiewicz, G. Huang and P. N. Prasad, *J. Phys. Chem.* (1994), in press.
10. Y. Pang, M. Samoc and P. N. Prasad, *J. Chem. Phys.*, **94**, 5282 (1991).
11. M. E. Orczyk, M. Samoc, J. Swiatkiewicz and P. N. Prasad, *J. Chem. Phys.*, **98**, 2524 (1993).

Effect of Aromaticity on the Second Hyperpolarizability of Conjugated Donor-Acceptor Molecules

G. BOURHILL^a, B. G. TIEMANN^{a,b}, J. W. PERRY^{*a,b} and S. R. MARDER^{*a,b}

^a*Jet Propulsion Laboratory, California Institute of Technology, Pasadena, CA 91109, USA*, ^b*The Beckman Institute, California Institute of Technology, Pasadena, CA 91125, USA*

Received 12 January 1994; accepted 4 February 1994

The second hyperpolarizabilities, γ , of a series of conjugated donor-acceptor molecules, with varying donor and acceptor strengths, containing diene, triene, phenyl and styryl bridges were measured, in solvents of varying polarity, by third harmonic generation. The γ values for chromophores containing phenyl or styryl bridges, and their solvent dependence, correspond to a lower degree of neutral/charge-transfer mixing than for polyenes of similar conjugation length. For the phenyl- or styryl-bridged molecules, γ increases with increasing donor and acceptor strength, suggesting that even for the julolidino/nitro combination, representing a strong donor/acceptor pair, γ has not been maximized. Barbituric acid acceptors, that can gain a degree of aromaticity upon polarization, on a phenyl-containing bridge, lead to γ values that are enhanced relative to analogous molecules with moderately strong acceptors, such as dicyanovinyl. The indanedione acceptor, whose conjugation length may increase upon polarization, also leads to large γ values.

INTRODUCTION

There is currently significant interest in understanding the relationships between molecular structure and nonlinear optical polarizabilities of conjugated organic molecules. Recently, considerable progress^{1,2} has been made in developing and understanding the relationship between the first hyperpolarizability, β , and a key structural parameter of conjugated donor-acceptor molecules: the bond length alternation (BLA) defined as the difference in length of adjacent carbon-carbon bonds. The magnitude and sign of BLA is dependent² on the degree of mixing between neutral and charge-transfer forms of the molecule. By using a two-state model,³ it has been shown¹ that for a given conjugated bridge, a particular combination of donor and acceptor strength is required to obtain the appropriate degree of mixing between neutral and charge-transfer states (and hence BLA) necessary to optimize β for structures of a fixed length. Additionally, it was shown that since the structure of the conjugated bridge can strongly influence the coupling of the donor and acceptor, and thereby the mixing of neutral and charge-separated states, the choice of bridge can have a controlling influence on the hyperpolarizability. In particular, conjugated bridges containing

* To whom correspondence should be addressed.

groups that are aromatic in the neutral resonance form can impede charge-transfer mixing. This is because aromatic stabilization energy is lost upon charge-transfer, leading to a larger energy gap between the neutral and charge-transfer forms, and thus to weaker mixing. By utilizing groups that gain aromaticity upon charge-transfer, it is possible to offset the loss of aromaticity in phenyl-type rings upon polarization and to achieve higher degrees of neutral/charge-transfer mixing. Dramatically enhanced values of β have been realized¹ for chromophores that possess, in the neutral form, one phenyl ring and a group that gains aromaticity upon charge-transfer, relative to the corresponding stilbene-type chromophores that possess two phenyl rings in the neutral resonance form.

Quite recently, experimental⁴ and theoretical⁵ studies have indicated that the second hyperpolarizability, γ , is also sensitive to the degree of neutral/charge-transfer mixing. For example, measurements of γ for donor-acceptor polyenes as a function of solvent polarity and acceptor strength, by which the mixing and thus the ground-state polarization and BLA were varied, showed⁴ a peaked behavior and a change in sign for γ , consistent with the trend predicted theoretically.

In this paper, we present results on γ for conjugated donor-acceptor molecules possessing, in the neutral form, phenyl rings and either conventional acceptors (such as formyl, nitro, and dicyanovinyl) or acceptors that can gain a degree of aromaticity upon charge-transfer (such as thiobarbituric acid). Dialkylaminophenyl molecules possessing thiobarbituric acid acceptors are shown to exhibit γ values that are comparable to those of dialkylaminonitrostyrenes and the longer dimethylaminonitrostilbene chromophore, and are enhanced compared to dialkylaminostyryl molecules with cyano or formyl acceptors, as well as to a dialkylaminophenyl molecule with a dicyanovinyl acceptor. The γ values, as well as their solvent dependence, for phenyl- and styryl-bridged molecules containing formyl and dicyanovinyl acceptors are compared to the values for analogous polyenes of comparable length.

EXPERIMENTAL

The solvents used in this study (acetonitrile, dichloromethane, 1,4-dioxane and carbon tetrachloride) were all spectral grade solvents obtained from Burdick and Jackson, Inc. The following compounds were purchased commercially and used as received: Aldrich Chemical Co., 4-dimethylaminobenzonitrile (purity 98%), 4-dimethylaminobenzaldehyde (99%), 4-dimethylaminocinnamaldehyde (98%), 4-diethylaminocinnamionitrile (97%); and Lancaster Synthesis, Inc., 4-nitro-N,N'-dimethylaniline (98%). The other compounds examined were prepared according to literature methods.⁶⁻¹¹

The second hyperpolarizabilities of the molecules studied were determined by third harmonic generation (THG) measurements on solutions using apparatus and methodology described elsewhere.¹² Briefly, measurements of the third harmonic intensity fringes, obtained by translating a thick-window wedged cell¹³ across the laser beam, are measured on a series of solutions of varying solute concentration and on the neat solvent. These fringes are fit to a sine-squared function to obtain the peak intensity and coherence length as a function of solute concentration. The concentration dependence of the normalized (relative to solvent) peak intensity is fit to an expression, derived from

a model for the solution third-order susceptibility that is linearly additive in the solute and solvent hyperpolarizability, in order to determine the solute hyperpolarizability. The model ignores interactions between molecules, but allows for a complex solute hyperpolarizability. The THG measurements were performed with a fundamental wavelength of 1907 nm. The third harmonic wavelength of 636 nm was therefore far removed from that of the lowest-lying electronic absorption of all chromophores studied. The fits to the concentration dependent THG data for all molecules reported here indicate negligible imaginary components ($<10\%$ of the real part) of the hyperpolarizability. The values of the hyperpolarizability of the four solvents used in this study, necessary to extract the solute γ from the concentration-dependent THG intensity plot, were obtained from the literature.¹⁴⁻¹⁶ The relative values were checked for consistency by measurements in our laboratory and were in all cases within 10% of the reported value.

RESULTS

The structures of the compounds studied in this paper are shown in Figures 1-3. The γ values for these molecules were determined in different solvents since the degree of mixing between neutral and charge-transfer states can be fine-tuned by varying the solvent polarity.¹⁷ The γ values of molecules containing a diene or benzene bridge are presented in Table 1 and those containing a triene or styryl bridge are presented in Table 2.

The diene 1 shows no solvent dependence of γ , whereas the dicyano molecule 2 exhibits a decrease in γ with increasing solvent polarity and a negative γ in CH_3CN . The five carbon cyanine 3 exhibits a negative γ . The values for compounds 7-9 have been reported previously⁴ and are included here for comparison. Note that the longer aldehyde 7 exhibits stronger solvent dependence and generally larger γ values than the shorter aldehyde 1. Also, compound 8 shows negative γ values which strongly decrease with increasing solvent polarity and whose magnitudes are larger than that for 2. Also, note the order of magnitude increase in γ for the longer cyanine 9 as compared to 3.

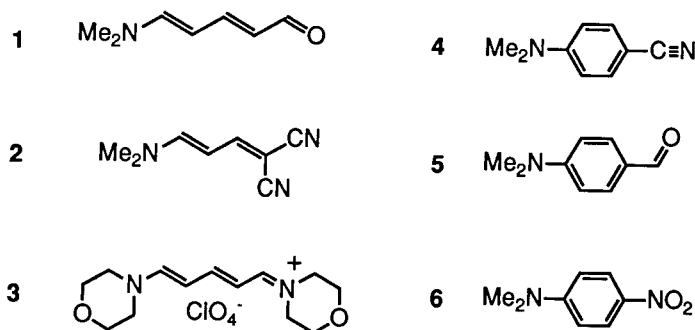


FIGURE 1 Structures of diene- and phenyl-bridged molecules examined. $\text{Me}\equiv\text{CH}_3$.

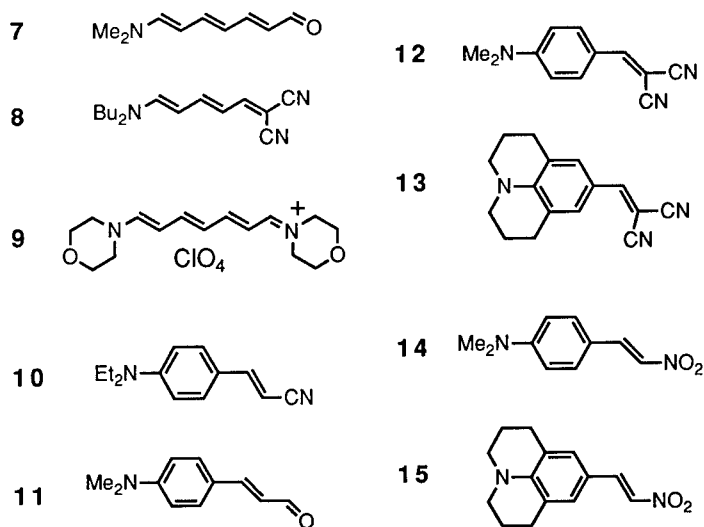


FIGURE 2 Structures of triene- and styryl-bridged molecules examined. Et \equiv C₂H₅, Bu \equiv n-C₄H₉.

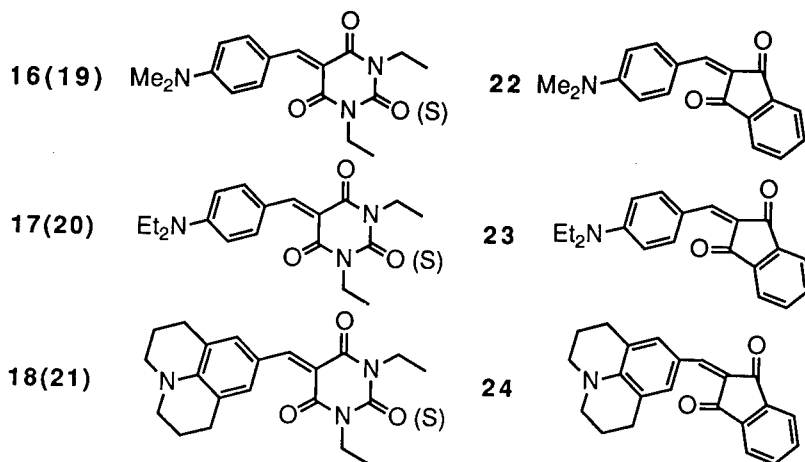


FIGURE 3 Structures of chromophores examined containing either diethylbarbituric acid, diethylthiobarbituric acid or indanedione acceptors.

The γ values for the benzene- (4–6) and styryl-bridged (10–15) molecules are essentially solvent independent except for compound 15, which has a julolidinyl donor, a styryl bridge and a nitro acceptor, and which exhibits an increase in γ in the most polar solvent. For benzene- and styryl-bridged molecules, γ increases as the acceptor strength is increased. For the styryl-bridged molecules, γ also increases as the donor strength is increased²⁰ on going from a dialkylamino to a julolidino donor.

Table 3 lists the γ values for molecules containing diethylbarbituric acid (16–18), thiobarbituric acid (19–21) and indanedione acceptors (22–24). The γ values for each of the molecules in Table 3 show no solvent dependence. The hyperpolarizability of

TABLE 1

Solvent-dependent second hyperpolarizabilities of molecules of similar conjugation lengths (7 atoms) but with different acceptor groups and bridging networks. γ values have units of 10^{-36} esu, with an estimated error of $\pm 15\%$. Insolubility precluded the determination of γ for some chromophores in particular solvents. Solvent polarity decreases from left to right. The wavelength of maximum absorption (in nm) is given within parentheses. There is excellent agreement between the γ values for 4–6 and those reported by Cheng *et al.*¹⁶

Molecule	Solvent			
	CH ₃ CN	CH ₂ Cl ₂	Dioxane	CCl ₄
1	+16 (360)	+17 (360)	+22 (354)	+20 (350)
2	–7 (374)	+5 (376)	+10 (370)	
3	–40 (416)			
4	+12 (292)	+11 (294)	+10 (288)	+13 (292)
5	+16 (336)	+15 (338)	+19 (330)	+17 (330)
6	+33 (394)	+32 (392)	+31 (382)	

TABLE 2

Solvent-dependent γ values for molecules possessing either a triene or styryl bridge. The conjugation length for all molecules is similar (9 atoms). Other details as for Table 1. Good agreement exists between the γ values for 11 and 12 and those reported by Cheng *et al.*¹⁸ A γ value of $+200 \times 10^{-36}$ esu for 11 has been reported by Puccetti and coworkers,¹⁹ the difference perhaps due to conventions used to define the hyperpolarizability.

Molecule	Solvent		
	CH ₃ CN	CH ₂ Cl ₂	Dioxane
7	+113 (418)	+105 (420)	+40 (402)
8	–120 (476)	–50 (480)	–25 (468)
9	–370 (516)	–325 (526)	
10	+68 (368)	+50 (372)	+51 (364)
11	+73 (378)	+65 (384)	+66 (372)
12	+82 (430)	+75 (432)	+66 (420)
13	+95 (456)	+81 (458)	+90 (444)
14	+190 (438)	+160 (442)	+170 (422)
15	+370 (478)	+230 (482)	+230 (454)

molecules possessing the thiobarbituric acid moiety are larger than those with the barbituric acid group and are the same as those with the indanedione acceptor. On increasing the donor strength from dimethylamino to diethylamino or julolidino donors, there is a concomitant increase in γ .

TABLE 3

Solvent-dependent second hyperpolarizabilities for molecules possessing diethylbarbituric acid, Diethylthiobarbituric acid and indanedione acceptor groups. Other details as for Table 1.

Molecule	Solvent		
	CH ₃ CN	CH ₂ Cl ₂	Dioxane
16	+ 100 (458)	+ 100 (460)	+ 120 (450)
17	+ 135 (464)	+ 117 (466)	+ 135 (456)
18		+ 140 (486)	+ 170 (474)
19	+ 200 (492)	+ 220 (494)	+ 230 (480)
20	+ 280 (498)	+ 250 (500)	+ 270 (486)
21		+ 280 (520)	
22	+ 220 (480)	+ 190 (480)	+ 220 (468)
23	+ 280 (486)	+ 245 (486)	+ 285 (475)
24		+ 272 (512)	

DISCUSSION

Neutral/Charge-Transfer Mixing and Bond Length Alternation

Recent calculations⁵ and experiments⁴ suggest that γ for simple donor-acceptor polyenes is correlated with changes in the molecular geometry of the conjugated carbon chain, i.e., the difference in length of adjacent carbon-carbon bonds, termed the bond length alternation (BLA). The BLA for donor-acceptor polyenes¹⁷ is determined by the degree of mixing between the two limiting charge-transfer resonance structures (Fig. 4). The mixing of the two limiting forms is dependent upon several factors including the relative energy of the two structures, as well as the electronic coupling between them. The energy difference between neutral and charge-transfer forms of simple donor-acceptor polyenes is essentially determined by the donor and acceptor strength and the solvent polarity. The BLA for a given energy difference between the two forms will be determined by the coefficient of each form in the lower energy mixed state, and by the structure of the two limiting forms. For a large energy difference between neutral and charge-separated forms (A in Fig. 4), the mixing is weak and the neutral form is the dominant contributor to the ground state (resulting in positive BLA), which then resembles an unsubstituted polyene. For strong donors and acceptors (B in Fig. 4) and polar solvents, the energy difference of the two forms will be small, leading to an increased mixing and reduced BLA. When both forms are of equal energy, the mixing is maximized and the ground-state possesses essentially zero BLA, analogous to a symmetrical cyanine (C in Fig. 4).²¹ Thus, by varying the donor and acceptor

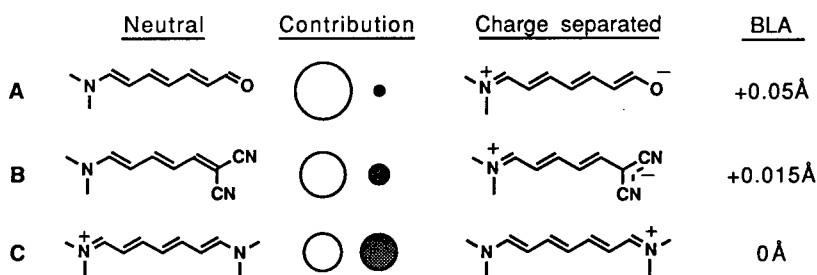


FIGURE 4 Neutral and charge-transfer resonance forms of donor-acceptor polyenes (A and B) and the two limiting resonance structures of a symmetrical cyanine (C). The size of the circles indicates the contribution of the adjacent form to the ground state. The bond length alternation values were determined by X-ray crystallographic studies on single crystals. For A, X-ray crystallographic and Raman spectroscopic studies have revealed¹⁷ that the neutral form contributes more to the ground-state geometry than the charge-separated form, whereas Raman and electronic absorption spectroscopy have revealed that the ground-state structure of B is cyanine-like in polar solvents¹² consistent with the small positive BLA in the solid state. The two canonical forms contribute equally for the cyanine, leading to zero bond length alternation.²¹

strength or the solvent polarity, the mixing of the two forms and thus the structure can be varied over a wide range.^{17,22}

Dependence of γ on Bond Length Alternation

Electric-field dependent quantum chemical calculations predict the relation between γ and BLA shown in Figure 5.⁵ The variation of γ can be understood in terms of a three-state model²³⁻²⁵ where γ is given by

$$\gamma \propto - \underbrace{\left(\frac{\mu_{ge}^4}{E_{ge}^3} \right)}_{N1} + \underbrace{\left(\frac{\mu_{ge}^2 \mu_{ee'}^2}{E_{ge}^2 E_{ee'}} \right)}_{P1} + \underbrace{\left(\frac{\mu_{ge}^2 (\mu_{ee} - \mu_{gg})^2}{E_{ge}^3} \right)}_{P2} \quad (1)$$

where g labels the ground state, e and e' label the two excited states, and μ and E are the dipole matrix element and transition energy, respectively, between the labelled states. The positive term, P2, can be related to the first hyperpolarizability β as $P2 = \beta(\mu_{ee} - \mu_{gg})/E_{ge}$. This term goes to zero for centrosymmetric polyenes (where $BLA \sim 0.12\text{\AA}$)²⁶ and for symmetric cyanines (where $BLA = 0$),²¹ since $\mu_{ee} - \mu_{gg}$ becomes negligible at these two limits.¹ Hence at the polyene- and cyanine-limit, γ is determined by the sum of two terms of opposite sign, N and P1. Theory^{23,24} and experiment^{4,27} give positive γ for polyenes and negative γ for cyanines, suggesting that $P1 > N$ for polyenes and $N > P1$ for cyanines. The P2 term would be expected to give a positive peaked behavior between these two limits, since $(\mu_{ee} - \mu_{gg})$ for the lowest energy transition has been shown to exhibit a peak over this range.¹ Thus, γ can be seen (Fig. 5) to be positive at the polyene limit, to increase as the neutral/charge-transfer mixing increases and the P2 term contributes, to exhibit a positive peak for an optimal degree of neutral/charge-transfer mixing, to cross zero where $N = P1 + P2$, and to reach a minimum (a negative peak) at the cyanine-limit where $1/E_{ge}$ and μ_{ge} are

maximized and $P2 = 0$. This trend has been mapped out experimentally⁴ using compounds 7–9, and solvents of varying polarity.

Solvent Dependence of γ for Donor-Acceptor Polyenes

The solvent dependence of γ for 1 and 2 is weaker and the values are smaller than those observed for 7 and 8, respectively. The smaller magnitudes are consistent with the expected length dependence of γ .¹⁹ If the dependence of γ on BLA, as depicted in Figure 5, is simply scaled by a factor when the length of the chain increases, then one would expect for the shorter molecule a weaker variation of γ for a given amount of structural change, thus a weaker variation with solvent polarity, except at the extrema. The weaker solvent dependence is possibly also due to the smaller dipole moment of the charge-separated form and larger energy difference between the neutral and charge-transfer forms for the shorter molecules. Since the molecules are shorter, the dipole moment of the charge-transfer form will be smaller than for the longer molecules. Thus, the dipolar stabilization energy afforded by solvents will be smaller than for the longer molecules, and the change of the degree of mixing over a given range of solvent polarities would be smaller. The trend of the solvent-dependent hyperpolarizabilities for 7–9 has been fully discussed elsewhere.⁴

Effect of Neutral Resonance Structure Aromaticity on γ

The presence of aromatic groups in the neutral resonance structure of conjugated donor-acceptor molecules introduces an additional contribution to the difference in

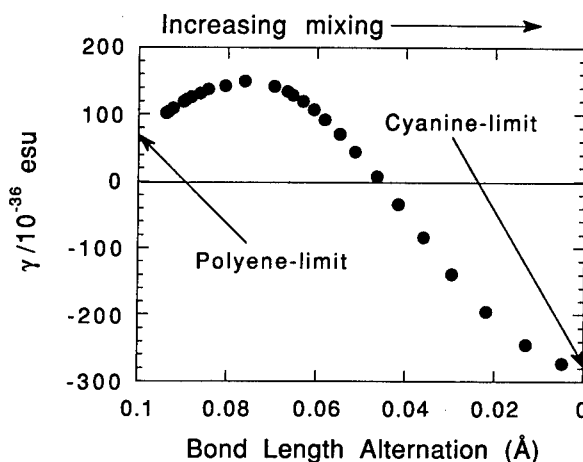


FIGURE 5 The dependence of the second hyperpolarizability of a donor-acceptor polyene (A in Fig. 4) on the degree of mixing between neutral and charge-transfer states and hence BLA. The hyperpolarizabilities were calculated⁵ using a finite-field approach for the molecule, which was geometry-optimized in the presence of an electric field (introduced using point charges). Varying the distance of the point charges from the molecule (hence varying the electric field strength) perturbed the geometry of the molecule from a small mixing limit (polyene-like with large positive BLA) to a strong mixing limit (cyanine-like with essentially zero BLA).

energy between the neutral and charge-transfer structures, and thus decreases their mixing. The aromatic stabilization energy of a phenyl group is lost upon charge-transfer since the ring adopts a quinoid structure. Thus, compared to a polyene of comparable length, one would expect a larger neutral/charge-transfer energy difference and a smaller mixing (or ground-state polarization) for a phenyl-containing chromophore. For a given donor and acceptor pair, the presence of an aromatic group would be expected to yield an effect on γ that would be equivalent to a shift towards more positive BLA (to the left in Fig. 5) for a donor-acceptor polyene.

From the results in Table 1 it can be seen that compounds 1 and 5, both possessing the weak formyl acceptor, have the same, solvent-independent γ values. This is likely due to the fact that the mixing is very weak in both cases. On going to a strong nitro acceptor on the aromatic ring, 6, γ increases, consistent with an increase in mixing (Fig. 5). However, use of a weaker dicyano substitution on the polyene, 2, leads to a sufficiently large mixing that BLA is smaller than the value required for maximum positive γ . Comparing the styryl-bridged with the triene-bridged chromophores, one sees more pronounced changes in the magnitude of the γ values and their solvent dependence. 7 shows stronger solvent dependence and larger maximum values of γ than does 11. In all solvents presented here, 8 shows negative γ values that drop rapidly with increasing solvent polarity, consistent with a high degree of mixing and BLA values which are approaching that of a cyanine.^{12,17} In comparison, compound 12, the phenyl-containing analogue to 8, displays positive γ values which are essentially independent of solvent. On going to the styryl-bridged molecules (10–15), γ increases with increasing donor or acceptor strength and for 15, γ increases with increasing solvent polarity, suggesting that these molecules have insufficient mixing to maximize γ . All of these results are consistent with the notion that neutral form aromaticity gives γ values that correspond to lower degrees of mixing or higher BLA for a donor-acceptor polyene. An alternative analogy is that substituting a phenyl for a pair of double bonds in a polyene chain produces an effect on γ equivalent to reducing the donor or acceptor strength.

Effect of Acceptors that Gain Aromaticity or Conjugation Length upon Charge-Transfer

Given the comparison amongst compounds in Tables 1 and 2, it is clear that in order to further increase γ for the phenyl-containing chromophores an increase in mixing between neutral and charge-transfer forms is required. By utilizing acceptors that gain aromaticity upon charge-transfer it is possible to lower the energy of the charge-separated resonance structure relative to that of the neutral form, and to increase the mixing. This is because the aromatic stabilization energy which is lost on polarizing the phenyl ring is offset by a gain of aromatic stabilization energy on polarizing the acceptor ring. Heterocyclic rings such as barbituric acid and thiobarbituric acid, when acting as acceptors in conjugated donor-acceptor molecules, can gain a degree of aromatic stabilization upon charge-transfer (A in Fig. 6). Indeed the results in Table 3 show that molecules containing the barbituric acid acceptor (16–18) have γ values larger than the analogous aldehyde (11) or dicyano (12, 13) substituted molecules. The

thiobarbituric acid group (19–21) gives an additional enhancement in γ , resulting in values comparable to those for the nitrostyrenes 14 and 15.

It is illustrative to compare the γ values of 19 (A in Fig. 6) and the conventional nonlinear optical chromophore dimethylaminonitrostilbene (DANS, B in Fig. 6). Although 19 possesses a conjugation length 2 atoms shorter than DANS, their electronic absorption energies and γ values are similar.¹⁶ These results are likely due to a diminished neutral/charge-transfer mixing in DANS compared to 19, since both rings in the stilbene bridge lose aromatic stabilization energy upon charge-transfer.

Interestingly large γ values have been obtained for molecules containing the indanedione acceptor (22–24). This acceptor does not gain aromaticity upon charge-transfer, but can provide an enhanced conjugation length upon polarization (Fig. 7). The phenyl ring of the indanedione is cross-conjugated to the donor and bridge portions of the molecule. In the charge-separated resonance structure, this phenyl ring becomes conjugated with the donor and bridge, leading to an increased overall conjugation length. Thus to the extent that the charge-separated resonance structure contributes to the actual structure, the increased conjugation length may provide an enhancement of γ .

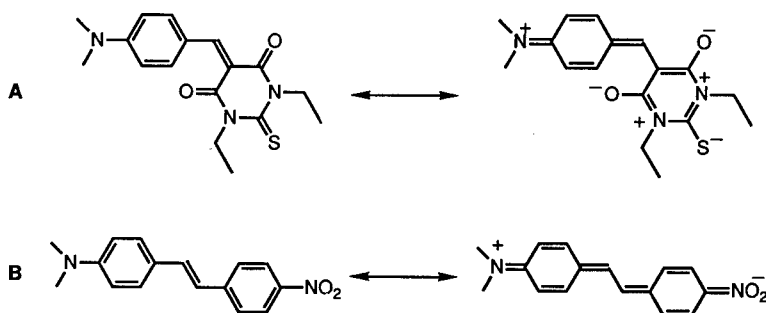


FIGURE 6 Two limiting charge-transfer resonance forms for A. A chromophore containing the thiobarbituric acid moiety which gains aromaticity upon polarization and B. The chromophore DANS which loses aromatic stabilization energy from both phenyl rings upon polarization. The greater energetic balance between neutral and charge-transfer states in A leads to increased neutral/charge-transfer mixing over that in B. Note that two other significant charge-separated resonance structures can be drawn for A, wherein the barbituric acid ring does not gain aromaticity and in which negative charge is localized on either of the oxygens.

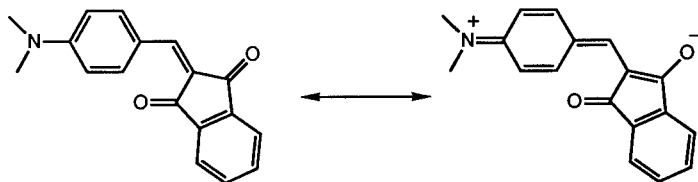


FIGURE 7 Two limiting charge-transfer resonance forms for the chromophore, 22, possessing the indanedione acceptor, which may increase the conjugation length upon polarization.

CONCLUSIONS

The results of this study reinforce the notion that the degree of neutral/charge-transfer mixing, and thus the polarization or, for polyene-containing bridges, the bond length alternation, is crucial in determining the hyperpolarizability for donor-acceptor molecules of a particular length. Structures with aromatic rings in the neutral resonance structure of conjugated donor-acceptor molecules generally lead to γ values and solvent dependence corresponding to a lower degree of neutral/charge-transfer mixing than for polyenes of similar conjugation length. As a result, substitution of phenyl- or styryl-bridged molecules with donors and acceptors of increasing strength lead to increased γ values, suggesting that even for the julolidino/nitro combination, γ has not been maximized. Use of groups that can gain a degree of aromaticity upon polarization, such as thiobarbituric acid, in conjunction with a phenyl-containing bridge, leads to a greater degree of charge-transfer character in the ground state, and γ values that are enhanced relative to molecules with moderately strong acceptors, such as dicyanovinyl. It is suggested that molecules with cross-conjugated groups, that become conjugated upon polarization, may also lead to large γ values.

ACKNOWLEDGEMENTS

This work was performed, in part, at the Center for Space Microelectronics Technology, Jet Propulsion Laboratory (JPL), California Institute of Technology and was supported, in part, by the Ballistic Missile Defense Organization/Innovative Science and Technology Office, through an agreement with the National Aeronautics and Space Administration (NASA). Support at the Beckman Institute by the Air Force Office of Scientific Research (Grant # F49620-92-J-0177) is also gratefully acknowledged. GB thanks the National Research Council and NASA for a Resident Research Associateship at JPL.

REFERENCES

1. S. R. Marder, D. N. Beratan and L.-T. Cheng, *Science*, **252**, 103 (1991).
2. S. R. Marder, C. B. Gorman, B. G. Tiemann and L.-T. Cheng, *J. Am. Chem. Soc.*, **115**, 3006 (1993).
3. J. L. Oudar, *J. Chem. Phys.*, **67**, 446 (1977).
4. S. R. Marder, J. W. Perry, G. Bourhill, C. B. Gorman, B. G. Tiemann and K. Mansour, *Science*, **261**, 186 (1993).
5. S. R. Marder, C. B. Gorman, B. G. Tiemann and L.-T. Cheng, *Proc. SPIE.*, **1775**, 19 (1992).
6. P. Scheibe, S. Schneider, F. Dörr and E. Daltrozzo, *Ber. Buns. Ges. Phys. Chem.*, **80**, 630 (1976).
7. S. S. Malhotra and M. C. Whiting, *J. Chem. Soc.*, 3812 (1960).
8. J. Becher, *Synthesis*, **8**, 589 (1980).
9. B. B. Corson and R. W. Stroughton, *J. Am. Chem. Soc.*, **50**, 2825 (1928).
10. L. G. S. Brooker, G. H. Keyes, R. H. Sprague, R. H. VanDyke, E. VanLare, G. VanZandt and F. L. White, *J. Am. Chem. Soc.*, **73**, 5326 (1951).
11. L. G. S. Brooker, G. H. Keyes, R. H. Sprague, R. H. VanDyke, E. VanLare, G. VanZandt, F. L. White, H. W. J. Cressman and S. G. Dent, *J. Am. Chem. Soc.*, **73**, 5332 (1951).
12. G. Bourhill, K. Mansour, B. G. Tiemann, C. B. Gorman, S. Biddle, S. R. Marder and J. W. Perry, *Proc. SPIE.*, **1863**, 208 (1993).
13. F. Kajzar and J. Messier, *Rev. Sci. Instrum.*, **58**, 2081 (1987).
14. G. R. Meredith, B. Buchalter and C. Hanzlik, *J. Chem. Phys.*, **78**(3), 1543 (1983).

15. F. Kajzar and J. Messier, *Phys. Rev. A.*, **32**(4), 2352 (1985).
16. L.-T. Cheng, W. Tam, S. H. Stevenson, G. R. Meredith, G. Rikken and S. R. Marder, *J. Phys. Chem.*, **95**, 10631 (1991).
17. S. R. Marder, J. W. Perry, B. G. Tiemann, C. B. Gorman, S. Gilmour, S. Biddle and G. Bourhill, *J. Am. Chem. Soc.*, **115**, 2524 (1993).
18. L.-T. Cheng, W. Tam, S. R. Marder, A. E. Stiegman, G. Rikken and C. W. Spangler, *J. Phys. Chem.*, **95**, 10643 (1991).
19. G. Puccetti, M. Blanchard-Desce, I. Ledoux, J.-M. Lehn and J. Zyss, *J. Phys. Chem.*, **97**, 9385 (1993).
20. M. Barzoukas, M. Blanchard-Desce, D. Josse, J.-M. Lehn and J. Zyss, in *Materials for Non-Linear and Electro-Optics*, M. H. Lyons ed., (Institute of Physics, Bristol, 1989), pp. 239-244.
21. P. Groth, *Acta. Chem. Scand. B.*, **41**, 547 (1987).
22. G. Bourhill, J.-L. Brédas, L.-T. Cheng, S. R. Marder, F. Meyers, J. W. Perry and B. G. Tiemann, *J. Am. Chem. Soc.*, **116**, 2619 (1994).
23. A. F. Garito, J. R. Hefflin, K. Y. Yong and O. Zamani-khamiri, *Proc. SPIE.*, **971**, 2 (1988).
24. B. M. Pierce, *Proc. SPIE.*, **1560**, 148 (1991).
25. C. W. Dirk, L.-T. Cheng and M. G. Kuzyk, *Int. J. Quant. Chem.*, **43**, 27 (1992).
26. R. H. Baughman, B. E. Kohler, I. J. Levy and C. Spangler, *Synth. Met.*, **11**, 37 (1985).
27. S. H. Stevenson, D. S. Donald and G. R. Meredith in *Nonlinear Optical Properties of Polymers* (Mat. Res. Soc. Symp. Proc. 109, Pittsburgh, 1988), pp. 103-108.

Nonlinear Optical Response of C_{60} Solutions at $\lambda = 1.06 \mu\text{m}$ in the Nanosecond Regime

VÉRONIQUE DENTAN, PHILIPPE ROBIN and JEAN-PIERRE HUIGNARD
*Laboratoire Central de Recherches, Thomson-CSF, Domaine de
Corbeville, 91404 Orsay, France*

Received 23 February 1994; accepted 16 March 1994

We investigate the nonlinear optical response of toluene C_{60} solutions at $\lambda = 1.06 \mu\text{m}$ in the nanosecond regime by means of a two-wave mixing experiment. We probe the transient index grating photoinduced in the sample either with one of the pulsed pump beam or with a CW low power laser. We thus demonstrate that the dominant nonlinear mechanism in C_{60} solutions with optical nanosecond-pulsed excitation is thermal in origin, even if absorption is very low. The diffraction efficiency can reach, in these experimental conditions, a value of the order of a few 10^{-3} for energy densities around 1 J/cm^2 .

INTRODUCTION

The recent success in synthesizing and purifying large quantities of C_{60} carbon clusters (fullerenes)¹ has fostered considerable interest on their nonlinear optical properties. Due to their closed-shell electronic configuration with highly delocalized electrons, fullerenes have been expected to exhibit large third-order non-resonant optical non-linearity. This nonlinearity is estimated through the value of either the macroscopic third-order susceptibility $\chi^{(3)}$ or the molecular third-order polarisability γ . So far, several measurements of these coefficients through degenerate four-wave mixing experiments (DFWM) at $\lambda = 1.06 \mu\text{m}$, a wavelength far away from any one-photon resonance of C_{60} , have been published.^{2–9} Results are listed in Table 1 which also specifies two relevant experimental parameters: the nature of the C_{60} sample (solid film or solution) and the pulse duration. Comparison of $\chi^{(3)}$ and/or γ values evidences a large discrepancy, with hyperpolarisabilities γ ranging from 0 to a few orders of magnitude more than that of linear conjugated polyenes. Possible differences in purification of the C_{60} samples should anyway remain small and cannot account for such a huge disparity in the results.

The aim of the experiment reported in this paper is therefore to clarify whether C_{60} solutions exhibit an off-resonant nonlinear optical response ($\lambda = 1.06 \mu\text{m}$) in the nanosecond time scale and, should that be the case, to identify the mechanism responsible for the observed nonlinearity. We demonstrate that index gratings can be written in C_{60} solutions through two-wave mixing (TWM) experiments, performed with nanosecond pulses at $\lambda = 1.06 \mu\text{m}$ (in the transparent region). Analysis of a probe

TABLE 1

Third-order optical susceptibility $\chi^{(3)}$ and molecular second-order hyperpolarisability γ measured at $\lambda = 1.06 \mu\text{m}$ by DFWM. Also specified are the pulse length and the nature of the sample used in the experiment. Italic typing stands for $\chi^{(3)}$ values of the solid extrapolated from the values measured in solution.

Sample	Pulse length	$\chi^{(3)} (10^{-12} \text{ esu})$	$\gamma (10^{-33} \text{ esu})$	Reference
solid film	35 ps	7	0,3	2,3
solution/toluene	10 ns	0	0	4
solution/toluene	10 ns	3300	160	5
(87% C_{60} -13% C_{70})				
solution/benzene	50 ps	60 10 ³	(110 \pm 10) 10 ³	6
			93	7
solution/toluene	35 ps	0	0	8
solution/benzene	30 ps		$-0.65 \leq \gamma \leq 0.24$	9

diffracted beam (ns pulse or CW) in terms of efficiency, response time and fringe spacing, yields clues about the origin of the nonlinearity.

EXPERIMENT

C_{60} (99% pure) was purchased from MGP-ISAR (France) and dissolved in toluene without further purification. Visible and near IR absorption spectrum of the C_{60} solution ($C = 8.3 \cdot 10^{-4} \text{ M/l}$) agrees with published data.¹⁰ The absorption coefficient of the solution at $\lambda = 1.06 \mu\text{m}$ is very weak, $\alpha = 0.22 \text{ m}^{-1}$. The solution is placed in a 10 mm thick spectrophotometer glass cell and the overall transmission coefficient is $T \approx 99,8\%$ at $\lambda = 1.06 \mu\text{m}$ (losses due to the cell windows will be neglected throughout the paper for simplicity).

TWM experiment is carried out using a *Q*-switch Nd:YAG laser with a pulse duration $2\tau \approx 8 \text{ ns}$ (FW1/e), with output energy up to 20 mJ, operating at low repetition rate ($< 1 \text{ Hz}$). The geometry for the experimental set-up is depicted in Figure 1. The incident s-polarised beam is split into two beams of approximately equal energy which

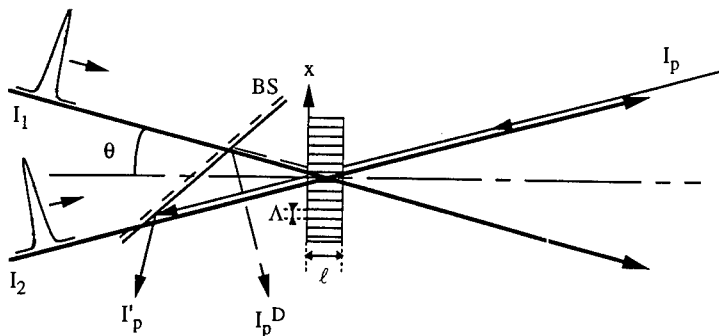


FIGURE 1 Scheme of the TWM experiment. Writing beams I_1 and I_2 are nanosecond (8 ns) pulses emitted by a *Q*-switched Nd:YAG laser at $\lambda = 1.06 \mu\text{m}$. The probe beam I_p is either one of the pump beam, strongly attenuated and delayed, or a low power CW He:Ne beam. In this last case, the angle of incidence of I_p in the grating is adjusted so that it satisfies the Bragg condition at $\lambda = 633 \text{ nm}$.

cross inside the sample. A lens, placed before the beam splitter BS, slightly focuses the beams in the sample in order to increase the peak energy density. The focal length is chosen depending on the fringe spacing Λ so that the number of fringes in the interference region excess 30. Typical values of total incident intensity in the sample are around 100 MW/cm². The interference pattern due to the two pulsed beams illuminates the sample with a spatially modulated intensity:

$$I(r, t) = I_T(r, t)(1 + \cos qx) \quad (1)$$

where $I_T(r, t) = I_1(r, t) + I_2(r, t) = I_T \exp(-t^2/\tau^2) \exp(-2r^2/\omega^2)$ is the total intensity and ω the waist radius in the sample. $q = 2\pi/\Lambda$ is the modulus of the grating wave vector and $\Lambda = \lambda/(2 \sin \theta)$ the fringe spacing. In the following, we will neglect the gaussian spatial envelope of the interference pattern.

We also neglect any amplitude grating contribution to the diffraction efficiency. The two-photon absorption of 40 cm/GW measured by Lindle and coworkers³ at 1.06 μ m on a C₆₀ solid film reduces to $1.5 \cdot 10^{-2}$ cm/GW in our solution. The corresponding diffraction efficiency in our experimental conditions would then be of a few 10^{-7} , which is 4 orders of magnitude smaller than the value we measure. The grating is then a pure phase grating.

RESULTS AND DISCUSSION

Grating Probed with a Delayed Pulse

The photoinduced index grating is first probed with one of the pulsed writing beams, strongly attenuated and reflected back into the sample. This allows to measure the diffraction efficiency η of the grating, which is defined as the ratio of the diffracted probe intensity I_P^D over the directly transmitted probe intensity I_P' . In our experimental conditions, we have the following relationship between η and the index modulation Δn :

$$\eta = \frac{I_P^D}{I_P'} = \left(\frac{\pi \ell \Delta n}{\lambda} \right)^2 \quad (2)$$

where ℓ is the sample thickness.

Furthermore, delaying the probe beam (0 to 15 ns delay) gives information about the dynamic of grating formation. Figure 2 shows the measured η and Δn values for pump probe delay ranging from 0 to 14 ns, for a fringe spacing $\Lambda = 49 \mu$ m and a total pump intensity $I_T = 122$ MW/cm². The time variation of η and Δn implies that the response of the solution is not instantaneous: Δn increases from $(0.5 \pm 0.1) \cdot 10^{-6}$ at 0 ns delay to $(1.5 \pm 0.3) \cdot 10^{-6}$ at ≈ 14 ns delay. Such a behaviour is inconsistent with the assumption that Δn arises from an electronic contribution, as Kerr effect has nearly instantaneous (fs) response time.

However, let us for the moment ignore this inconsistency and persist in interpreting the nonlinearity as a Kerr effect. We can therefore deduce $\chi^{(3)}$ and γ values from the measurement of Δn through the following relationships (in esu units):¹¹

$$\chi_r^{(3)} = \frac{n^2 c}{12\pi^2} \frac{\Delta n}{I_T} = NL^4 \gamma \quad (3)$$

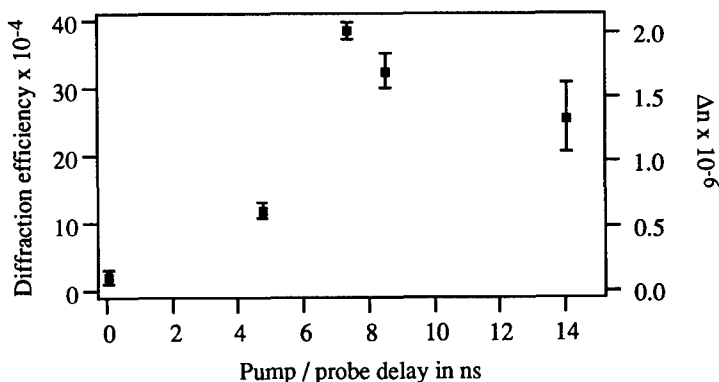


FIGURE 2 Diffraction efficiency and corresponding index modulation Δn measured when probing the grating with one of the writing beam, strongly attenuated and delayed. The fringe spacing is $\Lambda = 49 \mu\text{m}$ and the total incident intensity $I_T = 122 \text{ MW/cm}^2$.

N is the molecular density and $L = (n^2 + 2)/3$ a local field correction factor, which is given by the Lorentz-Lorenz formula¹² in the case of isotropic dilute solutions. Our experimental values, $\Delta n \approx 2 \cdot 10^{-6}$ and $I_T = 122 \text{ MW/cm}^2$, together with $n \approx 1.45$, lead to $\chi^{(3)} \approx 9 \cdot 10^{-13} \text{ esu}$. The extrapolated γ value ($N = 5 \cdot 10^{17} \text{ cm}^{-3}$), $\gamma \approx 460 \cdot 10^{-33} \text{ esu}$ is very large. If we compare it to other published values (see Tab. 1), we see that our value has the same order of magnitude that the one measured by Gong *et al.*⁵ Their DFWM experiment was performed with 10 ns pulses on C_{60} solutions, as our TWM experiment. On the contrary, our γ value is more than 3 orders of magnitude larger than the value measured by Kafafi and coworkers^{2,3} but they worked with shorter pulses (35 ps) and used C_{60} solid films. As these experimental conditions are much more appropriate to measure electronic contributions, we believe the second-order hyperpolarisability value $\gamma \approx 0.3 \cdot 10^{-33}$ given by Kafafi *et al.*, to be the most reliable one.

We then conclude that the nonlinearity observed on C_{60} solutions in a nanosecond time scale is not a Kerr effect. This conclusion is also supported by the slow temporal variation of the TWM signal as mentioned above (Fig. 2).

We may now evoke thermally induced effects to explain the nonlinearity. Thermal effects would indeed be consistent with the slow grating formation time. However, as the solution is highly transparent, it is not sure that absorption of incident energy is sufficient to induce any detectable index nonlinearity. We can roughly estimate the thermally induced index variation Δn . As the pulse duration is more than six orders of magnitude shorter than the thermal relaxation time τ_{th} ($\tau_{th} \propto \Lambda^2 / D$, where D is the thermal diffusion coefficient, is in the μs range in our experimental conditions), we can assume that the heating process is adiabatic. The amplitude of the temperature variation ΔT_0 is then simply given by:

$$\Delta T_0 = \frac{\alpha}{(\rho c_p)} \cdot F_T \quad (4)$$

where α and ρ are respectively the absorption coefficient and the density of the solution, c_p is the specific heat of the solvent and F_T the incident energy density. In our experimental conditions ($\alpha = 0.22 \text{ m}^{-1}$, $\rho c_p^{13} = 1.2 \cdot 10^6 \text{ J/m}^3/\text{°C}$, $F_T = 8.5 \cdot 10^3 \text{ J/m}^2$), we obtain $\Delta T_0 = 1.6 \cdot 10^{-3} \text{ °C}$.

This heat source in the solution induces an index variation

$$\Delta n_0 = \frac{dn}{dT} \cdot \Delta T_0 \quad (5)$$

A dn/dT value of several 10^{-4} °C^{-1} (which is common in solvents like toluene or benzene¹³) is then sufficient to achieve index variation around 10^{-6} , as we obtained in our measurement. From this simple analysis, we see that invoking a thermal nonlinearity gives the good order of magnitude for Δn .

Grating Probed with a CW Beam

To further check that the assumption of a thermal effect is valid, we probed the grating with a low power CW He-Ne laser. The idea was to measure the dynamic of the transient grating. The probe angle of incidence in the sample is adjusted to match the Bragg condition at $\lambda = 633 \text{ nm}$ and the diffracted beam is detected with a fast rise time ($< 1 \text{ ns}$) photodiode. Figure 3 shows how this signal evolves with time, for a fringe spacing $\Lambda = 32 \mu\text{m}$. We see that, as expected, the transient grating has a long decay time ($\approx 0.4 \mu\text{s}$). We also note that the maximum diffraction efficiency occurs several nanoseconds after the pump pulse. At last, we observe time-dependent oscillations in the diffracted signal.

This behaviour has been known and analysed for more than 20 years¹⁴ when it was shown that acoustic waves can be generated by the interference of two optical pulses in an absorbing medium. Absorption of 10 ns long spatially modulated excitation $\Delta I = I_T \cos qx$ induces a local and instantaneous temperature grating in the solution which lasts after the end of the excitation:

$$\Delta T(x, t) = \Delta T(t) \cos qx \quad \text{with} \quad \Delta T(t) = \Delta T_0 \exp\left(\frac{-t}{\tau_{th}}\right) \quad (6)$$

ΔT_0 is given by equation [4] above and $\tau_{th} = \rho c_p / (\kappa q^2)$ is the thermal relaxation time, κ is the thermal conductivity.

Thermal expansion in the liquid then sets up two counter-propagating acoustic waves with pulsation $\omega_s = 2\pi v_s / \Lambda$, v_s being the velocity of sound in the solvent.

The resulting density modulation can be written $\Delta \rho(x, t) = \Delta \rho(t) \cos qx$, where $\Delta \rho(t)$ is the solution of the acoustic wave equation:

$$\frac{\partial^2 \Delta \rho(t)}{\partial t^2} + \frac{1}{\tau_{ac}} \frac{\partial \Delta \rho(t)}{\partial t} + \omega_s^2 \Delta \rho(t) = -\omega_s^2 \beta \rho_0 \Delta T(t) \quad (7)$$

This equation writes as a classical propagation equation: the source term on the right-hand comes from heating in the material (β is the thermal dilatation coefficient) and the damping term is due to the viscosity v of the solvent: $\tau_{ac} = \rho / (v q^2)$. A detailed analysis would account for the transverse gaussian spatial dependence of the excitation

beams together with the gaussian temporal shape of the pump pulses. As mentioned in the beginning, we approximate the pump beams as plane waves of temporal rectangular profile with duration 2τ . The solution of equation [7] can then be written, in first approximation, as:¹⁵

$$\Delta\rho(t) = \Delta\rho_0 \left[C \exp\left(\frac{-t}{2\tau_{ac}}\right) \cos(\omega_s t) - \exp\left(\frac{-t}{\tau_{th}}\right) \right] \quad (8)$$

$\Delta\rho_0 = \beta\rho\Delta T_0$ is the amplitude of the maximum induced density modulation.

C appears as a contrast factor which depends on the pump pulse duration. In the limit of very short excitation, C equals unity.¹⁵ Indeed, with nanosecond pulses, C can vary between 0 and 1 depending on the fringe spacing. When C is close to 0, no time oscillations in the diffracted signal occur.¹⁶ This behaviour can be understood by splitting the nanosecond excitation ($I_T(t) = I_T$ for $|t| \leq \tau$ and 0 otherwise) into a sum of many successive short pulses. Each of these pulses creates 2 counter-propagating acoustic waves, hence a density modulation $d\Delta\rho(t) = \Delta\rho_0 \cos\omega_s t$ (acoustic damping and thermal relaxation during the pulse are neglected: τ_{ac} and τ_{th} are assumed to be much larger than τ). The total density modulation induced by the whole pulse is then the sum:

$$\Delta\rho(t) = \int_{-\tau}^{+\tau} \frac{\Delta\rho_0}{2\tau} \cos(\omega_s(t-u)) du = \Delta\rho_0 \frac{\sin\omega_s\tau}{\omega_s\tau} \cos(\omega_s t)$$

The contrast $C = \sin(\omega_s\tau)/(\omega_s\tau)$ is null when the condition $\omega_s\tau = m\pi$ (or $\Lambda = 2v_s\tau/m$) is met: there is a destructive interference process between the acoustic waves created during the whole nanosecond pulse. As an example, when $\Lambda = 2v_s\tau \approx 10.4\mu\text{m}$ in our experimental conditions, acoustic waves created during the first half of the pulse interfere destructively with those created during the second half, resulting in cancellation of the time-oscillations.

We now return to the qualitative discussion about the mechanism of formation of the transient grating. The density modulation given by equation [8] induces a refractive index modulation which is readily obtained by the Lorentz-Lorenz formula:¹²

$$\Delta n = \frac{(n^2 + 2)(n^2 - 1)}{6n} \frac{\Delta\rho}{\rho} \quad (9)$$

We then get a time-modulated (pulsation ω_s or period Λ/v_s), spatially periodic (period Λ) refractive index modulation in the form:

$$\Delta n(x, t) = \Delta n_0 \left[C \exp\left(\frac{-t}{2\tau_{ac}}\right) \cos(\omega_s t) - \exp\left(\frac{-t}{\tau_{th}}\right) \right] \cos(qx) \quad (10)$$

with

$$\Delta n_0 = \beta \frac{(n^2 + 2)(n^2 - 1)}{6n} \frac{\alpha}{\rho c_p} F_T \quad (11)$$

Equation [11] is a more detailed expression of equation [5].

We can now compare the diffracted signal shown in Figure 3 with the theoretical time dependence given by equation [10]. Table 2 shows how good is the agreement between the measured period of the time-dependent oscillations and the expected value

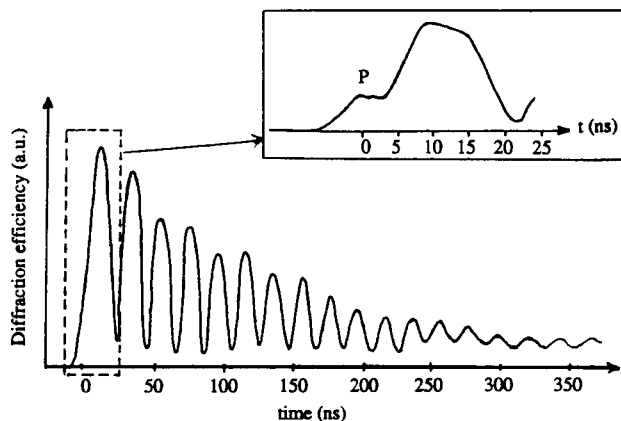


FIGURE 3 Grating probed with a low-power CW He:Ne laser. The fringe spacing is $\Lambda = 32 \mu\text{m}$. Inset is shown a detail where peak P represents the non-totally filtered pump pulse at $\lambda = 1.06 \mu\text{m}$.

TABLE 2

Comparison of the measured and theoretical temporal parameters of the transient TWM diffracted signal for two values of the fringe spacing Λ . T is the measured time-oscillation period and τ_e is the measured 1/e decay time of the signal. τ_{ac} and τ_{th} are respectively the acoustic wave attenuation time and the thermal relaxation time. The values of the thermal constants of the solvent used in the calculation are¹³: $v_s = 1300 \text{ m/s}$, $\rho c_p = 1.2 \cdot 10^6 \text{ J/m}^3/^{\circ}\text{C}$, $\kappa = 0.135 \text{ J/s/m}^2/^{\circ}\text{C}$, $v = 0.59 \text{ g/m/s}$ and $\rho = 0.87 \text{ g/cm}^3$.

$\Lambda (\mu\text{m})$	$T(\text{ns})$	$\Lambda/v_s (\text{ns})$	$\tau_e (\text{ns})$	$\tau_{ac} (\mu\text{s})$	$\tau_{th} (\mu\text{s})$
32	21	24.9	155	38	230
13.4	9.3	10.4	119	6.7	40.4

Λ/v_s . This point undoubtedly evidences that the mechanism for the formation of the transient grating is due to absorption and consecutive thermal expansion in the liquid.¹⁶ However, the decay time of the grating is much shorter than expected by the theory. This could be explained by the fact that we neglected the gaussian spatial dependence of the interference pattern and considered an infinite grating in the x direction.

CONCLUSION

We demonstrated that the transient grating induced by the interference pattern with nanosecond duration is due to the generation of acoustic waves in the C_{60} solution. We checked that this grating built up within a few nanoseconds and presented time-dependent oscillations of the diffracted signal at each acoustic cycle. We think that such a thermo-acoustic effect is a dominant mechanism in C_{60} solutions with nanosecond-pulsed excitation. Although the absorption is very low at $\lambda = 1.06 \mu\text{m}$ (the solution is transmitting 99.8% of the incident energy at this wavelength), it can lead to index

modulation with amplitude fairly high ($\approx 10^{-6}$) for incident energy density of the order of a J/cm². This may explain some of the discrepancies encountered in the literature about the nonlinear optical third-order properties of the fullerene C₆₀.

REFERENCES

1. W. Krätschmer, L. D. Lamb, K. Fostiropoulos and D. R. Huffman, *Nature*, **347**, 354 (1990).
2. Z. H. Kafafi, J. R. Lindle, R. G. S. Pong, F. J. Bartoli, L. J. Lingg and J. Milliken, *Chem. Phys. Lett.*, **188**, 492–496 (1992).
3. J. R. Lindle, R. G. S. Pong, F. J. Bartoli and Z. H. Kafafi, *Phys. Rev. B*, **48**, 9447–9451 (1993).
4. R. Vijaya, Y. V. G. S. Murti, G. Sundararajan, C. K. Mathews and P. R. Vasudeva Rao, *Opt. Commun.*, **94**, 353–356 (1992).
5. Q. Gong, Y. Sun, Z. Xia, Y. H. Zou, Z. Gu, X. Zhou and D. Qiang, *J. Appl. Phys.*, **71**, 3025–3026 (1992).
6. W. J. Blau, H. J. Byrne, D. J. Cardin, T. J. Dennis, J. P. Hare, H. W. Kroto, R. Taylor and D. R. M. Walton, *Phys. Rev. Lett.*, **67**, 1423–1425 (1991).
7. R. J. Knize and J. P. Partanen, *Phys. Rev. Lett.*, **68**, 2704 (1992).
8. Z. H. Kafafi, F. J. Bartoli, J. R. Lindle and R. G. S. Pong, *Phys. Rev. Lett.*, **68**, 2705 (1992).
9. N. Tang, J. P. Partanen, R. W. Hellwarth and R. J. Knize, *Phys. Rev. B*, **48**, 8404–8408 (1993).
10. T. W. Ebbesen, K. Tanigaki and S. Kuroshima, *Chem. Phys. Lett.*, **181**, 501–504 (1991).
11. F. Kajzar and J. Messier, Chapter III-2, pp 51–83 in “*Nonlinear optical properties of organic molecules and crystals*”, Vol. 2, Eds D. S. Chemla and J. Zyss, Academic Press (1987).
12. M. Born and E. Wolf, p 87 in “*Principle of optics*”, 6th edition, Pergamon Press (1987).
13. *Handbook of Chemistry and Physics*, 61st edition, CRC Press (1980–1981).
14. D. C. Auth, *Appl. Phys. Lett.*, **16**, 521–523 (1979) and references quoted therein.
15. J. R. Salcedo and A. E. Siegman, *IEEE J. Quant. Elect.*, **QE-15**, 250–256 (1979).
16. K. A. Nelson, R. J. D. Dwayne Miller, D. R. Lutz and M. D. Fayer, *J. Appl. Phys.*, **53**, 1144–1149 (1982).

Nonlinear Optics of Conjugated Polyacetylene Thin Films Produced by Different Preparation Techniques

W. SCHROF, J. R. WÜNSCH, A. ESSER*, K. H. HAAS* and H. NAARMANN
BASF AG, Polymers Research, D-67056 Ludwigshafen, FRG
**BASF Advanced Polymer Research, 2-1-6 Sengen, Tsukuba 305, Japan*

Received 12 January 1994; accepted 19 January 1994

Femtosecond Degenerate Four Wave Mixing (DFWM) and frequency tunable Third Harmonic Generation (THG) measurements were performed on all-trans polyacetylene thin films prepared by different processes: 1. gas phase polymerization (Ziegler-Natta) on a glass substrate, 2. spin-coating of a polyacetylene dispersion and 3. spin-coating of a soluble poly(phenyl vinyl sulfoxide) (PPVS) precursor polymer followed by a thermal polyene conversion. The conjugation lengths of the polyene thin films were analyzed using absorption and FT-Raman spectroscopy. The Ziegler-Natta material showed the longest conjugation followed by the Luttinger type polyacetylene dispersion. Thermal conversion of PPVS lead to the shortest chain length among these methods. This behavior was mirrored in the NLO measurements yielding resonantly enhanced $\chi^{(3)}$ values up to 10^{-7} esu (DFWM) and relaxation times less than 2 ps.

Keywords: nonlinear optics, polyacetylene thin films, DFWM, THG.

INTRODUCTION

BASF is participating in the Japanese 'Nonlinear Photonics Materials Project (NPM)' for the development of materials for all optical switching. Within this long-term project BASF is engaged in the field of conjugated organic oligomers and polymers.

Polyacetylene with its one-dimensional conjugated polymeric structure is one of the most promising candidates for a NLO active material.^{1–6} Unfortunately, polyacetylene shows several intrinsic problems concerning the preparation of thin films with acceptable optical quality: low optical transparency in the visible spectral range, high scattering losses, poor stability and processability. In this paper we report on three different ways to prepare polyacetylene thin films using the spin-coating technique:

- 1) Thin film acetylene polymerization on a spin-coated Ziegler-Natta catalyst
- 2) Spin-coating of a polyacetylene Luttinger-type dispersion
- 3) Spin-coating of a PPVS precursor followed by thermal conversion to the polyene

EXPERIMENTAL

Chemical Synthesis and Film Preparation

Ziegler-Natta-catalysts The BASF method⁷ allows to polymerize polyacetylene from the Shirakawa type⁸ (with ~80% cis units) at room temperature. Extending this method to coatings on glass or quartz substrates we were able to prepare even films at

room temperature under inert conditions which could be treated by heat yielding trans isomerized items. The thickness of the films measured by a mechanical profilometer ranged from 90 nm up to several 100 nm.

For the catalyst preparation 5 ml of Silicone Oil AV 1000 (Goldschmidt, Essen) and 31 ml of 100% aluminium triethyl were placed in a stirring flask rendered inert with argon. Then, 41 ml of distilled titanium tetrabutylate were added drop-wise to this solution over a period of one hour while the temperature was maintained at $40 \pm 2^\circ\text{C}$. All volatiles of the reaction, which were largely dissolved in the catalyst mixture, were subsequently removed by evacuating at room temperature for two hours.

The catalyst solution prepared this way was heated at a particular temperature (120°C) for a defined period (2 hr). Then, after cooling to room temperature this black catalyst system could be used for polymerization.

Thin films of the catalyst material were prepared by a spin coating process. Three drops of the catalyst were distributed on the surface of a quartz flat rotating at a speed of 3000 revolutions per minute.

For the polymerization the coated quartz flat was contaminated with acetylene gas for 1 minute yielding polyacetylene with a high cis-content of 80%. After this procedure the catalyst was washed out by extracting with toluene (10 times, each run 15 ml), dried under argon (1 h, 10^{-3} torr). Thermal isomerization (150°C) yielded in all-trans polyacetylene thin films.

Coated Polyacetylene dispersions Thin films of polyacetylene particles synthesized by a modified Luttinger-Green process^{9,10} and dispersed in an inert polymer matrix (polybutyrate or polyvinylpyrrolidone) were spin-coated on optical flats.

For the polymerization of acetylene 500 ml ethanol were placed in a stirring flask rendered inert with nitrogen. After cooling to -78°C 60 mg $\text{Co}(\text{NO}_3)_2 \cdot 6\text{H}_2\text{O}$ dissolved in 15 ml ethanol were added slowly (20 min) and stirred for a further hour, then 500 ml acetylene were pressed in and a solution of 150 mg NaBH_4 dissolved in 10 ml ethanol were added slowly through a dropping funnel (over 30 minutes). The colour the reaction mixture turned from colourless to purple. After stirring the solution for further 30 min at -78°C , the mixture was warmed to room temperature and allowed to stand for 3 hours before workup. Isolation of 300 mg polyacetylene having a cis-content of $\approx 85\%$ showed a high conversion rate.

The polyacetylene dispersed in ethanol was filtered, washed twice with 100 ml ethanol and dispersed again in 150 ml ethanol (Branson-ultrasound bath, 10 min, 10 kHz). 10 ml of this polyacetylene dispersion were diluted with 1 ml of 15 wt.% solution of polyvinylpyrrolidone (alternatively polymethylmethacrylate or polybutyrate) in ethanol (room temperature).

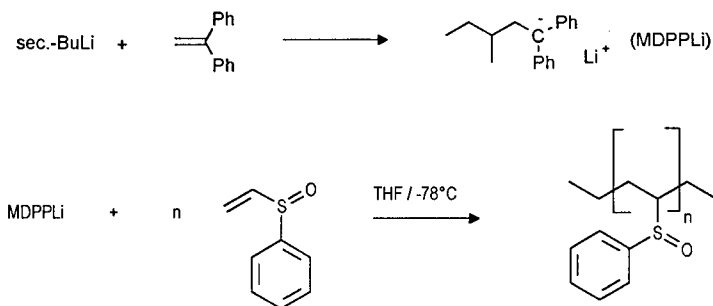
From this dispersion, containing the polyacetylene and the polymeric binder, 3 drops were spin-coated. Heating of the coating yielded an isomerized trans polyacetylene blend.

Spin-coating of a polyphenylvinylsulfoxide (PPVS) precursor followed by a thermal conversion to the polyene Phenyl vinyl sulfoxide (PVS)¹¹ is a reactive alkene bearing an electron-withdrawing phenyl-sulfoxide moiety. PVS has already been used as acetylene synthon in well known organic transformations like Diels-Alder reactions or Michael-additions. During investigations on the synthesis of polyene precursor polymers we polymerized PVS and tried the polymer analogous elimination reaction to

build up polyenes. The anionic polymerization of the PVS monomer with lithio-organyls leads to poly(phenyl vinyl sulfoxide) (PPVS) which can thermally be converted into polyacetylene by heating the precursor polymer PPVS.

The synthesis of polyacetylene from poly(phenyl vinyl sulfoxide) (PPVS) has potential advantages. First the polymerization of PVS proceeds through a stable carbanion so that the molecular weight distribution is expected to be narrow. Moreover, the control of molecular weight through the ratio of monomer to initiator is quite good, and the formation of high molecular weight PPVS should be possible. Another advantage is the good processability due to the good solubility of PPVS in common solvents. At least, PPVS is air-stable and could be converted thermally into polyacetylene right before analytical and spectroscopical investigations. Using the anionic polymerization procedure, it should be possible to build up block copolymers, i.e., polystyrenepolyacetylene (ex PPVS).

(a) *Synthesis of PPVS* As a matter of fact, PVS could not be polymerized with *n*-butyllithium or *sec*-butyllithium as initiator. This is because of a nucleophilic attack of these carbanions at the sulfur atom, causing an S_N2 displacement of the aryl group. Therefore we used (3-methyl-1,1-diphenyl pentyl)lithium (MDPPLi) to initiate the polymerization of PVS. This initiator has already been successful used for the anionic polymerization of styrene.

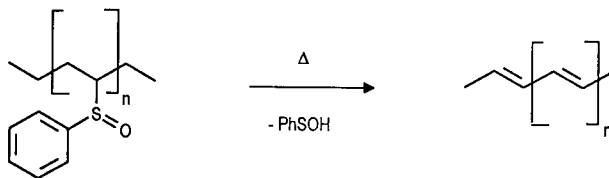


The monomer PVS, the solvent THF and the initiator-alkene 1,1-diphenylethylene (DPE) were purified thoroughly. PVS, purchased from Aldrich, was stirred over calcium hydride and distilled under high vacuum. This procedure is repeated two times and the monomer coming from the final distillation was collected in a flame dried flask. THF was refluxed 24 hours over sodium wire containing benzophenone. Once the purple red colour of the benzophenone dianion was obtained the THF was distilled and collected in a flame dried flask. To remove acidic traces DPE was purified by a short column filtration over basic Al_2O_3 . DPE was dissolved in THF and *sec*-butyllithium was added at room temperature until a redish colour appears and remains for 15 minutes. Now the calculated amount of *sec*-butyllithium was added and the mixture cooled to -78°C . PVS was added slowly through a drop-funnel. After complete addition the reaction was allowed to proceed for another hour at -78°C . After termination with an excess of degased methanol PPVS was precipitated in diethyl ether and dried under vacuum at room temperature. Since the PPVS tends to degrade slowly at room temperature, the samples were stored in a freezer at -20°C .

(b) *Preparation of thin films* PPVS is soluble in common organic solvents and stable on air exposure. Therefore spin-coating was used to prepare thin films. PPVS was dissolved preferentially in chloroform and tetrahydrofuran as a 1–10% (weight-%) solution of polymer in solvent. Due to its good solubility PMMA (lucryl C66) could be added to increase the optical quality of the polymer films prepared. The thickness of the films varied between 0.02–2.7 μm according to the polymer concentration of PPVS in the solvent and the rotation speed of the spin coater.

(c) *Thermal elimination of phenyl-sulfenic acid from PPVS under formation of polyenes* As described above phenylsulfoxides bearing an α -hydrogen eliminate phenyl sulfenic acid upon heating. The question arises if such a elimination process could be transformed on polymeric vinylsulfoxides like PPVS.

As depicted in the equation, we assumed that in analogy to the Diels-Alder cycloaddition-elimination process phenyl sulfenic acid is ejected and a polyene, i.e., a new kind of polyacetylene has been formed.



To remove the phenyl sulfenic acid the elimination process was conducted under dynamic vacuum ($p \leq 0.01$ mbar) at temperatures of $T = (100 \pm 20)^\circ\text{C}$. During thermal elimination of PPVS a crystalline deposit is formed on the unheated glass wall of the apparatus which is assumed to be phenyl sulfenic acid.

Experimental Instrumentation

Raman A Fourier-Transform Raman spectrometer (Bruker FRA 106) equipped with a diode pumped Nd-YAG laser was used to record the Raman spectra of polyene thin films. Because of the electronic coupling of the $\text{C}=\text{C}$ - and $\text{C}-\text{C}$ -stretching vibrations and the delocalized π -electrons the position and intensity of the Raman band will change as a function of the conjugation length, i.e., the chain length.^{12–14} The $\text{C}-\text{C}$ - and the $\text{C}=\text{C}$ -stretching vibrations ω will move to smaller wavenumbers when the conjugation length is increased as approximated by (eq. 1) (with A, B being constants (1450 cm^{-1} and 500 cm^{-1} , resp.¹⁴) and N the number of double bonds):

$$\omega[\text{cm}^{-1}] = A[\text{cm}^{-1}] + \frac{B[\text{cm}^{-1}]}{N} \quad (1)$$

The wavelength of 1064 nm assures that no short chain resonances will occur in the Raman spectra shifting the $\text{C}=\text{C}$ bands to higher energy values as published in the literature for Raman measurements using ion laser radiation.^{13,14}

Third harmonic generation (THG) To record spectra of the nonlinearity $\chi^{(3)}$, frequency tunable (1–2.5 μm) Maker fringe THG experiments¹ were performed using

an optical parametric oscillator pumped by a frequency tripled Nd-YAG laser as a light source. Quartz was used as reference.

Degenerate four wave mixing (DFWM) A fs-DFWM experiment¹ (see Fig. 1) was used to measure the magnitude and the relaxation behavior of the nonlinearity $\chi^{(3)}$. With this experiment relevant parameters for future device operation like refractive index change and maximum switching speed can be determined in contrast to THG. The light source of the DFWM experiment, a Kerr-lens modelocked Ti-Sapphire laser (Coherent, MIRA 900 F) delivered 100 fs pulses at a repetition rate of 76 MHz at a wavelength tunable from 715 nm to 1050 nm with a peak power of nearly 100 kW. The experiment was built up in a folded BOXCARS geometry, the probe pulses were delayed with respect to the grating forming pulses by a computer controlled optical delay stage. To improve the signal to noise ratio (S/N) of the diffracted DFWM-signal lock-in techniques were applied in combination with a mechanical mini-shaker or a chopper chopping two beams at different frequencies.

The $\chi^{(3)}$ -value of the sample(s) was calculated by a comparison with the signal of the reference (Ref) CS₂ ($\chi^{(3)} = 6 \cdot 10^{-13}$ esu) using (eq. 2):

$$\chi_s^{(3)} = \chi_{\text{ref}}^{(3)} \cdot \frac{n_s^2}{n_{\text{ref}}^2} \cdot \sqrt{\frac{I_{4s}}{I_{4\text{ref}}}} \cdot \sqrt{\frac{P_{\text{ref}}^3}{P_s^3}} \cdot \frac{\alpha \cdot e^{\alpha \cdot L_{\text{eff}s}/2}}{(1 - e^{\alpha \cdot L_{\text{eff}s}})} \cdot L_{\text{effref}} \quad (2)$$

- $L_{\text{eff}s}$: thickness of sample
- L_{effref} : effective thickness of reference
- n : refractive index
- α : absorption constant sample
- I_4 : DFWM-intensity
- P : average laser power

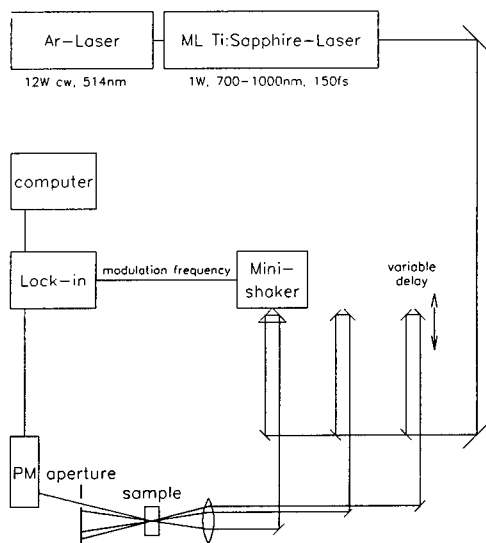


FIGURE 1 Schematic layout of the DFWM experiment.

RESULTS AND DISCUSSION

One major target of our development of polyene materials was to elongate the π -electron conjugation in order to get higher nonlinearities. Longer conjugation lengths should manifest in absorption edges shifted to lower energies and in Raman bands shifted to lower wavenumbers. Figure 2 shows the typical absorption spectra of the three different polyacetylene film preparations. The longest conjugation length was found with the Ziegler-Natta system followed by the polyacetylene dispersion and converted precursor material.

The same experimental findings were confirmed by Raman measurements shown in Figure 3, 4, 5 revealing Raman shifts of 1461, 1466.4 and 1489 cm^{-1} for the C=C-

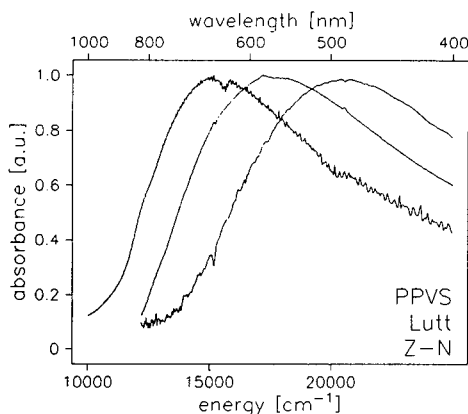


FIGURE 2 Absorption spectra of thin films of isomerized polyacetylene: the band edge of Ziegler-Natta polyacetylene is shifted to the lowest energies, followed by the polyacetylene dispersion and converted PPVS.

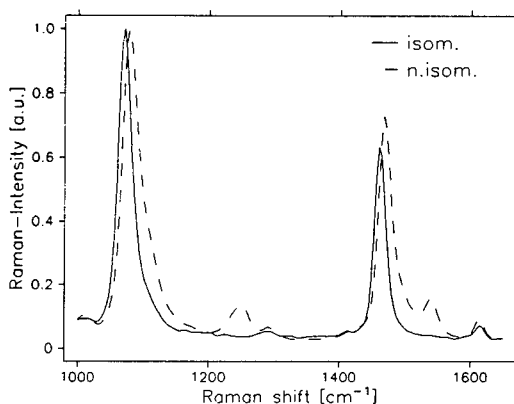


FIGURE 3 Raman shifts of C=C-(trans-configuration 1461.1 cm^{-1} (isomerized), and 1468.0 cm^{-1} (not isomerized), cis-band 1250.2 cm^{-1}) and of the C—C-stretching-vibrations (trans-configuration 1070 cm^{-1} (isom.), and 1078.0 cm^{-1} (not isom). resp.) of thin films of polyacetylene (Ziegler-Natta) before and after thermal isomerization.

stretching vibrations for the all-trans materials in the same sequence as above. Using (eq. 1) a much smaller conjugation was calculated for the precursor material ($N \approx 13$ compared to $N \approx 40$ for Ziegler-Natta and $N \approx 30$ for polyacetylene dispersions). This indicates that the thermal conversion process leads to a polyene interrupted by sp^3 -defects caused by an incomplete elimination of the phenylsulfoxide moiety. Thus, the conditions of the elimination process have to be optimized. The broad Raman bands of the converted PPVS films can be contributed to a broad distribution of chain lengths supporting the idea of statistical defects in the polyene chain.

DFWM-measurements were performed with the all-trans samples at wavelengths around 720 nm (partly resonant, at the edge of the tuning range of the modelocked Ti:Sapphire laser). A typical relaxation curve is given in Figure 6 for a spin-coated

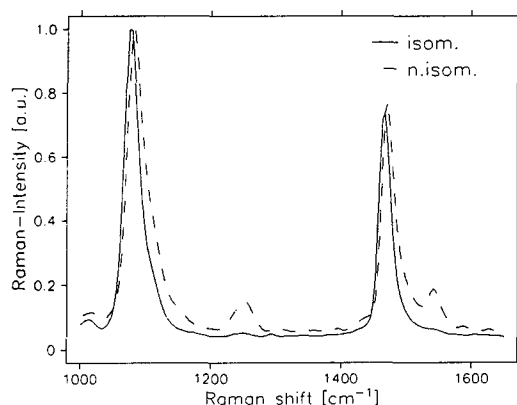


FIGURE 4 Raman shifts of $C=C$ -(trans-configuration 1466.4 cm^{-1} (isomerized), and 1470.8 cm^{-1} (not isomerized) resp., cis-configuration 1252 cm^{-1}) and $C-C$ -stretching vibrations (trans-configuration 1076.5 cm^{-1} (isom.), and 1081.8 cm^{-1} (not isom.), resp.) of thin films of a polyacetylene dispersion before and after thermal isomerization.

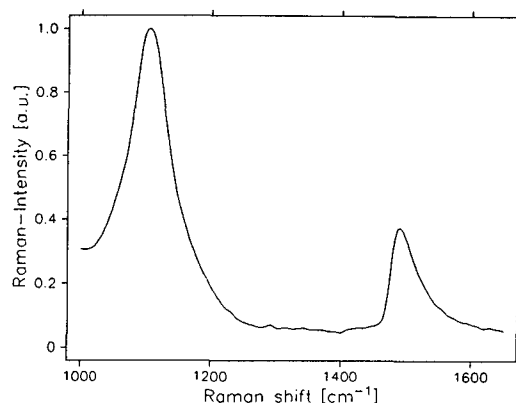


FIGURE 5 Raman shifts of $C=C$ -(1489 cm^{-1}) and $C-C$ -stretching vibration (1104 cm^{-1}) of a thin film of converted PPVS material (exclusively all-trans). The broad bands are attributed to a broad distribution of chain lengths.

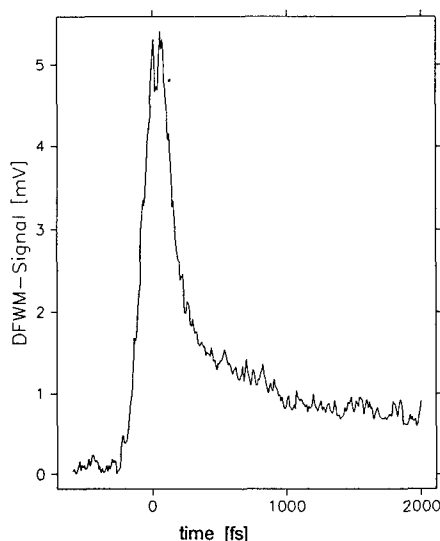


FIGURE 6 Ultrafast relaxation behavior of a thin film of a spin-coated polyacetylene dispersion.

polyacetylene dispersion. The relaxation curve consists of two parts, one decay being instantaneous (in the measurement limited by laser pulse width) and one decay time of the order of 1.5 ps.

The DFWM $\chi^{(3)}$ -values and the absorption constants α of the polyene films are given in Table 1. The highest nonlinearities of nearly 10^{-7} esu were found with films of polyacetylene dispersions. This may be attributed to the better optical quality of the dispersion film compared to the Ziegler-Natta samples since the film quality influences the intensity of the DFWM signal quite a lot. By changing the polyacetylene concentration of the dispersions and the spin-coating conditions the absorption constant α can be manipulated. The experimental findings show that $\chi^{(3)}$ scales linearly with α .

No DFWM signal of the converted PPVS samples could be detected so far around 720 nm with the DFWM experiment of Figure 1. This may be explained by a reduction of the resonance enhancement due to blue shifted absorption of the short chain lengths (see above).

TABLE 1
 $\chi^{(3)}$ values, relaxation times τ and absorption constants α of polyene thin films.

Polyene film	$\chi^{(3)}$ [esu]	$\chi^{(3)}/\alpha$ [esu-cm]	τ
Ziegler-Natta isomerized	$4 \cdot 10^{-8}$ (1P-DFWM) ($\alpha = 47000 \text{ cm}^{-1}$)	$8 \cdot 10^{-13}$	< 100 fs, 1.5 ps
PA-Dispersion (PVB) isomerized	$9.9 \cdot 10^{-8}$ (1P-DFWM) ($\alpha = 92000 \text{ cm}^{-1}$)	$1.1 \cdot 10^{-12}$	< 100 fs, 1.5 ps
	$4.8 \cdot 10^{-9}$ (1P-DFWM) ($\alpha = 3300 \text{ cm}^{-1}$)	$1.4 \cdot 10^{-12}$	< 100 fs, 1.5 ps
PPVS precursor	$1.7 \cdot 10^{-10}$ (THG)		

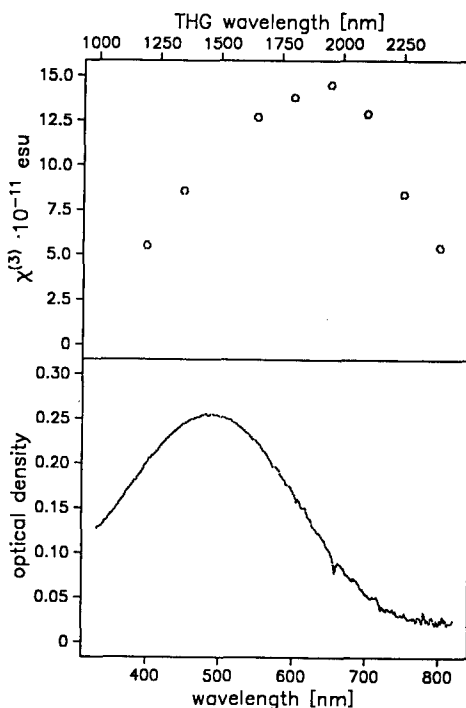


FIGURE 7 Wavelength dependence of $\chi^{(3)}$ -nonlinearity (upper trace) and absorption (lower trace) of converted PPVS thin films (75% PPVS, 25% PMMA).

Frequency tunable THG-measurements (Fig. 7) show relatively high $\chi^{(3)}$ values up to $1.7 \cdot 10^{-10}$ esu and a typical resonance behavior known for carotinoids.¹⁵ THG nonlinearities around 1650 nm of Ziegler-Natta and polyacetylene dispersion samples are of the same order of magnitude. The nonlinearities (THG) of converted PPVS samples did not change significantly when the molecular weight of the precursor material was varied from $M_p = 3000$ to 22500 indicating again that the thermal conversion leads to sp^3 -defects as mentioned above.

CONCLUSION

Femtosecond DFWM and frequency tunable THG measurements were performed on all-trans polyacetylene thin films prepared by different processes: 1. gas phase polymerization (Ziegler-Natta) on a glass substrate, 2. spin-coating of a polyacetylene dispersion and 3. spin-coating of a soluble PPVS precursor polymer followed by a thermal conversion into polyene. The conjugation lengths of the polyene thin films were analyzed using absorption and FT-Raman spectroscopy. The Ziegler-Natta material showed the longest conjugation followed by the Luttinger type polyacetylene dispersion. Thermal conversion of PPVS leads to the shortest chain lengths among these methods. This behavior was mirrored in the NLO measurements yielding resonantly

enhanced $\chi^{(3)}$ values up to 10^{-7} esu (DFWM) and relaxation times less than 2 ps for the Ziegler-Natta and the dispersion sample. The absorptive losses are still too high for a potential device operation.

ACKNOWLEDGEMENT

This work was performed under the management of Japan High Polymer Center as a part of Industrial Science and Technology Frontier Program supported by New Energy and Industrial Technology Development Organization.

REFERENCES

1. Prasad, Williams, *Introduction to Nonlinear Optical Effects in Molecules and Polymers*, Wiley, New York, 1991
2. *Conjugated Polymers*, Ed. Bredas, Silbey, Kluwer Academic Publishers, Dordrecht, 1991.
3. Krausz, Wintner, Leising, *Phys. Rev., Condens. Matter*, **39**, 3701 (1989).
4. Heeger, Moses, Sinclair, *Synth. Met.*, **15**, 95 (1986).
5. Sariciftci, Kobryanskii, Reghu, Smilowitz, Halvorson, Hagler, Mihailovic, Heeger, *Synth. Met.*, **53**, 161–74 (1989).
6. Fann, Benson, Madey, Etemad, Baker, Kajzar, *Phys. Rev. Lett.*, **62**, 1492 (1989).
7. Naarmann, *Electrically conducting polymers*, *Ullmann's Encyclopedia of Industrial Chemistry*, Vol. A21, p. 433 (1992) VCH Publishers, Weinheim. Naarmann, Theophilou, *Synthetic Metals*, **22**, 1 (1987).
8. Ito, Shirakawa, Ikeda, *J. Polym. Sci., Polym. Chem.*, **12**, 11 (1974).
9. Luttinger, *Chem. and Ind.*, **3**, 1135 (1960).
10. Green, Nehmé, Wilkinson, *Chem. and Ind.*, **3**, 1136 (1960).
11. Kanga, Hogen-Esch, Randrianalimanana, Soum, Fontanille, *Macromolecules*, **23**, 4235–4240 (1990); *ibid.* 4241–4246.
12. Schaffer, Chance, Silbey, Knoll, Schrock, *J. Phys. Chem.*, **94**, 4161 (1990).
13. Harada, Furukawa, Tasumi, Shirakawa, Ikeda, *J. Phys. Chem.*, **73**, 4746 (1980).
14. Brivio, Mulazzi, *Phys. Rev.*, **B30**, 876 (1984).
15. Haas, Ticktin, Esser, Fisch, Paust, Schrof, *J. Phys. Chem.*, **97**, 8675 (1993).

Femtosecond Time Resolved Measurement of the Nonlinear Refractive Index of Thiophene Oligomers in Solution

DAO VAN LAP, S. RENTSCH and H. NAARMANN*

Inst. Opt. and Q. E., Universität Jena, Max-Wien-Platz 1, 07743 Jena,

**BASF AG, Plastic Res. Lab., Ludwigshafen*

Received 12 January 1994; accepted 11 March 1994

Femtosecond time resolved measurements of the nonlinear refractive index have been performed by a deflection method and by a Kerr method as well. A colliding pulse laser amplifier system yields 75 fs pulses at 616 nm.

The amplified pulses (10^{11} W/cm²) generate an intensity induced refractive index in the sample $\Delta n = n_2 I$. A weak probe beam meeting the excited medium at various delay times will be deflected proportional to Δn .

n_2 -values were measured for thiophene oligomers in solution and partly at films. Hyperpolarizabilities of negative sign were obtained, the greatest value was $\gamma(6T) = -4.3 \cdot 10^{-33}$ esu.

The difference $n_{\parallel} - n_{\perp}$ obtained by deflection measurements agrees well with Kerr effect results. The γ values increase with the size of the thiophene oligomers.

INTRODUCTION

The dynamics of nonlinear processes in organic molecules and polymers is of scientific and technical interest as well.¹ The time behaviour of $\chi^{(3)}$ -susceptibilities in ps and fs region gives information about intra- and intermolecular processes.³ The relaxation of laser pulse induced refractive index is of interest for optical switching at all optical devices. Therefore, the elaboration of methods for time resolved studies of nonlinear properties is important. In this paper we used a deflection method² and a well known Kerr method³ for time resolved studies on thiophene oligomers.

EXPERIMENTAL

Nonlinear refractive index measurements were carried out by the deflection method and by optical Kerr effect measurement with fs time resolution.^{2,3} The laser radiation, generated by colliding pulse mode locking and amplified in a four stage amplifier with a repetition rate of 1 Hz consists of 75 fs pulses of 100 μ J energy at 616 nm with a beam diameter at the sample plane of 400 μ m. Both methods, deflection and Kerr effect were used in the same experimental arrangement with respect to the beam adjusting and the time delay shown in Figure 1.

In Figure 2 the schema of the deflection method is shown. A strong pump and a weak probe pulse meet on the aperture AP.

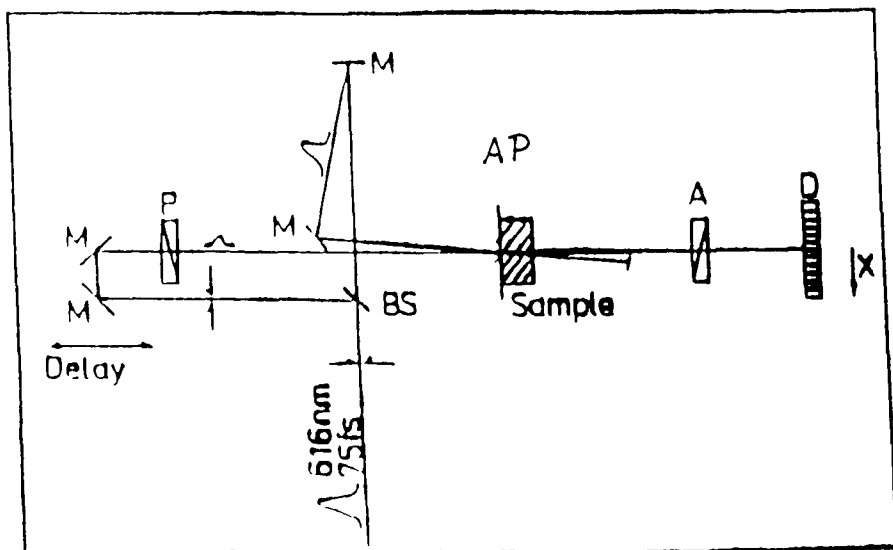


FIGURE 1 Scheme of time resolved measurement of nonlinear refractive index by deflection and by Kerr effect (M-mirror, BS-beam splitter, P-polarizer, A-analyser, Ap-aperture, S-sample).

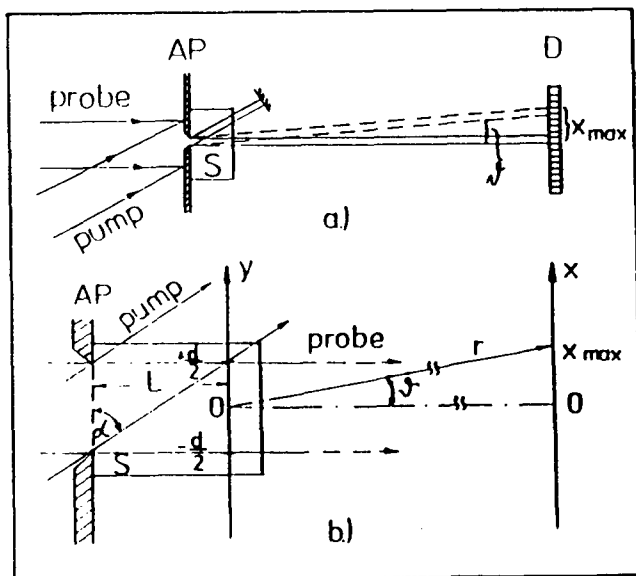


FIGURE 2 Scheme of beam deflection by pump beam induced refractive index (AP-aperture, S-sample, L-length, θ -deflection angle).

The sample S of the thickness l is placed directly behind the aperture slit.

The pump beam crosses the probe beam with the angle α and induces a refractive index change. The probe beam crosses the entrance plane perpendicularly. The probe beam will be deflected at the border plane between the pumped and nonpumped region

of the sample corresponding to the refractive law. The pump pulse induced deviation of the probe beam can be measured by a diode array placed at a distance r behind the sample.

It holds $\tan \vartheta = x_{\max}/r$, where x_{\max} is the maximum value of the displacement on the diode array. From the angle ϑ the index change Δn can be determined² using the formula

$$\Delta n(t) = \frac{\sin \vartheta(t)}{\tan \alpha} \quad (1)$$

In a solution, where the interaction between solvent and solute molecules can be neglected, χ^3 is given by

$$\chi^{(3)} = L^4(N_S\gamma_S + N_M\gamma_M)$$

with S for solvent and M for molecules of the densities N_S, N_M . Thereby is $L = (n^2 + 2)/3$ the local field factor and γ the second hyperpolarizability.

The reliability of the method was tested with fused silica SQ_1 . With a pump pulse intensity of $5.4 \cdot 10^{11}$ W/cm² we obtained $n_2 = (3.5 \pm 0.8) \cdot 10^{-16}$ cm²/W in agreement with:⁴ $n_2 = 3.31 \cdot 10^{-16}$ cm²/W and⁵: $n_2 = 2.73 \cdot 10^{-16}$ cm²/W for SQ_1 .

Figure 3 shows the registered probe beam profile on the diode array in dependence on the delay between pump and probe pulse. For any selected delay time 40 laser shots of a pulse energy within a fixed energy window were averaged. The time dependent position of the maximum is a measure for Δn . At the deflection arrangement the diode array located in a distance behind the sample measures the deviation from the "umpumped" direction. The pixel distance (25 μ m) allowed an angle accuracy of $6 \cdot 10^{-5}$ rad. The diaphragm AP at the front plane of the sample amounts to 150 μ m compared with 400 μ m beam diameter. So the intensity profil behind the diaphragm is nearly rectangular.

The Kerr method consists in a transmission measurement of the probe beam intensity after passing crossed polariser and analyser with the pumped or unpumped sample in between. Without pump pulse the probe beam transmission is zero. With a pump pulse polarization of 45° to that of the probe pulse the laser induced double refractive changes the polarization of the probe radiation. The phase angle between the parallel and perpendicular part of the probe beam amounts to

$$\Phi(t) = \frac{2\pi \Delta n_k(t)l}{\lambda_0} \quad (2)$$

($\Delta n_k = n_{\parallel} - n_{\perp}$, λ_0 -probe beam wavelength and l -interaction lengths of pump and probe pulse).

The probe beam transmission is given by

$$T(t) = \sin^2\left(\frac{\Phi(t)}{2}\right). \quad (3)$$

At the Kerr arrangement the intensity values of both polarization components (\parallel and \perp) of the probe beam were measured by a multiplier. The reliability of the methods has been proved by well known samples, SQ_1 and CS_2 .²

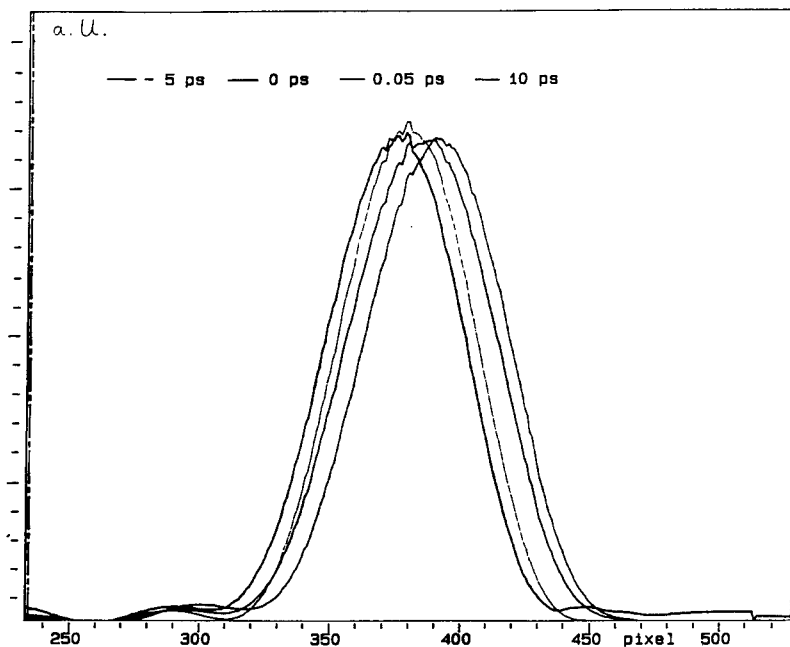


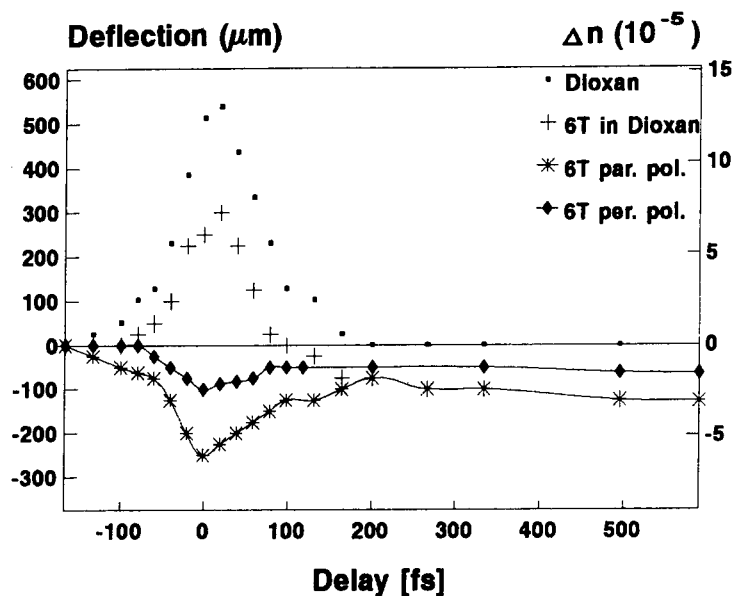
FIGURE 3 Deflection and beam profile of probe radiation at different delay times.

EXPERIMENTAL RESULTS AND DISCUSSION

Figure 4 shows the beam deflection on solved 6T and on neat dioxan at parallel and perpendicular polarization of probe to pump beam of $I = 3 \times 10^{11} \text{ W/cm}^2$. During the pump pulse duration we observed the strongest index change, the deflection follows the time course of the pump pulse. After that the deflection increases up to about 1 ps and remains constant up to more than 10 ps (not shown). The time dependence of parallel and perpendicular polarized beams is very similar. The deflection of the solution compared with the solvent shows negative n_2 -values for thiophene oligomers at 616 nm.

The deflection during the pump pulse is caused by pure electronic interaction of light and molecules and coherence interaction of the pump and probe pulses.

For interpretation of the non electronic part of n_2 , which exist many picoseconds, we use our results of time resolved spectroscopy.⁶ We found transient absorption bands for nT in the red spectral region. These bands were generated by one photon absorption (308 nm) and two photon absorption (616 nm) as well. The depletion of the ground state and occupation of excited states may cause the slow part of $n_2(t)$. Refractive index values are influenced by the number density of oscillators and their resonance absorption frequencies as well. We assume, that the negative n_2 values are caused by the induced change of the linear absorption,⁷ and therefore the long n_2 -lifetime reflects the relaxation of excited states.⁶ The results of n_2 measurements of a series of thiophene oligomers are represented in Table 1. In Table 2 the second hyperpolarizabilities

FIGURE 4 Time resolved deflection measurement on 6T in dioxan ($c = 10^3$ mol/l).TABLE 1
Nonlinear refractive index.

nT	Deflection		Kerr-Method	
	$n_{\parallel}(10^{-16})$ $\text{cm}^2/\text{W}^{1)}$	$n_{\perp}(10^{-16})$ $\text{cm}^2/\text{W}^{2)}$	$\Delta n = n_{\parallel} - n_{\perp}$ $(10^{-16})\text{cm}^2/\text{W}$	$\Delta n(10^{-16})\text{cm}^2/\text{W}$
1T	+13.0	+5.1	+7.9	
2T	-0.25	-0.12	-0.13	$+0.08 \pm 0.04$
3T	-0.33	-0.12	-0.21	-0.1 ± 0.08
4T	-0.60	-0.27	-0.33	-0.27 ± 0.08
5T	-1.39	-0.69	-0.70	-0.59 ± 0.1
6T	-2.93	-1.21	-1.72	-1.4 ± 0.1
8T in film				$-(5.1 \pm 0.2)10^3$

¹⁾ accuracy ± 0.2 .²⁾ accuracy ± 0.1 .TABLE 2
Molecular second hyperpolarizabilities.

nT	$\chi_{\parallel}^3(10^{-14})$ esu	This work $\gamma(\text{esu})10^{-34}$;	Ref. 1 $\gamma(\text{esu})10^{-34}$;
1T		+0.018	0.041
2T	-0.11	-3.9	0.22
3T	-0.15	-5.2	1.4
4T	-0.29	-9.1	8.0
5T	-0.68	-21	26
6T	-1.46	-44	100
8T (in film)	$-3.7 \cdot 10^{-11}$ esu	-50	-

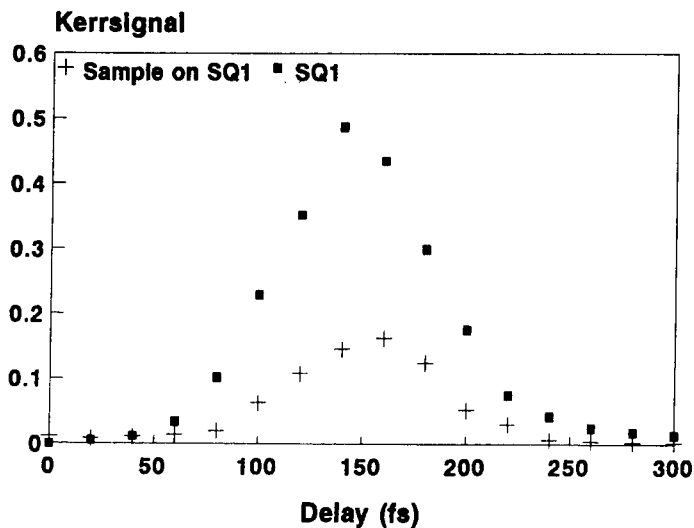


FIGURE 5 Time resolved Kerr effect measurement on a thiophene oligomer film on SQ 1 substrats.

calculated from n_2 are compared with results of DFWM experiments with fs pulses in films reported by Zhao *et al.*¹

Both series of results lie in the same order of magnitude, both show the increase of the nonlinear values with the number of monomers per molecules. A convergence of the values could not be observed up to $n = 6$. The different sign of γ in our work and in paper¹ is caused in our opinion, by the different employed intensities in both experiments (300 GW/cm² here, 400 MW/cm² in paper.¹ At low intensities the ground

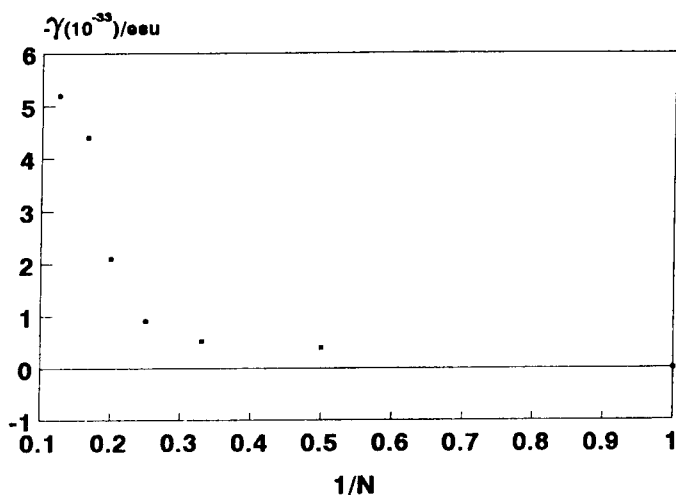


FIGURE 6 Size dependence of the hyperpolarizability γ of thiophene oligomers.

state depletion is negligible where as at high intensity an occupation of excited electronic levels by two (or multi) photon absorption is remarkable. Therefore nonlinearity of higher order than χ^3 may take part and may be responsible for the negative sign. The Kerr method described above was applied to thiophene solution and film as well. An 8T film on SQ1 substrate was measured and compared with the value for the pure substrate (Fig. 5). From the Kerr signal observed on a 200 nm thiophene film we obtained a value of $n_2 = -(4.2 \pm 1) 10^{-13} \text{ cm}^2/\text{W}$.

Measurements in solution were performed using in solution a 1 mm thick cuvette with windows of 100 μm thickness. Thereby the condition of small phase change ($\Phi < 0.5 \text{ rad}$) was kept.

The results of Kerr effect measurements together with the results of the deflection measurement, expressed as $\Delta n = n_{\parallel} - n_{\perp}$ are represented in Table 1.

The results of both methods are in good agreement. Figure 6 shows the hyperpolarizabilities in dependence on the inverse oligomer size.

REFERENCES

1. M. T. Zhao, B. P. Singh and P. N. Prasad, *J. Chem. Phys.*, **89**, 5535 (1988).
2. H.-S. Albrecht, P. Heist, J. Kleinschmidt and D. V. Lap, *Appl. Phys. B*, **57**, 193 (1993).
3. D. MeMorrow, W. T. Lotshav and G. A. Kenney-Wallace, *IEEE J.Q.E.*, **24**, 443 (1988).
4. C. deC. Chamon, C. K. Sun, K. A. Haus and J. G. Fujimoto, *Appl. Phys. Lett.*, **60**, 533 (1992).
5. P. W. Hellwart, *Progress in Quantum Electr.*, 5 part 1 (pergamon press, New York, 1977).
6. H. Chosrovian, D. Grebner, S. Rentsch and H. Naarmann, *Synth. Metals*, **52**, 213 (1992).
7. V. Philippart, M. Dumont, I. M. Munzi and F. Charra, *Appl. Phys. A*, **56**, 29 (1993).

Nonlinear Optical Properties of Tetraaryl Substituted Metal Dithiolene Complexes in the Near Infra-Red

S. N. OLIVER, S. V. KERSHAW, A. E. UNDERHILL*, C. A. S. HILL* and A. CHARLTON*

*Advanced Technologies Section, BT Laboratories, Martlesham Heath, Ipswich IP5 7RE, United Kingdom, *Department of Chemistry, University College of North Wales, Bangor, LL57 2UW, United Kingdom*

Received 12 January 1994; accepted 2 February 1994

The nonlinear refractive index, n_2 , of a series of tetraaryl substituted metal dithiolenes have been measured by degenerate four wave mixing. For the same ligand substitution the nonlinearity is shown to depend markedly on the metal in the series Ni, Pd, Pt. Saturation of the nonlinearity occurs to a greater or lesser extent in all cases. In at least one of these cases it is suggested that this is due to removal of electrons from the first directly excited state by excited state absorption. Excited state lifetimes in the range < 35 ps to several hundred ps are inferred by time delay studies. It is shown that there may be a power region of operation in some of these materials where large magnitude, fast nonlinearity could be accessed in a guided wave photonic switch application.

INTRODUCTION

Photonic switches in optical telecommunications systems will require materials that show a combination of high nonlinear refractive index and low loss in the near infra-red where fibre transmission losses are at a minimum. We have approached the search for such materials by looking for near-resonance enhancement of the nonlinearity while being prepared to trade off some increase in absorption and decrease in speed of response. Higher nonlinearities are needed to enable devices to be fabricated which are physically small and thus integratable with other components and which minimise problems of latency and stability. In practical all-optical switches, absorption might well be tolerable at levels comparable with waveguide fabrication losses. Temporal responses in the region of a few picoseconds would make optical switching attractive compared to electronic switching. Our choice of material has focused primarily on metal dithiolene complexes,^{1,2} the schematic structure of which is shown as I. By varying the metal, the ligands and the charge state a wide range of structures are available that show strong absorption throughout the visible and near infra-red.³ Estimation of molecular γ 's by CNDO methods also encouraged us by indicating that these materials would be good candidates for optical switching applications.⁴ Organometallic materials in general have recently been recognised as showing interesting nonlinear optical properties.⁵

Using information gained from studies in solution we have made host PMMA films with guest phenyl butyl nickel dithiolene (structure I, $M = \text{NiR}_1 = \text{phenyl}$, $R_2 = \text{n-butyl}$) at 20% loading which show n_2 values up to $10^{-8} \text{ cm}^2/\text{kW}$ at $1.064 \mu\text{m}$ but with absorption values of ten's of cm^{-1} . These films also showed increasing two photon absorption as the dithiolene loading increased.^{6,7} However this established that highly loaded polymer films could be made which retain the nonlinearity extrapolated from dilute solution. The majority of our further studies have concentrated on solutions to try to understand the behaviour of these materials and hence to enhance the useful nonlinear properties by structural modification. While we have previously reported that the optical nonlinearity does scale approximately with absorption for a range of derivatives at a fixed measurement wavelength of $1.064 \mu\text{m}^2$, it was not clear that this was an inescapable drawback for all materials of this type or indeed if the dispersion of $\chi^{(3)}$ and α would be the same. Another consideration of concern in the design of materials useful for optical switching is the time response of the nonlinearity. Our previous measurements have been limited by the temporal width of the 100 ps laser pulses used. Responses limited by 35 ps pulses at $1.064 \mu\text{m}$ in structurally related compounds have however been reported.⁸ Although the mechanism of the nonlinearity had not been established, at least in the case of materials with $\lambda_{\text{max}} > 250 \text{ nm}$ blue shifted from $1.064 \mu\text{m}$, a fast electronic nonlinearity was strongly indicated.⁷

We have now extended our investigations to derivatives of dithiolenes with four aryl substituents and containing platinum and palladium as the metal. We have measured nonlinearities of these derivatives in solution using 100 ps and 35 ps pulses (the shortest we can attain on our laser) and carried out further studies on the time response of the nonlinearity.

EXPERIMENTAL

Dithiolenes are of the general structure depicted as I. The specific derivatives discussed here are shown in Table 1. and were made at the University of Wales, Bangor, following procedures developed by Mueller-Westerhoff *et al.*⁹ Absorption spectra profiles of the 4-methylphenyl derivatives are shown in Figure 1.

Nonlinear optical measurements were made at $1.064 \mu\text{m}$ on solutions of the dithiolenes in dichloromethane by degenerate four wave mixing (DFWM) in the retroreflecting pump geometry. Pure dichloromethane shows no detectable nonlinearity in our

TABLE 1

Composition and spectroscopic data for compounds described in text. Data (apart from molar extinction coefficient, ϵ_{max}) are for solutions in dichloromethane at a concentration of $10^{18} \text{ molecules/cm}^3$ ($1.7 \times 10^{-3} \text{ M}$)

R_1	R_2	Metal	Abbreviation	λ_{max} nm	α at $1.064 \mu\text{m cm}^{-1}$	ϵ_{max}
Phenyl	n-Butyl	Ni	PhBut NiDT	800	0.14	
4-methylphenyl	4-methylphenyl	Ni	MePh ₄ NiDT	882	2.8	45,800
4-methylphenyl	4-methylphenyl	Pd	MePh ₄ PdDT	906	2.8	48,800
4-methylphenyl	4-methylphenyl	Pt	MePh ₄ PtDT	823	0.11	58,300
4-methoxyphenyl	4-methoxyphenyl	Pt	MeOPh ₄ PtDT	860	0.44	

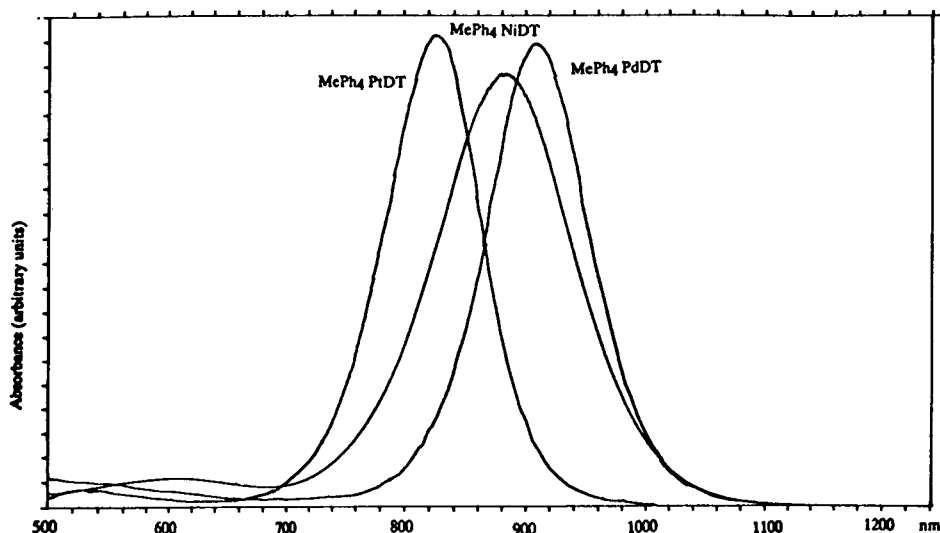
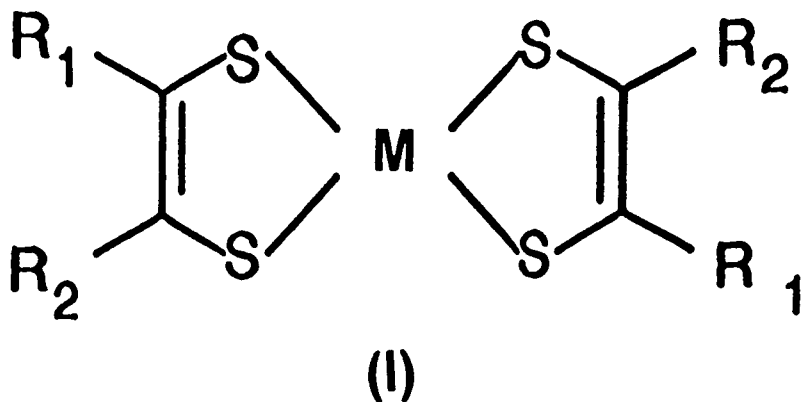


FIGURE 1 Absorption spectra profiles of the 4-methylphenyl dithiolenes. Quantitative spectroscopic data for these compounds and the others described in the text are given in Table 1.



experiments. The experimental set up has been described in detail by us elsewhere.² A brief description follows.

In DFWM two intense pump beams are formed from a single mode-locked pulse (100 ps or 35 ps) selected from the *Q*-switch envelope of a Nd:YAG laser and its retroreflected image from a plane dielectric mirror placed immediately behind the sample which is held in a 2 mm cuvette. A weak (10% of pump) beam is split off the forward pump and interacts with the two intense pump beams in the sample. This weaker beam is often referred to as the probe beam. All beams are parallel polarised so gratings can be set up between any permutation of pairs of beams. The phase conjugate (PC) beam, retroreflecting along the path of the forward going 10% beam, is split off and detected. Photomultipliers and energy meters are used to detect pump and PC energies (E_{pump} and E_{PC}). The square root of the reflectivity $R (= E_{\text{PC}}/E_{\text{pump}})$ is plotted

against input pump energy and the slope, G , of the plot ratioed to that from a reference CS_2 sample for which we take $\chi^{(3)}$ as $2.5 \times 10^{-20} \text{ m}^2/\text{V}^2$ (equivalent to an n_2 of $3.6 \times 10^{-11} \text{ cm}^2/\text{kW}$).^{10,11} From this can be derived the $\chi^{(3)}$ and hence n_2 of the solution.¹²

$$\frac{\chi^{(3)}_{\text{sample}}}{\chi^{(3)}_{\text{ref}}} = \frac{\alpha_{\text{sample}} L_{\text{ref}}}{T(1-T)} \times \frac{n_{\text{sample}}}{n_{\text{ref}}} \times \frac{G_{\text{sample}}}{G_{\text{reference}}}$$

where T is the transmission of sample, L is the reference path length and n the respective linear refractive indices

$$n_2 (\text{cm}^2/\text{KW}) = (3.77 \times 10^9 / n_{\text{sample}}^2) \cdot \chi^{(3)} (\text{m}^2/\text{V}^2)$$

Simple time delay studies were carried out by delaying one of the pumps by moving the back mirror away from the sample on a precision linear translation stage. Pump and probe temporal overlap can thus be varied. The PC energy was monitored as a function of displacement (converted to time delay) at constant input energy by averaging over 100 pulses at each displacement. Results are plotted relative to the PC at zero delay. Readings were taken on the outward and return travel of the translation stage.

RESULTS AND DISCUSSION

Degenerate Four Wave Mixing Using 100 ps and 35 ps Pulses

PhButNiDT is included as a benchmark material for this group of compounds which we have previously reported to have a n_2 of $2 \times 10^{-11} \text{ cm}^2/\text{kW}$ at the standard concentration of $10^{18} \text{ molecules/cm}^3$ as measured by DFWM or z-scan.¹³

Using 100 ps pulses the corresponding derived n_2 's for the other solutions in Table 1 are:-

MePh ₄ NiDT	$3.3 \times 10^{-10} \text{ cm}^2/\text{kW}$	$\alpha = 2.8 \text{ cm}^{-1}$
MePh ₄ PdDT	$1.9 \times 10^{-10} \text{ cm}^2/\text{kW}$	$\alpha = 2.8 \text{ cm}^{-1}$
MePh ₄ PtDT	$1.5 \times 10^{-11} \text{ cm}^2/\text{kW}$	$\alpha = 0.11 \text{ cm}^{-1}$
MeOPh ₄ PtDT	$3.6 \times 10^{-11} \text{ cm}^2/\text{kW}$	$\alpha = 0.44 \text{ cm}^{-1}$

Again in this series of materials a correlation between α and n_2 is observed but the nonlinear response of these materials are markedly different in their detail. In all cases saturation of the phase conjugate reflectivity with increasing input power occurs at a level which is material and concentration dependent. The reflectivity plots are shown in Figures 2 and 3 for MePh₄NiDT and MePh₄PdDT respectively. In each case the initial linear part of these plots, corresponding to a cubic dependence of phase conjugate on pump power, has been used for establishing $\chi^{(3)}$. Owing to the saturation limit at high input power and noise limited resolution at low power we are constrained to work in a fairly narrow input power region. We have previously shown that, by adjusting the concentration of solutions of saturating materials, that a good cubic response region can be obtained.² The value of $\chi^{(3)}$ per unit concentration obtained using this region is in very good agreement with those obtained from joining the origin in reflectivity plots to the data points taken before saturation begins. This justifies our use of the linear region shown in the Figures.

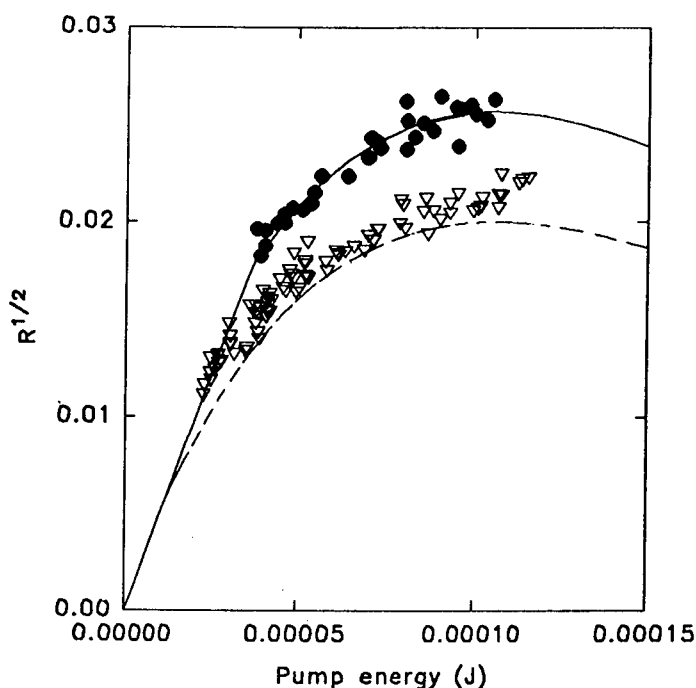


FIGURE 2 Phase conjugate reflectivity versus input pump energy for 0.54×10^{18} molecules/cm³ MePh₄NiDT in dichloromethane solution. Filled symbols are data points for 100 ps pulses and hollow symbols for 35 ps pulses. The solid line through the filled symbols is an empirical fit based on a cubic dependence of PC on input energy at low energy and a linear dependence after saturation. The dashed line is the expected response at 35 ps if the only effect is due to the increased power in the shorter pulses.

The pulse energies indicated in the plot for MePh₄NiDT correspond to power densities, I , before saturation of about 0.6 GW/cm^2 . A optical switching device requiring a π phase change in 1 cm length would require a $\Delta n (= n_2 I)$ of 5×10^{-5} . The power required for this is thus below the saturation level for the two dithiolenes above. The cross sectional area of a $2 \mu\text{m}$ diameter waveguide is $3 \times 10^{-8} \text{ cm}^2$ giving a power requirement of a few watts. The optical loss of such a guide would be about 12 dB. Clearly for device use some improvement in n_2 is required or alternatively a reduction in absorption so that longer devices are feasible.

Also shown as the hollow data points in Figures 2 and 3 are the results on the same solutions but using 35 ps pulses. In the case of MePh₄NiDT no difference in initial slope is seen and hence $\chi^{(3)}$ is the same but some difference in the saturation point is noted. For MePh₄PdDT a much greater difference is seen and only a very narrow cubic response region can be obtained using 35 ps pulses. A value of $\chi^{(3)}$ 1/3 rd that quoted above is cautiously estimated in this case.

The differences in the response using the two pulse widths is amplified at higher concentrations. The reflectivity plots for a derivative of MePh₄NiDT in which the methyl group is replaced with a n-heptyl to improve solubility are shown in Figure 4 for a concentration of 1.98×10^{18} molecules/cm³. The measured $\chi^{(3)}$ for this compound at 100 ps and at an equal concentration is virtually the same as for MePh₄NiDT but by

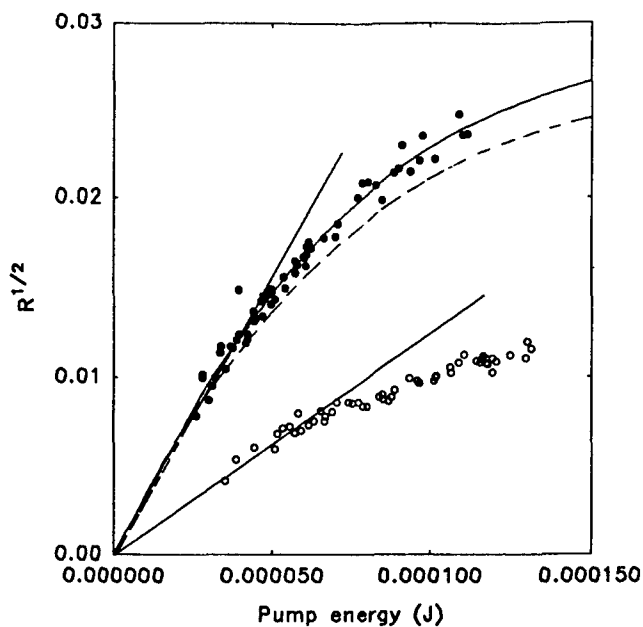


FIGURE 3 Phase conjugate reflectivity versus input pump energy for 0.65×10^{18} molecules/cm³ MePh₄ PdDT in dichloromethane solution. The symbols and lines have the same meaning as in Figure 2.

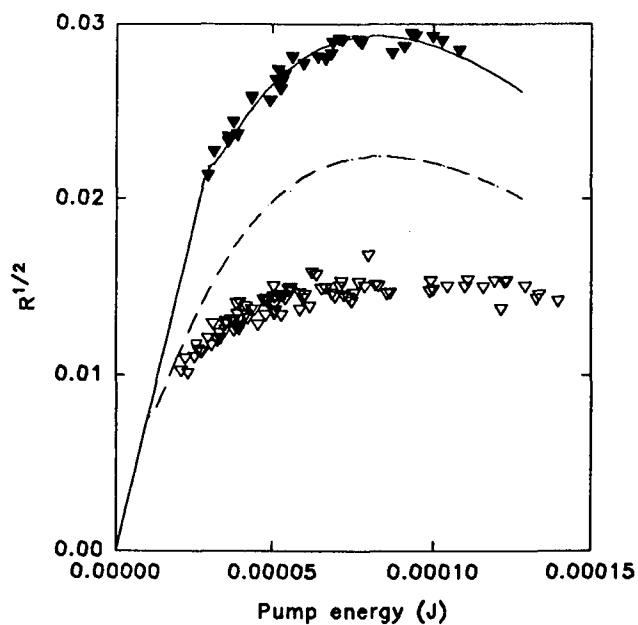


FIGURE 4 Phase conjugate reflectivity versus input pump energy for 1.98×10^{18} molecules/cm³ 4-n-heptylPh₄NiDT in dichloromethane solution. The symbols and lines have the same meaning as in Figure 2.

increasing the concentration four times a marked difference in saturation reflectivity using 35 ps pulses is seen. Maximum reflectivity is reduced for the more concentrated solution and there is some evidence of a smaller gradient and hence $\chi^{(3)}$.

For the MePh_4PtDT derivative a good cubic dependency of PC on pump energy was seen using 100 ps pulses. The reflectivity plot is shown in Figure 5. With 35 ps pulses only very low phase conjugate signals could be obtained at the highest energy pumps used.

For $\text{MeOPh}_4\text{PtDT}$ and 100 ps pulses a marked saturation is seen (Fig. 6) which is surprising for a material with relatively low absorption at the measurement wavelength. In our previous work on solutions of related materials which show absorption of this magnitude we had not seen saturation. For example PhBut NiDT at a similar concentration and sample thickness shows a similar α value at $1.064\text{ }\mu\text{m}$ but no saturation.

Further investigation of PhBut NiDT however reveals that saturation also occurs in this material at higher solution concentrations. Reflectivity plots for a 6×10^{18} molecules/ cm^3 solution of this material is shown in Figure 7. It can be seen that saturation occurs in this more highly absorbing solution when using 100 ps pulses. Using 35 ps pulses very low phase conjugate reflectivity was seen compared to that obtained with 100 ps pulses. Although the reflectivity plot is linear a less than cubic relationship between phase conjugate and input intensity is measured. No meaningful region of the plot can be used for the estimation of $\chi^{(3)}$. The lack of measurable phase conjugate with 35 ps pulses in this case is presumably a result of saturation at low reflectivity at low

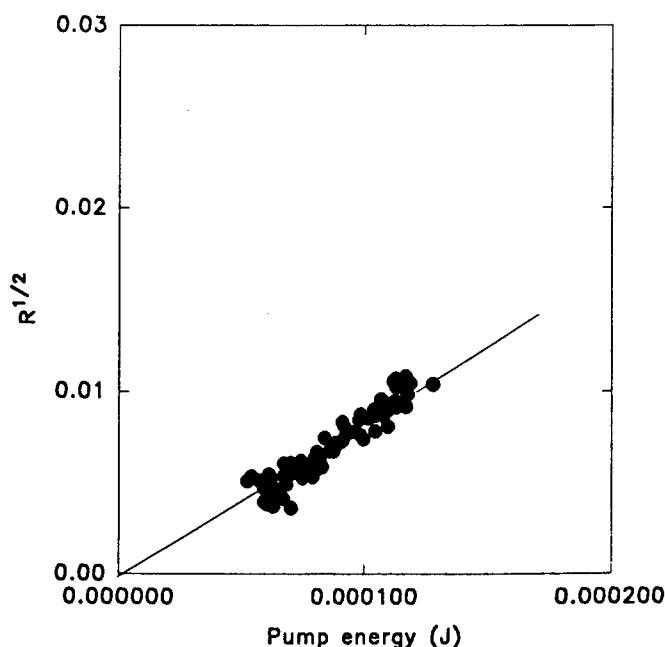


FIGURE 5 Phase conjugate reflectivity versus input pump energy for 0.74×10^{18} molecules/ cm^3 MePh_4PtDT in dichloromethane solution using 100 ps pulses.

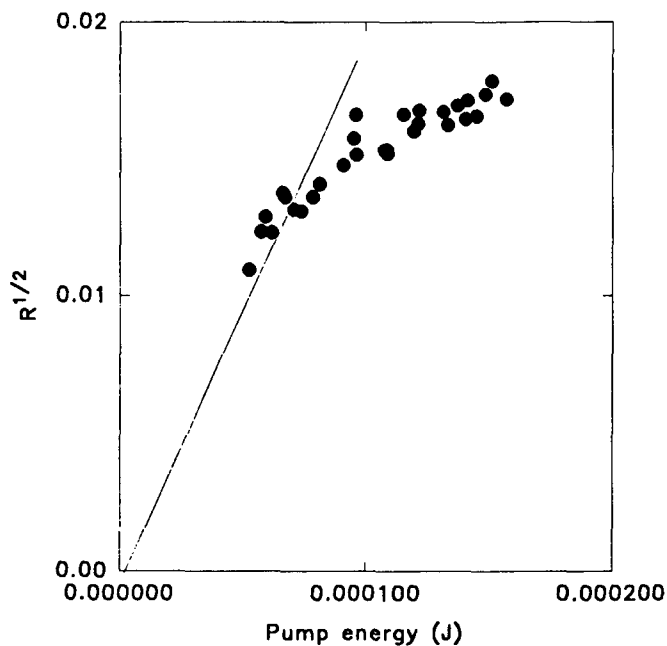


FIGURE 6 Phase conjugate reflectivity versus input pump energy for 1×10^{18} molecules/cm³ MeOPh₄ PtDT in dichloromethane solution using 100 ps pulses. The straight line corresponds to cubic dependence of phase conjugate on input energy.

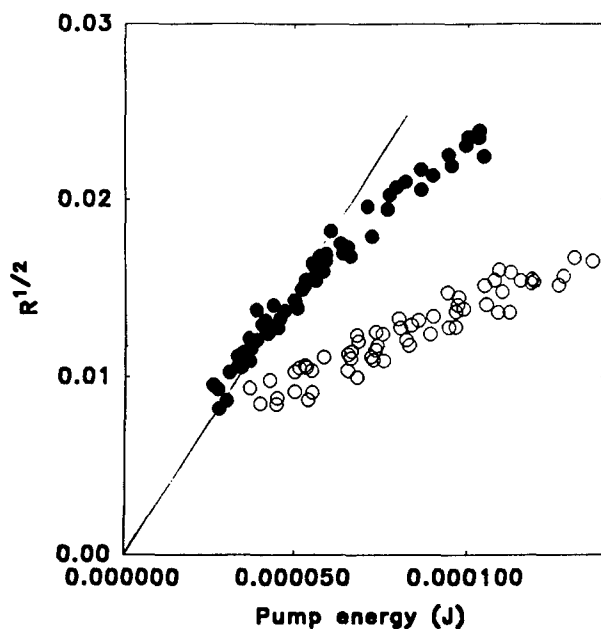


FIGURE 7 Phase conjugate reflectivity versus input pump energy for 6×10^{18} molecules/cm³ PhBut NiDT in dichloromethane solution. Filled symbols are data points using 100 ps pulses and hollow symbols for 35 ps pulses. The straight line corresponds to cubic dependence of phase conjugate on input energy.

input energy. This is a situation similar to that for the similarly absorbing MePh_4PtDT described above.

In comparison the reflectivity plots for CS_2 are coincident for the two pulse widths used and measured gradients are within the day to day variation seen with a fixed pulse width (typically 10% variation). This is expected since we measure and plot the integrated pulse energies, not intensities and this result for CS_2 shows that the beam diameter at the sample is the same in both cases.

The apparent different saturation point using the two pulse widths can be reconciled by the fact of saturation and consideration of our method of data collection and plotting. In the case of 35 ps pulses the intensity at the sample will be approximately 3 times higher so the PC will increase by 27 times for a third order process. Plotting $R^{1/2}$ vs input energy the slopes of the plot will remain the same in the absence of saturation. With saturation the equivalent input intensity at a point on the 35 ps plot will be much further into saturation on the 100 ps plot. For the way the data is presented in Figures 2–4 this effect shows up as a curve at lower saturating reflectivity for the shorter pulse width. In the case of MePh_4NiDT in Figure 1, it can be seen that the difference between the two pulse widths is accounted for by this effect. This is not the case for $\text{MePh}_4\text{Pd NiDT}$ or MePh_4NiDT at higher concentrations. In these cases a possible explanation is that slower processes contributing to the non-linearity are not being fully accessed with the shorter pulses. This could be due to intrinsically longer lived electronic states for the case where Pd is substituted for Ni and possible molecular aggregation effects with increasing concentration. Differences in ratio of $\text{Re:Im}\chi^{(3)}$ with concentration in these materials have been reported previously.⁷

These results coupled with our previous work seem to indicate that, in these tetraaryl derivatives, the nonlinearity arises from a real excitation with a lifetime in the sub 35 ps to 100 ps region. In the case of MePh_4NiDT the initial response is still pulse width limited at 35 ps indicating an excited state lifetime somewhat less than this. We have previously shown that, in solutions of this material, two photon absorption occurs the magnitude of which increases with concentration.²

Time Delay Studies

Figure 8 shows the time delay result for MePh_4NiDT in solution at both 100 ps and 35 ps pulse widths. Also shown are the responses for CS_2 where the plots are the autocorrelations of the laser pulses as the nonlinear grating decay time is only a few ps and much less than the laser pulse width in either case.

Figure 9 shows the effect of pulse energy on the decay time plot for MePh_4NiDT solution with 100 ps pulses. A clear difference between time response using pump energies in the saturating region (hollow symbols) and nearer the initial cubic non-linearity region (filled symbols) is shown. Even for these latter data some effect of saturation is thought to be present, but lower pump energies could not be used owing to the low PC signals at delays of more than 100 ps.

Figure 10 is the same plot at 100 ps for MePh_4PdDT where there is little difference between results for each pulse energy in line with the less pronounced saturation in this solution.

The result for a MePh_4PtDT solution is shown in Figure 11 and is closer to the expected response. It would be expected that an initial drop to half of the zero delay

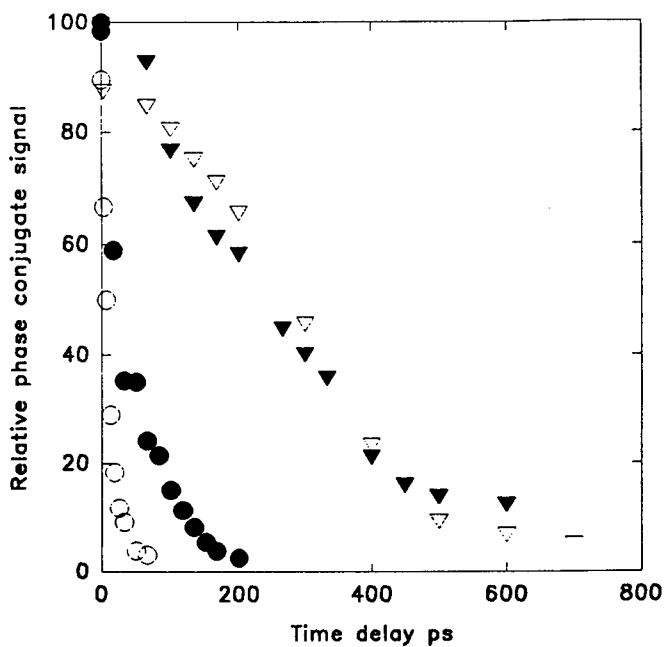


FIGURE 8 Effect of delaying the arrival of backward pump on the relative phase conjugate signal at two input pulse widths. Filled circles CS₂ – 100 ps, open circles CS₂ – 35 ps. Filled triangles 1.77×10^{18} MePh₄ NiDT – 100 ps, open triangles 1.77×10^{18} MePh₄ NiDT – 35 ps.

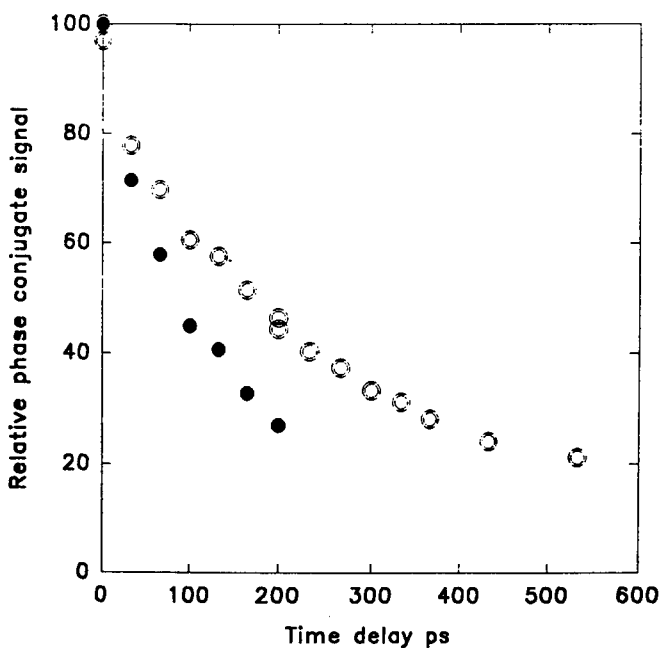


FIGURE 9 Relative phase conjugate signal decrease with delay time for 0.47×10^{18} MePh₄ NiDT at two input pulse energies and 100 ps pulses. Open circles – 125 μJ per pulse, filled circles 25 μJ per pulse.

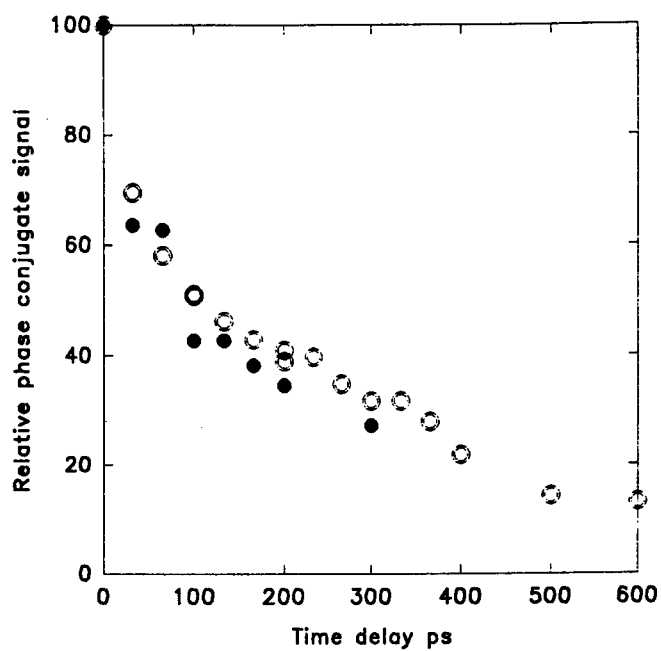


FIGURE 10 Time delay plot for 0.65×10^{18} MePh₄PdDT. Symbols have the same meaning as in Figure 9.

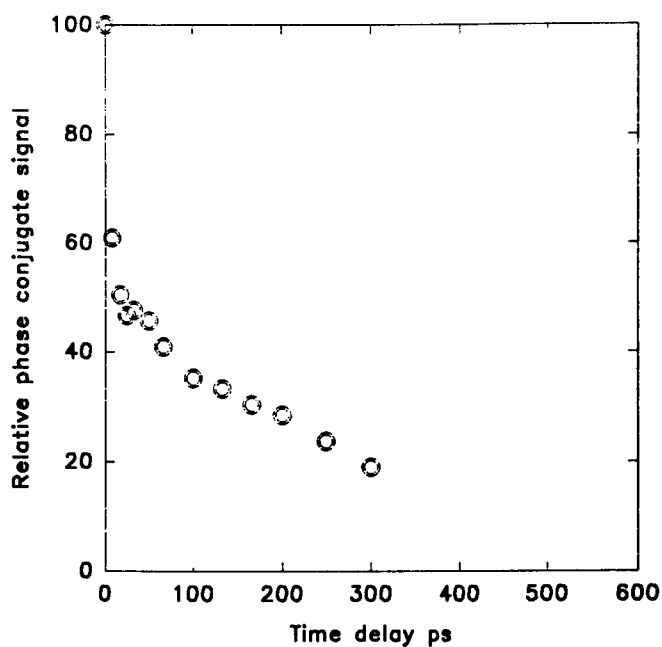


FIGURE 11 Time delay plot for 0.74×10^{18} MePh₄PtDT and 100 ps pulses.

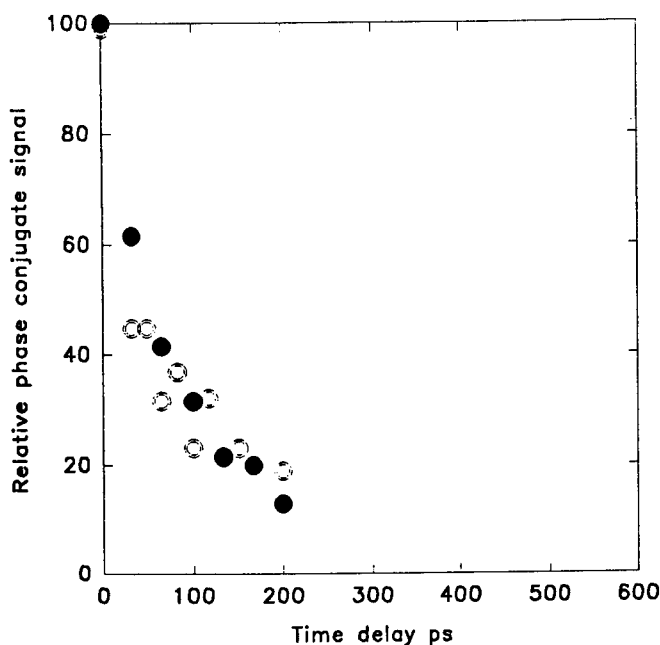


FIGURE 12 Time delay plot for 0.94×10^{18} PhBut NiDT and 100 ps pulses. Open circles — 80 μ J per pulse, filled circles 140 μ J per pulse.

contributing gratings (that due to the forward and backward pumps) disappearing leaving only the forward-probe grating to be probed by the retroreflecting pump. This is what is observed with the forward-probe grating decaying over a few hundred ps. A similar result is given by a PhButNiDT solution (Fig. 12) which shows no reflectivity saturation and hence no difference in decay time dependent on pump energy. In this case a slowest decay of 100–200 ps is indicated. The response of the tetraaryl derivatives of the other metals described above is governed by saturation and the grating decay plots show only the slowest decay component of the order of a few hundred ps. Faster decay times, coupled with large magnitude nonlinearity may be accessible by operating in the cubic region of the nonlinear response before saturation occurs. Indication that this could be the case is given by the decay curves shown at lower input pulse energies which show faster decay of the induced grating. It remains however to establish the limits of this by measurements using ps or sub ps pulses.

CONCLUSIONS

Large near resonant nonlinearities have been measured in tetraaryl metal dithiolenes and at least a component of the nonlinearity shown to have a response faster than 35 ps. Saturation of the nonlinearity limits the maximum usable index change available. The results given here however indicate that it may be possible to access a usable nonlinearity by operating below saturation at power levels compatible with guided

wave devices and current laser sources. Measurements further off resonance and using shorter laser pulses are required however to demonstrate this. These studies are currently underway at BT Laboratories.

ACKNOWLEDGEMENTS

We thank Jim Ainslie, Bob Manning and David Cotter at BT Labs for helpful guidance and comments.

REFERENCES

1. C. S. Winter, S. N. Oliver, R. J. Manning, J. D. Rush, C. A. S. Hill and A. E. Underhill, *J. Mater. Chem.*, **2**(4), 443 (1992).
2. S. V. Kershaw, S. N. Oliver, R. J. Manning, J. D. Rush, C. A. S. Hill, A. Underhill and A. Charlton, *Proc. SPIE*, **2025**.
3. U. T. Mueller-Westerhoff, B. Vance and D. I. Yoon, *Tetrahedron*, **47**(6), 909 (1991).
4. M. Papadopoulos, J. Waite, C. S. Winter and S. N. Oliver, *Inorg. Chem.*, **32**(3), 277 (1993).
5. H. S. Nalwa, *Appl. Organometallic. Chem.*, **5**, 349 (1991).
6. C. S. Winter, S. N. Oliver, J. D. Rush, C. Hill and A. E. Underhill, *J. Applied Phys.*, **71**(1), 512 (1992).
7. C. S. Winter, R. J. Manning, S. N. Oliver and C. Hill, *Optics Comm.*, **60** No. 1-3, 139 (1992).
8. Z. H. Kafafi, J. R. Lindle, S. R. Flom, R. G. S. Pong, C. S. Weisbecker, R. C. Claussen and F. J. Bartoli, *Proc. SPIE*, **1626**, 440 (1992). J. R. Lindle, C. S. Weisbecker, F. J. Bartoli, R. G. S. Pong, Z. H. Kafafi, *Mat. Res. Soc. Symp. Proc.*, **247**, 277 (1992).
9. U. T. Mueller-Westerhoff, A. Nazzari, R. J. Cox and A. M. Giroud, *Mol. Cryst. Liq. Cryst. (Lett.)*, **56**, 249 (1980).
10. W. E. Williams, M. J. Soileau, E. W. Van Stryland, *Opt. Commun.*, **50**, 256 (1984).
11. K. J. Witte, M. Galanti and R. Volk, *Opt. Comm.*, **34**, 278 (1980).
12. G. M. Carter, *J. Opt. Soc. Am. B*, **4**, 1018 (1987).
13. S. N. Oliver, C. S. Winter, J. D. Rush, A. E. Underhill and C. Hill, *Proc. SPIE*, **1775**, 110 (1992).

Third Harmonic Generation in New Crown Ether Substituted Metallotriazolehemiporphyrazines

M. A. DÍAZ-GARCÍA^a, I. LEDOUX^b, F. FERNÁNDEZ-LÁZARO^c, A. SASTRE^c,
T. TORRES^c, F. AGULLÓ-LÓPEZ^a and J. ZYSS^b

^a*Départamento Física de Materiales C-IV, Universidad Autónoma de Madrid*

^b*FRANCE TELECOM, CNET Paris B Département d'Electronique Quantique
et Moléculaire 196, Av. Henri Ravera, 92225 Bagneux, France,*

^c*Química Orgánica C-I, Universidad Autónoma de
Madrid, 28049 Madrid, Spain*

Received 12 January 1994; accepted 17 March 1994

The molecular hyperpolarizabilities γ of new highly soluble crown-ether substituted metallotriazolehemiporphyrazines (MThp) have been determined by third-harmonic generation (THG) in chloroform solutions. Two fundamental wavelengths (1.340 and 1.904 μm) have been used to investigate the dispersive behaviour. Both real and imaginary parts of γ have been measured from the concentration dependence of the THG susceptibility. Unfilled d-shell metal ions induce an enhancement of γ as compared to the metal-free molecule (H_2Thp). The highest values of the hyperpolarizability magnitude have been found for the Co-complexed compound (CoThp): $|\gamma| = 8.6 \times 10^{-33}$ esu ($\lambda = 1.340 \mu\text{m}$), $|\gamma| = 7.7 \times 10^{-33}$ esu ($\lambda = 1.904 \mu\text{m}$). A three-four level model has been used to account for the main experimental features, including the metal-induced enhancement of $|\gamma|$.

Keywords: third harmonic generation, metallotriazolehemiporphyrazines, three- and four-level models

INTRODUCTION

The current interest in photonic technologies has stimulated the search for high performance third-order nonlinear optical materials,^{1,2} such as π -conjugated organic molecules.^{1–4} In particular, metallorganic compounds⁵ present interesting features due to the presence of the metal, which may be used to optimize the nonlinear response. Thus, for example, the metallophthalocyanines⁶ offer a promising potential for large third-order nonlinearities. Their chemical versatility and stability allow the tailoring of their physico-chemical parameters, either by peripheral substitution or by central metal modification. Third harmonic generation experiments have been extensively made on these^{7–12} and related compounds,^{13–14} but unfortunately, most of them have been performed in thin films, where structure and order parameters are not well-defined, so that the third-order microscopic nonlinear optical response cannot be reliably inferred from the macroscopic one, contrary to the case of single-crystalline materials. Therefore, additional work at a molecular level is needed for a better understanding of the third-order response of these metallomacrocycles.

This paper reports on the preparation of new highly soluble crown-ether substituted metallotriazolehemiporphyrazines, whose structure is shown in Figure 1. These

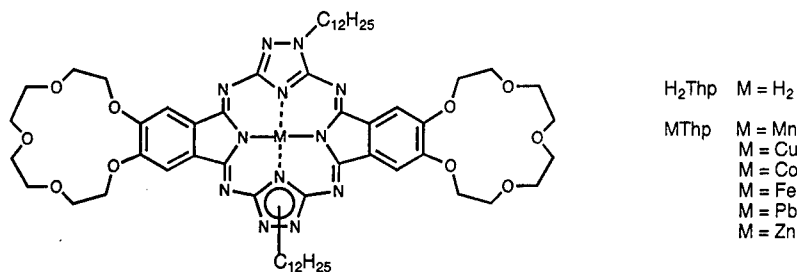


FIGURE 1 Chemical structure of crown-ether substituted metallotriazolehemiporphyrazines.

compounds are formal derivatives of phthalocyanines by replacement of two opposite isoindol rings by two 1,2,4-triazole subunits.

In a previous work¹⁵ sparingly soluble lipophilic-substituted metallotriazolehemiporphyrazines were synthesised and THG experiments were performed in chloroform solutions. Unfortunately, due to the limited solubility, only the real part of γ could be measured. Now, the real γ' and imaginary γ'' parts of the third-order molecular hyperpolarizabilities $\gamma(3\omega;\omega,\omega,\omega)$ ($\gamma = \gamma' + i\gamma''$) have been determined from the concentration dependence of the macroscopic THG susceptibilities $\chi^{(3)}(3\omega;\omega,\omega,\omega)$. Moreover, in order to gain information about the role of one- and two-photon resonances on γ values, experiments have been carried out at two fundamental wavelengths, 1.904 and 1.340 μm . Particular attention has been paid to the effect of metal complexation on both components of γ , which are enhanced for unfilled d-shell ions. Final data have been analyzed with a three-level model (metal-free compound) and a four-level model (metal-complexed compound).

EXPERIMENTAL TECHNIQUES

Synthesis

Metal complexes (MThp) were prepared by metallation of the free triazolehemiporphyrazine (H_2Thp), according to a procedure previously described for the synthesis of related compounds.¹⁵

Compound H_2Thp was synthesized as a mixture of regioisomers by condensation of 4,5(1,4,7,10,13-pentaoxatridecametilen)-1,3-diiminoisoindoline and dodecylguanazole.¹⁶

All compounds were characterized systematically by conventional techniques: IR, NMR, FAB-MS and UV-visible spectroscopies.

THG Experiments

The THG experiments have been performed in chloroform solutions, the third harmonic response being measured as a function of the concentration, using the Maker fringe technique with a liquid cell with thick windows in the wedge configuration.¹⁷ Measurements were made at fundamental wavelengths of 1.340 and 1.904 μm . The first one is emitted by a *Q*-switched $\text{Nd}^{3+}:\text{YAG}$ laser with 60 ns. pulse duration, while the second one is provided by a high pressure hydrogen cell pumped by a *Q*-switched

Nd³⁺:YAG laser (pulse duration 20 ns), leading to a Raman-shifted first Stokes radiation at 1.904 μm .

The method of analysis consists of two steps:

(1) A least-squares fit of the Maker fringes (harmonic intensity $J_{3\omega}$ as a function of cell translation x), given by the following equation,¹⁸ was carried out:

$$J_{3\omega}(C, x) = \left\{ \left(\frac{\chi^{(3)}}{\Delta\epsilon} \right)_G \left(\frac{t_{3\omega}^{GO}}{\beta^2} \right) (t_{3\omega}^{GL} t_{3\omega}^{LG} - \alpha\beta \exp(i\Delta\psi) (t_{\omega}^{GL} t_{\omega}^{LG})^3 \right. \\ \left. + \left(\frac{\chi^{(3)}}{\Delta\epsilon} \right)_L \left(\frac{\Delta\epsilon}{\chi^{(3)}} \right)_G (\alpha\beta \exp(i\Delta\psi) - 1) (t_{\omega}^{GL})^3 t_{3\omega}^{LG} \right\}^2 \quad (1)$$

where G and L refers to the window material and the liquid solution respectively. $t_{\omega}^{12}(3\omega)$ are the transmission factors between media 1 and 2, $\Delta\epsilon$ is the dielectric constant dispersion, $\Delta\psi$ the phase mismatch between the fundamental and harmonic waves and J_{ω} is the intensity of the fundamental wave. α and β are absorption factors given by

$$\alpha = \exp \frac{6\pi K_{\omega} l}{\lambda}; \quad \beta = \exp \frac{18\pi K_{3\omega} l}{\lambda} \quad (2 \& 3)$$

where λ is the excitation wavelength, K is the imaginary part of the refractive index and l is the liquid thickness, which depends on cell translation.

A fitting of equation (1) to the experimental $J_{3\omega}(C, x)$ values was performed for a number of concentrations (C). Therefore, the dispersion of the refractive index ($\Delta n = n_{\omega} - n_{3\omega}$) and the maximum harmonic intensity ($J_{3\omega}^M$) for each of concentration were determined.

(2) Then, a least-squares fit of the maximum intensity variation $J_{3\omega}^M$ (at fixed cell position x) as a function of concentration was carried out. For convenience, $J_{3\omega}^M$ was normalized with respect to the solvent. The macroscopic susceptibility $\chi^{(3)}$ appearing in equation (1) was written as a sum of the contributions of the solvent and the nonlinear molecule, that is

$$\chi^{(3)}_L = \frac{f\rho N_A}{(1+C)} \left\{ \frac{C(\gamma'_m + i\gamma''_m)}{M_m} + \frac{\gamma_s}{M_s} \right\} \quad (4)$$

where m and s refers to the nonlinear molecule and the solvent respectively, ρ is the density of the solution, N_A is Avogadro's number, M is the molecular weight and f is the local field factor, which in the Lorentz-Lorentz approximation reads

$$f = \left(\frac{n_{\omega}^2 + 2}{3} \right)^3 \frac{(n_{3\omega}^2 + 2)}{3} \quad (5)$$

This procedure allowed us to determine both: real (γ') and imaginary (γ'') parts of the averaged third order molecular hyperpolarizability ($\gamma = \gamma' + i\gamma''$), the hyperpolarizability of the solvent being known. It is important to note that the sign of γ'' is undetermined.

RESULTS

Optical Absorption Spectra

The electronic spectrum of H_2Thp compound is dominated by a strong absorption band in the near UV between 0.330 and 0.385 μm , similar to the B (Soret) band of phthalocyanines and porphyrins¹⁹ and several weak absorptions in the UV-visible region at 0.410–0.590 μm ($\pi \rightarrow \pi^*$ transitions). Additional absorptions due to metal-ligand and ligand-metal charge transfer (MLCT and LMCT respectively), as well as d–d transitions are observed in the electronic spectra of the metal complexes MThp in the 0.41–0.59 μm region and also between 0.5 and 0.7 μm . The spectra of H_2Thp and CoThp are displayed in Figure 2, as an example of the observed behaviour.

Third-order Nonlinear Hyperpolarizabilities

Real γ' and imaginary γ'' parts of $\gamma(3\omega:\omega, \omega, \omega)$, calculated by the previously described method, are listed in Table 1, together with the corresponding magnitude and phase. γ values are about one-order of magnitude lower than that measured by THG at 1.904 μm for the aromatic related compound, silicon-naftaphtalocyanine⁸ ($\gamma = -3.14 \times 10^{-33}$ esu). Higher values (as generally expected) have been determined from degenerate four-wave mixing (DFWM) at 1.064 μm for the magnitude of $\gamma(\omega:\omega, -\omega, \omega)$ in a number of metallophthalocyanines.⁹

From Table 1, a marked enhancement of both γ' and γ'' for unfilled d-shell metal ions is clearly apparent, particularly Fe and Co. γ' in CoThp is more than one order of

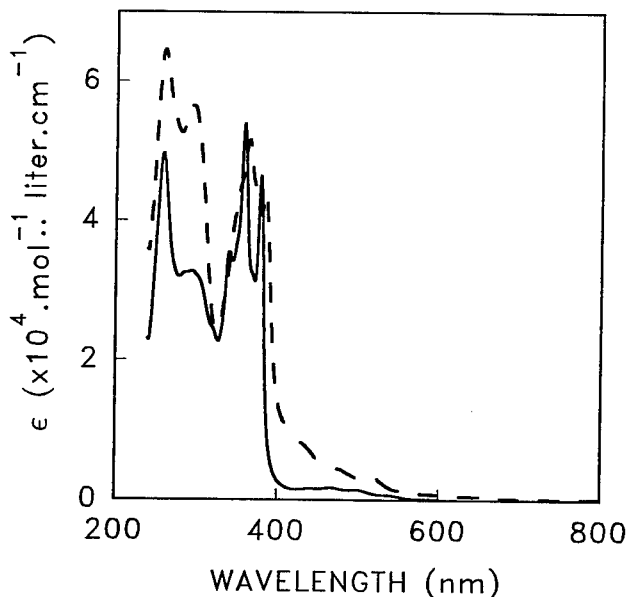


FIGURE 2 Optical electronic spectra of H_2Thp (Full line) and CoThp (Dashed line).

TABLE I

Third order microscopic hyperpolarizability γ of metallotriazolehemiporphyrines at 1.340 and 1.904 μm fundamental wavelengths. γ' , γ'' , $|\gamma|$, and ψ are real part, imaginary part, modulus and phase respectively. ϵ is the extinction coefficient at each wavelength from optical absorption spectra.

Metal	γ' ($\times 10^{-33}$) esu	γ'' ($\times 10^{-33}$) esu	$ \gamma $ ($\times 10^{-33}$) esu	$\psi(^{\circ})$	Log ϵ ($\text{mol}^{-1}\cdot\text{cm}^2$)
THG ($\lambda = 1.340 \mu\text{m}$)					
H ₂ Thp	-0.77	*	0.77	180	6.301
MnThp	-2.73	± 2.79	3.91	180 ± 45.6	6.479
FeThp	-2.98	± 3.23	4.39	180 ± 45.3	6.721
CoThp	-4.11	± 7.60	8.64	180 ± 61.6	6.847
NiThp	-1.60	± 1.89	2.48	180 ± 49.8	6.400
CuThp	-0.75	± 1.98	2.12	180 ± 69.3	6.304
ZnThp	-0.94	*	0.94	180	6.301
THG ($\lambda = 1.904 \mu\text{m}$)					
H ₂ Thp	+0.05	0	0.05	0	4.301
MnThp	-0.26	± 3.80	3.81	180 ± 86.1	5.568
FeThp	-0.50	± 2.80	2.84	180 ± 79.9	5.623
CoThp	-0.92	± 7.60	7.66	180 ± 83.1	5.643
NiThp	-0.31	± 1.89	1.92	180 ± 80.7	5.591
CuThp	-0.15	± 1.98	1.99	180 ± 85.7	5.255
ZnThp	+0.14	0	0.14	0	5.255

*(no reliable values)

magnitude higher than in H₂Thp. On the other hand, for ZnThp, with a d¹⁰ configuration, γ values are close to that of H₂Thp. Another interesting feature is the real character of γ for these two compounds, whereas the imaginary part is important for the metal-complexed molecules. This is particularly remarkable for excitation at 1.904 μm , where γ'' is one-order of magnitude higher than γ' .

The measured signs and magnitudes of the real part of the hyperpolarizability γ' for our crown-ether substituted metallotriazolehemiporphyrines, are respectively, equal and similar to those previously reported¹⁵ for the less soluble lipophilic substituted compounds.

DISCUSSION

In base to the new data obtained in this work, the dispersive behaviour of γ can be more thoroughly analyzed and the physical mechanisms discussed in more detail.

(a) *Three-level model for H₂Thp* For H₂Thp, a positive γ' was measured at 1.904 μm , which changes to negative when the excitation is performed at 1.340 μm . Since at 1.904 μm all frequencies ω , 2ω , and 3ω , are below one-photon resonances, a two-level model (the ground state $|0\rangle$ and the first excited state $|1\rangle$, allowed for one-photon transitions) would yield a negative sign and so it is not appropriate. Therefore, the simplest choice to analyze the data is a three-level model^{20,21} involving an additional one-photon forbidden (and two-photon allowed) level from the ground state ($|2\rangle$), which dominates the nonlinearity far from resonance. The situation is as depicted in

Figure 3. The three-level expression for $\gamma(3\omega: \omega, \omega, \omega)$ in centrosymmetric systems is^{22,23}

$$\gamma(3\omega: \omega, \omega, \omega) = \mu_{01}^2(-\mu_{01}^2 D_{11} + \mu_{12}^2 D_{12}) \quad (6)$$

where μ_{01} and μ_{12} are the dipolar moments for the $|0\rangle \rightarrow |1\rangle$ and $|1\rangle \rightarrow |2\rangle$ transitions, respectively. The dispersion factors D_{11} and D_{12} are as follows,

$$D_{11} = \frac{1}{(\Omega_{10} - 3\omega)(\Omega_{10} - \omega)(\Omega_{10} - \omega)} + \frac{1}{(\Omega_{10} - \omega)(\Omega_{10}^* + \omega)(\Omega_{10} - \omega)} \\ + \frac{1}{(\Omega_{10}^* + 3\omega)(\Omega_{10}^* + \omega)(\Omega_{10}^* + \omega)} + \frac{1}{(\Omega_{10}^* + \omega)(\Omega_{10} - \omega)(\Omega_{10}^* + \omega)} \quad (7)$$

$$D_{12} = \frac{1}{(\Omega_{10} - 3\omega)(\Omega_{20} - 2\omega)(\Omega_{10} - \omega)} + \frac{1}{(\Omega_{10} + \omega)(\Omega_{20}^* - 2\omega)(\Omega_{10} - \omega)} \\ + \frac{1}{(\Omega_{10}^* + \omega)(\Omega_{20}^* + 2\omega)(\Omega_{10} - \omega)} + \frac{1}{(\Omega_{10}^* + \omega)(\Omega_{20}^* + 2\omega)(\Omega_{10}^* + 3\omega)} \quad (8)$$

Here ω is the frequency of the applied optical field, and $\Omega_{ab} = \omega_{ab} - i\Gamma_{ab}/2$, where ω_{ab} is the energy difference (in energy units) between states a and b ($\omega_{ab} = 1/\lambda_{ab}^{\max}$, λ_{ab}^{\max} is the center of the absorption band associated with transition $a \rightarrow b$) and Γ_{ab} is the FWHM.

With this model one can qualitatively understand the positive sign of γ' for 1.904 μm excitation, due to the dominance of the positive term in equation (6). At 1.340 μm the negative term is enhanced, since 2ω may have crossed the resonance with the one-photon forbidden level (if it is located at a lower energy than the allowed level). This would change the sign of D_{12} to negative.

A quantitative analysis, based in equation (6) has also been carried out. The one-photon allowed level $|1\rangle$ was placed at the center of the envelope of the UV band (see Fig. 2), at $\lambda_{01}^{\max} = 0.358 \mu\text{m}$, with a line-width $\Gamma_{01} = 4329 \text{ cm}^{-1}$ and a transition dipole moment $\mu_{01} = 6.7 \text{ D}$, calculated by integration of the optical absorption spectrum.²⁴

Then, the phases of γ at 1.340 and 1.904 μm , and the ratio $\rho = |\gamma(1.340 \mu\text{m})|/|\gamma(1.904 \mu\text{m})|$ were fitted in terms of the excitation wavelength, by using the position

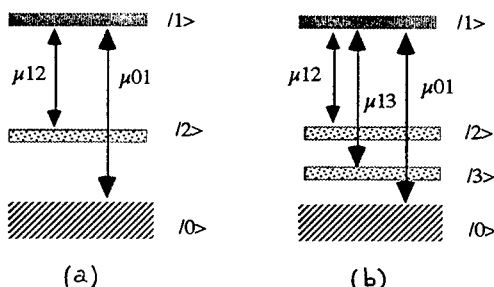


FIGURE 3 Schematic of the three- (a) and four-level (b) models. $|0\rangle$ ground state, $|1\rangle$ one-photon allowed state, $|2\rangle$ and $|3\rangle$ one-photon forbidden states.

(λ_{12}^{\max}) and line-width (Γ_{12}) of the one-photon forbidden level $|2\rangle$ as fitting parameters. The dipole moment μ_{12} was taken equal to μ_{01} , since it has been checked that its variation does not essentially modifies the above conclusion. A good agreement has been found when level $|2\rangle$ is placed at $\lambda_{12}^{\max} = 0.650 \mu\text{m}$ with a line-width $\Gamma_{12} = 2\Gamma_{01}$. The parameters and results of the fitting are summarized in Table 2.

(b) *Four-level model for MThp* When a metal with unfilled d-shells is introduced, additional electronic levels should be added to the scheme for a metal-free molecule. In principle, we will consider one additional one-photon forbidden d-excited level $|3\rangle$ (see Fig. 3), leading to a four-level model. It can now be used to account for the effects of metal-complexation on γ , including some other relevant features, such as the negative sign of γ' at $1.904 \mu\text{m}$. The four-level expression for γ writes,

$$\gamma(3\omega:\omega, \omega, \omega) = \mu_{01}^2 (-\mu_{01}^2 D_{11} + \mu_{12}^2 D_{12} + \mu_{13}^2 D_{13}) \quad (9)$$

where μ_{13} is the dipolar moment for the $|1\rangle \rightarrow |3\rangle$ transition, D_{13} is obtained from D_{12} (Eq. 8) by replacing the subscript "2" by "3" and the rest of the parameters are the same as for the three-level model.

In order to apply equation (9), we used for level $|2\rangle$ the parameters (λ_{12}^{\max} and Γ_{12}) previously fitted with the three-level model for H_2Thp . Then, we followed the same method as before, but using as fitting parameters the location λ_{13}^{\max} and line-width Γ_{13} of level $|3\rangle$, associated with the metal. As an illustration, we show in Table 2 the parameters used for CoThp . In this case, the best fit of the experimental data was obtained by placing level $|3\rangle$ at around $\lambda_{13}^{\max} = 1.100 \mu\text{m}$ with a line-width $\Gamma_{13} = \Gamma_{01}$. Similar accordance has been obtained for other MThp, with somewhat different positions and widths of level $|3\rangle$.

From our linear optical spectra, there is no evidence of bands in the $1\text{--}1.3 \mu\text{m}$ region. However, very weak parity-forbidden (and so two-photon allowed) d–d transitions in this range of wavelengths have been reported in metallophthalocyanines and

TABLE 2

Fitting parameters which provided the best fit to the THG data for H_2Thp (three-level model) and CoThp (four-level model), where $|0\rangle$ is the ground state, $|1\rangle$ is the one-photon allowed level, $|2\rangle$ and $|3\rangle$ are one-photon forbidden (two-photon allowed) levels. (λ_{ab}^{\max}) center of transition ab , (Γ_{ab}) line-width, (μ_{ab}) transition dipole moment, $\rho = |\gamma|(\lambda = 1.340 \mu\text{m})/|\gamma|(\lambda = 1.904 \mu\text{m})$ and (ψ) Phase of γ (in degrees). "Exp" refers to experimental values and "fit" refers to values obtained from the fit with the three- (four) level model.

Level $ 1\rangle$	Level $ 2\rangle$	Level $ 3\rangle$
$\lambda_{01}^{\max} = 0.358 \mu\text{m}$	$\lambda_{02}^{\max} = 0.650 \mu\text{m}$	$\lambda_{03}^{\max} = 1.100 \mu\text{m}$
$\Gamma_{01} = 4329 \text{ cm}^{-1}$	$\Gamma_{02} = 8658 \text{ cm}^{-1}$	$\Gamma_{03} = 4329 \text{ cm}^{-1}$
$\mu_{01} = 6.7 \text{ D}$	$\mu_{12} = 6.7 \text{ D}$	$\mu_{13} = 6.7 \text{ D}$
	3-LEVEL MODEL	4-LEVEL MODEL
ρ^{exp}	15.7	1.1
ρ^{fit}	9.2	1.5
$\psi^{\text{exp}}(\lambda = 1.340 \mu\text{m})$	—	180 ± 61.6
$\psi^{\text{fit}}(\lambda = 1.340 \mu\text{m})$	88	103
$\psi^{\text{exp}}(\lambda = 1.904 \mu\text{m})$	0	180 ± 83.1
$\psi^{\text{fit}}(\lambda = 1.904 \mu\text{m})$	24	100

naphthalocyanines.⁹ Therefore, excited d levels seem to be good candidates for the level $|3\rangle$ introduced in our model.

The changes in γ observed with the d-shell occupancy, from d^5 (Mn^{2+}) to d^9 (Cu^{2+}), are probably related to changes in the location, width and strength, of the IR d-d transitions. An exhaustive study would require additional experimental data (at different excitation wavelengths) in order to determine these parameters more precisely. Although our fitting is only indicative and cannot be taken as a rigorous proof for the adequacy of our model, it gives a reasonable description of some main features of the nonlinear response. Furthermore, as mentioned above, the trend we have observed in the variation of γ with the transition metal ions, agrees with that reported for the structurally related metallophthalocyanines⁹ by using the DFWM technique at 1.064 μm . In that work it was more difficult to explain this behaviour, because of the existence of optical nonlinear mechanisms, which are not present in our THG experiments. Therefore, our results confirm that the effect has a purely electronic origin.

REFERENCES

1. D. S. Chemla and J. Zyss, *Nonlinear Optical Properties of Organic Molecules and Crystals* (Academic Press, New York, 1987) Vols. 1 and 2.
2. S. R. Marder and J. W. Perry, *Adv. Mater.*, **5**, 804 (1993) and references therein.
3. J. Zyss, "Molecular Nonlinear Optics" J. Zyss, Ed., Academic, 1993.
4. P. N. Prasad and D. J. Williams, *Introduction to Nonlinear Effects in Molecules and Polymers*, (J. Wiley, New York 1991).
5. H. S. Nalwa, *Appl. Organomet. Chem.*, **5**, 349 (1991); *Adv. Mater.*, **5**, No. 5 (1993).
6. C. C. Leznoff and A. B. P. Lever, *Phthalocyanines. Properties and Applications*, (VCH publishers, Inc. 1989, 1993). Vols. 1, 2 and 3.
7. Z. Z. Ho, C. Y. Ju and W. M. Hetherington III, *J. Appl. Phys.*, **62**, 716 (1987).
8. N. Q. Wang, Y. M. Cai, J. R. Hefflin and A. F. Garito, *Mol. Cryst. Liq.*, **189**, 39 (1990).
9. J. S. Shirk, J. R. Lindle, F. J. Bartoli, Z. H. Kafafi, A. W. Snow and M. E. Boyle, *Int. J. Opt. Phys.*, **1**, 699 (1992).
10. A. Ground, A. Kaltbeitzel, A. Mathy, R. Schwarz, C. Bubeck, P. Vermehren and M. Hanack, *J. Phys. Chem.*, **96**, 7450 (1992).
11. H. S. Nalwa, A. Kakuta and A. Mukoh, *J. Phys. Chem.*, **97**, 1097 (1993).
12. H. S. Nalwa, T. Sautim, A. Kakuta and I. Iwayanagi, *J. Phys. Chem.*, **97**, 10515 (1994).
13. D. V. G. L. N. Rao, F. J. Aranda, J. F. Roach and D. E. Remy, *Appl. Phys. Lett.*, **58**, 1241 (1991).
14. K. S. Suslick, C. T. Chen, R. Meredith and L. T. Cheng, *J. Am. Chem. Soc.*, **114**, 6928 (1992).
15. M. A. Díaz-García, I. Ledoux, F. Fernández-Lázaro, A. Sastre, T. Torres, F. Agulló-López and J. Zyss, *J. Phys. Chem.*, **98**, 4495 (1994).
16. F. Fernández-Lázaro, J. De Mendoza, O. Mo, S. Rodríguez-Morgade, T. Torres, M. Yañez, J. Elguero, *J. Chem. Soc., Perkin Trans.*, **2**, 797 (1989); F. Fernández-Lázaro; Ph.D. Thesis, Universidad Autónoma de Madrid, 1992.
17. F. Kajzar and J. Messier, *Rev. Sci. Instrum.*, **58**, 2081 (1987).
18. F. Kajzar, *Spring. Proc.*, **36**, 108 (1989).
19. E. Ortí and J. L. Brédas, *J. Chem. Phys.*, **89**, 1009 (1988).
20. M. Barzoukas, P. Frémaux, D. Josse, F. Kajzar, J. Zyss, *MRS Symp. Proc.*, **109**, 71 (1988).
21. J. Messier, F. Kajzar, C. Sentein, M. Barzoukas, J. Zyss, M. Blanchard-Desci, J. M. Lehn, *Mol. Cryst. Liq. Cryst. Sci. Technol. Sec. B. Nonlinear Optics*, **2**, 53 (1992).
22. B. Orr and J. F. Ward, *Mol. Phys.*, **20**, 531 (1971).
23. J. F. Ward, *Rev. Mod. Phys.*, **37**, 1 (1985).
24. R. S. Mulliken, *J. Chem. Phys.*, **7**, 14 (1939).

Molecular Design of Quinoid Dyes for 3rd Order NLO Materials

MASARU MATSUOKA, ATSUSHI OSHIDA, AKIRA MIZOGUCHI*,
YASUHIRO HATTORI* and AKIRA NISHIMURA*

*Department of Applied Materials Science, University of Osaka Prefecture,
Sakai, Osaka 593, Japan, *New Chemistry R & D Laboratories,
Sumitomo Electric Ind. Ltd., Konohana, Osaka 554, Japan*

Received 12 January 1994; accepted 21 March 1994

Molecular design and syntheses of new quinoid dyes for 3rd order nonlinear optical materials were undertaken. Quinoid dyes have large π -conjugated systems with an intramolecular charge-transfer chromophoric system. This system has large photo-induced polarization which is favorable for 3rd order NLO materials. Strong intra- and intermolecular hydrogen bonding of some quinoid dyes produce a planar molecular stacking to form "molecular sheet", and strong intermolecular charge-transfer interactions between molecular layers produce three dimensional molecular stacking which play a great role to produce a large $\chi^{(3)}$ value. We found two types of new quinoid dyes, 4,8-dihydroxy-2,6-bis(butylamino)-1,5-naphthoquinone and 1,4-dithio-keto-3,6-diphenyl-pyrrolo-[3,4-c]-pyrrole, which were one of the candidates for 3rd order NLO materials.

INTRODUCTION

There is currently extensive interest in the development of 3rd order nonlinear optical materials. The large 3rd order NLO susceptibilities $\chi^{(3)}$ have been reported in a series of polymer materials such as polydiacetylenes and so on. We intend to develop new organic materials from a series of dye chromophores. Dye chromophores have large π -conjugated systems and generally have intramolecular charge-transfer chromophoric systems and then seems to be good candidates for 3rd order NLO materials. A large and planar structure of dye molecules with strong intra- and intermolecular hydrogen bonding is favorable for producing planar molecular stacking to form "molecular sheet", and strong intermolecular charge-transfer interactions between molecular layers produce strong three dimensional intermolecular interactions that lead to strong and precise molecular stacking in crystals or in thin films for NLO devices. Quinoid dyes have strong intramolecular charge-transfer chromophoric systems in which amino and hydroxy groups act as donor moieties and a para-quinone group acts as an acceptor moiety. In addition, amino and hydroxy groups act as hydrogen donors, and quinone carbonyl groups act as hydrogen acceptors, and consequently effective three dimensional molecular stacking is obtained by intra- and intermolecular hydrogen bonding and intermolecular charge-transfer interactions in the solid state. In this paper, some quinoid dyes which have strong intermolecular hydrogen bonding and intermolecular charge-transfer interactions are evaluated as 3rd order NLO materials by the THG method.

RESULTS AND DISCUSSION

The $\chi^{(3)}$ values and spectral data for some quinoid dyes are summarized in Table 1. The relative intensity of their powder efficiency against that of PDA-PTS (polydiacetylenep-toluene-sulfomethyl) were measured to evaluate dye materials. Their $\chi^{(3)}$ values were measured by the Maker fringe method in the vapor deposited thin films onto a fused silica and were correlated with their chemical structures. Intermolecular interactions of dye molecules can be evaluated from the differences of λ_{\max} values ($\Delta\lambda$) between these in solution and a thin film. It is generally known that λ_{\max} value in the solid state shifts to longer wavelength of $0.03 \sim 0.08 \mu\text{m}$ compared with that in solution. It is a result of strong intermolecular interactions of dye molecules in the solid state. Dyes 1, 3, 4, 5 and 6 showed $\chi^{(3)}$ value of 10^{-12} esu order which are general for organic compounds but dye 2 showed $\chi^{(3)}$ of 4.8×10^{-11} esu at $1.9 \mu\text{m}$.¹ That is considerably large value for such a small molecule. The $\Delta\lambda$ value of $0.12 \mu\text{m}$ is the biggest for dye 2, however for others it is small. From these results, dye 2 was proposed to have some special intermolecular interactions in solid state. The synthesis of dye 2 has been reported previously² but the structural identification of dye 2 was conducted by NOESY nmr spectra and X-ray diffraction analysis.¹

An X-ray diffraction analysis of single crystal of dye 2 was carried out and the structure was confirmed.¹ Dye 2 belongs to P1 space group and its partial crystal structure is shown in Figure 1. Intramolecular hydrogen bonding is observed between the hydroxy proton and the quinone carbonyl group, and the amino hydrogen and the quinone carbonyl group. In addition, intermolecular hydrogen bonding is also observed between the amino hydrogen and the quinone carbonyl group of a neighboring molecule. This intermolecular hydrogen bonding controls the molecular packing and thus, dye 2 exhibits molecular packing in a so called "molecular sheet".

Molecular overlap for each of the molecular layer is shown in Figure 2. The distance between the layer is about 3.3 \AA which is almost the summation of van der Waals radius

TABLE I
THG responses and spectral data of some quinonoid dyes.

Dye	λ_{\max}		$\Delta\lambda$ (μm)	PE ^{a)}	$\chi^{(3)}$ ($\times 10^{-13}$)	WL ^{b)} (μm)	Film thickness (μm)
	Soln. (μm)	Film. (μm)					
1	0.48	0.49	0.01	0.9	4.7	1.9	1.8
	0.48	0.49	0.01	0.1	40	2.1	0.4
2	0.50	0.62	0.12	0.6	480	1.9	0.2
	0.50	0.62	0.12	0.2	160	2.1	0.08
3	0.50	0.50	0	—	< 10	1.5 ~ 1.2	—
4	0.65	0.71	0.06	< 0.1	26	1.9	0.12
5a	0.60	0.66	0.06	—	10	1.9	0.14
5b	0.71	0.68	-0.03	—	39	1.9	0.27
6	0.52	0.56	0.04	—	< 10	1.9	0.35
7	0.51	0.55	0.04	—	< 10	1.5 ~ 1.2	0.1
8	0.62	0.68	0.06	—	170	2.1	0.1
		0.80	0.18				

^{a)} THG powder efficiency against PDA-PTS.

^{b)} Wavelength of laser.

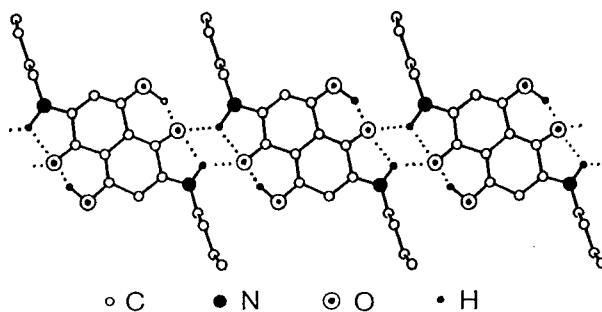


FIGURE 1 Intra- and intermolecular hydrogen bondings in crystals of dye 2 to form "molecular sheet".

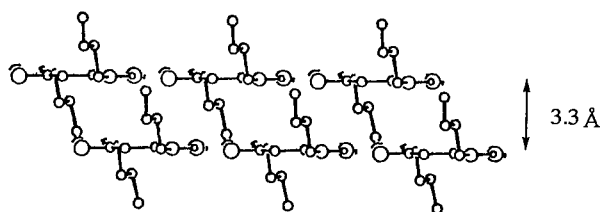


FIGURE 2 Molecular stacking in P1 space group and overlap of molecular layer in crystals of dye 2.

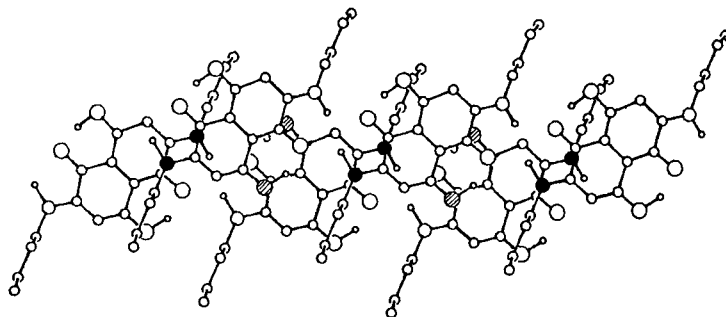


FIGURE 3 Four centered intermolecular charge-transfer intermolecular interactions from the view of π -molecular plane in crystals of dye 2.

of each element, and then intermolecular interaction between molecular layer was proposed. The two butyl groups are oriented perpendicular to the planar π -molecular plane and are oriented in the opposite side.

Overlaps of molecular layers from the view of π -molecular plane are shown in Figure 3. Four centered intermolecular charge-transfer interactions were observed between the molecular layer; amino nitrogen and hydroxy oxygen act as donors, and quinone carbonyl carbon acts as an acceptor. The distance between the nitrogen and the carbon is 3.31 Å and that of the oxygen and the carbon is 3.35 Å. These results indicate that strong interatomic charge-transfer interactions play a great role to produce strong three dimensional molecular packing which enabled to produce large polarization of π -electrons under laser irradiation. It may cause to produce large $\chi^{(3)}$ value.

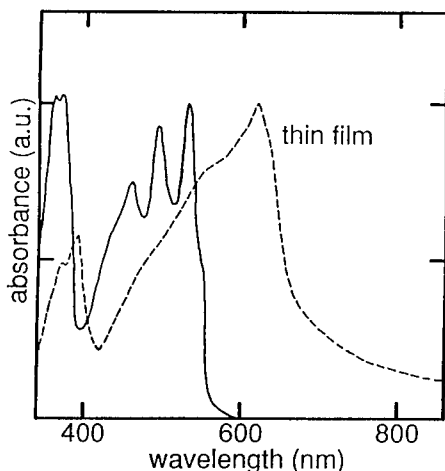


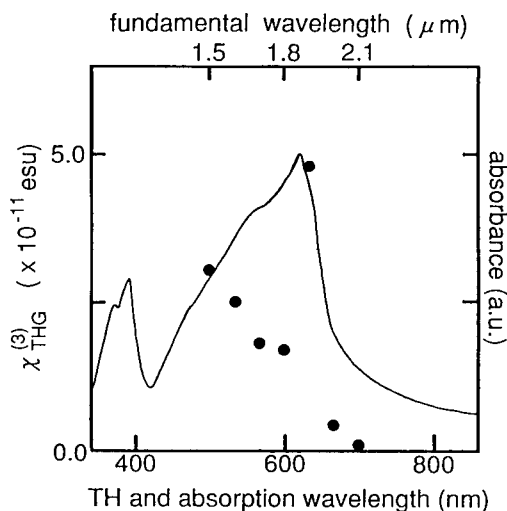
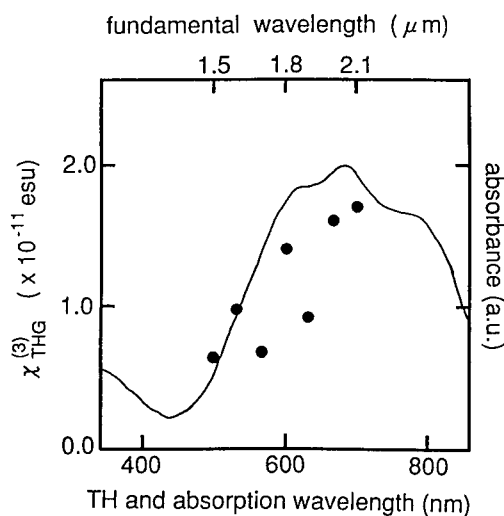
FIGURE 4 Differences in absorption spectra of dye 2 in solution and in thin film.

A comparison of $\chi^{(3)}$ values of dyes 2 and 3 is quite interesting. They are similar in their chemical structure and absorption spectra in solution. But their absorption spectra in thin films are quite different as indicated in Table 1 and Figure 4. Their calculated γ value is almost same; 50×10^{-36} esu for dye 2 and 34×10^{-36} esu for dye 3.¹ However, their $\chi^{(3)}$ value is quite different; 4.8×10^{-11} esu at $1.9 \mu\text{m}$ for dye 2 and 1×10^{-12} esu order in the range from 1.5 to $2.1 \mu\text{m}$ for dye 3. These differences in $\chi^{(3)}$ values may be due to the differences in molecular stacking of each molecules in solid state. None of intermolecular hydrogen bonding was observed in case of dye 3, but that of dye 2 was characterized by X-ray diffraction analysis as discussed above.

The $\chi^{(3)}$ value of dye 2 is affected by the pumping wavelength of laser and their relationship is correlated to absorption spectra (Fig. 5). The maximum $\chi^{(3)}$ value of 4.8×10^{-11} esu was observed at $1.9 \mu\text{m}$ which is well corresponded to the maximum absorption at 620 nm of thin film.

From these results, it is concluded that three dimensional molecular packing by intermolecular charge-transfer interactions is effective to enlarge $\chi^{(3)}$ value and will be one of the way to search new 3rd order NLO materials.

On the other hand, some type of pyrrolo-pyrrole pigments³ have been known to form similar three dimensional molecular packings by intermolecular hydrogen bonding and intermolecular charge-transfer interactions.^{4,5} These are 1,4-diketo-3,6-diphenyl-pyrrolo-[3,4-c]-pyrrole 7 and its thio analogue 8. Preliminary evaluation of pigments 7 and 8 by the THG method indicated that pigment 8 showed large $\chi^{(3)}$ value of 1.7×10^{-11} esu at the fundamental wavelength of $2.1 \mu\text{m}$, but pigment 7 showed $\chi^{(3)}$ value of less than 10^{-12} esu order at any fundamental wavelength of $1.5 \sim 2.1 \mu\text{m}$. The correlation between $\chi^{(3)}$ value and fundamental wavelength of pigment 8 is shown in Figure 6, and the maximum $\chi^{(3)}$ value was obtained at λ_{max} of thin film. It has been reported that pigments 7 and 8 showed strong intermolecular hydrogen bonding to form "molecular sheet", and pigment 8 showed strong intermolecular charge-transfer

FIGURE 5 Wavelength dependence of $\chi^{(3)}$ in thin film of dye 2.FIGURE 6 Wavelength dependence of $\chi^{(3)}$ in thin film of dye 8.

interactions but pigment 7 did not show such interactions. The difference in $\chi^{(3)}$ values of pigments 7 and 8 was well correlated with the difference in the intermolecular charge-transfer interactions. The $\Delta\lambda$ value of 7 is $0.04\ \mu\text{m}$ but those of 8 are 0.04 or $0.18\ \mu\text{m}$ depending on crystal morphology by solvent vapor treatment.⁵ The THG measurement of various solvent-vapor treated thin films of pigments 7 and 8 are in progress now. Further results will be reported elsewhere.

ACKNOWLEDGEMENT

The authors would like to thank Dr. A. Iqbal in Ciba-Geigy, Marly, for providing pigments 7 and 8. This work was partially supported by Ciba-Geigy Foundation (Japan) for the Promotion of Science, and by a Grant-in-Aid for Scientific Research No. 05805073 from the Ministry of Education, Science and Culture.

REFERENCES

1. Y. Hattori, A. Mizoguchi, M. Kubata, T. Uemiya, G. Tanaka and M. Matsuoka, *Electronics Letters*, submitted.
2. M. Matsuoka, T. Takei and T. Kitao, *Chemistry Letters*, 627 (1979).
3. A. Iqbal, M. Jost, R. Kirchmayr, J. Pfenninger, A. C. Rochat and O. Wallquist, *Bull. Soc. Chim. Belg.*, **97**, 615 (1988).
4. J. Mizuguchi and G. Wooden, *Ber. Bunsenges. Phys. Chem.*, **95**, 1264 (1991).
5. J. Mizuguchi, A. C. Rochat and G. Rihs, *ibid*, **96**, 607 (1992).

New $\chi^{(3)}$ Materials for Electro Optic and All Optical Signal Processing Based on Metal Complexes

A. S. DHINDSA¹, A. E. UNDERHILL¹, S. OLIVER² and S. KERSHAW²

¹Department of Chemistry, University of Wales, Bangor, Gwynedd, LL57 2UW, UK, ²BT Laboratories, Martlesham Heath, Ipswich, UK

Received 12 January 1993; accepted 1 March 1994

The non-linear susceptibility ($\chi^{(3)}$) of a series of metal complexes of diaminomaleonitrile and o-phenylenediamine have been measured by degenerate four wave mixing. The results indicate that the values of $\chi^{(3)}$ in these nitrogen-donor ligand systems are comparable to those found for the sulphur-donor metal dithiolenes.

INTRODUCTION

In the last decade, research on the third-order non-linear optical properties of materials has attracted considerable interest because of their potential use in unconventional optical devices such as all optical logic, optical image processor, phase conjugation mirror, optical switches and optical data storage.^{1–3}

Large non-linearities have been reported for conjugated polymers where the optical non-linearity is thought to arise from the extensive delocalisation of the π -electron system.^{2,3} The ultrafast, low-loss, off-resonant optical non-linearities observed in organic polymers have led to an extensive study of these materials; but, their practical use is likely to be limited due to the small size of the non-linearities.^{4,5} Recently, a report on waveguides fabricated from easily processed polydiacetylenes, showed that the material in a device format was dominated by two-photon absorption and also suffered from scattering problem.⁶ A large optical non-linearity was also observed for organic metals such as α -[BEDT-TTF]₂I₃ by Huggard *et al.*,⁷ in 1987, but their use in optical devices also suffers from problems of processibility and linear loss due to absorption.

In the past few years, several research groups^{8–11} have focussed their attention on the third order non-linear optical properties of metal complexes with centrosymmetric square planar structures. For example, metallophthalocyanines where third-harmonic generation (THG) and degenerate four wave mixing (DFWM) techniques have been used to study the non-linear optical (NLO) properties.^{12,13} It has been demonstrated that the third-order optical coefficient of platinum-cumylphenoxyphthalocyanine is about 45 times higher than that of the free phthalocyanine ligand and that the coefficient varies dramatically upon changing the central metal atom coordinated to the phthalocyanine ring.¹²

Recently, metal dithiolene complexes have been the focus of attention for their third order non-linear optical properties.^{14–18} The dithiolene complexes possess a delocalised π -electron system and show strong near-IR absorption bands. The position of

the near-IR absorption band can be tuned by varying the substituent groups on the dithiolene ligand and by changing the central metal atom. The non-linear susceptibility (χ^3), linear absorption, α , and two photon absorption co-efficient, β , of nickel and platinum complexes with various substituted dithiolene ligands have been measured at 1064 nm by DFWM technique. These measurements show very large resonance enhanced molecular non-linearities for these systems, and it has been emphasised that the "figure of merit" based on the non-linear refractive index and linear and two photon absorption coefficients are compatible for their use in simple demonstrator optical devices.¹⁷⁻¹⁹

Kafafi *et al.*,^{20,21} have recently reported the results of their DFWM studies on solutions of o-aminobenzenethiol and benzenedithiol complexes of cobalt(III), nickel(II) and platinum(II). The nickel complex, $\text{Ni}(o\text{-NHC}_6\text{H}_4\text{S})_2$, in solution at 1064 nm has a large non-linearity, χ^3 , of the order of 2×10^{-9} e.s.u. Several mechanisms have been proposed to explain these large non-linearities. It is clear from the above studies that the non-linearities of the square planar complexes with delocalised π -system ligands vary with the presence of different substitutions on the ligands and with changing the nature of donor atoms. There is, therefore, a need to explore the relationship between the structure of the ligand and the NLO properties to aid the preparation of compounds with improved properties. The present investigations are focussed on nickel and platinum complexes of o-phenylenediamine and diamino-maleonitrile ligands of the type shown below:

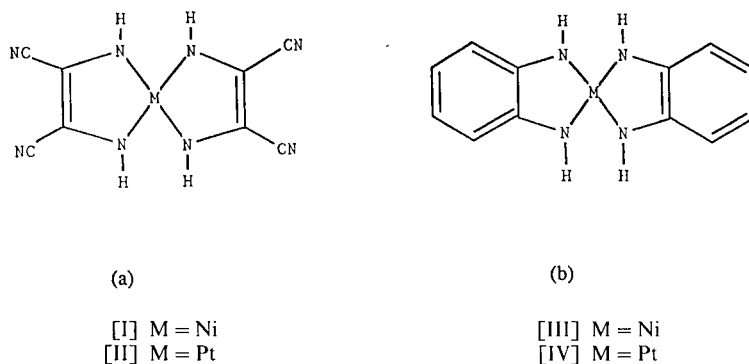


FIGURE 1 Schematic structures of metal complexes with (a) diaminomaleonitrile and (b) o-phenylenediamine ligands.

Our interest in these materials was aroused because of the fact that they are centrosymmetric square planar complexes and can exist with a range of charges. They show a strong visible/near-IR absorption band due to a ligand to metal symmetry allowed charge transfer transition and their structure is characteristic of delocalised π -electron conjugated system having semiquinoneimine type of coordination to the metal atom.²² In particular, it is interesting to compare the change in NLO properties on varying the nature of donor atom from sulphur to nitrogen in a closely related molecular systems.

EXPERIMENTAL

Diaminomaleonitrilenickel(II) and diaminomaleonitrileplatinum(II) complexes [I] and [II], were synthesised by a modification of the procedure described by Miles and coworkers.²³

[Ni(C₄H₂N₄)₂]. To a stirred solution of diaminomaleonitrile (1.10 g, 10 mmol) in 50 ml of methanol was added slowly a solution of nickel(II) chloride hexahydrate (1.16 g, 5 mmol) in methanol (40 ml). A solution of triethylamine (2.10 g, 21 mmol) in 15 ml of methanol was slowly added. The solution turned an intense blue green after 15 minutes and was filtered. The solution was then evaporated almost to dryness under vacuum and the product was repeatedly washed with water. The product was extracted with acetone and purified by recrystallisation twice from acetone (yield 20%).

[Pt(C₄H₂N₄)₂]. The complex [II] was synthesised similarly to that described for Complex (I) but using a solution of potassium tetrachloroplatinate(II) in a 1:1 water and methanol mixture and adding only a small quantity of triethylamine (less than 5 equivalent to that of diaminomaleonitrile).

M[C₆H₄(NH₂)₂]₂. Bis(o-phenylenediamino)metal(II) complexes of nickel, [III], and platinum, [IV], were prepared by the method reported by Balch and Holm.²⁴ Typically, to a solution of the metal(II) salts, i.e., nickel(II)chloride or potassium tetrachloroplatinate(II), in water was added o-phenylenediamine dissolved in warm water in the presence of aqueous ammonia and the solution left stirring in air for 24 hours. The products were purified by extraction into acetone.

Optical Measurements

The absorption spectra of the complexes in DMF solutions were measured on a Beckman DK2A Spectrophotometer and the position of the visible/near-IR band is given in Table 1.

Third order non-linear optical measurements were made on solutions of the complexes (approximately 10¹⁸ molecules per ml) in DMF using the retroreflection DFWM technique at 1064 nm using a Nd:YAG laser.

In the DFWM experiment two intense pump beams were formed from a single mode-locked pulse (100 ps) selected from the Q-switch envelope of a Nd:YAG laser and its retroreflected image from a plane dielectric mirror placed immediately behind the sample. The sample solution was placed in a 2 mm cuvette. A weak (10% of pump)

TABLE 1
Results for complexes I to IV and (TBA) [Ni(BDT)₂] corrected to 10¹⁸ molecules/cc.

Complex	Formula	λ_{\max} (nm)	$\alpha(\text{cm}^{-1})$ at 1064 m	$\chi^{(3)}$ (10 ⁻¹³ esu)	γ_{xxx} (10 ⁻³² esu)
I	[Ni(C ₄ H ₂ N ₄) ₂]	680	0.28	1.4	4.2
II	[Pt(C ₄ H ₂ N ₄) ₂]	630	0.03	not measureable	—
III	[Ni(C ₆ H ₄ N ₂) ₂]	790	0.26	5.1 × 10	15.3
IV	[Pt(C ₆ H ₄ N ₂) ₂]	710	0.20	1.6 × 10	4.8
[Ni(BDT) ₂] ⁻	[Ni(C ₆ H ₄ S ₂) ₂] ⁻	881	0.84	3.4 × 10	10.3

probe beam was split off the forward pump beam and interacted with the two pump beams in the sample. All beams were parallel polarised. The phase conjugate (PC) signal retroreflecting along the path of the probe was split off and detected. Photomultipliers and energy meters were used to detect the pump and PC energies. The square root of the reflectivity $R (= E_{\text{PC}}/E_{\text{pump}})$ was plotted against input pump energy and the slope, G , of the plot ratioed to that from a reference CS_2 sample for which we take $\chi^{(3)} = 1.8 \times 10^{-12}$ esu.^{25,26} From this can be derived the $\chi^{(3)}$.

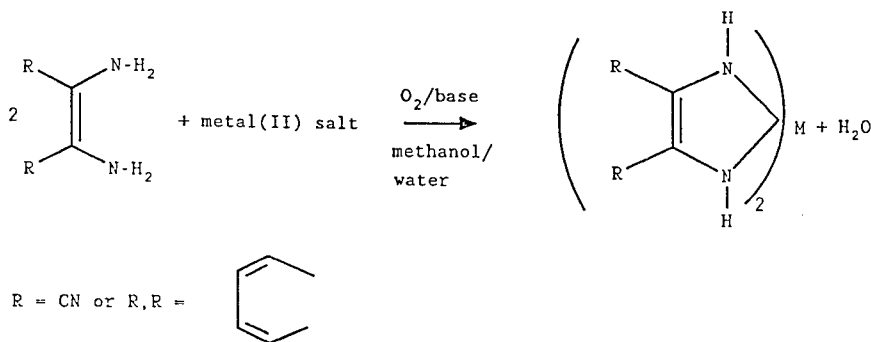
$$\frac{\chi^{(3)}_{\text{sample}}}{\chi^{(3)}_{\text{ref}}} = \frac{\alpha_{\text{sample}} L_{\text{ref}}}{T(1-T)} \times \frac{n_{\text{sample}}}{n_{\text{ref}}} \times \frac{G_{\text{sample}}}{G_{\text{reference}}}$$

where T is the transmission of sample, L is the reference path length and n the linear refractive indices.

RESULTS AND DISCUSSION

Preparation of Compounds

Both diaminomaleonitrile and *o*-phenylenediamine react with metal (II) salts in basic media and after aerial oxidation to give the required complexes according to the equation:



However, when the synthesis of complexes I and II was attempted using 2-methylpiperidine as the base as described by Miles and coworkers,²³ either a very low yield or an impure/decomposed product was obtained repeatedly. This method was improved by using triethylamine as the base. The complexes, III and IV, of *o*-phenylenediamine were easily obtained but their purification by extraction into acetone is difficult and time consuming due to their low solubility.

Linear Optical Properties

The visible/near-IR spectra of the nickel(II) complexes of diaminomaleonitrile[I] and *o*-phenylenediamine [III] are shown in Figure 2. The most important feature is a very

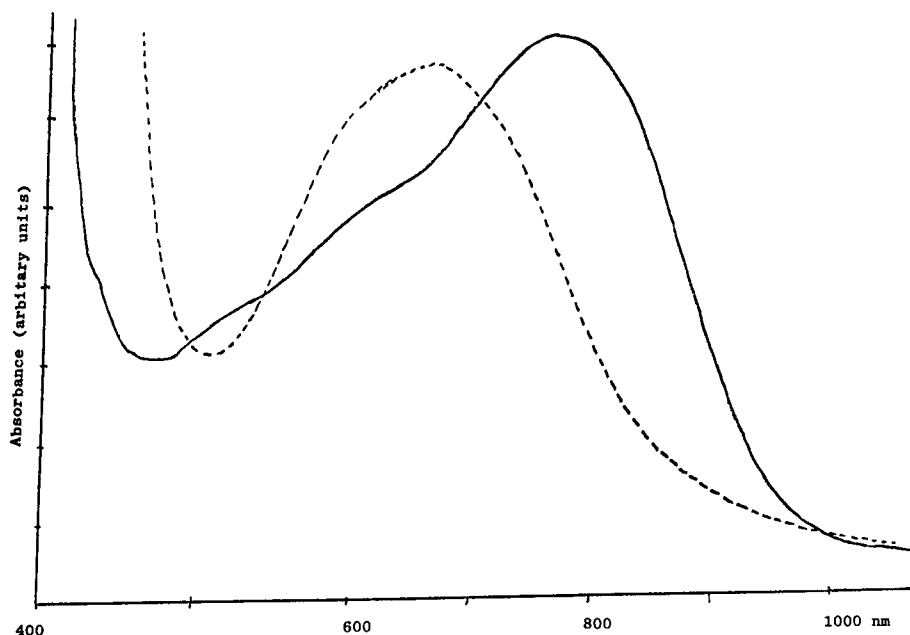


FIGURE 2 Visible-near-IR spectra of complex I (dotted line) and complex III (solid line).

strong band observed around 650 nm for complex I and around 780 nm for complex III. The origin of this intense band is generally believed to arise from the ligand to metal symmetry allowed charge transfer transition. The position of this band varies with the nature of substituents on the five membered ring and also depends upon the nature of the central metal ion (see Table 1). In the case of the diaminomaleonitrile complexes, the electron withdrawing cyano groups shift the position of this band dramatically from the near IR region into visible region as compared with the o-phenylenediamine complexes. In the o-phenylenediamine complexes, the appearance of this band at low energy could be due to extensive delocalisation of the π -electron system involving the presence of the benzene rings. The effect of replacing the nickel ion by platinum results in a slight blue shift of this absorption band. The change in the position of this band with the nature of substituent on the ligands or the metal ion are very important and enable the band to be tuned to a desirable wavelength to create a resonant or near-resonant condition with the excitation wavelength for their use in non-linear optics. Moreover, neutral diaminomaleonitrile complexes of the type $[M(C_4H_2N_4)_2]$ where $M = Ni, Pd$ and Pt , can be reduced to their monoanionic form $[M(C_4H_2N_4)_2]^-$ which results in a dramatic shift of the position of this charge transfer band towards the red region (around 1050 nm), thus further enhancing the scope for broadening the range of the absorption band for tuning it to the laser frequency.²⁷

The position of λ_{max} and of the linear absorption measured at 1064 nm is given in the Table. For all the compounds there is a long slowly decreasing tail on the low energy side of the absorption band which extends into the near-IR.

Non-linear Optical Properties

Figure 3 shows a typical plot of the phase conjugate reflectivity against the pump intensity for carbon disulphide and for the complex III.

For complex III a cubic dependence of phase conjugate energy upon pump energy was observed. However, for the other samples the dependence of phase conjugate energy upon pump energy was less than cubic and thus could be due to saturation effects. Similar effects have been observed with dithiolenes and are discussed more fully elsewhere.²⁸ These effects will result in a lower value of $\chi^{(3)}$ to that which would be obtained in the absence of saturation.

Table 1 summarises the values of measured $\chi^{(3)}$ for all the materials (complexes I to IV) along with that of tetrabutylammonium bisbenzenedithiolatenickel(II) (TBA) $[\text{Ni}(\text{BDT})_2]$ for comparison. The molecular susceptibility, γ_{xxxx} , was calculated using the expression.

$$\gamma = \frac{\chi^{(3)}}{NL^4} \quad \text{where} \quad L = \frac{(n_0^2 + 2)}{3}$$

The value of n_0 was equated to the n_D^{20} value for DMF (1.43) as the solutions were dilute and refractive index dispersion of the pure solvent is expected to be small. The values of α for $[\text{Ni}(\text{BDT})_2]^-$ agree with those previously reported when the difference in the value assumed for CS_2 is taken into account.²⁰

Results of the NLO measurements on complexes in Table 1 show that the $\chi^{(3)}$ of these materials in DMF solutions at concentrations of 10^{18} molecules per cc are of the order of 10^{-13} esu. The most significant feature is the similarity of the value of $\chi^{(3)}$ of the metal complexes of the nitrogen-donor ligands to those of the previously studied sulphur-donor compounds. For example the phenyl/butyl substituted nickel dithiolene exhibits a $\chi^{(3)}$ value of $\sim 1.2 \times 10^{-12}$ esu at a similar concentration of 10^{18} molecules per cc.¹⁶ This suggests that the non-linearities are predominantly associated with the delocalised

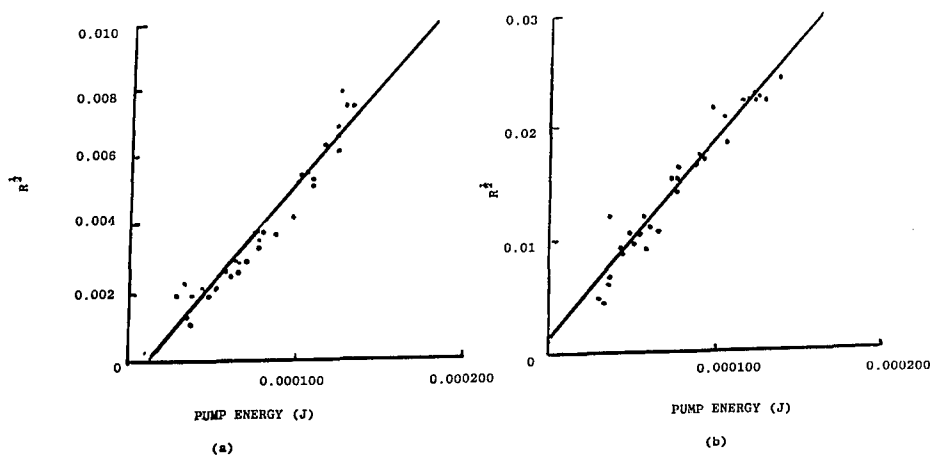


FIGURE 3 Plots of the degenerate four wave signal of complex III (a) in DMF solutions of about 10^{18} molecules/cc and pure CS_2 (b).

π -system and not critically dependent on the donor atom. Similar results have been observed in complexes containing both nitrogen and sulphur donor atoms.^{20,21}

Care must be exercised in attempting to make a detailed comparison of the $\chi^{(3)}$ values of the various compounds. As mentioned previously, values of $\chi^{(3)}$ in Table 1 apart from Compound III are likely to have been lowered due to saturation effects. Resonance enhancement of $\chi^{(3)}$ will also occur to a different extent in these compounds depending on the position of λ_{\max} relative to the laser wavelength. Finally the linear absorption of 1064 nm also varies from compound to compound although the values of $\chi^{(3)}$ do not scale with α in a simple fashion. Further work on the NLO properties of these compounds is in progress.

ACKNOWLEDGEMENT

We thank SERC for support (to ASD and AEU).

REFERENCES

1. D. J. Williams, ed, *Nonlinear Optical Properties of Organic and Polymeric Materials*, (American Chemical Society, Washington DC, 1983); P. N. Prasad and D. J. Williams "Introduction to Nonlinear optical effects in molecules and Polymers", Wiley, New York, 1991.
2. J. R. Lindle, F. J. Bartoli, C. A. Hoffman, O. K. Kim, Y. S. Lee, J. S. Shirk and Z. H. Kafafi, *Appl. Phys. Lett.*, **56**, 712 (1990).
3. X. F. Cao, J. P. Tiang, D. P. Boch, R. W. Hellwarth, L. P. Yu and L. Dalton, *J. Appl. Phys.*, **65**, 5012 (1989).
4. G. M. Carter, Y. J. Chen and S. K. Triparthy, *Opt. Eng.*, **24**, 609 (1985).
5. K. Rochford, R. Zanonì, G. I. Stegeman, W. Krug, E. Miao and M. W. Beranek, *Appl. Phys. Lett.*, **58**, 13 (1991).
6. P. D. Townsend, J. L. Tachel, G. L. Baber, J. A. Shelburne and S. Etemard, *Appl. Phys. Lett.*, **55**, 1829 (1989).
7. P. G. Huggard, W. Blau and D. Schweitzer, *Appl. Phys. Lett.*, **51**, 2183 (1987).
8. J. W. Wu, J. R. Heflin, R. A. Norwood, K. Y. Wong, O. Zamini-Khamiri, A. E. Gavito, P. Kalyavaraman and J. Sonnik, *J. Opt. Soc. Am. B*, **6**, 707 (1989).
9. M. K. Casstevens, M. Samoc, J. Pfeleger and P. N. Prasad, *J. Chem. Phys.*, **92**, 2019 (1990).
10. H. Sasabe, T. Wada, M. Hosoda, H. Ohkawa, A. Yamada and A. F. Gaviot, *Mol. Cryst. Liq. Cryst.*, **189**, 155 (1990).
11. R. A. Norwood and J. R. Sounik, *Appl. Phys. Lett.*, **60**, 295 (1992).
12. J. S. Shirk, J. R. Lindle, F. J. Bartoli, C. A. Hoffman, Z. H. Kafafi and A. W. Snow, *Appl. Phys. Lett.*, **55**, 1287 (1989).
13. J. S. Shirk, J. R. Lindle, F. J. Bartoli, Z. H. Kafafi and A. W. Snow, in "Materials for Nonlinear Optics: Chemical Perspectives", S. R. Mardav, J. E. Sohn and G. D. Stucky, Eds; ACS Symposium Series, **455**, 626 (1991).
14. T. Fukaya, M. Mizuno, S. Murata and A. Mito, *SPIE*, **1626**, 135 (1992).
15. C. S. Winter, S. N. Oliver, J. D. Rush, C. A. S. Hill and A. E. Underhill, "Organic Molecules for Nonlinear Optics and Photonics", J. Messier *et al.*, Ed., 383 (1990).
16. C. S. Winter, S. N. Oliver, R. J. Manning, J. D. Rush, C. A. S. Hill and A. E. Underhill, *J. Mater. Chem.*, **2**, 443 (1992).
17. C. S. Winter, S. N. Oliver, J. D. Rush, C. A. S. Hill and A. E. Underhill, *Mol. Cryst. Liq. Cryst.*, **235**, 181 (1993).
18. C. S. Winter, C. A. S. Hill and A. E. Underhill, *Appl. Phys. Lett.*, **58**, 107 (1991).
19. S. N. Oliver, C. S. Winter, R. J. Manning, J. D. Rush, C. Hill and A. E. Underhill, *Nonlinear Optical Properties of Organic Materials V, SPIE*, **1775**, 111 (1992).
20. Z. H. Kafafi, J. R. Lindle, S. R. Flom, R. G. S. Pong, C. S. Weisbecher, R. C. Clansen and F. J. Bartoli, *SPIE*, **1626**, 440 (1992).
21. Z. H. Kafafi, J. R. Lindle, C. S. Weisbecher, F. J. Bartoli, J. S. Shirk, T. H. Yoon and O. K. Kim, *Chem. Phys. Lett.*, **179**, 79 (1991).
22. G. S. Hall and R. H. Soderberg, *Inorg. Chem.*, **7**, 2300 (1968).
23. M. G. Miles, M. B. Hursthouse and A. G. Robinson, *J. Inorg. Nucl. Chem.*, **33**, 2015 (1971).
24. A. L. Balch and R. H. Holm, *J. Am. Chem. Soc.*, **88**, 5201 (1966).
25. W. E. Williams, M. J. Soileau, E. W. Van Stryland, *Opt. Comm.*, **50**, 256 (1984).
26. K. J. Witte, M. Galanti and R. Volk, *Opt. Comm.*, **34**, 278 (1980).
27. F. C. Seftleber and W. E. Geiger, *Inorg. Chem.*, **17**, 3615 (1978).
28. S. N. Oliver, S. V. Kershaw, A. E. Underhill, C. A. S. Hill and A. Charlton, these proceedings.

Nonlinear Optical Properties of J-Aggregated Merocyanine Dye Microcrystals in Polymer Matrices

H. MATSUDA¹, E. VAN KEUREN¹, A. MASAKI¹, K. YASE¹, A. MITO²,
C. TAKAHASHI², H. KASAI³, H. KAMATANI³, S. OKADA³
and H. NAKANISHI³

¹National Institute of Materials and Chemical Research, Tsukuba 305 (Japan)

²National Research Laboratory of Metrology, Tsukuba 305 (Japan)

³Tohoku University, Institute for Chemical Reaction Science,
Sendai 980 (Japan)

Received 12 January 1994; accepted 11 February 1994

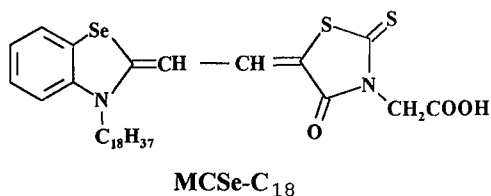
We found that microcrystals of an amphiphilic merocyanine dye (MCSe-C₁₈) dispersed in water could be stably converted to the J-aggregate form. The absorption maximum shifts to 610 nm (J1 state) or 630 nm (J2 state) from 550 nm in the non-J state and shows the sharp excitonic peak with a half-width at room temperature of roughly 40 nm or 30 nm, respectively. The maximum of the modulus of $\chi^{(3)}$ was observed to be approximately 2.5×10^{-12} esu for the J2 state microcrystals (10 wt. %) in a poly(vinyl alcohol) matrix, which is 20 times larger than that of non-J state microcrystals (10 wt. %). The change in the phase of $\chi^{(3)}$ from 0 deg. at 700 nm to 180 deg. at 550 nm can be explained by the 3-photon resonance of the excitons. The figure of merit $|\chi^{(3)}|/\alpha$ reaches a maximum value of 5.7×10^{-12} esu· μm at a wavelength of 670 nm. This is 1.5 and 20 times greater than at non-resonant (720 nm) and excitonic peak (630 nm) wavelengths, respectively. From this result, we surmise that the enlargement of nonlinear optical properties can be obtained by sharpening the absorption peak and using a wavelength near band edge.

INTRODUCTION

Organic π -conjugate systems have been studied in the hope of developing all-optical computing devices using the non-linear refractive index.¹ Among the several possible methods for obtaining enlarged third-order non-linear optical susceptibilities ($\chi^{(3)}$), the formation of the so-called J-aggregate state of organic dyes has recently received much attention. In the J-aggregate state, the excitons are confined to a mesoscopic region and quantum size effects are expected to produce large nonlinear optical properties.² In particular, pseudoisocyanine, known as one of the few compounds to have a J-aggregate state in pure aqueous solution,³ has been investigated with interest focused on the very sharp exciton band absorption.^{4,5} However, the stability of the J-state pseudoisocyanine is poor.

The amphiphilic merocyanines (see the chemical structure MCSe-C₁₈ below, for example), are also known to form J-aggregate states which are more stable than those of pseudoisocyanine.⁶ The merocyanine dyes have found use as materials for photoelectric or photoelectrochemical devices because of their high quantum efficiency.^{7,8} Derivatives with long alkyl groups attached have been developed in order to obtain an ordered structure in mono-molecular layers such as Langmuir-Blodgett films.⁹ We

have already reported the $\chi^{(3)}$ value of MCSe-C₁₈ being enhanced about ten times by the formation of J-aggregates in both three-photon resonant and non-resonant regions by third harmonic generation (THG).¹⁰ We found that the microcrystals of an amphiphilic merocyanine dye dispersed in water could be stably converted to the blue/violet J-aggregate having a sharper absorption spectrum of excitons than that in a bulk thin film or an LB film.¹¹ In the present study, the nonlinear optical properties of the J-aggregate microcrystals of MCSe-C₁₈ dispersed in polymer matrices are further evaluated, in particular by THG measurement. We present the modulus $\chi^{(3)}$ and the phase around the absorption maximum (from 720 to 500 nm of TH wavelength) and discuss the three-photon resonant effect.



EXPERIMENTAL

Materials and J-Aggregate Microcrystal Formation

The MCSe-C₁₈ was obtained from the Japanese Research Institute for Photosensitizing Dyes and used without further purification. As a polymer matrix, commercially available poly(vinyl alcohol) (PVA) or gelatin was used. The J-aggregate microcrystals were made by dropping a 1 ml acetone solution of MCSe-C₁₈ (approximately 5 mM) into a 10 ml aqueous ammonia solution dissolved with matrix polymers. After storing the solution mixture below 10°C for about 1 day, the color changed from red to blue-violet, indicating J-aggregate formation. The size of the microcrystals was observed with a Hitachi SEM S-900 scanning electron microscope. For the preparation of thin film samples by spin coating, the solution mixture was dried by a freeze-drying method and then a small amount of water was added to make a suitable viscous solution.

Optical Measurements

UV, Visible and near IR spectra of the thin film samples were measured using a Shimadzu UV-3100 spectrometer. The refractive index was measured at a wavelength of 700 nm using a Shimadzu AEP-100 ellipsometer and the dispersion of the refractive index was calculated from the absorbance data using the Kramers-Kronig relation. The film thickness was determined with a Tencor Instruments Alpha-step 300 surface height profiler, which drags a stylus across the sample surface.

Third harmonic generation (THG) measurements were carried out between 1.47 and 2.16 μm of pumping wavelength, which was generated by mixing beams from a Q-SW Nd:YAG laser and a dye laser using a LiNbO₃ crystal (Spectra Physics, DCR-10 system). The pulse width is approximately 5 ns, the repetition rate is 10 Hz, and the

incident energy per pulse on a sample is roughly 2 mJ. The THG was analyzed by the Maker fringe method. The apparatus was automatically controlled by personal computer. The $\chi^{(3)}$ value was evaluated by fitting to the following equation.^{12,13} A reference value of $\chi^{(3)} = 1 \times 10^{-14}$ esu was used for fused quartz at all pumping wavelengths.¹⁴

Equation for the determination of $\chi^{(3)}$

$$I_{3\omega} = \left| T_1 \frac{\chi_s^{(3)}}{\Delta \epsilon_s} e^{-i\Delta\psi_s/2} \sin \frac{\Delta\psi_s}{2} + T_2 \frac{|\chi_f^{(3)}| e^{-i\phi}}{\Delta \epsilon_f} e^{-i\Delta\psi_f/2} \sin \frac{\Delta\psi_f}{2} \right|^2 I_\omega^3$$

where: $\chi^{(3)}$ is the third order susceptibility, ϕ is the phase of $\chi^{(3)}$ of the film, $\Delta\epsilon = \epsilon(\omega) - \epsilon(3\omega) = n_\omega^2 - n_{3\omega}^2$, $\Delta\psi = 6\pi t/\lambda_\omega (n_\omega \cos\theta_\omega - n_{3\omega} \cos\theta_{3\omega})$ is the phase mismatch between the waves at ω and 3ω in the medium, $n_{\omega,3\omega}$ is the refractive index, t is the film thickness, $\theta_{\omega,3\omega}$ is the angle the wave inside the material makes with the normal, $T_{1,2}$ are transmission factors depending on the boundary conditions and f, s refer to the film and substrate, respectively.

RESULT AND DISCUSSIONS

The acetone solution of MCSe-C₁₈ is red-colored in the non-J state, having a broad-band absorption with a maximum at 550 nm and a half-width of roughly 150 nm. Just after dispersing MCSe-C₁₈ acetone solution in water, the solution mixture is also red-colored and transparent, like a homogeneous organic solution, although there exist microcrystals in it. Using a scanning electron microscope, the microcrystals were observed to have sizes of several tens of nm. During the time the solution is stored below 10°C (1 day) with a catalytic amount of ammonia, the color gradually changed to blue/violet, with an absorption maximum at 610 nm or 630 nm and a 40 nm or 30 nm half-width, respectively. Both of these low energy bands indicate the formation of J-aggregate states.⁶ After conversion to the J-aggregate state, the size of the microcrystals was observed to be the same as that of the non-J state. The first state, having the absorption maximum at 610 nm is called the J1 state; the second one is the J2 state. X-ray diffraction patterns show that J1 and J2 states have spacing distances of 31 Å and 33 Å respectively. Therefore, the molecular packing in the J1 state is different from that in the J2 state. At very low concentrations of MCSe-C₁₈, (less than 1 μM in aqueous solution), the formation of J1 or J2 state can be controlled by the ratio between the amounts of organic solvent and water in the mixture.¹⁵ However, such control was difficult in this investigation because of the presence of the polymer matrices. At the higher concentrations of MCSe-C₁₈ with respect to the polymer matrix (15–20 wt.%), the J1 state was obtained; at the lower concentrations (5–10 wt.%) the J2 state was obtained.

In Figure 1 typical examples of Maker fringe patterns from both the J-aggregate microcrystals in polymer matrix on a quartz substrate and from only the quartz substrate are shown. Since the film thickness is small enough to be less than the coherence length, both fringes obtained come from the substrate. The shift of the local fringe minimum between the film on the substrate and only the substrate is related to

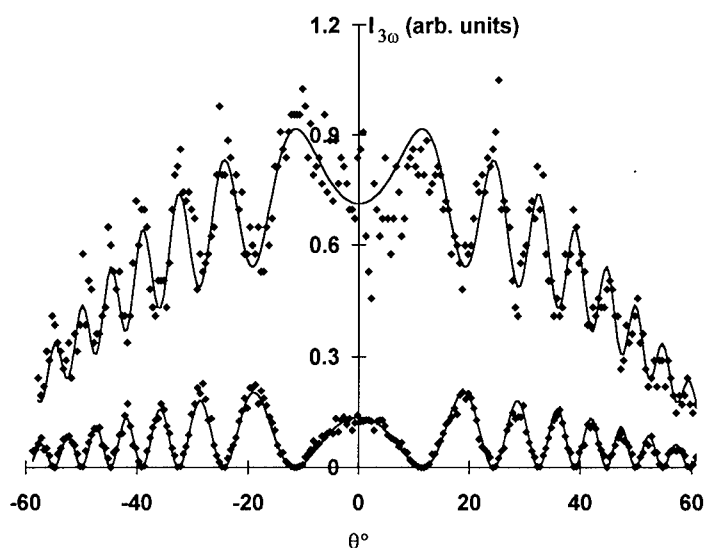


FIGURE 1 Typical THG Maker fringes plots from a merocyanine dye thin film. Lower curves: substrate, the intensity times 5; upper curves: sample film + substrate, points: data, solid lines: theoretical fits.

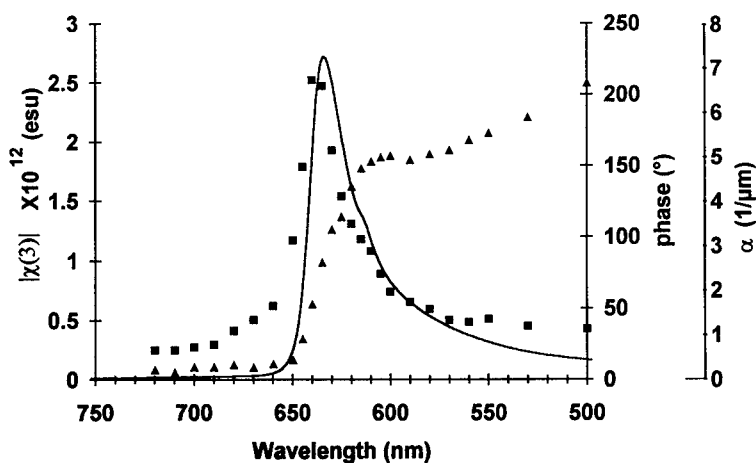
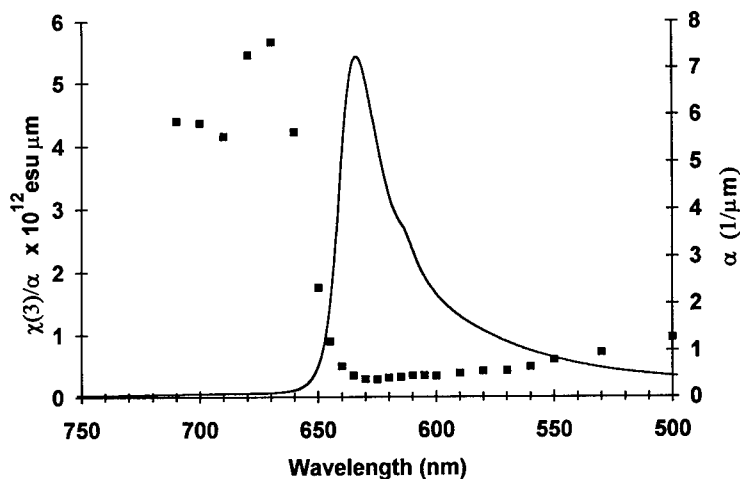


FIGURE 2 Modulus and phase of $\chi^{(3)}$ vs. TH wavelength for 10% merocyanine film in J2 state. ■: modulus of $\chi^{(3)}$; ▲: phase of $\chi^{(3)}$; line: absorbance.

the phase of $\chi^{(3)}$. The dispersion of modulus and phase of $\chi^{(3)}$ vs. TH wavelength are shown with the absorption coefficient in Figure 2. The phase of $\chi^{(3)}$ changes from 0 deg. around 700 nm to 180 deg. below 570 nm and is 90 deg. at the absorption maximum. The three-photon resonant effect can be clearly observed at the absorption maximum of 630 nm where only the imaginary part of $\chi^{(3)}$ contributes to the non-linear optical process. At TH wavelengths slightly longer than that at the absorption maximum, the modulus of $\chi^{(3)}$ increases while the phase remains small. This indicates that the real part

FIGURE 3 Figure of merit ($|\chi^{(3)}|/\alpha$) vs. TH wavelength.

of $\chi^{(3)}$ increases at the band-edge by a resonant effect. In order to see the effect clearly, a figure of merit, $|\chi^{(3)}|/\alpha$, is plotted vs. the TH wavelength in Figure 3. The figure of merit reaches a maximum value of 5.7×10^{-12} esu μm at a wavelength of 670 nm. This is 1.5 and 20 times greater than at non-resonant (720 nm) and excitonic peak (630 nm) wavelengths, respectively. Such a maximum of the figure of merit can be observed because of the sharp band-edge of excitonic absorption made by the formation of J-aggregate state. In other words, at the band edge the absorption decreases rapidly away from resonance while the real part of $\chi^{(3)}$ is still large due to resonance effects. This result suggests that by sharpening the absorption peak and using a wavelength near band-edge, significant enhancement of non-linear optical properties can be obtained.

In Table 1, the nonlinear optical properties of MCSe- C_{18} microcrystals in a polymer matrix are summarized for several samples. It is clearly seen that the J2 state has the largest non-linear optical properties compared to the non-J and J1 states. This is due to the fact that the J2 state has the sharpest absorption peak. Preparation of samples of

TABLE 1
Summary of THG measurements for merocyanine dye microcrystals in polymer matrices.

State	Concentration (wt%)	Film thickness (μm)	λ max (nm)	Half width of α (nm)	Maximum $ \chi^{(3)} $ ($\times 10^{-12}$ esu)	$ \chi^{(3)} $ at 700 nm div. by conc. ($\times 10^{-14}$ esu(wt%) $^{-1}$)
J2 state	5	1.02	630	27	0.806(635 nm)	2.1
	10	0.749	634	28	2.52(640 nm)	2.4
	10	0.593	632	26	2.23(635 nm)	2.5
J1 state	15	0.542	610	40	1.94(615 nm)	1.5
	20	0.227	609	43	2.77(610 nm)	1.6
non-J state	10	0.368	553	146	0.119(590 nm)	0.68

merocyanine dyes in the J2 state at higher concentrations in a polymer matrix is now in progress.

REFERENCES

1. P. W. Smith and W. J. Tomlinson, *IEEE Spectrum*, June 1981, p. 26.
2. E. Hanamura, *Phys. Rev. B*, **37**, 1273 (1988), *ibid* **38**, 1228(1988).
3. E. E. Jelley, *Nature*, **139**, 631(1937).
4. S. Kobayashi and F. Sasaki, *Nonlinear Optics*, **4**, 305(1993).
5. E. Daltrozso, G. Scheibe, K. Gschwind and F. Haimerl, *Photo. Sci. Eng.*, **18**, 441(1974).
6. K. Iriyama, F. Mizutani and M. Yoshiura, *Chem. Lett.*, 1399(1980).
7. D. L. Morel, A. K. Ghosh, T. Feng, E. L. Stogryn, P. E. Purwin and A. Fishman, *Appl. Phys. Lett.*, **32**, 495(1978).
8. G. A. Chamberlain and R. E. Malpas, *Faraday Discuss. Chem. Soc.*, **70**, 299(1980).
9. M. Sugi and S. Iizima, *Thin Solid Films*, **68**, 199(1980).
10. H. Tomiyama, H. Matsuda, S. Okada and H. Nakanishi, *Nonlinear Optics, Fundamentals, Materials and Devices*, Ed. by S. Miyata, p. 305 (Elsevier Science Pub., 1992).
11. H. Kasai, H. S. Nalwa, H. Oikawa, S. Okada, H. Matsuda, N. Minami, A. Kakuta, K. Ono, A. Mukoh and H. Nakanishi, *Jpn. J. Appl. Phys., Part 2*, **31**, L1132 (1992).
12. F. Kajzar and J. Messier, *Nonlinear Optical Properties of Organic Molecules and Crystals*, **2**, eds. by D. S. Chemla and J. Zyss, p. 51 (Academic Press, 1989).
13. T. Hasegawa, K. Ishikawa, T. Koda, K. Takeda, H. Kobayashi and K. Kubodera, *Synth. Metals*, **49-50**, 123 (1992).
14. A. Mito, C. Takahashi, H. Matsuda, S. Okada and H. Nakanishi, *Proc. Inter. Conf. Lasers'92*, p. 908 (STS press, Maclean VA, 1993).
15. F. Mizutani, S. Iijima and K. Tsuda, *Bull. Chem. Soc. Jpn.*, **55**, 1295 (1982).

The Third-Harmonic Generation in Gold and Nickel Bis-Dithiolene Complexes

T. BJØRNHOLM*, T. GEISLER*^{+,1}, J. C. PETERSEN⁺, D. R. GREVE*
and N. C. SCHIØDT*

*Centre for Interdisciplinary Studies of Molecular Interactions(CISMI),
Chemistry Department, SYMBION, University of Copenhagen,
Fruebjergvej 3, DK-2100 Copenhagen, Denmark,

⁺ Danish Institute of Fundamental Metrology, Lundtoftevej 100,
Bldg. 307, DK-2800 Lyngby, Denmark

Received 25 February 1994; accepted 16 March 1994

Optical third-harmonic generation (THG) has been used in a study of thin films of n-butylammonium salts of Au- and Ni-bis-dithiolene complexes (bis-(benzene-1,2-dithiolato)(Au(III) or Ni(III)))[−] and (bis-(4,5 dimethoxy-benzene-1,2 dithiolato) (Au(III) or Ni(III)))[−] as guests in a polymer matrix of PMMA (polymethylmethacrylate). The third-order nonlinear hyperpolarizabilities, $\gamma(-3\omega; \omega, \omega, \omega)$, derived from the THG measurements at 1064 nm are $5-8 \cdot 10^{-48} \text{ m}^5/\text{V}^2$ which is orders of magnitude smaller than the $\gamma(-\omega; \omega, -\omega, \omega)$ -values reported for similar metal complexes measured by the degenerate four wave mixing (DFWM) and the Z-scan techniques. The Ni containing compounds have an intense NIR-transition which is vanishing in the Au containing compounds. This NIR transition does not seem to contribute to the THG response since both the Ni and Au containing compounds have THG γ -values of the same magnitude. A THG γ -value of $2 \cdot 10^{-48} \text{ m}^5/\text{V}^2$ is obtained for the neutral Ni(dipdt)₂ (bis-(1,2-diphenylethene-1,2-dithiolato-S,S')Ni(III)) which is included for comparison with previously reported data measured by DFWM.

INTRODUCTION

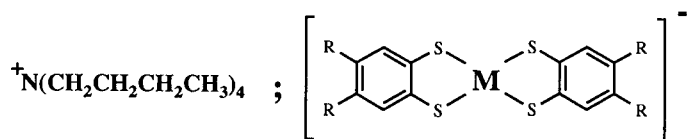
Organic materials displaying nonlinear optical (NLO) effects are of interest because of their relative large and fast nonresonant nonlinearities with origin in the delocalized π -electron system.^{1–3} They possess considerable potential for applications in devices used for optical information processing in optical communication systems.⁴

Organometallic systems, where organic ligands are attached to a metal center are also expected to possess enhanced nonlinear optical properties due to coupling to an intense near infrared absorption transition allowing the transfer of electron-density between the ligand and the metal atom.⁵ An enhancement in the third-order optical nonlinearity has e.g., been observed in metallocyanine relative to that of the metal-free compound.⁶ The presence of a low-lying electronic state associated with the ligand was suggested as a possible source for the enhancement.⁶ Recent studies of metal dithiolene complexes^{7–12} have shown promise for obtaining high values of the nonlinear refractive index which is proportional to the nonlinear susceptibility

¹ Present address: Institute of Physics, University of Aalborg, 9220 Aalborg, Denmark.

$\chi^{(3)}(-\omega; \omega, -\omega, \omega)$. The possibility of maximising the figures of merit (FOM) by tuning the near infra-red absorption band was shown for metal dithiolene derivatives with different substituent groups on the dithiolene ligands⁸ and by varying the metal atom.¹⁰ The effect of metal substitutions has been investigated for complexes of the benzenedithiol (bdt) ligand $M(bdt)_2^-$,^{11,12} and an enhancement in $\chi^{(3)}$ of two orders of magnitude were obtained by metal atom substitution.¹¹ The above mentioned investigations were performed using the two different techniques, degenerate four wave mixing (DFWM) and Z-scan. For bis-(benzene-1,2-dithiolato)Ni(III)⁻ ($Ni(bdt)_2^-$) it was shown by DFWM at 1064 nm that the response time was limited only by the pulse time, indicating a nonlinear response time of less than 35 psec.¹² THG has previously been used in a study of the metal-dithiolene complexes, (e.g., $n-Bu_4N[Ni(dmbdt)_2]$), in solutions.¹³ These studies showed that the $\chi^{(3)}(-3\omega; \omega, \omega, \omega)$ -values were two to three orders of magnitude lower than the $\chi^{(3)}(-\omega; \omega, -\omega, \omega)$ -values obtained by DFWM studies. This was attributed to the different contributions to $\chi^{(3)}$ encountered in the two measurements.¹³

In order to reveal the significance of the ligand to metal charge transfer transition in connection with the coherent nonlinear properties measured by THG, we have used the two metals Ni and Au (Fig. 1), respectively, since the strong near infra-red band present in the Ni containing compounds becomes very weak when Ni is replaced by Au. Ab initio calculations show that both compounds possess transitions which have ligand-to-metal character among the lowest lying excitations.^{14,15} For the Ni-complexes these transitions are symmetry allowed while they are forbidden in Au-complexes. This difference is reflected in the oscillator strength of the transitions which differ by two orders of magnitude. We have applied the THG Maker fringe technique^{16,17} in a study of a series of thin films of these molecules (Fig. 1). For comparison with the DFWM results presented in⁹ the neutral $Ni(dipdt)_2$ compound has been included in this study (Fig. 1).



$Ni(bdt)_2NBA : R = H, M = Ni$

$Ni(dmox)_2NBA : R = OCH_3, M = Ni$

$Au(bdt)_2NBA : R = H, M = Au$

$Au(dmox)_2NBA : R = OCH_3, M = Au$

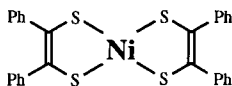


FIGURE 1 Molecular structure of the metal complexes studied. The neutral molecule is in the text labelled $Ni(dipdt)$.

EXPERIMENTS

The gold complexes were prepared by mixing alcoholic solutions of NaAuCl_4 , the ligand and the hydrated sodium acetate by filtration and precipitation with a tetra-*n*-butylammonium salt (BF_4^- or PF_6^-).¹⁴ The Ni-complexes were prepared similarly (using $\text{NiCl}_2 \cdot 6\text{H}_2\text{O}$) except for using preformed disodium dithiolate and for allowing the reaction mixture to stand in contact with air to oxidize the initially formed dianionic complex.¹⁸ All metal complexes were recrystallized and their composition found to be in accordance with the theoretical values from microanalysis.

Thin polymer/metal-complex films were formed by casting from chlorobenzene solutions of the PMMA polymer doped with approximately 10 weight percent of the metal-complex corresponding to a concentration of the order of 10^{20} molecules cm^{-3} . The film thicknesses were measured by profilometry and calculated from the optical density.

Absorption spectra were measured by a Perkin Elmer Lambda 9 spectrophotometer.

The experimental set-up for the THG measurements is illustrated in Figure 2. The laser was a 10 pps *Q*-switched Nd:YAG laser operating at 1064 nm with a pulse duration of 10 nsec. The beam was directed through filters, polarizing optics and focused on the sample by a 300 mm lens. The sample was mounted on a rotational stage so that the angle of incidence of the laser beam could be varied. The thin film side of the sample was facing the detector. The polarization of the electrical field was parallel to

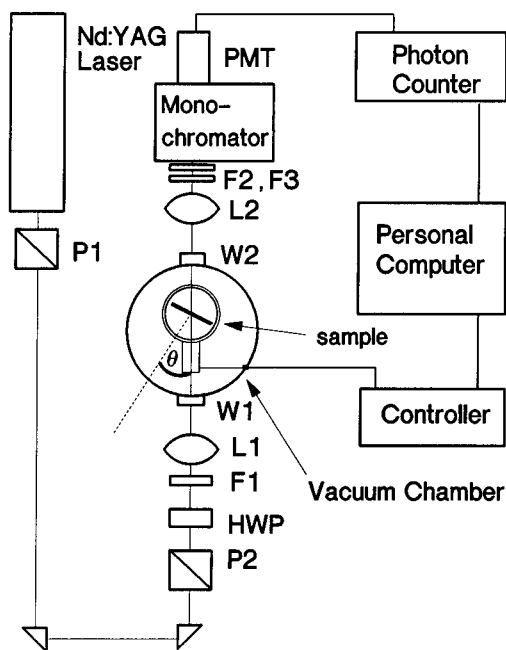


FIGURE 2 The experimental setup used for the THG measurements. P_1 , P_2 are polarizers; F_1 , F_2 , and F_3 are color filters; L_1 , L_2 are lenses; W_1 , W_2 are windows and HWP is a halfwave plate.

the rotation-axis and care was taken that the incident beam and the rotation-axis coincided. The sample and the rotational stage were contained in a vacuum chamber to avoid interference from air. The third harmonic beam at 354.6 nm was detected in a transmission geometry using a photomultiplier in connection with a photoncounter. A combination of infrared filters and a monochromator were used to block other wavelengths. A Personal Computer was used to control the rotational stage and for data collection. Each data point was obtained by sampling signals from 300 laser pulses.

The third-order optical susceptibilities of the thin films (f), $\chi_f^{(3)}$, were determined relative to that of the fused silica substrate (s), $\chi_s^{(3)}$, using the Maker fringe technique.¹⁶ The expression for the intensity, $I_{3\omega}$, of the third harmonic radiation is given by¹⁷

$$I_{3\omega}(\theta) = C |\alpha^{-1} [A(1 - e^{-i\Delta\phi_s}) + B\rho(\alpha\beta e^{i\Delta\phi_f} - 1)]|^2 I_\omega^3, \quad (1)$$

where I_ω is the intensity of the fundamental, θ the angle of incidence, and C a constant. The Maker fringe oscillations are due to the phase mismatch between the free and bound waves at 3ω represented by the quantities $\Delta\phi_i = \phi_{i,\omega} - \phi_{i,3\omega}$ and $\phi_{i,j} = 3\omega l_{i,j} n_{i,j} \cos \theta_{i,j} / c$, where $i = s$ for the substrate, $i = f$ for the film, j can be either ω or 3ω . l_i denotes the thickness of the substrate or the film, $n_{i,j}$ are the real parts of the indices of refraction and $\theta_{i,j}$ are the internal angles of propagation. The factors A and B arise from the Fresnel transmission factors and boundary conditions at each interface.¹⁶ The factors α and β are included in order to account for any absorption in the film at the harmonic and fundamental wavelength, respectively.¹⁷ The quantity ρ is defined by

$$\rho = \frac{\chi_f^{(3)} \Delta \varepsilon_s}{\chi_s^{(3)} \Delta \varepsilon_f} = \left| \frac{\chi_f^{(3)}}{\chi_s^{(3)}} \right| \left| \frac{\Delta \varepsilon_s}{\Delta \varepsilon_f} \right| e^{i\psi}, \quad (2)$$

where $\Delta \varepsilon_i = \varepsilon_{i,\omega} - \varepsilon_{i,3\omega}$ are the dielectric constant dispersion and $\varepsilon_{i,j} = (n_{i,j} + i\kappa_{i,j})^2$, where $\kappa_{i,j}$ denote the imaginary part of the refractive indices. For the substrate we have $\kappa_{s,j} = 0$. The relative phase between $\chi_f^{(3)}$ and $\chi_s^{(3)}$ is denoted by ψ . The phase of $\chi_s^{(3)}$ is assumed to be zero.¹⁶

At present the index of refraction of the thin films is not known accurately. However, for a film with a thickness much smaller than the THG coherence length,¹⁶ $l_{c,f} = \lambda / (6|n_f^\omega - n_f^{3\omega}|)$ it can be shown that the third-harmonic generated in the film is not strongly dependent of the refractive index. However, due to absorption the imaginary part has to be taken into consideration. The imaginary part of the refractive index at ω and 3ω are determined from absorption spectra of the films, and the real parts are assumed to be close to those of the polymer-host PMMA ($n_f^\omega = 1.48$ and $n_f^{3\omega} = 1.50$).

When $\chi_f^{(3)}$ has been determined the isotropic orientational average of the second hyperpolarizability⁴

$$\langle \gamma \rangle = \frac{1}{5} (\gamma_{xxxx} + \gamma_{yyyy} + \gamma_{zzzz} + 2(\gamma_{xxyy} + \gamma_{xxzz} + \gamma_{yyzz})) \quad (3)$$

can be obtained from the following expression⁴

$$\chi_f^{(3)} = N_s L \langle \gamma \rangle \quad (4)$$

where N_s is the number density of oligomer molecules and L is a correction factor due to the local-field effects. We use the Lorentz approximation for the local-field effects which leads to⁴

$$L = \left(\frac{n_{\omega}^2 + 2}{3} \right)^3 \frac{n_{3\omega}^2 + 2}{3} \quad (5)$$

where $n_{\omega(3\omega)}$ is the linear refractive index of the film at ω and 3ω , respectively. We use a correction factor of $L = 4.0$.

RESULTS

The Ni bis-dithiolene complexes possess a strong electronic transition in the near infrared region (Fig. 3a). The transition is red-shifted in complexes with electron donating substituents indicating a ligand-to-metal character of the transition. Similar red-shifted transitions are observed in the spectrum of the Au complexes. In comparison to

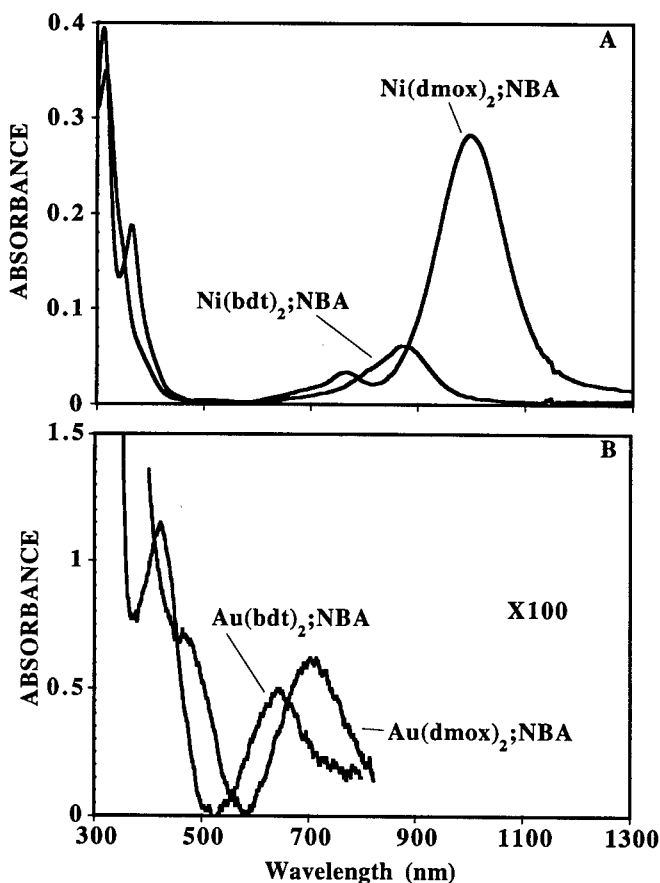


FIGURE 3 Electronic spectra of the mono anionic metal complexes in solution (10^{-5} M, CH_2Cl_2).

the Ni complexes these transition are found to be approximately 100 times less intense (Fig. 3b, Table 1).

The films used in the THG measurements were less than 500 nm thick. Examples of experimental THG Maker fringe patterns obtained from the films are shown in Figures 4a, b. In the figures are shown both the data obtained from the film-on-substrate sample and those obtained from the same substrate in the same position with the film carefully removed by chloroform. The lines represent theoretical fits to Eq. (1) of the experimental data of the film sample and of the bare substrate, respectively. The symmetric and reproducible Maker fringe patterns obtained indicate that the films are homogeneous. The analysis of the THG measurements of $\chi^{(3)}(-3\omega; \omega, \omega, \omega)$ reveal values of $\langle \gamma \rangle$ of approximately $5 - 8 \cdot 10^{-48} \text{ m}^5/\text{V}^2$. For the Au complexes the $\chi_f^{(3)}$ values were real, whereas for all the Ni complexes $\chi^{(3)}$ had a positive imaginary component. However, due to the lack of knowledge about the accurate values of the refractive indices the exact phases cannot be determined. Compared to the intensity of the electronic transition in the near infrared no strong correlation between extinction coefficient for the NIR-transition, and is observed as summarized in Table 1.

DISCUSSION

The following observations are noted: (1) $\gamma(-3\omega; \omega, \omega, \omega)$ values of metal-bisdithiolene complexes are of the same order of magnitude as $\gamma(-3\omega; \omega, \omega, \omega)$ values for conjugated π -electron systems with the same number of delocalized π -electrons (e.g., bis-styryl-benzenes).^{21,22} (2) $\gamma(-3\omega; \omega, \omega, \omega)$ is insensitive to the intensity of the excitation in the NIR-region of the spectrum. Non of these observations are in accordance with the notion that the main contribution to γ originates from an intense NIR-transition which possess pronounced transfer of electron density from ligand of metal. In an effort to understand this we have performed *ab initio* molecular orbital calculations of the $\text{Au}(\text{bdt})_2^-$ -complex which show that the highest occupied molecular orbital (HOMO) has almost pure ligand character while the LUMO is a mixed ligand and metal orbital.¹⁴ Similar results are obtained for the Ni-complex.¹⁵ The calculated mixing of ligand and metal orbitals in the LUMO-state of $\text{Au}(\text{bdt})_2^-$ indicates that the excited state charge distribution is delocalized over the entire molecule as it is for the ground state. The resulting polarization of the molecule upon excitation is consequently not as

TABLE I
Hyperpolarizabilities of the investigated metal complexes.

Compound	λ nm	ϵ	$\langle \gamma \rangle^c 10^{-48} \text{ m}^5/\text{V}^2$
$\text{Au}(\text{bdt})_2^-$	640 ^a	70 ^a	6.0
$\text{Au}(\text{dmox})_2^-$	715 ^a	100 ^a	8.3
$\text{Ni}(\text{bdt})_2^-$	875 ^b	3500 ^b	5.0
$\text{Ni}(\text{dmox})_2^-$	996 ^b	20000 ^b	6.2
$\text{Ni}(\text{dipdt})_2$	854 ^b	30000 ^b	2.2

^a Lowest lying electronic transition.

^b Most intense NIR transition.

^c For conversion to electrostatic units see Ref. 20.

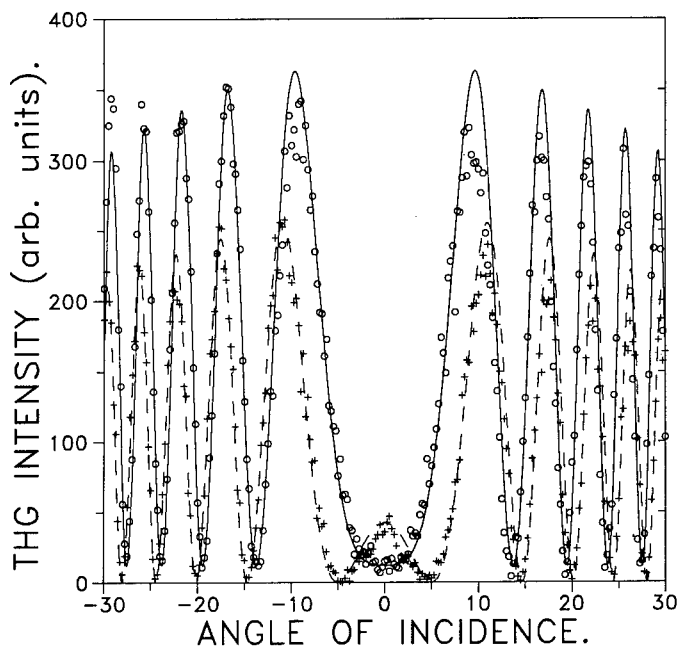


FIGURE 4a The experimental fringe pattern from a 1 mm thick fused silica substrate (the film removed by chloroform) is shown (daggers) together with the pattern from a 420 nm thick film of $\text{Au}(\text{bdt})_2^-$ (approx. 10wt%) on the substrate (open circles). The lines are theoretical fits.

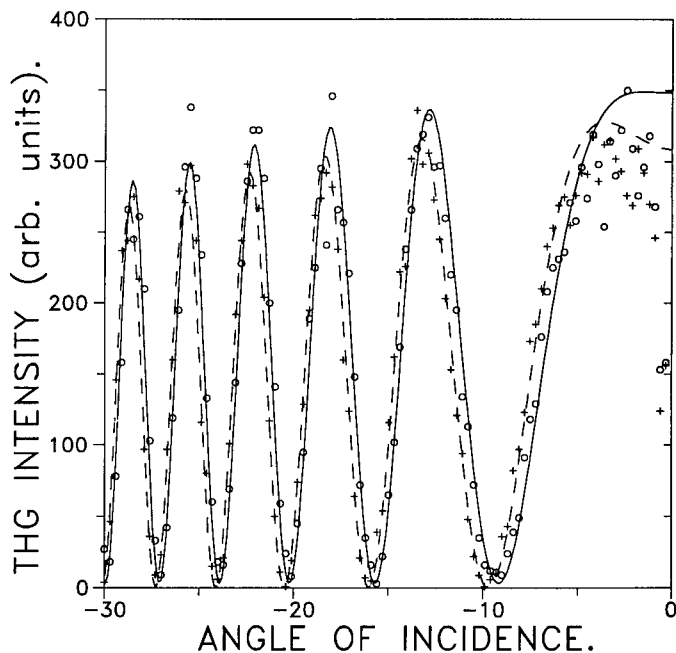


FIGURE 4b The experimental fringe pattern from a 1 mm thick fused silica substrate (the film removed by chloroform) is shown (daggers) together with the pattern from a 190 nm thick film of $\text{Ni}(\text{bdt})_2^-$ (approx. 10wt%) on the substrate (open circles). The lines are theoretical fits.

pronounced as expected for a pure ligand to metal transition providing a natural explanation for the observed data.

The THG $\langle\gamma\rangle$ -value of $5 \cdot 10^{-48} \text{ m}^5/\text{V}^2$ obtained for the $\text{Ni}(\text{bdt})_2^-$ is approximately 70 times less than the corresponding $\langle\gamma\rangle$ -value of $360 \cdot 10^{-48} \text{ m}^5/\text{V}^2$ ($25.8 \cdot 10^{-35} \text{ esu}$) measured by DFWM at 1064 nm by Kafafi *et al.*^{11,12} The response time of the DFWM signal was pulse width limited at 35 ps. However, the measured ratio of the tensor components χ_{xxxx} and χ_{yyyy} suggested that an excited state with a lifetime of less than 35 ps contributed to the observed nonlinearity.¹² The static molecular hyperpolarizability has been calculated by Craig and Williams¹⁹ for the neutral $\text{Ni}(\text{bdt})_2$ using CNDO/S molecular orbital technique in connection with the finite field method. It was shown that the non-diagonal element within the plane of conjugation, $\chi_{xxyy} \approx 1.68 \cdot 10^{-48} \text{ m}^5/\text{V}^2$, is the most significant element. Neglecting the other elements this leads to $\langle\gamma\rangle = \frac{2}{5} \gamma_{xxyy} \approx 0.67 \cdot 10^{-48} \text{ m}^5/\text{V}^2$.²⁰ This value is approximately one order of magnitude less than the experimental value obtained for the $\text{Ni}(\text{bdt})_2^-$. Since the calculated value is the static value and the experimental value may be influenced by resonance enhancement due to the absorption at 3ω (355 nm), this is considered to be a reasonable agreement. Similar observations were made in a recent study of thienylenes etynylenes.²²

For both the Ni- and Au-complexes the addition of electron donating methoxy substitutes give rise to a slight enhancement in the γ -values. The absorption spectra are also showing a change at the third-harmonic wavelength upon "substitution" (see Figs. 3a, b). Therefore the enhancement of γ could be due to a three-photon resonance enhancement or it could simply be due to more participating electrons.²³

CONCLUSIONS

Nickel and gold bis-dithiolene complexes have similar values of $\gamma(-3\omega; \omega, \omega, \omega)$ despite a large difference in the intensity of the optical "ligand-to-metal" transition. Pure electronic contributions to NLO-properties (measured by THG at 1064 nm) are orders of magnitude smaller than the values obtained by degenerate four wave mixing.

REFERENCES

1. D. S. Chemla and J. Zyss (Eds.), *Nonlinear Optical Properties of Organic Molecules and Crystals*, Vol. I, II, (Academic Press, New York 1987).
2. S. R. Marder, J. E. Sohn and G. D. Stucky (Eds.), *Materials for Nonlinear Optics: Chemical Perspectives*, (ACS Symposium Series 455, 1991).
3. J. Messier, F. Kajzar and P. Prasad (Eds.), *Organic Molecules for Nonlinear Optics and Photonics*, (Kluwers Academic Publishers, Dordrecht 1991).
4. P. N. Prasad and D. J. Williams, *Introduction to Nonlinear Optical Effects in Molecules and Polymers*, (Wiley, New York, 1991).
5. H. S. Nalwa, *Appl. Organomet. Chem.*, **5**, 349 (1991).
6. J. S. Shirk, J. R. Lindle, F. J. Bartoli, C. A. Hoffman, Z. H. Kafafi and A. W. Snow, *Appl. Phys. Lett.*, **55**, 1287 (1989).
7. C. Maloney and W. Blau, *J. Opt. Soc. Am.*, **B4**, 1035 (1987).
8. C. S. Winter, S. N. Oliver, J. D. Rush, C. A. S. Hill and A. E. Underhill, *J. Appl. Phys.*, **71**, 512 (1992).
9. C. S. Winter, S. N. Oliver, R. J. Manning, J. D. Rush, C. A. S. Hill and A. E. Underhill, *J. Mater. Chem.*, **2**, 443 (1992).
10. S. N. Oliver, C. S. Winter, R. J. Manning, J. D. Rush, C. Hill and A. E. Underhill, *SPIE*, **1775**, 110 (1992).

11. Z. H. Kafafi, J. R. Lindle, S. R. Flom, R. G. S. Pong, C. S. Weisbecker, R. C. Claussen and F. J. Bartoli, *SPIE*, **1626**, 440 (1992).
12. J. R. Lindle, C. S. Weisbecker, F. J. Bartoli, R. G. S. Pong and Z. H. Kafafi, *Mat. Res. Soc. Symp. Proc.*, **247**, 277 (1992).
13. T. Fukaya, M. Mizuno, S. Murata and A. Mito, *SPIE*, **1626**, 135 (1992).
14. N. C. Schiødt, P. Sommer-Larsen, T. Bjørnholm, M. F. Nielsen, J. Larsen and K. Bechgaard, *Inorg. Chem.*, submitted.
15. Z. S. Herman, R. F. Kirchner, G. H. Loew, U. T. Mueller-Westerhoff, A. Nazzari and M. C. Zerner *Inorg. Chem.*, **21**, 46 (1982).
16. F. Kajzar, J. Messier and C. Rosilio, *J. Appl. Phys.*, **60**, 3040 (1986).
17. J. B. van Beek, F. Kajzar and A. C. Albrecht, *J. Chem. Phys.*, **95**, 6400 (1991).
18. M. J. Baker-Hawkes, E. Billig and H. B. Gray, *J. Am. Chem. Soc.*, **88**, 4870 (1966).
19. B. I. Craig and C. R. J. Williams, *Appl. Phys.*, **B56**, 331 (1993).
20. The following conversions have been used: $1 \text{ au} = 0.503717 \cdot 10^{-39} \text{ esu}$; $1 \text{ esu} = 13.97 \cdot 10^{-15} \text{ m}^5/\text{V}^2$.
21. T. Geisler, T. Bjørnholm, J. C. Petersen, H. G. Madsen and K. Bechgaard, in preparation.
22. T. Geisler, J. C. Petersen, T. Bjørnholm, E. Fischer, J. Larsen, C. Dehu and J.-L. Bredas, G. V. Tormos, P. N. Nugara, M. P. Cava, R. M. Metzger, *J. Phys. Chem.*, to appear.
23. P. N. Prasad and B. A. Reinhardt, *Chem. Mater.*, **2**, 660 (1990).

The Third Order Nonlinear Optical Response of a Soluble form of Polyisothionaphthene

S. J. BURBRIDGE, H. PAGE, A. DRURY, A. P. DAVEY, J. CALLAGHAN
and W. BLAU

Department of Pure and Applied Physics, Trinity College Dublin, Dublin 2

Received 30 January 1994; accepted 21 March 1994

The third order nonlinearity of a low bandgap conjugated organic polymer has been assessed. Degenerate four-wave mixing experiments (at 1.064 μm using picosecond pulses from a passively mode locked Nd:YAG laser) on solutions of the polymer have permitted the determination of the microscopic third order nonlinearity ($\chi^{(3)}$). The polymer exhibits unusual behaviour which is solution concentration dependent. This behaviour is thought to be due to aggregation effects and strongly suggests that the bulk response of the material is large, the third order nonlinearity being of the order of ten times greater than that of polythiophene.

Following preliminary studies, a sample of the same polymer with a greater average molecular weight was also measured and was found, within an order of magnitude, to possess the same third order nonlinearity.

INTRODUCTION

The third order nonlinear optical properties of conjugated organic semiconducting polymers has been the subject of intense investigation for the past 15 years. It is hoped that such materials will find use in optical switching devices based on planar waveguides.¹

Many different classes of such polymers have been investigated² in the search for a material which exhibits a sufficiently large third order nonlinear optical response for use in all optical switching devices. To date, a material which meets all device requirements has still not been identified.

Our own work has focused on the development of semiconducting polymers for use in devices which would operate in the near-infrared region. Such devices would find application primarily in optical telecommunications systems. The Kramers-Kronig relationship states that the magnitude and sign of the nonlinear refractive index at a fixed wavelength is strongly dependent on the position of resonance for any sample to be investigated. For the purposes of our own work, this has involved the investigation of narrow gap semiconducting polymers whose band edge tails into the near-infrared region. In the past, investigations have avoided such systems, concentrating on conjugated polydiacetylenes which exhibit optical transparency in the near infrared. Loss measurements in PDA waveguides have demonstrated however, that absorption forms only a small fraction of overall losses, scattering in waveguides proving to be a far greater problem.³

The work reported here describes investigation of the microscopic third order nonlinear optical response of a narrow gap semiconducting polymer based on the polyisothionaphthene (PITN) family (see Fig. 1)

The electrical properties of this polymer have been extensively investigated,⁴ however, its lack of solubility has prevented any study of the nonlinear optical properties since no form of high optical quality sample has been available. The polymer studied here is a form of PITN which is soluble in common organic solvents (Fig. 2). The synthesis of this polymer is detailed elsewhere.⁵

The fact that this material is soluble permits the investigation of its nonlinear optical properties in solution and the fabrication of thin film waveguide structures using spincoating techniques. The investigation of the microscopic third order nonlinearity of two different forms of this material in chloroform solutions is described herein.

EXPERIMENTAL

The experimental method employed in these studies was that of Forced Light Scattering from Laser Induced Gratings, a technique which may be viewed as a degenerate four wave mixing process in the forward direction.⁶ The light source is an amplified, passively mode-locked Nd^{3+} :YAG laser emitting linearly polarised pulses of 50 ± 25 psec duration and of wavelength $\lambda = 1.064 \mu\text{m}$ at a repetition rate of 3 Hz. Peak powers of up to 50MW were readily available. The experimental method is described in detail elsewhere⁷ and the set-up is depicted schematically in Figure 3. It is based on the interference at the sample of two spatially and temporally overlapped beams, producing a spatial modulation of the intensity dependent refractive index of the material. This modulation acts as a diffraction grating from which the pulses may self diffract. Under

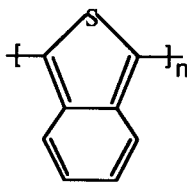


FIGURE 1 The Chemical Structure of polyisothionaphthene (PITN).

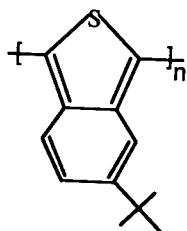


FIGURE 2 The Chemical Structure of Poly(3-*tert*-butyl)isothionaphthene.

thin grating conditions,⁶ satisfied experimentally by keeping the angle between the two beams small, ($< 1^\circ$), an expression relating the diffraction efficiency, η into the first order, to the third order material nonlinearity may be derived;

$$|\chi^{(3)}| = \frac{4\epsilon_0 c n^2 \lambda \sqrt{\eta}}{3\pi d I_0} \quad (1)$$

where c is the speed of light, ϵ_0 is the permittivity of free space, n is the refractive index of the sample, d is the sample thickness and I_0 is the input pulse intensity. In the experiments reported here, $d = 1$ mm and n is taken to be the refractive index of the solvent, because of the low fractional volume of solute. Equation (1) holds for materials which are transparent at the operating wavelength. Although there is some small absorption at the operating wavelength, the effective refractive index and thus the effective sample thickness may be considered to be that of the refractive index of the solvent and the sample cell path length respectively.

It can be seen from equation (1) that verification of the presence of a true third order nonlinear process may be performed by monitoring the intensity dependence of the diffraction efficiency. For a true third order process;

$$\eta = \frac{I_1}{I_0} \propto I^2 \quad (2)$$

where I_1 is the intensity diffracted into the first order. Such a verification is important as fifth and seventh order processes, originating in two and three photon resonant enhancement of the material nonlinearities, have been observed in organic conjugated materials.^{7,8}

$|\chi^{(3)}|$ may have both real and imaginary components originating from the solute as well as a contribution from the solvent, $\chi_{\text{solvent}}^{(3)}$, which is purely real and positive in the case of most organic solvents, including chloroform.⁹ For the concentration range employed in this work the solute fractional volume is negligible. Thus,

$$|\chi^{(3)}| = \{(\chi_{\text{solvent}}^{(3)} + \text{Re } \chi_{\text{sol}}^{(3)})^2 + (\text{Im } \chi_{\text{sol}}^{(3)})^2\}^{1/2} \quad (3)$$

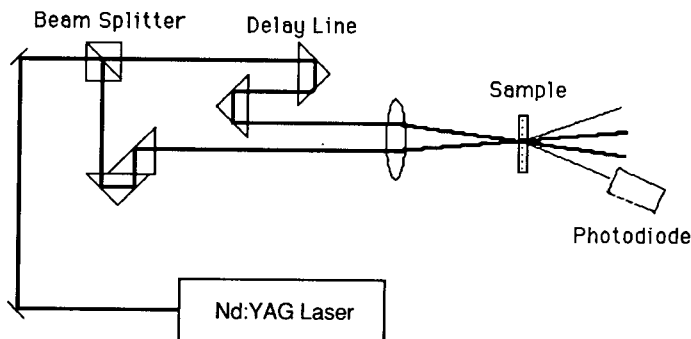


FIGURE 3 Experimental Setup for Self-diffraction Technique.

where $\text{Re}\chi_{\text{sol}}^{(3)}$ and $\text{Im}\chi_{\text{sol}}^{(3)}$ are the real and imaginary components of the material nonlinearity. By monitoring the concentration dependence of $|\chi^{(3)}|$, the contribution $\chi_{\text{sol}}^{(3)}$ due to the solvent may be extracted and the magnitude of $\text{Re}\chi_{\text{sol}}^{(3)}$ and $\text{Im}\chi_{\text{sol}}^{(3)}$ may be determined. Furthermore the sign of $\text{Re}\chi_{\text{sol}}^{(3)}$ may be determined from the concentration dependence of the real part of $|\chi^{(3)}|$.

The second molecular hyperpolarisability, (γ) is given by,

$$|\gamma| = \frac{|\chi^{(3)}|}{N_A C L_L^4} \quad (4)$$

where C is the oligomer concentration, N_A is Avagadro's constant and L_L is the Lorentz local field factor, which for practical purposes is taken to be that of a linear molecule and is given by $L_L = 1$.¹⁰

RESULTS

Linear Absorption

Two different types of sample were studied; one of low molecular weight (with an average of 5 repeat units per chain), and one of far higher molecular weight (of the order of 80 repeat units on average).¹¹ The absorption spectrum of the higher molecular weight sample is shown in Figure 4.

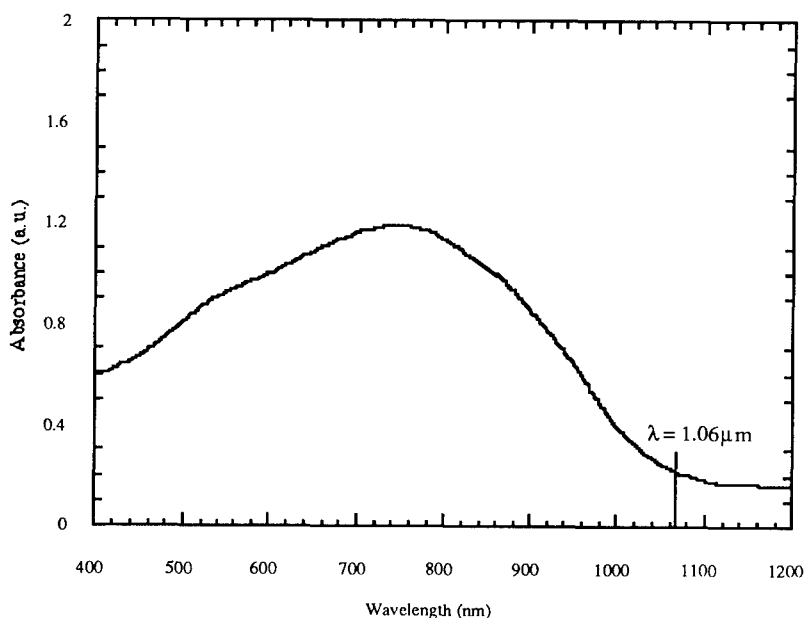


FIGURE 4 Absorption Spectrum of Higher Molecular Weight PTBITN. (NOTE—The absorption bandtail for the lower molecular weight material disappears at 950 nm).

Nonlinear Optical Response of the Low Molecular Weight Sample

Figure 5 shows the concentration dependence of diffraction efficiency. As already described, theory predicts a parabolic behaviour. It is clear however, that there is a deviation from such behaviour in this case. At low concentration, the dependence of diffraction efficiency is parabolic. At a certain limit however, this dependence begins to deviate before returning at higher concentrations to a second parabolic behaviour.

Such behaviour is not well understood but is clearly due to some form of interaction between polymer chains. However, this behaviour has been consistently observed in a variety of organic materials both monomeric and polymeric.¹²

For the purposes of calculating a microscopic nonlinearity (γ), points in the low concentration region (where no interchain interaction occurs) are used. The fit employed in this case along with the points is shown in Figure 6. It should be noted that errors (including scattering) are minimised by sampling each data point over 100 shots. The best fits in each case were found to be parabolic.

The values of γ obtained from this fit are given in Table 1. As can be seen by comparison with the values given for polythiophene (a structurally related conjugated polymer), the nonlinear optical response is quite large.

Nonlinear Optical Response of the High Molecular Weight Sample

Figure 7 shows the variation of Diffraction Efficiency with concentration. As before, there is a significant deviation from the behaviour predicted by theory. It is interesting to note that the deviation is quite similar to that of the low molecular weight sample.

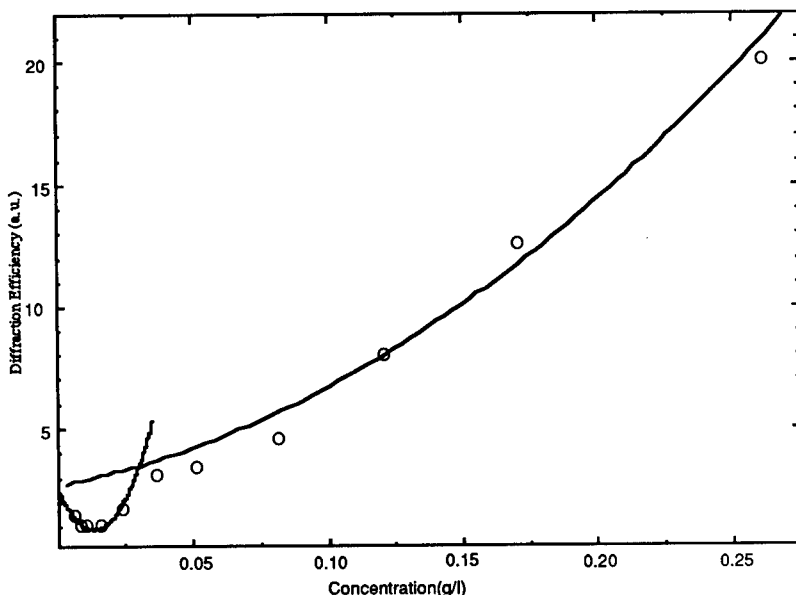


FIGURE 5 Concentration Dependence of Diffraction Efficiency for the Low Molecular Weight Sample.

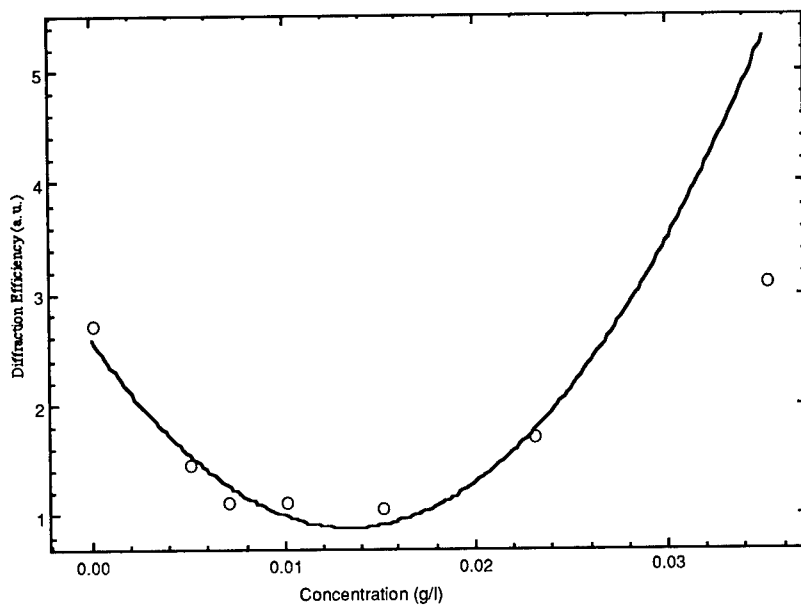


FIGURE 6 Fit of Concentration to Diffraction Efficiency for the Low Molecular Weight Sample.

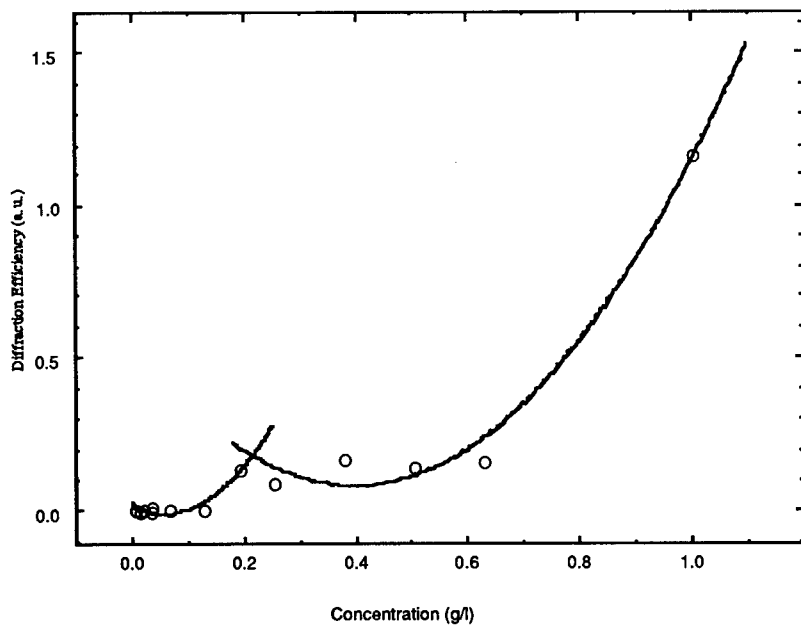


FIGURE 7 Concentration Dependence of Diffraction Efficiency for the High Molecular Weight Sample.

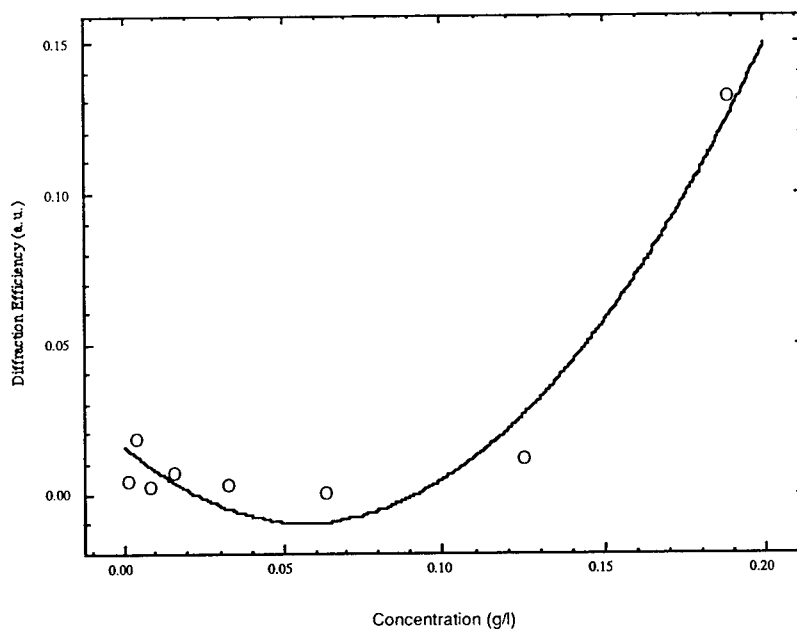


FIGURE 8 Fit of Concentration to Diffraction Efficiency for the High Molecular Weight Sample.

TABLE I
Values of γ for the Polymer compared to Polythiophene.

Compound	$\gamma_{Re} (m^5 V^{-2})$	$ \gamma _{Im} (m^5 V^{-2})$	$ \gamma (m^5 V^{-2})$
Poly(3-t-butyl)Isothionaphthene (Low Molecular Weight)	-9×10^{-45}	6×10^{-45}	1×10^{-44}
Poly(3-t-butyl)Isothionaphthene (High Molecular Weight)	-1×10^{-45}	3×10^{-45}	4×10^{-45}
Polythiophene ¹³	-6×10^{-46}	1×10^{-45}	1×10^{-45}

Figure 8 shows the fit employed to calculate the values of γ for the high molecular weight sample.

The γ values obtained (given in Table 1) are similar to the other polymers listed. It should be noted however, that for this sample the wavelength of measurement lies in the band edge, whereas for the other compounds in Table 1 the measurement may be considered to have been performed off-resonance.

CONCLUSIONS

Nonlinear optical properties of high and low molecular weight narrow bandgap conjugated organic polymers were studied. Concentration dependence of diffraction efficiency shows unusual behaviour. In the sample where the primary absorption is shifted towards the wavelength of measurement, no increase in the real and imaginary

components of nonlinearity was observed. The marginal decrease in the values for γ may also be ascribed to an increase in aggregation. Further work aims to probe the change in nonlinearity through the wavelength region of 1.0–1.5 μm , and to explore the effect of aggregation more thoroughly.

ACKNOWLEDGEMENTS

This work was funded by the RACE 2017 (HIPOS) project, sponsored by the EC Commission.

REFERENCES

1. G. I. Stegeman and R. H. Stolen, *J. Opt. Soc. Am. B*, **6**, 652 (1989).
2. H. S. Nalwa, *Adv. Mater.*, **5**, 341 (1993).
3. W. Krug, E. Miao, M. Derstine, J. Valera, *J. Opt. Soc. Am. B*, **6**, 4 (1989).
4. M. Kobayashi, N. Colaneri, M. Boysel, F. Wudl and A. Heeger, *J. Chem. Phys.*, **82/12**, 5717 (1985).
5. A. Drury, A. Davey, S. Burbridge, H. Page and W. Blau, *The Synthesis of the Narrow-Gap, Nonlinear, Organic Polymer Poly(tertbutylisothianaphthene)*. Poster Presentation, ICONO1.
6. "Laser Induced Gratings", H. J. Eichler, P. Gunter and D.W. Pohl, *Springer Series in Optical Sciences*, **50**, Springer Verlag. (1986).
7. H. J. Byrne, W. Blau and K. Y. Jen, *Synth. Metals.*, **32**, 229 (1989).
8. J. M. Nunzi and D. Grec, *J. Appl. Phys.*, **62**, 2198 (1987).
9. P. D. Maker, R. W. Terhune and C. M. Savage, *Phys. Rev. Lett.*, **12**, 507 (1964).
10. "The Principles of Nonlinear Optics", Y. R. Shen, Wiley Interscience (1984).
11. A. Drury, *Synthesis of Organic Polymers for Nonlinear Optical Applications*. MSc Thesis, Trinity College, Dublin, (1993).
12. H. J. Byrne and W. Blau, *Springer Series in Solid-State Sciences*, **107**, 190 (1992).
13. H. J. Byrne, *On the Origins and Nature of the Nonlinear Optical Properties of Organic Conjugated Polymers*, PhD Thesis, Trinity College, Dublin (1989).

The Design of New Organic Materials with Enhanced Nonlinear Optical Properties: Incorporation of Bipolaronic Charge States

CHARLES W. SPANGLER^a, MINGQIAN HE^a, PEIKANG LIU^a,
 ERIC G. NICKEL^a, JOYCE LAQUINDANUM^a and LARRY R. DALTON^a

^aDepartment of Chemistry, Northern Illinois University, DeKalb, IL 60115

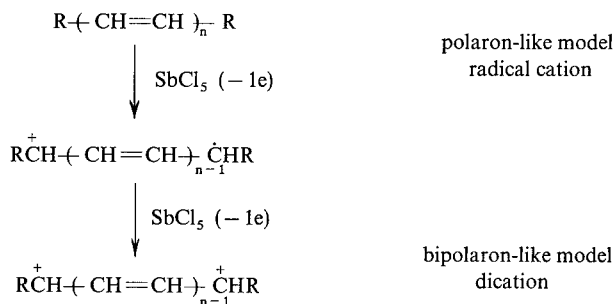
^bDepartment of Chemistry, University of Southern California,
 Los Angeles, CA 90089

Received 12 January 1994; accepted 16 March 1994

Bipolaron-like dications can be produced by oxidative doping of a wide variety of pi-conjugation sequences. These charge states can be stabilized either by mesomeric interaction with electron-donating groups or by stabilizing the quinoid structures produced upon oxidation by incorporation into an aromatic structure. Theoretical prediction of bipolaronic enhancement of third order response has now been confirmed in several conjugated oligomers related to polyacetylene wherein stabilization and processibility enhancement has also been achieved.

INTRODUCTION

The formation of stable bipolaron-like dications in short oligomeric conjugation sequences of electroactive polymers has been described extensively over the past five years. Our group has modeled polaron and bipolaron formation in diphenyl,¹ dialkyl,² and bis-thienyl polyenes^{3–5} by either FeCl₃ or SbCl₅ doping in solution as shown in Scheme 1. Fichou and coworkers have obtained similar results for the oxidative doping of a series of polythiophene oligomers,^{6,7} as has Guay and coworkers.⁸



SCHEME 1 Formation of polaron-like and bipolaron-like model radical cations and dications by oxidative doping.

In all of our studies, oxidation with SbCl_5 in CH_2Cl_2 results in an immediate bleaching of the $\pi-\pi^*$ transition with the simultaneous appearance of new absorption bands in the VIS or NIR spectral region depending on oligomer length and the identity of the polyene end caps (R). In most cases the transitory P-like radical cation can be observed spectroscopically (VIS-NIR or ESR), however in all cases studied to date, the bipolaron-like dication is the dominant species in solution. The use of thienyl end groups in place of either phenyl or alkyl provides additional resonance stabilization of the bipolaron, and/or greater solubility.

CHARGE STATE ENHANCEMENT OF NONLINEARITY

The question of charge state enhancement of NLO response has received increasing attention during the past few years. DeMelo and Silbey have postulated that enhancement of third order hyperpolarizability γ may be possible by incorporating delocalized charge states in the π -conjugation sequence of electroactive polymers such as polyacetylene.^{9,10} Their results indicated that both P and BP charge states could lead to enhancement. More recently, Birge and coworkers¹¹ also calculated the effect of BP charge state incorporation on γ_{xxxx} for an oligomeric series of disubstituted diphenyl polyenes. Using an INDO-PSDGI finite perturbation procedure, which includes 200 single and 400 double excitations, they also found BP enhancement of γ_{xxxx} but with a much lower power dependency than DeMelo and Silbey predicted. Birge's work shows a difference in power dependency between γ_{neutral} and γ_{BP} of 0.4, which corresponds to a threefold increase in γ_{xxxx} for a 20 carbon atom chain. We recently reported¹² that such enhancement is found when bis-anthracenyl polyenes are oxidized in solution. For example when the bis-anthracenyltetraene, stabilized by decylthio groups in the 10, 10 positions, is oxidized in a saturated CH_2Cl_2 solution, the following is observed.

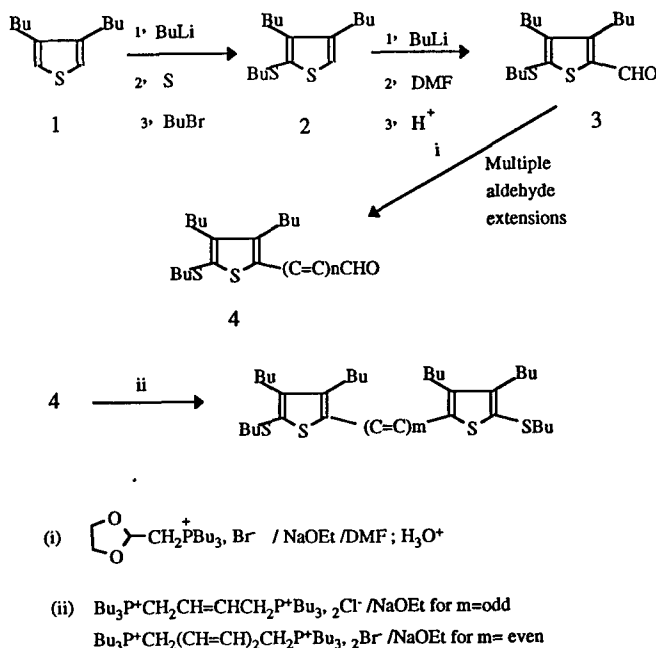
Compound	$\chi_{\text{iii}}^{(3)}(-\omega; \omega, \omega, -\omega)$ (esu)	
$\text{C}_{10}\text{H}_{21}\text{S}-\text{An}-(\text{C}=\text{C})_4-\text{An}-\text{SC}_{10}\text{H}_{21}$	neutral	doped
	7×10^{-14}	67×10^{-13}

Due to the extremely dilute solution used in the degenerate four-wave mixing experiment (0.21 weight %) dictated by the relative insolubility of the polyene, this result may not appear to be very exciting. However, this is one of the largest third order nonlinearities yet measured for a small molecule and scales to a projected $\chi^{(3)}$ of ca. 10^{-8} esu if the anthracenyl moiety could be incorporated in a typical copolymer.

BIS-THIENYL POLYENES INCORPORATING SOLUBILIZING GROUPS

The recent synthesis of bis-thienyl polyenes incorporating butyl substituents on the 3 and 4 positions of the thienyl end caps by our group has recently been described.¹³ Although increased solubility was achieved up to the octaene oligomer length, the nonaene, and decaene were not soluble enough to obtain third order susceptibility measurements in solution *via* degenerate four wave mixing (DFWM) (ca. 10^{-3} M

solubility required). We have previously shown that alkylthio substituents increased the solubility in the anthracenyl polyenes, as well as thienyl polyenes, and also provide increased mesomeric stabilization of the BP charge states. Therefore we have synthesized a new series of bisthienyl polyenes as outlined in Scheme 2.



SCHEME 2 Synthesis of Bis-Thienyl Polyenes.

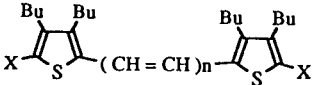
The synthesis details for these materials will be reported elsewhere,¹⁴ however, the absorption spectra of the neutral and oxidized species are shown in Table 1.

PRELIMINARY CHARACTERIZATION OF THE THIRD ORDER PROPERTIES OF BIS-THIENYL POLYENES

Preliminary $\chi^{(3)}$ evaluation of the neutral and oxidatively doped polyenes are being studied at 532 and 1064 nm by degenerate four wave mixing in conventional back-beam geometry. The $\chi^{(3)}$ values for selected polyenes are shown in Table 2. Absorption characteristics for $X = \text{H}$ and $X = \text{BuS}$ heptaenes are shown in Figures 1 and 2.

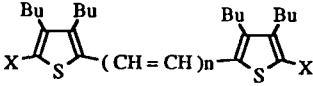
At 532 nm the $n = 5$, $X = \text{H}$ polyene has little or no absorption. For this material, an enhancement of ca. $3X\chi^{(3)}$ neutral is observed, which agrees remarkably well with the theoretical prediction of Birge and coworkers.¹¹ For $n = 7$ and 8 , $X = \text{H}$, the doped sample absorption lies far from the DFWM irradiation frequency, whereas the neutral species display significant resonance enhancement. However at 1064 nm, $n = 5, 7$ and 8 all show the same degree of BP enhancement. Thus, it is clear that for these samples, additional measurement at red-shifted frequencies are required for a comparison of

TABLE 1
Absorption Spectra of Bis-Thienyl Polyenes and Polyene Bipolarons.

			
x	n	λ_{\max} neutral (nm) ^a	λ_{\max} bipolaron (nm) ^a
H	3	422, 399, 380	655, 593
H	4	443, 418, 396	661, 600
H	5	462, 435, 412	715, 679
H	6	480, 450, 426	809, 719
H	7	496, 464, 439	849, 790
H	8	510, 477, 450	914, 855
H	9	521, 489, 461	971, 892
H	10	534, 499, 471	1022, 950
BuS	3	424	643
BuS	4	439	657
BuS	5	451	705
BuS	6	466	754
BuS	7	476	801
BuS	8	488	849

^a 10^{-5} M solutions in CH_2Cl_2 ; underlined peak equals peak of maximum absorption.

TABLE 2
Preliminary DFWM $\chi^{(3)}$ studies of Bis-Thienyl Polyenes.

				
x	n	λ (nm)	$\chi^{(3)}$ neutral (10^{-13} esu) ^a	$\chi^{(3)}$ doped (10^{-13} esu) ^a
H	5	532	2.7	7.8
H	7	532	43.0	11
H	8	532	258	14
H	5	1064	0.54	1.4
H	7	1064	0.85	3.2
H	8	1064	0.66	2.7
BuS	3	532	1.3	^b
BuS	4	532	9.5	^b
BuS	5	532	48.0	^b
BuS	6	532	170	^b
BuS	7	532	300	^b
BuS	8	532	1000	^b

^a all solutions corrected to 10^{-3} M.

^b measurements currently underway.

neutral and doped species. For the BuS series, the neutral $\chi^{(3)}$ series shows remarkable enhancement with increasing length at 532 nm. This resonance enhancement spans 3 orders of magnitude. At the current time, we are examining the real and imaginary contributions to this remarkable enhancement to determine if these materials might

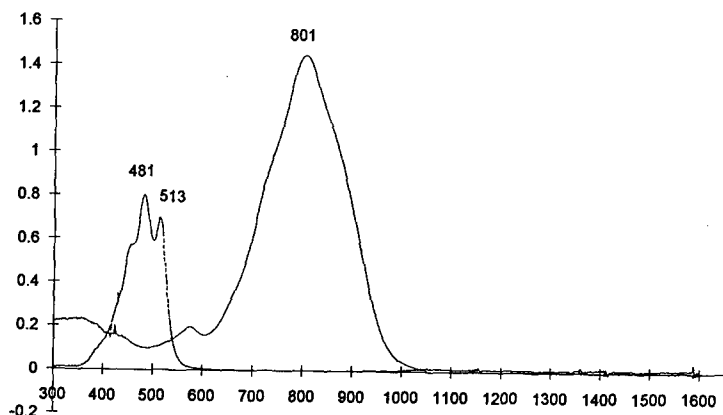


FIGURE 1 Absorption spectra of Bis-Thienylheptaene Bipolaron (X = H).

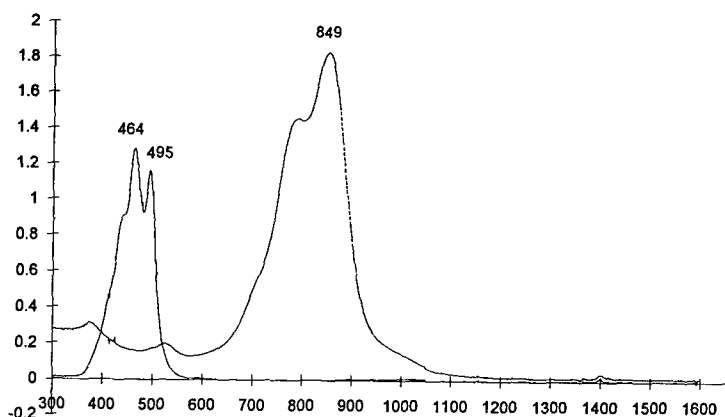


FIGURE 2 Absorption spectra of Bis-Thienylheptaene Bipolaron (X = BuS).

function as optical limiters in thin film composites. At this concentration level, for example, the calculated γ values for $n = 7$, $X = \text{BuS}$ and $n = 8$, $X = \text{BuS}$, are 1.2 and 4.1×10^{-29} esu. These values, although resonance enhanced are quite large, and are among the largest such values reported for such small oligomeric structures.

CONCLUSIONS

It would appear from these preliminary results that small oligomeric polyene molecules have extremely interesting third-order properties either in the neutral or doped state. Bipolaronic enhancement seems to be a quite general phenomenon, and is of the same order of magnitude as predicted by theory. At the current time, it is not clear whether doping of the thienyl polyene series will yield as dramatic results as our previously

reported anthracenyl polyene series. However, it now seems possible that the synthesis of even longer conjugation lengths is possible, so that the length dependence of γ for either neutral or oxidized species and the question of saturation may be experimentally accessible in the near future.

ACKNOWLEDGEMENTS

This research was supported in part by the Air Force Office of Scientific Research Grant #AFOSR-90-0060, and partial support is also acknowledged to the Donors of the Petroleum Research Fund, administered by the American Chemical Society. DFWM measurements were carried out by Mr. Nansheng Tang.

REFERENCES

1. C. W. Spangler, L. S. Sapochak and B. D. Gates, *Organic Materials for Nonlinear Optics*, R. Hann and D. Bloor, eds. (Royal Society of Chemistry, London, 1989) pp. 57–62.
2. C. W. Spangler and R. A. Rathunde, *J. Chem. Soc. Chem. Commun.*, **26** (1989).
3. C. W. Spangler, P.-K. Liu, A. A. Dembek and K. O. Havelka, *J. Chem. Soc., Perkin 1*, 799 (1991).
4. C. W. Spangler, P.-K. Liu and K. O. Havelka, *J. Chem. Soc., Perkin 2*, 1207 (1992).
5. C. W. Spangler and P.-K. Liu, *J. Chem. Soc., Perkin 2*, 1959 (1992).
6. D. Fichou, G. Horowitz, B. Xu and F. Garnier, *Synthet. Met.*, **39**, 243 (1990).
7. D. Fichou, B. Xu, G. Horowitz and F. Garnier, *Synthet. Met.*, **41–43**, 463 (1991).
8. J. Guay, P. Kasal, A. Diaz, R. Wu, J. Tour and L. H. Dao, *Chem. Mat.*, **4**, 254 (1992).
9. C. P. DeMelo and R. Silbey, *Chem. Phys. Lett.*, **140**, 537 (1987).
10. C. P. DeMelo and R. Silbey, *J. Chem. Phys.*, **88**, 2567 (1988).
11. J. R. Tallent, R. R. Birge, C. W. Spangler and K. O. Havelka, AIP Conf. Proc. 262, Molecular Electronics-Science and Technology (New York, 1992) pp. 191–203.
12. E. G. Nickel, C. W. Spangler, N. Tang, R. Hellwarth and L. Dalton, *Nonlinear Optics*, **6**, 000 (1993).
13. C. W. Spangler, M. Q. He, J. Laquindanum, L. Dalton, N. Tang and R. Hellwarth, *Polym. Prepr.*, **34**(2), 384 (1993).
14. C. W. Spangler and M. Q. He, *J. Chem. Soc., Perkin 2* (submitted).

Determination of Real and Imaginary Part of $\chi^{(3)}$ Values in Thiophene Oligomers by z-Scan Method

J. HEIN, H. BERGNER, M. LENZNER and S. RENTSCH

*Institute of Optics and Quantum Electronics,
Friedrich-Schiller-University, Jena, Max-Wien-Platz 1, D-07743 Jena, FRG*

Received 12 January 1994; accepted 28 February 1994

Using the single beam z-scan technique with single pulses at 532 nm from a frequency doubled and passive mode-locked Nd:YAG laser the values of real and imaginary part of third order optical nonlinear susceptibility $\chi^{(3)}$ in solutions of thiophene oligomers have been determined for different numbers of repeat units ($n = 2 \dots 6$). The values of the real part of $\chi^{(3)}$ were found to be negative, the contribution of each repeat unit to this value increases with increasing chain length. In solutions of dioxane (10^{-3} mol/l) we measured n_2 -values in the order of 10^{-13} esu, whereas two photon absorption coefficients of about 0.1 cm/GW were found.

Numerous studies deal with experimental determination of $\chi^{(3)}$ with various methods of nonlinear optics, e.g., THG, DFWM, ellipsometry.^{1,2} In the case of conjugated polymers the relation between the number of repeat units and the nonlinear refraction index n_2 was subject to extended experimental and theoretical investigations.^{2–4} One found that the π -electron system is responsible for the nonlinear refraction index and that, with increasing chain length, not only the absolute value of $\chi^{(3)}$ is increasing but even the net contribution of each additional repeat unit is growing.

Various authors reported measurements of $\chi^{(3)}$ -effects in thiophene oligomers and polymers far from the resonant region with different methods. For instance a wavelength dependent $\chi^{(3)}(-3\omega, \omega, \omega, \omega)$ was measured in the range of $0.8 \dots 1.9 \mu\text{m}^5$ by direct generation of the third harmonic. Time-resolved measurements were performed by Wong and Vardeny⁶ in polythiophenes at 620 nm, theoretical work and experimental results from DFWM in thiophene oligomers have been presented.³

Our measurements were done on thiophene oligomers $n\text{T}$ with $n = 2 \dots 6$ repeat units which are soluble in organic solvents. Preceding investigations at these oligomers revealed a clear recognizable size dependence of linear optical properties such as the absorption coefficient α .⁷ In this paper we report on size dependence of the nonlinear properties of thiophene oligomers measured with the help of z-scan technique.

The z-scan method, first published by Sheik-bahae *et al.*,⁸ is often used for determination of $\chi^{(3)}$ because of its simplicity, high sensitivity, and the possibility of measurements in a large wavelength range.^{6,9–11} The optical refractive nonlinearity as well as the two photon absorption coefficient can be obtained, too.

In our experimental setup (Fig. 1) nonlinear absorption and nonlinear refraction are measured simultaneously. The smaller part of the transmitted beam reflected at a beam splitter (BS in Fig. 1) is used to measure the nonlinear absorption (removed aperture) with a separate detector (D3). We used single pulses of a frequency doubled

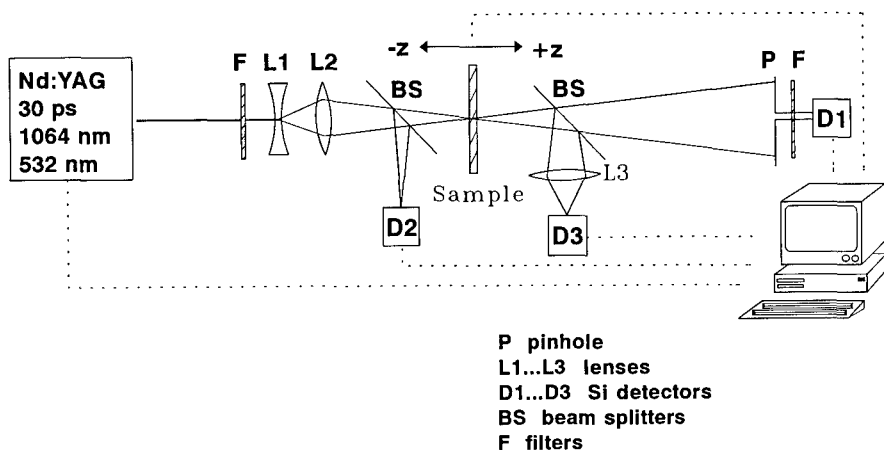


FIGURE 1 z-scan experimental setup.

mode-locked Nd:YAG laser with a pulse duration of 30 ps. With a low repetition rate of 1 Hz we made sure to exclude thermal effects, by using solutions of the thiophene oligomers rather than thin solid films we prevented effects from damage of the sample and photothermal effects.

Following the theory of z-scan published by Sheik-bahae *et al.*,⁸ we have to obey the following conditions for our experimental setup in order to use the given simple analysis that yields the nonlinear refractive index:

$$l < \frac{z_0}{\Delta\Phi_0}, \text{ where the diffraction length } z_0 = \frac{k\omega_0^2}{2} \quad (1)$$

$$d \ll z_0.$$

ω_0 is the waist radius of the Gaussian beam, l is the thickness of the sample and d is the distance between the sample and the detector. $\Delta\Phi_0$ denotes the on-axis phase shift caused by the nonlinear refractive index of the sample and $k = 2\pi/\lambda$ is the wavenumber in free space. The equations (1) are the conditions for having a thin sample and for using the far field of the laser beam, respectively. $\Delta\Phi_0$ is given by:

$$\Delta\Phi_0 = kn_2 I_0 l_{\text{eff}} \quad \text{with} \quad l_{\text{eff}} = \frac{1 - e^{-\alpha l}}{\alpha} \quad (2)$$

where α is the linear absorption coefficient of the sample and I_0 is the on-axis irradiance in the focal plane. The nonlinear refractive index n_2 causes refractive index changes $\Delta n = n_2 I$.

The rather extensive analysis of z-scan transmittance yields some simple equations for the conditions given in equations (1), a cubic nonlinearity, and a small nonlinear phase change $|\Delta\Phi_0| \ll 1$. The geometry-independent normalized on-axis transmittance is then:

$$T(z, \Delta\Phi_0) = 1 - \frac{4\Delta\Phi_0(z/z_0)}{((z/z_0)^2 + 1)((z/z_0)^2 + 9)} \quad (3)$$

Looking for the extrema in (3) gives two easy obtainable quantities, namely, the maximum transmittance change ΔT over the scanning path z and the spatial distance Δz between peak and valley of the transmitted intensity. They can be used to determine the nonlinear refractive index n_2 :⁸

$$\Delta T = 0.406(1 - S)^{0.25} |\Delta \Phi_0| \quad (4)$$

$$\Delta z = 1.7z_0$$

The so called linear aperture transmittance S is given by $S = 1 - \exp(-2r_a^2/\omega_a^2)$, where r_a is the aperture radius and ω_a the beam radius in the aperture plane. The correction factor $(1 - S)^{0.25}$ can be neglected if the aperture is chosen to be small, which is usually the case in order to achieve a sufficient sensitivity of this method. In our experimental setup we placed the aperture in a distance of 1.5 m from the focal plane (giving $\omega_a = 6.5$ mm) and with an aperture of 2 mm diameter we achieved $S = 0.05$. The on-axis intensity I_0 can be calculated from the total pulse energy and the diffraction length z_0 . In conclusion, we can perform absolute measurements of n_2 within the error limits of pulse energy, pulse duration, and diffraction length z_0 .

The part of the experiment determining the nonlinear absorption coefficient is also described by Sheik-bahae *et al.*⁸ In case of a temporally Gaussian-shaped pulse the total transmittance $T(z)$ of the sample is given by:

$$T(z) = \sum_{m=0}^{\infty} \frac{(-q(z))^m}{(m+1)^{3/2}} \quad \text{with} \quad q(z) = \frac{\beta I_0 l_{\text{eff}}}{\left(1 + \frac{z^2}{z_0^2}\right)} \quad (5)$$

where β is the two-photon-absorption coefficient. These nonlinear absorption curves are necessary to extract the nonlinear refractive index from the experimental z-scan results in these cases, where multiphoton absorption is present.

In the experiments reported here we used thiophene oligomers nT with different numbers of monomers ($n = 2 \dots 6$). The solubility of nT up to $n = 5$ was satisfying, however, the solubility of hexathiophene turned out to be too low to get appropriate concentrations for distinguishing the nonlinearities of oligomer and solvent. Therefore, we used 2,5-didecylhexathiophene which exhibits a much higher solubility than hexathiophene. Generally it is assumed that additional decyl groups do not have a significant influence on the nonlinearity of the thiophene oligomer. This seems to be justified because the electrons of these groups do not contribute to the π -electron system of the thiophene backbone.

The oligomers were solved in dioxane with a concentration of 10^{-3} mol/l. The measurements were carried out in a cuvette of 1 mm thickness which fulfills the condition of a thin sample in the first of equations (1).

Figure 2 shows the transmittance of 6T and 4T as a function of the sample position z which was calculated as the ratio between the measured intensities at detectors D3 and D1 (Fig. 1). The beam radius in the focal plane was measured to be 26 μm . The single pulse energy of 12 μJ results in an on-axis irradiance in the focal plane of 19 GW/cm² within an error of 20% caused by the error of z_0 and the deviation of the pulse duration.

According to the absorption spectra⁸ a two photon process is very likely. From time resolved excite and probe measurements¹³ we can exclude the occurrence of an excited

state absorption (ESA), thus only two photon absorption (TPA) can act as a nonlinear absorption process in this case of wavelength and pulse width. A fit of the experimental results using equation (5) justifies the assumption of a third order absorptive nonlinearity. The results as well as the fit curve (solid line) are shown in Figure 2 and the resulting two photon absorption (TPA) coefficients are listed in Table 1.

We accomplished additional measurements in sample 6T by varying the excitation intensity. The results are listed in Table 1, too.

A linear absorption that had to be considered with $\alpha = 1.4 \text{ cm}^{-1}$ was present in the case of didecylhexathiophene (6T) only. Hence from equation (2) we get an effective sample thickness of $l_{\text{eff}} = 0.93 \text{ mm}$.

The two photon absorption coefficients in Table 1 (β_{rel} is the TPA coefficient related to the concentration of the oligomer in the solvent) are increasing with increasing chain

TABLE I
Two Photon Absorption Coefficients of Dioxane and Thiophene
Oligomers with 4 and 6 Monomers (4T,6T) at 532 nm.

Sample	Intensity	$\beta/10^{-1} \text{ cm/GW}$	$\beta_{\text{rel}}/\text{cm-l/GW-mol}$
dioxane	19 GW/cm ²	0.26	0.22
4T	19 GW/cm ²	1.1	275
6T	11 GW/cm ²	3.3	550
6T	19 GW/cm ²	3.4	570
6T	35 GW/cm ²	2.3	380

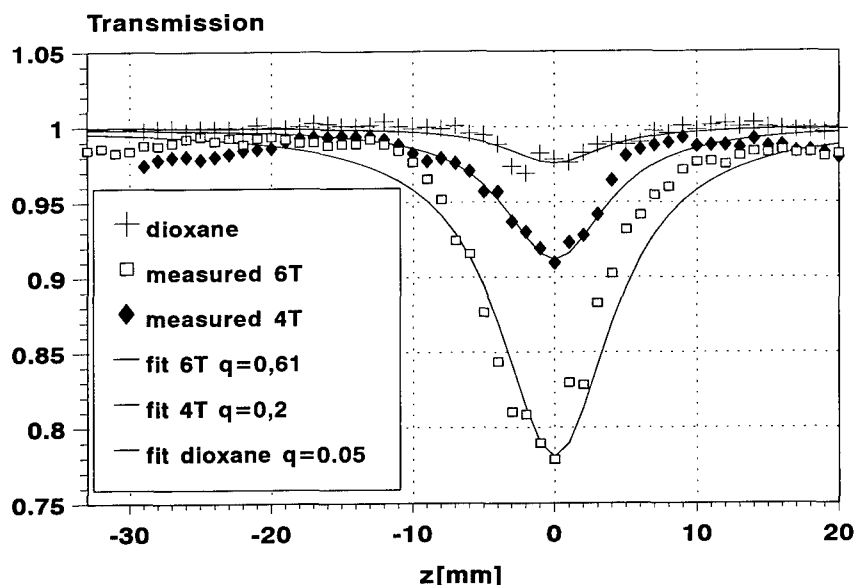


FIGURE 2 Position dependence of sample transmittance (without aperture) measured at 4T and 6T in dioxane (10^{-3} mol/l) and pure dioxane.

length. This effect is not solely caused by the higher number of π -electrons because the TPA coefficient is increasing faster than the number of these electrons.

The lower values for 6T, measured at higher excitation intensities, are caused by a saturation of TPA. At these intensities the absorbed photon number per volume is already in the order of the concentration of molecules in the solution.

Figure. 3 and Figure. 4 show a set of z-scan measurements with the samples 4T, 5T, and 6T, respectively. First we did a z-scan of the plain solvent dioxane and with the help of the equations (2) and (4) we calculated a positive nonlinear refractive index of $n_2 = 4.9 \times 10^{-6} \text{ cm}^2/\text{GW}$. In the z-scan measurements of the dissolved oligomers one can notice a reduced peak and valley amplitude and therefore a reduced nonlinear refraction index. This can be explained only by a negative n_2 of the thiophene oligomers for the following reasons.

According to Zhao *et al.*,³ the molecular second hyperpolarizability γ is given by

$$\gamma [\text{esu}] = \frac{\chi^{(3)}}{L^4 N} \quad (6)$$

with the local field factor L in Lorentz-Lorenz approximation and N the density of molecules. By assuming equal refractive indices for solvent and solutions the nonlinear quantities $\chi^{(3)}$ are simply additive in a solution of noninteracting particles.

The values of n_2 were calculated by fitting the experimental data with equation (3) with additional consideration of the TPA coefficient obtained from the experimental data.

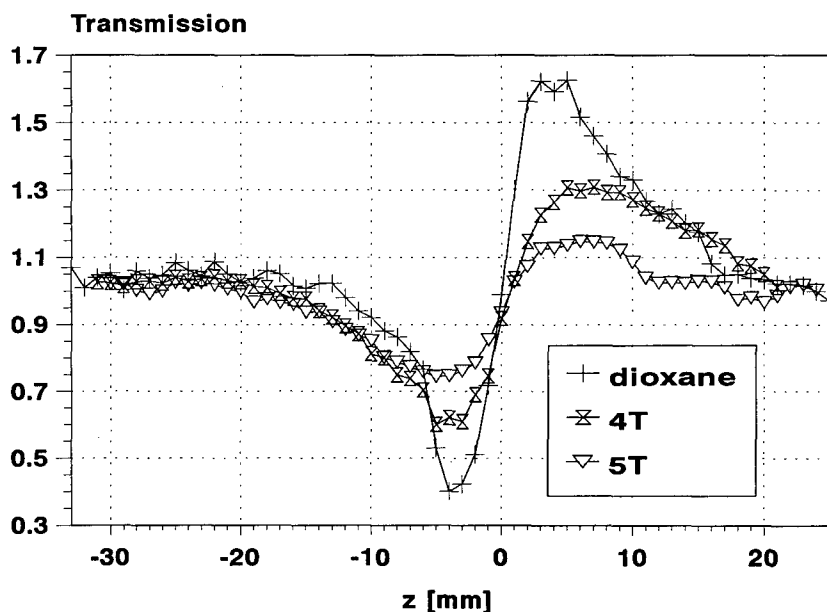


FIGURE 3 Results of z-scan measurements at 4T, 5T and pure dioxane with the same concentration and laser pulse intensity.

TABLE 2
Coefficients of Nonlinear Refraction of Dioxane and Thiophene Oligomers with Different Chain Lengths Measured at 532 nm.

Sample	$n_2/10^{-6}\text{cm}^2/\text{GW}$	$n_2/10^{-13}\text{esu}$	$\gamma/10^{-33}\text{esu}$ per molecule	$\gamma/10^{-33}\text{esu}$ per monomer
dioxane	4.9	16	0.08	0.08
2T	> -0.5	> -1.6	> -8	> -4
3T	-0.5	-1.6	-9.6	-3.2
4T	-2.3	-7.7	-45	-11.3
5T	-3.2	-10.6	-62	-12.3
6T	-3.5	-12	-70	-11.7

In Table 2 we listed the experimental results from Figures 3 and 4 as well as the results obtained for 2T and 3T oligomers. The n_2 -values for 2T are too small compared with the nonlinearity of the solvent in order to decide whether they are positive or negative. The second and third column in Table 2 give the values of n_2 in SI-units and in esu, respectively and the last columns give the second hyperpolarizability γ per monomer and per molecule calculated by using (6).

In the case of didecylhexathiophene (6T) we performed some additional measurements in order to prove the claim that the solution consists of noninteracting molecules. In a solution of half the normal concentration (0.5×10^{-3} mol/l) we found a clear linear dependence of the nonlinearity on the concentration (see Fig. 4).

The first point in discussing these results has to be the negative value of n_2 in the thiophene oligomers at a wavelength of 532 nm. As already stated for other materials¹¹

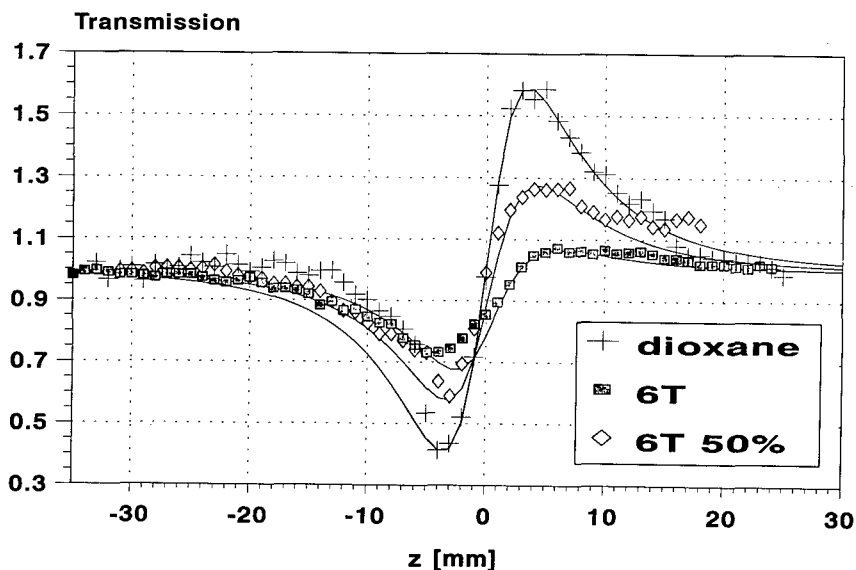


FIGURE 4 Results of z-scan measurements at 6T and a solution of half the concentration.

this is caused by the vicinity of the TPA absorption band where TPA resonance of bound electrons dominates the nonlinear refraction, whereas at larger wavelengths the electronic resonance gives positive values of n_2 . The change of sign of the bound-electronic nonlinearity was also found in some inorganic semiconductors,⁹ where it was finally explained using a nonlinear Kramers-Kronig relation between the real and imaginary parts of $\chi^{(3)}$. Although the scaling of our experimental values to a certain power of the band gap energy E_G did not give the desired effect, this explanation serves well with regard to the negative value of the n_2 of thiophene oligomers at 532 nm.

Regarding the chain length dependence of the nonlinear refractive index it is obvious and also in accordance with former publications of other authors^{2,3} that the contribution of each monomer to the nonlinear refraction is not constant but increasing with increasing chain length. This can be explained in a similar way as for the TPA coefficient because nonlinear refraction as well as nonlinear absorption is caused by bound electrons (the extended π -electron system in the case of our oligomers). A power law dependence as suggested in several publications^{2,12} cannot—in such a simple way—apply to results of nonlinear refraction taken in the vicinity of the two-photon-absorption edge, because of the possibility of resonance detuning changing if the chain length is varied. Further wavelength dependent measurements with a tunable laser source which solve this problem are in preparation.

From Table 2 it is evident that the highest measured hyperpolarizability γ per monomer was obtained for the 5T oligomer. Because of the different chemical structure of the derivative 6T we cannot decide whether this value is solely caused by the chain length.

ACKNOWLEDGEMENT

The authors gratefully acknowledge the providing of the samples by Dr. H. Naarmann.

REFERENCES

1. *Organic Molecules for Nonlinear Optics and Photonics*, Ed. by J. Messier, F. Kajzar and P. Prasad, NATO ASI Series E: *Applied Science*, **194**, (1991).
2. H. Thienpont, G. L. J. A. Rikken, E. W. Meijer, W. T. ten Hoeve, H. Wynberg, *Phys. Rev. Lett.*, **65**, (1990), p. 2141.
3. M. T. Zhao, B. P. Singh, P. N. Prasad, *J. Chem. Phys.*, **89**, (1988), p. 5535.
4. D. N. Beratan, J. N. Onuchic, J. W. Perry, *J. Phys. Chem.*, **91**, (1987), p. 2696.
5. D. Fichou, F. Garnier, F. Charra, F. Kajzar, J. Messier from *Organic Materials for Nonlinear Optics*, Ed. by R. A. Hann, D. Bloor, London (1989), p. 177.
6. K. S. Wong, Z. V. Vardeny, *Synthetic Metals*, **49–50**, (1992), p. 13.
7. H. Chosrovian, D. Grebner, S. Rentsch, H. Naarmann, *Synthetic Metals*, **52** (1992), p. 213.
8. M. Sheik-bahae, A. A. Said, E. W. van Stryland, *IEEE Journal of Quantum Electronics*, **26**, (1990), p. 760.
9. M. Sheik-bahae, D. J. Hagan, E. W. van Stryland, *Phys. Rev. Lett.*, **65**, (1990), p. 96.
10. F. Henari, J. Callaghan, H. Stiel, W. Blau, D. J. Cardin, *Chem. Phys. Lett.*, **199**, (1992), p. 144.
11. Lina Yang, R. Dorsinville, R. R. Alfano, W. K. Zou, N. L. Yang, *Optics Lett.*, **16**, (1991), p. 758.
12. J. L. Bredas, C. Adant, D. Beljonne, F. Meyers, Z. Shuai, *Synthetic Metals*, **55–57**, (1993), p. 3933.
13. D. V. Lap, D. Grebner, S. Rentsch, H. Naarmann, *Chem. Phys. Lett.*, **211**, (1993), p. 135.

Resonant Third-Order Optical Response in the Metallo-Phthalocyanines at 1064 nm

F. J. BARTOLI, J. R. LINDLE, J. S. SHIRK, S. R. FLOM, A. W. SNOW
and M. E. BOYLE

Naval Research Laboratory, Washington, D.C. 20375, U.S.A

Received 12 January 1994; accepted 21 March 1994

The mechanism for the third-order nonlinear response at 1064 nm is investigated systematically for a series of metal-substituted phthalocyanines. Previous measurements of time-resolved degenerate four-wave mixing at 1064 nm are reviewed and analyzed. The nonlinear response, which occurs on a picosecond time scale, is shown to be strongly correlated with the magnitude of the linear absorption coefficient. New measurements of nonlinear transmission are reported for several of these compounds. The data are compared to results of new calculations based on two-level and multi-level models for $\chi^{(3)}$ and the nonlinear absorption coefficient. The nonlinear response in the near infrared is for the most part inconsistent with the predictions of a two-level model, but can be understood in terms of optical pumping of a multi-level system.

The phthalocyanines are an attractive class of nonlinear optical (NLO) materials, possessing a highly delocalized π -electronic structure and low-lying electronic states. Recent studies¹ have shown that central metal and peripheral substitution introduces charge transfer states offering new pathways for an enhanced third-order nonlinear optical response. The metallo-bis(phthalocyanines), in which two phthalocyanine rings are coordinated to a single trivalent (+3) metal ion, possess an intervalence transition associated with an unpaired electron residing on the phthalocyanine rings. More extended stacked structures, consisting of many phthalocyanine rings bridged axially by metal agents, have also been synthesized and studied. This rich variety of substituted phthalocyanines has already led to enhancement by nearly three orders of magnitude in the third order optical susceptibility, $\chi^{(3)}$, measured by degenerate four-wave mixing (DFWM) at 1064 nm.^{2,3} Relevant optical and photophysical properties for this molecular system have been recently reviewed.³

Although, there is a large body of experimental evidence on the substituted phthalocyanines demonstrating large increases in $\chi^{(3)}$ at infrared wavelengths, no comprehensive understanding of the mechanisms involved has emerged to date, and no quantitative agreement with predictions of theoretical models has been established. Previously reported DFWM measurements,^{4,5} performed at visible wavelengths near the peak of the strongly absorbing Q-band in several phthalocyanines, have been attributed to optical pumping of this absorption band. Similarly, saturation of the Q-band absorption was reported⁶ for silicon naphthalocyanine near the peak absorption at 810 nm, and found to agree with the results of a two-level model. However, no such association has been made at wavelengths in the near-infrared region where optical transitions are generally only weakly allowed and the absorption coefficient small.

In the present work, the mechanism for the third-order nonlinear response at 1064 nm is investigated systematically for a series of metallated macrocycles. Previous picosecond DFWM measurements¹⁻³ are summarized for solutions of H₂ and metal-substituted tetrakis(cumulphenoxy)phthalocyanines (MPc(CP)₄) (M = Co, Ni, Cu, Zn, Pd, and Pt), and a series of metallo-bis-phthalocyanines (MPc₂) (M = Sc, Y, Nd, Eu, Gd, Yb, and Lu) and their anions (MPc₂⁻). New measurements of nonlinear transmission (NLT), employing techniques described elsewhere,⁷ are reported for several of these compounds. The DFWM and NLT results are compared to the theoretical predictions using two-level and multi-level models for $\chi^{(3)}$ and the nonlinear absorption coefficient.

THEORETICAL CALCULATIONS

The third-order optical susceptibility for an excited-state population grating is calculated below using two-level and multi-level models. In the two-level approximation, $\chi_{xxxx}^{(3)}$ may be written,^{2,8-10}

$$\chi_{xxxx}^{(3)}(\omega) \approx -\frac{10^{-7} n_0^2 c^2 \alpha_0(\omega)}{96 \pi^2 \omega I_s(\omega)}(\delta + i). \quad (1)$$

Here $\chi_{xxxx}^{(3)}$ is given in esu, c is the speed of light expressed in cm/s, n_0 the refractive index, $\alpha_0(\omega)$ the linear absorption coefficient in cm⁻¹, and $I_s(\omega)$ the saturation intensity in W/cm², all at the measurement frequency ω . $\delta = (\omega - \omega_0)/\Delta\omega$ is the offset of ω from the band center, ω_0 , normalized to $\Delta\omega$, the half-width at half maximum of the band. Equation 1 gives both the real (refractive) and the imaginary (absorptive) parts of $\chi_{xxxx}^{(3)}$, both of which contribute to the degenerate four wave-mixing signal. Neglecting effects of stimulated emission, one can express the saturation intensity for a two-level system as $I_s(\omega) = \hbar\omega/\sigma_0(\omega)\tau$, where $\sigma_0(\omega)$ is the absorption cross-section of the ground electronic state and τ is the excited state lifetime. Eq. 1 can be rewritten as

$$\chi_{xxxx}^{(3)}(\omega) \approx -\frac{10^{-7} n_0^2 c^2 \tau \alpha_0(\omega)}{96 \pi^2 \hbar \omega^2} \sigma_0(\omega)(\delta + i). \quad (2)$$

If $\sigma_0(\omega)$ is replaced in Eq. 2 by $\alpha_0(\omega)/N$, (N = number density), $\chi_{xxxx}^{(3)}$ is seen to vary as the square of the low intensity absorption coefficient $\alpha_0(\omega)$ for a two-level saturable absorber.

For a multi-level system, Eq. 2 can be generalized

$$\chi_{xxxx}^{(3)}(\omega) \approx -\frac{10^{-7} n_0^2 c^2 \tau \alpha_0(\omega)}{96 \pi^2 \hbar \omega^2} [\sigma_1(\omega)(\delta_1 + i) - \sigma_0(\omega)(\delta + i)] \quad (3)$$

where $\delta_1 = (\omega - \omega_1)/\Delta\omega$ is the normalized offset of the measurement frequency from the excited absorption band center.

In nonlinear transmission experiments, the absorption coefficient $\alpha(\omega)$ to first order varies linearly⁷ with optical intensity I , i.e.,

$$\alpha(\omega) \approx \alpha_0(\omega) + \beta(\omega)I. \quad (4)$$

The imaginary part of $\chi_{xxxx}^{(3)}$ can be determined directly from the measured nonlinear coefficient $\beta(\omega)$ using the expression¹¹

$$\text{Im}(\chi_{xxxx}^{(3)}) = -\frac{10^{-7} n^2 c^2}{96 \pi^2 \omega} \beta(\omega) \quad (5)$$

where $\chi_{xxxx}^{(3)}$ is again given in esu and $\beta(\omega)$ is in cm/W. In the two-level approximation, $\beta(\omega)$ is given by

$$\beta(\omega) = -\frac{\alpha_0(\omega) \tau}{\hbar \omega} \sigma_0(\omega). \quad (6)$$

For a multi-level electronic system, the nonlinear coefficient can be written as

$$\beta(\omega) = \frac{\alpha_0(\omega) \tau}{\hbar \omega} (\sigma_1(\omega) - \sigma_0(\omega)) \quad (7)$$

where $\sigma_1(\omega)$ is the excited-state absorption cross-section at ω . For the case of strong excited-state absorption, where $\sigma_1(\omega) \gg \sigma_0(\omega)$, Eq. 7 becomes

$$\beta(\omega) \approx \frac{\alpha_0(\omega) \tau}{\hbar \omega} \sigma_1(\omega). \quad (8)$$

Note that $\beta(\omega)/\alpha_0(\omega)$ is independent of $\alpha_0(\omega)$ for a reverse saturable absorber (Eq. 8), but depends linearly on $\alpha_0(\omega)$ for a two-level saturable absorber (Eq. 6).

RESULTS AND DISCUSSION

Values of $\chi_{xxxx}^{(3)}/\alpha_0$ determined by DFWM¹⁻³ at 1064 nm are plotted in Figure 1 as a function of linear absorption coefficient α_0 over a large range of variation of α_0 . The magnitude of $\chi_{xxxx}^{(3)}$ for these compounds is closely correlated with α_0 , although there are some notable exceptions. The abscissa coordinate α_{0n} is the absorption coefficient extrapolated to neat material.¹² The results suggest that the measured nonlinear response is dominated by a population grating contribution involving resonant excitation of low-lying electronic states. Time resolved DFWM measurements at 1064 nm exhibited a laser pulse-width limited temporal response for all molecules considered here, indicating the excited state lifetime is significantly less than 10 ps.

To investigate further the resonant excitation of these states, nonlinear transmission measurements were performed at 1064 nm for solutions of PtPc(CP)₄, YPc₂, and ScPc₂ in chloroform, and the nonlinear coefficient $\beta(\omega)$ was determined. These results are illustrated in Figure 2 for PtPc(CP)₄. While positive values of $\beta(\omega)$ were obtained for PtPc(CP)₄ and YPc₂, indicating that these compounds are reverse saturable absorbers, ScPc₂ behaved as a saturable absorber, i.e., α decreases with increasing intensity. These results are summarized in Table 1. Since ScPc₂ is a saturable absorber, Eq. 6 was used to obtain a value of $\tau = 1$ ps from the measured β . A 1 ps lifetime appears to be reasonable for the upper-level of the intervalent transition, since very strong vibronic coupling is expected in such states¹³ leading to efficient internal conversion. If this value for τ is assumed, Eq. 2 can be used to calculate $\chi_{xxxx}^{(3)}/\alpha_0(\omega)$ for a two-level

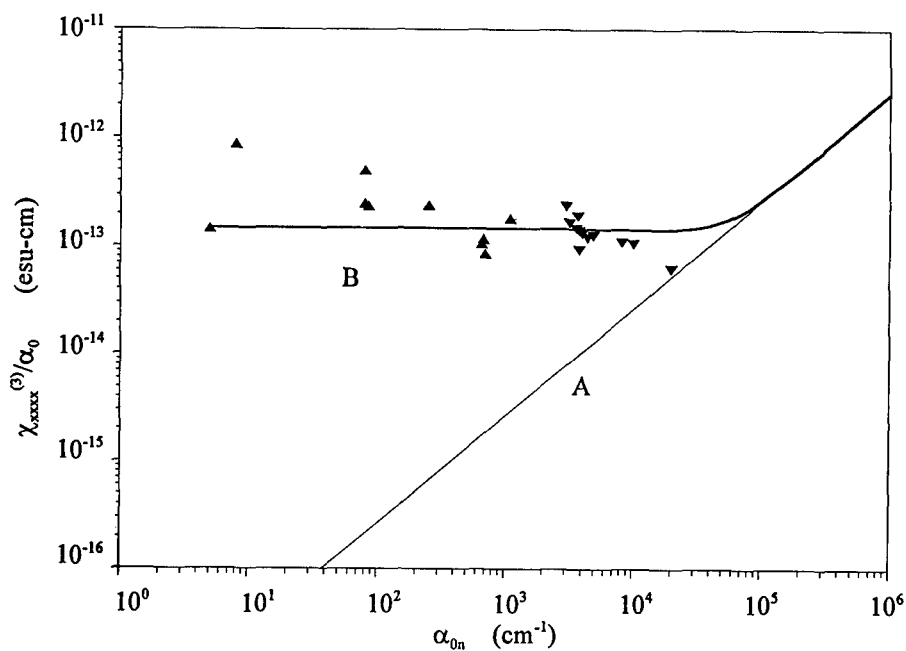


FIGURE 1 $\chi_{xxxx}^{(3)}/\alpha_0$ determined by DFWM at 1064 nm (Ref. 2-3) as a function of α_{0n} for solutions of H_2 , Zn, Cu, Ni, Co, Pd, and Pt tetrakis-(cumulphenoxy)phthalocyanines (triangles), and Sc, Lu, Yb, Y, Gd, Eu and Nd bis-phthalocyanines and their anions (inverted triangles). The calculated $\chi_{xxxx}^{(3)}/\alpha_0$ was determined using Eq. 2 for a two-level saturable absorber (A) and Eq. 3 for a multi-level system (B).

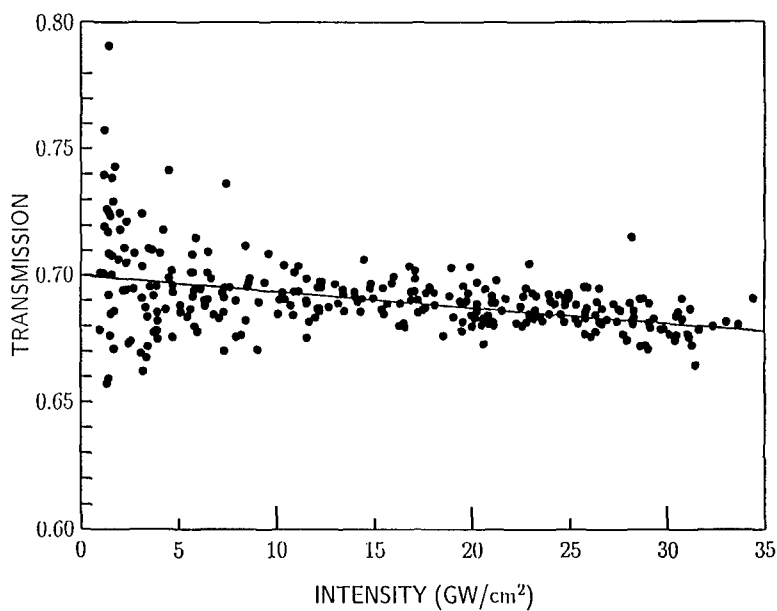


FIGURE 2 Nonlinear transmission measurements for a 16 mM $PtPc(CP)_4/CHCl_3$ solution using 35 ps pulses at 1064 nm.

TABLE I
Nonlinear Transmission Results for PtPc(CP)₄, ScPc₂ and YPc₂ at 1064 nm.

Sample	Conc. (mM)	β (cm/GW)	α (cm ⁻¹)	β/α (cm ² /GW)	$\text{Im}(\chi_{xxxx}^{(3)})/\alpha$ (esu-cm)	$ \chi_{xxxx}^{(3)} /\alpha$ (esu-cm)
PtPc	16	0.16	14.8	0.011	1.2×10^{-15}	2.0×10^{-13}
ScPc ₂	0.2	-0.3	3.4	-0.088	-1.0×10^{-14}	4.4×10^{-14}
YPc ₂	0.27	0.07	0.85	0.082	9.4×10^{-15}	1.1×10^{-13}

saturable absorber as a function of $\alpha_0(\omega)$. This is shown as curve A in Figure 1, where for convenience a value of $\delta = 0$ was assumed. Except for ScPc₂, which has the largest absorption coefficient, there is poor agreement between the two-level model (curve A) and the experimental data at 1064 nm.

The results in Figure 1 suggest that the NLO response for the majority of phthalocyanines must be treated in terms of multiple level model. Curve B in Figure 1 represents $\chi_{xxxx}^{(3)}/\alpha_0(\omega)$ for a multi-level system as a function of $\alpha_0(\omega)$, calculated using Eq. 8. In this calculation, the product $\tau\sigma_1\delta_1$ is on the order of 2×10^{-28} s-cm². These values for $\chi_{xxxx}^{(3)}/\alpha_0(\omega)$ compare quite well with experimental data over several orders of magnitude variation in α . The multi-level model is also found to successfully treat other nonlinear organic systems, such as transition-metal complexes of o-aminobenzenethiol¹⁴ at 1064 nm, and the polythiophenes¹⁵ and a series of alternate aromatic-quinoidal co-polymers^{16,17} at visible wavelengths. The latter are shown in Figure 3, where

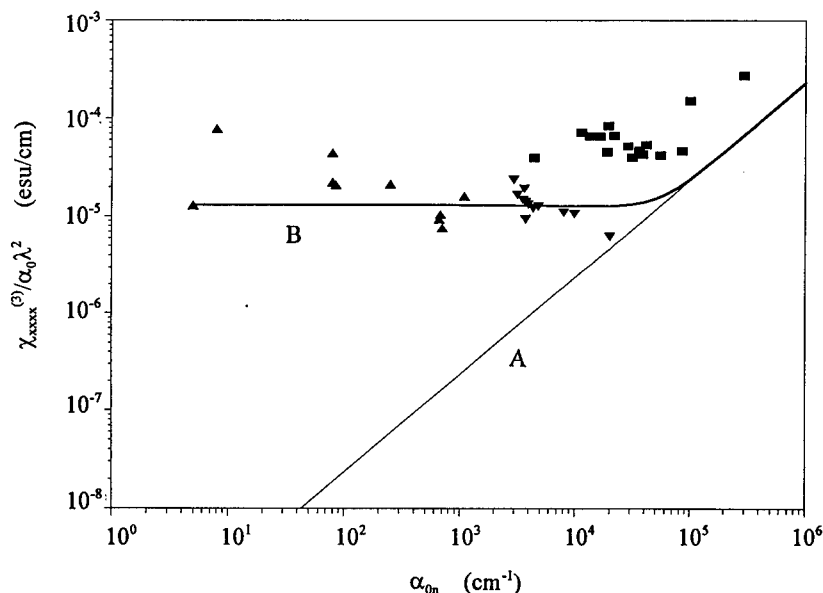


FIGURE 3 $\chi_{xxxx}^{(3)}/(\alpha_0 \lambda^2)$ as a function of α_{0n} for solutions of the tetrakis-(cumulphenoxo)-phthalocyanines (triangles) and bis-phthalocyanines (inverted triangles) at 1064 nm. The squares represent polythiophene and polydithieno(3,2-b,2',3'-d)thiophene films at 532–630 nm (Ref. 15) and solutions of several mixed quinoidal aromatic polythiophene copolymers at 532 nm (Refs. 16 and 17). The calculated $\chi_{xxxx}^{(3)}/(\alpha_0 \lambda^2)$ was determined using Eq. 2 for a two-level saturable absorber (A) and Eq. 3 for a multi-level system (B).

$\chi_{xxxx}^{(3)}/(\alpha_0\lambda^2)$ is plotted as a function of α_0 , again extrapolated to neat material. λ^2 is included in the denominator of the ordinate to account for the differences in excitation wavelength. The data at 1064 nm is qualitatively similar to that obtained in the visible under resonant excitation. We note again that all these materials included in Figure 3 have been observed to have short excited state lifetimes. Better agreement between theory and experiment could be achieved for the polythiophenes and mixed quinone aromatics by accounting for differences in refractive index and using a somewhat larger value of τ .

The last two columns of Table 1 show that the $\text{Im}(\chi_{xxxx}^{(3)})$ determined by nonlinear transmission is appreciably smaller than $|\chi_{xxxx}^{(3)}|$ obtained from DFWM, suggesting that $\text{Re}(\chi_{xxxx}^{(3)}) \gg \text{Im}(\chi_{xxxx}^{(3)})$. This was verified by z-scan measurements on several of these compounds.¹⁸ Hence, it appears that the nonlinear response associated with optical pumping of electronic states in these systems is primarily real.

In summary, this work demonstrates for the first time that the nonlinear optical susceptibility measured in the near infrared by degenerate four-wave mixing may be understood in terms of optical pumping of a multi-level system for a large number of metal-substituted phthalocyanines and bis-phthalocyanines. Usually, the nonlinear response is inconsistent with the predictions of a two-level model and has a large real component associated with optically induced changes in the refractive index. Structural modification of these molecules will permit the design of materials with improved figures-of-merit such as $\chi^{(3)}/\alpha$ and $\text{Re}(\chi^{(3)})/\text{Im}(\chi^{(3)})$ of interest for device applications.

REFERENCES

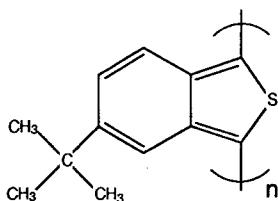
1. J. S. Shirk, J. R. Lindle, F. J. Bartoli, C. A. Hoffman, Z. H. Kafafi and A. W. Snow, *Appl. Phys. Lett.*, **55**, 1287 (1989).
2. J. S. Shirk, J. R. Lindle, F. J. Bartoli and M. E. Boyle, *J. Phys. Chem.*, **96**, 5847 (1992).
3. J. S. Shirk, J. R. Lindle, F. J. Bartoli, Z. H. Kafafi, A. W. Snow and M. E. Boyle, *Int. J. Nonlinear Opt. Phys.*, **1**, 699 (1992).
4. P. N. Prasad, M. K. Casstevens, J. Pflieger and P. Logsdon, *SPIE Proc.*, **878**, 106 (1988).
5. M. K. Casstevens, M. Samoc, J. Pflieger and P. N. Prasad, *J. Chem. Phys.*, **92**, 2019 (1990).
6. J. W. Wu, J. R. Heflin, R. A. Norwood, K. Y. Wong, O. Zamani-Khamiri, A. F. Garito, P. Kalyanaraman and J. Sounik, *J. Opt. Soc. Am. B*, **6**, 707 (1989).
7. E. W. Van Stryland, H. Vanherzeele, M. A. Woodall, M. J. Soileau, A. L. Smirl, S. H. Guha, T. F. Bogess, *Opt. Eng.*, **24**, 613 (1985).
8. H. M. Gibbs, "Optical Bistability: Controlling Light with Light", (Academic Press, Orlando, 1985).
9. T. Y. Chang, *Opt. Eng.*, **20**, 220 (1981).
10. M. A. Kramer, W. R. Tomkin and R. W. Boyd, *Phys. Rev. A*, **34**, 2026 (1986).
11. P. Liu, W. L. Smith, H. Lotem, J. H. Bechtel and N. Bloembergen, *Phys. Rev. B*, **17**, 4620 (1978).
12. The absorption coefficient α_0 is obtained by a lowest-order extrapolation from solution data to neat material, neglecting aggregation and local field effects. This is employed as the abscissa in Figures 1 and 2 to permit comparison among solutions of differing concentrations and thin films.
13. K. Y. Wong and P. N. Schatz, *Prog. Inorg. Chem.*, **28**, 369 (1981).
14. Z. H. Kafafi, J. R. Lindle, C. S. Weisbecker, F. J. Bartoli, J. S. Shirk, T. H. Yoon and O. K. Kim, *Chem. Phys. Lett.*, **179**, 79 (1991).
15. R. Dorsinville, L. Yang, R. R. Alfano, R. Zamboni, R. Danieli, G. Ruani and C. Taliani, *Opt. Lett.*, **14**, 1321 (1989).
16. S. A. Jenekhe, W. C. Chen, S. Lo and S. R. Flom, *Appl. Phys. Lett.*, **57**, 126 (1990).
17. S. A. Jenekhe, S. K. Lo and S. R. Flom, *Appl. Phys. Lett.*, **54**, 2524 (1989).
18. J. R. Lindle, F. J. Bartoli, J. S. Shirk and M. E. Boyle (unpublished results).

The Synthesis of the Narrow-Gap, Nonlinear, Organic Polymer Poly(*tert*butylisothianaphthene)

A. DRURY, A. P. DAVEY, S. BURBRIDGE, H. PAGE and W. BLAU
*Department of Pure and Applied Physics, University of Dublin,
Trinity College, Dublin 2, Ireland*

Received 4 February 1994; accepted 6 March 1994

Polyisothianaphthene (PITN) has been shown to be a low band-gap polymer ($E_g \sim 1$ eV) with good semiconducting and photoelectrical properties. However it is difficult to process and characterise due to its insolubility in common organic solvents. The synthesis of Poly(*tert*butylisothianaphthene) (PTBITN), a new soluble derivative of PITN, is described in this paper. Preliminary characterisation shows that this polymer (structure below) has optical properties similar to those of PITN.

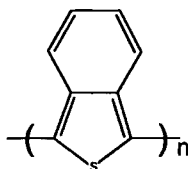


PTBITN

INTRODUCTION

This work describes the synthesis and characterisation of a new polymer (PTBITN) which has one of the highest known third order nonlinearity constants [$\chi^{(3)}$] recorded so far.

The parent polymer PITN, has been well studied. It has been found to have a band gap of ~ 1 eV^{1,2} and films (prepared by electrochemical deposition) became highly conducting and transparent after p-doping.² However, the disadvantage of PITN is its insolubility in common organic solvents which greatly limits studies of its properties.

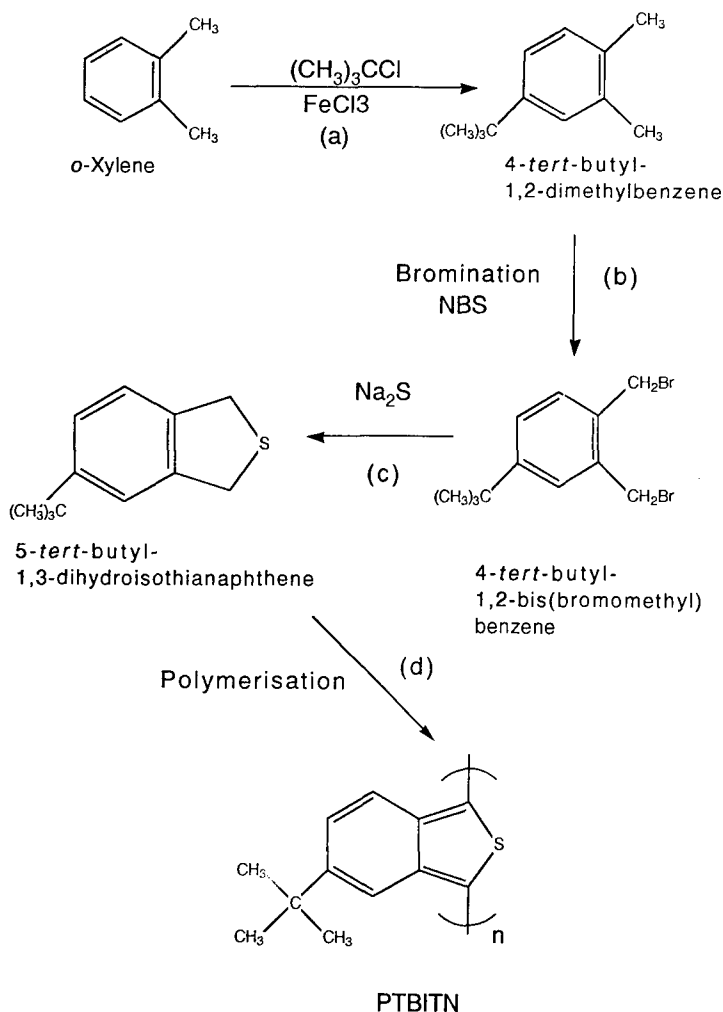


Polyisothianaphthene or Poly(benzo[c]thiophene)

In 1985 Bredas *et al.*,³ performed a theoretical study (based on Valence Effective Hamiltonian $\langle \text{VEH} \rangle$ band structure calculations) on the influence of substituents on the electronic structure of PITN. They concluded that simple substituents on the PITN molecule (e.g., dimethyl, dimethoxy or dicyano) would not affect the size of the band gap in any significant way. We would therefore expect PTBITN to have a similar band gap to PITN (i.e., $E_g \sim 1 \text{ eV}$).

SYNTHESIS

PTBITN was made by polymerisation of the monomer 5-*tert*-butyl-1,3-dihydroisothianaphthene. The synthetic route can be summarised as follows:



The reaction steps (a) to (d) can be described as follows:

(a) *Synthesis of 4-tert-butyl-1,2-dimethylbenzene* This was prepared by adding *tert*-butyl chloride to *o*-xylene with ferric chloride (FeCl_3) as catalyst.⁴

(b) *Bromination of 4-tert-butyl-1,2-dimethylbenzene* The bromination of *tert*-butyl-*o*-xylene was done using *N*-bromosuccinimide (NBS) in carbon tetrachloride (CCl_4) with benzoyl peroxide (BPO) as catalyst. The best results were obtained when the reaction was performed in the dark in a nitrogen atmosphere and the product isolated by vacuum distillation.⁵

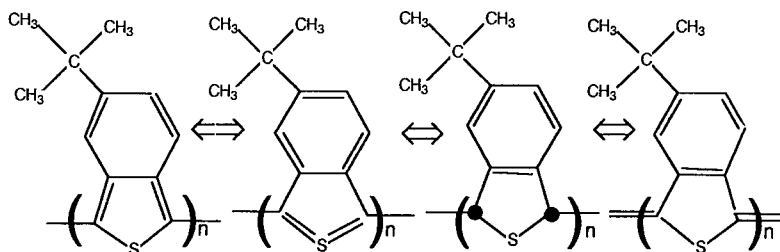
(c) *Preparation of 1,3-dihydro-5-tert-butylisothianaphthene* This was prepared by adding the 4-*tert*-butyl-1,2-bis(bromomethyl)benzene prepared above to a solution of anhydrous sodium sulfide (Na_2S) in ethanol. Again the best results were obtained when the reaction was done under nitrogen. A pure product is obtained by vacuum distillation, but the crude product (extracted with methylene chloride) can be used directly in the next stage.⁶

(d) *Polymerisation* The polymerisation methods used for PITN were tried but very low yields were obtained for the chemical cationic oxidative polymerisation with H_2SO_4 and FeCl_3 and the product could not be characterised. Polymerisation by UV and γ rays also proved unsuccessful. The oxygen-promoted solid-state polymerisation yielded a very low molecular weight product. A low molecular weight polymer was also obtained by benzoyl initiated free-radical polymerisation. The best results were obtained by polymerisation with Ferric chloride using the method of Pomerantz *et al.*⁷ The full experimental details are given in the Appendix.

ELECTRONIC AND OPTICAL PROPERTIES

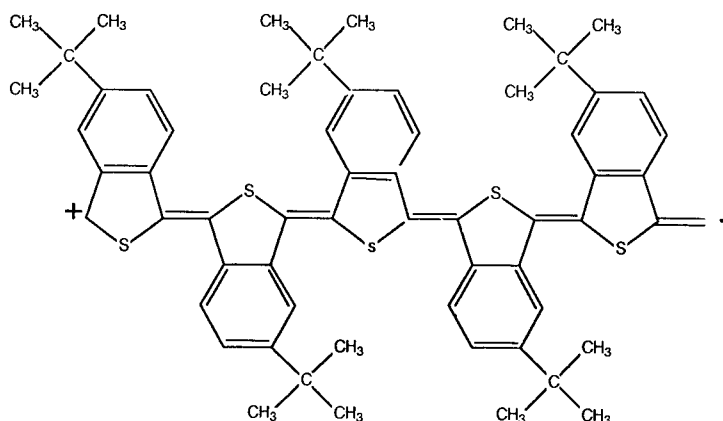
The electronic properties of polythiophenes arise from the delocalised π -electrons along the polymer backbone.

π conjugation in PTBITN would also be increased in the excited state due to the formation of a quinoidal structure which provides a rigid coplanar arrangement of



Resonance Structures for PTBITN

repeated units:



Quinoidal Structure for PTBITN

Recent work on doping PITN and PTT (polythieno[3,5-*c*] thiophene) with electron donors (*n*-doping) shows that the linear polarizability is greatly increased. This is probably not only due to charge transfer from the dopant atoms, but also to the induced quinoid-like structure of the polymer.⁸

NONLINEAR OPTICAL PROPERTIES

The second hyperpolarizability of PTBITN measured by Hugh Page⁹ and Simon Burbridge¹⁰ using four-wave mixing at 1.064 μm in chloroform gave the following values of $|\gamma|$:

Low mol. wt. polymer	High mol. wt. polymer
$\gamma_{\text{Re}} = -9 \times 10^{-45} \text{ m}^5/\text{V}^2$	$\gamma_{\text{Re}} = -1 \times 10^{-45} \text{ m}^5/\text{V}^2$
$ \gamma \text{ Im} = 6 \times 10^{-45} \text{ m}^5/\text{V}^2$	$ \gamma \text{ Im} = 3 \times 10^{-45} \text{ m}^5/\text{V}^2$
$ \gamma = 1 \times 10^{-44} \text{ m}^5/\text{V}^2$	$ \gamma = 4 \times 10^{-45} \text{ m}^5/\text{V}^2$

These are higher than values obtained for poly(alkylthiophenes),¹¹ which supports the "quinoid structure" theory. However there may be some contribution from resonance enhancement as the absorption band edge tails into the near infrared.¹⁰

SUMMARY

We describe herein the synthesis of a soluble derivative of polyisothianaphthene. Two forms of this polymer have been produced, one of high molecular weight and one of low

molecular weight. Solution measurements indicate that these polymers possess a very large nonlinearity in the near infrared and would thus have useful applications in the field of nonlinear optics.

ACKNOWLEDGEMENTS

We thank Peggy Brehon and John O'Brien for NMR results and Noel Daly for GPC's. The research was supported by a grant from the C.E.C. (RACE projects 1020 and 20120).

REFERENCES

1. M. Kobayashi, N. Colaneri, M. Boysel, F. Wudl and A. J. Heeger, *J. Chem. Phys.*, 82/12:5717 (1985).
2. N. Colaneri, M. Kobayashi, A. J. Heeger and F. Wudl, *Synth. Met.*, 14:45 (1986).
3. J. L. Bredas, A. J. Heeger and F. Wudl, *J. Chem. Phys.*, 85/8:4673-4678.
4. Larner and Peters, *J. Chem. Soc.*, 680-682 (1952).
5. Pini *et al.*, *Macromolecules*, 20/1:58-62 (1987).
6. Cava and Deana, *J. Am. Chem. Soc.*, 81:4266 (1958).
7. M. Pomerantz, J. J. Tseng, H. Zhu, S. J. Sproull, J. R. Reynolds, R. Uitz, H. J. Arnott and M. L. Haider, *Synth. Met.*, 41-43:825-830 (1991).
8. J. L. Bredas, M. Dory, B. Themans, J. Dehalle and J. M. Andre, *Synth. Met.*, 28:D533-D542 (1989).
9. H. Page, MSc Thesis, Trinity College Dublin (1991).
10. S. Burbridge, H. Page, A. Drury, A. P. Davey and W. Blau, Poster Presentation ICONO 1.
11. H. J. Byrne, PhD Thesis, Trinity College Dublin, Ireland (1989).

APPENDIX

Experimental Details

Synthesis of 4-tert-butyl-1,2-dimethylbenzene 106.2 g (1 mol) O-Xylene and 92.1 g (1 mol) *tert*-butyl chloride were well mixed (magnetic stirrer). 1.1 g anhydrous ferric chloride was added slowly (30 min.) at room temperature. When the evolution of hydrogen chloride had stopped excess *tert*-butyl chloride (20.5 g) was added and the mixture stirred for a further hour. It was then heated in a water bath for 15 min. (turning brown at approx. 65°C) and filtered through charcoal (125 g). The resulting yellow solution was distilled and various fractions of colourless liquid were collected (b.p = 155-175°C, 185-200°C, 205-210°C). The highest boiling fraction was found to be 4-*tert*-butyl-1,2-dimethylbenzene.

Yield = 90.6 g (55.8%). Structure was confirmed by ^1H NMR at 80 MHz (CDCl_3 + TMS) δ = 1.3, 2.2, 7.1.

Preparation of 1,2-bis(bromomethyl)-4-tert-butylbenzene 8.125 g *tert*-butyl-*o*-xylene (0.05 mols), 17.8 g *N*-bromosuccinimide (0.1 mol), 0.2 g benzoyl peroxide and 50 ml dry carbon tetrachloride were placed in a 250 ml round-bottomed flask and refluxed with magnetic stirring in the dark under nitrogen for 3 hrs. The mixture was left overnight at room temperature (under the same conditions) then it was filtered (to remove succinimide) and concentrated in vacuo. The product was collected by vacuum distillation (116-118°C at 0.12 mm Hg).

Yield = 4.66 g (29%). ^1H NMR at 60 MHz (CDCl_3 + TMS) δ = 1.25, 4.6, 7.25.

Preparation of 1,3-dihydro-5-tert-butylisothianaphthene 1.05 g (0.013 mol) anhydrous sodium sulfide dehydrate was dissolved in 75 mls dry ethanol in a 250 ml round-bottomed 2-necked flask fitted with a magnetic stirrer and condenser. 3.98 g (0.012 mol) 1,2-bis(bromomethyl)4-tert-butylbenzene was added dropwise during 30 mins. The solution went from pale blue to bright yellow. It was refluxed for 1 hour and the ethanol removed in vacuo. The remaining brown-black oil was dissolved in methylene chloride and filtered to remove sodium bromide. The CH_2Cl_2 was removed in vacuo and the final product obtained by vacuum distillation ($p = 6 \times 10^{-2}$ torr, $t = 88^\circ\text{C}$). Yield = 1.53 g (64%). ^1H NMR at 80 MHz ($\text{CDCl}_3 + \text{TMS}$) $\delta = 1.2, 3.35, 7.15$.

Polymerisation of 5-tert-butyl-1,3 dihydroisothianaphthene

1. *Oxygen promoted solid-state polymerisation* 1 g of the monomer (5-tert-butyl-1,3-dihydroisothianaphthene) was left uncovered in air in a glove-box for 3 weeks. IR spectra were taken at regular intervals and finally UV and NMR ($\sigma = 1.3, 7.25$ at 80 MHz in CDCl_3 and TMS) after washing with methanol to remove monomer. Gel Permeation Chromatography (GPC) indicated a polymer of weight average molecular weight $M_w = 13,091$ and number average molecular weight $M_n = 5,569$.

2. *Chemical Cationic Oxidative Polymerisation with Ferric Chloride* 3.6 mmols of 5-tert-butyl-1,3-dihydroisothianaphthene (0.7 g) was placed into a 3-necked flask equipped with condenser and drying tube, dropping funnel and inlet for dry air. 0.5 g anhydrous ferric chloride dissolved in 50 mls chloroform was added (20 min.). The solution was warmed to 50°C and stirred for 24 hrs, with air bubbling through. The resulting black solution was then washed with water to remove FeCl_3 . 20 mls concentrated ammonia was added and the solution stirred for 30 min. at room temperature. It was washed several times with water and dried over magnesium sulphate. The solvent was removed in vacuo and the low molecular weight fractions removed by soxhlet extraction with methanol. Yield = 0.25 g (36.5%).

The experiment was repeated using monomer recovered from the methanol wash giving a total yield of 53.1%.

GPC showed a high molecular weight polymer of weight average molecular weight $M_w = 49,362$ and number average molecular weight $M_n = 10,842$. The structure was confirmed by NMR (300 MHz, $\text{CDCl}_3 + \text{TMS}$, $\delta = 1.25, 7.23$).

3. *Free Radical Polymerisation* 0.75 g 5-tert-butyl-1,3-dihydroisothianaphthene was dissolved in 200 mls CCl_4 . A pinch (0.1 g) benzoyl peroxide was added and the mixture heated under reflux (in a nitrogen atmosphere) for 24 hrs. Upon filtration a black powder was obtained. This was washed with methanol and dried in vacuo. GPC indicated a polymer of $M_w = 3,901$ and $M_n = 3,862$.

Determination of $\chi^{(3)}$ -Parameters of Solutions and of Thin Layers by Coherent Antistokes Raman Scattering (CARS)

W. WERNCKE, M. PFEIFFER, T. JOHR, A. LAU, S. WOGGON,
S. SCHRADER*, H.-J. JÜPNER and W. FREYER
*Max-Born-Institut für Nichtlineare Optik und Kurzzeitspektroskopie,
Institut für Angewandte Chemie, D-12489 Berlin-Adlershof, Germany

Received 12 January 1994; accepted 8 March 1994

CARS susceptibilities $\chi^{(3)}(-\omega_A, \omega_p, \omega_p, -\omega_S)$ are determined at excitation under non resonant as well as under electronic resonance conditions. For the first time quantitative results are obtained even from very thin layers ($d_l = 10$ nm). This is demonstrated for oligomeric paraphenylene vinylene and for tetracene where a dispersion curve at the edge of the absorption band has been obtained.

A series of bisdimethylaminomethine dyes with different chain lengths is investigated and negative signs of their zero frequency susceptibilities are obtained. Results are compared with recent theoretical predictions.

INTRODUCTION

Contrary to the case of first order molecular hyperpolarizabilities β , a sufficient knowledge about the required molecular structure to acquire high second order molecular hyperpolarizabilities γ is still lacking though in recent years numerous experimental as well as theoretical contributions on this topic have been published. Some of these papers dealt with long chain like polyenes and polymethines being with respect to differences in the sign of γ even contradicting.

The tools to study experimentally the macroscopic third order susceptibilities $\chi^{(3)}$ are Degenerate Four Wave Mixing (DFWM), Third Harmonic Generation (THG) or Coherent Antistokes Raman Scattering (CARS).

We have shown that $\chi^{(3)}$ of dissolved substances as well as their dispersions caused by electronic resonances can be determined by CARS. Applying this technique it is possible to determine all parts (imaginary and real part of the Raman resonant and non-Raman resonant contributions) of $\chi^{(3)}(-\omega_A, \omega_p, \omega_p, \omega_S)$ at the Antistokes frequency $\omega_A = 2\omega_p - \omega_S$, at arbitrary pump and Stokes waves ω_p, ω_S . This method of $\chi^{(3)}$ determination will be sketched first. Then we will demonstrate for the first time how this method can be extended to very thin layers, being important because of their technological relevance and for investigation of unsoluble materials, and show some first applications to oligomeric paraphenylene vinylene and tetracene layers.

In addition results concerning non-Raman resonant molecular susceptibilities of a homologous series of polymethine dyes will be reported and compared with theoretical predictions.

DETERMINATION OF $\chi^{(3)}$ -PARAMETERS OF DISSOLVED MATERIALS

The basic idea of this method is to analyse the CARS line shape $I_{\text{CARS}}(\delta)$ of a Raman active vibration (frequency ω_R , line width Γ , $\delta = \omega_R - [\omega_P - \omega_S]$). The intensity $I_{\text{CARS}}(\delta)$ and the third order susceptibility are connected:

$$I_{\text{CARS}}(\delta) \propto |\chi^{(3)}|^2$$

In general the total third order susceptibility in the vicinity of a Raman line contains a non Raman resonant contribution χ^{NR} and a Raman resonant contribution $\chi^{\text{R}}/(\delta + i\Gamma)$ approaching χ^{R}/Γ at vibrational resonance:¹

$$\chi^{(3)}(-\omega_A, \omega_P, \omega_P, -\omega_S) = \chi^{\text{NR}} + \frac{\chi^{\text{R}}}{\delta + i\Gamma}$$

χ^{NR} is the analogue to the $\chi^{(3)}$ value measured by THG and DFWM. The three types of $\chi^{(3)}$, χ^{NR} , χ^{DFWM} and χ^{THG} become equivalent in the case of static limit where all radiation field frequencies tend to zero.

Usually the non-Raman resonant part χ^{NR} is not negligible compared to the Raman resonant contribution. This results in line shapes which are the sum of a constant, a dispersion-like, and a Lorentzian contribution² and these shapes can be analysed to determine the different $\chi^{(3)}$ contributions.

However near to electronic resonances where both χ^{NR} and χ^{R} can be complex valued

$$(\chi^{\text{NR}} \equiv B' - iB'', \chi^{\text{R}} \equiv VR - iJ)$$

this information is insufficient to determine all real and imaginary parts independently. For the total third order susceptibility of a solution the following relation holds:

$$\begin{aligned} \chi_{\text{total}}^{(3)} &= \frac{N_{\text{solvent}} \chi_{\text{solvent}} + N_{\text{solute}} \chi_{\text{solute}}}{N_{\text{solvent}} + N_{\text{solute}}} \\ &\Rightarrow I_{\text{CARS}} \propto |\chi_{\text{total}}|^2 \end{aligned} \quad (1)$$

where N are the concentrations (number/cm⁻³) of solute and solvent molecules respectively.

Varying the concentration in a solution changes the total susceptibility and therefore the respective line shapes containing together sufficient data to determine all parts of the third order susceptibility of a given solute unambiguously.³ However this technique can be applied only if the linear (or at least a known) dependence on concentration between molecular and macroscopic susceptibilities can be assumed. Investigation e.g., of aggregates exhibiting a concentration dependence of the molecular polarizabilities or of thin solid layers require different techniques.

INVESTIGATIONS OF THIN LAYERS

To determine $\chi^{(3)}$ values of layers, the method described above has been extended. The alterations of the CARS line shapes in solutions of changed concentrations are due to "local" interferences of the $\chi^{(3)}$ -contributions of the different components. Assuming

two different media e.g., a layer of the thickness d_l and the substrate of the thickness d_s as shown in Figure 1 "non local" interference of radiations originating from the contributions χ_l and χ_s occur.

For two components as in Figure 1 the intensity of the CARS-signal I_{CARS} can be written as:

$$I_{\text{CARS}} \propto \left| \chi_s + k \frac{n_s d_l}{n_l d_s} \chi_l \right|^2 \quad (2)$$

where k is a factor taking into account the influence of layer's absorption α at the wavelengths of the different radiations λ_A , λ_P and λ_S respectively

$$k = \frac{e^{(2\alpha_P + \alpha_S - \alpha_A)d_l} - 1}{(2\alpha_P + \alpha_S - \alpha_A)d_l},$$

and n_i are the respective refractive indices.

The relation is valid under the conditions that

- for the substrate the phase matching condition $\Delta \vec{k} = 2\vec{k}_P - \vec{k}_S - \vec{k}_A = 0$ is fulfilled as indicated in Figure 1 ($k_i = 2\pi n_i/\lambda_i$ is the wave vector) and
- the absorption within the substrate is negligible.

A non-zero phase mismatch, that will usually occur within the layer due to different dispersions of substrate and layer, can be neglected as far as $|\Delta \vec{k}| d_l \ll \pi/2$ holds. This is valid for the layers we used ($d_l < 1 \mu\text{m}$). As the relation (1) is analogous to (2) the $\chi^{(3)}$ contributions of the layer can be determined by CARS line shape analysis in a similar way as in solutions but changing d_s/d_l ratios. Contrary to solutions the absorption losses in the layer have to be taken into account. Absolute values can be calibrated with respect to the substrate of known susceptibility.

EXPERIMENTAL TECHNIQUE

For our experiments a multiplex CARS set up as described in⁴ was used. It is based on a narrow band and a broad band dye laser which are pumped by the second and third harmonic of a ns-pulsed Nd:YAG laser respectively. Spectra are recorded by a CCD-optical multichannel analyser, the data being further processed by a personal

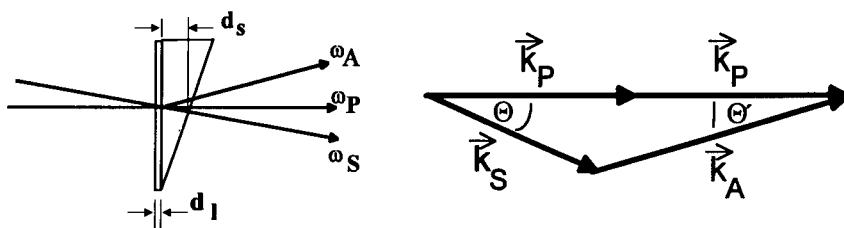


FIGURE 1 Geometry of the beams for CARS line shape analysis of a thin layer (left) Phase matching diagram (right).

computer. Materials were either dissolved in dimethylformamide or in trifluoroethanol, or sublimated by vacuum deposition as thin layers (5 nm–600 nm) on wedged quartz substrates. Due to the geometry of the substrate as shown in Figure 1 it is possible to change the interaction length within the substrate from 0.1 mm–1 mm by shifting the substrate perpendicular to the laser beams.

EXPERIMENTAL RESULTS

CARS-Susceptibility of Oligomeric Paraphenylene Vinylene Outside the Electronic Resonance

First CARS spectra of chain stretching vibrations of oligomeric tetra butyl paraphenylene vinylene (OPV-4)⁵ H (Fig. 2a (A)) from a 100 nm layer on a 0.2 mm quartz substrate and are shown in Figure 2b.

The absorption spectrum of OPV-4 is shown in the insert. The apparent tail in the absorption spectrum towards longer wavelengths is caused by reflection losses and has to be corrected to determine pure absorption losses.⁶ The CARS-excitation conditions as indicated in the insert are far outside the absorption band and can be considered as “off-resonant”.

The asymmetry in the CARS spectra in Figure 2b is mainly due to interferences between the Raman-resonant contribution of OPV-4 (being real valued outside the absorption) and the non-Raman resonant contribution of the substrate. The susceptibilities of the observed chain vibrations at 1625 cm^{-1} and 1588 cm^{-1} prove to be real valued and can be fitted with $R_1/\Gamma_1 = 1 \cdot 10^{-11}\text{ esu}$ and $R_2/\Gamma_2 = 4.5 \cdot 10^{-11}\text{ esu}$ respectively, values which are extremely high taking into account the off-resonant excitation conditions.

Generally high Raman susceptibilities are accompanied by other high non Raman resonant $\chi^{(3)}$ contributions. As suggested by Zerby *et al.*, this may be due to large

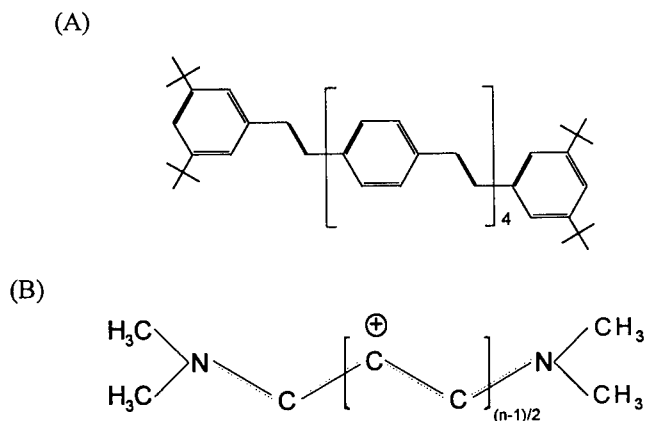


FIGURE 2a Molecular structures of paraphenylvinylene (“OPV-4”) (A) and of bisdimethylaminomethine dyes (B).

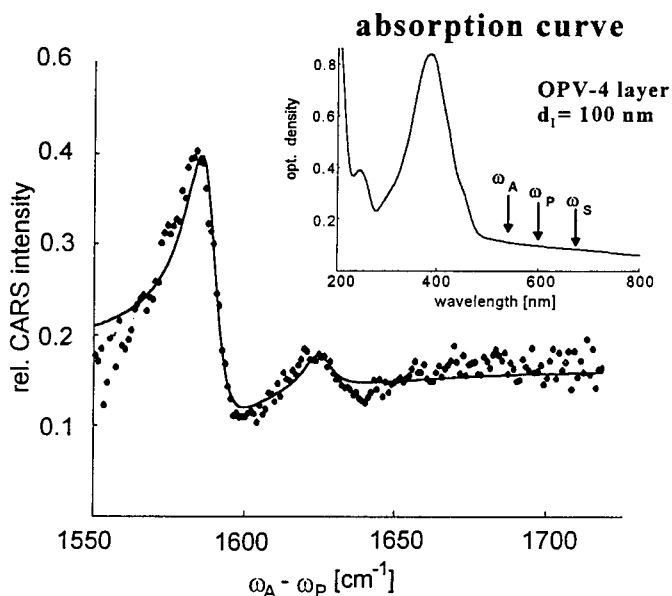


FIGURE 2b CARS-spectrum of a OPV-4 layer ($d_l = 100$ nm) deposited on quartz ($d_s = 0.2$ mm) dots: experimental data; solid curve: fit of the CARS-line shape Insert: Absorption curve of OPV-4, CARS excitation conditions.

nuclear relaxation contributions to other nonlinear susceptibilities (e.g., χ^{THG}) caused by strong electron phonon coupling.⁷

The B' contribution can be neglected in the fitting procedure of the above CARS-spectra. Therefore it should be considerable lower than the Raman-resonant contribution. This is in agreement with THG-measurements⁸ where for OPV-4 off-resonant conditions values of appr. $5 \cdot 10^{-12}$ esu have been determined.

CARS Susceptibilities of Tetracene Under Strict Resonance Conditions

CARS line shapes of the 1543 cm^{-1} ring stretching vibration of tetracene deposited as a layer with $d_l = 95$ nm were recorded varying the substrate thickness from 0.1–1.2 mm. Figure 3a shows the absorption spectrum of the tetracene layer. CARS excitation conditions related to the absorption band are indicated.

For $\lambda_p = 570$ nm the best CARS line shape fit was obtained for $R/\Gamma = 3 \cdot 10^{-10}$ esu $J/\Gamma = 7.5 \cdot 10^{-10}$ esu, $B' = 6 \cdot 10^{-11}$ esu $B'' = -6 \cdot 10^{-11}$ esu respectively.

Changing the excitation condition in tuning λ_p from 585 nm to 545 nm but letting $\omega_p - \omega_s$ fixed to the 1543 cm^{-1} -vibration a R/J-dispersion curve of the tetracene layer at the absorption edge was obtained.

For comparison we calculated R/J-curves by transform-theory⁹ taking into account the measured absorption spectra of the layer as shown in Figure 3a. As can be seen in Figure 3b the calculated R/J phase approximately fits the experimental curve.

Deviations occurring with respect to the modulus may be due to the Davydov splitting occurring at the absorption edge¹⁰ but they may also be caused by damages of the

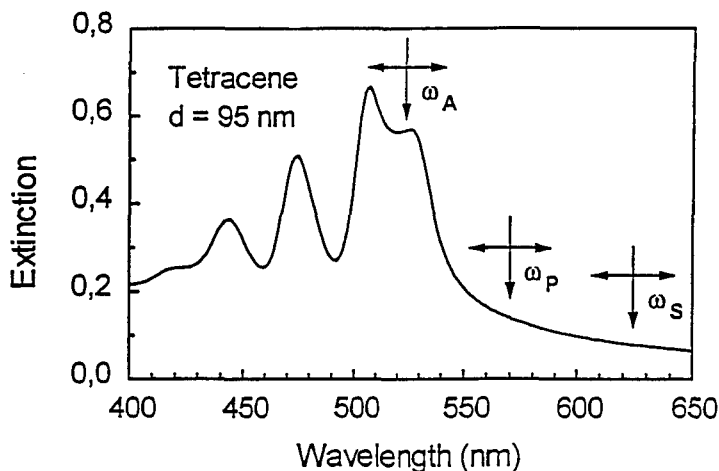


FIGURE 3a Absorption-curve of a 95 nm layer of tetracene (vertical bars in the absorption-curve indicate wavelength used for fourwave mixing; horizontal bars indicate tuning range).

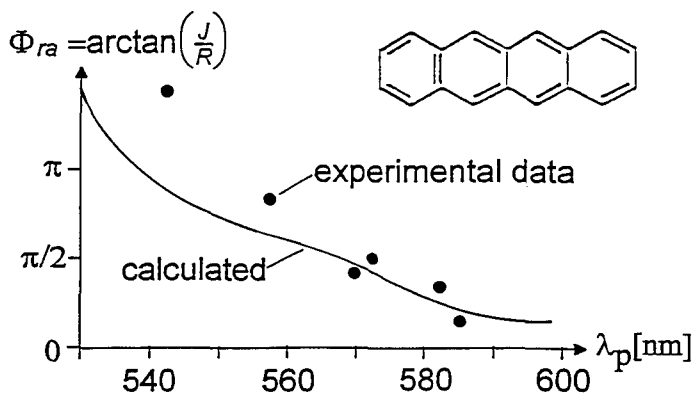


FIGURE 3b R-iJ phase of the 1543 cm^{-1} -ring vibration of a 95 nm tetracene layer calculated from the absorption spectrum (solid line); R/J phase determined from CARS line shapes of the 1543 cm^{-1} vibration (dots).

sample which become more perturbing if λ_p approaches the absorption maximum. In addition influences of reflection and scattering losses in the tetracene layers have to be taken into account. These effects have to be investigated more in detail.

Non Raman Resonant Susceptibilities of Polymethine Dyes of Different chain lengths

Bisdimethylaminomethine dyes $[(\text{CH}_3)_2\text{N}(\text{CH})_n\text{N}(\text{CH}_3)_2]^+ \text{X}^-$, $\text{X}^- = \text{ClO}_4^-$ / see Figure 2a (B)/ exhibiting different chain lengths $n = 3, 5, 7$ are model compounds of simple polymethines.

The susceptibilities of these dyes have been determined by Third Harmonic Generation (THG) by Stevenson *et al.*, avoiding any direct interference of electronic resonances.¹¹ An increase of the modulus of the susceptibility in lengthening the chain and positive signs of susceptibilities for $n=3,5$ but a negative sign for $n=7$ has been reported. While theoretical calculations roughly reproduce the enhancements they either predict positive¹³ or negative^{12,14} non-linear polarizabilities.

We have reinvestigated the bisdimethylaminomethine dyes outside electronic resonance conditions but applying CARS as a probe for the non-Raman resonant susceptibilities. The polymethines were dissolved either in trifluoroethanol or in dimethylformamide up to concentrations of 10^{-1} mol/l. Even at the highest concentration we could not find any change of the shape of the absorption curves indicating that there does not appear any aggregation.

Real and imaginary part of the susceptibilities B' , B'' of the solutions have been determined by CARS line shape analysis of solvent Raman lines of known susceptibility.

For all dyes at sufficient high concentration we observed a reversed dispersive line shape, which can be explained only by a B' -contribution of the solute being negative and exceeding the χ^{NR} contribution of the solvent. ($B' = N_{\text{solute}} L^4 b'$, where b' is the real part of the molecular non Raman-resonant hyperpolarizability of the dye and L^4 is the local field correction) Furthermore, from the line shape fits a negligible value of the imaginary part B'' can be concluded indicating that under our excitation conditions any resonant two photon contributions can be excluded.

Absorption maxima, excitation conditions, measured and calculated molecular susceptibilities¹² as well as data derived from results published by other groups^{11,13} are summarised in Table 1.

For comparison the different susceptibilities were normalised to "zero frequency hyperpolarizabilities" $\gamma(0)$ with respect to their different excitation conditions:

$$\gamma_{\text{THG}} \sim \gamma(0) D_1(3\omega) D_2(2\omega) D_1(\omega), \quad b' \sim \gamma(0) D_1(\omega_A) D_1(\omega_P) D_2(2\omega_P)$$

where $D_i(\omega) = \omega_i / (\omega_i - \omega)$ contain the one photon and two photon denominators respectively. Here it is assumed that (i) excitation is far from resonance and that the dominating one photon transition is the lowest $\pi\pi^*$ -transition ($\omega_1 = \omega_{\text{abs}}$) given in Table 1, (ii) two photon transitions to electronic levels ω_2 far above the first one photon allowed transition are relevant only. Such an assumption is supported by calculations of the electronic levels of simple polymethines¹⁴ and by transient absorption measurements, where e.g., for the heptamethine a strong $S_1 - S_N$ absorption at 420 nm has been

TABLE 1

Measured and calculated off resonant molecular third order susceptibilities of the series of bisdimethylaminomethine dyes.

Molecule	λ_{abs}	λ_A, λ_P	b'	$\gamma(0)$	$\gamma(0)$	$\gamma(0)$	$\gamma(0)$
	[nm]	[nm]	[esu] CARS exp.	$ \gamma(0)_{\text{TRI}} $ CARS exp.	$ \gamma(0)_{\text{TRI}} $ THG exp. ¹¹	$ \gamma(0)_{\text{TRI}} $ calc. ¹²	$ \gamma(0)_{\text{TRI}} $ calc. ¹³
TRI	315	490, 571	$-0.3 \cdot 10^{-34}$	-1	+1	-1	+1
PENTA	414	490, 571	$-10 \cdot 10^{-34}$	-7.2	+10.8	-5	+7.2
HEPTA	514	586, 610	$-90 \cdot 10^{-34}$	-22.4	-32	-15	+28

observed.¹⁵ For the pentamethine the respective $S_1 - S_N$ absorption is shifted to shorter wavelengths with respect to the heptamethine.¹⁶

It turns out that the measured increase of CARS- and THG-zero frequency hyperpolarizabilities are comparable, but contrary to THG all values obtained by CARS exhibit a negative sign.

Negative signs of our experimental b' -values are not expected to result from a negative two photon denominator. They are in agreement with semiempirical calculations for the zero frequency susceptibilities as obtained in¹²⁻¹⁴ being a consequence of a negative molecular transition moment occurring in π -electron systems with perfect bond equalization.

Albert *et al.*,¹³ calculated significant bond alternations in the chains resulting in positive signs for the whole series of dyes as shown in Table 1.

For explanation of the change of the signs of the measured THG susceptibilities Pierce¹⁴ suggested a polymethine ground state with an alternating π -bond order due to a polar methine structure for the tri- and for the pentamethine but a more symmetric structure for the heptamethine.

Taking into account our new results this assumption may not be necessary.

CONCLUSIONS

We have demonstrated how CARS line shape analysis can be applied for determination of third order susceptibility parameters not only of dissolved material but of thin layers as well. The technique can be used outside and under strict resonance conditions and it allows to determine the respective $\chi^{(3)}$ -dispersion curves.

Negative non-Raman resonant susceptibilities for the investigated series of polymethines with different chain lengths are obtained. This result is consistent with quantum chemical calculations assuming a symmetric "ideal" polymethinic structure.

ACKNOWLEDGEMENT

We are very grateful to Prof. Dr. K. Müllen, Max-Planck-Institut für Polymerforschung, Mainz for providing the OPV samples and to the Deutsche Forschungsgemeinschaft for financial support.

REFERENCES

1. J. W. Nibler and G. V. Knighten in "Raman Spectroscopy of Gases and Liquids", Topics in Current Physics, **11** Weber, pp. 253-299. Ed. A. (1979).
2. J. W. Fleming and C. S. Johnson, *J. Raman Spectrosc.*, **8**, 284 (1979).
3. M. Pfeiffer, A. Lau and W. Werncke, *J. Raman Spectrosc.*, **17**, 425 (1986).
4. A. Lau, W. Werncke and M. Pfeiffer, *Spectrochim. Acta Rev.*, **13**, 191 (1990).
5. R. Schenk, H. Gregorius, K. Meerholz, J. Heinz and K. Müllen, *J. Am. Chem. Soc.*, **113**, 2634 (1991).
6. D. Neher, A. Kaltbeitzel, A. Wolf, C. Bubeck and G. Wegner, *J. Phys. D. Appl. Phys.*, **24**, 1193 (1991).
7. M. del Zoppo, C. Castiglioni, M. Veronelli and G. Zerbi, *Synth. Metals*, **55-57**, 3919 (1993).
8. A. Mathy, thesis, University Mainz, Mainz (1992).
9. M. Pfeiffer, A. Lau and W. Werncke, *J. Raman Spectrosc.*, **15**, 20 (1984).

10. W. Hofberger, *Phys. Stat. Sol. (a)*, **30**, 271 (1975).
11. S. H. Stevenson, D. S. Donald and G. R. Meredith, *Mat. Soc. Symp. Proc.*, **109**, 103 (1988).
12. M. Pfeiffer, W. Werncke, A. Lau and W. Freyer, in "Electronic Properties of Polymers", Springer Series in Solid-State Sciences **107**, Eds. H. Kuzmany, M. Mehring, S. Roth, pp. 150 (1992).
13. I. D. L. Albert, P. K. Das and S. Ramasesha, *J. Opt. Soc. Am. B*, **10**, 365 (1993).
14. B. M. Pierce, in "Nonlinear Optical Properties of Organic Materials IV" Ed. K. D. Singer, *Proc. Soc. Photo-Opt. Instrum. Eng.*, **1560**, 148 (1991).
15. S. Rentsch and B. Wilhelmi, *J. Mol. Struct.*, **114**, 1 (1984).
16. S. Rentsch; private communication.

Nonlinear Optical Properties of Fullerenes and their Derivatives

S. R. FLOM, R. G. S. PONG, F. J. BARTOLI and Z. H. KAFABI*
U. S. Naval Research Laboratory, Washington D.C. 20375, U.S.A.

Received 21 March 1994; accepted 22 March 1994

The nonlinear optical (NLO) response of pure C_{60} and chemically modified C_{60} has been studied at selected wavelengths in the visible region. The electronic and chemical structure of C_{60} was altered by photopolymerization, oxygen doping or by formation of charge transfer complexes in the ground (ex. C_{60} :TMPD) or excited (ex. C_{60} /MEH-PPV) states. The magnitude of the NLO response for C_{60} was largely unaffected by photopolymerization or oxygen-doping whereas significant enhancements were observed for the charge transfer complex C_{60} :TMPD and the C_{60} /MEH-PPV composite. The dynamics of the NLO response and its laser fluence dependence were altered by these chemical modifications.

INTRODUCTION

Since the discovery of the synthesis of Buckminsterfullerenes,¹ many studies have engaged in identifying the nonlinear optical (NLO) properties^{2–8} of this fascinating new form of carbon. The symmetry and structure, unique to the fullerenes, have been among the attractions to this class of carbon-based materials. The fullerenes exhibit third-order optical responses comparable to those of conjugated organic polymers. In the near-infrared the response has been characterized as electronic with two- or three-photon resonance enhancement at some wavelengths.^{5,8} The origin of the resonant NLO response in solid fullerene films has been identified as molecular and is associated with localized excitations on the molecules.³

Recently, we have undertaken the studies of chemically modified fullerenes using linear absorption spectroscopy, degenerate four-wave mixing (DFWM) and nonlinear transmission (NLT) to further understand and enhance the NLO response observed in the fullerenes. The chemical modifications of fullerenes include photopolymerization of thin films of C_{60} , oxygen doping of C_{60} thin films, formation of 1:1 charge transfer complexes of C_{60} with N,N,N',N'-tetramethyl-1,4-phenylenediamine (TMPD) in 1-chloronaphthalene solutions and using C_{60} as a dopant, 1:1 by weight, in thin films of a polyphenylenevinylene derivative. These studies compare the NLO response of chemically modified fullerenes to that of C_{60} . In addition, they demonstrate the degree to which the NLO response varies with these chemical and structural changes.

* Author to whom correspondence should be addressed.

EXPERIMENTAL SECTION

C₆₀ (99.99%) was obtained from Strem Chemicals or from Bluegrass fullerenes (Lexington, KY 99 + %) and used after outgassing in vacuum below the fullerenes' sublimation temperature. Thin films were formed through vacuum vapor deposition (400°C) onto optical substrates held at ambient temperature. For the photopolymerized samples the newly formed film was irradiated under vacuum using the output of a HeCd laser, or a 300 W Hg arc lamp as described previously.⁹ Oxygen doped samples were prepared¹⁰ by a 25 hr exposure of the freshly prepared C₆₀ film to 1 atm of room temperature O₂ with simultaneous irradiation of the sample with either the output of a 75 W Xe lamp or that of an Ar ion laser.

Pfaltz and Bauer were the suppliers of 1-chloronaphthalene (95%) while N,N,N',N'-tetramethyl-1,4-phenylenediamine and chlorobenzene were obtained from Aldrich. Poly-[2-methoxy, 5-(2'-ethylhexyloxy)-p-phenylenevinylene], MEH-PPV, was purchased from Uniax (Santa Barbara, CA) in a chlorobenzene solution (3.3 mg/ml). Films of C₆₀/MEH-PPV were prepared by adding 3.3 mg of C₆₀ to one ml solution of MEH-PPV which was then spin coated onto CaF₂ substrates.

Absorption spectra were taken using a Perkin-Elmer Lambda 9 spectrophotometer. The laser system used for the DFWM and NLT measurements consists of a dye laser (Coherent model 702) that is synchronously pumped by the second harmonic of a CW mode-locked Nd:YAG laser (Coherent, Antares). The output of the dye laser is amplified by a three stage dye amplifier (Continuum, PTA 60) that is pumped by the second harmonic of the output of a regenerative Nd:YAG amplifier (Continuum, RGA60). The laser system provides 1.2 ps (FWHM) pulses with energies up to 1 mJ.

DFWM measurements are performed using the phase conjugate geometry. Intensity is varied by rotating a half wave plate between crossed polarizers. The dependence of the signal on the incident intensity is fit by least squares to a cubic expression, and the cubic coefficient a_3 is compared to the cubic coefficient $a_{3\text{ref}}$ extracted from an identical experiment using CS₂ as a standard reference. The third-order optical susceptibility is determined by means of the expression,

$$|\chi_{ijkl}^{(3)\text{eff}}| = |\chi_{ijkl}^{(3)\text{ref}}| \left(\frac{a_3}{a_{3\text{ref}}} \right)^{\frac{1}{2}} \left(\frac{n}{n_{\text{ref}}} \right)^2 \left(\frac{l_{\text{ref}}}{l} \right) \left(\frac{\alpha l}{e^{-\alpha l/2}(1 - e^{-\alpha l})} \right) \quad (1)$$

where the "eff" superscript denotes an effective value of $\chi^{(3)}$, n is the refractive index, l is the path length and α is the linear absorption coefficient of the sample. The value of the measured $\chi^{(3)}$ is denoted effective to encompass processes whose lifetimes are longer than the laser pulse width. Time resolved measurements are accomplished by delaying the arrival of the back pump beam.

NLT experiments are performed by directing the output of the laser system into the sample and collecting all of the transmitted light. From the slope of the intensity dependence of the transmitted light, the coefficient of the nonlinear absorption α_{nl} is obtained using,

$$T(I) = (1 - R)^2 e^{-\alpha_0 l} \left[1 - \frac{\alpha_{nl}(1 - R)(1 - e^{-\alpha_0 l})}{\alpha_0 2\sqrt{2}} I \right] \quad (2)$$

where R is the reflection coefficient of the sample and I is the peak intensity of the gaussian laser pulse. Equation 2 is based on the assumptions that the intensity dependence of the absorption coefficient, α , varies linearly with intensity,

$$\alpha(I) = \alpha_0 + \alpha_{nl} I \quad (3)$$

and that $(\alpha_{nl} I / \alpha_0) < 1$. The coefficient of nonlinear absorption is related to the imaginary part of $\chi^{(3)\text{eff}}$ as follows:

$$\text{Im } \chi_{xxxx}^{(3)\text{eff}} = \frac{10^{-16} n^2 c^2}{96 \pi^2 \omega} \alpha_{nl} \quad (4)$$

where $\chi^{(3)\text{eff}}$ is expressed in esu and α_{nl} is in cm/GW; c is the speed of light in cm/s, n is the refractive index and ω is the optical frequency.

RESULTS AND DISCUSSION

Poly-C₆₀ and C₆₀—O₂

The measured absorption spectra of C₆₀ photopolymer and C₆₀—O₂ are quite similar to that of C₆₀ with slightly broader spectral features in the visible region. Table 1 summarizes the measured NLO properties of these chemically modified fullerenes in comparison to C₆₀ at different wavelengths. The variation of the $\chi^{(3)\text{eff}}$ from sample to sample is small, and indicates that structural changes through oxygen doping or polymerization does not radically affect the magnitude of the NLO response. Further, the ratio of $\chi_{xyyx}^{(3)\text{eff}} / \chi_{xxxx}^{(3)\text{eff}}$ remains unusually small. This small ratio was observed earlier for the fullerenes and was explained in terms of a rapid loss of the orientation at correlation of the transition dipole moment of the triply degenerate excited states of C₆₀.³ Apparently, the structural change of the molecule, i.e., disrupting its symmetry, does not change the degeneracy of the electronic excited states that participate in the NLO mechanism at these resonant wavelengths.

Figure 1 shows the early temporal response of the DFWM signal observed for films of C₆₀ photopolymer and C₆₀—O₂ at 590.5 nm at different laser intensities. The response exhibits rapidly decaying components and a slower component (not shown in Fig. 1) that persists for more than a nanosecond. These dynamics are quite similar to those exhibited by pristine films of fullerenes.³ The fast components were previously attributed to the decay of singlet excitons. For the photopolymer, a strong fluence

TABLE I
Linear and Nonlinear Optical Properties of C₆₀, Poly-C₆₀ and C₆₀—O₂.

Fullerene	λ nm	α cm ⁻¹	$\chi_{xxxx}^{(3)\text{eff}} 10^{-11}$ esu	$\chi_{xyyx}^{(3)\text{eff}} / \chi_{xxxx}^{(3)\text{eff}}$
C ₆₀	590.5	9800	52	< 0.006
Poly-C ₆₀	590.5	16,000	84	< 0.005
C ₆₀ —O ₂	590.5	14,000	43	< 0.007
C ₆₀	675	1500	8.2	< 0.07
Poly-C ₆₀	675	4800	8.7	< 0.03
C ₆₀ —O ₂	675	4600	9.5	< 0.03

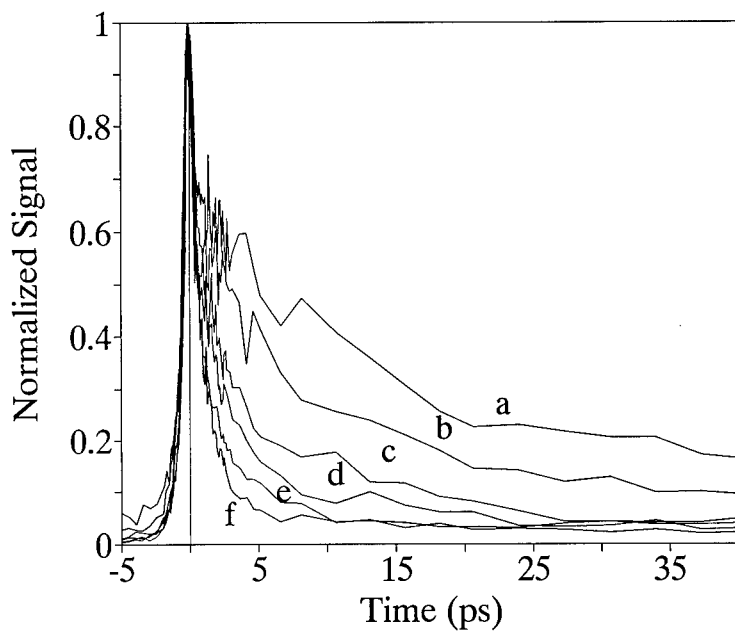


FIGURE 1(A) The early temporal response of the NLO signal of poly-C₆₀ measured at 590.5 nm as a function of laser fluence (a) 0.36, (b) 0.55, (c) 0.82, (d) 1.4, (e) 2.7 and (f) 6.8 mJ/cm².

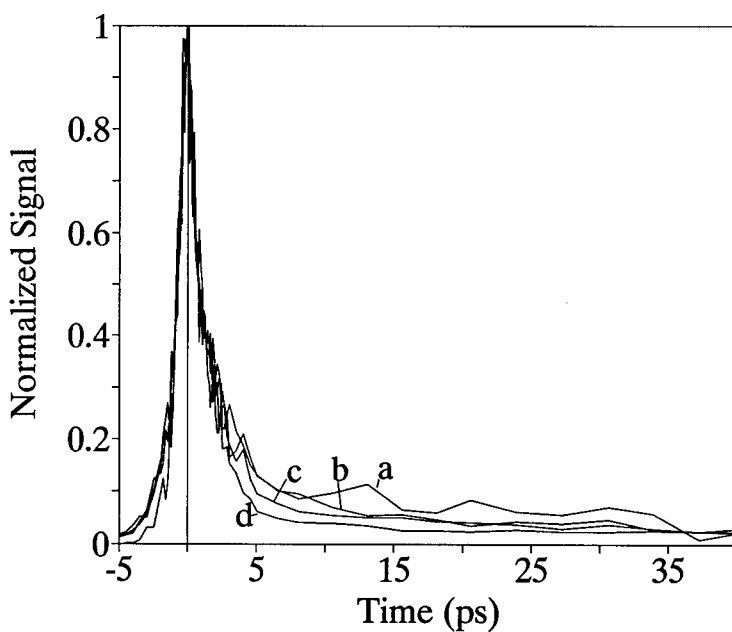


FIGURE 1(B) The early temporal response of the NLO signal of C₆₀-O₂ measured at 590.5 nm as a function of laser fluence (a) 0.76, (b) 1.5, (c) 3.3 and (d) 7.1 mJ/cm².

dependence is observed with the decay becoming much faster at higher fluences. Fluence dependence arises from bimolecular exciton-exciton annihilation which competes with unimolecular decay processes. At the lowest fluence, the decay seems to be slower than that observed for pristine films at the same fluence. This result suggests that exciton migration may occur at a slower rate in the photopolymerized film. In contrast, the decay displayed in Figure 1B for the oxygen-doped fullerene shows a much weaker dependence on the fluence. It is possible that oxygen doping shortens the lifetime of the singlet exciton through enhanced intersystem crossing while photopolymerization may slow the apparent response through disruption of exciton migration.

C₆₀: TMPD Charge Transfer Complex

Figure 2 shows the absorption spectrum obtained from a chloronaphthalene solution with equilibrium concentrations of 1.1 M TMPD, 5.3 mM C₆₀ and 2.8 mM of the C₆₀: TMPD charge transfer (CT) complex. Also shown in the figure are spectra of the fullerene and the electron donor compound adjusted to the approximate height of their contribution to the mixed solution. A new absorption band that is dependent on the concentrations of both C₆₀ and TMPD appears with $\lambda_{\text{max}} = 725$ nm and has been assigned to the charge transfer complex between C₆₀ and TMPD. An equilibrium constant of 0.51 was calculated for the charge transfer complex which has an extinction coefficient of 1400 l/mole-cm at 675 nm.

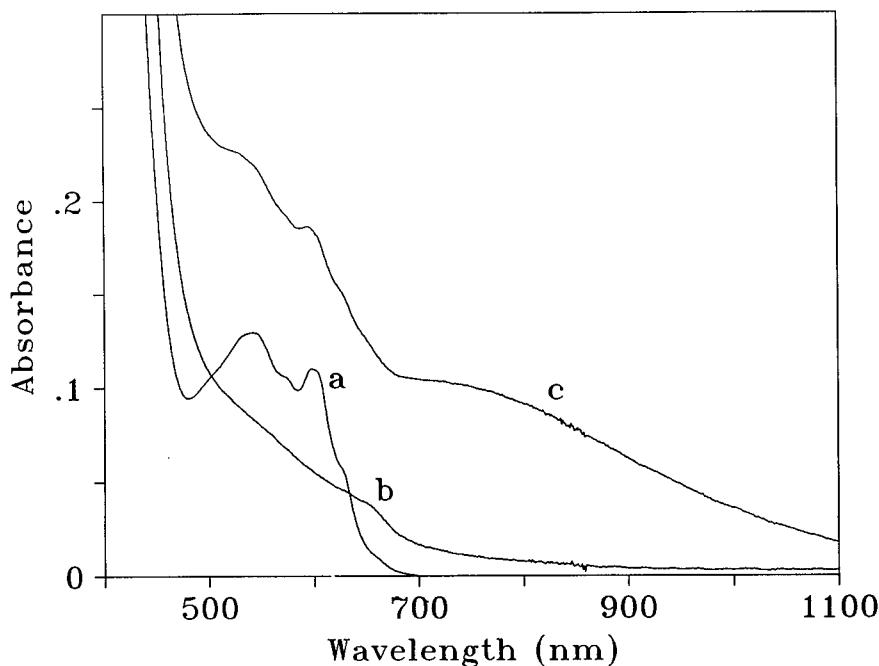


FIGURE 2 The absorption spectra of 1-chloronaphthalene solutions of (a) C₆₀, (b) TMPD and (c) C₆₀/TMPD.

DFWM experiments at 675 nm were carried out on five solutions of C_{60} and TMPD with varying concentrations. Neither C_{60} nor TMPD solutions exhibited a DFWM signal that was distinguishable from that of the solvent. Hence, only an upper limit to $|\chi^{(3)}|$ of solutions of pure C_{60} or TMPD may be obtained. Solutions containing both molecules gave a strong NLO signal that changed with concentration. The DFWM signal exhibited a cubic power dependence characteristic of a third-order effect, and increased with the concentration of the C_{60} :TMPD CT complex. Figure 3 shows the dependence of the solution $\chi^{(3)}$ on equilibrium CT complex concentration. Least squares analysis of the data yields an effective second hyperpolarizability of 7.1×10^{-33} esu for the charge transfer complex. Extrapolation to the pure C_{60} :TMPD complex yields $\chi^{(3)} = 1.2 \times 10^{-10}$ esu. Comparing this value with an upper-limit value of 7×10^{-12} esu (extrapolated from solution measurements to the fullerene in the solid state), one concludes that the third-order optical response of C_{60} has been greatly enhanced by complexation with a good electron donor such as TMPD.

In order to further understand the nature of the NLO response of the charge transfer complex, nonlinear transmittance studies have been undertaken to determine the absorptive contribution to the third-order optical coefficient of the C_{60} :TMPD CT complex. At 675 nm, it was found that solutions of the charge transfer complex act as "reverse saturable absorbers" in that their transmittance decreases with increasing incident laser intensity. Solutions of C_{60} also demonstrate reverse saturable absorption (RSA). The nonlinear absorption coefficient, α_{nl} , for a 13.9 mM chloronaphthalene

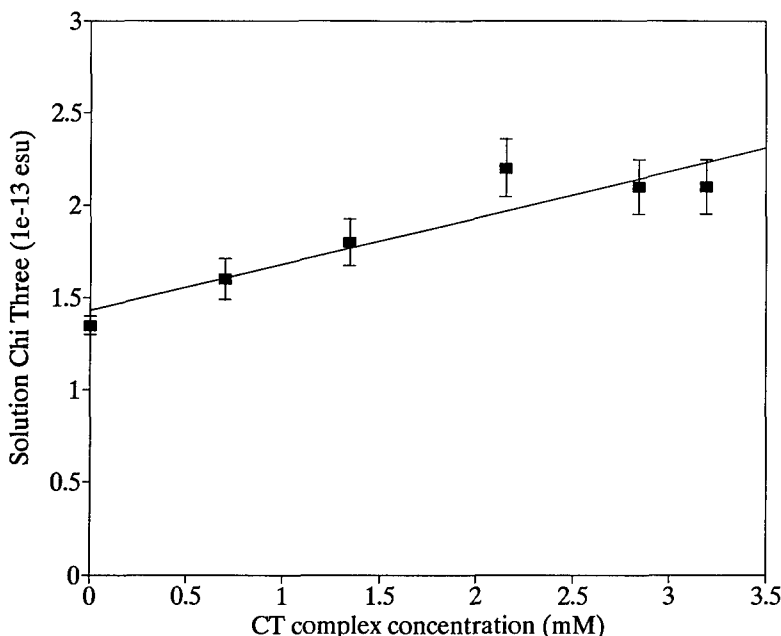


FIGURE 3 The third-order optical susceptibility of 1-chloronaphthalene solutions of C_{60} /TMPD as a function of molar concentration of the C_{60} :TMPD charge transfer complex.

solution of C_{60} is 0.093 cm/GW. Using equation 4, one obtains $\text{Im}\chi^{(3)\text{eff}} = 8.4 \times 10^{-15}$ esu which extrapolates to a value of 3.8×10^{-12} esu for pure C_{60} . This lower limit along with the upper-limit of 7.1×10^{-12} esu obtained from the DFWM study brackets the contributions of isolated C_{60} molecules to the response of a C_{60} /TMPD film. Note that these values are more than an order of magnitude smaller than that shown in Table 1 for solid C_{60} .

Analysis of the concentration dependence of the NLO response for the CT solutions has been performed taking into account contributions from C_{60} and TMPD solutions. At 675 nm, TMPD is a saturable absorber so the sign of α_{nl} (and $\text{Im}\chi^{(3)\text{eff}}$) is negative. Table 2 lists the derived nonlinear absorption coefficient $\alpha_{nl,CT}$ after subtraction of contributions from C_{60} and TMPD solutions, using $\alpha_{nl,CT} = \alpha_{nl,solution} - (\alpha_{nl,TMPD} \pm \alpha_{nl,C_{60}})$. Also listed in the table are the equilibrium CT concentrations as well as the calculated values for $\text{Im}\chi^{(3)\text{eff}}$. By extrapolating to the bulk an $\text{Im}\chi^{(3)\text{eff}} = 3.9 \times 10^{-11}$ esu was obtained as compared to $|\chi^{(3)\text{eff}}| = 1.2 \times 10^{-10}$ esu deduced from the DFWM measurements at the same wavelength. This comparison shows that absorptive contributions to the third-order optical response of the CT complex are significant. Direct optical excitation into the CT band accesses higher excited states with larger absorption cross-sections than that of the ground state and contribute to the enhanced NLO response observed for the complex.

C_{60} /MEH-PPV Composite

Figure 4 shows absorption spectra of the C_{60} /MEH-PPV composite film and the separate components. The spectrum of the composite material is quite similar to a composite of the spectra of C_{60} and MEH-PPV. The significant difference is that the peak near 340 nm for the composite material is narrower and blue shifted relative to that observed in the pure C_{60} film. On the other hand, this peak is strikingly similar in position and width to that measured for solutions of C_{60} . This resemblance between liquid solutions of C_{60} and C_{60} /MEH-PPV solid film is an indication that C_{60} is dispersed in the composite film.

DFWM and NLT experiments were conducted on films of C_{60} , MEH-PPV and C_{60} /MEH-PPV at 590.5 nm. Results from NLT measurements indicate that both C_{60} and C_{60} /MEH-PPV act as reverse saturable absorbers while MEH-PPV is a saturable absorber at this same wavelength. The DFWM signal of the MEH-PPV film exhibits a small third-order response and its intensity dependence contains a fifth-order

TABLE 2
Third-Order Optical Susceptibilities of Solutions of C_{60} /TMPD Measured at 675 nm by Nonlinear Transmission and Degenerate Four-Wave Mixing.

C_{60} /TMPD mM	$\alpha_{nl,CT}$ cm/GW	$\text{Im}\chi_{xxxx}^{(3)\text{eff}} 10^{-14}$ esu	$ \chi_{xxxx}^{(3)\text{eff}} 10^{-14}$ esu	$\text{Im}\chi_{xxxx}^{(3)\text{eff}}/ \chi_{xxxx}^{(3)\text{eff}} $
0.7	0.13	1.2	2.5	0.48
1.3	0.19	1.7	4.5	0.38
2.1	0.24	2.2	8.5	0.26
2.8	0.29	2.6	7.5	0.35
3.2	0.31	2.8	7.5	0.38

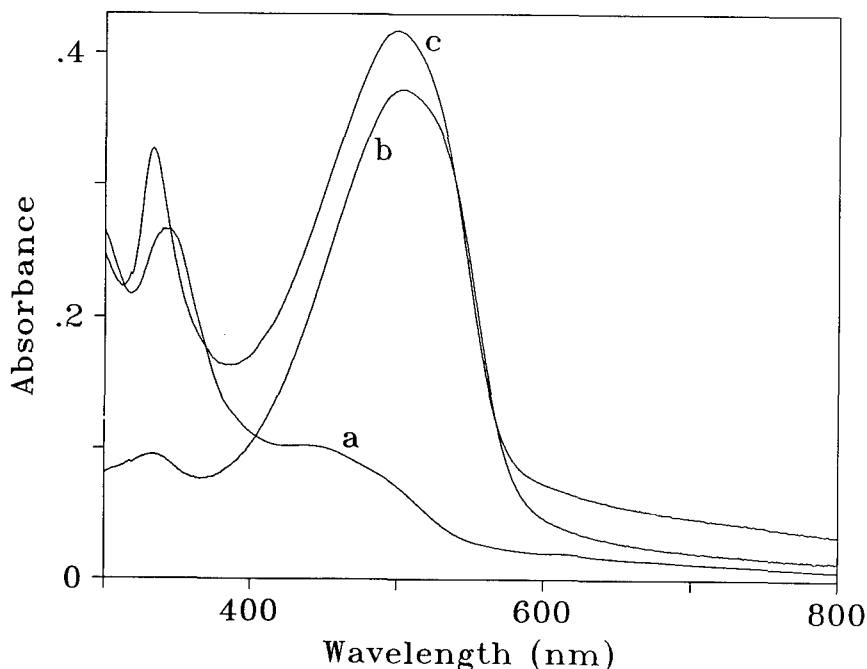


FIGURE 4 The absorption spectra of films of (a) C_{60} , (b) MEH-PPV and (c) C_{60} /MEH-PPV.

component. $\chi_{xxxx}^{(3)}$ on the order of 3×10^{-10} esu was deduced for MEH-PPV, consistent with previously reported values¹¹ for PPV. This value is also similar to that measured for C_{60} at 590.5 nm and shown in Table 1. A larger NLO signal than that exhibited by the separate components was measured for the C_{60} /MEH-PPV composite film. It shows a cubic power dependence, similar to that observed for films of pure C_{60} , at moderate laser intensities. The NLO signal becomes markedly subcubic at higher intensities with no obvious contribution from a fifth-order component. The third-order optical susceptibility of the composite material appears to be larger than the sum of the susceptibilities of the two components in the solid state. If one assumes that the fullerene in solid MEH-PPV behaves more like C_{60} in solution, one may speculate that the measured enhancement in the NLO response is even more pronounced. This is due to the fact that the directly measured $\chi_{xxxx}^{(3)} = 5 \times 10^{-10}$ esu for a film of C_{60} is at least 70 times larger than that deduced from solutions of C_{60} .

In the cross-polarized configuration, both MEH-PPV and C_{60} /MEH-PPV films display a cubic intensity dependence. For MEH-PPV, a ratio of $\chi_{xyyx}^{(3)}/\chi_{xxxx}^{(3)} = 1/3$ is measured, consistent with either an electronic or an excited state third-order optical process. For the composite film, the ratio is of the order of 0.07, much smaller than the ratio measured for the MEH-PPV film, and is inconsistent with a purely nonresonant electronic process. However, it is much larger than the upper-limit value given for C_{60} in Table 1. The differences between the measured ratios for C_{60} and C_{60} /MEH-PPV must arise from different NLO mechanisms.

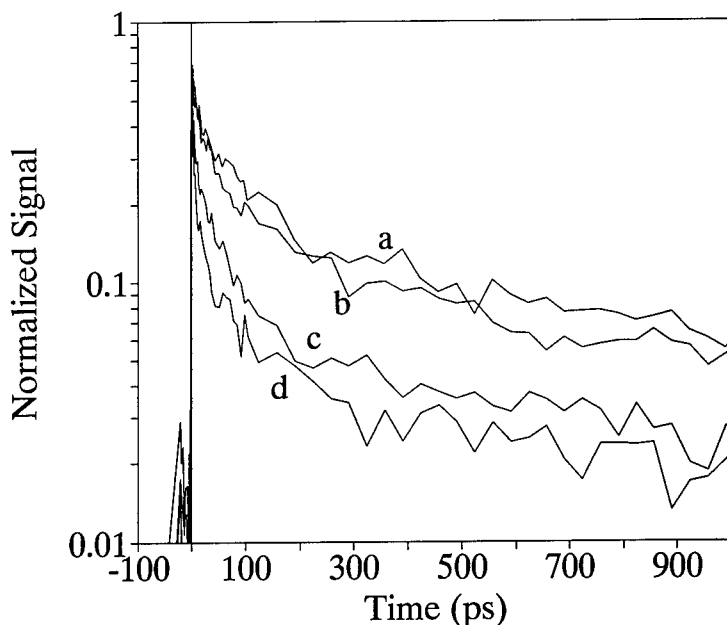


FIGURE 5 The temporal response of the degenerate four-wave signal of a film of C_{60} /MEH-PPV measured at 590.5 nm as a function of laser fluence (a) 0.45, (b) 1.1, (c) 3.2 and (d) 5.0 mJ/cm^2 .

Figure 5 shows the dynamics of the NLO response for the film of the C_{60} /MEH-PPV composite. There are multiple decay processes contributing to the temporal response on the pico- and nanosecond time scale. The early temporal response is characterized by a fast component that shows a strong fluence dependence. This response is qualitatively similar to that measured for films³ of pure C_{60} but quite different from that exhibited by MEH-PPV film whose signal is very nearly pulse-width (1.2 ps) limited. However, quantitatively the response is more complex than that observed for films of pure C_{60} . The presence of a kinetic component that decays on the hundreds of picosecond time scale strongly suggests that a new process occurring that is unique to the composite film. Recently, a very rapid photo-induced electron transfer from the excited state of MEH-PPV onto C_{60} has been reported to occur on a picosecond time scale.¹² This charge-separated state in the composite films is metastable at low temperatures. Direct excitation into the tail of the π - π^* transition of MEH-PPV may access this state via fast electron transfer from the conducting polymer to C_{60} . The present NLO results are consistent with the formation of an excited-state charge transfer complex between MEM-PPV and C_{60} .

CONCLUSIONS

In summary, the present study demonstrates that chemical modification of C_{60} has varying effects on the NLO response. The presence of oxygen in films of C_{60} has little effect

if any on the magnitude of its third-order optical susceptibility. Photopolymerization of the fullerene enhances its physical properties without negatively affecting its NLO response. In addition, altering the chemical and electronic structure by formation of charge transfer complexes with C_{60} in the ground or excited state, result in a greatly enhanced NLO response. The dynamics of the NLO response and its laser fluence dependence are also influenced by these chemical modifications.

ACKNOWLEDGEMENTS

The authors would like to thank Professor P. C. Eklund and Dr. A. M. Rao for providing initial samples of poly- C_{60} and $C_{60}-O_2$. Mr. Charles Merritt prepared one of the photopolymerized C_{60} samples used in this study. Financial support from the Office of Naval Research is greatly appreciated.

REFERENCES

1. W. Kratschmer, L. D. Lamb, K. Fostiropoulos and D. R. Huffman, *Nature*, **347**, 354 (1990).
2. Z. H. Kafafi, J. R. Lindle, R. G. S. Pong, F. J. Bartoli, L. J. Lingg and J. Milliken, *Chem. Phys. Lett.*, **188**, 492 (1992).
3. S. R. Flom, R. G. S. Pong, F. J. Bartoli and Z. H. Kafafi, *Phys. Rev. B*, **46**, 15598 (1992).
4. Z. H. Kafafi, F. J. Bartoli, J. R. Lindle and R. G. S. Pong, *Phys. Rev. Lett.*, **68**, 2705 (1992).
5. J. R. Lindle, R. G. S. Pong, F. J. Bartoli and Z. H. Kafafi, *Phys. Rev. B*, **48**, 9447 (1993).
6. F. Z. Henari, S. Mac Namara, O. Stevenson, J. Callaghan, D. Weldon and W. J. Blau, *Advan. Mater.*, **5**, 930 (1993).
7. S. J. Qin, W. M. You and Z. B. Su, *Phys. Rev. B*, **48**, 7562 (1993).
8. F. Kajzar, C. Taliani, R. Danieli, S. Rossini and R. Zamboni, *Chem. Phys. Lett.*, **4**, 418 (1994).
9. A. M. Rao, P. Zhou, K. -A. Wang, G. T. Hager, J. M. Holden, Y. Wang, W. -T. Lee, X. -X. Bi, P. C. Eklund, D. S. Cornett, M. A. Duncan and I. J. Amster, *Science*, **259**, 955 (1993).
10. A. M. Rao, K. -A. Wang, J. M. Holden, Y. Wang, P. Zhou, P. C. Eklund, C. C. Eloi and J. D. Robertson, *J. Mater. Res.*, **8**, 1 (1993).
11. B. P. Singh, P. N. Prasad and F. E. Karasz, *Polymer*, **29**, 1940 (1988).
12. N. S. Sariciftci, L. Smilowitz, A. J. Heeger and F. Wudl, *Science*, **258**, 1474 (1993).

Z-Scan Measurement of Third and Fifth Order Nonlinearities in Single Crystal PTS at 1064 nm

BRIAN L. LAWRENCE, MYOUNGSIK CHA, WILLIAM E. TORRUELLAS,
GEORGE I. STEGEMAN¹, SHAHAB ETEMAD² and GREGORY BAKER³

¹*CREOL, University of Central Florida, Orlando, FL 32826,*

²*Bell Communications Research, Red Bank, NJ 07701,*

³*Department of Chemistry, Michigan State University,
East Lansing, MI 48824*

Received 21 March 1994; accepted 22 March 1994

Z-scan at 1064 nm was used with single, 35 psec pulses to measure the third and fifth order nonlinear refraction and absorption in single crystal PTS (p-toluene sulfonate). Nonlinear effects higher than third order were found at intensities greater than 0.5 GW/cm². As a result detailed analysis of the Z-scan data was necessary to deduce n_2 and n_3 where $\Delta n = n_2 I + n_3 I^2$, and α_2 and α_3 defined by $\Delta \alpha = \alpha_2 I + \alpha_3 I^2$. At this wavelength both n_2 and α_2 were positive and n_3 and α_3 were found to be negative.

INTRODUCTION

PTS (poly[2,4-hexadiyne-1,6-diol-bis-p-toluene-sulfonate]) has been a “promising” third order nonlinear material since the early work of Sauteret and coworkers.¹ Using third harmonic generation with a fundamental wavelength of 2600 nm, they measured a very large third order susceptibility $\chi^{(3)}$ ($-3\omega; \omega, \omega, \omega$), albeit with very large uncertainties. Assuming that their experiment allowed a non-resonant value to be estimated, they deduced $n_2 \sim 2 \times 10^{-12}$ cm²/W with n_2 defined by $n = n_0 + n_2 I$ where n is the refractive index and I the intensity. (In fact, this value has turned out to be an excellent estimate to the value of the non-resonant $n_2 = (2.2 \pm 0.3) \times 10^{-12}$ cm²/W recently measured at 1600 nm.)² This early result focussed attention on conjugated polymers in general, and PTS in particular as promising material systems for large nonlinearities. It was realized at an early stage that the strong coupling to two photon states was both a potential problem due to two photon absorption as well as an important mechanism contributing to the very large nonlinearity. Large two photon absorption coefficients were measured in the 1970s in the near infrared, of order of 100s of cm/GW.³ Interest was revived in the 1980s when it was realized that such large nonlinearities could be used for waveguide switching devices. Although technically difficult, the fabrication of single crystal channel waveguides has been demonstrated.⁴ Multiple measurements of both the nonlinearity and two photon absorption coefficient were reported at 1064 nm by Thakur and coworkers.^{5–8} For single crystal PTS a range of very large values of n_2 has been measured at 1064 nm, specifically 3×10^{-11} cm²/W,⁵ 5.5×10^{-12} cm²/W,⁶ 1.1×10^{-12} cm²/W⁷ and 1.5×10^{-11} cm²/W.⁸ The spread is too

large to be attributed to approximations made in the different measurement techniques and probably implies variation in sample quality and preparation technique. Such large coefficients, if accompanied by sufficiently low linear and nonlinear losses, could make this material useful for all-optical applications. Although the linear loss has been demonstrated to be small, a range of two photon absorption coefficients α_2 (50 cm/GW to 120 cm/GW) has also been reported.^{3,7,8} As a result, the two photon figure of merit $T = 2\lambda\alpha_2/n_2$, which needs to be less than unity for useful applications, varies from 0.3 to 22.⁹ That is, it is not clear whether PTS is a useful nonlinear material or its response is dominated fully by two photon absorption at 1064 nm. This spectrum of values and the fact that n_2 and α_2 were frequently reported in different publications and hence potentially on different samples encouraged us to evaluate the two photon figure of merit on the same sample. Here we report single-pulse, picosecond, z-scan measurements on single crystal PTS which allow us to sort out the large uncertainty in the possible values of T , and hence to assess the potential of PTS for switching devices.

Z-Scan Technique with Higher Order Nonlinearities

The Z-scan technique is a proven, high resolution method for measuring the absolute value of the intensity-dependent refractive index and multi-photon absorption coefficient.¹⁰ The standard analysis of Z-scan results assumes $\alpha(I) = \alpha_1 + \alpha_2 I$ and $n(I) = n_1 + \Delta n(I) = n_1 + n_2 I$, where α_1 and n_1 are the linear (intensity-independent) absorption coefficient and refractive index, respectively. α_2 and n_2 are the nonlinear absorption coefficient and nonlinear refractive index associated with $\chi^{(3)}(-\omega; \omega, -\omega, \omega)$. Using these intensity-dependent coefficients, a Fresnel diffraction calculation can be performed for a high intensity beam focussed in the nonlinear medium.¹⁰ In the Z-scan technique gaussian input beams are commonly assumed so that the input intensity at the front surface of the sample can be written as:

$$I(z, r, t) = I_0 \frac{w_0}{w(z)} \exp\left(-\frac{2r^2}{w^2(z)} - t^2\right) \quad (1)$$

where $w^2(z) = w_0^2(1 + z^2/z_0^2)$ is the beam radius, $z_0 = \pi w_0^2/\lambda$ is the diffraction length of the beam, $z = 0$ is chosen operationally to be zero at the center of the sample and λ is the wavelength, all in free space. I_0 represents the on-axis, peak intensity at the focus where the beam has an effective waist w_0 .

Most Z-scan measurements are made in the "thin sample" approximation, that is the sample length $L < z_0$. Hence the intensity does not change significantly over the sample thickness due to diffraction.¹⁰ Under this assumption, the intensity and phase inside the material are given by the two equations:

$$\frac{dI}{dz'} = -\alpha(I)I \quad (2)$$

and

$$\frac{d\Delta\phi}{dz'} = \Delta n(I) \frac{2\pi}{\lambda} \quad (3)$$

where z' is the propagation distance in the sample, not the sample position, and $\Delta\phi$ is the cumulative nonlinear phase distortion. Equations (2) and (3) can be solved

numerically, assuming an input intensity of the form given in equation (1), to give the intensity and accumulated phase shift at the output facet of the crystal. The expression for the electric field at the output face of the sample may now be given by:

$$E_{\text{out}}(z, r, t) = \sqrt{\frac{2}{c\epsilon_0 n}} I_{\text{out}}(z, r, t) \exp\left(-\Delta\phi(r, t, z) - \frac{\pi r^2}{\lambda R(z)}\right) \quad (4)$$

where $I_{\text{out}}(z, r, t)$ is the output intensity obtained by solving equation (2), $\Delta\phi(z, r, t)$ is the nonlinear phase shift obtained by solving equation (3), and $R(z) = z(1 + z_0^2/z^2)$ is the radius of curvature of the wavefront. The electric field at the aperture may now be calculated by applying a zeroth-order Hankel transform to include the propagation from the sample to the aperture. This gives [11]:

$$E_{ap} = \frac{1}{j\lambda z_a} \exp\left(\frac{j\pi}{\lambda}\left(2z_a + \frac{r^2}{z_a}\right)\right) H_0 \left[E_{\text{out}} \exp\left(\frac{j\pi r^2}{\lambda z_a}\right) \right]_{\rho = \frac{r}{\lambda z_a}} \quad (5)$$

where z_a is the distance from the output face of the sample to the aperture and H_0 represents a zeroth-order Hankel transform. The power transmitted through the aperture is calculated by integrating the E_{ap} over the aperture area, assuming an aperture radius of r_a , giving:

$$P_T(t) = c\epsilon_0 n_0 \pi \int_0^{r_a} |E_{ap}(z, r, t)|^2 r dr \quad (6)$$

where ϵ_0 is the permittivity of free space. Finally, the transmittance is obtained by integrating over the temporal pulse shape, and normalizing to the input energy:

$$T(z) = \frac{\int_{-\infty}^{\infty} P_T(t) dt}{S \int_{-\infty}^{\infty} P_i(t) dt} \quad (7)$$

where $P_i = \pi w_0^2 I_0(t)/2$ is the peak input power in the sample, and $S = 1 - \exp(-2r_a^2/w_a^2)$ is the linear transmittance of the aperture (w_a is the undistorted beam radius at the aperture). As shown by the Van Stryland group at CREOL, measurements of this transmittance as a function of sample position for both small and open apertures allow n_2 and α_2 to be evaluated.

This analysis is not sufficient for finding n_2 and α_2 in two cases. One, if the sample is not "thin" and a detailed calculation of the beam evolution through the sample is needed. Second, if there are higher order nonlinear effects present it is necessary to introduce additional terms, for example of the form $\Delta n(I) \propto n_3 I^2$ and $\Delta \alpha(I) \propto \alpha_3 I^2$ for instantaneous (relative to the pulse width) nonlinearities. This is frequently the case for organic molecular systems in which many one and two photon states can contribute to the large nonlinearity. Good examples are π -conjugated polymers, such as PTS, which have become increasingly important, either through improved nonlinear optical response, or improved sample quality. In such systems, the higher order nonlinear effects may no longer be negligible, and must be accounted for. Similar effects have been seen in semiconductors, where they have been attributed to free carrier generation; the manifestation of these higher-order nonlinearities in the z-scan technique has been extensively studied.¹² Therefore, we must include these effects in the analysis and understand the ramifications of adding higher-order intensity dependencies on the Z-scan technique.

We limit the inclusion of the additional nonlinearities in our case to apparent $\chi^{(5)}$ effects: The quality of our data, i.e., signal to noise, does not merit inclusion of yet even higher order effects. Due to the general nature of Eqns. 1–3, adding the fifth-order effects is a reasonable task. In fact, we may include these by assuming $\Delta n(I) = n_2 I + n_3 I^2$ for the intensity-dependent refractive index, and similarly $\Delta \alpha(I) = \alpha_2 I + \alpha_3 I^2$ for the nonlinear absorption. In order to maintain suitable conditions under which the usual slowly varying envelope approximation should still be valid, we found that we had to solve equations (2) and (3) with smaller distance increments to avoid large spurious phase distortions. Nevertheless, the propagation and integration methods are still valid.

Inclusion of the fifth-order nonlinearity has serious implications for the appearance and analysis of Z-scan data. Previous inclusion of fifth-order nonlinear effects has been performed where such effects were assumed to originate from free-carrier scattering in semiconductors. That effect primarily contributed to nonlinear refraction via an appropriate cross-section, σ , and no additional nonlinear absorption terms were added.¹² In this paper, we take a slightly more general approach in which we do not assume any specific mechanism for the higher-order nonlinearity, and instead use coefficients to reflect both the higher-order, intensity-dependent refractive index and absorption.

In order to more clearly understand the manifestations of fifth order effects, we will discuss the absorption and refraction separately at first, saving the complex case of including both effects simultaneously for later. Assuming $\alpha_2 > 0$, there are primarily two interesting cases of nonlinear absorption; one where α_3 is positive and the other where it is negative. Under low-intensity irradiation, the higher-order effects are negligible relative to the usual two photon absorption. With high-intensity illumination, the higher-order effects can dominate.

First we consider the case of positive α_3 . This case can occur for excited state absorption by an excited state population generated by two photon absorption. If α_3 can be neglected, the width of the open aperture Z-scan curve is given primarily by the input beam waist and does not depend on α_2 . However, when the α_3 term also contributes significantly to the absorption, the observed Z-scan minimum is deeper than for $\alpha_3 = 0$ and the curves become progressively narrower with increasing input intensity. Simulated examples are shown in Figures 1 and 2. (Note that in the simulations discussed in this paper we assumed $\alpha_2 = 60 \text{ cm/GW}$, $\alpha_3 = \pm 20 \text{ cm}^3/\text{GW}^2$, $n_2 = 5 \times 10^{-4} \text{ cm}^2/\text{GW}$ and $n_3 = \pm 5 \times 10^{-4} \text{ cm}^4/\text{GW}^2$.) This behavior cannot be correctly modelled by assuming an effective α_2 , $\alpha_{2\text{eff}}$, defined by

$$\alpha_{2\text{eff}} = \alpha_2 + \alpha_3 I_0 \quad (8)$$

where, for example, $I_0 = I_p/2$ and I_p is the peak, on-axis intensity. Such a definition has the appropriate desired result for multiphoton absorption in the sense that the net intensity-dependent absorption increases, i.e., the value of $\alpha_{2\text{eff}}$ obtained from Eqn. 8 also increases as the intensity increases. However, a more complete analysis shows that the width of the Z-scan curve decreases (see Figs. 1 and 2 for simulations), as observed experimentally, and to compensate for this narrowing, the beam waist needs to be reduced in the $\alpha_{2\text{eff}}$ -based analysis. This is, of course, incorrect since the input beam size has not changed for a very thin sample. As a result, for sufficiently large

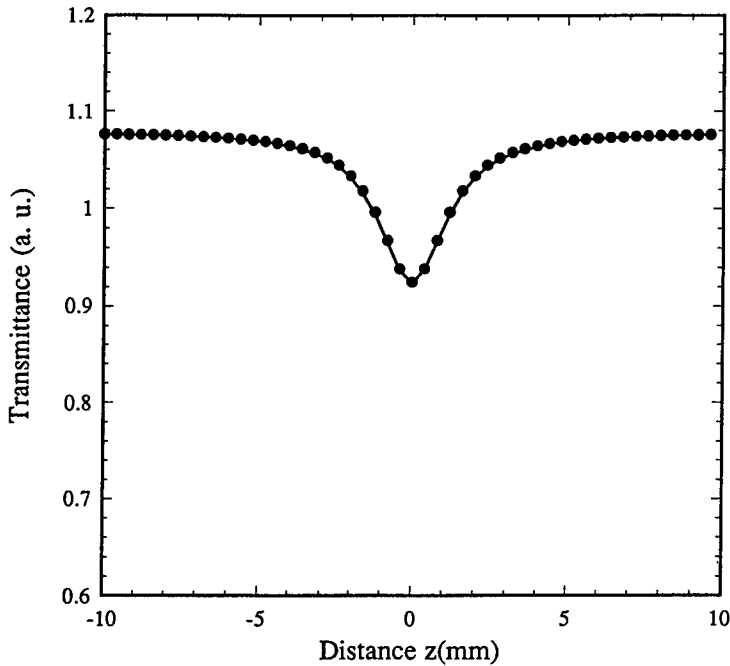


FIGURE 1 Simulated low intensity Z-scan curves for positive α_2 and α_3 ($I_p = 0.4 \text{ GW/cm}^2$). The circles show the calculated curve using $\alpha_{2\text{eff}}$ and the solid line shows the curve calculated using both α_2 and α_3 .

intensities and/or large α_3 , Eqn. 8 is not a useful approximation and the Z-scan calculation must specifically include the higher-order contribution to the absorption, $\alpha_3 I^2$.

Similar effects occur for the case of negative α_3 . This is potentially a much more interesting case for which the physical origin is currently under investigation. As the intensity is increased, the higher-order effects first lead to a reduction in the effective nonlinear absorption coefficient. Modelling this effect simply as $\alpha_{2\text{eff}} = \alpha_2 + \alpha_3 I_0$ is again inadequate and leads to a consequent effective widening of the beam waist when an α_2 based Z-scan analysis is performed. At high intensities, the broadening of the Z-scan curve continues, and is accompanied by a flattening of the transmission curve at the peak absorption value, as shown in Figures 3 and 4. Again it is clear that the higher order absorption terms must be included consistently in the analysis.

We turn now to a discussion of the effects of higher order nonlinearities on nonlinear refraction as measured by the Z-scan technique. The distortion from the usual Z-scan curves can be quite dramatic, especially for the case when n_2 and n_3 are opposite in sign. Here we consider only the case of positive n_2 because it is relevant to our experiments. As in the preceding discussion, we treat separately the two cases of positive n_3 and negative n_3 . (The effects of n_3 on a negative n_2 material are analogous, but simply reversed in sign.) Third-order effects dominate in the presence of low-intensity light and as the intensity is increased, the higher-order effects appear. For a positive n_3 material (with $n_2 > 0$) we can again test whether assuming that n_3 effects can be approximated by

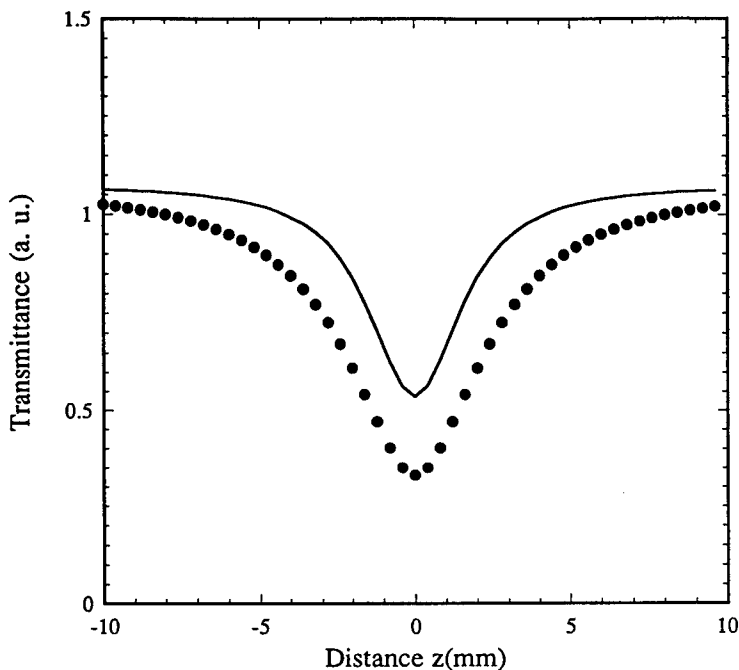


FIGURE 2 Simulated high intensity Z-scan curves for positive α_2 and α_3 ($I_p = 5 \text{ GW/cm}^2$). The circles show the calculated curve using $\alpha_{2\text{eff}}$ and the solid line represents the curve calculated using α_2 and α_3 .

an effective $n_{2\text{eff}}$ is useful where

$$n_{2\text{eff}} = n_2 + n_3 I_0. \quad (9)$$

The true Z-scan curve is significantly narrower and the peak to valley transmission change increased when compared to the same curve obtained from a purely n_2 type of response. Although the value of $n_{2\text{eff}}$ evaluated from Eqn. 9 does indeed increase with increasing intensity, the beam waist needs to be erroneously decreased to accurately fit the data.

The case of a material with a negative n_3 (with $n_2 > 0$) is more interesting. As the intensity is increased, the nonlinear index change can actually change sign at high enough input intensities. As shown in the simulation in Figure 5, dramatic changes can occur in the Z-scan curves, leading in some cases to erroneous conclusions about not just the magnitude but even the sign of the nonlinearity being measured, as well as the presence or absence of higher order effects. In general, the higher-order effects first lead to a broadening of the Z-scan curve, and a reduction in the peak to valley transmission change. As a result, the $n_{2\text{eff}}$ (Eqn. 9) is reduced while the beam waist is apparently (but erroneously) increased. However, as the intensity reaches a point at which the higher-order effects truly dominate, the fifth-order effects totally distort the shape of the Z-scan curve, again see Figure 5. In some cases the experimental Z-scan curves have the appearance of a typical Z-scan with strong two photon absorption and a nonlinearity n_2 of opposite sign to that actually used in the simulation. Thus calculations based on

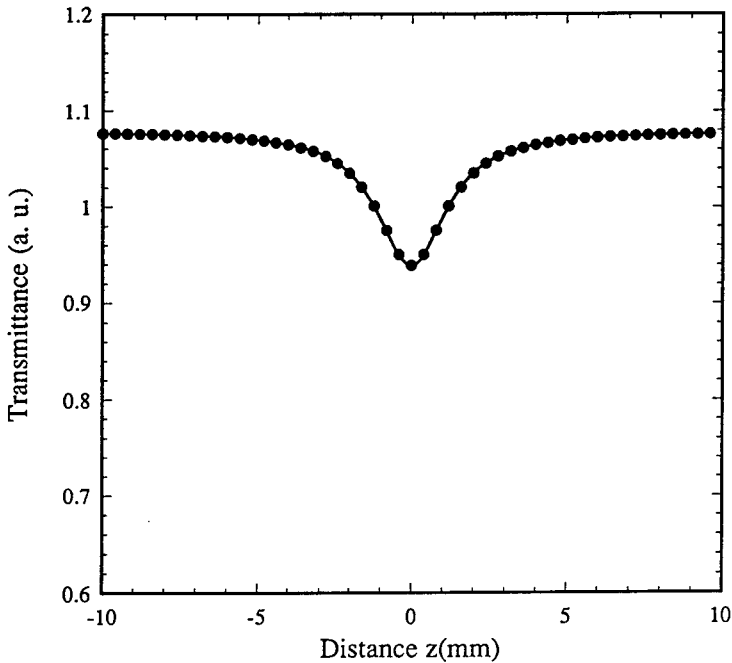


FIGURE 3 Simulated low intensity Z-scan curve for positive α_2 and negative α_3 ($I_p = 0.4 \text{ GW/cm}^2$). The circles are based on $\alpha_{2\text{eff}}$ and the solid line on including both α_2 and α_3 in the calculation.

only a n_2 (and α_2) to fit the Z-scan curves result in a nonlinear refractive index that has a changed sign, and a substantially reduced beam width. In fact, the observation of a reduction in effective beam width in a Z-scan experiment is correlated with the need to include higher-order effects in the analysis.

Finally, we deal with the more complex issue of including both the higher-order absorption and refraction in the Z-scan technique, our experimental situation. A detailed description of these effects is not possible due to the variety of effects that can occur, especially when $T > 1$. Put very simply, at high intensities the Z-scan curve can show practically no resemblance to the standard shape normally observed for open or closed aperture scans. Furthermore, inclusion of the fifth-order effects also complicates the material characterization in the sense that there are additional fitting parameters which need to be evaluated, i.e., n_3 and α_3 in addition to n_2 and α_2 . Namely, in order to accurately characterize the nonlinear properties of a material using the Z-scan technique, a series of both opened and closed aperture scans are necessary for different peak input intensities.

EXPERIMENTS ON PTS

The single crystal PTS samples were grown from saturated acetone solution and thermally polymerized in vacuum. The platelets varied in thickness from 0.1 to a few

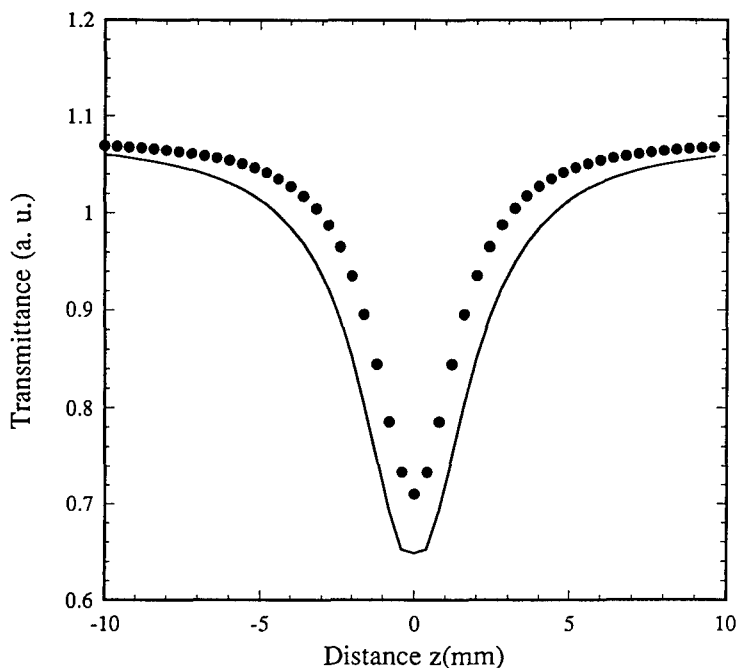


FIGURE 4 Simulated high intensity Z-scan curve for positive α_2 and negative α_3 ($I_p = 3 \text{ GW/cm}^2$). The circles are based on $\alpha_{2\text{eff}}$ and the solid line on including both α_2 and α_3 in the calculation.

millimeters, with several millimeters of cross-section. In general the interior of such crystals contains flaws and cracks and it was necessary to search over the surface of many samples to find those with small enough stray scattering to obtain good z-scan data. For such samples, no stray light correction was required or performed. The orientation of the nonlinear axis was verified by measuring the polarized transmission, i.e., maximum absorption occurs along the axis associated with the conjugation direction. By comparing the linear transmission of two perpendicular polarizations we concluded that most of the transmission losses were due to absorption along the polymer backbone, and not due to scattering.

We performed a series of both opened and closed aperture Z-scans on these PTS crystals with different input peak intensities. A minimum intensity of 400 MW/cm^2 was needed in order to obtain a useful Z-scan with our mode locked and Q-switched Nd:YAG laser operating at a 10 Hz with 35 ± 5 picosecond pulses. The spatial profile for successful Z-scan measurements is critical and our laser output was first spatially filtered in air through a $25 \mu\text{m}$ diameter pinhole and then collimated, with special care taken to avoid introducing additional aberrations to the phase front. A 10 cm focal length lens focussed 0.2 to $2 \mu\text{J}$ of the 1064 nm radiation into a $20 \mu\text{m}$ spot on a single crystal PTS sample $210 \mu\text{m}$ thick as measured by a digital micrometer. The optical damage threshold was estimated experimentally to be $\geq 25 \text{ GW/cm}^2$ at our wavelength (1064 nm) and pulse widths (35 psec). In other experiments we found the damage threshold to vary with wavelength and pulse width.

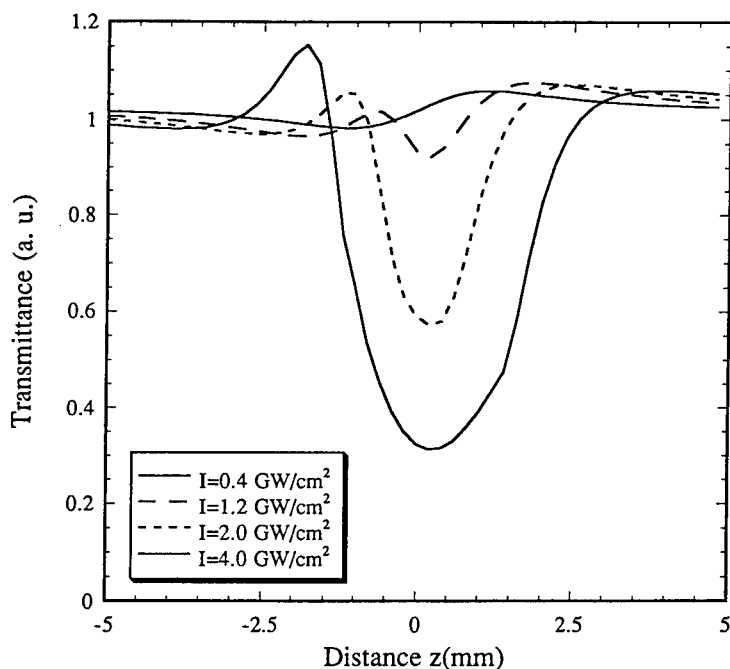


FIGURE 5 Simulated Z-scan curves for positive n_2 and negative n_3 at four different intensities. The curve with the smallest peak-to-valley transmission change resembles the usual Z-scan curve. At higher intensities, the curve no longer resembles the standard case, until finally at the highest intensity shown it resembles a Z-scan with a different sign for n_2 and significant nonlinear absorption, although none was assumed in the simulation.

Typical Z-scan results obtained at two different peak input intensities, one high and one low, are shown in Figure 6 for incident light polarization along the conjugation axis. We explicitly verified that no nonlinear effects were observed with Z-scan for orthogonally polarized light. As usual, the open aperture Z-scan was used to deduce both the multi-photon absorption coefficients, as well as the laser beam parameters such as the beam waist (low-intensity data only) and the position of the focus. These parameters were needed to consistently fit the closed aperture Z-scan results. Because of the large transmission changes due to both the strong multi-photon absorption and large nonlinear phase shifts, a full Z-scan diffraction calculation had to be performed to extract useful information. The methodology, both experimental and numerical, was verified by calibration measurements on CS_2 for which values of n_2 are known, giving comparable results to those of VanStryland within $\pm 30\%$. This experiment was also used to fix w_0 . An additional check was performed on experimental alignment, namely that data was retained only when low intensity ($< 50 \text{ MW/cm}^2$) scans gave no observable change on transmission for both the open and closed aperture cases. Because of recently reported conflicting Z-scan data, the experimental procedure, including intensity scans, was reproduced 3 times on two different samples to establish sample and measurement reproducibility.⁸

It is in principle possible to deduce all of the nonlinear parameters from a single closed and open aperture Z-scan experiment. This would require a perfectly characterized input beam, including both the amplitude and phase fronts, as well as excellent signal-to-noise characteristics. The approach we chose was to perform a series of experiments with different input intensities. The goal was to produce a self-consistent set of values for both the nonlinear coefficients as well as the optical beam parameters. Because multiple sets of data are used which essentially contain the same information, an iterative procedure is needed to efficiently converge to the appropriate nonlinear parameters. We first fit the high and low intensity open aperture data until the calculations converged to a set of material and experimental parameters. Then the fits to the intermediate intensity data were checked for consistency and we found only minor changes were needed in the parameters α_2 and α_3 . This analysis is also useful for confirming the beam waist w_0 obtained from the CS_2 calibration discussed earlier, vital to analyzing the closed aperture scans. The closed aperture data was fit in the same manner, i.e., starting with the highest and lowest intensity scans and then fine-tuning and checking for consistency with the intermediate intensity data. Examples of the resulting fits at low and high intensities are shown in Figures 6. This extended

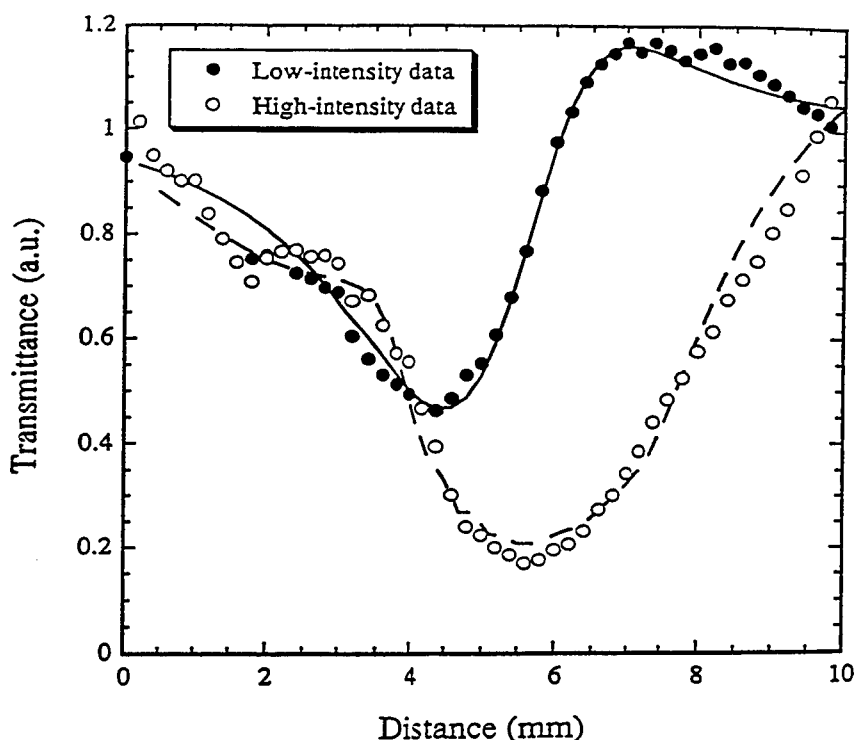


FIGURE 6 Nonlinear transmission for an aperture $S = 0.5$. The filled circles indicate low-intensity data (focussing, $I = 0.9 \text{ GW/cm}^2$), and the open circles indicate high-intensity data (defocussing, $I = 9 \text{ GW/cm}^2$). Note the shifts from the center position of the two minima as well as the sharp slope changing sign. In both cases the curves show an effect dominated by two photon absorption.

calculation gave $n_2 = 5(\pm 1) \times 10^{-3} \text{ cm}^2/\text{GW}$, $n_3 = -5(\pm 1) \times 10^{-3} \text{ cm}^4/\text{GW}^2$, $\alpha_2 = 100(\pm 20) \text{ cm/GW}$ and $\alpha_3 = -5(\pm 1) \text{ cm}^3/\text{GW}^2$. The uncertainties reflect the iterative fit to all of the data as well as uncertainties in the experimental parameters.

DISCUSSION

It is interesting to compare the actual values of $\Delta n = n_2 I + n_3 I^2$ obtained from the detailed analysis to those obtained by forcing a fit to the individual Z-scan with just a single value for the n_2 at each peak input intensity, i.e., using an $n_{2\text{eff}}$ approach. The latter result is shown in Figure 7. From this graph one might conclude that an intensity of 10 GW/cm^2 (pulsed input) is required for the nonlinearity to change sign. Based on the more detailed analysis of the data, the effect of the higher order nonlinearity is to reverse the sign of the nonlinear index change at a cw intensity of only 1 GW/cm^2 ! This shows the necessity of the detailed analysis to make useful predictions for intensities at which the contributions from both nonlinear terms are comparable. Note, however, if only n_2 is required, it is estimated quite well by the zero intensity intercept in Figure 7.

Our values for n_2 and α_2 compare well with some of the measurements reported in the literature. For example, our n_2 of $5 \times 10^{-12} \text{ cm}^2/\text{W}$ compares well with that reported in reference 6 ($n_2 = 5.5 \times 10^{-12} \text{ cm}^2/\text{W}$), obtained by using a modified Sagnac

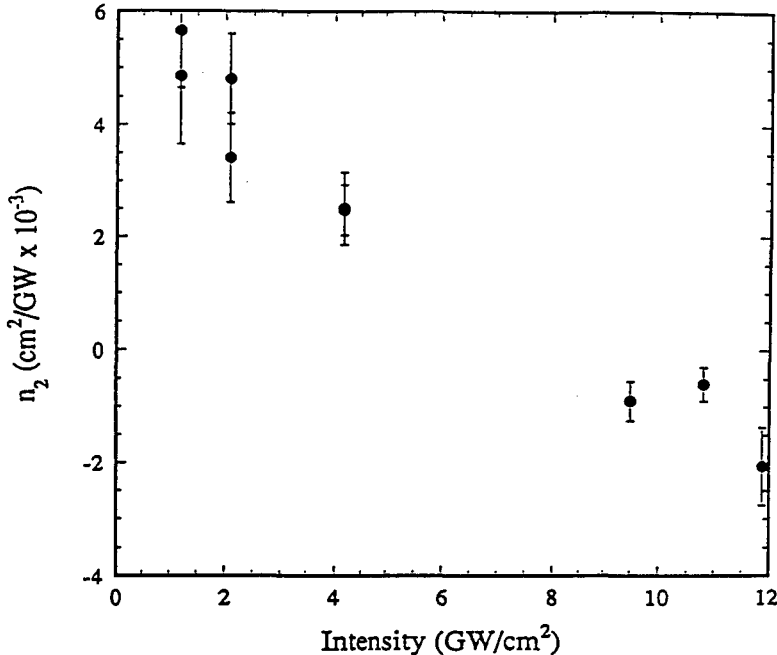


FIGURE 7 Variation of the effective nonlinear refractive index coefficient n_2 as a function of the intensity, as measured with 35 psec pulses at 1064 nm from a 10 Hz Nd:YAG laser. The analysis used assumed $\Delta n = n_2 I$.

ring interferometer in which any slow thermal effects are avoided by design. In our experiments thermal effects are minimized by virtue of the low repetition rate and short duration of the pulses employed. For α_2 our value 100 cm/GW agrees well with the value of 120 cm/GW reported in reference 13. The uncertainty in our measured value α_2 is probably due to thickness variations in PTS known to occur because of its laminar (stratified) structure. Repeated measurements performed on the same or a nearby spot were repeatable to $\pm 15\%$, verifying the technique's reproducibility.

One of the key results of this study is that higher order effects are not only present but are important in PTS. Similar higher order effects have been observed previously in other diacetylenes similar to PTS, for example also at 1064 nm in the red form of poly-4BCMU in solution using degenerate four wave mixing.¹³ In that case, increasing the intensity led to an increase in $n_2(I)$ from a negative to a positive value, the opposite to PTS, and to an increase in the two photon absorption coefficient, again opposite to the PTS case. Some of the features were interpreted in terms of a Stark shift and saturation of the two photon level which was modelled to occur at a lower energy than the energy of the two photons being absorbed. In our case, there are multiple two photon states with the energy of the two photons being absorbed lying between two neighboring two photon states located at 2.05 and 2.7 eV. Using those two-photon states, in addition to the one photon excited state at 2 eV, in Charra's and Nunzi's model could explain qualitatively the effects described here.¹³ The interpretation in reference 13 also included contributions from excited species in a three level model. Clearly the origin of these intensity dependencies merits further investigation which will require lasers with different pulse widths.

There are two figures of merit used to assess the suitability of a nonlinear material for all-optical switching devices.¹⁴ If linear absorption dominates the loss, $W = \Delta n / \alpha \lambda > 1$ is needed. Here $W > 1$ for $I > 22 \text{ MW/cm}^2$, based on the attenuation coefficients reported in reference 15. When two photon absorption (α_2) dominates the loss, $T = 2\alpha_2 \lambda / |n_2|$ should be less than unity. For PTS, $T > 3$ at 1064 nm. Therefore we conclude that PTS is marginal for all-optical applications at 1064 nm. Note, however, that recent results show that PTS is ideally suited for all-optical switching at 1600 nm.²

In conclusion we have investigated the complex nonlinear refractive index of PTS at 1064 nm. We found that higher order effects were very important, requiring measurements over a range of input intensities and a detailed non-standard analysis of the Z-scan data in order to obtain the nonlinear parameters. This higher-order intensity dependence led to extended calculations including $n_3 I^2$ and $\alpha_3 I^2$ terms. In fact we found the higher order effects to be so strong that the nonlinear index change actually changed sign at intensities of order 1 GW/cm^2 , perhaps explaining the large range of values reported for n_2 . As a result single intensity scans for material systems with higher-order nonlinear effects are no longer sufficient.

ACKNOWLEDGEMENT

The CREOL research was supported by AFOSR (91-0339). We gratefully acknowledge the help of Eric Van Stryland's group in implementing and understanding the details of the Z-scan technique.

REFERENCES

1. C. Sauteret, J. P. Hermann, R. Frey, F. Pradere, J. Ducuing, R. H. Baughman and R. R. Chance, *Phys. Rev. Lett.*, **36**, 956 (1976).
2. B. Lawrence, M. Cha, J. U. Kang, W. Torruellas, G. I. Stegeman, G. Baker, J. Meth and S. Etemad, "Large Purely Refractive Nonlinear Index of Single Crystal P-Toluene Sulfonate (PTS) at 1600 nm", *Electron Lett.*, in press.
3. M. Lequime and J. P. Hermann, *J. Chemical Physics*, **26**, 431 (1977).
4. M. Thakur, B. Verbeek, G. C. Chi and K. J. O'Brien, *Mat. Res. Soc. Symp. Proceeding*, **109**, 41 (1988).
5. D. M. Krol and M. Thakur, *Appl. Phys. Lett.*, **56**, 1406 (1990).
6. M. C. Gabriel, N. A. Whitaker, C. W. Dirk, M. G. Kuzyk and M. Thakur, *Opt. Lett.*, **16**, 1334 (1991).
7. S.-T. Ho, M. Thakur and A. LaPorta, ' $\chi^{(3)}$ measurement of PTS polydiacetylene waveguides at 1.06 μm using single beam nearly degenerate forward four-wave mixing', Digest of International Quantum Electronics Conference 1990, paper QTUB5, vol.8, (*Optical Society of America*, Washington DC 1990), pp. 40-42.
8. M. Thakur and R. Quintero-Torres, Technical Digest of ACS/OSA Topical Meeting on Organic Thin Films for Photonic Applications, (*Opt. Soc. Am.*, Washington, 1993), pp. 215-18.
9. V. Mizrahi, K. W. DeLong, G. I. Stegeman, M. A. Saifi and M. J. Andrejco, *Opt. Lett.*, **14**, 1140 (1989).
10. M. Sheik-Bahae, A. A. Said, T.-H. Wei, D. J. Hagan, E. W. Van Stryland, *IEEE J. Quantum Electron.*, **26**, (1990).
11. J. Gaskill, *Linear Systems, Fourier Transforms and Optics*, (J. Wiley & Sons, New York, 1978), pp. 349-68.
12. A. A. Said, M. Sheik-Bahae, D. J. Hagan, T. H. Wei, J. Wang, J. Young and E. W. VanStryland, *J. Opt. Soc. Am. B*, **8**, 405 (1992).
13. J. M. Nunzi and F. Charra, *Nonlinear Optics*, **1**, 19 (1991).
14. G. I. Stegeman and E. M. Wright, *J. Optical and Quant. Electron.*, **22**, 95 (1990).
15. M. Thakur, R. C. Frye and B. I. Greene, *Appl. Phys. Lett.*, **56**, 1187 (1990).

Mechanism of Optical Nonlinearity of Conjugated Polymers

TAKAYOSHI KOBAYASHI

*Department of Physics, Faculty of Science, University of Tokyo,
Hongo 7-3-1, Bunkyo-ku, Tokyo 113, Japan*

Received 12 January 1994; accepted 12 March 1994

Ultrafast nonlinear optical responses in conjugated polymers are investigated by femtosecond transient spectroscopy. Absorbance changes due to “instantaneous” processes which decay within the pulse duration of 100 fs, self-trapped exciton, and triplet exciton are resolved in time. The spectra of the corresponding nonlinear optical susceptibilities are obtained by considering the pulse duration and response times. The “instantaneous” nonlinear optical response consists of several nonlinear effects, i.e., hole burning, coherent coupling between pump polarization and probe field, Raman gain, inverse Raman scattering, and induced-phase modulation.

INTRODUCTION

Conjugated polymers have been extensively investigated both experimentally and theoretically as model compounds of one-dimensional electronic systems. Recently, their large and ultrafast optical nonlinearities have attracted great interest as candidate materials to be applied in nonlinear optical devices.^{1,2}

Nonlinear optical responses in PDA's have been studied by time-resolved nonlinear spectroscopies, i.e., degenerate four-wave mixing,^{3,4} coherent-Raman scattering,⁵ inverse Raman spectroscopy,⁶ optical Kerr effect,^{7,8} the Raman-induced Kerr effect,⁹ and absorption saturation.^{10–12} However, these works measured only a few wavelengths or near the exciton resonance (1.8–2.2 eV). The nonlinear optical responses in the whole visible and near-infrared region (1.1–3.0 eV) have been investigated by femtosecond pump-probe spectroscopy and several ultrafast nonlinear optical effects, i.e., coherent coupling between pump polarization and probe field, Raman gain, inverse Raman scattering, induced-phase modulation, and perturbed free-induction decay, have been observed.^{13–15}

In this paper, the ultrafast nonlinear optical response and relaxation kinetics in blue-phase PDA-3BCMU (3-butoxycarbonyl methylurethane) epitaxially grown on a KCl substrate have been investigated by femtosecond absorption spectroscopy. The transient absorbance changes are time-resolved in the wide spectral region extending from 1.2 to 2.8 eV. The spectral changes were attributed to four components with different time responses. They are “instantaneous” processes, free excitons, STE's, and triplet excitons. The corresponding nonlinear optical susceptibilities of these components are estimated by considering the pulse duration and response times of the nonlinear processes. The spectrum of the “instantaneous” response can be explained by

a model including the coupling between excitons and vibrational modes. Several nonlinear optical effects, such as hole burning, coherent coupling, and Raman processes, are observed. The relaxation processes of photogenerated excitons in epitaxially grown PDA-3BCMU are compared with those in PDA-3BCMU cast film.

EXPERIMENT

The femtosecond absorption spectroscopy was done using an amplified colliding-pulse mode-locked dye laser (628 nm (1.97 eV), about 100 fs). In this study, the diacetylene monomers were epitaxially grown on a single crystal of KCL[001] surface cleaved in air and heated at 150°C for 30 min in a vacuum chamber before deposition, and polymerized using UV light.

DECAY DYNAMICS OF EXCITONS

The photoinduced absorption spectra of PDA-3BCMU of 0.13 μm thickness at 290 K are shown in Figure 1 together with the stationary absorption and pump spectra. The

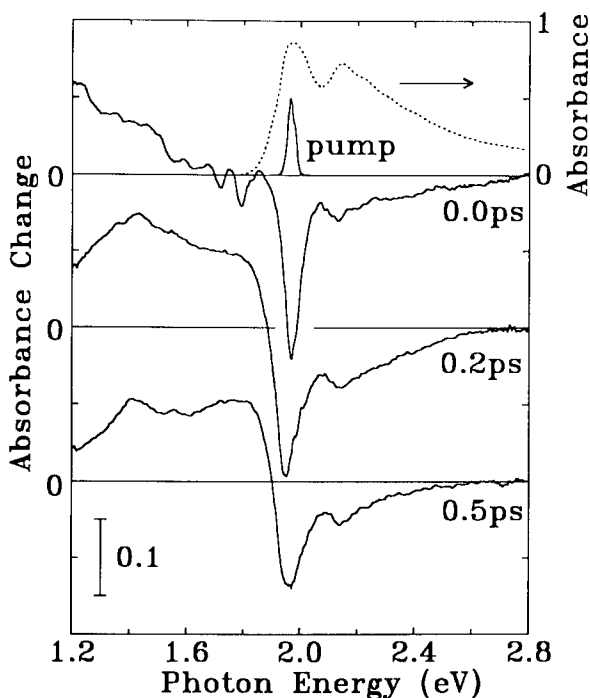


FIGURE 1 Transient absorption spectra of blue-phase PDA-3BCMU on the KCl substrate at 290 K. The stationary absorption (dotted curve) and pump spectra are shown together.

time dependencies at various probe photon energy are fitted to

$$\Delta A(t) = \Delta A_0 \delta(t) + \Delta A_f \exp(-t/\tau_f) + \Delta A_s \{\exp(-t/\tau_s) - \exp(-t/\tau_f)\} + \Delta A_c, \quad (1)$$

where the first term is the term which responds within pulse duration and ΔA_f corresponds to the absorbance change due to nonthermal (self-trapped exciton) STEs. When the time constant τ_f is fixed to 150 fs in Figure 2, the time constant τ_s is obtained as 1.4 ± 0.1 ps. This is consistent with the decay time constant obtained at 1.84 eV.

NONLINEAR OPTICAL RESPONSES DUE TO EXCITONS

The imaginary part of the nonlinear susceptibility due to the instantaneous processes is estimated and shown in Figure 3. Here, the transmittance change due to IPM is corrected in the ΔA_0 spectrum. The spectrum has two negative minima at 1.71 and 1.79 eV, and small dispersion type structures at 2.15 and 2.23 eV. These structures can be explained by calculating $\chi^{(3)}$ using a model shown in Figure 3. Here, zero-phonon ($v=0$) and one-phonon ($v=1$) states of major four vibrational modes are taken into consideration in both exciton (S_1) and ground level (S_0). Among six levels only the ground vibrational level ($v=0$) in the ground electronic state (S_0) is populated. Since the spectral bandwidth of the pump pulse (0.03 eV) is much smaller than the phonon

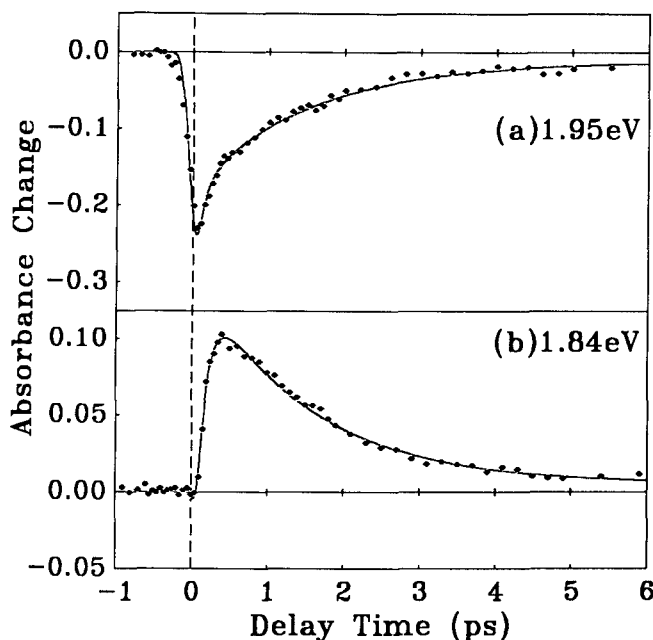


FIGURE 2 Time dependence of absorbance changes at (a) 1.95 eV and (b) 1.84 eV. Solid curves are the best fit of Eqs. (1) to the data at 1.95 and 1.84 eV, respectively. The time constants τ_f and τ_s are (a) 150 fs and 1.4 ps and (b) 150 fs and 1.5 ps, respectively. The resolution times at 1.95 and 1.84 eV are obtained by a cross-correlation method as 200 and 150 fs, respectively.

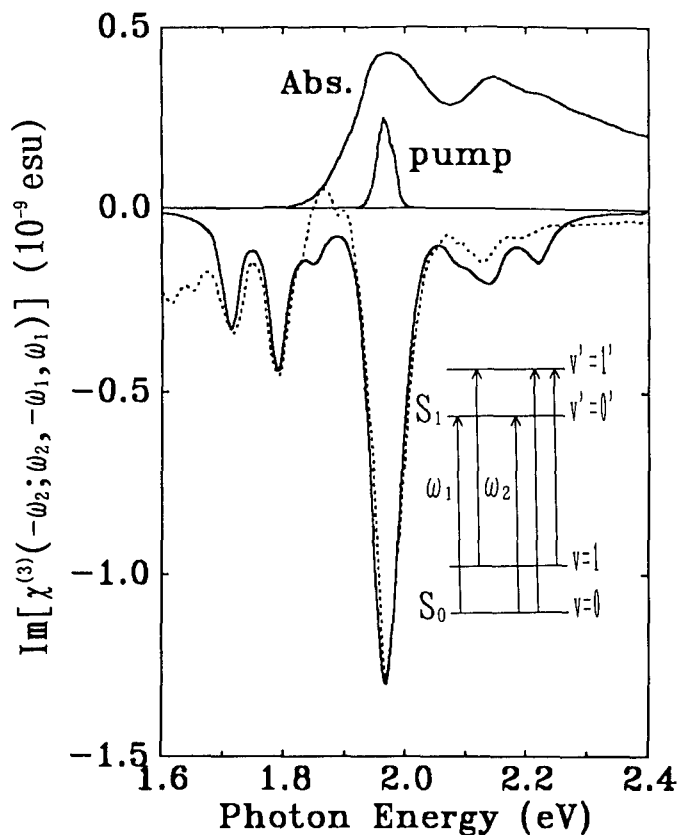


FIGURE 3 The total calculated nonlinear susceptibilities (solid curve) and the observed nonlinear susceptibility of the "instantaneous" processes (dotted curve). The stationary absorption and pump spectra are shown together.

energies (0.11–0.26 eV) and the 1.97 eV pump pulse (ω_1) is resonant with the 0–0' and 1–1' transitions, the pump resonances with the 0–1' and 1–0' transitions are neglected. The nonlinear susceptibilities of three probe resonant transitions (0–0', 1–0' and, 0–1') are calculated using two-level and three-level density matrix models.

$\chi^{(3)}$ corresponding to the 0–0' exciton transitions is calculated using a two-level model and given by

$$\chi_{00'}^{(3)} = \frac{|\mu_{00'}|^4}{\hbar^3} \left\{ \frac{4\Gamma_x/\gamma_x}{[(\omega_1 - \omega_x)^2 + \Gamma_x^2](\omega_2 - \omega_x + i\Gamma_x)} \right. \quad (2a)$$

$$+ \frac{2}{(\omega_1 - \omega_x - i\Gamma_x)(\omega_2 - \omega_x + i\Gamma_x)(\omega_2 - \omega_1 + i\gamma_x)} \quad (2b)$$

$$\left. - \frac{2}{(\omega_2 - \omega_x + i\Gamma_x)^2(\omega_2 - \omega_1 + i\gamma_x)} \right\}, \quad (2c)$$

where ω_1 and ω_2 are the frequencies of the pump and probe fields, respectively, and $\mu_{00'}$, ω_x , Γ_x , and γ_x are the dipole moment, the transition frequency, the transverse relaxation rate, and the longitudinal relaxation rate of the exciton, respectively.

$\chi^{(3)}$ corresponding to the 1-0' transition is calculated using a three-level model as

$$\chi_{10'}^{(3)} = \frac{|\mu_{00'}|^2 |\mu_{10'}|^2}{\hbar^3} \left\{ \frac{2\Gamma_x/\gamma_x}{[(\omega_1 - \omega_x)^2 + \Gamma_x^2](\omega_2 - \omega_x + \omega_i + i\Gamma_x)} \right. \quad (3a)$$

$$\left. + \frac{1}{(\omega_1 - \omega_x - i\Gamma_x)(\omega_2 - \omega_x + \omega_i + i\Gamma_x)(\omega_2 - \omega_1 + \omega_i + i\Gamma_i)} \right\}, \quad (3b)$$

where $\mu_{10'}$ is the dipole moment of the 1-0' transition and ω_i and Γ_i^{-1} are the frequency and the decay rate of each phonon modes, respectively.

Since the pump pulse is resonant with both the 0-0' and 1-1' transition, the nonlinear susceptibility for the 0-1' transition is rather complicated and obtained as

$$\chi_{01'}^{(3)} = \frac{|\mu_{00'}|^2 |\mu_{01'}|^2}{\hbar^3} \left\{ \frac{2\Gamma_x/\gamma_x}{[(\omega_1 - \omega_x)^2 + \Gamma_x^2](\omega_2 - \omega_x + \omega_i + i\Gamma_x)} \right. \quad (4a)$$

$$+ \frac{1}{(\omega_1 - \omega_x - i\Gamma_x)(\omega_2 - \omega_x - \omega_i + i\Gamma_x)(\omega_2 - \omega_1 - \omega_i + i\Gamma_x)} \quad (4b)$$

$$\left. - \frac{1}{(\omega_2 - \omega_x - \omega_i + i\Gamma_x)^2(\omega_2 - \omega_1 - \omega_i + i\Gamma_i)} \right\} \quad (4c)$$

$$- \frac{|\mu_{11'}|^2 |\mu_{01'}|^2}{\hbar^3} \frac{1}{(\omega_2 - \omega_x - \omega_i + i\Gamma_x)^2(\omega_2 - \omega_1 - \omega_i + i\Gamma_i)} \quad (4d)$$

where $\mu_{11'}$ and $\mu_{01'}$ are the dipole moments of the 1-1' and 0-1' transitions, respectively. The common level of the transition in the terms (4a)–(4c) is the ground level (S_{00}), while the common level of the term (4d) is the excited level (S_{11}).

The imaginary parts of each term and the total of the calculated nonlinear susceptibilities are shown in Figures 4 and 3 with the observed spectrum. Here, the phonon energies of the C=C and C≡C stretching vibrational modes are determined from the observed Raman gain signal as 0.180 eV and 0.257 eV, respectively. The observed pump spectrum is also used for the calculation, respectively. The reported values of PDA-TS are used for the cross sections of each transition and $\Gamma_i = 0.003$ eV.¹⁶ The relaxation rates Γ_x and γ_x and the width of the inhomogeneous broadening are used as variable parameters to fit both the third-order nonlinear susceptibility and stationary absorption spectra. Then the calculation with $\Gamma_x = 0.03$ eV and $\gamma_x = 0.03$ eV gives a good fit as shown in Figure 3.

The terms (2a), (3a), and (4a) of which spectra are shown in Figure 4(a) correspond to the level population term of the transient transmittance change calculated using a two-level system. The three terms are hole burning, stimulated emission, and hole burning of phonon sidebands, respectively. The terms (2b), (3b), and (4b) correspond to the pump polarization coupling terms. The term (2b) is due to the coherent coupling between pump polarization and probe field. The terms (3b) and (4b) are the stimulated

Raman signals in Stokes (Raman gain) and anti-Stokes sides, respectively. The terms (2c) and (4c) correspond to the perturbed free induction decay term. The last term (4d) is the inverse Raman scattering.

The peaks due to Raman gain at 1.71 and 1.79 eV are clearly reproduced in the calculated nonlinear susceptibility. The small peaks at 2.14 and 2.22 eV are due to both the phonon sideband hole and inverse Raman scattering. When the pump pulse is near resonant to the exciton transition, the inverse Raman signal has dispersive structure. The inverse Raman signal in this study is diminished by inhomogeneous broadening of the exciton transition and the broad pump spectrum because of the overlapping of the dispersive structure. The calculated spectrum differs slightly from the observed spectrum around 1.6 and 1.85 eV. It is mainly due to the deviation of the decay kinetics from the biexponential function given by Eq. (1). The relaxation from the nonthermal STE to the quasi-thermal STE has the time constant of 150 fs, but the transient absorbance change due to the spectral shift cannot be exactly fitted to the exponential function. Therefore, the small deviations appear in the time-resolved spectrum.

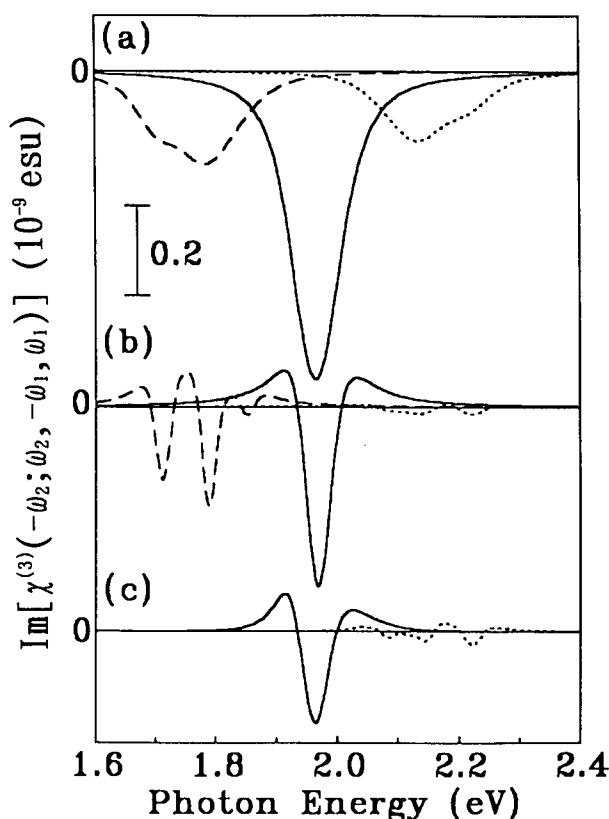


FIGURE 4 The third-order nonlinear susceptibilities calculated using the inset method. (a) Level population terms, Eq. (2a) (solid curve), Eq. (3a) (dashed curve) and Eq. (4a) (dotted curve). (b) Pump polarization coupling terms, Eq. (2b) (solid curve), Eq. (3b) (dashed curve) and Eq. (4b) (dotted curve). (c) Perturbed free induction decay terms, Eq. (2c) (solid curve), and Eqs. (4c) + (4d) (dotted curve).

The imaginary part of the third-order nonlinear susceptibility spectra $\text{Im}[\chi_{1111}^{(3)}(-\omega_2; \omega_2, -\omega_1, \omega_1)]$ are estimated also from ΔA_f and ΔA_s spectra. The nonlinear susceptibility $\text{Im}[\chi_f^{(3)}]$ shown in Figure 5(a) is due to the nonthermal STE with the response time of 150 fs. The spectrum has a negative peak at 1.93 eV and is positive below 1.8 eV. $\text{Im}[\chi_s^{(3)}]$ in Figure 5(b) is due to the quasi-thermal STE. The response time of $\chi_s^{(3)}$ is 1.5 ps. The spectrum has a positive peak at 1.82 eV and a negative peak at 1.96 eV. The peak value of $\text{Im}[\chi_s^{(3)}]$ is 1.0×10^{-8} esu. It is larger than $\text{Im}[\chi_f^{(3)}]$ because the response time of the quasi-thermal STE is ten times longer than that of the nonthermal STE. The nonlinear susceptibility of PDA-3BCMU epitaxially grown on KCl is larger than that of PDA-3BCMU cast film,¹⁴ because the main chains of the polymers align to the polarization of the pump and probe beams and the inhomogeneous broadening is narrower.

Figure 6 shows the nonlinear susceptibility spectrum $\text{Im}[\chi_{TE}^{(5)}]$ due to the triplet exciton. The $\text{Im}[\chi_{TE}^{(5)}]$ has a positive peak at 1.42 eV and a negative peak at 1.94 eV. Since the triplet excitons are generated by the fusion of two singlet excitons, ΔA_c increases proportionally with the square of the pump intensity. Therefore, the observed response corresponds to the fifth-order nonlinearity. Here, the lifetime of the triplet exciton is assumed to be 44 μs using the reported lifetime in PDA-TS. If pump pulses of 1 ps duration and 100 GHz repetition rate (10 ps interval) are used for excitation, the pulses with the peak intensity of about 300 kW/cm² give the same amount signal due to triplet excitons as the ultrafast nonlinear optical responses due to free excitons and

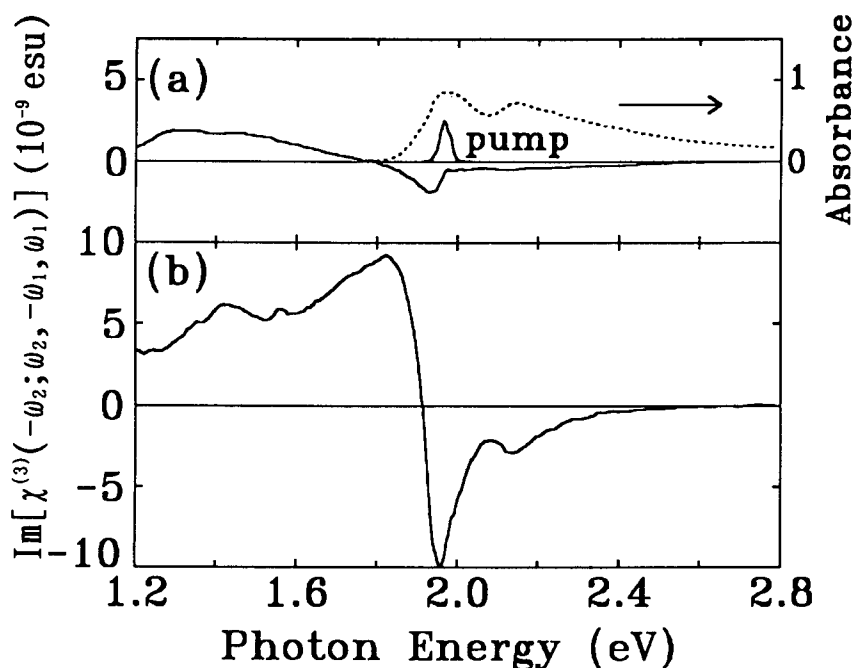


FIGURE 5 The third-order nonlinear susceptibilities due to (a) nonthermal self-trapped excitons, (b) quasithermal self-trapped excitons.

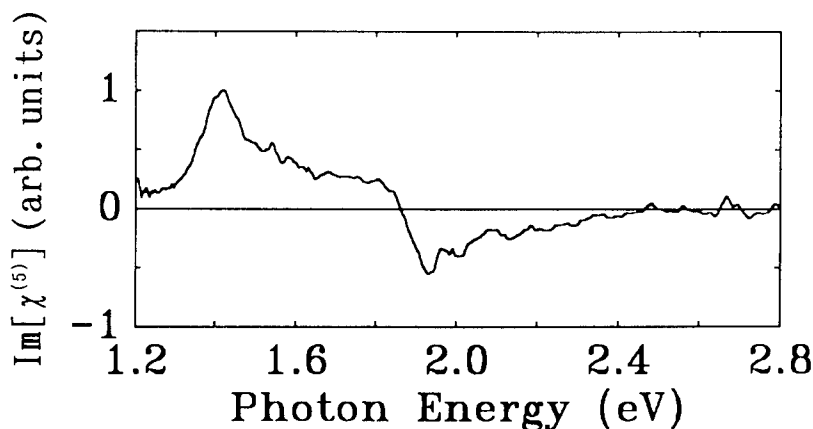


FIGURE 6 The fifth-order nonlinear susceptibility due to triplet excitons.

STEs. Since slow nonlinear optical effects prevent the ultrafast responses, attention must be paid to their properties for applications in devices at high repetition rate.

CONCLUSION

The ultrafast nonlinear optical responses in the blue-phase PDA-3BCMU epitaxially grown on a KCl substrate have been investigated. The relaxation kinetics of the photoexcitations can be explained in terms of a STE using the same model as other conjugated polymers. The relaxation processes have the same time constants as a PDA-3BCMU cast film and other blue-phase PDA's. The relaxation processes of excitons in PDA's in the femtosecond to picosecond time range up to 10 ps are insensitive to the sample morphology and the side groups. This indicates that the ultrafast relaxation process in PDA's is due to intrinsic processes, such as self-trapping, thermalization, and tunneling, which are not much affected by structural defects or impurities.

The ultrafast nonlinear optical responses of epitaxially grown blue-phase PDA-3BCMU in KCl single crystal are time-resolved and separated into four components including an "instantaneous" nonlinear response term which decays within 100 fs in a nonthermal STE, quasi-thermal STE, and triplet exciton. The spectra of the nonlinear optical susceptibilities are determined by taking into account of the pulse duration and response times. The spectrum of the instantaneous nonlinear optical response is explained using a model of the twolevel system with vibrational modes coupled to the excitonic transition. The instantaneous nonlinear response consists of several nonlinear effects, i.e., hole burning, coherent coupling between pump polarization and probe field, Raman gain, hole burning of phonon sidebands, and inverse Raman scattering. The contribution of the induced-phase modulation to the observed absorbance change is also estimated.

The nonlinear optical effects due to the nonthermal and quasi-thermal STEs are the saturation of the excitonic absorption and the transition from the photoexcited lowest ^1Bu exciton to a biexciton and/or a higher exciton with ^1Ag symmetry. The response times of the nonlinear processes are 150 fs and 1.5 ps at 290 K, respectively. The imaginary part of $\chi^{(3)}(-\omega_2; \omega_2, -\omega_1, \omega_1)$ due to the quasi-thermal STE has a peak minimum of -1.0×10^{-18} esu at $\hbar\omega_1 = 1.97$ eV and $\hbar\omega_2 = 1.95$ eV.

REFERENCES

1. T. Kobayashi, in *Polymers for Lightwave and Integrated Optics*, L. A. Hornak ed., Dekker (New York) (1989), p. 543.
2. T. Kobayashi, *IEICE Trans. Fundamentals*, **E-75A**, 38 (1992).
3. G. M. Carter, J. V. Hryniewicz, M. K. Thakur, Y. J. Chen and S. E. Meyler, *Appl. Phys. Lett.*, **49**, 998-1000 (1986).
4. T. Hattori and T. Kobayashi, *Chem. Phys. Lett.*, **133**, 230 (1987).
5. J. Swiatkiewicz, X. Mi, P. Chopra and P. N. Prasad, *J. Chem. Phys.*, **87**, 1882-1886 (1987).
6. G. J. Blanchard, J. P. Heritage, *J. Chem. Phys.*, **93**, 4377 (1990).
7. P. P. Ho, N. L. Yang, T. Jimbo, Q. Z. Wang and R. R. Alfano, *J. Opt. Soc. Am. B*, **4**, 1025-1029 (1987).
8. F. Charra and J. M. Nunzi, in *Organic Molecules for Nonlinear Optics and Photonics*, J. Messier *et al.*, eds. Kluwer (Dordrecht), (1991), p.359.
9. T. Kobayashi and M. Yoshizawa, *Synth. Metals*, **41-43**, 3129 (1991).
10. F. Kajzar, I. Rothberg, S. Etemad, P. A. Chollet, D. Grec, A. Boudet and T. Jedju, *Opt. Commun.*, **66**, 55 (1988).
11. M. Sinclair, D. Mcbranch, D. Moses and A. J. Heeger, *Appl. Phys. Lett.*, **53**, 2374 (1988).
12. B. I. Greene, J. Orenstein and S. Schmitt-Rink, *Science*, **247**, 679 (1990).
13. M. Yoshizawa, M. Taiji and T. Kobayashi, *IEEE J. Quantum Electron.*, **QE-25**, 2532-2539 (1989).
14. T. Kobayashi, M. Yoshizawa, U. Stamm, M. Taiji and M. Hasegawa, *J. Opt. Soc. Am. B*, **7**, 1558 (1990).
15. M. Yoshizawa, A. Yasuda and T. Kobayashi, *Appl. Phys. B*, **53**, 296 (1991).
16. D. N. Batchelder and D. Bloor, *J. Phys.*, **C15**, 3005 (1982).

Femtosecond Phase Spectroscopy with a Frequency-Domain Interferometer

#EIJI TOKUNAGA⁽¹⁾, §AKIRA TERASAKI⁽¹⁾ and TAKAYOSHI KOBAYASHI^{(1),(2)}

⁽¹⁾*Department of Physics, Faculty of Science, University of Tokyo,
7-3-1 Hongo, Bunkyo-ku, Tokyo 113, Japan,*

⁽²⁾*Frontier Research Program, RIKEN (The Institute of Physical
and Chemical Research), 2-1 Hirosawa, Wako, Saitama 351-01, Japan*

Received 12 January 1994; accepted 16 March 1994

A frequency-domain interferometer for femtosecond phase spectroscopy was developed and applied to the determination of the time-resolved dispersion relations (difference phase and transmission spectra) for $\text{CdS}_x\text{Se}_{1-x}$ doped glass. The experimental results were qualitatively well reproduced by the numerical calculation based on the third-order perturbation theory for the pump-probe measurement. It was proved that induced amplitude and induced phase modulations of probe pulses cause the distortion from the Kramers-Kronig relations.

INTRODUCTION

Femtosecond absorption spectroscopy is extensively used for the measurement of difference transmission spectra (DTS). However, the DTS gives only the imaginary part of the nonlinear susceptibility, so that the information of the excited state in materials is incomplete. In order to obtain the complete information, recently we developed femtosecond phase spectroscopy,¹ which is complementary to femtosecond absorption spectroscopy. We modified the arrangement of the pump-probe method to make a frequency-domain interferometer (FDI). In contrast to the previous interferometers,^{2–7} the FDI utilizes frequency-domain interference instead of spatial interference, so that difference phase spectra (DPS), which are the counterparts of DTS, can be obtained without need of a complicated experimental arrangement.

By the Kramers-Kronig (K-K) relations⁸ the real part of the susceptibility can be calculated from the imaginary part, and even for the nonlinear susceptibility the extended relations are applicable if the causality condition is satisfied for a response function.^{9,10} However, no such general relations exist in time-resolved spectroscopy because the causality condition is not satisfied.¹¹ Hence, the real part of the nonlinear susceptibility should be measured directly and the FDI is an only way to access the DPS at present.

Present address: # Institute for Solid State Physics, University of Tokyo, 7-22-1 Roppongi, Minato-ku, Tokyo 106, Japan,

§ Department of Chemistry, Faculty of Science, University of Tokyo, 7-3-1 Hongo, Bunkyo-ku, Tokyo 113, Japan.

In this paper, to prove the applicability and usefulness of the FDI, we have measured the DPS and DTS in $\text{CdS}_x\text{Se}_{1-x}$ doped glass (Toshiba R63 filter) and extracted general features of time-resolved dispersion relations. The results did not show a large discrepancy from the K-K relations compared with the results for CS_2 in Reference 11.

EXPERIMENTAL

Figure 1 shows the experimental arrangement of the FDI. The laser source is a standard combination of a colliding-pulse mode-locked ring dye laser and a six-pass amplifier pumped by a copper vapor laser, generating pulses of 620-nm wavelength, 60-fs duration, 2- μJ pulse energy, and 10-kHz repetition rate.¹² At the FDI, the pulses are divided into three, i.e., pump, probe, and reference pulses. The probe is delayed by τ from the pump, and at a Michelson interferometer, the reference and probe are displaced temporally by T for frequency-domain interferometry. In order to avoid the effect of the pump on the reference, the displacement T is set in such a way that the reference arrives at the sample earlier than both pump and probe. The transmitted reference and probe spectra are detected by a spectrometer with a multichannel photodiode array. By blocking the pump beam at ca. 5 Hz with a mechanical shutter, the spectra with and without excitation are taken alternately to obtain the difference spectra as a function of τ with a fixed T . By blocking the reference beam, the ordinary pump-probe measurement can be performed to obtain DTS.

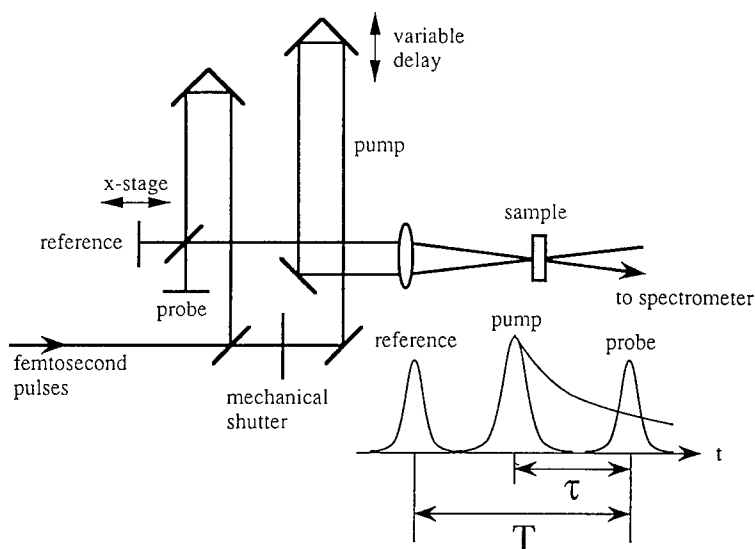


FIGURE 1 The experimental setup of the frequency-domain interferometer, and time sequence of pump, probe, and reference pulses with separation τ and T .

RESULTS AND DISCUSSION

The pump pulse energy was $0.3 \mu\text{J}$ and the excitation density was ca. 3.8 mJ/cm^2 . The polarizations of all the pulses were parallel and the experiments were performed at room temperature. Figure 2 shows signals observed by the FDI for the R63 filter at $\tau = 20 \text{ fs}$ and $T = 410 \text{ fs}$. The interference spectra with and without excitation (curves a and b) in the upper panels were taken for four seconds. Details of the method for deriving the DPS are given in the captions of Figure 2. Figure 3 shows DPS and DTS in the R63 filter for several time delays. Figure 4 shows the time evolution of the phase change averaged over the probed spectral region, which was obtained by the Fourier transformation of the interference spectra.⁷ The average transmission change showed the same dynamics as that of the phase.

The following features are extracted for respective delays in Figure 3. At -100 fs , oscillatory behavior is seen in both DPS and DTS. The oscillatory structure in DTS for

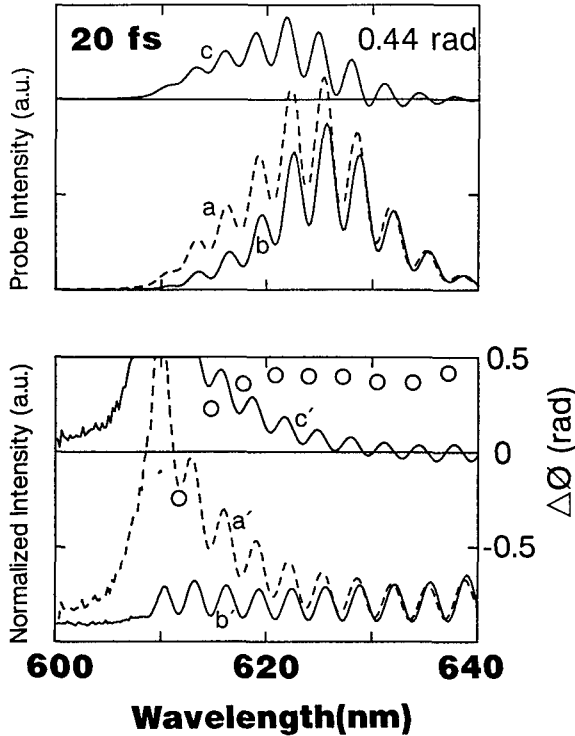


FIGURE 2 Signals obtained by the FDI for the R63 filter at $\tau = 20 \text{ fs}$ and $T = 410 \text{ fs}$.

Upper panels: directly observed interference spectra with excitation (curves a) and without excitation (curves b); the difference interference spectra (curves c) are also shown. The average phase shift, 0.44 rad , was calculated by the Fourier transform of curves a and b in order to use the information of the whole fringes.⁷ Lower panels: curves a, b, and c have been normalized by the transmitted probe spectra to obtain a', b', and c', respectively. The open circles (DPS) are calculated from the fringe-valley shifts between curves a' and b' as $2\pi(\lambda_i - \lambda_i^{\text{ex}})/(\lambda_{i+1} - \lambda_i)$ where λ_i^{ex} and λ_i are the i -th fringe-valley wavelengths with and without excitation, respectively, and $\lambda_{i+1} > \lambda_i$.

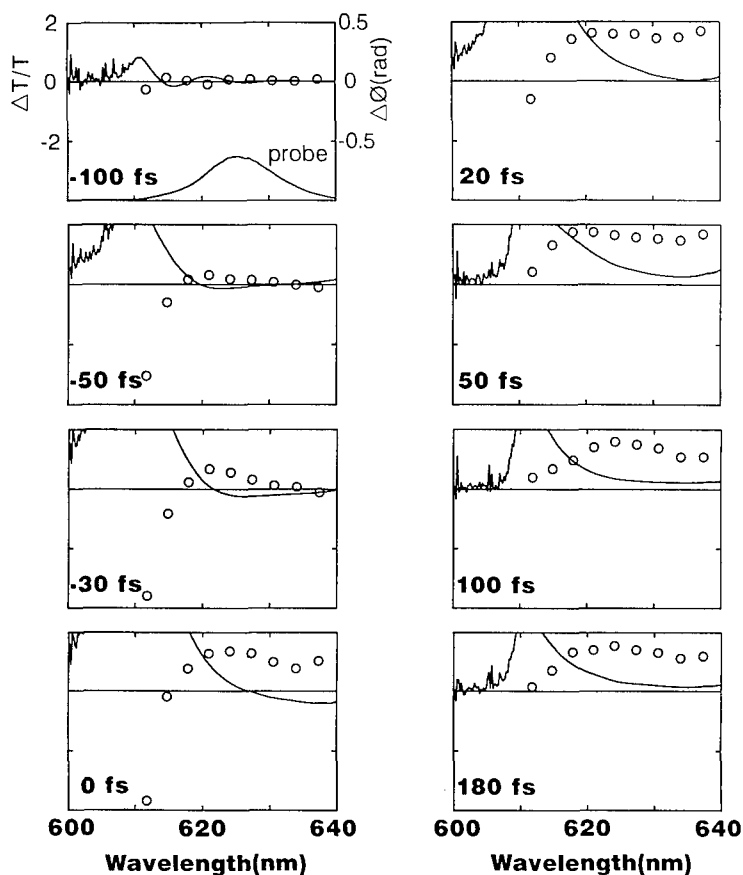


FIGURE 3 DTS (solid lines) and DPS (open circles) for the R63 filter.

negative time delays is well known as transient oscillations which are caused by the coherent coupling effect,^{13–19} but the present result is the first observation of the oscillating structure in DPS to the best of our knowledge. From -50 fs to 0 fs, the absorption saturation grows around 610 nm, accompanied by the negative transmission change for the longer wavelengths. From the oscillatory features of the DTS at -100 fs and -50 fs and the fact that the oscillating period of transient oscillations is inversely proportional to the time delay, this negative change should not be assigned to induced absorption but to transient oscillations with a longer period. In other words, the signals contain a blue shift in the transmitted probe spectra as well as the absorption saturation. This is evidenced by the rapid rise of the DPS from negative to zero delay, which should cause induced phase modulation (IPM)^{20–23} of the probe pulse. In this process, the probe pulse is phase modulated by the rapid change in the refractive index in the medium to show the frequency shift which is proportional to the time derivative of the phase change. Without the DPS, one cannot tell whether the transmission change is due to the absorption change or to the spectral shift of the probe. At 100 fs and 180 fs, both phase and transmission changes decrease with wavelength from 620 to

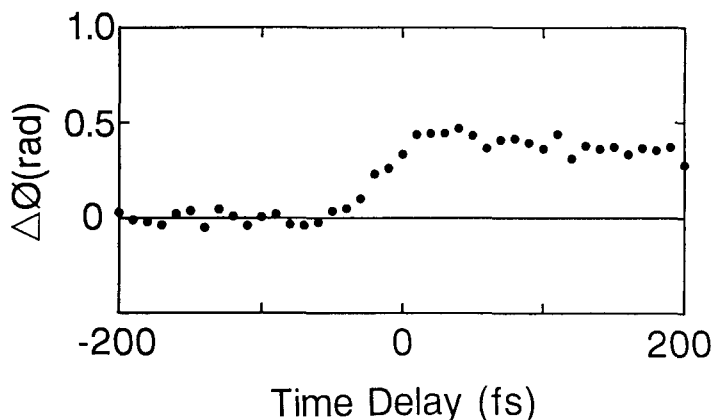


FIGURE 4 Average phase change in the probed spectral region as a function of time delay. The average transmission change shows the same dynamics.

640 nm, while at 20 fs and 50 fs they increase from ca. 635 nm. Since this behavior can hardly be explained in terms of semiconductor dynamics, it should also be attributed to the transient oscillations with longer periods. For longer delays than 100 fs, both DPS and DTS are almost the same as those at 100 fs.

Because of the limited spectral range, quantitative evaluation on the K-K relations cannot be made, but at least it is known that the DPS and DTS qualitatively satisfy the K-K relations: an absorption decrease around 610 nm is accompanied by a decrease in the refractive index for the longer wavelength side. However, from the fact that the spectral shift due to IPM does not depend on the phase itself but on the changing rate of the phase, it is suggested that the K-K relations are not valid in Figure 3. This will be discussed later.

SIMULATION

Since both phase and transmission changes show the same dynamics as a function of τ as shown in Figure 4, the system can be approximated as a two-level system. This is mainly because the excitation is near the band edge, so that the contribution of intraband relaxation is insignificant compared with interband contribution. The relaxation from the bottom in the conduction band to the top of the valence band can be regarded as a two level. Therefore, the experimental results for R63 filter can be numerically simulated by the third-order perturbation theory for a two-level system in the pump-probe measurement, which is deduced by solving the optical Bloch equations in the perturbation approximation¹⁵ as follows:

$$P^{(3)}(t) = \chi^{(3)}(t) \otimes E_{pr}(t) = 2\mu f_2(t) \otimes [E_{pr}(t)N^{(2)}(t)], \quad (1)$$

where \otimes denotes convolution operation and $N^{(2)}(t)$ is the population change:

$$N^{(2)}(t) = f_1(t) \otimes [E_{ex}(t)P_{ex}^{(1)*}(t) - E_{ex}^*(t)P_{ex}^{(1)}(t)]/2\mu. \quad (2)$$

The equation (1) is called the level population term. The coherent coupling term, which consists of the pump polarization coupling term and the perturbed free induction decay term,¹⁵ was also calculated but not shown here because it makes little qualitative difference from the following two reasons. First, since the same pulses are used for both pump and probe, the coherent coupling term gives exactly the same signals as the level population term at zero delay. Second, since the phase relaxation time of Toshiba R63 filter is much shorter than the pulse duration,²⁴ the coherent coupling effect is not significant except near zero delay. In Eqs. (1) and (2), $E_{ex}(t)$ and $E_{pr}(t)$ are pump and probe fields given by

$$\begin{cases} E_{ex}(t) = E_2(t + \tau) \exp[i\omega_{ex}(t + \tau)], \\ E_{pr}(t) = E_1(t) \exp(i\omega_{pr}t), \end{cases} \quad (3)$$

$P_{ex}^{(1)}(t)$ is the pump induced polarization:

$$P_{ex}^{(1)}(t) = 2\mu N_0 f_2(t) \otimes E_{ex}(t), \quad (4)$$

and $f_1(t)$ and $f_2(t)$ are population and polarization response functions:

$$\begin{cases} f_1(t) = i(\mu/\hbar)\theta(t) \exp(-t/T_1), \\ f_2(t) = -(i/2)(\mu/\hbar)\theta(t) \exp[(i\Omega - 1/T_2)t], \end{cases} \quad (5)$$

where ω_{ex} and ω_{pr} are pump and probe angular frequencies, respectively, μ is the dipole moment, N_0 is the equilibrium population difference, T_1 and T_2 are energy and phase relaxation times, respectively, Ω is a transition frequency, and $\theta(t)$ is a step function:

$$\theta(t) = \begin{cases} 1 & t > 0 \\ 0 & t < 0. \end{cases} \quad (6)$$

It is assumed that the pulses are Fourier-transform-limited and have a hyperbolic-secant envelope:

$$E_{1,2}(t) = \text{sech}[2 \ln(1 + \sqrt{2}) t / \tau_{pr,ex}], \quad (7)$$

where $\tau_{pr,ex}$ are the FWHM's of the probe and pump intensity profiles $I_{pr,ex}(t) = E_{1,2}^2(t)$, respectively. We obtain from Eq.(1)

$$\chi^{(1)}(\omega) = F[P_{pr}^{(1)}(t)]/E_{pr}(\omega) = 2\mu N_0 f_2(\omega) \quad (8)$$

$$\begin{aligned} \chi^{(3)}(\omega, \tau) &= F[P^{(3)}(t)]/E_{pr}(\omega) \\ &= 2\mu f_2(\omega) F[E_{pr}(t) N^{(2)}(t)]/E_{pr}(\omega) \end{aligned} \quad (9)$$

Since $N^{(2)}(t)$ depends on τ such that $N^{(2)}(t) = N^{(2)'}(t + \tau)$ [$N^{(2)}(\omega) = \exp(i\omega\tau) N^{(2)'}(\omega)$], Eq. (9) can also be expressed by

$$\chi^{(3)}(\omega, \tau) = 2\mu f_2(\omega) \frac{\exp(i\omega\tau)}{E_{pr}(\omega)} \int d\omega' E_{pr}(\omega') \exp(-i\omega'\tau) N^{(2)'}(\omega - \omega'). \quad (10)$$

Assuming $N^{(2)}(t)$ and $I_{pr}(t)$ at delay zero as shown in Figure 5 with the following parameters:

$$T_1 = 10 \text{ ps}, \quad T_2 = 30 \text{ fs}, \quad \tau_{pr} = \tau_{ex} = 60 \text{ fs}, \quad \Lambda (= 2\pi c/\Omega) = 610 \text{ nm},$$

$$\lambda_{pr}(= 2\pi c/\omega_{pr}) = 620 \text{ nm} \quad \text{and} \quad \lambda_{ex}(= 2\pi c/\omega_{ex}) = 620 \text{ nm},$$

the numerical calculation of Eq. (9) leads to the results in Figure 6, where the real and imaginary parts of $\chi^{(3)}$ are proportional to DPS and DTS, respectively, as $\Delta\Phi \propto -\text{Re}\chi^{(3)}$ and $\Delta T/T \propto -2\text{Im}\chi^{(3)}$. Here we made reasonable assumptions for this material that the energy relaxation time is much longer ($T_1 = 10$ ps) and the phase relaxation time is shorter ($T_2 = 30$ fs) than the pulse duration and that the excitation is off-resonant. The simulation satisfactorily reproduces the typical features of the experimental results in Figure 3.

In contrast to $\chi^{(1)}$, $\chi^{(3)}$ exhibits characteristic transient oscillating structure, which is due to the $\exp(i\omega\tau)$ factor in Eq. (10). Note that the level population term gives transient oscillations as well as the coherent coupling term. As discussed in Reference 23 the transient oscillations by the level population term as in Figure 6 are due to the induced amplitude and induced phase modulations of the probe pulse. The negative transmission change near zero delay is well reproduced by the simulation. Since we assumed the two-level system in which excited-state absorption is prohibited, the negative change is unequivocally attributed to the pulse modulation effects. All the other unusual features pointed out in results and discussion are well reproduced by the simulation, recognized as a part of the transient oscillations with longer periods.

COMPARISON WITH THE K-K RELATIONS

As shown in Eq. (9), time-resolved dispersion relations depend on both $f_2(\omega)$ and $F[E_{pr}(t)N^{(2)}(t)]/E_{pr}(\omega)$. The factor $f_2(\omega)$ satisfies the K-K relations because $f_2(t) = 0$ over $t < 0$, satisfying the causality principle, while the factor $F[E_{pr}(t)N^{(2)}(t)]/E_{pr}(\omega)$

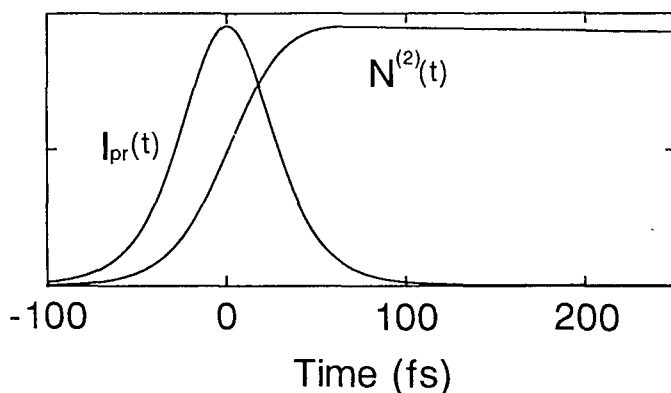


FIGURE 5 $I_{pr}(t)$ and $N^{(2)}(t)$ assumed for the calculation in Figure 6. $I_{pr}(t)$ is placed at delay zero.

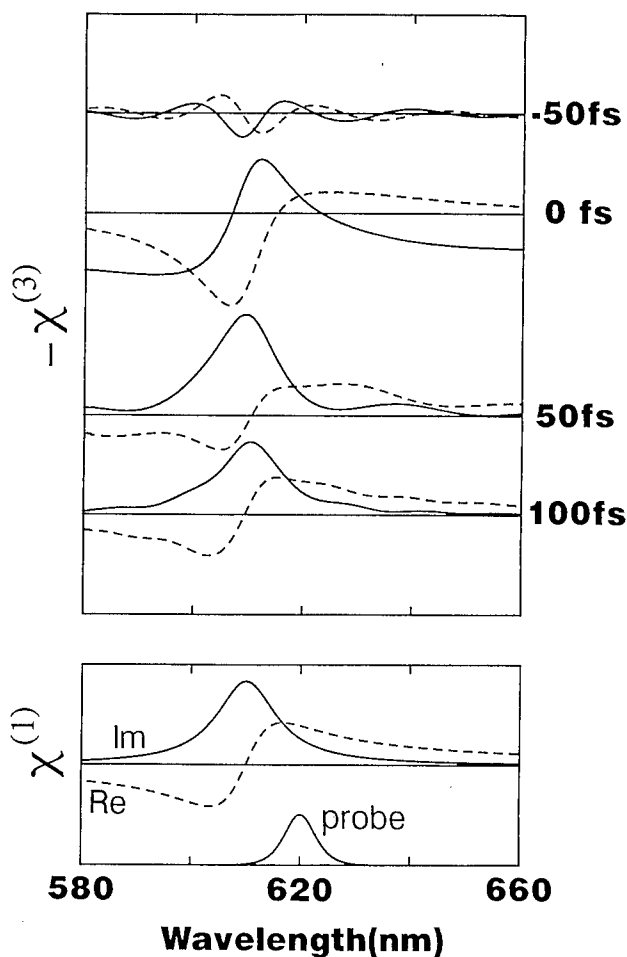


FIGURE 6 Numerical simulations for the R63 filter. Upper part: real (dashed curves) and imaginary (solid curves) parts of $\chi^{(3)}(\omega, \tau)$ calculated from Eq. (9) on the conditions: $T_1 = 10$ ps, $T_2 = 30$ fs, $\tau_{pr} = \tau_{ex} = 60$ fs, $\Lambda = 610$ nm, and $\lambda_{pr} = \lambda_{ex} = 620$ nm. $-2\text{Im}\chi^{(3)}$ and $-\text{Re}\chi^{(3)}$ are proportional to DTS and DPS, respectively. Lower part: $\chi^{(1)}(\omega)$ and the probe spectrum. The pump pulse is the same as the probe.

represents the induced modulation of the probe pulse and does not satisfy the K-K relations.¹¹ If $E_{pr}(t) = \delta(t)$, the latter is simply reduced to $N^{(2)'}(\tau)$, a constant value, and then $\chi^{(3)}(\omega, \tau)$ satisfies the K-K relations. That is, the distortion from the K-K relations is caused by the induced modulation effects of the probe pulse, and the modulation effects manifest themselves as long as a probe pulse duration is finite.

The degree of discrepancy from the K-K relations, depends on experimental conditions such as pulse widths, relaxation times, time delays, and a frequency detuning. We can see the degree of the applicability of the K-K relations to time-resolved data from the conditions (A) to (D) derived in Reference 11.

At 100 fs and 180 fs, $\Delta\phi(t)$ is nearly steady within the probe pulse duration as seen in Figure 4 to satisfy the condition (A), so that the probe pulse is not subject to the modulation effects. Hence, the K-K relations hold approximately. This is demonstrated also in Figure 6, where $\chi^{(3)}(\omega)$ at 100 fs is almost proportional to $\chi^{(1)}(\omega)$ because $N^{(2)}(t)$ is nearly steady within the probe pulse duration as shown in Figure 5.

At negative delays also, the K-K relations hold qualitatively in both experimental and calculated results. In this case the condition (C) is satisfied, i.e., $\Delta\phi(t)$ rises at the trailing edge of the probe pulse. This is a special case in which induced modulation spectra satisfy the K-K relations.

At zero delay, the K-K relations do not hold even approximately because $\Delta\phi(t)$ is changing over the whole probe-pulse duration. As shown in Figure 6, the induced modulation effects distort the signals at zero delay such that they show the dispersion relations substantially different from those at 50 fs or 100 fs.

Compared with the results for CS_2 in Reference 11, however, qualitative features of the dispersion relations for the R63 filter are still consistent with the K-K relations. For CS_2 , the results show qualitative differences from the K-K relations such as the sign-reversed K-K relations and both DTS and DPS being even functions. This is because the wavelength dependence for CS_2 is caused only by the modulation effects due to $f_2(\omega)$ being constant in the nonresonant region, while for the R63 filter $f_2(\omega)$ has a strong wavelength dependence to give a larger contribution to $\chi^{(3)}(\omega)$ than the induced modulation effects.

CONCLUSION

We have developed a frequency-domain interferometer for femtosecond phase spectroscopy to extract the general features of time-resolved dispersion relations by using $\text{CdS}_x\text{Se}_{1-x}$ doped glass as a sample. The time-resolved spectra consist of two factors, an intrinsic susceptibility change in a material and transient oscillations whose oscillating period is inversely proportional to the time delay. The former satisfies the K-K relations while the latter does not. That is, the distortion from the K-K relations is caused by the induced modulation effects of the probe pulse. Since the modulation effects cannot be avoided as long as a probe pulse has a finite duration, this fact tells us that the DPS is obtained only by direct measurement with a frequency-domain interferometer.

ACKNOWLEDGMENTS

This work was carried out at Frontier Research Program, RIKEN (The Institute of Physical and Chemical Research) by the support of Prof. A. F. Garito, Drs. A. Yamada, H. Sasabe, and T. Wada. The authors would like to express sincere thanks for their support when T. K. was involved in the program, and to Drs. T. Hattori and M. Yoshizawa for their valuable advice.

REFERENCES

1. E. Tokunaga, A. Terasaki and T. Kobayashi, *Opt. Lett.*, **17**, 1131 (1992).
2. J.-M. Halbout and C. L. Tang, *Appl. Phys. Lett.*, **40**, 765 (1982).
3. Y. Li, G. Eichmann and R. R. Alfano, *Appl. Opt.*, **25**, 209 (1986).
4. D. Cotter, C. N. Ironside, B. J. Ainslie and H. P. Girdlestone, *Opt. Lett.*, **14**, 317 (1989).
5. N. Finlayson, W. C. Banyai, C. T. Seaton, G. I. Stegeman, M. O'Neill, T. J. Cullen and C. N. Ironside, *J. Opt. Soc. Am. B*, **6**, 675 (1989).
6. M. J. LaGasse, K. K. Anderson, H. A. Haus and J. G. Fujimoto, *Appl. Phys. Lett.*, **54**, 2068 (1989).
7. K. Minoshima, M. Taiji and T. Kobayashi, *Opt. Lett.*, **16**, 1683 (1991).
8. For example, L. D. Landau and E. M. Lifshitz, *Electrodynamics of Continuous Media* (Addison-Wesley, Reading, MA, 1960), or A. Yariv, *Quantum Electronics*, 3rd edition (Wiley, New York, 1988).
9. F. Bassani and S. Scandolo, *Phys. Rev. B*, **44**, 8446 (1991), and references therein.
10. H. Kishida, T. Hasegawa, Y. Iwasa, T. Koda and Y. Tokura, *Phys. Rev. Lett.*, **70**, 3724 (1993).
11. E. Tokunaga, A. Terasaki and T. Kobayashi, *Phys. Rev. A*, **47**, R4581 (1993).
12. A. Terasaki, M. Hosoda, T. Wada, H. Tada, A. Koma, A. Yamada, H. Sasabe, A. F. Garito and T. Kobayashi, *J. Phys. Chem.*, **96**, 10534, (1992).
13. C. H. Brito-Cruz, R. L. Fork, W. H. Knox and C. V. Shank, *Chem. Phys. Lett.*, **132**, 341 (1986).
14. B. Fluegel, N. Peyghambarian, G. Olbright, M. Lindberg, S. W. Koch, M. Joffre, D. Hulin, A. Migus and A. Antonetti, *Phys. Rev. Lett.*, **59**, 2588 (1987).
15. C. H. Brito-Cruz, J. P. Gordon, P. C. Becker, R. L. Fork and C. V. Shank, *IEEE J. Quantum Electron.*, **QE-24**, 261 (1988).
16. M. Joffre, D. Hulin, A. Migus, A. Antonetti, C. Benoit a la Guillaume, N. Peyghambarian, M. Lindberg and S. W. Koch, *Opt. Lett.*, **13**, 276 (1988).
17. M. Lindberg and S. W. Koch, *Phys. Rev. B*, **38**, 7607 (1988).
18. J. P. Sokoloff, M. Joffre, B. Fluegel, D. Hulin, M. Lindberg, S. W. Koch, A. Migus, A. Antonetti and N. Peyghambarian, *Phys. Rev. B*, **38**, 7615 (1988).
19. M. Joffre, D. Hulin, A. Migus and A. Antonetti, *J. Mod. Opt.*, **35**, 1951 (1988).
20. R. L. Fork, C. V. Shank, C. Hirlimann, R. Yen and W. J. Tomlinson, *Opt. Lett.*, **8**, 1 (1983).
21. R. R. Alfano and P. P. Ho, *IEEE J. Quantum Electron.*, **QE-24**, 351 (1988).
22. T. Hattori, A. Terasaki, T. Kobayashi, T. Wada, A. Yamada and H. Sasabe, *J. Chem. Phys.*, **95**, 937 (1991).
23. E. Tokunaga, A. Terasaki, T. Wada, K. Tsunetomo, Y. Osaka and T. Kobayashi, *J. Opt. Soc. Am. B*, **10**, No.12 (1993) in press.
24. A. Nakamura and T. Tokizaki, *Solid State Physics*, **24**, 931 (1989), in Japanese.

Spectral Dispersion of Third Harmonic Generation in Squaraines

JAMES H. ANDREWS¹, JOHN D. V. KHAYDAROV¹, KENNETH D. SINGER¹,
 DIANA L. HULL² and KATHY C. CHUANG²

¹*Case Western Reserve University Department of Physics, Cleveland,
 OH 44106–7079, ²NASA Lewis Research Center, Cleveland,
 Ohio 44135–3191*

Received 12 January 1994; accepted 11 February 1994

We measured the third-harmonic spectrum of each of two squaraine dyes dissolved in chloroform. Our measurements were made over a range of fundamental frequencies for which the third harmonic is above the exceptionally strong, narrow peak in each dye's linear absorption spectrum, but below its uv absorption band. By fitting the experimental dispersion of the third order susceptibility, γ , to a four-level sum-over-states model, we determine the strength and location of the lowest lying two-photon transition. In each case, we find that the 2^1Ag state appears just above the 1^1Bu state in energy and that the $1^1\text{Bu} \rightarrow 2^1\text{Ag}$ transition moment makes a significant contribution to the nonlinearity. We also find that a significant contribution to γ comes from one or more higher-lying two-photon states ($n^1\text{Ag}$) in the ultraviolet with $1^1\text{Bu} \rightarrow n^1\text{Ag}$ transition moments comparable to the $1^1\text{Ag} \rightarrow 1^1\text{Bu}$ transition moment. Using our results, we predict the electronic contribution to the near infrared dispersion of the Optical Kerr effect for one of these dyes.

INTRODUCTION

The two-level model has been used successfully to understand the second order susceptibility (β) of organic nonlinear dyes.¹ Multiple configuration interaction quantum chemical calculations have shown, however, that transitions to two-photon states are necessary for determining the magnitude and sign of the third order molecular nonlinear susceptibility $\gamma_{ijkl}(-\omega_4; \omega_1, \omega_2, \omega_3)$ in conjugated organic and polymeric materials, especially polyenes.^{2,3} These studies show that at least a three-level model with a high-lying two-photon state is necessary for the characterization of third-order nonlinearities. Experimentally locating and characterizing two-photon states using an all optical technique, probing electronic contributions to the nonlinear susceptibility, is of considerable interest for understanding such systems.

For third harmonic generation in a one-dimensional system, the sum-over-states expression for $\gamma(-3\omega; \omega, \omega, \omega)$ obtained from perturbation theory simplifies to⁴

$$\gamma_{xxxx}(-3\omega; \omega, \omega, \omega) = \frac{e^4}{4\hbar^3} \left[\sum_{l,m,n} D_{lmn}(-3\omega; \omega, \omega, \omega) \langle x \rangle_{gl} \langle \bar{x} \rangle_{lm} \langle \bar{x} \rangle_{mn} \langle x \rangle_{ng} - \right. \\ \left. - \sum_{l,n} D_{ln}(-3\omega; \omega, \omega, \omega) \langle x \rangle_{gl} \langle x \rangle_{lg} \langle x \rangle_{gn} \langle x \rangle_{ng} \right] \quad (1)$$

where g is the ground state and l, m, n are the excited states of the system, $\langle x \rangle_{gl}$ are the g and l matrix elements of the position operator, and the barring operation \bar{x} represents $x - \langle x \rangle_{gg}$. The frequency dependence is found in the “ D ” factors where

$$D_{lmn} = [(\Omega_{ng} - \omega)(\Omega_{mg} - 2\omega)(\Omega_{lg} - 3\omega)]^{-1} + [(\Omega_{ng}^* + \omega)(\Omega_{mg} - 2\omega)(\Omega_{lg} - \omega)]^{-1} \quad (2)$$

$$+ [(\Omega_{ng}^* + \omega)(\Omega_{mg}^* + 2\omega)(\Omega_{lg} - \omega)]^{-1} + [(\Omega_{ng}^* + \omega)(\Omega_{mg}^* + 2\omega)(\Omega_{lg}^* + 3\omega)]^{-1}$$

and

$$D_{ln} = [(\Omega_{lg} - \omega)(\Omega_{lg} - 3\omega)(\Omega_{ng} - \omega)]^{-1} + [(\Omega_{lg}^* + \omega)(\Omega_{lg} - \omega)(\Omega_{ng} - \omega)]^{-1} \quad (3)$$

$$+ [(\Omega_{lg} - \omega)(\Omega_{lg}^* + \omega)(\Omega_{ng}^* + \omega)]^{-1} + [(\Omega_{lg}^* + \omega)(\Omega_{lg}^* + 3\omega)(\Omega_{ng}^* + \omega)]^{-1}.$$

Here, $\Omega_{ng} \equiv \omega_{ng} - i\Gamma_{ng}$ and $*$ represents complex conjugation. The quantity $\hbar\omega_{ng}$ is the energy of the excited state n above the ground state and $\hbar\Gamma_{ng}$ is the width of this excited state.

For a simplified four-level model, if we assume that the higher excited states are pure two-photon states, not accessible from the ground state in a dipole transition, the expression for γ for third harmonic generation becomes⁵

$$\gamma_{xxxx}(-3\omega; \omega, \omega, \omega) = \frac{\mu_{01}^2}{4\hbar^3} (\mu_{12}^2 D_{121} + \mu_{13}^2 D_{131} + \Delta\mu_{01}^2 D_{111} - \mu_{01}^2 D_{11}), \quad (4)$$

where D_{1n1} ($n = 2, 3$), D_{111} , and D_{11} represent the permuted sums of the relevant energy denominators as described above, $\mu_{ab} = e\langle x \rangle_{ab}$, and $\Delta\mu_{01} = e(\langle x \rangle_{11} - \langle x \rangle_{00})$. For our purposes, the most fully resonating term for each is

$$D_{1n1} \rightarrow [(\omega_{10} - 3\omega - i\Gamma_{10})(\omega_{n0} - 2\omega - i\Gamma_{n0})(\omega_{10} - \omega - i\Gamma_{10})]^{-1} \quad (5)$$

$$D_{111} \rightarrow [(\omega_{10} - 3\omega - i\Gamma_{10})(\omega_{10} - 2\omega - i\Gamma_{10})(\omega_{10} - \omega - i\Gamma_{10})]^{-1} \quad (6)$$

$$D_{11} \rightarrow [(\omega_{10} - 3\omega - i\Gamma_{10})(\omega_{10} - \omega - i\Gamma_{10})(\omega_{10} - \omega - i\Gamma_{10})]^{-1}. \quad (7)$$

Of course, for a centrosymmetric molecule, $\Delta\mu_{01} \equiv 0$ and the resonance predicted by (6) at $\omega_{10} = 2\omega$ cannot contribute.

In many molecular materials, the positive contribution from a two-photon excited state transition in $\mu_{1n}^2 D_{1n1}$ competes strongly with and dominates over the negative contribution from the purely “two-level” term in $\mu_{01}^2 D_{11}$ so that γ is positive for input frequencies far below the first excited state⁶ (for third harmonic generation, the D factors are positive definite for $3\omega < \omega_{10}$). Recent studies^{5,7,8} of certain centrosymmetric derivatives of squaric acid, however, show an unusually large and, off-resonance, inherently negative γ . These molecules appear to represent a class of materials, in this case a cyanine-like dye of donor-accepter-donor structure, for which the $\mu_{01}^2 D_{11}$ contribution dominates. This $D^+ \rightarrow A^- \leftarrow D^+$ character is expected to lead to considerable intramolecular charge transfer in both the ground and excited states.

Linear cyanines and polyenes have been modeled theoretically in detail by Pierce³ who found that, below resonance, $\gamma < 0$ for all-*trans* linear centrosymmetric cyanines, in contrast to polyenes. As with polyenes, Pierce’s calculations predict important contributions from two-photon (Ag) states on γ . The lowest Ag state for these cyanines is energetically above the lowest one-photon (Bu) state, unlike linear polyenes for which the order of these two states is reversed due to strong electron correlations. Recently,

Zhou and coworkers⁹ theoretically modeled a squaraine dye and similarly predicted a negative off-resonant γ with significant contributions from certain two-photon states. Most importantly for comparison to the measurements described in this paper, both Pierce and Zhou predict that the lowest lying ($n = 2$) two-photon state makes a negligible contribution to γ . Instead, Pierce predicts for linear centrosymmetric cyanines³ and Zhou predicts for a centrosymmetric squaraine dye⁹ that higher two-photon states ($n > 2$) will be much more significant than the 2^1Ag state due to much larger transition moments with the first excited (1^1Bu) state. These higher two-photon states appear in the ultraviolet but the excitation energy to the 2^1Ag state is predicted to be in the visible region of the spectrum.

Pierce and others have also reported that the magnitude of γ is strongly dependent upon the extent of bond alternation which is strongly a function of the end groups on the molecule and the molecular environment, i.e., the solvent used.^{3,10} Centrosymmetric squaraines are expected to have a degenerate ground state, as in linear cyanine dyes. Squaraines differ from linear cyanines most significantly, however, by the presence of the central square ring which is depleted in electrons and by their more two-dimensional character. The nature of the solvent and the charge-transfer characteristics of the end groups on the dye may also affect the conformational structure of the molecules, and the molecular associations in solution. Some squaraines, such as the forms studied by Zhou⁹ appear to have a quinoidal character in phenyl groups attached to the central square ring.¹¹

Our work is intended to test the strength, location, and purity of the lowest lying two-photon transition by fitting the measured dispersion of γ in the vicinity of the 2^1Ag two-photon resonance to a sum-over-states model with a minimum number of levels consistent with the linear absorption spectrum of the dye. We use third harmonic generation to probe the sign and magnitude of the near-resonant contribution found in the D_{121} denominator at $\omega_{02} = 2\omega$ because it does not require detection of the output signal at a highly absorbed frequency. We have measured the third-harmonic response of the squaraine dyes, ISQ and C16-TSQ, shown with their absorption spectra in chloroform in Figure 1. Our measurements were made over a range of fundamental frequencies (ω) for which the third harmonic is energetically above the exceptionally strong, yet relatively narrow, absorption peak in each dye's linear absorption spectrum (at 654 nm for ISQ and 668 nm for C16-TSQ), but below the ultraviolet absorption band which begins for each dye around 400 nm. Previous studies of ISQ have shown it to have an exceptionally high γ . In methylene chloride, $\langle\gamma_{xxxx}\rangle_{1111}(2\omega; \omega, \omega, 0)$ was $-3.5(\pm 0.5) \times 10^{-34}\text{esu}$ at $1.91\text{ }\mu\text{m}^5$ and, in a PMMA film, $|\langle\gamma_{xxxx}\rangle_{1133}(\omega; \omega, 0, 0)|$ was $68 \times 10^{-34}\text{esu}$ at 799 nm.⁸

EXPERIMENTAL PROCEDURE

To study the spectral dispersion of the third harmonic generated in low concentration solutions of the squaraine dyes, we used a synchronously pumped optical parametric oscillator (SPOPO) which produces tunable high power picosecond pulses from 0.4–2.5 μm . Our SPOPO is pumped by the third harmonic (355 nm) of a pulsed Nd:YAG laser with a combination of hybrid active-passive mode-locking and passive

negative feedback similar to the system described in Reference 12. Third-harmonic pulse trains consist of about 40 11-picosecond pulses separated by 8 nanosecond intervals. The energy of a single pulse of third harmonic radiation can be as high as $50\text{ }\mu\text{J}$. Our SPOPO operation is unique in that, by increasing the cavity length of the SPOPO to compensate for the dispersive walk-off between the pump and oscillating SPOPO pulses, we obtained compressed pulses on the order of 3-picoseconds without a fully commensurate loss of pulse energy. The resulting peak power input to our experiment was increased using this technique as compared to operating the SPOPO at a cavity length optimized for low threshold. We achieved further increases in the peak pulse power of the laser and, consequently, of the SPOPO output, by adjusting the threshold energy of the negative feedback element. In this case, the number of pulses decreased but the power of the initial pulses increased by more than an order of magnitude. Some stability was sacrificed by this adjustment, but by appropriately referencing our experimental output, we did not find this to be a problem. Further details on the SPOPO used in this experiment and our technique for pulse compression are published elsewhere.¹³

To measure the third harmonic response in solution, we used a wedged liquid cell with thick (5 cm) input and output windows in the manner first described in Reference.¹⁴ Our wedge angle was $0.5 \pm 0.04^\circ$ and the average thickness of the liquid in the cell was about 0.2 mm. We focused the idler of the SPOPO into our cell with a 20 cm lens leading to a confocal parameter estimated to be on the order of 1–2 mm. The tight focus

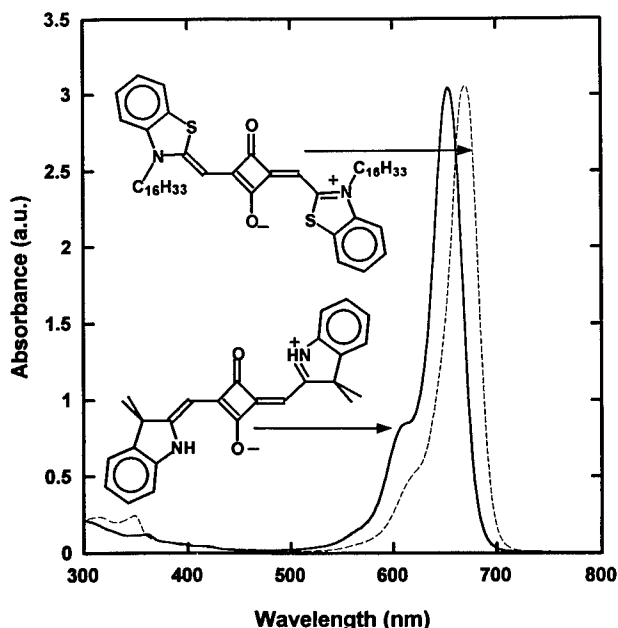


FIGURE 1 Chemical structure and optical absorption spectrum of ISQ (solid line) and C16-TSQ (dashed line) in chloroform. For ISQ, the peak molar absorptivity in chloroform is $\epsilon_M = 175,000\text{ M}^{-1}\text{cm}^{-1}$. For C16-TSQ, $\epsilon_M = 280,000\text{ M}^{-1}\text{cm}^{-1}$.

and thick windows assure us that the contribution to our signal from air can be neglected. Our cell differs from previously reported designs in that it uses cylindrical windows (1 in. diameter) fitted without adhesives directly into a custom bored teflon holder. This design enables us to use the cell for long periods with strong organic solvents, yet easily disassemble and clean it when necessary. Because our experimental procedure required that we switch between different dye solutions and pure solvent, we fit the cell with a teflon tube drain and steel valve to permit easy drainage and rinsing of the cell *in situ*.

Figure 2 shows the experimental setup. After the OPO idler beam passes through the cell, the third harmonic generated is deflected by a heat transmitting mirror (45° cold mirror) into the sample photomultiplier tube (PMT). The infrared input beam is filtered of any remaining third harmonic and is focused onto a glass slide whose third harmonic output serves to divide out shot-to-shot fluctuations in the input pulse power. We found this particular sample/reference arrangement to yield a much better signal-to-noise ratio than others.

By translating the wedged cell across the beam, we recorded the third harmonic Maker fringes for each dye solution and for pure chloroform at each wavelength. The fringes were then analyzed to determine the mean third harmonic fringe amplitude (\bar{A}_{thg}) and coherence length (l_c) in the manner described in Reference 6 including the effects of the measured third harmonic absorption of the dye solutions in the cell. We chose chloroform as a solvent in part because it absorbs only weakly at a few very narrow regions in the near IR due to the presence of only one C—H bond.

The ratio of the amplitude of the fringes from the dye-chloroform solutions (L) and from the pure chloroform reference (R) is given by

$$\frac{\bar{A}_{thg}^L}{\bar{A}_{thg}^R} = \frac{|(T_{GL}/\Delta n_G^2)\chi_G^{(3)} - (T_L/\Delta n_L^2)\chi_L^{(3)}(t_\omega^L)^3|^2}{|(T_{GR}/\Delta n_G^2)\chi_G^{(3)} - (T_R/\Delta n_R^2)\chi_R^{(3)}(t_\omega^R)^3|^2} \quad (8)$$

where G refers to the BK-7 glass windows of the cell, Δn^2 is the difference $n_{3\omega}^2 - n_\omega^2 = (n_{3\omega} + n_\omega)\lambda/6l_c$, and the transmission factors are

$$t_\omega^X = \frac{2n_\omega^G}{n_\omega^G + n_\omega^X}, \quad T_X = \frac{n_\omega^X + n_{3\omega}^X}{n_{3\omega}^G + n_{3\omega}^X}, \quad T_{GX} = \frac{n_\omega^G + n_{3\omega}^X}{n_{3\omega}^G + n_{3\omega}^X}. \quad (9)$$

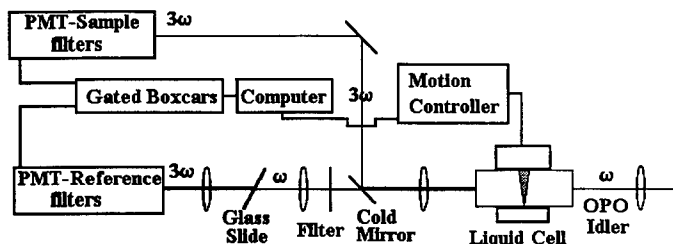


FIGURE 2 Experimental geometry used for third harmonic generation.

The second hyperpolarizability of the squaraine molecules is determined from $\chi_L^{(3)}$ and $\chi_R^{(3)}$ for low dye concentrations from the relation:

$$\chi_L^{(3)} \approx \frac{m_{\text{chloroform}}}{m_{\text{total}}} \chi_R^{(3)} + (f^\omega)^3 f^{3\omega} N \langle \gamma' + i\gamma'' \rangle_{\text{dye}}, \quad (10)$$

where m is the mass, f represents the appropriate Lorentz local field factors, N is the number density determined from the weight fraction and the molecular mass of the particular dye (with C16-TSQ being slightly more than twice as heavy per molecule than ISQ), $\langle \gamma \rangle \approx \gamma_{xxx}/5$ for a one-dimensional molecule, and γ' and γ'' are the real and imaginary second hyperpolarizabilities of the dissolved dye.

To fit the data to a particular model of the excited states, we used a value of 0.58×10^{-14} esu for $\chi_{BK-7\text{Glass}}^{(3)}$ obtained from Reference 6 at $1.907 \mu\text{m}$ and adjusted it for each of our experimental wavelengths using Miller's rule and the refractive index dispersion data calculated from the BK-7 refractive index dispersion relation.¹⁵ For chloroform, we similarly used the value of 0.875×10^{-14} esu at $1.064 \mu\text{m}$ obtained from Reference 14 (modified for differences in the conventions used to define $\chi^{(3)}(-3\omega; \omega, \omega, \omega)$) and we adjusted this value for the relevant wavelengths using Miller's rule and a fit refractive index dispersion relation for chloroform. Our fits were not qualitatively sensitive to the susceptibilities used for glass and chloroform.

DATA AND MODEL FITS

Figures 3 and 4 show the experimentally determined intensity ratios for the specified concentrations of ISQ and C16-TSQ in chloroform, together with our least squares fits. On each graph, a ratio of unity implies that the presence of the dye at this concentration does not change the amplitude of the third harmonic fringes from the amplitude obtained for pure chloroform. Because there are no sign changes in the nonlinearity of chloroform which is positive and only slowly increasing with increasing frequency in this region, we can infer the location and strength of a significant two-photon resonance in the dye solutions from our fit to the shape of the dispersion to the predictions of Eq. (4). By using the linear absorption spectrum to determine μ_{01} , ω_{01} and Γ_{01} , we find that the dispersion of the third harmonic in this region is very sensitive to the location and strength of the 2^1Ag two-photon transition. We determine μ_{01} in each case by integrating over a Gaussian fit to the main linear absorption peak in the manner described in reference [16]. The fit parameters used for each graph are given in Table 1, where errors were estimated from the reasonableness of the fits and uncertainties in the determination of μ_{01} from the linear absorption spectra.

For ISQ (Fig. 3), we fit the data to the four-level model given by Eq. (4) with $\Delta\mu_{01} \equiv 0$. The inset to the figure shows the only two types of transitions used in the fit. For C16-TSQ (Fig. 4), a four-level model with "pure" two-photon levels was unable to account even qualitatively for an unmistakable secondary oscillation in the ratio of the third harmonic at around 1.3 to $1.4 \mu\text{m}$ fundamental. To fit this feature, we first tried without success to include terms in our model representing direct transitions between the ground and the two-photon states (μ_{0n} transitions). These terms led to large

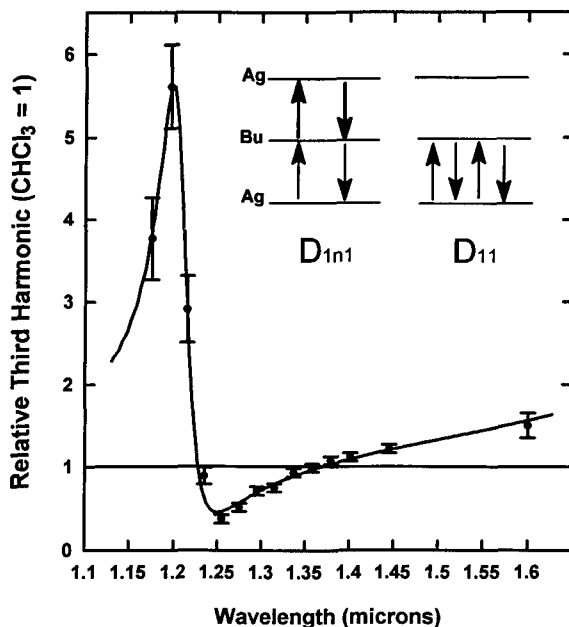


FIGURE 3 Ratio of the third harmonic fringe amplitudes of $0.215 \pm 0.02\%$ ISQ by wt. in chloroform to the fringe amplitudes of pure chloroform. Errors were estimated only from the uncertainties in the measured Maker fringe amplitudes due to absorption of the third harmonic. The solid line is a four-level fit using the parameters listed in Table 1 with level diagrams for the relevant virtual transitions shown schematically on the inset.

divergences between the data and our fit at longer wavelengths. In the absence of absorption at the fundamental, the sum-over-states expression for the third harmonic requires that the feature be accounted for by an additional competing "resonance" near either half (2ω) or one-third (3ω) of the fundamental wavelength for the oscillation. For this feature to be of a three-photon character (3ω), it should also be observable in the linear absorption spectrum. As shown in Figure 1, the solutions are relatively

TABLE 1
Four-level fit parameters for dispersion of third harmonic of $0.215 \pm 0.02\%$ ISQ and $0.43 \pm 0.02\%$ C16-TSQ by wt. in chloroform.

ab levels	10	20	n0
ISQ	$(\Delta\mu_{01} \equiv 0)$		
$\omega_{ab}(\text{eV})$	1.896 ± 0.004	2.05 ± 0.01	3.3 ± 1
$\Gamma_{ab}(\text{meV})$	45 ± 3	33 ± 6	360 ± 120
$\mu(\text{Debye})$	$\mu_{01} = 10.3 \pm 1.4$	$\mu_{12} = 4.8 \pm 1$	$\mu_{1n} = 9.5 \pm 3$
C16-TSQ	$(\Delta\mu_{01} = 1.3 \pm 0.5 \text{ Debye})$		
$\omega_{ab}(\text{eV})$	1.87 ± 0.006	2.02 ± 0.01	3.7 ± 1
$\Gamma_{ab}(\text{meV})$	42 ± 3	50 ± 15	250 ± 120
$\mu(\text{Debye})$	$\mu_{01} = 11.8 \pm 1.4$	$\mu_{12} = 4 \pm 1$	$\mu_{1n} = 11 \pm 3$

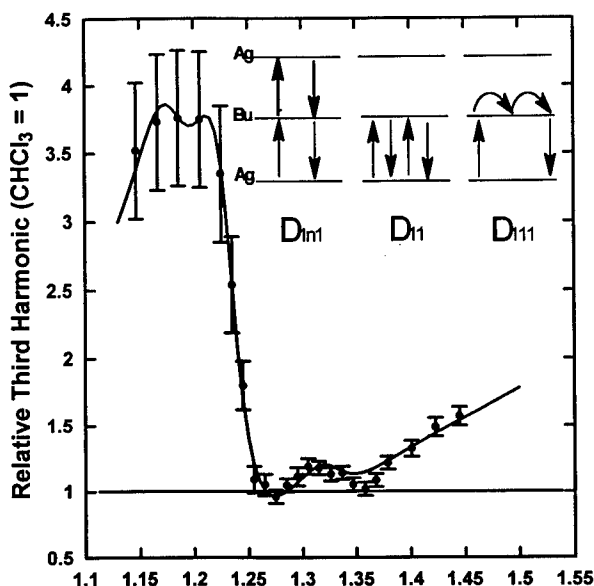


FIGURE 4 Ratio of the third harmonic fringe amplitudes of $0.43 \pm 0.02\%$ C16-TSQ by wt. in chloroform to the fringe amplitudes of pure chloroform. Errors were estimated only from the uncertainties in the measured Maker fringe amplitudes due to absorption of the third harmonic. The solid line is a modified four-level fit using the three-level parameters listed in Table 1 with level diagrams for the relevant transitions shown on the inset and a weak additional Bu level to include an effect of the ultraviolet absorption below 400 nm as described in the text.

transparent between 400 and 500 nm. Thus, we expect a resonant transition at around 2ω , corresponding to 650–700 nm, the location of the dominant linear absorption peak on Figure 1. Our best fit was then obtained by assuming that C16-TSQ is weakly noncentrosymmetric with the dipole transition shown on the inset to Figure 4. In this case, the contribution to D_{111} at $2\omega = \omega_{01}$ approximately reproduces the feature at $1.31 \mu\text{m}$ shown in that Figure. The use of a simplified model with just these three types of transitions is consistent with the predictions of Dirk, Cheng, and Kuzyk.⁵

For C16-TSQ, there are also features in the data below $1.2 \mu\text{m}$ that diverge from a model with just one one-photon excited state. We believe these features, which may also be present to a lesser extent or at shorter wavelengths with ISQ, are due to the onset of a three-photon absorption in the near uv spectrum of the dye. We included a narrow ($\sim 70 \text{ meV}$) and weak, fifth level of odd parity ($\mu_{04} \sim \mu_{24} \sim 3.6 \text{ Debye}$) around 390 nm in our fit for C16-TSQ, consistent with the onset of the ultraviolet absorption band shown in Figure 1. The terms involving transitions between this higher-lying Bu state and the high-lying Ag states were ignored since they contributed no additional features in this wavelength region. The addition of just this single fourth level is only a first approximation to the ultraviolet absorption band and implies the presence of a slight fluctuation in the third-harmonic as a function of wavelength at just below $1.2 \mu\text{m}$. While our measurements were, in general, not spectrally fine enough to resolve this feature, we did observe a similar dip at around $1.18 \mu\text{m}$ at different dye concentrations.

The presence of the fourth level has little effect on the fit to our data above $1.2\text{ }\mu\text{m}$. Only the four-level transitions used in the fit are shown on the inset to Figure 4.

DISCUSSION

With both dyes, we find that the 2^1 Ag state appears just above the 1^1 Bu state in energy and has a transition moment from the first excited state that is moderately smaller than that between the ground and 1^1 Bu state. As has been predicted for linear cyanines,³ these results differ from those obtained both experimentally and theoretically on linear polyenes where the 2^1 Ag state is *below* the 1^1 Bu state.^{2,6} For polyenes, the transition moment from the 1^1 Bu state to the dominant two-photon state (not necessarily the 2^1 Ag state) is reported to be larger than the $1^1\text{ Ag} \rightarrow 1^1\text{ Bu}$ transition moment, thus resulting $\gamma > 0$ far off-resonance.

The 2^1 Ag transition moments determined by our experimental fits ($\mu_{12} = 4.8$ Debye for ISQ and $\mu_{12} = 4.0$ Debye for C16-TSQ), however, are more than an order of magnitude larger than that predicted by Zhou⁹ for a similar squaraine dye ($\mu_{12} = -0.34$ Debye) using quantum chemical calculations. Those calculations predict large two-photon transition moments (~ 10 Debye) only for high-lying two-photon states (the 3^1 Ag , 4^1 Ag , or 5^1 Ag states in the ultraviolet). We find that the 2^1 Ag state plays a significant role in determining the shape of the nonlinear dispersion for third harmonic generation and predict that this state is the second most significant excited state (after the 1^1 Bu state) to third harmonic measurements in the *near* IR region due to the near-resonant denominator and the significant transition moment.

Our measurements confirm the predictions of Pierce and Zhou, however, that high-lying two-photon states must be included in modeling γ for these materials. With respect to both ISQ and C16-TSQ, we find at least one high-lying two-photon state is required to fit the data using the μ_{01} transition moment strength determined from the linear absorption spectra. A simple three-level model with only one two-photon state is inadequate. If the higher-lying two-photon states are not included, we would need to underestimate the μ_{01} transition moments by $\sim 30\%$ to obtain a reasonable fit.

The parameters of higher-lying two-photon states are not well determined by the fits to our data. We can fit our data with either one or two high-lying two-photon states of a broad range of widths, strengths, and locations (all above 3 eV). The width, strength, and locations of these states are interdependent parameters in our fits and are not precisely determined in this work. However, it is seen that all reasonable fits to high-lying two-photon states merely contribute a relatively constant imaginary part to γ in the spectral region of our measurements. While our measurements precisely characterize the 2^1 Ag state, further measurements are needed to characterize the higher-lying two-photon states.

The location and width of the 2^1 Ag state varies little in any of our fits, regardless of the strength of μ_{01} or the parameters of the high-lying two-photon states. The uncertainty in μ_{12} is almost entirely determined by the uncertainty in μ_{01} . As an additional check, we attempted to fit the resonant behavior at $\geq 1.2\text{ }\mu\text{m}$ using a three-photon transition to around 400 nm , but the transition moments required for even vague qualitative fits were far larger than could be justified by the weak near

ultraviolet absorptions shown in Figure 1. Similarly, we tried unsuccessfully to use the high energy shoulder of the linear absorption spectrum peak to fit our results. The results for the 2ω resonance in this case were at wavelengths too long to fit our data.

Our third harmonic generation measurements and dispersion fit for ISQ are qualitatively consistent with and complement previously reported ISQ third-order measurements.^{5,7,8,17} By analyzing the quadratic electroabsorption spectrum for films of ISQ doped PMMA on ITO glass, Poga and coworkers¹⁷ were able to identify a two-photon state in ISQ at about 600 nm (2.07 eV). We expect that this is the same two-photon state contributing to our third harmonic spectrum, differences in our fit parameters being at least in part attributable to the different molecular environments, PMMA vs. chloroform, and the different mechanisms involved, quadratic electro-optic vs. third harmonic generation, the former having an orientational contribution that was accounted for by looking at the temperature dependence of the effect.¹⁷

Our results should also be compared to third harmonic measurements by Aramaki and coworkers on trans- β -carotene films.¹⁸ Their work also probed the 2Ag state by fitting the spectral dispersion of β -carotene films to a four-level model involving the 1Bu and 2Ag states and a higher-lying n Ag state. As predicted for polyene-like molecules, they located the 2Ag state energetically below the 1Bu state. Also, they found the 1Bu–2Ag transition moment to be smaller than the 1Bu– n Ag transition moment and predicted a μ_{12}/μ_{01} ratio of 0.27, comparable to the results shown in our Table 1, though the authors express significant uncertainty in these results. We expect that when the 2Ag state is energetically below the 1Bu state, as in polyenes, third-harmonic spectral dispersion measurements will locate the 2Ag state less precisely due to competition between the $\omega \rightarrow \omega_{10}/3$ and the $\omega \rightarrow \omega_{20}/2$ resonances which may appear in overlapping regions of the third harmonic spectrum.

In Figure 5, we show the real and imaginary parts of the predicted nonlinear refractive index, n_2 , for an approximately 1% solution of ISQ in the near infrared region. This n_2 dispersion curve was obtained by substituting the fit parameters from our third harmonic four-level fit into the sum-over-states expression applicable to $\gamma_{\text{Kerr}}(-\omega; \omega, \omega, -\omega)$. The resonant behavior is dominated in this case by

$$D_{121}^{\text{Kerr}} \rightarrow [(\omega_{10} - \omega - i\Gamma_{10})^2 (\omega_{20} - 2\omega - i\Gamma_{20})]^{-1}. \quad (11)$$

As can be seen in Figure 4, we expect ISQ to exhibit a negative intensity dependent refractive index below $1.2 \mu\text{m}$ which may be useful for device purposes. We also predict significant two-photon absorption, however, in the region where the real part of n_2 is largest. This absorption may limit the usefulness of ISQ for device purposes in this wavelength range. More careful direct measurements should be made to explore this region for possible device application. Based on comparisons with the electroabsorption studies of Reference 17, we expect that in a polymer environment such as PMMA, the two-photon resonance may be broadened and, so, the width of the two-photon absorption, limiting the practical value of the relevant figure of merit, $\text{Re}[n_2]/\text{Im}[n_2]$.¹⁹

The additional features found in the third harmonic spectrum of C16-TSQ will require further study. Our prediction of noncentrosymmetry in the model for C16-TSQ, but not ISQ, needs to be justified by the differences in structure between the molecules. In this regard, we are planning to measure the dipole moment of each dye in

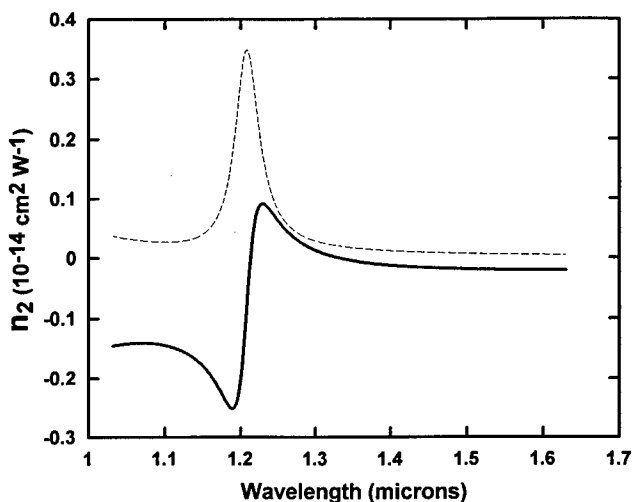


FIGURE 5 Predicted nonlinear refractive index (solid line-real part, dashed line-imaginary part) due to the optical Kerr effect using the fit parameters from Table 1 for about 1% solution of ISQ in chloroform.

chloroform by more direct means. One possible explanation is that the long C_{16} -alkyl chain on TSQ increases the two-dimensional character of the dye perhaps by enhancing the presence of a cis-conformation in the dye solution which would be noncentrosymmetric. While both molecules are zwitterionic in character, ISQ dissolves through a proton exchange leaving the molecule more neutral than TSQ. Also, the hydrophobic nature of the C_{16} -alkyl chain on TSQ suggests it is more likely to lead to molecular associations in solution. Finally, the presence of sulfur may change the nature of the conjugation from that shown in Figure 1. Further analysis of these and similar molecules is ongoing in an attempt to address these concerns.

Additional measurements are also needed to determine more exactly the strengths and locations of the significant high-lying two-photon states of the dye. To further understand these squaraines it may also be necessary to measure their third harmonic spectrum in other solvents so as to explore the effect of the polarity of the solvent on the nature of the electronic states. As seen by Marder and co-workers,¹⁰ in solvents of different polarity there can be different levels of charge-transfer state present, leading to different levels of bond alternation and different contributions from the one- and two-photon states of the molecule. Thus the degree of bond alternation may significantly affect the magnitude and sign of γ . This work as well as further studies of the nonlinear spectrum of these and related dyes is in progress.

ACKNOWLEDGEMENTS

The authors are grateful to C. Dirk and M. Kuzyk for providing the ISQ used in this study. We also thank J. R. Heflin and M. Kuzyk for very helpful discussions. J. H. Andrews acknowledges support from the NASA Lewis Research Center in the

form of a Graduate Researchers Fellowship. This work has also been supported in part by AFOSR grant no. F49620-93-1-0202.

REFERENCES

1. K. D. Singer, J. E. Sohn, L. A. King, H. M. Gordon, H. E. Katz and C. W. Dirk, *J. Opt. Soc. Am. B*, **6**, 1339 (1989).
2. J. W. Wu, J. R. Heflin, R. A. Norwood, K. Y. Wong, O. Zamani-Khamiri, A. F. Garito, P. Kalyanaraman and J. Sounik, *J. Opt. Soc. Am. B*, **6**, 707 (1989).
3. B. M. Pierce, *Proc. SPIE*, **1560**, 148 (1991).
4. M. G. Kuzyk and C. W. Dirk, *Phys. Rev. A*, **41**, 5098 (1990).
5. C. W. Dirk, L.-T. Cheng and M. G. Kuzyk, *Int. J. of Quant. Chem.*, **43**, 27 (1992).
6. J. R. Heflin, Y. M. Cai and A. F. Garito, *J. Opt. Soc. Am. B*, **8**, 2132 (1991).
7. M. G. Kuzyk, J. E. Sohn and C. W. Dirk, *J. Opt. Soc. Am. B*, **7**, 842 (1990).
8. C. W. Dirk and M. G. Kuzyk, *Chem. Mat.*, **2**, 4 (1990).
9. Q. L. Zhou, R. F. Shi, O. Zamani-Khamari and A. F. Garito, *Nonlinear Optics*, **6**, 145 (1993).
10. G. Bourhill, J.-L. Bredas, L.-T. Cheng, A. C. Friedli, C. G. Gorman, S. R. Marder, F. Meyers, J. W. Perry, B. M. Pierce, J. Skindhoj and B. G. Tiemann, *OSA Tech. Digest*, **17**, 46 (1993).
11. R. W. Bigelow and H.-J. Freund, *Chem. Phys.*, **107**, 159 (1986).
12. A. Agnesi, G. C. Reali, V. Kubecek, S. Kumazaki, Y. Takagi and K. Yoshihara, *J. Opt. Soc. Am. B*, **10**, 2211 (1993).
13. J. D. V. Khaydarov, J. H. Andrews and K. D. Singer, *Opt. Lett.*, **19**, 831 (1994).
14. F. Kajzar and J. Messier, *Rev. Sci. Instrum.*, **58**, 2081 (1987).
15. *Optical Glass* [Schott Glass Technologies Inc. catalog] (Schott Glass, Duryea, Pa., 1990).
16. C. W. Dirk, H. E. Katz, M. L. Schilling and L. A. King, *Chem. Mat.*, **2**, 700 (1990); *errata* **3**, 207 (1991).
17. C. Poga, M. G. Kuzyk, S. Martinez and C. W. Dirk, *Proc., SPIE*, **2025**, 363 (1993).
18. S. Aramaki, W. Torruellas, R. Zanon and G. I. Stegeman, *Opt. Comm.*, **85**, 527 (1991).
19. V. Mizrahi, K. W. DeLong, G. I. Stegeman, M. A. Saifi and M. J. Andrejco, *Opt. Lett.*, **14**, 1140 (1989).

Large Effective $\chi^{(3)}$ by Cascading of $\chi^{(2)}$ in Crystal Cored Fibers

P. VIDA KOVIC^a, J. ZYSS^a, D. KIM^b, W. TORRUELLAS^b and G. STEGEMAN^b

^aFRANCE TELECOM/CNET/PAB, 196, Avenue Henri Ravera,
92220 Bagneux, France, ^bC.R.E.O.L. University of Central Florida,
Orlando, FL 32826, U.S.A.

Received 6 April 1994; accepted 11 April 1994

Very large nonlinear shifts ranging from $\pi/4$ to $\pi/2$ are observed at relatively modest input intensities, in single crystal cored fibers of 4-(N,N-dimethylamino)-3-acetamidonitrobenzene (DAN). A series of experiments unambiguously ascribe their origine in a cascading sequence of second harmonic generation followed by down frequency conversion. The nonlinear shifts and corresponding n_2 values extracted from independent observations of self-phase modulation and direct interferometric measurements reach 10^{-12} cm²/W at relatively modest input intensities ranging from 30 to 60 MW/cm².

INTRODUCTION

Organic materials are well known to exhibit enhanced nonlinear optical properties as compared to those of classical inorganic compounds (i.e., LiNbO₃),¹ as evidenced by considerable experimental and theoretical work over the last two decades. These materials are mainly made of highly dipolar molecules, derived from the para-nitroaniline. The origin of large second-order molecular hyperpolarisabilities lies in conjugated π -electron systems where electron delocalisation is assymetrically enhanced by substituting donor- and acceptor groups at the opposite sites. Several outstanding noncentrosymmetrical crystals with molecular ordering optimised at the crystal level toward efficient second harmonic generation, have been grown and characterised during the last decade. Some of them, such as N-(4-Nitrophenyl)-(L)-prolinol (NPP),² 3-Methyl-4-Nitropyridine-1-Oxide (POM),³ and 4-(N, dimethyl-amino)-3-acetamidonitrobenzene (DAN)⁴ have been successfully used for demonstration of parametric amplification,⁵ parametric oscillation,⁶ etc.

In contrast with earlier molecular engineering strategies where cubic nonlinearities at the macroscopic level were thought to originate from cubic molecular hyperpolarizability we show in our work that quadratic molecular media optimised for efficient second order parametric interactions, may be suitable for applications in the field of ultrafast low-power all optical signal processing.⁷ This is based on recent demonstrations of cascading of second order processes in noncentrosymmetric mineral materials leading to significant third order effects.^{8–10} In the first part of our work (Sect. 1), we will briefly introduce fundamental features of cascading, while in the second part (Sect. 2) we will describe experiments performed on DAN crystal cored fibers. Finally, we will discuss our results and conclude on some possible applications (Sect. 3).

CASCADING OF SECOND ORDER PROCESSES

The domain of all optical signal processing has been traditionally related to $\chi^{(3)}$ processes.⁷ Indeed, the operation of such key devices as non-linear Mach-Zender interferometers or non-linear directional couplers is based on the non-linear phase shifts accumulated by the fundamental beam (at the frequency ω), over the propagation. The basic underlying mechanism is the self-action of the beam through an intensity dependent refractive index given by

$$n(I) = n_0 + n_2 \cdot |E|^2 = n_0 + \gamma \cdot I \quad (1)$$

where n_0 is the refractive index at low intensity, n_2 and γ are the nonlinear refractive index coefficients, while I is the local intensity.

The physical mechanisms responsible for the intensity dependent refractive index will strongly relate to the nature of the materials. The usual origin of refractive index changes are thermal, electrostriction and electronic processes or any combination of them.⁷ Although, thermal or resonant electronic nonlinear changes of refractive index are very large, such dissipative phenomena will exhibit high losses and/or relatively slow response time.

Nonlinear change of the refractive index based on purely non-resonant electronic processes would be more consistent with ultrafast signal processing. Moreover, in order to decrease the power of operation and to open the possibility for further integration, the waveguide format based on highly non-linear materials is preferable. Thus the search for new materials with high values n_2 's driven by ultrafast processes has been strongly boosted during the last decade.⁷ We have summarized in Table 1 range of n_2 values measured for materials of interest for all optical signal processing⁷. Clearly only semiconductor doped glasses and conjugate polymers exhibit both relatively high and fast n_2 's. Although, nonlinear Mach-Zender interferometers and nonlinear directional couplers have been successfully realized from silica glasses and semiconductors, powers needed for the operation of these devices are still too high.⁷ From this Table n_2 's of small organic molecules seem very far from desired level.

In 1992 Stegeman and coworkers⁸ have shown a fundamentally new way of reaching potentially large nonlinear shifts in quadratic noncentrosymmetric materials. The large nonlinear shifts observed in a single crystal of KTP⁸ have been identified as the consequence of a cascading process involving second harmonic generation in a phase

TABLE 1
The nonlinear refractive index ranges for various materials relevant for low power all optical signal processing.

Material	$n_2(\text{cm}^2/\text{W})$
Silica glasses	3×10^{-16}
Semiconductor doped glasses	$10^{-15} - 10^{-14}$
Semiconductors	$ 10^{-14} - 10^{-12} $
Polymers (polydiacetylene type)	$ 10^{-14} - 10^{-11} $
Small molecules and polymers with small active groups	$\leq 10^{-14} $

mismatched configuration. In a very schematical picture this process result from the following sequence:

$$\omega + \omega \rightarrow 2\omega - \omega \rightarrow \omega \quad (2)$$

During the propagation of the fundamental beam (ω) in a noncentrosymmetrical medium in a phase mismatched configuration a second harmonic (or a sum-frequency, if fundamental beams of different frequency are involved) is generated. This process is followed by a down-conversion ($2\omega - \omega \rightarrow \omega$). The fact that the process is coherent and phase mismatched is responsible for a nonlinear phase shift experienced by the fundamental beam. Indeed, when the second harmonic should deliver the energy back to the fundamental beam, it "sees" different phase velocity due to the phase mismatch. To permit however the transfer of the energy, the second harmonic will excite the medium in such a way that the resulting polarisation (proportional to $\int d_{\text{eff}} E_{2\omega} E_{\omega}^* dz$) is in quadrature with the polarization due to fundamental beam (proportional to $\int d_{\text{eff}} E^{\omega} E^{\omega} dz$). The polarization in quadrature will then shift the phase of the fundamental beam to facilitate the energy exchange between second harmonic and fundamentals beams. *This is the key mechanism for producing very large nonlinear phase shifts, which is completely different from that involved in purely cubic materials.* The phase shift obtained by cascading second order process has been shown^{9,10} to oscillate with the period depending on the propagation distance, input intensity, phase mismatch and is roughly proportional (in the limit of small pump depletion) to the well known figure of merit for second order nonlinear parametric processes.¹

Observation of phase change of the fundamental due to cascading has been reported in the past.¹² But, this effect has been considered as limiting factor for efficient second harmonic generation. The first study to point out cascading as a useful phenomenon toward all optical signal processing was published in Reference 13. However, the rational starting point for the theoretical and experimental understanding of cascading in the domain of all optical signal processing can be found in the seminal works of Stegeman and coworkers.⁸⁻¹⁰ In what follows we will base our discussion on these works.

The coupled equations describing second harmonic generation are as follows:

$$\frac{dE_{\omega}}{dz} = -i\kappa(-\omega; 2\omega, \omega) E_{2\omega} E_{\omega}^* e^{-i\Delta\beta z} \quad (3a)$$

$$\frac{dE_{2\omega}}{dz} = -i\kappa(-2\omega; \omega, \omega) E_{\omega}^2 e^{i\Delta\beta z} \quad (3b)$$

where z is the propagation distance, $\Delta\beta = 2k(n_{2\omega} - n_{\omega})$ is the wave vector mismatch between coupled modes, $n_{2\omega}$ and n_{ω} are the effective refractive indices of guided modes at corresponding frequencies, $k = 2\pi/\lambda_{\text{vac}}$ is the free space wavenumber, κ is proportional to the effective nonlinear coefficient (d_{eff}) depending on the polarizations of the fundamental and second harmonic beams through the tensorial structure of $\chi^{(2)}$, and transverse field distribution of modes. We neglect here absorption and the contribution from pure $\chi^{(3)}$ processes.

The complete solution of this set of coupled equations is well known from early studies by Bloembergen *et al.*,¹⁴ and can be obtained in a closed form via elliptic integrals. Instead, we will adopt a simplified approach giving a more immediate insight into the main features of cascading processes.

If we assume no initial second harmonic, we obtain a second order differential equation for E_ω by eliminating $E_{2\omega}$ from (3a) as follows:

$$\frac{d^2 E_\omega}{dz^2} + i\Delta\beta \frac{dE_\omega}{dz} - \Gamma^2 \left(1 - 2 \left| \frac{E_\omega}{E_0} \right|^2 \right) E_\omega = 0 \quad (4)$$

where τ is a parameter given by:

$$\Gamma = \frac{\omega d_{\text{eff}} |E_0|}{c \sqrt{n_{2\omega} n_\omega}} \quad (5)$$

E_0 is the input amplitude of the fundamental.

In the case of a phase mismatched configuration, small pump depletion, $|E_\omega|$ remains equal to $|E_0|$. The electric field of the fundamental can be expressed as

$$E_\omega(z) = |E_0| \exp(-i\Delta\Phi^n(z)) \quad (6)$$

where $\Delta\Phi^n(z)$ is z -dependent nonlinear phase of the fundamental beam.

At the exit interface after the interaction length L , the total nonlinear phase change is given by:

$$\Delta\Phi^n(L) \approx \frac{\Delta\beta L}{2} \left(1 + \frac{\sqrt{2\Gamma}}{\Delta\beta^2} \right) \quad (7)$$

For the $\Gamma/\Delta\beta \ll 1$, the case of large mismatch and/or low fundamental intensity, the phase change due to cascading is formally similar to the Kerr effect. We can then define an effective n_2 :

$$n_2^{\text{eff}} = -\frac{4\pi L}{c\epsilon_0 \lambda} \frac{d_{\text{eff}}^2}{n_{2\omega} n_\omega^2} \frac{1}{\Delta\beta L} \quad (8)$$

Two striking features follow from this relatively simple equation: firstly, the sign of the effective refractive index follows the sign of the phase mismatch. Secondly, the effective nonlinear index is proportional to the figure of merit for second order parametric processes. Beyond this simple, however illustrative model, small phase mismatch and/or high second harmonic conversion rate could require numerical solution of coupled equations to precisely account the nonlinear phase change due to cascading.^{9,10}

EXPERIMENTAL

Fabrication of DAN Fibers

Due to its high effective d_{eff} coefficients ($d_{\text{eff}} \sim 27$ pm/V at $1.064 \mu\text{m}$ for Type I phase matching) and its availability in both single crystalline⁴ and crystalline cored fiber¹⁵ formats with adequately oriented dielectric axis, DAN has been selected as a relevant candidate for first cascading experiments in organic media.

Several years ago the problem of orientation of dielectric axis and its influence on efficient second harmonic generation in organic crystal cored fibers¹⁶ had been addressed. It had been shown that nonlinear organic materials belonging to the orthorhombic crystallographic class, (encompassing the majority of highly nonlinear

organic materials) naturally grow in capillaries with their twofold axis parallel to the fiber axis. In this configuration SHG is symmetry forbidden. Modifying the crystal orientation is a rather involved task although some success has been observed with meta-nitroaniline (m-NA) and N-(4-Nitrophenyl)-N-methylaminoacetonitrile (NPAN).¹⁷ In spite of persistent research efforts, a limited number organic materials have been found to grow spontaneously with adequate orientation in capillaries. One of them, DAN belonging to the monoclinic crystallographic class (point group 2) grows with its unique twofold axis perpendicular to the fiber axis, leading to a favorable orientation for efficient Type I second harmonic generation. The best result has been obtained in a 6 μm DAN cored fiber optimized for Cerenkov type SHG, where 1.5% second harmonic conversion rate has been measured for 1 mW average input power at 1,064 μm .¹⁵

DAN fibers used in our experiments have been grown from the melt by a modified Bridgman-Stockbarger method. We have used different Schott glasses (from the SF-series) for the fabrication of capillaries with the core diameters ranging from 2 to 10 μm . The crystal quality of the core has been examined between crossed polarizers. The precise DAN crystal orientation in fibers is shown in Figure 1. In this configuration efficient second harmonic generation requires the fundamental mode at ω polarized in the X-Z dielectric plane resulting in a second harmonic polarized along the twofold axis Y. These polarizations have transverse components with respect to the propagation axis in keeping with basic electromagnetic requirements.

Optical Measurements

In 1990, Yamashita and coworkers¹⁸ have observed a very strong spectral broadening of a 250 fs pulses produced by an amplified colliding pulse mode-locked laser source at 625 nm, in a 3.9 mm long DAN fiber. The nonlinear refractive index n_2 estimated from this self-phase modulation experiment was as large as 17 000 that of silica glass. This result had been surprising, as the modest hyperpolarizabilities of small para-nitroaniline-like molecules are not expected to display such efficient third order effects.

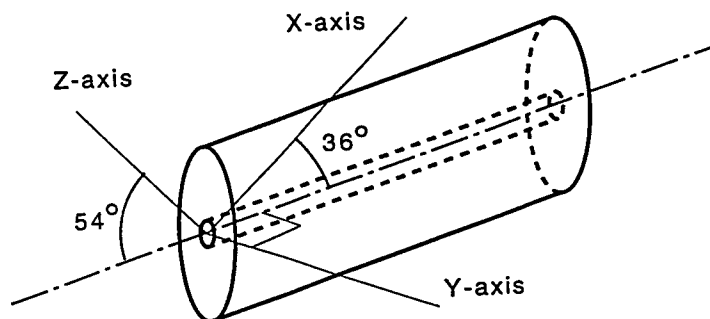


FIGURE 1 Orientation of the dielectric axes of DAN single crystal in a capillary tube.

Third Harmonic Generation To elucidate this unsettled issue, we have performed several third harmonic Maker fringe experiments on 1 μm thick PMMA films doped with different concentrations of DAN (Fig. 2). The films have been spin coated on glass substrates. The light source was a Raman shifted YAG laser delivering 8 ns pulses at 1.904 μm . For this fundamental wavelength, the third harmonic is well outside the absorption band of a DAN molecule thus precluding resonant enhancement of $\chi^{(3)}$.

By subtracting the contribution of the substrate,¹⁹ the average molecular $\chi^{(3)}$ of DAN has been estimated to be positive and only 4 times larger than $\chi^{(3)}$ (SiO_2). This result has been compared to third harmonic generation measurements performed under similar conditions on the PMMA films doped with other para-nitroaniline derivatives such as NPP and NPAN. The variations of $\chi^{(3)}$ between these molecules were of the order of 20% only, thus reflecting variations in the proximity of the absorption band and the strength of electron-acceptor and -donor groups of corresponding molecules. From this value and by using an oriented gas approach¹ the $\chi^{(3)}$ of DAN crystals is evaluated to be 100–150 times larger than $\chi^{(3)}$ of silica glass, but still two orders of magnitude lower than results obtained by Yamashita and coworkers.¹⁸ Even with a more sophisticated approach, molecular $\chi^{(3)}$ of DAN cannot explain such a large discrepancy.

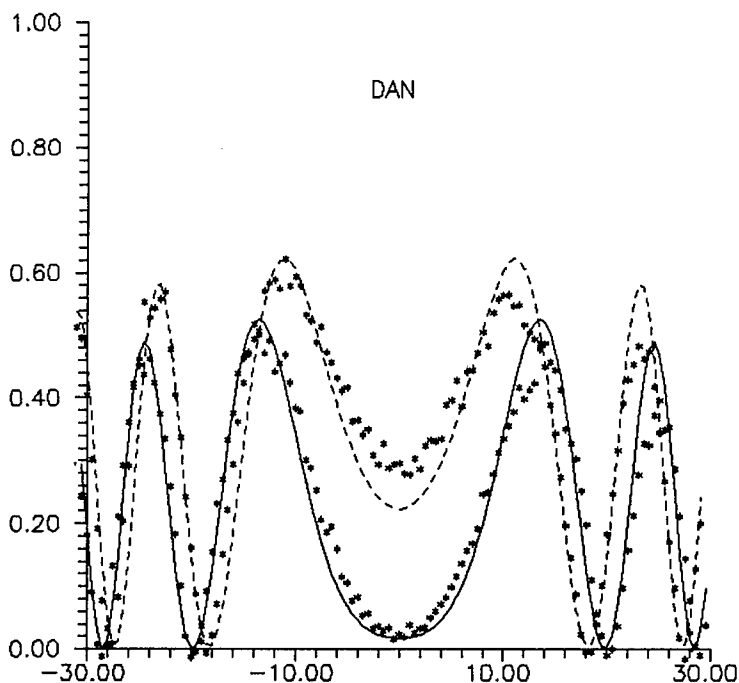


FIGURE 2 Third harmonic Maker fringes, obtained by the angular tuning of a 1 μm thick PMMA film doped with DAN, spin coated on a glass substrate. The fundamental wavelength is 1.904 μm : —third harmonic Maker fringes of substrate; —+—third harmonic Maker fringes of substrate and film.

Self-Phase Modulation To prevent any contribution from resonant interactions to an enhancement of $\chi^{(3)}$, we have undertaken self-phase measurements at $1.55 \mu\text{m}$. The laser source was an additively-pulse-mode locked color center laser generating 600 fs pulses at 76 MHz repetition rate. A multimode 2.6 mm long, $5 \mu\text{m}$ core DAN/SF 15 fiber has been used. The wavelengths of generated beams have been carefully measured by a calibrated 0.5 m monochromator. The clearly observed spectral broadening corresponding to an induced phase shift of $\pi/2$ and a factor of 1.75 has been achieved with a modest 2.5% coupling efficiency (Fig. 3). The estimated value of n_2 is as large as $|6 \pm 3| \times 10^{-13} \text{ cm}^2/\text{W}$ at $0.3 \text{ GW}/\text{cm}^2$ input intensity. The important point is that the spectral broadening is only observed in the presence of generated second harmonic. In addition a small amount of the third harmonic probably generated via a sum of the second harmonic and the fundamental beam, has also been observed (Fig. 4).

The importance of the presence of second harmonic light as a condition towards for the observation of spectral broadening has been clearly evidenced in the case of DAN/SF1 single mode fiber. Here, the absence of second harmonic has resulted in an undetectable spectral broadening meaning that the intrinsic $\chi^{(3)}$ of DAN is much smaller than that due to cascading processes. Even for an intensity approaching the damage threshold of fibers ($\approx 1 \text{ GW}/\text{cm}^2$), the spectral broadening was negligible in the limit of precision of our observation method.

Interferometric Measurements We have used a nonlinear Mach-Zender interferometer at $1.32 \mu\text{m}$ with a remarkable resolution of $\pi/100$ for more precise direct measurements of the value and the sign of n_2 . The setup and operation of this

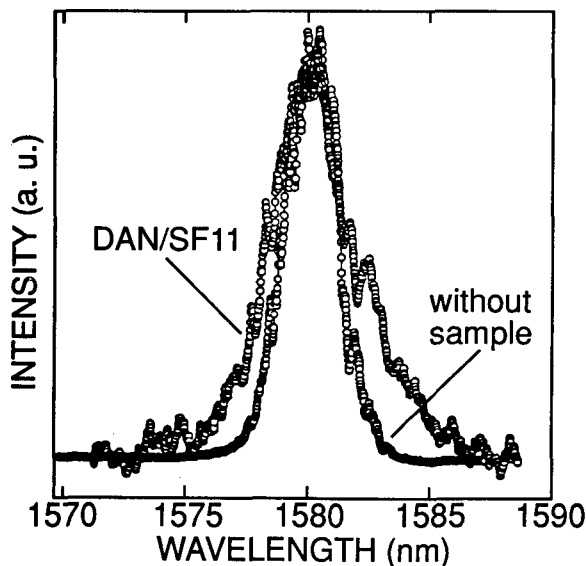


FIGURE 3 Spectral broadening due to cascading of second order processes observed in a DAN/SF11 fiber. The wavelength of the fundamental is $1.58 \mu\text{m}$, and the spectral broadening factor is 1.75. The estimated n_2 is $|6 \pm 3| \times 10^{-13} \text{ cm}^2/\text{W}$ at an input intensity of $0.3 \text{ GW}/\text{cm}^2$.

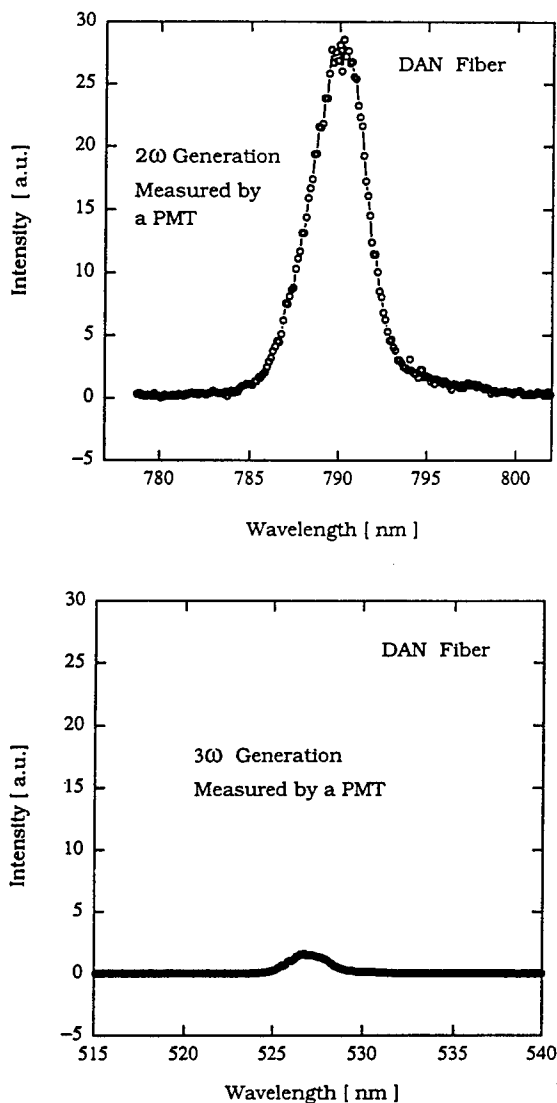


FIGURE 4 a) The second harmonic generated in a DAN/SF11 b) Third harmonic generation in a DAN/SF11 fiber. The intensity ratio second harmonic over third harmonic intensity is less than 1%. The wavelength of the fundamental is 1.55 μm .

interferometer have been described in details in Reference 20. The light source is a mode-locked Nd:YAG operating at 1.32 μm and providing 90 ps pulses at 76 MHz repetition rate (see Fig. 5). An electro-optic slicer synchronized to the mode locker permits to select one high intensity pulse with a 2 KHz repetition rate.

The 4.28 mm long DAN fiber with 7 μm core diameter used in the interferometric measurements is clad by SF1 glass. The linear losses of DAN/SF1 fiber of 0.62 dB/cm

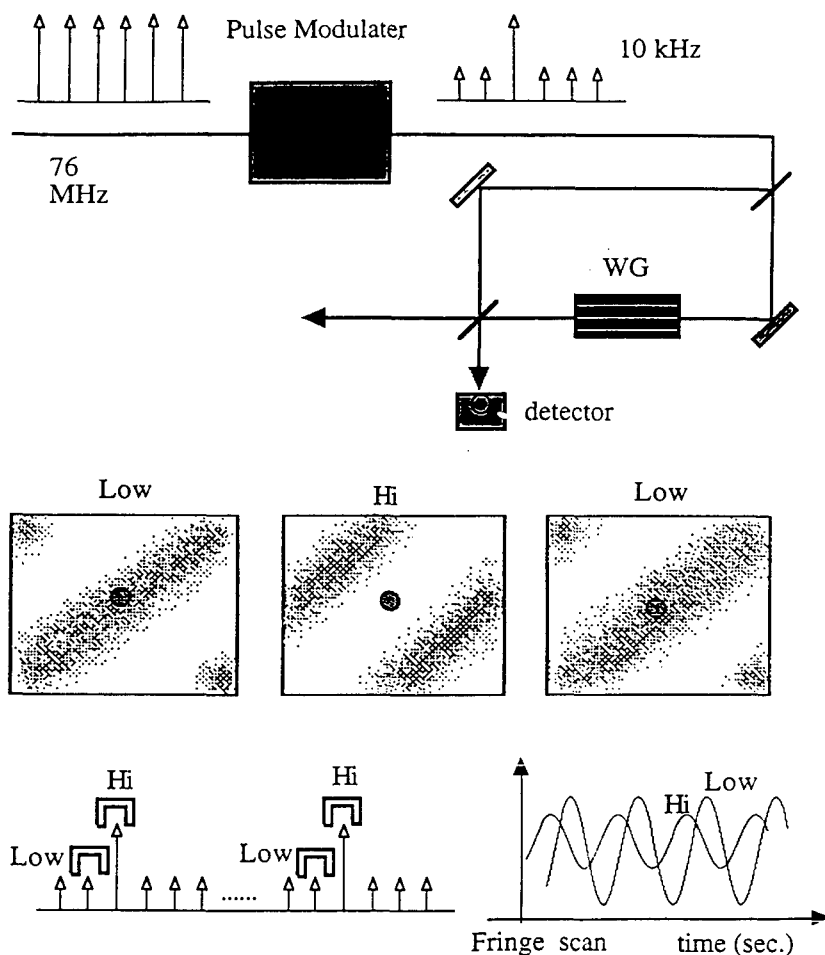


FIGURE 5 Setup and operation of a nonlinear Mach-Zender interferometer. Top: setup of the Mach-Zender interferometer; Middle: fringe displacement following the arrival of a high intensity pulse; Bottom: time behavior of fringes for low and high intensity pulses.

(mostly due to defect scattering along the fiber) have been measured by using an IR camera and a frame grabber.

This fiber accommodates the three lower modes polarized parallel to the X - Z plane at $1.32\ \mu\text{m}$ but cuts off guided second harmonic modes polarized along the twofold crystal axis Y . The only possible phase matched of second harmonic generation in this case results from the optical Cerenkov effect, where one of the guided modes at $1.32\ \mu\text{m}$ is matched to the continuum of second harmonic radiation modes, weakly guided by the cladding. The coupling efficiency of the fundamental beam was 10.4%. From the fringe displacement triggered by the arrival of the strong intensity pulse, phase shifts ranging from $-\pi/8$ to $-\pi/4$ have been measured for relatively small input intensities of 30 to $60\ \text{MW}/\text{cm}^2$ (see Fig. 6). The corresponding $n_2 = -(9 \pm 4) \times 10^{-13}\ \text{cm}^2/\text{W}$ is very large and negative. The sign has been calibrated by shifting one of the mirrors of the

interferometer resulting in a well defined direction of the fringe displacement. In addition a small amount (about 3% of the global second harmonic generated in this Cerenkov type fiber) but very distinct second harmonic guided in the core has been observed. To be sure that this signal is really second harmonic, we have measured the global intensity of second harmonic (guided by the cladding and the core) and the intensity guided by the core in function of the input intensity. The results are summarized in the Figure 7, and confirm the quadratic intensity dependence, characteristic of second harmonic generation. The polarization of second harmonic is checked

$$n_2^{\text{eff}}(1320 \text{ nm}) = -8 \times 10^{-4} \text{ (cm}^2/\text{GW)}$$

$$\Delta\Phi = 0.25 \pi$$

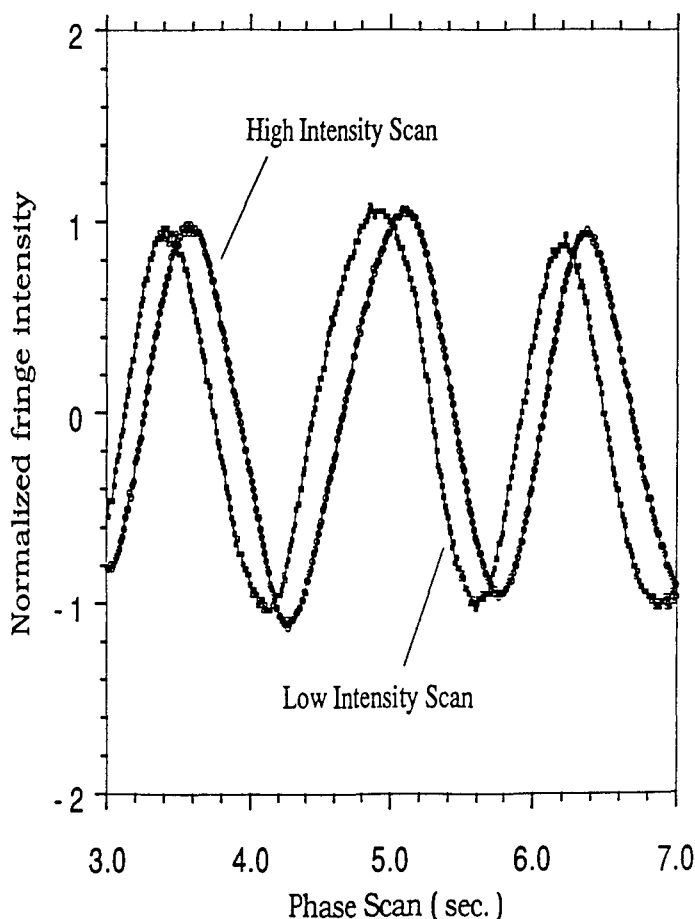


FIGURE 6 Interferometric phase scan of fringes displacement obtained in a DAN/SF1 fiber at 1.32 μm . The observed phase shift of $\pi/4$ corresponds to $n_2 = -8 \times 10^{-13} \text{ cm}^2/\text{W}$.

to be parallel to the Y axis. Here again, the presence of the guided second harmonic is prerequisite towards further observation of a large phase shift.

DISCUSSION AND CONCLUSIONS

Our third harmonic generation measurements in DAN doped PMMA thin films have clearly demonstrated that molecular hyperpolarizabilities cannot be at the origin of very large third order effects observed in crystal cored fibers. These results have been confirmed by EFISH measurement of molecular hyperpolarizability of DAN. It is

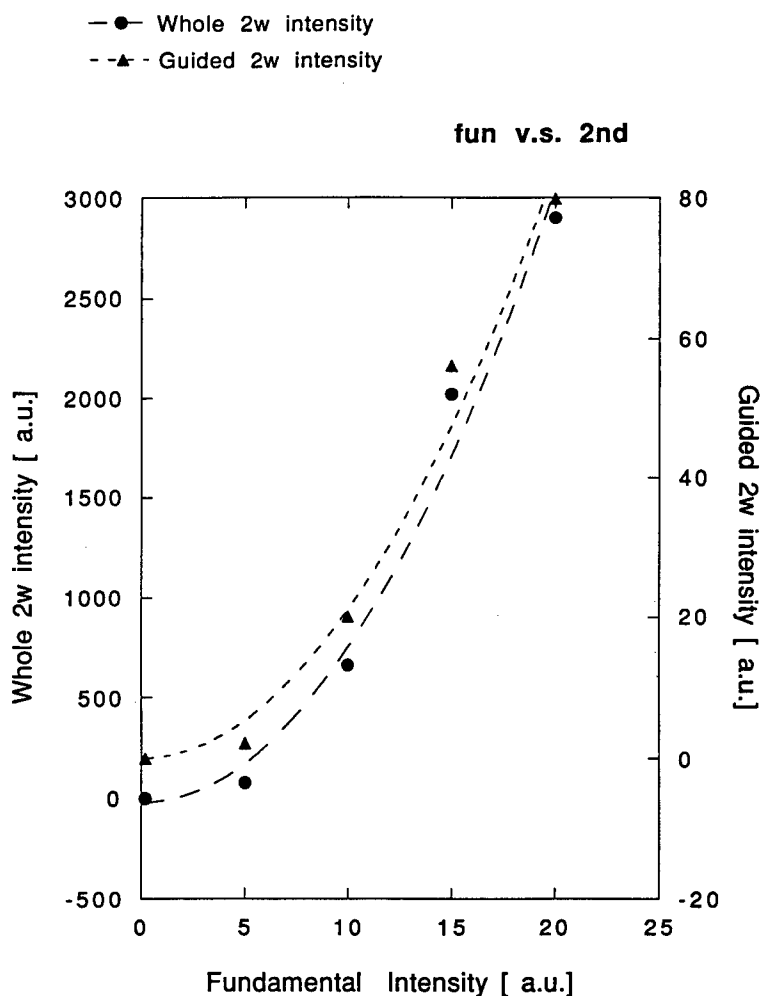


FIGURE 7 Intensity of Cerenkov second harmonic generated in a DAN/SF1 fiber as function of intensity of the fundamental beam at $1.32 \mu\text{m}$. —●— Whole second harmonic intensity guided in both cladding and core. —▲— the second harmonic intensity guided in the core. Note the difference in scales.

difficult to imagine that this molecular hyperpolarizabilities can give rise, due to crystal organization, to such an enhancement of the $\chi^{(3)}$. Although the oriented gaz approach rests on simplifying approximations, it is well adapted towards the estimation of $\chi^{(2)}$ of dipolar media. In the case of $\chi^{(3)}$, this approach is adapted at least for the estimation of the order of magnitude of $\chi^{(3)}$.

Our self phase modulation experiments have clearly confirmed the results previously obtained by Yamashita and coworkers.¹⁸ The measurements of the spectral broadening centered at 1.55 μm have shown that a very large effective n_2 ($\approx 10^{-12} \text{ cm}^2/\text{W}$) is involved in the self phase modulation process without resonant contributions from significant neighbouring levels. The correlation between relatively low level generated second harmonic signals and spectral broadening is clearly established. *There can be no spectral broadening in DAN fibers without the presence of the second harmonic signal.* This allows to conclude that the large spectral broadening in DAN fibers is due to the cascading of second order processes.

The observation of very large nonlinear shifts at relatively low input intensities in our interferometric measurements performed on Cerenkov fibers were surprising. As already stressed, the second harmonic is guided in the cladding in this type of fibers. Only 3% of the total second harmonic generated in our experiments is guided by the core, and is sufficient to produce phase shifts of the fundamental wave through cascading as large as $-\pi/8$ to $-\pi/4$. The second harmonic generation rate in this fiber was smaller than 1% for input intensities in the range of 30 to 60 MW/cm^2 . The image of the two lower fundamental modes propagating in the core and the corresponding second harmonic modes does not change with increasing input intensity of the fundamental. It means that no spatial structure has been induced in the core of fibers due to strong nonlinear interactions (Fig. 8). We have recently made a numerical simulation of the propagation of beams in a Cerenkov fiber in the presence of cascading and found that our experimental results were fully supported by this simulation. A detailed reports of the numerical results will be published elsewhere.²¹

Very large nonlinear shifts due to the cascading of two second order processes recently been observed in a single KTP crystal as well as in quasi phase matched KTP waveguides.²² It has been found that effective n_2 due to the cascading effect in the mismatched configuration, is one to two orders of magnitude larger than that corresponding to pure cubic nonlinearity. These results are now fully confirmed by our experiments performed in fibers with cores made of the strongly nonlinear organic material DAN. We have performed additional Z-scan measurements on DAN single crystal which have permitted to confirm the main features of cascading.¹¹ By angular tuning of the mismatch in a Type I phase-matching configuration for second harmonic generation in DAN, the sign and value of n_2 change at both sides of the phase-matching configuration where n_2 cancels as expected from theory.

In conclusion, our results clearly evidence the potential of organic nonlinear materials in the domain of low power all optical signal processing. Indeed, with materials such as NPP,² for which the figure of merit for the second order parametric processes is almost one order of magnitude larger than that of DAN, a n_2 value larger than $10^{-11} \text{ cm}^2/\text{W}$ is expected. Organic crystal cored fibers can have immediate application for femtosecond pulse compression without amplification, as was demonstrated by Yamashita's group.

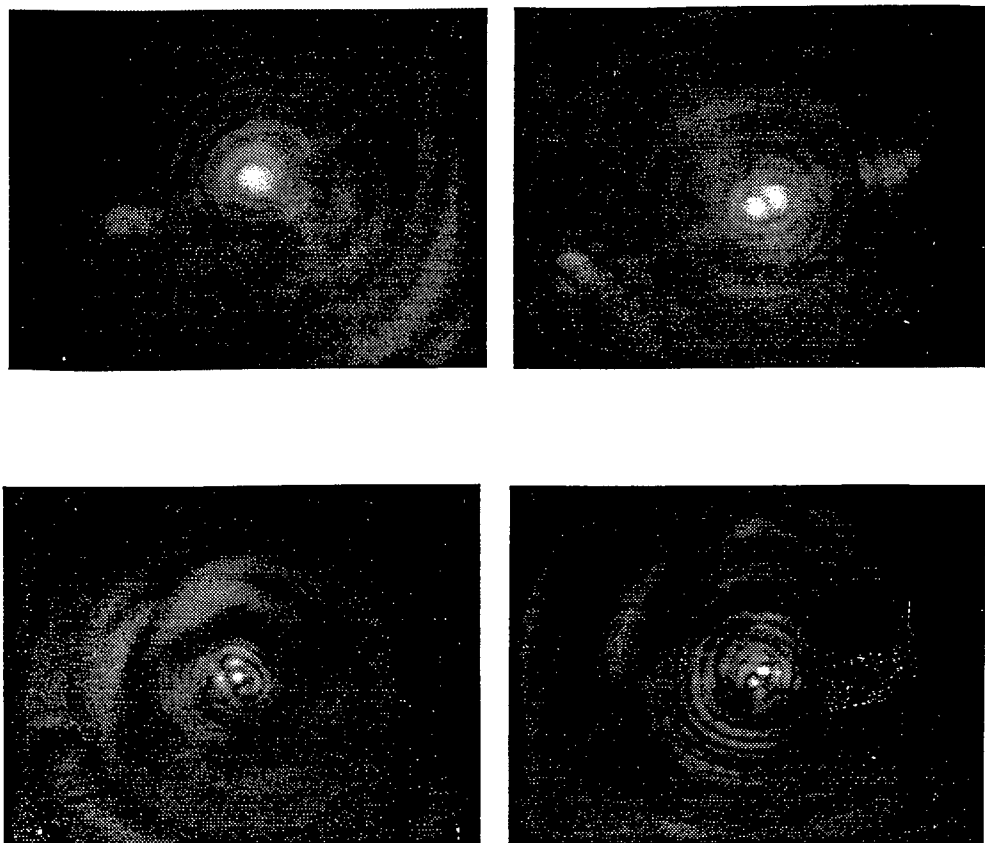


FIGURE 8 Mode patterns of the fundamental and Cerenkov second harmonic at the exit of a DAN/SF1 fiber. Top: the two lower modes at the fundamental wavelength (1.32 μm); Bottom: the two lower modes of the second harmonic. These patterns do not change with increasing input intensity.

With the development and thermal stabilizing of nonlinear second order properties of polymers, it is possible to conceive a new generation of very fast low power all optical signal processing waveguiding devices based on cascading processes.

REFERENCES

1. Nonlinear Optical Properties of Organic Molecules and Crystals., D. S. Chemla and J. Zyss, (Academic Press, Orlando 1987) and Molecular Nonlinear Optics: Materials, Physics and Devices, J. Zyss Ed. (Academic Press, Boston, 1994).
2. I. Ledoux, C. Lepers, A. Perigaud, J. Badan and J. Zyss *Opt. Comm.*, **80**, 149 (1990).
3. J. Zyss, D. S. Chemla and J. F. Nicoud, *J. Chem. Phys.*, **74**, 4800 (1981) (POM); J. Zyss, I. Ledoux, R. Hierle, R. Raj and J. Oudar, *IEEE J. Quantum Electron.*, **QE-21**, 1286 (1985); D. Josse, R. Hierle, I. Ledoux and J. Zyss, *Appl. Phys. Lett.*, **53**, 2251 (1988) (POM).
4. J.-C. Baumert, R. J. Twieg, G. C. Bjorklund, J. A. Logan and C. W. Dirk, *Appl. Phys. Lett.*, **51**, 1484 (1987); P. Kerkoc, M. Zygonik, K. Sutter, Ch. Bosshard and P. Günter, *J. Opt. Soc. Am.*, **7**, 313 (1990).
5. I. Ledoux, J. Badan, J. Zyss, A. Migus, D. Hulin, J. Etchepare, G. Grillon and A. Antonetti, *J. Opt. Soc. Am. B*, **4**, 987 (1987).

6. D. Josse, S. X. Dou, J. Zyss, P. Andreazza and A. Pèrigaud, *Appl. Phys. Lett.*, **61**, 121 (1992).
7. G. I. Stegeman and C. T. Seaton, *J. Appl. Phys.*, **58**, R57 (1985); G. I. Stegeman and R. H. Stolen, *J. Opt. Soc. Am. B*, **5**, 2 (1988); G. I. Stegeman, *Nonlinear Optics: Fundamentals, Materials and Devices*, p. 337, Ed. by S. Miyata, (Elsevier, 1992); G. I. Stegeman, *Guided Wave Nonlinear Optics*, p. 11, Ed. D. B. Ostrowski and R. Reinisch, (Kluwer, 1992).
8. R. DeSalvo, D. J. Hagan, M. Sheik-Bahae, G. I. Stegeman, E. W. Van Stryland and H. Vanherzeele, *Optics Lett.*, **17**, 28 (1992).
9. G. Assanto, G. Stegeman, M. Sheik-Bahae and E. Van Stryland, *Appl. Phys. Lett.*, **62**, 1323 (1993).
10. G. I. Stegeman, M. Sheik-Bahae, E. Van Stryland and G. Assanto, *Optics Lett.*, **18**, 13 (1993).
11. D. Y. Kim, W. E. Toruellas, J. Kang, C. Bosshard, G. Stegeman, P. Vidakovic, J. Zyss, W. Moerner, R. Twieg and G. Bjorklund, submitted to *Optics Lett.*
12. J. -M. R. Thomas and J. -P. E. Taran, *Opt. Commun.*, **4**, 329 (1972).
13. N. R. Belashenkov, S. V. Gagarinskii and M. V. Inochkin, *Opt. Spectrosc.*, **66**, 1383 (1989).
14. C. Flytzanis and N. Bloembergen, *Prog. Quant. Electron.*, **4**, 271 (1976).
15. R. Heckingbottom, J. R. Hill, G. E. Holdcroft, P. L. Dunn, P. Pantelis and J. D. Rush, *Nonlinear Optics of Organics and Semiconductors*, (Springer Verlag, 1989).
16. P. Vidakovic, M. Coquillay and F. Salin, *J. Opt. Soc. Am. B*, **4**, 998 (1987).
17. P. Vidakovic, *Nonlinear Opt.*, **4**, 253 (1993); R. Morita and P. V. Vidakovic, *Appl. Phys. Lett.*, **61**, 2854 (1992).
18. M. Yamashita, K. Torizuka and T. Uemiya, *Appl. Phys. Lett.*, **57**, 1301 (1990).
19. W. E. Toruellas, R. Zanoni, G. I. Stegeman, G. R. Mohlmann, E. W. P. Erdhuisen and W. H. G. Horsthuis, *J. Chem. Phys.*, **94**, 6851 (1991).
20. D. Y. Kim, M. Sundheimer, A. Otomo, G. I. Stegeman, W. H. G. Horsthuis, F. R. Möhlman, *Appl. Phys. Lett.*, **63**, 290 (1993).
21. W. E. Toruellas, R. Shiek, D. Y. Kim, G. Krijnen, G. I. Stegeman, P. Vidakovic and J. Zyss, submitted to *Optics Lett.*
22. M. L. Sundheimer, Ch. Bosshard, E. W. Van Stryland, G. Stegeman and J. D. Bierlein, *Optics Lett.*, **18**, 1397 (1993).

Resonance Raman Scattering and Photoinduced Infrared Absorption in Different Forms of Polyanilines and Substituted Polyanilines

S. QUILLARD, G. LOUARN, K. BERRADA, S. LEFRANT, K. A. COPLIN*,
S. W. JESSEN* and A. J. EPSTEIN*

*Laboratoire de Physique Cristalline, Institut des Matériaux,
44072 NANTES Cédex 03; France*

**Department of Physics, Ohio State University, COLUMBUS,
OH 43210 USA*

Received 11 February 1994; accepted 21 March 1994

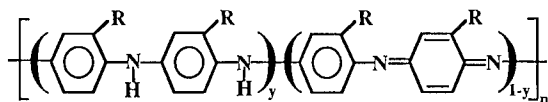
Resonant Raman spectra of the three forms of polyaniline bases, namely emeraldine, leucoemeraldine and pernigraniline, are presented for different excitation wavelengths. A complete assignment of the fundamental Raman and i.r. vibrational modes is proposed and a force field is determined for the polyaniline polymers in the fully reduced, half-oxidized and fully oxidized forms, respectively. Force constants are determined in a rather accurate way and in good consistency with the nature of the chemical bonds. Such a determination turns out to be significant to interpret modifications occurring in the electronic structure between neutral and protonated emeraldine polymers. At the same time, it demonstrates the important changes of the electronic distribution around the nitrogen atom. The exact knowledge of the different vibrational modes of the different forms of polyanilines is also used to interpret experimental spectra obtained in photoinduced i.r. absorption in which a one-to-one correspondence between observed peaks and Raman modes can be established. All these results can easily be transposed in substituted polyanilines for which some vibrational modes are silent for symmetry reasons as observed experimentally in both Raman and photoinduced i.r. spectra.

INTRODUCTION

Since the first work on polyacetylene published by Shirakawa *et al.*,¹ a number of novel concepts about conducting polymers have emerged, implying the formation of defect states such as solitons, polarons and bipolarons characteristic of the strong electron-lattice coupling in these materials.² Such defects can be put in evidence in doped or photoexcited polymers by studying Raman and i.r. active vibrational modes or subgap electronic transitions.^{3–8} In this context, polyanilines appear to be one of the best candidates to illustrate the rich chemistry and physics of conducting polymers,⁹ since, as mentioned before, their chemical structure can be varied from the fully reduced base to the fully oxidized base forms.

Polyanilines and substituted polyanilines relate to a large class of polymers since several forms of these compounds can be obtained.¹⁰ These different forms are described by two parameters: the average oxidation state and the degree of protonation.¹¹ In their nonconductive undoped (or base) form, polyanilines and substituted

polyanilines may be described in general by the formula scheme depicted below:



where y can be varied continuously from 1 for the completely reduced polymer to zero for the completely oxidized one. Conversion to a conductive form can be accomplished by either protonation or electronic doping.¹² The terms leucoemeraldine, emeraldine and pernigraniline used in the following discussion will refer to the different oxidation states of the polymer where $y = 1$, ~ 0.5 and 0 respectively. In this work, we have focused on one hand our attention on the three forms of polyaniline which are the fully reduced non protonated form (Leucoemeraldine Base; LB), the half oxidized base form (Emeraldine Base; EB) and the fully oxidized non protonated form (Pernigraniline Base; PB), and on the other hand on the substituted emeraldine forms (poly-*o*-toluidine; POT and polyethylaniline; PEA).

Our purpose is to obtain information on the structure of these polymers via their vibrational properties by using classical spectroscopies such as Resonance Raman Scattering (RRS) and infrared absorption. Following a procedure already used successfully in many other conducting polymers, we have adopted a preliminary model in which the polymers have a planar geometry, and therefore we have focused our study on the in-plane modes which reflect in particular the conducting backbone structure.¹³ Finally, we have correlated our Raman data to photoinduced i.r. absorption spectra¹⁴ for which a good consistency is obtained.

EXPERIMENTAL RESULTS

The chemical synthesis of the three different forms of polyaniline have already been described in details elsewhere.¹⁵ The emeraldine polymeric form has also been synthesized in our laboratory by classical electrochemical route in acidic media (HCl 1M).¹⁶ The same procedure has been used to obtain the different substituted polymers presented in this paper.¹⁷

Resonance Raman Scattering (RRS) spectra were recorded with standard equipment in a 90° scattering geometry and either argon or krypton laser lines were used. The laser beam power was limited to 20 mW. All experiments were performed at room temperature.

Polyanilines have been for many years the subject of both experimental and theoretical structural and electronic studies.¹⁸⁻²¹ In spite of these different reports, no complete analysis and no definitive assignment have been reported for all fundamental vibrations of these different forms of polyaniline (PANI, POT and PEA).

In this paper, we present experimental Raman spectra of a series of samples including LB, EB and PB and substituted forms POT and PEA, in order to make a complete vibrational assignment for all fundamental vibrations. From these results and from other spectra obtained on model compounds^{22,23} and on the basis of normal

coordinates calculations, we could determine a good set of force constants for all the compounds studied.

Raman and infrared spectra of model compounds for the reduced polymer have been presented in the 400–1700 cm^{-1} range in previous papers.^{22,23} These Raman spectra have been obtained with an excitation wavelength of $\lambda_L = 457.9$ nm.

The spectrum of LB is presented Figure 1(a). It exhibits several bands characteristic of the benzene ring such as those peaked at 1618 and 1181 cm^{-1} (in model compounds, they are observed at 1603 and 1183 cm^{-1} in diphenylamine (DPA), and at 1618 and 1182 cm^{-1} in phenyl capped dimer (PCD)), which correspond to a C—C stretching vibration and a C—H bending vibration respectively. The band at ≈ 1219 cm^{-1} in LB (1220 cm^{-1} in DPA, 1222 cm^{-1} in PCD) is related to the symmetric C—N stretching vibration. The two bands at 993 and 1031 cm^{-1} in DPA are found rather weak in PCD and are not observed in the polymer. This is consistent with the polymeric nature of the compound studied. On the other hand, let notice that the main feature observed in the Raman spectrum of LB is the band peaked at 1618 cm^{-1} . This vibrational mode is related to paradisubstituted benzene rings and can be used as a criterion to check the polymerization state, together with the disappearance of the two modes at 993 and 1031 cm^{-1} , due to monosubstituted rings.

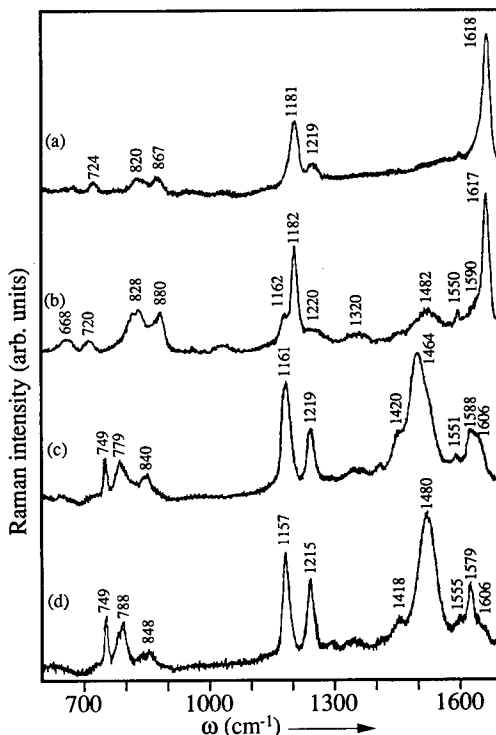


FIGURE 1 Raman spectra of powders of (a) leucoemeraldine base ($\lambda_L = 457.9$ nm), (b) and (c) emeraldine base ($\lambda_L = 457.9$ nm and 647.1 nm respectively) and (d) pernigraniline base ($\lambda_L = 647.1$ nm).

As for aniline, vibrational spectra of p-benzoquinone and its deuterated derivatives have been studied by several different groups.^{24,25} These studies turn out to be fruitful in the understanding of the fully oxidized polymer data.

The Raman spectrum of PB is presented in Figure 1(d). Two different excitation wavelengths have been used for the fully oxidized polymer (PB) which exhibits two main transitions on its UV-VIS optical absorption spectrum:^{10,26} $\lambda_L = 457.9$ nm is expected to enhance "reduced units" (presented in a previous work²³) and $\lambda_L = 647.1$ nm "oxidized units" (Fig. 1(d)). The C=N stretching mode observed at 1519 cm^{-1} in oxidized phenyl capped dimer (OPCD)²³ is shifted to 1480 cm^{-1} in the polymer ($\lambda_L = 647.1$ nm) showing a slight frequency dispersion. Keeping in mind the resonance effects observed by using different excitation wavelengths and by comparing the two spectra of PB, we have assigned the Raman band at 1579 cm^{-1} for $\lambda_L = 647.1$ nm (1582 cm^{-1} for $\lambda_L = 457.9$ nm) to a C=C stretching vibration of the quinoid ring, while the peak at 1157 cm^{-1} ($\lambda_L = 647.1$ nm) is due to a C—H bending vibration of the quinoid ring. At $\lambda_L = 457.9$ nm, we observe two bands at 1553 and 1612 cm^{-1} , no longer present with the red excitation wavelength. These bands are related to the benzene ring (C—C stretching). The symmetric C—H bending vibration of the benzene ring can be characterized by a Raman band at 1181 cm^{-1} in the fully reduced polymer. The similar vibration localized on the quinoid ring is obtained at 1157 cm^{-1} in the fully oxidized polymer. Consequently, this can also be a qualitative measurement of the degree of oxidation.

Figures 1(b) and (c) show Raman spectra ($600\text{--}1700\text{ cm}^{-1}$) at room temperature of the emeraldine base in powder form measured with two different excitation wavelengths. The main fundamental bands of the emeraldine base was first reported by Furukawa *et al.*²⁷ In a series of infrared and Raman measurements of different compounds, some of them being ^{15}N substituted, Furukawa was able to isolate individual C—N and C=N stretching vibrations and to correlate them with the nature of the chemical bonds of the molecules. The downward shift of the Raman band observed at 1479 cm^{-1} (^{15}N shift, 17 cm^{-1}) indicates a significant dependence with the C=N bond. The presence of two carbon-nitrogen bonds with a different nature in emeraldine and pernigraniline base was confirmed experimentally by the observation of a second band at 1219 cm^{-1} . This one was corroborated by a theoretical calculation of the bond lengths performed in both compounds.²⁸ The length of the C=N bond was calculated to be $\approx 0.12\text{ \AA}$ shorter than the C—N bond. The C—H bending modes occur in two different frequency ranges $1150\text{--}1200\text{ cm}^{-1}$ and $800\text{--}900\text{ cm}^{-1}$. In this first range we observe two bands at 1162 cm^{-1} assigned to the C—H quinoid ring and 1182 cm^{-1} assigned to the C—H benzenoid ring. This interpretation finds support from the resonant Raman spectra at 457.9 and 647.1 nm in which we observed these two bands selectively. From our early studies of pernigraniline base, we assign the three bands around $1550\text{--}1620\text{ cm}^{-1}$ to the carbon-carbon stretching modes of the benzene rings.

In Tables 1 and 2, we have collected all Raman frequencies and the corresponding assignments proposed for LB, PB and EB in the $600\text{--}1700\text{ cm}^{-1}$ frequency range.

For comparison, Raman spectra of the emeraldine base form of PANI (obtained after deprotonation of electrochemical samples) are presented in Figure 2 (a and b) for two different exciting wavelengths: 457.9 and 647 nm. At 457 nm, we observe two

TABLE 1

Experimental and calculated Raman frequencies (600–1700 cm^{-1} range) of in-plane vibrations of LB and experimental Raman frequencies of EB, with the corresponding assignment.

LEUCOEMERALDINE		EMERALDINE	DESCRIPTION OF VIBRATIONS
BASE		BASE	
Exp.	Calc.	457,9 nm	
1618	1620	1617	C—C stretching (8a)
1597	1588	≈ 1590 (1482) (1320)	C—C stretching (8b) oxidized structure oxidized structure
1219	1217	≈ 1220	C—N stretching (X-sens.)
1181	1168	1185 (1162)	C—H bending (9a) oxidized structure
867	878	880	ring deformation (1)
820		828	amine def. (X-sens.)
724		720	amine def. (X-sens.)
667	669	668	ring deformation (6a)
603	610		ring deformation (6b)

TABLE 2

Experimental and calculated Raman frequencies (600–1700 cm^{-1} range) of in-plane vibrations of PB and experimental Raman frequencies of EB, with the corresponding assignment. (B: Benzenoid ring, Q: Quinoid ring).

PERNIGRANILINE		EMERALDINE	DESCRIPTION OF VIBRATIONS
BASE		BASE	
Exp.	Calc.	647,1 nm	
1612	1614	1618	C—C stretching B
1579	1581	1590	C=C stretching Q
1555	1591	1555	oxidized structure
1480	1496	1484	oxidized structure
1418	1417	1420	C—N stretching (X-sens.)
—	1265		C—H bending (9a)
1215	1207	1219	oxidized structure
1157	1155	1160	ring deformation (1)
		840	amine def. (X-sens.)
788	800	780	amine def. (X-sens.)
750	705	748	ring deformation (6a)
		640	ring deformation (6b)

intense bands at 1620 and 1186 cm^{-1} , which respectively correspond to C—C stretching and C—H bending of the reduced structure, the leucoemeraldine base. The bands around 1220 and 1590 cm^{-1} come also from the reduced structure. The bands at 1479 and 1420 cm^{-1} correspond to the oxidized structure and the band at 1331 cm^{-1} to the remaining protonated units.

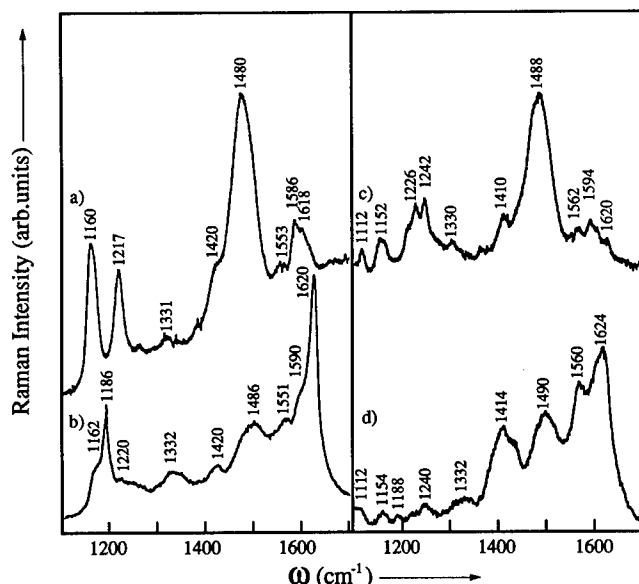


FIGURE 2 Raman spectra of electrochemical films of (a) and (b) emeraldine base ($\lambda_L = 647.1$ nm and 457.9 nm respectively), (c) and (d) poly-o-toluidine emeraldine base ($\lambda_L = 647.1$ nm and 457.9 nm respectively).

In the same way, Raman spectra of POT were recorded at 457.9 and 647 nm (Figs. 2 c and d). Main vibrational modes can be attributed similarly to those observed in polyaniline, and numerous new ones appear due to the change in symmetry. Also, the band at 1186 cm^{-1} , due to a C—H bending vibration mode in polyaniline, is no longer observed in the substituted polymer (POT). All these results, as well as a complete assignment of the vibrational modes, are reported on Table 3.

TABLE 3
Comparison between experimental Raman frequencies of emeraldine in PANI and POT (1100–1700 cm^{-1} range).

PANI-EMERALDINE		POT-EMERALDINE		DESCRIPTION OF VIBRATIONS
457,9 nm	647,1 nm	457,9 nm	647,1 nm	
1620	1618	1624	1620	C—C stretching (8a)
1590	1586	—	1594	C—C stretching (8b)
1551	1553	1560	1562	Oxidized structure
1486	1480	1490	1488	Oxidized structure
1420	1420	1414	1410	C—N stretching (X-sens)
1132	1331	1132	1330	oxidized structure
—	—	1240	1242	CH ₃ "twisting"
1220	1217	—	1226	C—N stretching (X-sens)
1186	—	1188	—	C—H bending (9a)
1162	1160	1154	1152	ring deformation (1)
—	—	1112	1112	C—CH ₃ stretching.

Raman data can be correlated with photoinduced i.r. absorption of all polymers as shown on Figure 3. In the PANI case, the results show strong absorption at 1144 and 1574 cm^{-1} and bleachings at 1510 and 1599 cm^{-1} .¹⁴ But for POT and PEA, the band at 1144 cm^{-1} has disappeared whereas another band comes up at 1550 cm^{-1} . This is well consistent with the symmetry change occurring in substituted polymers.

VIBRATIONAL ANALYSIS

In our model, calculations of the force field and frequencies are carried out using the dynamical matrix and with the hypothesis that molecules and polymers are planar, allowing us to separate in-plane and out-of-plane vibrations. We also assume that the polymeric chains are infinite and have no defects. Calculated Raman frequencies are presented in Tables 1 and 2 in the frequency region 600–1700 cm^{-1} for LB and PB. Notice that translation modes have not been taken into account.

For both the "reduced structure" (LB) and the "oxidized structure" (PB), we have built a valence force field characterized by a set of force constants expressed in terms of internal coordinates, as defined previously.²³ Using geometric parameters obtained by MNDO calculations,^{28,29} we have performed dynamical calculations allowing the determination of these different force constants.

A comparison of the vibrational frequencies of the different compounds reveals a close similarity in the magnitude of similar modes, in spite of the fact that rings are mono or parasubstituted and that the substituents change (amine or imine group). Therefore, force constants corresponding to common groups are expected to be

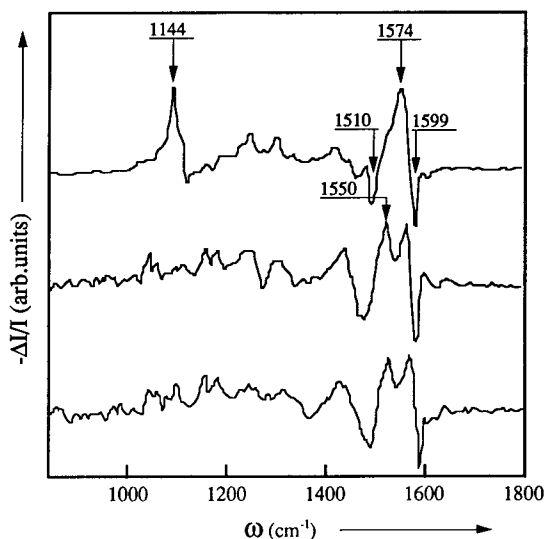


FIGURE 3 Photoinduced infrared absorption spectra of (a) polyaniline, (b) poly-o-toluidine and (c) polyethylaniline.

transferable from one molecule to the other. However, only a few of these force constants are of real importance for the calculated modes, and among them, the most interesting ones are those concerning C—C and C—N bonds because they are directly related to the electronic structure. The initial values of force constants (for in plane-vibrations) related to the non perturbed and perturbed benzene rings are kept very close to those found in benzene and oligophenyls as reported in previous works.^{30,31} Concerning the oxidized structure, we have started calculations on the p-benzoquinone molecule. The interaction constants for which values were not available were taken as zero in the starting calculations. The parameters obtained in this compound are supposed to be close to those of the non perturbed quinoid ring. In this way, the number of parameters is reduced to 13 for the "reduced part" and to 18 for the "oxidized part". Complete sets of force constants will be published elsewhere.³² In this paper, we have only chosen the main parameters which are strongly correlated to the electronic structure of the polymeric chain. These main values are reported in Table 4.

Force constants were refined by a fitting procedure and their variations were limited to about 10% of their initial values. This is a way to keep our parameters physically reasonable. Force constants concerning the C—C bonds (F_t^2 and $F_t'^2$) were kept close to those of benzene ring, leading to values such as 6.32 mdyn/Å, in agreement with calculations performed by Kostic *et al.* ($K_3 = 6.24$ mdyn/Å).³³

For comparison and from the study on PB, our model provide similar parameters concerning the quinoid ring. These calculations lead to force constants of the quinoid ring such as $FQ_t^2 = 8.19$ mdyn/Å for the carbon-carbon double bond and $FQ_t'^2 = 4.53$ mdyn/Å for the single bond of the ring. These values are very similar to those obtained for p-benzoquinone: $FQ_t^2 = 8.70$ mdyn/Å and $FQ_t'^2 = 4.83$ mdyn/Å by of Pietilä *et al.*²⁵ Furthermore, we can notice that the corresponding force constant in benzene is calculated at 6.32 mdyn/Å, intermediate between these two values.

TABLE 4
Main force constants of the reduced structure (benzenoid ring and amine group) and of the oxidized structure (quinoid ring and imine group).

Main force constants relative to the benzenoid ring				Main force constants relative to the amine group (—NH—)			
Stretch		Bend		Stretch		Bend	
F_s^2	5.08	$F\alpha^2$	0.99	FR^2	5.31	$F\delta^2$	0.63
F_t^2	6.32	$F\phi^2$	0.50	$F_s'^2$	6.21	$F\delta'^2$	1.45
$F_t'^2$	6.32	$F\alpha'^2$	0.82				
		$F\phi'^2$	1.07				
Main force constants relative to the quinoid ring				Main force constants relative to the imine group (=N—)			
Stretch		Bend		Stretch		Bend	
F_s^2	5.08	$FQ\alpha^2$	1.13	FQR^2	5.00	$FQRQR'$	0.49
FQ_t^2	8.19	$FQ\phi^2$	0.30	FQR'^2	9.19	$FQRQt$	0.42
$FQ_t'^2$	4.53	$FQ\alpha'^2$	0.55			$FQtQR'$	0.55
		$FQ\phi'^2$	1.02			$FQ\phi'^2$	1.02
		$FQ1\phi^2$	0.60			$FQ1\phi'^2$	0.60

This study on both forms of polyaniline (LB and PB) allowed also the determination of the parameters of the interrering group: amine group in the reduced case, imine group in the oxidized case. The force constant related to carbon-nitrogen bond of the amine group (FR^2) is found at 5.31 mdyn/Å, a value which is consistent with others obtained for similar single bonds: 4.80 mdyn/Å in the PPV³⁴ and at 5.31 mdyn/Å in PTV³⁵ (both for an interrering C—C stretching vibration).

The C=N stretching vibration of the imine group is experimentally peaked at 1480 cm⁻¹ in the Raman spectrum of PB, and it is calculated at 1496 cm⁻¹. The force constant related to this double bond (FQR^2) provide a large contribution to this vibration and has been calculated at 9.19 mdyn/Å. In the imine group, the C—N stretching vibration is observed at 1215 cm⁻¹ close to the similar mode in the reduced polyaniline (at \approx 1220 cm⁻¹). The parameter FQR^2 is then equal to 5.00 mdyn/Å in the "oxidized part" while FR^2 is found to be 5.31 mdyn/Å in the "reduced part". We can also already notice a good relationship between these force constants and the geometric parameters.

CONCLUSION

In this paper, we have made a complete interpretation of the Raman and i.r. vibrational modes of the different forms of polyaniline: leucoemeraldine base, emeraldine base and pernigraniline base. In addition, we present a study of substituted polymers. By the use of a valence force field model, we obtain two sets of force constants concerning the reduced and the oxidized structure respectively. These parameters are consistent with the quinoid or benzenoid character of the ring and with the imine or amine group. Despite similarities, the valence force field for oxidized structure clearly differs from that of reduced structure.

We have also presented a Raman study of substituted polymers. Experimental data are consistent with the symmetry changes occurring in these new forms of polyaniline. In addition, Raman data are strongly correlated with photoinduced i.r. absorption of all polymers as shown in Figure 3. In particular, strong absorptions are observed at 1144, 1574 cm⁻¹ bleachings at 1510 and 1599 cm⁻¹. These features can easily be interpreted by considering the main vibrational features observed in the Raman spectra. This consistency appears also clearly in substituted emeraldine POT in which the photoinduced i.r. absorption band at 1144 cm⁻¹ has disappeared (together with the 1186 cm⁻¹ Raman band). A detailed analysis of these data can be found elsewhere.¹⁴

Further studies are in progress in an attempt to understand the modifications of the vibrational properties observed in these polymers after protonation.

REFERENCES

1. C. K. Chiang, C. R. Fincher Jr, Y. W. Park, A. J. Heeger, H. Shirakawa, E. J. Louis, S. C. Gau, A. G. MacDiarmid, *Phys. Rev. Lett.*, **39**, 1098 (1977).
2. R. R. Chance, D. S. Boudreaux, J. L. Brédas and R. Silbey in *Handbook of Conducting Polymers*, edited by T. A. Skotheim (Dekker, New York, 1986), p.825 and the references cited therein.
3. J. L. Brédas in proceeding of the 1991 Nobel Symposium on Conjugated Polymers and Related Materials, edited by W. R. Salaneck (Oxford Univ. Press, 1993).

4. A. P. Monkman, D. Bloor, G. C. Stevens, J. C. H. Stevens and P. Wilson, *Synth. Metals*, **29**, E277 (1989).
5. R. P. McCall, J. M. Ginder, J. M. Leng, H. J. Ye, S. K. Manohar, J. G. Masters, G. E. Asturias, A. G. MacDiarmid and A. J. Epstein, *Phys. Rev. B*, **41**, 5202 (1990).
6. M. G. Roe, J. M. Ginder, T. L. Gustafson, M. Angelopoulos, A. G. MacDiarmid and A. J. Epstein, *Phys. Rev. B*, **40**, 4187 (1990).
7. R. H. Friend, D. D. C. Bradley and P. D. Townsend, *J. Phys. D: Appl. Phys.*, **20**, 1367 (1987).
8. Y. Furukawa, A. Sakamoto and M. Tasumi, *J. Phys. Chem.*, **93**, 5354 (1989).
9. A. G. MacDiarmid and A. J. Epstein, *Faraday Discuss. Chem. Soc.*, **88**, 317 (1989).
10. J. G. Masters, Y. Sun, A. G. MacDiarmid and A. J. Epstein, *Synth. Metals*, **41**, 715 (1991).
11. A. Ray, G. E. Asturias, D. L. Kershner, A. F. Richter, A. G. MacDiarmid and A. J. Epstein, *Synth. Metals*, **29**, E141 (1989).
12. A. Ray, A. F. Richter, A. G. MacDiarmid and A. J. Epstein, *Synth. Metals*, **29**, E151 (1989).
13. G. Louarn, J. Y. Mevellec, J. P. Buisson and S. Lefrant, *J. Chim. Phys.*, **89**, 987 (1992).
14. R. P. McCall, M. G. Roe, J. M. Ginder, J. Kusomoto and A. J. Epstein, *Synth. Metals*, **29**, 433–438 (1989).
15. A. G. MacDiarmid, J. C. Chiang, A. F. Richter, N. L. D. Somasiri and A. J. Epstein in *Conducting Polymers*, edited by L. Alcacer (D. Reidel Publishing Company, 1987) p.105.
16. W. S. Huang, B. D. Humprey and A. G. MacDiarmid, *J. Chem. Sc. Faraday Trans.*, **1**, **82** 2385 (1986).
17. M. Leclerc, J. Guay and L. H. Dao, *Macromolecules*, in press.
18. F. Ueda, K. Mukai, I. Harada, T. Nakajima and T. Kawagoe, *Macromolecules*, **23**, 4925 (1990).
19. I. Harada, Y. Furukawa and F. Ueda, *Synth. Metals*, **29**, E303 (1989).
20. A. P. Monkman in *Conjugated Polymeric Materials: Opportunities in Electronics, Optoelectronics and Molecular Electronics*, **182**, edited by J. L. Brédas and R. R. Chance (Kluwer Academic publishers, 1990) p.273.
21. N. S. Sariciftci, M. Bartonek, H. Kuzmany, H. Neugebauer and A. Neckel, *Synth. Metals*, **29**, E193 (1989).
22. S. Quillard, G. Louarn, J. P. Buisson, S. Lefrant, J. Masters and A. G. MacDiarmid, *Synth. Metals*, **49–50**, 525 (1992).
23. S. Quillard, G. Louarn, J. P. Buisson, S. Lefrant, J. Masters and A. G. MacDiarmid, *Synth. Metals*, **55–57**, 475 (1993).
24. A. Giraldo and C. Pecile, *J. Mol. Spectrosc.*, **77**, 374 (1979).
25. L.-O. Pietilä, K. Palmö and B. Mannfors, *J. Mol. Spectrosc.*, **116**, 1 (1986).
26. Y. Sun, A. G. MacDiarmid and A. J. Epstein, *J. Chem. Soc., Chem. Commun.*, **7**, 529 (1990).
27. Y. Furukawa, F. Ueda, Y. Hyodo, I. Harada, T. Nakajima and T. Kawagoe, *Macromolecules*, **21**, 1297 (1988).
28. S. Stafström and B. Sjögren, O. Wennerström and T. Hjertberg, *Synth. Metals*, **16**, 31 (1986).
29. J. J. Langer, *Synth. Metals*, **20**, 35 (1987).
30. S. Zeraoui, J. P. Buisson, J. Y. Mevellec and S. Lefrant, *Synth. Metals*, **55–57**, 487 (1993).
31. G. Louarn, L. Athouël, G. Froyer, J. P. Buisson and S. Lefrant, *Synth. Metals*, **57**, 4757 (1993).
32. S. Quillard, G. Louarn, S. Lefrant and A. G. MacDiarmid, to be published.
33. R. Kostić, D. Rakostić, I. E. Davidova and L. A. Gribov, *Phys. Rev. B*, **45**, 728 (1992).
34. S. Lefrant, E. Perrin, J. P. Buisson, H. Eckhardt and C. C. Han, *Synth. Metals*, **29**, E91 (1989).
35. G. Louarn, J. Y. Mevellec, J. P. Buisson, S. Lefrant and H. Eckhardt in *Electronic Properties of Polymers*, edited by H. Kuzmany, M. Mehring and S. Roth (Springer-Verlag, Berlin, 1992), p. 298.

Chainlength Dependence of Cubic Optical Nonlinearities in Polyene Oligomers: Saturation and Scaling Law

IFOR D. W. SAMUEL¹, ISABELLE LEDOUX¹, CHRISTOPHE DHENAUT¹, JOSEPH ZYSS^{1*}, HAROLD H. FOX, RICHARD R. SCHROCK and ROBERT J. SILBEY

¹*France Telecom-CNET-Centre Paris B-Laboratoire de Bagneux, 196 Avenue Henri Ravera, 92220 Bagneux, France,* ²*Department of Chemistry, Massachusetts Institute of Technology, Cambridge, Massachusetts 02139, U.S.A.*

Received 6 May 1994; accepted 6 May 1994

Early theoretical and experimental studies have pointed-out the interest of highly extended conjugated molecules (e.g., polyenes) for optimization of nonlinear quadratic and cubic hyperpolarizabilities at the molecular level. The role of the conjugation length, of the bond alternation, and the influence of side or chain-end substituents was intensively explored using various theoretical methods. However, the experimental investigations that would be required to validate these models remained limited to short-length oligomers, owing to the poor stability of polyenic moieties beyond a limited number n of carbon-carbon double bonds. We report solution measurements of γ as a function of chainlength in long chain (up to 240 double bonds) model polyene oligomers, in which the synthetic difficulties were overcome by modern living polymerisation techniques. We observe, for the first time in such molecules, a saturation of the increase of γ with chainlength. The onset of the saturation occurs for chainlengths considerably longer than expected from theory. The influence of donor and acceptor end-chain substituent is also investigated.

INTRODUCTION

The ever developing research on the nonlinear optical (NLO) behaviour of organic molecules and polyenes has been driven by interest both in using organic materials in NLO devices and understanding the electronic processes underlying NLO effects.¹ In all the molecules investigated to-date, the magnitude of the first and second hyperpolarizabilities, β and γ , respectively, depends on the extent of π electron conjugation.^{1–3} Thus, a firm knowledge of the relationship between the molecular hyperpolarizability and the length of the molecule is necessary for the development of new NLO organic materials and for the understanding of the electronic origin of their NLO behaviour. On the other hand, actual figures of merit for material and device applications such as parametric gain or optical switching refer to the macroscopic susceptibilities $\chi^{(2)}$ and $\chi^{(3)}$. In this context, the molecular engineering goal is the optimization of

the molecular hyperpolarizability density β/V or γ/V , where V is the molecular volume, rather than the molecular hyperpolarizability itself.⁴

Within this domain of investigation, polyene oligomers are of particular interest as model systems for one-dimensional (1D) conjugated molecules. This family of compounds displays large second-order hyperpolarizability γ values⁵⁻¹² and possibly high β ¹³⁻¹⁷ ones in the case of donor-acceptor substituted materials. In the case of these strongly 1D systems, optimization of $\chi^{(2)}$ or $\chi^{(3)}$ is equivalent to that of the β/n or γ/n ratios, where n is the number of carbon-carbon double bonds. For moderate n values, it is expected that β and γ vary exponentially with n , in the form $\beta \propto n^a$ and $\gamma \propto n^b$. A number of theoretical models have predicted values of the exponent b ranging from 3 to 5.4.¹⁸⁻²⁹ However, there should be an asymptotic limit for β or γ values for large n 's.^{4,18,24-32} Therefore, an optimal conjugated system dimension, beyond which extending the chainlength would not only be pointless, but even detrimental in terms of hyperpolarizability density γ/n , should exist. This trend has been rationalized for γ hyperpolarizabilities by the introduction of the electron delocalization length, corresponding to the quadratic mean deviation of the electron position in a one-electron model, as derived from the chain bond alternation. Therefore, for large n , γ would be linear in n and γ/n would become constant. This saturation is predicted to occur at different n values in different models: Hückel models which do not include electron correlation tend to predict saturation at rather large n 's ($n > 50$), whereas theoretical models including electron correlation predict saturation at smaller n values ($n \approx 20$ or even less). These calculations are generally believed to be semi-quantitative; but they could be serious in error if the parameters used in the semiempirical Hamiltonian (PPP) are not valid for large molecules.

There exist few experimental investigations on the cubic hyperpolarizabilities γ of polyene oligomers.⁵⁻¹² Whereas theories focused on the most basic conjugated system, the all-*trans* polyene, experimentalists have examined substituted polyenes such as symmetric or asymmetric donor and/or acceptor carotenoids. Unsubstituted all-*trans* polyenes exhibit problematic physical properties, such as insolubility or polycrystallinity in the solid state, preventing a quantitative γ estimation for polyenes having more than 6 double bonds. For these reasons, experimental determination of a or b could only be performed on substituted polyene oligomers, the maximal number of carbon-carbon double bonds remaining rather weak, owing to stability or solubility problems encountered in larger species. More recently, a method for solubilizing and stabilizing all-*trans* polyenic units was proposed, using triblock copolymers of polynorbornene-polyene-polynorbornene.³³ Polynorbornene can be replaced by poly-methyl-tetracyclododecene. The b values of these all-*trans* compounds appeared to be similar to those of substituted polyene oligomers like carotenoids. However, the conjugation length remains limited ($n \leq 16$), owing to specific problems in synthesizing longer compounds.

The controlled synthesis of long-chain conjugated oligomers has recently become possible as a result of progress in living polymerization techniques.³⁴ We will report here measurements of γ as a function of n in soluble long-chain substituted polyene oligomer with up to 240 double bonds.³⁵ The influence of donor and acceptor substituents, symmetrically substituted at the chain ends, on the γ values is also investigated.

MOLECULES

Molecular Structure and Stability

The molecules investigated in the present work are sketched in Figure 1. They were synthesized by living cyclopolymerization of 1,6-heptadiyne derivatives, using well-defined molybdenum alkylidene complexes as initiators. Series of symmetric diphenyl-capped polyenes, "pull-pull" polyenes containing *p*-cyanophenyl end groups, and "push-push" polyenes containing *p*-dimethylamino end groups, have been prepared. These systems contain one phenyl ring in the center of the molecule.³⁴ The polymeric chain contains randomly distributed five- and six-membered non-conjugated rings, their relative proportions varying with the catalyst and the nature of the polyene itself. The π -electron system runs the entire length of the chain, and the average number of double bonds has been estimated by measuring the number average molecular weight. The three phenyl rings have been counted as 1.5 double bonds each. Polydispersities are narrow ($M_w/M_n \leq 1.25$) (here M_n is the number average molecular weight, M_w the experimental molecular weight measured by GPC on-line viscometry). The degree of polymerization is somewhat higher than indicated by the stoichiometry.

The thermal and oxidative stability of these polyenes is enhanced greatly over the stability of analogous unsubstituted polyenes. A THF solution in air of the longest polyene reported here ($n = 240$) displays a significant degradation of the polymer within one or two days. Over a period of several weeks, the fraction of long conjugated chains decreases while the fraction of short chains increases.

Linear Optical Properties and Conjugation

The optical absorption maximum (λ_{\max}) of the polyenes depends on the number of double bonds and on the nature of end groups, as indicated in Table 1. The observed values of λ_{\max} for a given number of double bonds do not correspond to the extrapolation of the values observed in shorter all-*trans* unsubstituted polyenes.³³⁻³⁴ This implies that the polymer is not rigid and the π orbitals therefore do not fully overlap. A significant solvatochromic shift observed between λ_{\max} values in acetonitrile and THF (up to 20 nm for $n = 240$) could be explained in terms of changes in polymer conformation in the different solvents.³⁴ In particular, the central phenyl ring is probably twisted out of conjugation with the polyene chains, therefore reducing λ_{\max} effectively to the

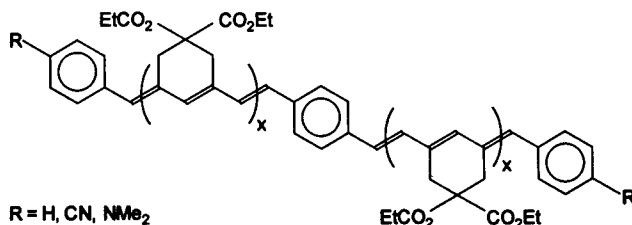


FIGURE 1 Molecular structure of the polyene oligomers studied in this work.

TABLE I

Summary of data for model polyene oligomers: n is the average number of double bonds in the sample; λ_{\max} is the wavelength of maximum of the absorption in tetrahydrofuran solution; $\gamma_{\text{THG}} = \gamma(-3\omega; \omega, \omega, \omega)$ is measured by third harmonic generation at 1.907 μm . The relative error on γ values does not exceed 15%. $\gamma(0)$ is the "static" hyperpolarizability deduced from the two-level model proposed in the text.

N (R = H)	λ_{\max} (nm)	$\gamma(\text{R} = \text{H})$ 10^{-34} e.s.u.)	$\gamma(0)$ $(10^{-34}$ e.s.u.)	N (R = CN)	λ_{\max} (nm)	$\gamma(\text{R} = \text{CN})$ $(10^{-34}$ e.s.u.)	N (R = NMe ₂)	λ_{\max} (nm)	$\gamma(\text{R} = \text{NMe}_2)$ $(10^{-34}$ e.s.u.)
							16	464	111
				18	454	51			
				21	470	92			
28	466	81	35						
				34	492	97			
39	486	141	54						
							41	508	174
							43	510	180
50	516	247	78				50	528	270
				52	528	256			
68	530	553	155						
88	538	1025	267						
				101	546	765			
							117	548	657
152	530	2731	629						
240	552	3794	854						

value expected in a polyene of approximately half the length. It is clear that the conjugation of π -electrons in these substituted polyenes strongly differs from that of the purely all-*trans* unsubstituted material. We could therefore expect exponent values a and b to be significantly smaller than those reported in more planar structures, the conjugation degree being apparently significantly weaker.

In the case of push-push and pull-pull polyenes, the difference in λ_{\max} between these two respective series is relatively large for small n values, but this difference diminishes as the polymer length increases. The smaller effect of substitution in longer molecules was previously observed in the shorter carotenoid derivatives reported in Reference 10. It can be accounted for by a decrease of the relative contributions of the end groups to the global electronic distribution over the conjugated chain, leading to λ_{\max} values similar to each other and close to the value of the corresponding unsubstituted polyenes. The "convergence" between λ_{\max} values for different end groups occurs probably slightly above $n = 50$.

EXPERIMENTAL NLO TECHNIQUE

γ values of polyenic molecules were measured by the well-known Third Harmonic Generation (THG) technique³⁶ in solution in tetrahydrofuran. Considering that λ_{\max} reaches 550 nm for the longest species, the fundamental wavelength was chosen at $\lambda = 1.907 \mu\text{m}$. Therefore, the THG wavelength at 636 nm is just below the onset of the electronic absorption band of the molecules. The laser source is a Nd³⁺:YAG laser emitting 1.06 μm nanosecond pulses; the fundamental beam at 1.907 μm was generated

by a hydrogen Raman cell at 40 bars pumped at $1.06\ \mu\text{m}$. Excitation intensities at $1.907\ \mu\text{m}$ are of order $100\ \text{MW}\cdot\text{cm}^{-2}$ and the concentrations of solutions are in the range of 10^{-6} to 10^{-3} M. Data analysis was performed as previously described in Reference 36.

EXPERIMENTAL RESULTS

Polyenes without Donor or Acceptor Endgroups

The results of these measurements are shown in Table 1 and Figure 2. γ reaches a giant value of $3794 \pm 500 \times 10^{-34}$ esu for $n = 240$ double bonds. However, for small n values, the rate of increase of γ with n is slower than that measured in previous experiments on shorter molecules: here b peaks at 2.6, compared to $b = 3.6$ as observed for all-*trans* oligomers, with n in the range 10–16.^{11–12} The graph of γ/n as a function of n clearly shows that γ/n saturates, so that the predicted exponential behaviour $\gamma = kn^b$ is not valid for long chain polyenes. The saturation is even more evident in Figure 3, which shows $b = d[\ln(\gamma)]/d[\ln(n)]$: this quantity would have a constant value of b for a simple power-law dependence. The observed behaviour is far more complex: there is a maximum of b for $n \sim 60$ double bonds, and b decreases towards 1 (which corresponds to $\gamma \propto n$) for the longest molecules.

Since most theoretical models have been elaborated on the basis of static hyperpolarizabilities, it is necessary to estimate γ at zero frequency (see Table 1 and Figure 4)

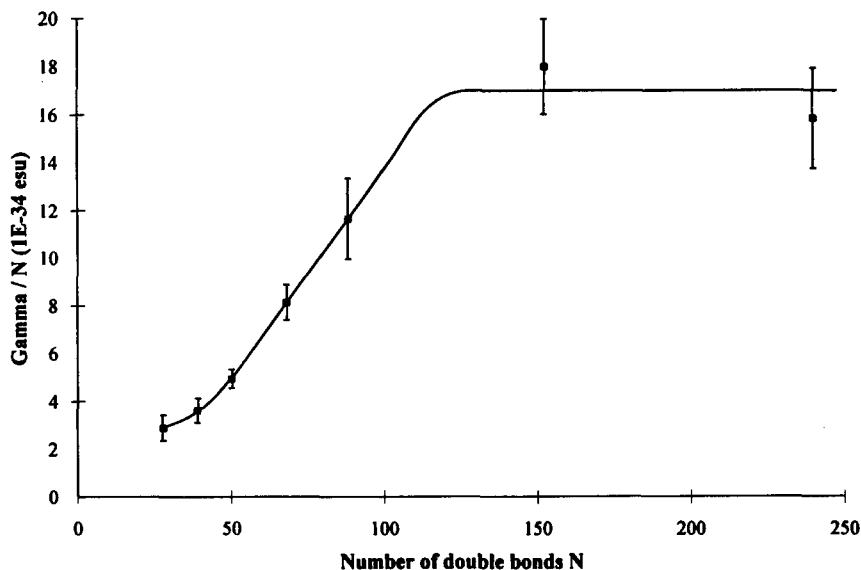


FIGURE 2 Values of $\gamma(-3\omega; \omega, \omega, \omega)/n$ as a function of number of double bonds n for the polyene oligomers of Figure 1 as measured by THG at $1.907\ \mu\text{m}$. The solid line is a guide for the eye.

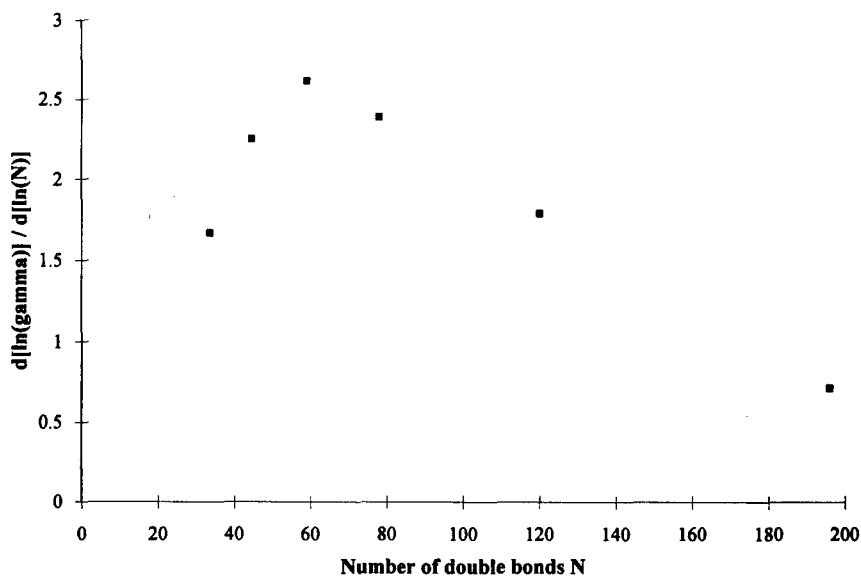


FIGURE 3 Plot of $d[\ln(\gamma)]/d[\ln(n)]$ as a function of chainlength for the data in Figure 1.

from the experimental data using a two-level model:

$$\gamma(0) = \left(1 - \frac{\lambda_{\max}^2}{\lambda^2}\right) \left(1 - \frac{9\lambda_{\max}^2}{\lambda^2}\right) \gamma(-3\omega; \omega, \omega, \omega)$$

where λ_{\max} is the wavelength of the maximum of the absorption, and $\lambda = 1.907 \mu\text{m}$ is the wavelength at which the measurement was made. This two-level model is probably a crude approximation of a more general multilevel model,^{8,37} usually, besides the well-identified one- or three-photon level corresponding to the observed λ_{\max} values presently reported in Table 1, the presence of an additional two-photon level is assumed⁸ on the basis of various theoretical and a few experimental studies in polyenes. However, it appears that, owing to the similar energies of these two levels, they cannot contribute simultaneously to resonance enhancement in polyenic species. In our case, the contribution of the three-photon resonance is predominant, and the "two-level" model is approximately valid.

Owing to the strong red shift of λ_{\max} values when increasing n , the saturation behaviour of the polyenes could significantly change after resonance corrections. In particular, the saturation of $\gamma(0)/n$ could occur at smaller n values than $\gamma(-3\omega; \omega, \omega, \omega)$. However, as illustrated in Figure 4, the saturation behaviour of $\gamma(0)$ is very similar to that of $\gamma(-3\omega; \omega, \omega, \omega)$.

Push-Push and Pull-Pull Polyenes

In contrast to short oligomers, there is no evidence of significant modification of γ values, for similar n 's, upon introduction of donor or acceptor end groups at the

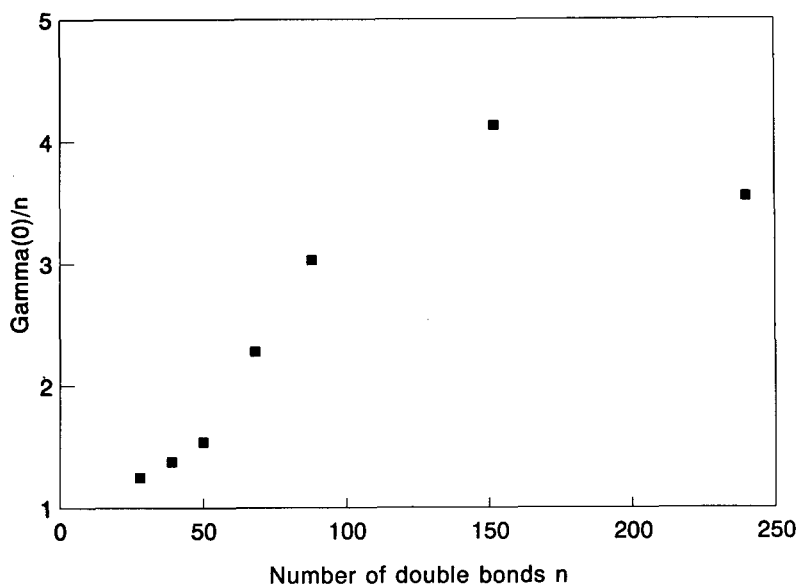


FIGURE 4 Values of $\gamma(0)/n$ as a function of n , deduced from $\gamma(-3\omega; \omega, \omega, \omega)/n$ using the two-level model discussed in the text.

extremities of the conjugated chain, as clearly evidenced from Table 1 and Figure 5. The experimental error being of the order of 20% on these particular compounds, it can be deduced from Figure 5 that the behaviour of γ/n with respect to n is similar for the three polyenic families investigated in this work.

DISCUSSION

Huge γ values are evidenced in partially resonant measurement conditions: the highest value, obtained for $n = 240$, reaches 3.7×10^{-31} e.s.u. This corresponds to a relative increase of almost two orders of magnitude as compared to β -carotene¹⁰ or all-*trans* copolymers.¹¹⁻¹² Of course the enhancement is lower for γ/n , which is three times larger than in the case of the best materials of References 10-12. Such values are, to the best of our knowledge, the largest $\gamma(-3\omega; \omega, \omega, \omega)$ ever reported. Even estimated "static" $\gamma(0)$ values remain close to 10^{-31} e.s.u. Similar orders of magnitude -in more resonant conditions than in our case- are reported in Reference 38 on γ values of tetrasubstituted cumulenenic compounds measured by degenerate Four-wave-mixing (DFWM) at 602 nm. However, in this configuration, where linear absorption is predominant, the purely electronic contribution to γ could not be separated from the global DFWM response, and no estimation of the static $\gamma(0)$ value could be undertaken.

To our knowledge, this is the first observation of a saturation of the increase of γ with chainlength in polyenic molecules. The shape of Figure 2 qualitatively resembles the predictions of several theories, but the number of double bonds at which the onset of

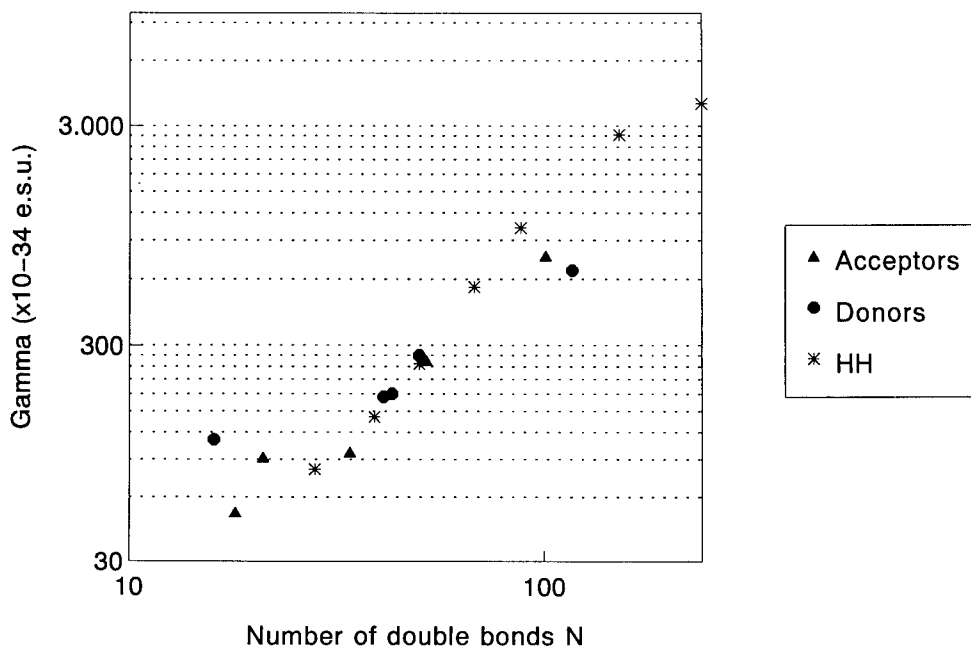


FIGURE 5 Plot of $\gamma(-3\omega; \omega, \omega, \omega)$ as a function of n of push-push, pull-pull and non-substituted polyenes.

saturation is observed ($n \sim 120$) is much larger than these theories suggest. The form of Figure 3, with a maximum of b followed by a decrease towards 1 for large n , is qualitatively similar to the calculations of Mukamel and Wang³¹⁻³² in their electron-hole anharmonic oscillator model, and of Spano and Soos²⁷ in Hückel theory. This behaviour may also arise in other models—but to date only these authors have published a figure corresponding to Figure 3. However, whilst we observe a maximum of b slightly above 2.5 for $n \sim 60$, and b approaches 1 for $n \sim 200$, Mukamel and Wang (using a Hubbard potential $U = 11.26$ eV in a PPP model³¹) calculate a maximum of b for $n \sim 5$, and that b falls to 1 for $n = 21$ in the case of ideal polyene (bond alternation $\delta = 0.07$).³² A further difference is that the maximum value of b in our measurements is 2.6, compared with ~ 7 calculated by Mukamel and Wang. In the work of Spano and Soos (with the same bond alternation $\delta = 0.07$) saturation is also predicted to occur in relatively short chains; the maximum of b is calculated to be at $n \sim 15$.

This behaviour could indicate that the bond alternation δ in our molecules could be strongly larger than that of model polyenes. In Mukamel's theory, much lower b values are predicted for high δ values: for $\delta = 0.7$, b_{\max} does not exceed 4.5. The difference between experimental and predicted b values would be smaller for high δ values.

All these theories refer to idealized planar, all-*trans* isolated gas phase polyene oligomers. Our measurements are made in solution, and the molecules are not true polyacetylene oligomers. As suggested by electronic absorption spectra, there may be some conformational disorder of the molecules in solution, which could reduce the extent and the degree of electron delocalisation, leading to possibly high bond

alternation values. The connection between chainlength and conjugation length with disorder is at present a challenge to theory.³⁹ Furthermore, the phenyl ring in the centre of the molecule might also reduce the extent of electron delocalisation, the actual conjugation length being possibly reduced by a factor of 2 if the phenyl moiety strongly limits the conjugation between the two parts of the molecule. Although the implications of such effects for the saturation behaviour are still uncertain, we may consider that a reduction in the extent of electron delocalization would tend to reduce the chainlength at which saturation occurs, and thus does not provide a more satisfactory explanation of why we observe saturation at considerably greater chainlengths than predicted in theory. A more consistent explanation would refer to probable strong discrepancies between the "nominal" conjugation length deduced from the molecular mass, and the actual conjugation length, limited by strong conformation -or other kinds of defect in the conjugated hydrocarbon chain- that decomposes the molecules in several non-interacting conjugated parts. As pointed out before, the central phenyl ring could be an example of such "defects" that breaks the conjugation between the two extremities of the molecules. Therefore, the surprising high n value corresponding to saturation could be overestimated owing to such conjugation defects.

The effect of the end groups is observed to be small in such long molecules. Symmetric substitution by electron donor or acceptor group does not significantly affects the behaviour of γ values with n , at least in the case of the few chain-end substituted molecules investigated here. As already pointed-out from linear absorption spectra, the electronic contribution of the end groups to the nonlinear response becomes relatively small as compared to that of the whole π -electron conjugated chain. In addition, the possible defects which may strongly reduce the actual conjugation length could also prevent the polarizing effects of the end group from extending over a large number of π electrons.

CONCLUSION

In conclusion, we have taken advantage of recent advances in controlled synthesis to study the scaling of γ with chainlength in long chain model polyene oligomers. Huge γ values, of purely electronic origin, were reported. We have observed, for the first time to our knowledge, a saturation of γ as a function of n in polyenic materials. The saturation occurs for chainlengths n considerably larger than expected in existing theories, which suggests that existing calculations may not give an adequate description of the electronic properties of long conjugated molecules, and that strong discrepancies between the idealized and the actual polyene structures make comparisons between experimental and theoretical studies problematic. A more precise understanding of the chain conformation would be required to provide even a qualitative account of the nonlinear optical behaviour of long chain polyene oligomers.

REFERENCES

1. J. Zyss and D. S. Chemla, Eds, *Nonlinear Optical Properties of Organic Molecules and Crystals*, Volumes 1 and 2, Academic Press, Orlando, 1987. J. Zyss, Ed., *Molecular Nonlinear Optics: Materials, Physics and Devices*, Academic Press, Boston, 1993.

2. J.-L. Oudar and H. Le Person, *Opt. Comm.*, **15**, 258 (1975).
3. J.-L. Oudar, *J. Chem. Phys.*, **67**, 446 (1977).
4. J. O. Morley, V. J. Docherty and D. Pugh, *J. Chem. Soc. Perkin Trans.*, **2**, 1351 (1987).
5. J. P. Hermann and J. Ducuing, *J. Appl. Phys.*, **45**, 5100 (1974).
6. J. F. Ward and D. S. Elliott, *J. Chem. Phys.*, **69**, 5438 (1978).
7. M. T. Zhao, B. P. Singh and P. N. Prasad, *J. Chem. Phys.*, **89** (1988).
8. J. Messier, F. Kajzar, C. Sentein, M. Barzoukas, J. Zyss, M. Blanchard-Desce and J. -M. Lehn, *Mol. Cryst. Liq. Cryst.*, -sec B: *Nonlinear Optics*, **2**, 53 (1992).
9. C. W. Spangler, K. O. Havelka, M. W. Becker, T. A. Kelleher and L. T. Cheng, *SPIE Proc.*, **1560**, 139 (1991).
10. G. Puccetti, M. Blanchard-Desce, I. Ledoux, J.-M. Lehn, J. Zyss, *J. Phys. Chem.*, **97**, 9385 (1993).
11. G. S. W. Craig, R. E. Cohen, R. R. Schrock, R. J. Silbey, G. Puccetti, I. Ledoux and J. Zyss, *J. Am. Chem. Soc.*, **115**, 860 (1993).
12. G. S. W. Craig, R. E. Cohen, R. R. Schrock, C. Dhenaut, I. Ledoux and J. Zyss, *Macromolecules*, **27**, 1875 (1994).
13. M. Blanchard-Desce, I. Ledoux, J. -M. Lehn, J. Malthête and J. Zyss, *J. Chem. Soc. Chem. Comm.*, **737** (1988).
14. M. Barzoukas, M. Blanchard-Desce, D. Josse, J. -M. Lehn and J. Zyss, *Chem. Phys.*, **133**, 323 (1989).
15. R. A. Huilts and G. L. J. Hesselink, *Chem. Phys. Lett.*, **156**, 209 (1989).
16. L. -T. Cheng, W. Tam, S. R. Marder, A. E. Stiegman, G. Rikken and C. W. Spangler, *J. Phys. Chem.*, **95**, 10643 (1991).
17. M. Blanchard-Desce, J. M. Lehn, M. Barzoukas, I. Ledoux, J. Zyss, *Chem. Phys.*, **181**, 281 (1994).
18. K. C. Rustagi and J. Ducuing, *Opt. Comm.*, **10**, 258 (1974).
19. G. P. Agrawal, C. Cojan, C. Flytzanis, *Phys. Rev. B*, **17**, 776 (1978).
20. O. Zamani-Khamiri and H. F. Hameka, *J. Chem. Phys.*, **73**, 5693 (1980).
21. C. P. de Melo and R. Silbey *Chem. Phys. Lett.*, **140**, 537 (1987).
22. J. R. Heflin, K. Y. Wong, O. Zamani-Khamiri, A. F. Garito, *Phys. Rev. B*, **38**, 1573 (1988).
23. B. M. Pierce, *J. Chem. Phys.*, **91**, 791 (1989).
24. Z. Shuai and J. L. Brédas, *Phys. Rev. B*, **44**, 5962 (1991).
25. T. C. Kavanaugh and R. J. Silbey, *J. Chem. Phys.*, **95**, 6924 (1991).
26. Z. G. Soos, G. W. Hayden, P. C. M. McWilliams, in *Conjugated Polymeric Materials: Opportunities in Electronics, Optoelectronics, and Molecular Electronics*, J. L. Brédas and R. R. Chance Eds. NATO Advances Study Institute Series, Vol. E182, Kluwer, Dordrecht (1990).
27. F. C. Spano and Z. G. Soos, *J. Chem. Phys.*, **99**, 9265 (1993).
28. D. N. Beratan, J. N. Onuchic and J. W. Perry, *J. Phys. Chem.*, **91**, 2696 (1987).
29. G. J. B. Hurst, M. Dupuis and E. Clementi, *J. Chem. Phys.*, **89**, 385 (1988).
30. Z. G. Soos and S. Ramasesha, *J. Chem. Phys.*, **90**, 1067 (1989).
31. S. Mukamel and H. X. Wang, *Phys. Rev. Lett.*, **69**, 65 (1992).
32. H. X. Wang and S. Mukamel, *Nonlin. Opt.*, **5**, 281 (1993).
33. K. Knoll and R. R. Schrock, *J. Am. Chem. Soc.*, **111**, 7989 (1989).
34. H. H. Fix, M. O. Wolf, R. O'Dell, B. Lin, R. R. Schrock and M. S. Wrighton, *J. Am. Chem. Soc.*, (1994).
35. I. D. W. Samuel, I. Ledoux, C. Dhenaut, J. Zyss, H. H. Fox, R. R. Schrock and R. J. Silbey, *Science*, 1994 (in press).
36. F. Kajzar and J. Messier, *Rev. Sci. Inst.*, **58**, 2081 (1987).
37. M. Barzoukas, P. Fremaux, D. Josse, F. Kajzar and J. Zyss, *Mat. Res. Soc. Symp. Proc.*, **109**, 171 (1988).
38. I. Kminek, J. Klimovic and P. N. Prasad, *Chem. Mater.*, **5**, 357 (1993).
39. G. Rossi, R. R. Chance and R. J. Silbey, *J. Chem. Phys.*, **90**, 7594 (1989).

Local-Field Effects and Preresonance Amplification of Coherent Anti-Stokes Raman Scattering in Thin Anthracene Monocrystals at Low Temperatures

PEETER KUKK, EDA REINOT and MARGUS RÄTSEP

*Institute of Physics, Estonian Academy of Sciences, Riia 142,
EE2400 Tartu, Estonia*

Received 12 January 1994; accepted 21 March 1994

In this paper, preresonant amplification of the CARS signal near the 0–0 excitonic transition of an anthracene monocrystal at 25097 cm^{-1} will be analysed. All experiments were performed at liquid helium temperatures and for particular measurements the most intensive line in the CARS spectra of anthracene at 1403 cm^{-1} was used. In order to find out the dependence of the CARS signal on the refractive index (or frequency) the dependence of the peak intensity of this CARS line on the pumping laser frequencies, or the CARS excitation profile, was measured. Experimental results were compared with different model calculations.

INTRODUCTION

The essential increase of activities in the field of local-field effects in the last years has been connected with the theoretical and experimental investigation of the second- and third-order nonlinear optical processes in thin films, nanostructures and at the surfaces of different materials.¹ Local-field effects in samples can be divided into two groups.² Geometric local-field effects take into account the changes of the electromagnetic field intensity inside the sample due to the reflections of the optical beam from the surface of the sample. This type of local-field factors can be found by solving the macroscopic Maxwell equation with correct boundary conditions. The microscopic local-field effects are caused by dipolar interactions between molecules. In this case the calculation of the response of an interacting ensemble of molecules to the electromagnetic field is reduced to the calculation of the response of isolated molecules interacting with the local field. At optical frequencies Lorentz-Lorenz type expressions are often used to describe the microscopic local field. These expressions are valid for isotropic media, but, due to their simplicity, they are often used to describe also Langmuir-Blodgett monolayers as well as biaxial organic monocrystals.³

In our previous paper the influence of geometric local-field effects on coherent anti-Stokes Raman scattering (CARS) spectra was analysed. It was shown that the interference effects in the CARS signal generated in thin samples with reflective surfaces are determined by the interference of the pumping and the CARS waves inside the sample.⁴

In this paper, preresonant amplification of the CARS signal near the 0-0 excitonic transition of an anthracene monocrystal at $\omega_{\text{ex}} = 25097\text{ cm}^{-1}$ will be analysed. All

experiments were performed at liquid helium temperatures, where the optical constants of these crystals are well determined.⁵ For particular experimental measurements the most intensive line of the CARS spectrum of anthracene at $\Omega = 1403 \text{ cm}^{-1}$ was used. In order to find the dependence of the CARS signal on the refractive index (or frequency) the dependence of the peak intensity of this CARS line on the pumping laser frequency, or the so-called CARS excitation profile, was measured. Experimental results were compared with different model-calculations based on polariton-mediated Raman scattering, the semiclassical and the transform theory, and the Lorentz-Lorentz type formula to allow for local-field effects.

MODEL CALCULATIONS

The intensity of the CARS signal at the frequency $\omega_3 = 2\omega_1 - \omega_2$, generated by two pumping lasers with the frequencies ω_1 and ω_2 , is determined by the following formula:⁶

$$I(\omega_3) = ML[\chi^{(3)}]^2 I(\omega_1)^2 I(\omega_2) [\sin(\Delta kl)/\Delta k]^2, \quad (1)$$

where M is the approximate constant, $\chi^{(3)}$ is the third-order non-linear susceptibility; $I(\omega_i)$ are the intensities of the light field at the frequency ω_i ; l is the thickness of the sample; Δk is the phase mismatch; L is proportional to the Lorentz-Lorentz-type local-field correction,⁷ where included are also refractive indices which appear in formula (1) due to the ratio between the electric field amplitude E and the intensity I , $I = cnE^2/(8\pi)$.

$$L = \frac{(n_1^2 + 2)^2}{9n_1} \frac{(n_2^2 + 2)^4}{81n_2^2} \frac{(n_3^2 + 2)^2}{9n_3}, \quad (2)$$

where n_i is the refractive index at the frequency ω_i .

CARS process in a solid-state low-temperature sample near its exciton (or polariton) resonance has, to our knowledge, not been elaborated theoretically. In literature may be found four models which more or less describe experiments done in the present work. Frequency dependence of the polariton-mediated Raman scattering near the exciton resonance at ω_{ex} has been investigated in several papers.^{8,9} CARS signal is proportional to the multiplication of two Raman scattering cross-sections,¹⁰ and its frequency dependence may be calculated according to the following formulae:

$$\chi^{(3)} \propto [(\omega_3^2 - \omega_{\text{ex}}^2)((\omega_3 - \Omega)^2 - \omega_{\text{ex}}^2)(\omega_1^2 - \omega_{\text{ex}}^2)((\omega_1 - \Omega)^2 - \omega_{\text{ex}}^2)]^{-1}, \quad (3)$$

$$\chi^{(3)} \propto [v_g(\omega_1)v_g(\omega_3)]^{-1/2}, \quad (4)$$

where v_g is the group velocity of the polaritons.

According to the semiclassical model the resonant amplification of the CARS signal due to the exciton resonance may be described by a single resonant denominator:¹¹

$$\chi^{(3)} \propto [\omega_3^2 - \omega_{\text{ex}}^2 + 2i\omega_{\text{ex}}\Gamma]^{-1}. \quad (5)$$

In the transform theory the CARS excitation profile is calculated by using the first order linear susceptibilities, $\chi^{(1)}$.¹⁰ In the transparency region of the sample, where the

absorption of the laser beams is absent, $\text{Im}(\chi^{(1)}) = 0$, the CARS excitation profile is mainly determined by the refractive index of the sample, $n^2 - 1 \sim \text{Re}(\chi^{(1)})$. In this case

$$\chi^{(3)} \propto (n_3^2 - n_1^2)(n_1^2 - n_2^2). \quad (6)$$

For particular numerical calculations the dependence of the refractive index, n_i (Fig. 1), and the group velocity, v_g , on frequency has been calculated according to the polariton model.¹² The frequencies of the laser beams (indicated by arrows in Fig. 1) were chosen to ensure an essential change of the refractive index at the CARS frequency, ω_3 .

The theoretical curves characterizing the dependence of the local-field factor (formula 2) and the squares of nonlinear susceptibilities (formulae 3–6) are depicted in a semilogarithmic scale in Figure 2. The theoretical dependences calculated according to formulae 3 and 6, coincide with the precision of the width of the line in Figure 2. All curves have been normalized so that at the CARS frequency, $\omega_3 = 24700 \text{ cm}^{-1}$, they are equal to 1. In any case, the preresonance amplification of the CARS signal was larger according to nonlinear susceptibility than according to the local-field correction. This means that in this particular case the extent of local-field effects in CARS spectra can be determined with the accuracy limited by the precision of determining the nonlinear susceptibility.

EXPERIMENTAL

A CARS spectrometer, based on two excimer-pumped dye lasers, generated light pulses with the duration of 10 ns, the energy of 50 μJ and the spectral width of 1 cm^{-1} . The lasers were operating on Coumarin 120 and Stilben 3 dye solutions. Two dye laser

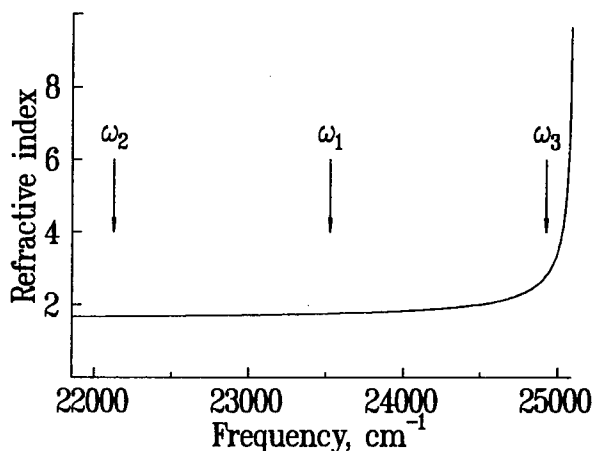


FIGURE 1 The calculated refractive index of an anthracene monocystal near its 0-0 excitonic transition at 25097 cm^{-1} at liquid helium temperatures. The crystallographic axis b of the monocystal is parallel to the polarization of the laser beams. The arrows marked with ω_1 , ω_2 and ω_3 indicate the frequencies of the pumping lasers and the CARS signal, respectively.

beams were focussed onto the sample (spot diameter 50–70 μm) with a 11-cm focal length lens. The generated CARS signal was spatially and spectrally filtered by a Raman-quality monochromator, detected with a photomultiplier and processed with a BOXCAR integrator connected to a computer.¹³ Anthracene monocrystals were prepared by sublimation in the atmosphere of argon. For the CARS experiments, wedge-shaped samples with a clear surface area of about 20 mm² and the thickness of 30–100 μm were selected. The shape of the sample was essential for the elimination of the geometric local-field effects caused by multiple reflections of the pumping laser beams from the surfaces of the crystal. Anthracene monocrystals are biaxial crystals and for the CARS experiments the crystallographic axis *b* of the crystal was oriented parallel to the polarization of the pumping laser beams.¹⁴

Due to a very strong dependence of the refractive index on frequency it is impossible to ensure the fulfilment of the phase-matching condition. For example, at $\omega_3 = 24700 \text{ cm}^{-1}$ the phase-matching angle is equal to 33°. In our experimental setup with a liquid helium cryostat the maximal angle between the two laser beams entering the sample was restricted to 5.5°. Due to this experiments were carried out under completely non-phase-matched conditions ($\Delta k \sim 10^4 \text{ cm}^{-1}$).

RESULTS AND DISCUSSIONS

The CARS excitation spectra were measured by scanning the laser frequency ω_2 at fixed values of ω_1 and the peak intensity of the CARS line corresponding to the $\Omega = 1403 \text{ cm}^{-1}$ Raman transition of anthracene was measured. The experimental points measured with the step of ω_3 equal 15 or 30 cm^{-1} are depicted in Figure 3 as a function of the CARS frequency. For guiding the eye these points are connected with straight lines. To compare the shapes of the excitation profiles they have been

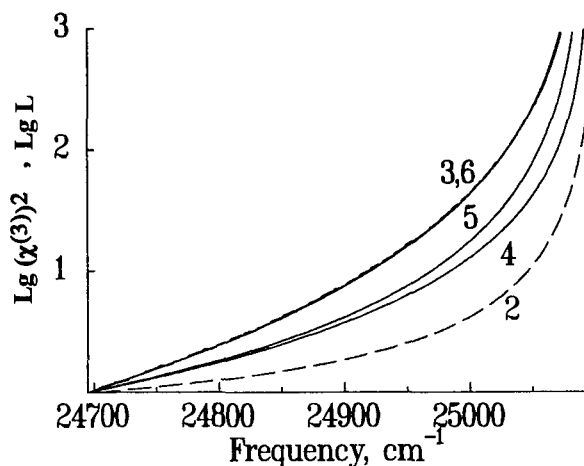


FIGURE 2 Theoretical dependence of the local-field factor and the squares of nonlinear susceptibilities on the frequency (numbers indicate the corresponding formula in the text).

normalized with respect to their values at $\omega_3 = 24940 \text{ cm}^{-1}$. The decrease of the angle between the two laser beams from 4.7 to 2.1° led to the lowering of the CARS signal by about 60 times and to the shift of the excitation profile by 15 cm^{-1} towards lower frequencies, but at the same time the shape of the excitation profile remained almost unchanged. The overall change of the measured CARS intensity between 24700 and 25000 cm^{-1} was about 40 times. At higher frequencies, $\omega_3 > 25000 \text{ cm}^{-1}$, the experimental signal decreased due to the tail of a high-intensity absorption band at 25097 cm^{-1} .

In the low-frequency region the measured excitation spectra coincide rather well with the theoretically predicted dependence calculated according to the polariton-mediated Raman scattering or transform theory and taking also into account the local-field correction (formulae 3 or 5 and 2). Other two theoretical formulae (4 and 5) gave less pronounced frequency dependence of the CARS excitation profile as compared to experimental results. A small decrease of the angle, from 4.7 to 2.1° , between two pumping laser beams led to a 5% change of the calculated Δk values. On one hand, as it was expected, this small change did not reflect in the shape of the experimentally measured profile, but on the other hand, however, this small change of Δk did not explain an about 60 times decrease of the measured excitation profile intensity. This discrepancy indicated that the simple formula commonly used for the calculating of Δk was not applicable for our particular case (biaxial monocrystal). For this reason the frequency dependence of Δk was not taken into account on calculating the theoretical curve in Figure 3 and as the exact determination of the ratio between the phase-mismatch and absorption coefficient was problematic, the theoretical excitation profile was calculated only for the transparency spectral region of the sample and not for the

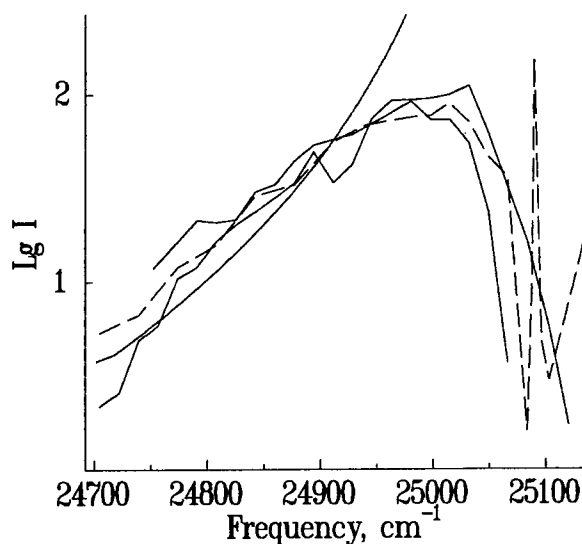


FIGURE 3 Normalized CARS excitation profiles measured from two anthracene monocrystals (solid and dashed curves) and at two different angles, 2.1° and 4.7° , between the two pumping beams entering the sample (two solid curves). Model calculations (formula 6 and 2) are shown by a smooth curve.

region of $\omega_3 < 25000 \text{ cm}^{-1}$, where the approximation $\text{Im}(\chi) = 0$ was not valid any more. These problems connected with phase-mismatch in biaxial monocrystals need further theoretical and experimental investigations.

The presence of geometric local-field effects due to backreflections from the surfaces in the crystals with parallel surfaces led to the appearance of an interference structure in the experimental CARS excitation profile. In this case the signal changed in the same frequency interval about 5000 times. This interesting experimental result indicated that multiple reflections of the light beams in the sample lead to the compensation of the large phase-mismatch.¹⁵

CONCLUSION

The experimentally observed dependence of the CARS signal on frequency in the transparency region of the sample coincides well with the numerical calculations made according to the polariton-mediated Raman scattering or transform theory and local-field approximation. Strong dependence of the refractive index and nonlinear susceptibility on the frequency allowed the estimation of the extent of local-field effects in CARS spectra only with the accuracy of the determining of nonlinear susceptibility. These two effects can be spectrally separated by investigating the impurity systems where the refractive index is mainly determined by the host and nonlinear susceptibility, by the impurity. Experimental investigations in this direction are in progress now.

ACKNOWLEDGEMENTS

The authors are grateful to I. Tehver and T. Reinot for valuable discussions. This work was supported partially by the International Science Foundation.

REFERENCES

1. Organic Molecules for Nonlinear Optics and Photonics, Ed. J. Messier, F. Kajzar and P. Prasad, (Kluwer Academic Publishers, Dordrecht, 1991).
2. G. Cnossen, K. E. Drabe and D. A. Wiersma, *J. Chem. Phys.*, **97**, 4512 (1992).
3. A. Bree and R. Zwarich, *J. Raman Spectrosc.*, **18**, 37 (1987).
4. P. Kuk, *J. Raman Spectrosc.*, **23**, 483 (1992).
5. J.-M. Sajer, M. Orrit and Ph. Kottis, *Chem. Phys.*, **94**, 415 (1985).
6. R. J. Carlson and J. C. Wright, *Appl. Spectrosc.*, **43**, 1195 (1989).
7. Chr. Flytzanis and N. Bloembergen, Progress in Quantum Electronics, ed. J. H. Sanders and S. Stenholm (Pergamon, New York, 1976), Vol. 4, p. 271–300.
8. B. Bendow, Electronic Structure of Noble Metals and Polariton-Mediated Light Scattering (Springer-Verlag, Berlin-Heidelberg-New York, 1978).
9. A. A. Maksimov and I. I. Tartakovskii, *Sov. J. Exper. and Theor. Physics*, **94**, 293 (1988).
10. A. V. Lukashin and M. D. Frank-Kamenetskii, *J. Raman Spectrosc.*, **12**, 234 (1982).
11. S. D. Kramer and N. Bloembergen, *Phys. Rev. B*, **14**, 4654 (1976).
12. J. Aaviksoo, A. Freiberg, J. Lippmaa and T. Reinot, *J. of Luminesc.*, **37**, 313 (1987).
13. P. Kuk and A. Freiberg, *J. Chem. Phys.*, **97**, 118 (1992).
14. P. Kuk, E. Reinot, and T. Haldre, *Proc. Estonian Acad. Sci. Phys. Math.*, **38**, 411 (1989).

Picosecond Light-Induced Dichroism in Thin Films of Phenylene-Vinylene Oligomers

J. M. NUNZI^a, F. CHARRA^a, N. PFEFFER^a, T. P. NGUYEN^b and V. H. TRAN^c

^aLeti (CEA-Technologies Avancées), DEIN-SPE, Groupe Composants Organiques, Centre d'Etudes de Saclay, F91191 Gif-sur-Yvette cedex
Tel: 33(1) 69 08 68 12 Fax: 33(1) 69 08 76 79 E-mail: nunzi@roitelet. saclay. cea. fr

^bLaboratoire de Physique Cristalline, Institut des Matériaux, 2 rue de la Houssinière, F44072 Nantes cedex 03, France
^cLaboratoire des Matériaux Organiques à Propriétés Spécifiques, UPR-CNRS, BP 24, F69390 Vernaison, France

Received 27 April 1994; accepted 9 May 1994

Resonant third-order optical nonlinearities due to the singlet and triplet anisotropic photoinduced absorptions are spectrally resolved in phenylene-vinylene oligomers using picosecond Kerr-ellipsometry. Photoinduced-absorption line shapes of the triplet-triplet absorptions are strongly oligomer-size dependent. A broadening which is observed for oligomers with more than five phenyl rings strongly reduces the response, showing that intermediate-sized oligomers optimize the resonant optical nonlinearity.

INTRODUCTION

Conjugated polymers have received a large interest owing to their large third-order nonlinear optical susceptibilities $\chi^{(3)}$.¹ Oligomers with a well-defined length can be considered as model compounds. They make possible the experimental check of the effect of conjugation on nonlinear optical properties and identification of the transition between molecule and polymer behaviours. Such chain-length dependences have been successfully studied in the case of the nonresonant third-harmonic nonlinear optical susceptibility $\chi^{(3)}(3\omega; \omega, \omega, \omega)$ with thiophene oligomers.^{2,3} However, experiments aimed at characterising optical modulation devices involve index nonlinearities $\chi^{(3)}(\omega; \omega_p, -\omega_p, \omega_i)$.⁴ Additionally, from a practical point of view, energy consideration makes resonant excitations the only reasonable candidates for parallel all-optical modulation applications in organic molecules.⁵ The thiophene oligomers with length ≤ 6 possess exceptionally-large resonant index nonlinearities in the pico and nanosecond regimes owing to their narrow singlet $S_1 \rightarrow S_n$ ⁶ and triplet $T_1 \rightarrow T_n$ ⁷ transient excited-state absorptions. This spectral concentration effect is due to the particular Franck-Condon reorganization of the carbon atoms which takes place in the excited states of the oligomers.⁵ Indeed, their conjugated polyene-like backbone undergoes a reduction of alternance between single and double bonds after excitation from the ground to the lowest excited state.⁸ It thus appears important to check if spectral

concentration occurs in other oligomers than the thiophene series and also if it saturates with chain-length as linear absorption does. In this paper, we present results of photoinduced-absorption measurements in oligomers of the poly (para-phenylenevinylene)(PPV) series. We identify $S_1 \rightarrow S_n$ and $T_1 \rightarrow T_n$ transient absorptions and we compare the present picosecond experiments performed on thin films with other millisecond experiments performed on solutions of similar phenylenevinylene oligomers.⁹

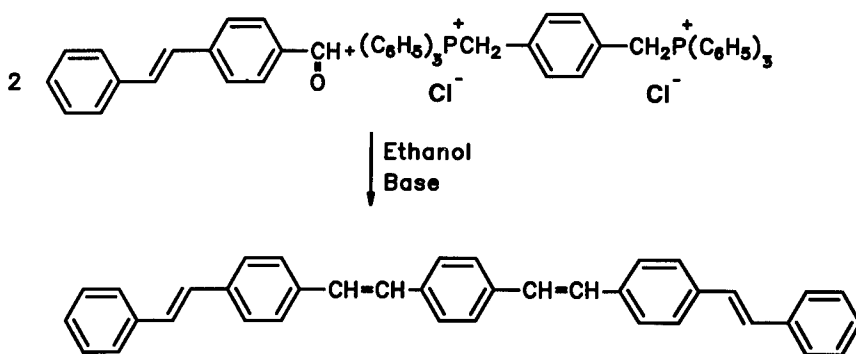
EXPERIMENT

Two oligomers of the phenylenevinylene series were synthesized (Fig. 1). In this study, the 5-phenyl, 4-vinyl compound is abbreviated 4PV and the 7-phenyl, 6-vinyl compound is abbreviated 6PV. All two compounds have been synthesized by Wittig reaction. Compound 6PV (Fig. 1b) is prepared according to the method described in Reference 10. Compound 4PV (Fig. 1a) is synthesized using *p*-xylene-bis (triphenylphosphonium chloride) and 4-stilbenecarboxaldehyde. 4PV is clear-yellow and melts at about 370°C with decomposition. 6PV is brown-yellow. It begins to melt at 400°C and decomposes at 415–420°C. Studied samples were $\ell \approx 1000$ Å-thickness thin-film vacuum-deposited onto 1 mm-thick ordinary glass substrates. Vacuum deposition by sublimation is an efficient purification method for those non-soluble oligomers. Films were weakly crystalline and birefringence free.

Picosecond photoinduced absorption was measured using the Kerr-ellipsometry technique.¹¹ It is derived from a classical Kerr-gate experiment (Fig. 2a) in which the anisotropic excitation produced by a linearly-polarized optical pump in the initially isotropic material is monitored. The pump beam is the $\lambda_p = 355$ nm third-harmonic derived from a 10 Hz-Nd:YAG laser with pulse duration $\tau_p = 25$ psec. Its fluence at the sample is 0.8 mJ/cm^2 ($I_p \approx 30 \text{ MW/cm}^2$). The probe beam is the broad-band visible continuum generated by focussing the 1064 nm laser-pulse into a D₂O cell. The transmission T of the sample is probed through nearly crossed ($90^\circ \pm \theta$) polarizers

a)

4PV



b)

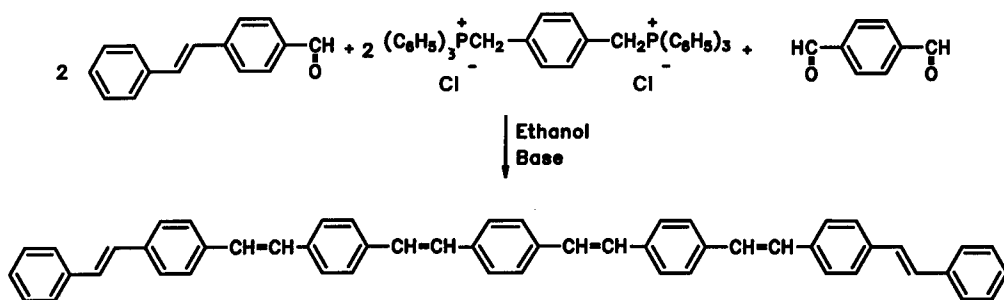
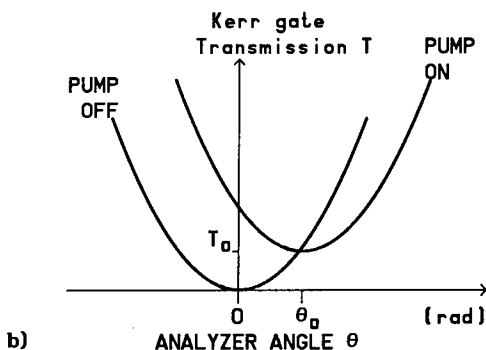
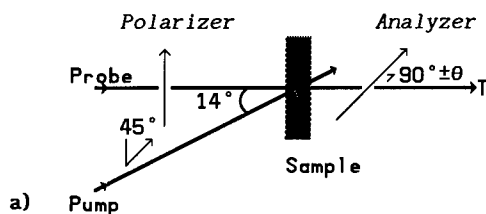
6PV


FIGURE 1 Synthesis scheme and chemical structures of 4PV (a) and 6PV (b) oligomers.


 FIGURE 2 Kerr ellipsometry characterization technique of photoinduced absorptions. Pump and probe beams incident onto the sample are polarized at 45° to each other (a). Transmission T of the modified Kerr-gate is analyzed with an angle θ close to extinction, alternatively with and without pump excitation (b).

(Fig. 2b). Light transmitted through the gate is dispersed onto an amplified optical multichannel analyser covering the $\lambda_t = 420$ to 950 nm probe-wavelength range. Pump and probe polarizations make a 45° angle. In the isotropic film, the pump induces an optical anisotropy which consists both of induced dichroism and birefringence. They

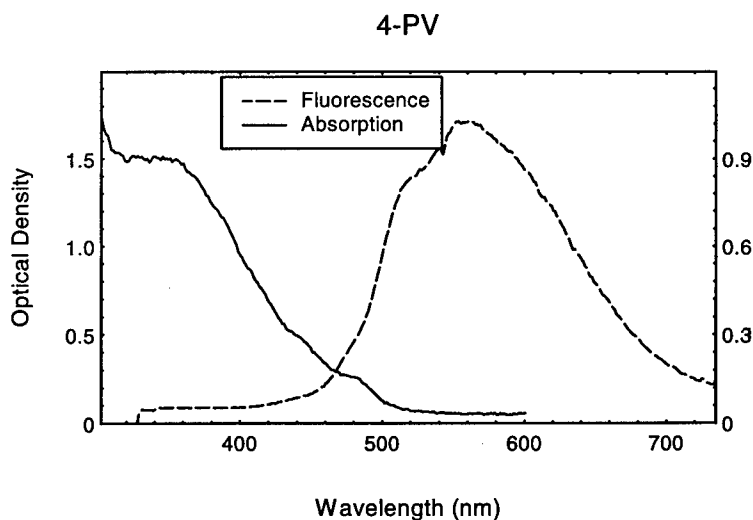
are linked to the tensor components of the imaginary and real parts of $\chi^{(3)}(\omega_i; \omega_p, -\omega_p, \omega_i)$, respectively. For each probe wavelength, the dichroism corresponds to a rotation of the transmitted probe polarization and it can be partly compensated by an analyzer rotation of an angle θ_0 with respect to the initial extinction position $\theta = 0$ in Figure 2b. This extinction angle θ_0 does not depend on probe intensity, sample transmission or apparatus response: it is the measurement of the nonlinear absorption changes experienced by the probe. The accuracy of the determination is essentially limited by pump fluctuations. We perform the operation for each probe wavelength λ_i using a computer treatment. In the small signal case, the measured angle θ_0 is proportional to the imaginary part of the nonlinear susceptibility of the solution:

$$\theta_0 = \left(\frac{3\pi\ell I_p}{2\varepsilon_0 \lambda_i n_i n_p c} \right) \text{Im}(\chi_{xxxx}^{(3)} - \chi_{yyxy}^{(3)}), \quad (1)$$

where ℓ is the sample thickness, I_p the pump intensity, n_i and n_p the refractive indices at probe and pump wavelengths. The imaginary part of $\chi^{(3)}$ reflects the absorption variations and in regions where the film is transparent, it gives the photoinduced absorptions.

RESULTS

UV-visible absorption spectra of the 4PV and 6PV oligomer thin films are drawn as the solid lines in parts *a* and *b* of Figure 3, respectively. Room temperature luminescence spectra are drawn as the broken lines in the same figure. Luminescence quantum efficiency is lower than 10%. The transient anisotropic photoinduced absorptions probed during the picosecond 355 nm UV-excitation are depicted in Figure 4. The transient photoinduced absorptions probed at 600 psec delay after picosecond 355 nm



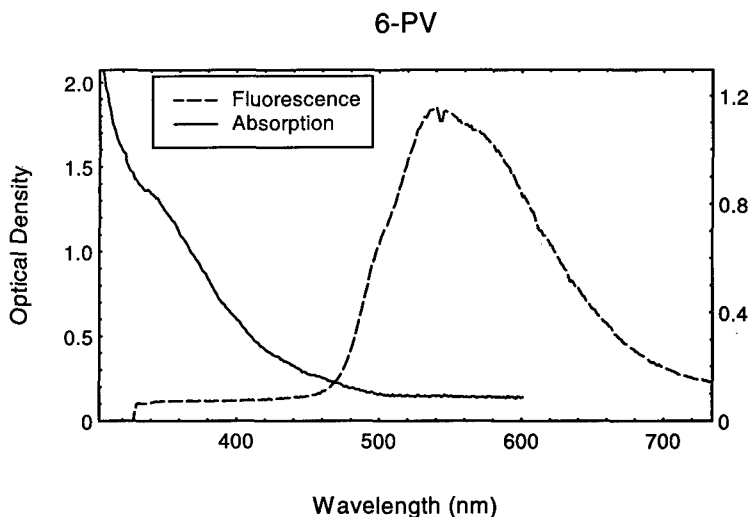


FIGURE 3 Optical density of absorption (solid line) and photo-luminescence (broken line, arbitrary units) spectra of 4PV (a) and 6PV (b) oligomer thin-films. UV transmission is cut at 320 nm by the ordinary glass substrate. Optical excitation is performed on the film side.

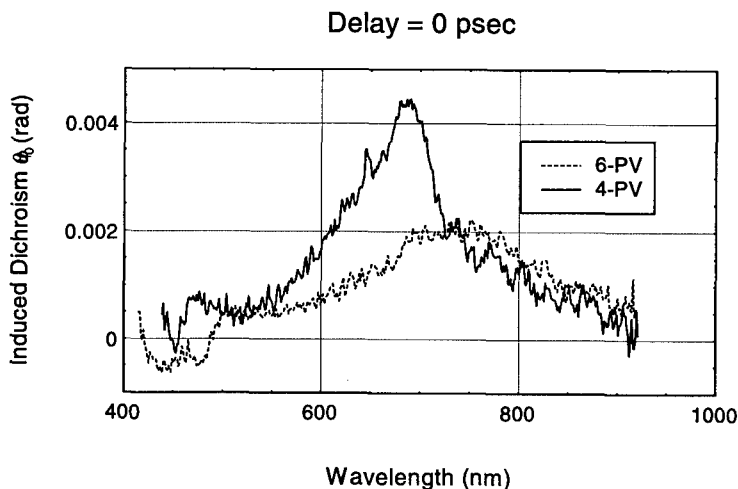


FIGURE 4 Anisotropic photoinduced absorption (dichroism) induced during 355 nm UV-excitation in 4PV (solid line) and 6PV (broken line) oligomers.

UV-excitation are depicted in Figure 5. Solid lines are for 4PV and broken lines are for 6PV transient spectra.

DISCUSSION AND CONCLUSIONS

Transient absorption is recorded in the red to near-IR transparency region of the oligomers. It lies in the region of the triplet $T_1 \rightarrow T_n$ absorptions which have been

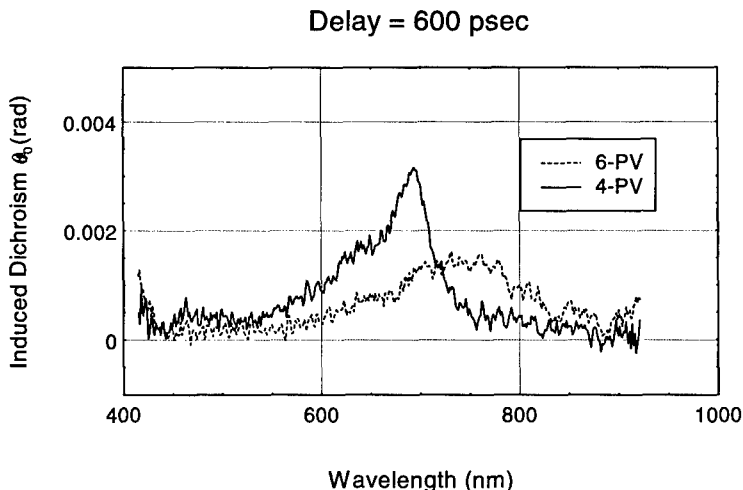


FIGURE 5 Anisotropic photoinduced absorption (dichroism) induced at 600 psec delay after pulsed 355 nm UV-excitation in 4PV (solid line) and 6PV (broken line) oligomers.

calculated¹² and measured¹³⁻¹⁵ for PPV type polymers (1.4 eV). As luminescence quantum efficiency is low, absorption features living more than 600 psec can indeed be associated with non-radiative states such as the triplets. For the 4PV oligomer, the 600 psec-delay absorption in Figure 5 is sharp and well resolved, with a 0.16 eV (1290 cm^{-1}) blue-shifted vibronic replica which may have the same vibrational origin as the one observed in the luminescence spectrum in Figure 3a. Its maximum peaks at 680 nm (1.82 eV), at the same energy as the triplet state previously observed in the millisecond regime in an end-capped 4PV oligomer.⁹ For the 6PV oligomer, the 600 psec absorption in Figure 5 is broader and unstructured. Its red-most maximum peaks at 770 nm (1.61 eV), at the same energy as the triplet state observed in an end-capped 6PV oligomer.⁹ This confirms observation of the $T_1 \rightarrow T_n$ absorptions in our experiments. Zero-delay spectra in Figure 4 contain the 600 psec-triplet spectra superimposed on a flat background with $\approx 5 \times 10^{-4}$ rad-dichroism magnitude. Assuming isotropically distributed molecules in the film and slow orientational diffusion, we get $\chi_{xxxx}^{(3)} = 3\chi_{yyyy}^{(3)}$. Equation 1 thus yields the imaginary part of the nonlinearity associated with this flat background: $\chi_{xxxx}^{(3)} \approx 3 \times 10^{-17} \text{m}^2/\text{V}^2$ (2×10^{-9} esu). This *instantaneous* flat background absorption may be associated with the blue tail of the $S_1 \rightarrow S_n$ excited state absorption whose theoretically predicted maximum lies in the 2000 nm wavelength-region (0.5 eV).¹² As concerns the triplet excited-state absorption, we cannot estimate its decay-time which is much larger than our probed 600 psec delay-range. We can thus give the ratio of $\chi^{(3)}$ over the photoabsorption lifetime (the effect is cumulative in the impulsive regime). Equation 1 thus yields the imaginary part of the nonlinearity associated with the $T_1 \rightarrow T_n$ absorption maximum: $\chi_{xxxx}^{(3)}/\tau = 8 \times 10^{-6} \text{m}^2 \text{V}^{-2} \text{s}^{-1}$ for 4PV at $\lambda_i = 680$ nm, where τ is the photoabsorption lifetime. The 6PV nonlinearity is half smaller and the reduction in size is compensated by the increase in spectral width in Figure 5. The peak area is preserved as the sum-rule for absorptions. Importantly,

Kerr-ellipsometry measures *anisotropic* effects. Such molecular property is not maintained over large distances in isotropic media, and energy migration may result in a signal decay. Moreover, the triplet absorption signal is quasi-constant in our probed delay-range. Weak spectral diffusion is thus to be expected, as opposed to kHz-regime experiments.⁹ The experiment is thus an extensive probe of the distribution of different energy-level structures present in the film. However, though absorption and emission spectra in Figure 2 are broad (0.5 eV fwhm), the 680 nm triplet-absorption of 4PV is narrow (0.17 eV fwhm). This indicates that the oligomer undergoes homogenization of the conformations in the excited state, as did the thiophene oligomers.^{6,7} Additionally, the magnitude of the 0.16 eV vibronic replica is reduced by a factor 2 from ground to triplet state absorption, indicating a reduction of C—C bond alternance, as predicted theoretically.¹² No such spectral narrowing is observed with 6PV triplet state absorption which is ≈ 0.3 eV fwhm. This means that the oligomer does not undergo homogenization of the conformations in the excited state. The experimental consequence is that the resonant nonlinearity does not increase with conjugation length above the 4PV oligomer size, as does the maximum triplet absorption wavelength. This shows that such intermediate-sized oligomers optimize the resonant optical nonlinearity: they exhibit *spectral concentration*.⁵

ACKNOWLEDGEMENTS

Work performed at Saclay was supported by the *Direction des Recherches, Etudes et Techniques*. We thank André Lorin for thin-film evaporation.

REFERENCES

1. P. N. Prasad and D. J. Williams, *Introduction to nonlinear optical effects in molecules and polymers*, Wiley (New York, 1991).
2. D. Fichou, F. Garnier, F. Charra, F. Kajzar and J. Messier, in *Organic Materials for Nonlinear Optics*, R. Hann, D. Bloor, Eds., Royal Soc. Chem. 176 (London, 1989).
3. H. Thienpont, G. L. J. A. Rikken, E. W. Meijer, W. ten Hoeve and H. Wynberg, *Phys. Rev. Lett.*, **65**, 2141 (1990).
4. F. Kajzar, J. Messier, J. M. Nunzi and P. Raimond, in "Polymers for Lightwave and Integrated Optics: Technology and Applications", L. A. Hornak, Ed., Marcel Dekker 595 (New York, 1992).
5. J. M. Nunzi, F. Charra and N. Pfeffer, *Journal de Physique III*, **3**, 1401 (1993).
6. F. Charra, D. Fichou, J. M. Nunzi and N. Pfeffer, *Chem. Phys. Lett.*, **192**, 566 (1992).
7. J. M. Nunzi, N. Pfeffer, F. Charra and D. Fichou, *Chem. Phys. Lett.*, **215**, 114 (1993).
8. D. Beljonne, Z. Shuai and J. L. Brédas, *J. Chem. Phys.*, **98**, 8819 (1993).
9. H. S. Woo, O. Lhost, S. C. Graham, D. D. C. Bradley, R. H. Friend, C. Quattrocchi, J. L. Brédas, R. Schenk and K. Müllen, *Synth. Met.*, **59**, 13 (1993).
10. G. Drefahl and G. Plötner, *Chem. Ber.*, **94**, 907 (1961).
11. N. Pfeffer, F. Charra, J. M. Nunzi, *Opt. Lett.*, **16**, 1987 (1991).
12. Z. Shuai and J. L. Brédas, Nature of photoexcitations in poly (paraphenylene vinylene) and its oligomers, *Chem. Phys. Lett.*, in press (1994).
13. X. Wei, B. C. Hess, Z. V. Vardeny and F. Wudl, *Phys. Rev. Lett.*, **68**, 666 (1992).
14. L. Smilowitz and A. J. Heeger, *Synth. Met.*, **48**, 193 (1992).
15. A. R. Brown, K. Pichler, N. C. Greenham, D. D. C. Bradley, R. H. Friend and A. B. Holmes, *Chem. Phys. Lett.*, **210**, 61 (1993).

Nonlinear Optical Properties of Organic MIS Structures¹

FABRICE CHARRA

*leti (CEA–Technologies Avancées), DEIN-SPE,
Centre d'Études de Saclay, F-91 191 Gif-sur-Yvette–Cedex, France*

Received 31 March 1994; accepted 18 April 1994

An important particularity of organic semiconductors is their strong coupling between charge-transport and optical properties. By applying a voltage on a Metal-Insulator-Semiconductor (MIS) structure charges can be injected in the semiconductor under well-controlled conditions. Based on these principles, new mechanisms of electro-optic coupling and all-optical coupling (i.e., nonlinear optical) phenomena appear in organic MIS devices. The use of these properties for the characterization of charge-transport and for light-modulating devices are discussed. The example of the association in a MIS structure of electro-optic coupling and photo-conductivity is discussed. It leads to a new type of electrically-controlled photochromic device.

INTRODUCTION

Organic thin films attract a growing interest in view of their semiconducting properties. Low molecular-weight organics such as anthracene¹ or metallophthalocyanines^{2,3} as well as π -conjugated polymers such as polyacetylene (PA),⁴ poly-3-alkylthiophene (P3ATs),⁵ or polyphenylene-vinylene (PPV)⁶ derivatives, as been used as the active semiconductor of electronic or photonic thin-film devices: photovoltaic cells, Schottky diodes, Field-Effect Transistors (FETs) or Light-Emitting Diodes (LEDs). Conjugated oligomers of thiophene (α -*n*T), paraphenylene (*n*P), or paraphenylene-vinylene (*n*PV, with *n* phenyl rings and (*n* – 1) vinylene double bonds) represent an intermediate case which combines good molecular and solid-state ordering with high carrier mobilities: the performances of FETs have been significantly enhanced by using α -6T as the semiconductor.⁷ Parallely, the electronic transport properties of organics are also studied with the aim of achieving organic photorefractive materials.

As for neutral excited states (Frenkel excitons), electric-charge carriers are stored in organic semiconductors as localized states. This results from strong electron-photon coupling and is in sharp contrast with mineral semiconductors where electrons and holes are delocalized over a large number of sites. These charge carriers are charged solitons in PA, singly-charged polarons or doubly-charged bipolarons in conjugated

¹ Proceedings of ICONO'1, Val-Thorens 9–13, 1994.

polymers with a nondegenerate ground state.⁸ They are radical ions, bications or bianions in low-molecular-weight organics. Ionic states of intermediate-sized oligomers can be considered as models of polarons or bipolarons of the respective polymer.

From this viewpoint, polymethine or cyanine dyes represent a particular case since they can be considered as low-molecular-weight models of the positively-charged soliton of PA (see Fig. 1). Such dyes are known for their large absorption coefficients and their narrow absorption lines. From this observation, we can infer that solitons in PA will present such strong spectral signatures. More generally, as a consequence of their localization, charge carriers of organic semiconductors can present sharp spectral features with large optical cross sections in the visible or the near infrared. Such properties can be achieved in mineral semiconductors only by confinement of the electronic wavefunction within quantum wells. Thus, the optical properties of organic semiconductors will be significantly influenced by the presence or the absence of charge carriers. Hence an important particularity of organic semiconductors is their intrinsically-strong coupling between charge-transport and optical properties. Moreover, the hopping nature of both charge- and excitation-transport phenomena confer several new features to this opto-electronic coupling, especially as concerns luminescence phenomena.^{5,9} A device based on electro-modulated fluorescence has been suggested.¹⁰

A third way, besides photogeneration or chemical oxydation or reduction, for generating charges in a semiconductor is the electrode injection achieved by applying a voltage on a Metal-Insulator-Semiconductor (MIS) structure. This method provides a very simple and accurate control of the number and sign of injected charged species. On the contrary to other methods, this permits unbalanced total charges in the semiconductor. The FET mechanism takes advantage of the changes in the *electrical conductivity* of the semiconductor induced by such a charge injection in a MIS device, to control the current between the source and the drain. In this paper, we give a review of the charge-induced changes in *optical properties* of organic semiconductors as part of MIS devices. This yields new types of electro-optic coupling phenomena but also all-optical coupling (i.e., nonlinear optical) phenomena such as electrically-controlled photochromism.

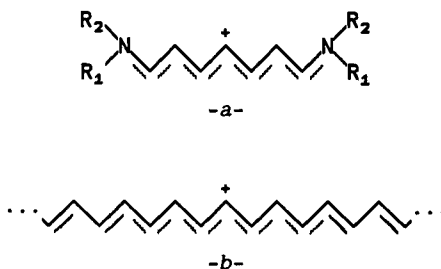


FIGURE 1 Polymethine dyes (-a-) as a model of positively-charged soliton in PA (-b-). Similarly, Galvinoxyl radicals and Oxonol dyes can be considered as models of, respectively, neutral and negative solitons.

ELECTRO-OPTICAL PROPERTIES

Electro-modulated spectroscopic measurements are undertaken as shown on Figure 2. Although the active material is usually centrosymmetric, an electro-optic effect (proportional to the electric-field) is made possible by the macroscopic noncentrosymmetry of the MIS structure itself. When a good electrical contact is achieved between the molecular semiconductor and the injecting electrode, the MIS structure can be viewed as a planar capacitor with the molecular semiconductor as one arm, and with a surface capacity $C_1 = \epsilon_i/t_i$ where ϵ_i is the dielectric constant of the insulator and t_i its thickness. Charge carriers are injected by field effect and stored at the insulator-semiconductor interface. For an applied voltage V , the total injected charge is $Q = \epsilon_i V/t_i$. The maximum electric field V/t_i that can be applied on a good dielectric (e.g., Si_3N_4 , $\epsilon = 6.5 \epsilon_0$) is of the order of $5 \times 10^8 \text{ V m}^{-1}$. Then the maximum number of injected charges is of the order of $2 \times 10^{17} \text{ m}^{-2}$. If the charged species have the absorption cross section of a good dye, $\sigma = 10^{-19} \text{ m}^2$ (i.e., an extinction coefficient $\epsilon = 2 \times 10^5 \text{ l mol}^{-1} \text{ cm}^{-1}$) at a wavelength λ , the optical absorption of the charged layer at this wavelength will be of about 2%. The Electro-Modulated Absorption (EMA) spectroscopy can be carried out through a transparent electrode by reflection on a metallic electrode (see Fig. 2). A maximum EMA signal of a few percent can then be expected.⁴ However, the reflectivity variations usually achieved are in most cases in the range 10^{-2} – 10^{-5} and are detected by lock-in amplification. A large EMA signal (0.64%) has been observed in polyacetylene.⁴ By comparing EMA with doping-induced absorption spectra, the authors have attributed the origin of this absorption to charged solitons. They have also estimated a high absorption cross-section ($1.2 \times 10^{-19} \text{ m}^2$) at 0.8 eV, which confirms the above discussion.

Recent experiments have shown that the origin of the EMA signal in α -6T is the radical cation (model polaron) α -6T $^{\cdot+}$ (see Fig. 3).¹¹ As a matter of fact, the peak at 1.50 eV in Figure 3 (broken line) can be identified with a similar absorption band that

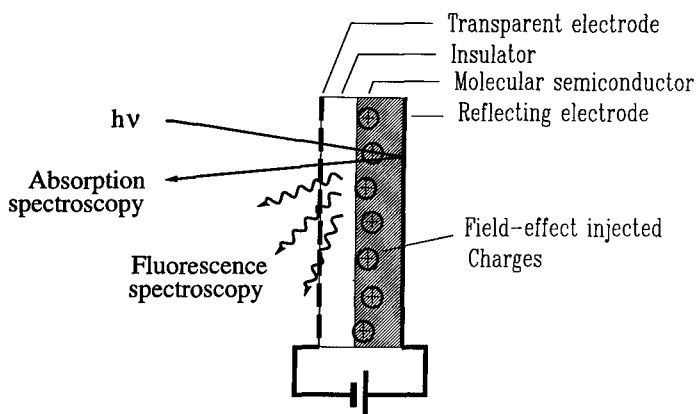


FIGURE 2 Electro-modulated spectroscopy measurements: charges are injected in the molecular semiconductor from the back metallic electrode. Absorption or fluorescence measurements are taken through the transparent electrode. The locations of the insulator and of the molecular semiconductor can be interchanged.

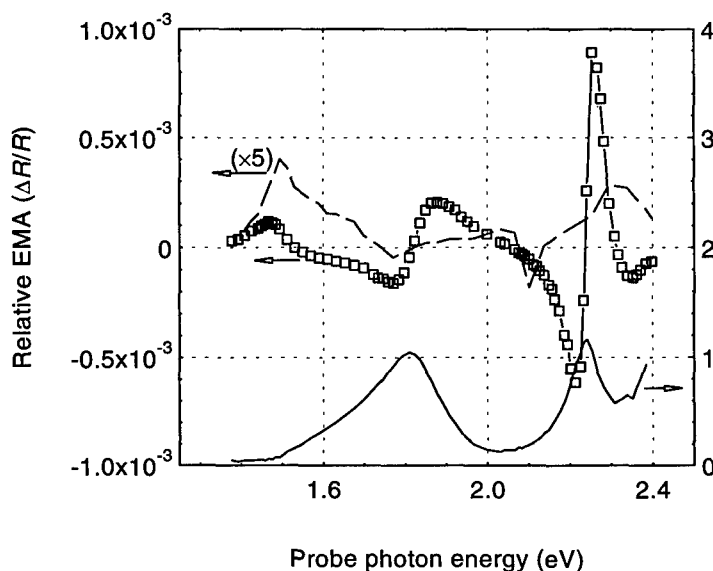


FIGURE 3 Relative EMA spectra of two types of MIS devices both made with a 300-nm evaporated thin film of α -6T as the organic semiconductor. For sample A (broken line, measured at 1 kHz, 10 V), α -6T has been evaporated on a highly transparent (300 Ω/\square) Indium-oxide coating used as the injecting electrode. A 300 nm insulating layer of water-soluble poly-acrylic acid has been spin coated on it. Finally a reflecting silver electrode was evaporated. For sample B (squares, 40 Hz, 5 V), a 47 nm alumina layer was grown by anodization of a reflecting alumina electrode. α -6T has been deposited on it and a 10-nm gold electrode has been evaporated on the top. Since the gold electrode is only partially transparent, Fabry-Perot (substrate-mode) dips can be observed in the reflection spectra R : the solid line is a plot of $\text{Log}_{10}(R)$.

appear following a stoichiometrically-controlled chemical oxydation of α -6T in solution.¹² The maximum signal magnitude is $\sim 10^{-4}$. EMA signals with the same order of magnitude have been observed in PAT⁵ and in PPV, as long as polarons are formed.¹³ In that last case, an absorption cross section of bipolarons as large as that of solitons in PA is mentioned. It thus appears that the nature of the conjugated chain, particularly the existence of a degenerate ground state, influences by orders of magnitudes the absorption cross sections of their charge carriers.

However, a quantitative analysis of EMA signal magnitude should account for the precise optical structure of the multilayer MIS device. As a matter of fact, light-absorbing charges are located within a very thin channel at the semiconductor-insulator interface. Depending on the optical path from the reflecting electrode to this interface, interferences will occur between the direct and reflected light. This will have a drastic influence on the absorbing efficiency of the charged layer. For example, at particular wavelengths, this interference can cancel out the resulting optical electric field. In that case electric-dipole absorptions, which become unable to absorb energy, have no effect on the reflection coefficient and the EMA spectrum drops to zero, independently to the actual absorption spectrum of the charged species. An illustration of this interference effect can be found in Reference 11 where two types of MIS samples, with very different insulator thicknesses, have been tested. In the first sample (A), the insulator was a 300-nm acrylic-polymer film. In the second sample (B), it was a 47-nm

alumina layer. Although the number of injected charges was 3.6 times larger in sample B than in sample A, the amplitude of induced absorption is larger by a factor 1.2 only. As a matter of fact, in sample B the α -6T-insulator interface was separated from the reflecting metal by only $\lambda_{\max}/10$ at the maximum absorption wavelength $\lambda_{\max} = 820$ nm. Since a metal reflection imposes nearly a "node" of electric field, the efficiency of electric-dipole absorptions is lowered by the proximity of such a reflection. However, a careful account of the precise optical structure of the samples, taking from the literature the optical constants of the different involved materials, leads to a good agreement between the absorption cross section of injected charge carriers estimated from sample A: $3.8 \times 10^{-21} \text{ m}^2$, and from sample B: $4.0 \times 10^{-21} \text{ m}^2$.

Even more dramatic effects occur when poorly-transparent electrodes are used. This is illustrated in Figure 3, where we compare the relative EMA spectra ($\Delta R/R$) of sample A, made with a highly transparent Indium-oxide electrode (broken line) and sample B, made with a 10-nm semi-transparent gold electrode (squares). Whereas the main feature of sample A is the 1.50-eV absorption attributed to α -6T $^{+\cdot}$, a strong highly-structured signal is observed with sample B above 1.7 eV, in addition to the α -6T $^{+\cdot}$ peak. Its maximum (9×10^{-4} at 2.25 eV) is ten-times larger than the 1.50-eV maximum of both samples A and B. Absorption peaks at 1.8 eV and 2.22 eV are observed on the reflection spectrum. Since these maxima depend upon incidence angle and sample thickness, these peaks should be attributed to Fabry-Perot (FP) resonances (also called substrate modes). These FP peaks are particularly sensitive to index variations. This property permits accurate measurements of electro-optic or nonlinear optical constants.¹⁴ Here, the dispersion of EMA spectrum is nearly proportional to the derivative of the reflection spectrum with respect to photon energy. Hence, it corresponds to a blue shift of the FP modes, i.e., to a decrease of the optical path between electrodes. Its magnitude corresponds to a *polarizability* variation of $\delta\alpha = -2.8 \times 10^{-38} \text{ C} \cdot \text{m}^2/\text{V}$ at 2.0 eV upon doping of α -6T, consistent with the visible-to-infrared transfer of oscillator strength. FP resonances affect the EMA signal even when highly transparent electrodes are used. For example, the slight dispersion around 2.1 eV of sample-A EMA spectrum can be attributed to a FP effect. These observations have two consequences. First, since both index and absorption variations contribute to EMA, spectral assignments can only be made by comparison of several samples with different structures or thicknesses, and by comparison with regular reflection spectrum. This analysis yields information on both absorption and polarizability of charged species. Second, the optical overintensities at FP resonances can yield large enhancements of the EMA signal. If the thicknesses are such that FP dips coincide with absorption peaks of injected charges, electro-optical modulation with large contrast can be expected. Since this works in a reflection configuration, it could be of great interest from an application point of view.

NONLINEAR OPTICAL PROPERTIES

The previous section dealt only with the coupling between charge-carriers and photons. In order to get an all-optical coupling (i.e., a nonlinear optical effect) a charge photogeneration process should be introduced in the system. This could be done by insertion of a photoconducting layer as for liquid-crystal light valves. Here, a simpler

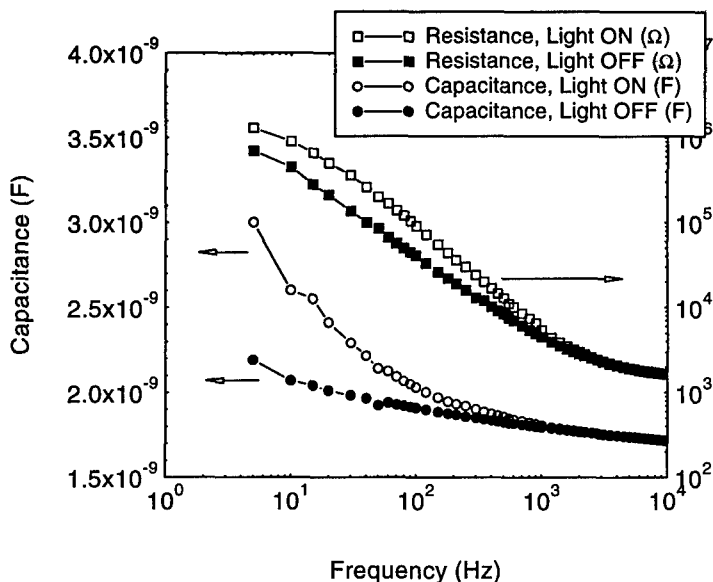


FIGURE 4 Photoimpedance measurements on a 0.7-cm^2 MIS device with 250-nm evaporated 5PV film as the semiconductor. The insulator was a 690-nm spin-coated layer of polymethylmethacrylate, and an Indium-oxide coating was used as the transparent electrode. The resistance (squares) and capacitance (circles) of the equivalent serial model ($Z = R + 1/jC\omega$), with (open marks) and without (filled marks) a 10 W/m^2 light-excitation in the 450–520 nm wavelength range. The test voltage amplitude was 0.5 V. No effect is observed when the excitation wavelength is larger than 520 nm, optical gap of 5 PV.

way is to use in the MIS device a semiconductor which is also photoconducting. Such a semiconductor can be 5PV.¹⁵ The photoinjection of charges in 5PV in a MIS structure has been demonstrated by photoimpedance measurements (see Fig. 4). An electrical modelization of the sample, taking the frequency-dependent dielectric constant and losses of polymethylmethacrylate from the literature, shows that in the dark, 5PV behaves as an insulator with a dielectric constant $\epsilon = 2.8\epsilon_0$. When the sample is submitted to a modest light excitation, an increase in the capacitance is observed at low frequency. Parallely, an increase in the equivalent serial resistance is measured. The frequency-dependent photoimpedance is well fitted by assuming the photogeneration of charge carriers with lifetime limited by trapping or recombination. The lifetime-mobility product ($\tau\mu$) ponderated by the quantum efficiency of the photogeneration ρ is estimated to $\rho\tau\mu = 5 \times 10^{-16}\text{ m}^2/\text{V}$. These results confirm that charge-injection in the 5PV MIS device must be assisted by light.

Figure 5 shows the EMA spectra of the 5PV MIS device with and without photoexcitation (from Ref. 15). From the above results, the quantum efficiency of charge injection under a 15-V polarization is of the order of 3%, but it can be larger because of the field dependence of the charge-generation quantum efficiency ρ . As expected, a EMA-signal is only observed in the presence of the excitation light. The signal is also strongly dependent on the frequency of the applied voltage: a cutting frequency of 10 Hz has been measured under the excitation-light intensity of 0.1 W/m^2 . This cutting frequency was nearly proportional to the excitation-light intensity. Hence, the 5PV MIS-structure behaves

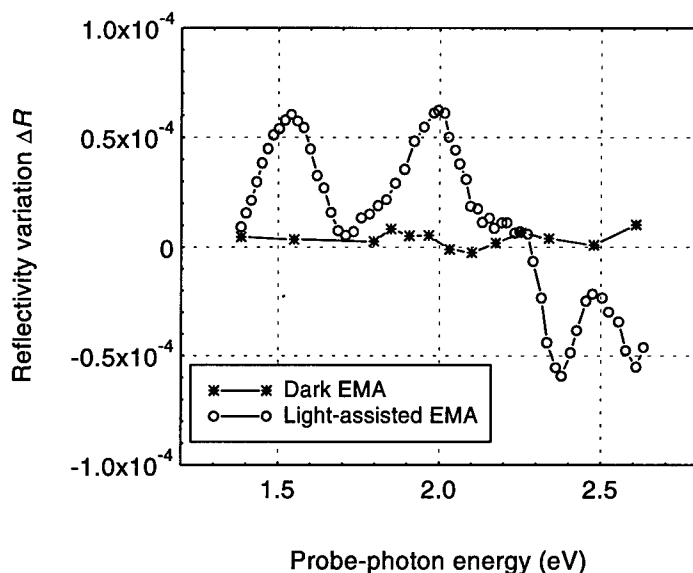


FIGURE 5 Absolute EMA spectra of a MIS device with 5PV as the semiconductor, with (open circles) and without (stars) a 0.1 W/m^2 light-excitation in the 450–520 nm wavelength range. The frequency of modulating voltage was 7 Hz and its amplitude 15 V. As for photoimpedance, no effect is observed when the excitation wavelength is larger than 520 nm.

as a photochromic device with an integration-time dynamically-controlled by the electric field. This property can be used to match the working frequency with the excitation intensity. The photochromic sensitivity is $10^{-2} \text{ m}^2/\text{J}$ which is the same order of magnitude as typical photochromics like bacteriorhodopsin. The remarks made in Section 2 as concerns the contrast of modulation and its possible amplification by FP resonances remain valid here. This electrically-controlled photochromic effect can be compared with photorefractivity, in the sense that it results from the association of electro-optic and photoconducting properties. However, whereas photorefractivity is a bulk effect, the thin-film aspect of MIS devices could be interesting for many applications, such as image converters¹⁶ or two-colour real-time holography.

CONCLUSION

The inherent strong coupling between charge-transport and optical properties present in organic semiconductor makes possible the optical spectroscopy of MIS devices. This has proved to be very useful for the characterization of charge-carriers and charge-transport processes in these materials. For this purpose, special attention must be paid to a careful optical modelization of these multilayer structures. This is especially true when poorly transparent electrodes are used, generating strong Fabry-Perot resonances. In this review, we have emphasized the aspects linked with possible applications. The maximum contrast is attained by association of charge carriers with large

absorption cross sections with FP resonances. The optimization of absorption cross sections would benefit from investigations on the relations between absorption and molecular structure of charged conjugated species.

New opto-electronic mechanisms appear specifically in organic MIS devices. These are electro-optic coupling phenomena but also nonlinear optical phenomena. For example, the association of electro-optic coupling and photoconductivity in a MIS structure yield a new type of electrically-controlled photochromic device.

REFERENCES

1. M. Pope and C. E. Swenberg, "Electronic processes in organic crystals", *Monographs on the physics and chemistry of materials*, **39**, Oxford University press (Oxford, 1982).
2. J. Simon, J. J. André, "Molecular Semiconductors", Springer (Berlin, 1985).
3. W. J. Pietro, *Adv. Mat.*, **6**, 239 (1994).
4. J. H. Burroughes, C. A. Jones and R. H. Friend, *Nature*, **335**, 137 (1988).
5. K. E. Ziemelis, A. T. Hussain, D. D. C. Bradley, R. H. Friend, J. Rühle and G. Wegner, *Phys. Rev. Lett.*, **66**, 2231 (1991).
6. R. N. Marks, J. J. M. Halls, D. D. C. Bradley, R. H. Friend and A. B. Holmes, *J. Phys., Condens. Matter*, **6**, 1379 (1994).
7. G. Horowitz, X. Peng, D. Fichou, F. Garnier, *J. Appl. Phys.*, **67**, 528 (1990).
8. For a review see e.g., A. J. Heeger, *Phil. Trans. R. Soc., London*, **A-314**, 17 (1985).
9. J. Kalinowski and J. Godlewski, *Acta Phys. Pol.*, **A-46**, 523 (1974).
10. P. Dyreklev, O. Inganäs, J. Paloheimo and H. Stubb, *J. Appl. Phys.*, **71**, 2816 (1992).
11. F. Charra, M. P. Lavie, A. Lorin and D. Fichou, *Synth. Met.*, **65**, 13 (1994).
12. D. Fichou, G. Horowitz, B. Xu and F. Garnier, *Synth. Met.*, **39**, 243 (1990).
13. A. R. Brown, K. Pichler, N. C. Greenham, D. C. C. Bradley, R. H. Friend and A.B. Holmes, *Chem. Phys. Lett.*, **210**, 61 (1993).
14. H. Uchiki and T. Kobayashi, *J. Appl. Phys.*, **64**, 2625 (1988).
15. F. Charra and V. H. Tran, to be published (1994).
16. J. M. Nunzi, F. Charra and N. Pfeffer, *J. Phys.*, III France, **3**, 1401 (1993).

Monte Carlo Simulations of Charge Transport through Doped Polymer Thin Films for Second Order Nonlinear Optics

T. A. PASMORE, J. D. HARPER, J. TALBOT and H. S. LACKRITZ*
*School of Chemical Engineering, Purdue University, West Lafayette,
Indiana 47907-1283*

Received 12 January 1994; accepted 24 March 1994

Charge transport through doped polymer thin films has been simulated using Monte Carlo techniques. The simulation is based upon the Gaussian Disorder model and can incorporate differing site configurations. The dependencies on the electric field strength and temperature have been examined and the expected time of flight behavior observed. From comparison of the lattice and pseudo-random site configurations, we find qualitatively identical results, indicating dependence on the average site location as opposed to the individual locations.

INTRODUCTION

Charge transport through molecularly doped polymer thin films has been investigated in order to understand its effects in applications such as electrophotography and photonics.^{1–6} The characterization of charge mobility during electric field poling is crucial for the design and fabrication of second order nonlinear optical devices, since the high poling fields necessary to induce chromophore orientation also induce charge transport. Generally, the carrier mobility is large enough that current through the films is readily observed.⁶

A site-to-site hopping mechanism has been used to describe non-ohmic, dispersive charge transport through a variety of systems.^{7,8} While stochastic modeling can be done using this mechanism, the resulting expressions are often based on mathematical constructs which have little or no physical significance. The continuous time random walk model (CTRW) of Montroll, Scher, and Lax is a classic illustration of this type of theory.^{9,10} The microscopic properties of the carriers are specified by making various assumptions about the nature of the individual inter-site transitions. Because most laboratory experiments, including the conventional time of flight techniques, measure macroscopic quantities, the practical applicability of the CTRW cannot be tested directly. However, by using Monte Carlo techniques to simulate transport through doped polymer systems at the microscopic level, averages can be taken over a large number of iterations and scaled to the macroscopic level for comparison with experimental results. Silver and Cohen constructed the first series of simulations designed using the CTRW model and were able to qualitatively predict both proper pulse shape and temperature dependence of the time of flight current through α -Se.¹¹ Bassler and

coworkers have since refined the simulation approach using the Gaussian Disorder Model (GDM), which gives a better physical representation of hopping functionalities than the CTRW can provide.^{12,13}

In this paper we report on Monte Carlo simulations of charge transport through molecularly doped polymer thin films. We have used the GDM and applied it to novel configurations in order to compare electric field and temperature functionalities. The model and simulation procedures are described in Section 2, while Section 3 contains the results and discussion. Finally, comparisons will be drawn between the original simulation technique of Bassler and our novel approach.

MONTE CARLO SIMULATION METHOD

The discrete nature of the hopping mechanism is easily described in terms of a generalized stochastic master equation,

$$\frac{dp(\vec{x}, t | \vec{x}_0, t_0)}{dt} = \sum_{\vec{x}'} \left[\frac{W(\vec{x} - \vec{x}' | \vec{x}_0) p(\vec{x}', t | \vec{x}_0, t_0)}{W(\vec{x}' - \vec{x} | \vec{x}_0) p(\vec{x}, t | \vec{x}_0, t_0)} - \right] \quad (1)$$

where $W(\vec{x} - \vec{x}' | \vec{x}_0)$ is the probability of making a transition from \vec{x}' to \vec{x} after starting from \vec{x}_0 and $p(\vec{x}, t | \vec{x}_0, t_0)$ is the probability of the occupation of site \vec{x} at time, t .¹⁵ This equation provides not only the basis for the CTRW, but also the microscopic probability balance, where the first term in the summation represents the probability of entering site \vec{x} from site \vec{x}' , and the second term in the summation represents the probability of leaving site \vec{x} for site \vec{x}' . It can be used to predict the transitional probabilities and the resulting discrete time dependence associated with the hopping motion of the carriers.

The simulation model we are using is based on the GDM. From this model the transition probability is defined as,

$$P_{ij} = \frac{v_{ij}}{\sum_{k \neq i} v_{ik}} \quad (2)$$

where P_{ij} is a normalized function of the hopping frequency, v_{ij} , which is defined as,

$$v_{ik} = v_0 \exp(-\gamma |r_{ik}|) \quad (3)$$

when

$$\begin{aligned} \varepsilon_k - \varepsilon_i + eE(x_k - x_i) &\leq 0 \\ v_{ik} &= v_0 \exp(-\gamma |r_{ik}|) \exp\left(\frac{-(\varepsilon_k - \varepsilon_i)}{kT}\right) \exp\left(\frac{-eE(x_k - x_i)}{kT}\right) \end{aligned} \quad (4)$$

when

$$\varepsilon_k - \varepsilon_i + eE(x_k - x_i) > 0$$

where v_0 is a constant, γ is a distance scaling constant, r_{ik} is the inter-site distance, ε_k is the individual site energy, e is the charge of an electron, E is the applied electric field,

and x_k is the distance from the origin in the x direction (parallel to the electric field). If any work is done by the carrier in its hop from site i to site j , there is a penalty added to the probability based exponentially on the work and if the transition is energetically favorable nothing is added. This results in a function that is both energetically and spatially dependent, $v_{ik} \neq v_{ki}$. It is interesting to note that neither (3) nor (4) were derived for polymeric systems. The inter-site distance term, $\exp(-\gamma|r_{ik}|)$, was derived for electronic conduction in amorphous glasses containing transition metal ions at or near absolute zero,¹⁶ while the term which describes the work done by the electric field, $\exp(-eE(x_k - x_i)/kT)$, was found for electronic impurity conduction at low concentrations for semiconductors, again, at or near absolute zero.¹⁷ The effect of the host material on the individual sites is not completely neglected, however. The material dependence on the hopping transport is accounted for by the site energy, given by

$$\varepsilon_k = \frac{eX\sigma}{kT} \quad (5)$$

where X is a Gaussian random number, and σ is the disorder parameter. The disorder parameter is material dependent and represents the influence of the host on the energy levels of the sites. It has been estimated that 0.1 eV corresponds to host polymeric systems.¹³ The physical justification for using this model is that we can relate polymer structural and polarization variations by varying the site energies through the disorder parameter.

The hopping time is defined as the time between the arrival of the carrier on a site and its subsequent arrival at the next site. It is calculated in the simulation by

$$t_{ik} = \left\lceil \frac{\log(Z)}{\sum_{j \neq i} v_{ij}} \right\rceil \quad (6)$$

where Z is a uniform random variable. By summing up all the times over the course of a carrier path, the connection between microscopic and macroscopic time scales can be made, allowing the scaling of individual hops to determine an average carrier mobility.

The simulation operates using a serial hopping algorithm. Once the configuration of sites has been constructed, the carriers are individually injected at the $z = 0$ surface and allowed to hop until they reach the $z = 40$ surface. By allowing just a single carrier at a time to travel through the system, we are able to both better approximate the microscopic conditions at low carrier concentrations and in turn neglect the effects of carrier-carrier (coulomb) interactions. To obtain the macroscopic properties of interest, the process is simply repeated numerous times and the data averaged over all carrier pathways. A more thorough discussion of the simulation procedure can be found elsewhere in the literature.¹³

The configuration of hopping sites is modeled in the GDM formalism as a cubic lattice with uniform, finite spacing. In this system the site energy and electric field are used to obtain directional variations in the transition probabilities. We have also employed a "pseudo-random" configuration to increase the variance across the system without sacrificing computer time or memory. This configuration is fabricated by moving the sites from integer lattice positions to local non integer random positions within the lattice cells. This allows for a more accurate calculation of the transition

probabilities, while simplifying the site addressing and reducing memory and CPU requirements.

RESULTS AND DISCUSSION

The relative current versus time results from the lattice configuration are displayed in Figures 1 and 2. These simulations qualitatively exhibit the conventional time of flight characteristics, a short time plateau followed by a long sloping tail. These features indicate a finite transit time which can be found from the length of the initial plateau, and the presence dispersive transport which is evident from the lengthy approach to the equilibrium value of zero current flow.

The expected temperature and electric field dependencies can also be seen in these figures. Increasing either temperature or field strength in turn causes an increase in carrier mobility. The dependence of the mobility on the electric field may appear to be much greater than that of temperature, but the limited range of applicable temperatures restricts the resulting current response. Although changing the temperature of the system effects both the effective field and the width of the Gaussian distribution, the large range of the electric field strength can overwhelm these dependencies producing extreme changes in the slope of the system, as evidenced here.

In Figures 3 and 4 the pseudo-random or off lattice results are plotted as a function of temperature and electric field strength as done in the previous two figures. Both

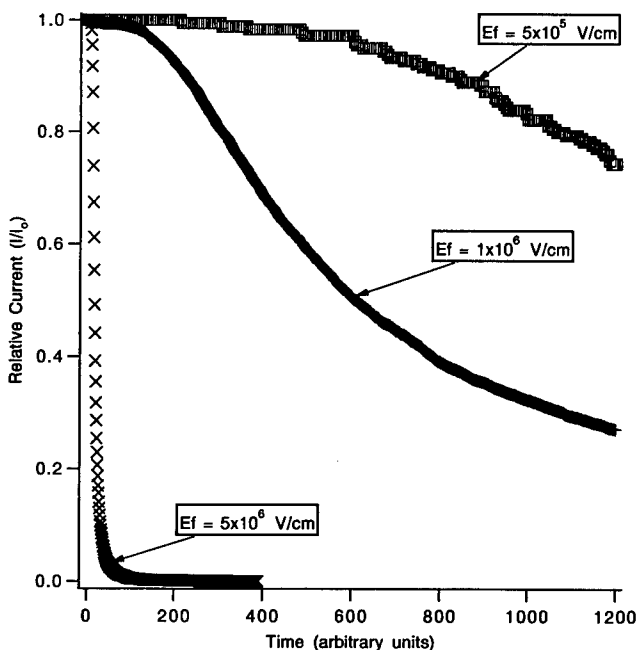


FIGURE 1 Plot of current vs. time for the lattice configuration at 298 K.

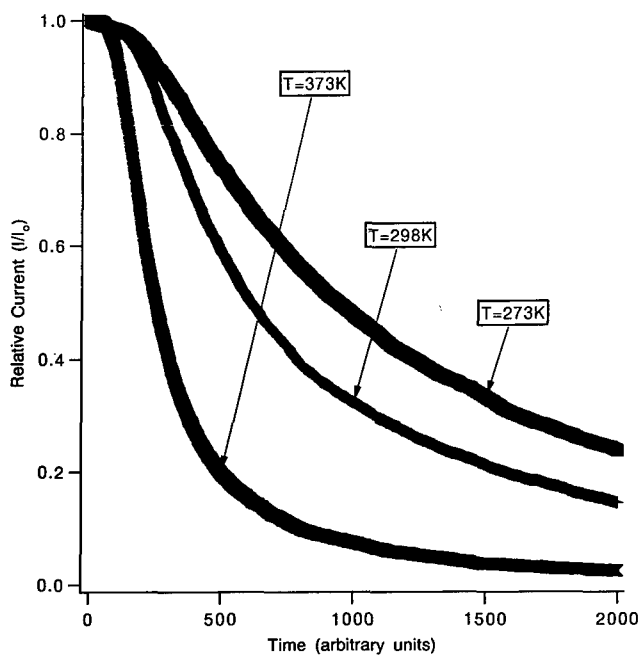


FIGURE 2 Plot of current vs. time for the lattice configuration at 1×10^6 V/cm.

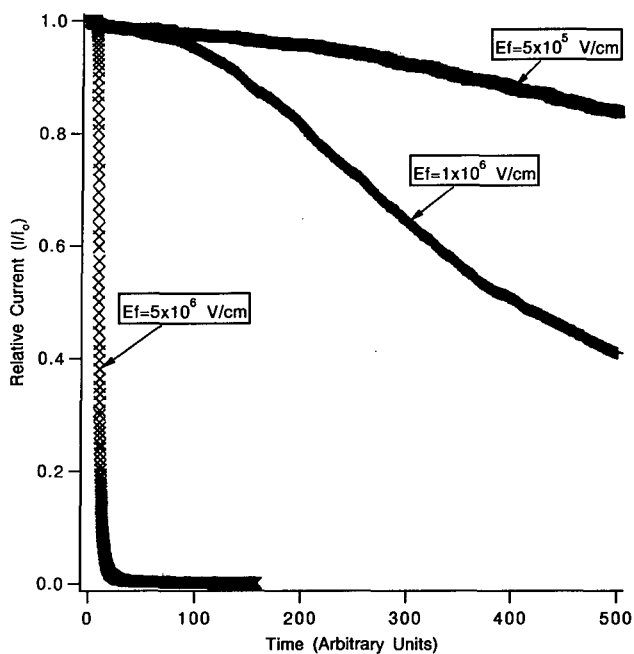


FIGURE 3 Plot of current vs. time for the pseudo-random configuration at 298 K.

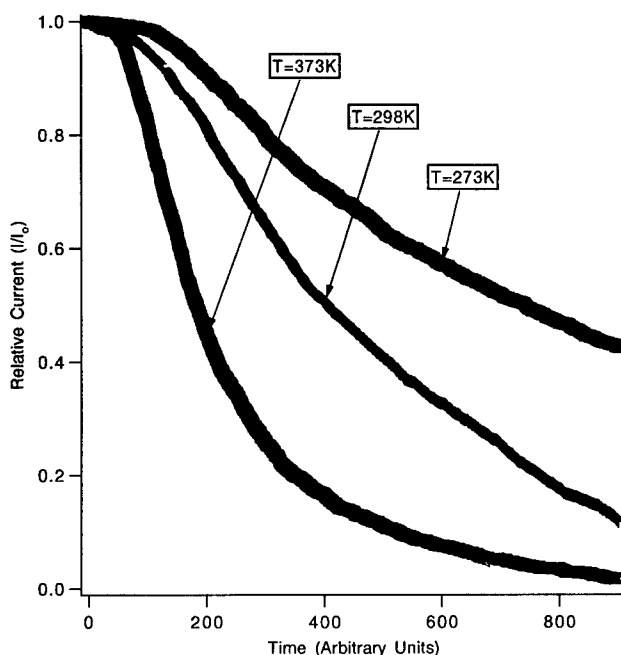


FIGURE 4 Plot of current vs. time for the pseudo-random configuration at 1×10^6 V/cm.

dependencies show very similar behavior to the results from the lattice configuration. This indicates that the macroscopic scaling of the current with respect to each configuration is independent of the configuration itself. Since the sites of the pseudo-random configuration are confined within the lattice cubes, long range order is maintained throughout the system. Thus, averaging over the entire system produces a distribution with a mean centered in the lattice cubes. This in turn illustrates that the current is dependent on the macroscopic average position, instead of the individual microscopic locations. The positional variations average out over the course of numerous carrier pathways. Under these conditions the only quantitative difference is in the time scaling between the two configurations. This, most likely, is the result of the microscopic site variations.

CONCLUSIONS

In conclusion, we have shown that the simulation results exhibit time of flight characteristics and are qualitatively independent of the choice of lattice or pseudo-random configuration, due to the dependence on the average site position. These results, however, can only be used within the constraints imposed by the assumptions of the model. While this model gives qualitatively predictive results, it lacks the quantitative accuracy necessary for almost all poling applications. The search for a better model has lead to the creation of the Law of Corresponding States model.¹⁸ It is designed to

take the selection of the host material into account. Our goal, currently, is to construct a model that will give qualitative results specifically for doped polymer under general poling conditions.

ACKNOWLEDGEMENTS

This investigation was supported by grants from the National Science Foundation and the Air Force Office of Scientific Research.

REFERENCES

1. M. A. Abkowitz, *Phil. Mag. B*, **65**, 817 (1992).
2. P. M. Borsenberger and H. Bassler, *J. Imaging Sci.*, **35**, 79 (1991).
3. W. Kohler, D. R. Robello, P. T. Dao, C. S. Willand and D. J. Williams, *J. Chem. Phys.*, **93**, 9157 (1990).
4. A. Peled, L. B. Schein and D. Glatz, *Phys. Rev. B*, **41**, 10835 (1990).
5. A. S. DeReggi and M. G. Broadhurst, *Ferroelectrics*, **73**, 351 (1987).
6. J. G. Simmons, G. S. Nadkarni and M. C. Lancaster, *J. Appl. Phys.*, **41**, 538 (1970).
7. J. A. Giacometti and O. N. Oliveira, *IEEE Trans. Elec. Insul.*, **27**, 924 (1992).
8. G. Pfister and H. Scher, *Adv. Phys.*, **27**, 747 (1978).
9. M. Pollak, *Phil. Mag. B*, **36**, 1157 (1977).
10. H. Scher and E. Montroll, *Phys. Rev. B*, **12**, 2455 (1975).
11. H. Scher and M. Lax, *Phys. Rev. B*, **7**, 4491 (1973); H. Scher and M. Lax, *Phys. Rev. B*, **7**, 4502 (1973).
12. M. Silver and L. Cohen, *Phys. Rev. B*, **15**, 3276 (1977).
13. G. Schonherr, H. Bassler and M. Silver, *Phil. Mag. B*, **44**, 47 (1981).
14. H. Bassler, *Phys. Stat. Sol. (b)*, **175**, 15 (1993).
15. G. F. Leal Ferreira, *Phys. Rev. B*, **16**, 4719 (1977).
16. N. F. Mott, *J. Non-Cryst. Solids*, **1**, 1 (1968).
17. A. Miller and E. Abrahams, *Phys. Rev.*, **120**, 745 (1960).
18. R. H. Young, *Phil. Mag. B*, **69**, 577 (1994).

Transport Dynamics of Singlet Guest Excitations in High-Concentration *p*-Terphenyl Crystals

ARND KRÜGER¹, CAROLA KRYSCI^{1*}, DANKWARD SCHMID¹ and
H. PETER TROMMSDORFF²

¹*Lehrstuhl für Festkörperspektroskopie (IPkM), Heinrich-Heine-Universität, D-40225 Düsseldorf, FRG*

²*Laboratoire de Spectrométrie Physique, Université Joseph-Fourier Grenoble I, B. P. 87, F-38402 St. Martin d'Hères, France*

Received 17 February 1994; accepted 15 March 1994

Picosecond transient grating experiments were used to examine singlet excitation transfer among pentacene guests in *p*-terphenyl crystals as a function of temperature and guest concentration. Transient population gratings were created by exciting the origin of the $S_1 \leftarrow S_0$ transition of pentacene in the O_4 site of the triclinic *p*-terphenyl crystal and were probed by Bragg-diffracting a time-delayed pulse of the same frequency. The onset of delocalization of the singlet excitations with increasing guest concentration is manifest in fast transient grating decays, which becomes slower with rising temperature. In the range of 8.5 to 20 μm , the decay is independent of the grating constant. These observations are explained by the existence of singlet excitations delocalized over resonant O_4 sites and trapping by the other lower-lying guest sites of pentacene.

Keywords: *picosecond transient grating spectroscopy, resonant energy transfer, mixed molecular crystals*

INTRODUCTION

Energy Transfer is an important part of the collective response of an ensemble of molecules to optical excitation. For excited singlet states the transition dipole-transition dipole interaction results in excitation energy transfer between resonant molecules.^{1–7} The dipole-dipole interaction is also responsible for the formation of extended states such as, in pure crystals, exciton states with well defined wave vectors.^{4–6} For identical chromophores dispersed at random in a host medium, the description becomes more complex and can only be approached by statistical theories and methods. In different host environments, the excited singlet state (S_1) energies of identical molecules are not strictly equal but spread a distribution, ΔE , of values. In mixed crystals, typical inhomogeneous broadenings are in the range of $\Delta E \approx 1 \text{ cm}^{-1}$ for a given crystallographic site, while excitation energies of inequivalent sites may differ by as much as several 100 cm^{-1} .^{8,9} These latter values are also typical for inhomogeneous broadenings in disordered solids (glasses).^{10,11} The dipole-dipole

* Correspondence to: Dr. Carola Krysci Lehrstuhl für Festkörperspektroskopie (IPkM) Heinrich-Heine-Universität, D-40225 Düsseldorf, FRG Tel: 49-2113114813, Fax: 49-2131667287 email: CKRYSCI@ze8.rz.uni-duesseldorf.de

interaction energies, V , between the chromophores are also distributed as are the intermolecular distances and orientations. The average value of the interaction energy can be changed by adjusting the concentration of guest molecules and thereby the average distance between them. Another important parameter governing the energy transport is the temperature, since the loss of coherence by thermal fluctuations limits the development of delocalized states, so that the description of the quantum states, involved in the transport process, is changed. Both fluctuations of the excitation energy and fluctuations of the dipole-dipole interaction (due to the relative motions of molecules, principally changes of relative orientation) contribute to this dephasing of the excited singlet states. The nature of the excitation energy transport is thus determined by the relative magnitude of the average values of the dipole-dipole interaction, V , its distribution, ΔV , the inhomogeneous distribution of excitation energies, ΔE , as well as the rate of dephasing, $1/T_2$. When V dominates ΔV , ΔE , and $\hbar T_2$, the excitation energy transport is coherent, while it becomes an incoherent hopping process, when the inverse is true, and the excited singlet states are essentially localized. In the intermediate region (reached by changing the guest concentration c_G , i.e., V , or the temperature and thereby T_2) the behavior is more complex and can change from coherent transfer at short times to incoherent hopping at longer times.

The proper understanding of excitation energy transport in molecular crystals is not only of academic interest, but is also important in many practical applications (e.g., sensitization processes, phosphors, laser gain media, etc.) as well as in biological systems (e.g., light harvesting antenna). In addition the nonlinear optical response (NLO) of coherent extended states has in recent years attracted much interest (e.g., in pure crystals, aggregates, or clusters), since the collective response is expected to enhance the NLO response. In fact, such potential enhancement will occur only near resonance and will vanish at higher temperatures, when dephasing dominates the excitation exchange in a very analogous way as transport mechanisms change from coherent to incoherent.

In a transient grating experiment, two time-coincident and spatially overlapping excitation pulses generate, within a sample, a pattern of interference fringes. Light absorption by resonant guest states creates a grating of excited state populations and corresponding refractive index changes. The temporal evolution of this grating is measured by monitoring the intensity of a Bragg-diffracted probe pulse as a function of delay time. In the absence of guest-guest dipolar couplings (i.e., at low guest concentrations), the lifetime of the excited singlet state, e.g., the fluorescence lifetime τ_F , determines the decay rate of the transient population grating. In sufficiently highly doped crystals, guest-to-guest energy transfer may destroy the grating pattern by spatially redistributing the population of excitations over several resonant guest sites and by making more efficient the trapping of the excitation by lower-energy guest sites. In this case, therefore, the decay of the transient grating is determined by both, the excited-state lifetime and the transport dynamics of the excitation energy.

In this contribution we present and discuss studies of singlet excitation energy transport in the crystalline model system of pentacene guests dissolved in single crystal matrices of *p*-terphenyl, where the excitation transport is monitored as a function of guest concentration and temperature via transient grating techniques. First indications of resonant energy transfer between the pentacene guests in dilute *p*-terphenyl and

naphthalene crystals in the range 10^{-7} – 10^{-5} mol/mol were obtained from photon echo experiments.^{12–14} In our transient grating experiments on pentacene guests in *p*-terphenyl crystals at 10^{-5} mol/mol, we could not verify a guest concentration effect on the time evolution of the transient grating. Instead in the high-concentration regime from 3×10^{-4} to 3×10^{-3} mol/mol, the transient grating decays with a significantly faster decay than twice the rate of fluorescence decay of non-interacting pentacene guests in highly dilute samples. The transient grating decay rate was found to decrease with rising temperature, but is independent of the grating constant in the range of 8.5 to 20 μm .

EXPERIMENTAL

Transient grating experiments were performed using 4 ps-pulses at a repetition rate of 45 Hz with pulse energies between 0.3 and 1 μJ . The pulses were produced by a mode-locked argon-ion laser (Coherent, INNOVA 20) pumping synchronously a rhodamine 6G dye laser (Coherent, CR 599-04) equipped with a cavity dumper (Coherent, CR 7200) and were amplified in a two-stage optical amplifier (coumarin 153 in methanol) pumped by an excimer laser (Lambda Physik, EMG 101). The output beam was divided by beam splitters into two excitation beams of equal intensity (45%) used to generate the transient grating and a weak probe beam (4%). The excitation beams were crossed in the sample at intersection angles of 1.7 or 3.9° resulting in fringe spacings (i.e., the grating constant) of 20 and 8.5 μm . The intensities of first-order Bragg diffracted signal and of the transmitted reference signal were detected by two phototubes (Hamamatsu, R1328U-03) and a fast-gated boxcar averager (Stanford Research System, SR250, with a fast sampler module SR255). A personal computer (IBM compatible AT-286) was used to control the experiment and to record and to process the data.¹⁵

p-Terphenyl (Merck, scintillation grade) was purified by extensive zone-refining (over 180 passes). Pentacene (Aldrich, 99.8%) was used as supplied. Mixed single crystals of *p*-terphenyl:pentacene at high guest concentrations (3×10^{-4} – 3×10^{-3} mol/mol) were grown from the melt using standard Bridgman techniques. Guest concentration was determined by recording absorption spectra at room temperature and calibrating these against the room-temperature spectrum of a rather weakly doped crystal of known concentration around 10^{-5} mol/mol. The guest concentration of the diluted sample was calculated, with an uncertainty of $\pm 25\%$, from the peak optical density, the FWHM of the absorption line, the sample thickness and using the literature value of the transition dipole moment of pentacene.¹⁶ Crystal platelets with a thickness ranging from 20 to 75 μm and extinctions between 1.3 and 2.5 were obtained by cleavage parallel to the crystallographic *ab* plane and were mounted in a helium cryostat (Cryovac, Konti-IT) providing temperatures variable between 2 and 300 K.

EXPERIMENTAL RESULTS AND DISCUSSION

All transient gratings were created by exciting the electronic origin or the first vibronic transition of pentacene in the O_4 site of *p*-terphenyl, i.e., at 17065 cm^{-1} and

17332 cm^{-1} . The grating decay was probed at the wavelength of excitation energy. In comparison with the lower-energy O_1 and O_2 sites the fluorescence lifetime of pentacene in O_4 is not only shorter by 60% ($\tau_F(O_4) = 9.4\text{ ns}$) but also independent of temperature between 2 and 100 K.¹⁶ In order to evidence guest-to-guest energy transfer, the time dependence of the transient grating was measured as a function of the guest concentration c_G ranging from $3 \times 10^{-4}\text{ mol/mol}$ to the highest accessible concentration of about $3 \times 10^{-3}\text{ mol/mol}$. To ensure that guest-to-guest energy transfer is responsible for the concentration effect, transient grating decays created under different optical density conditions in the same sample were compared. The same transient grating decay was observed for wavelengths corresponding to the first vibronic transition and to the pure electronic origin of O_4 , even though the optical density is higher by a factor of six in the latter case.¹⁵

Figure 1 presents transient grating decay curves recorded for various excitation pulse energies in a sample with a guest concentration $c_G = 5.3 \times 10^{-4}\text{ mol/mol}$ at 2 K. The decay curves show a fast initial drop of the diffraction efficiency followed by a much slower decay. When the power of the excitation pulse is increased from $W_{\text{exc}} = 0.35\text{ }\mu\text{J}$ to $W_{\text{exc}} = 1\text{ }\mu\text{J}$, the amplitude and the slope of the fast component become larger, while no significant changes are observed for the slow component of the decay curve. Clearly,

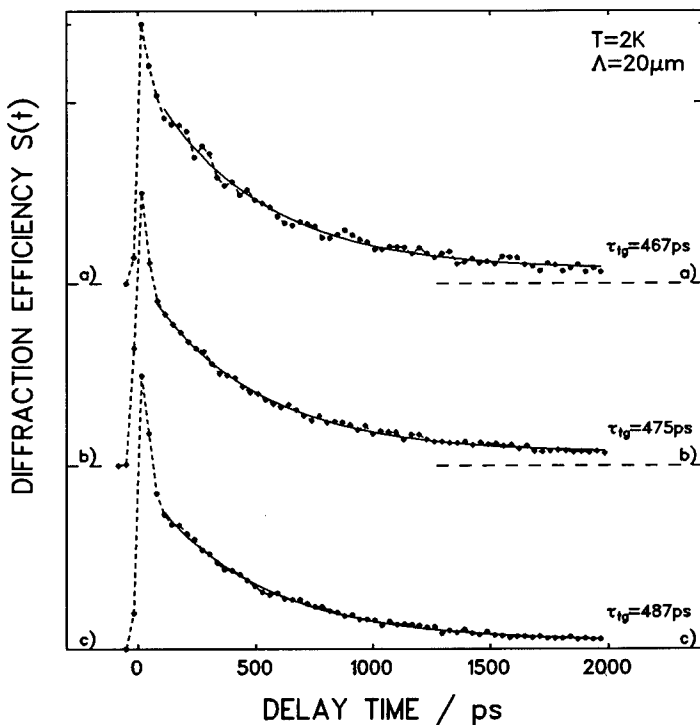


FIGURE 1 Transient grating decay curves obtained from excitation into the pure electronic origin of O_4 ($T = 2\text{ K}$, $c_G = 1.2 \times 10^{-3}\text{ mol/mol}$, $\Lambda = 20\text{ }\mu\text{m}$) for different energies of the excitation pulse: $W_{\text{exc}} = 0.35\text{ }\mu\text{J}$ (top), $W_{\text{exc}} = 0.5\text{ }\mu\text{J}$ (middle) $W_{\text{exc}} = 1\text{ }\mu\text{J}$ (bottom).

nonlinear processes such as superfluorescence and singlet-singlet annihilation contribute to the fast decay. Since these phenomena are not the subject of this paper, we have limited the analysis and discussion of the experimental data to the dominant slow component of the transient grating decay curves. As demonstrated in Figure 1, the slow decay can be well represented by a single exponential (solid line) with decay times of $\tau_{ig} = 477 \pm 10$ ps. The experimental data sets shown in Figure 2 are typical for the dramatic differences observed in the transient grating decay as a function of guest concentration. All the decay times, obtained from the fit to a straight line (full line), are much shorter than half the fluorescence lifetime ($\tau_F/2 = 4.7 \text{ ns}^{16}$) and decrease considerably with rising guest concentration from $\tau_{ig} = 1002$ ps at $c_G = 4.9 \times 10^{-4}$ mol/mol (a) to $\tau_{ig} = 362$ ps at $c_G = 2.1 \times 10^{-3}$ mol/mol (d). This behavior agrees with the qualitative expectation that the increase of dipole-dipole interactions due to shorter guest-guest distances at higher concentrations favors the delocalization of excitation energy (e.g., efficient guest-to-guest energy transfer), thereby decreasing the lifetime of the grating. The quantitative investigation of these changes as a function of temperature and grating constant Λ , in addition to concentration, provides significant insight in the nature and the dynamics of the excitation energy transfer process. The observed independence of the grating decay dynamics on the grating constant decay for Λ between 8.5 and $20 \mu\text{m}$ confines the guest-to-guest energy transfer to a distance scale smaller than microns. When, on the other hand, the temperature increases from 2 to

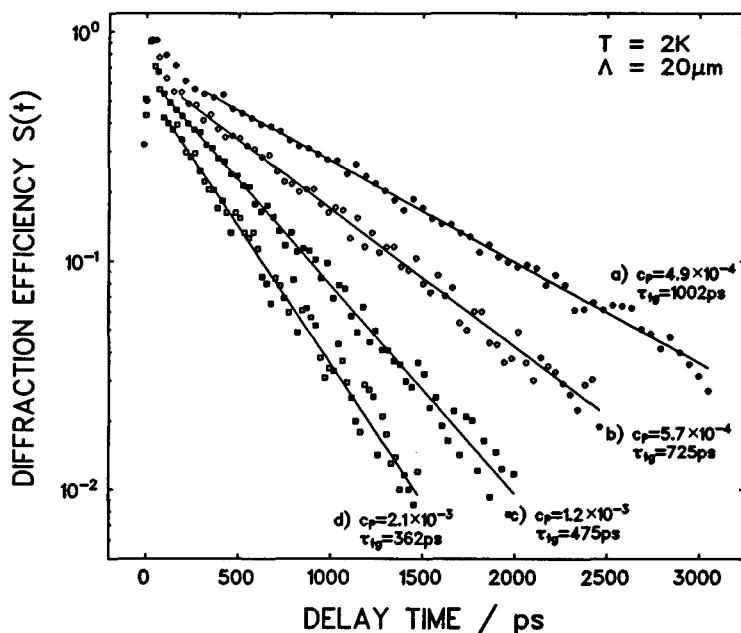


FIGURE 2 Transient grating decays recorded subsequent to excitation into the pure electronic origin of O_4 ($T = 2 \text{ K}$, $\Lambda = 20 \mu\text{m}$) for different guest concentrations: (a) $c_G = 4.9 \times 10^{-4}$ mol/mol with $\tau_{ig} = 1002$ ps, (b) $c_G = 5.7 \times 10^{-4}$ mol/mol with $\tau_{ig} = 725$ ps, (c) $c_G = 1.2 \times 10^{-3}$ mol/mol with $\tau_{ig} = 475$ ps, (d) $c_G = 2.1 \times 10^{-3}$ mol/mol with $\tau_{ig} = 362$ ps; the intensity scale is logarithmic.

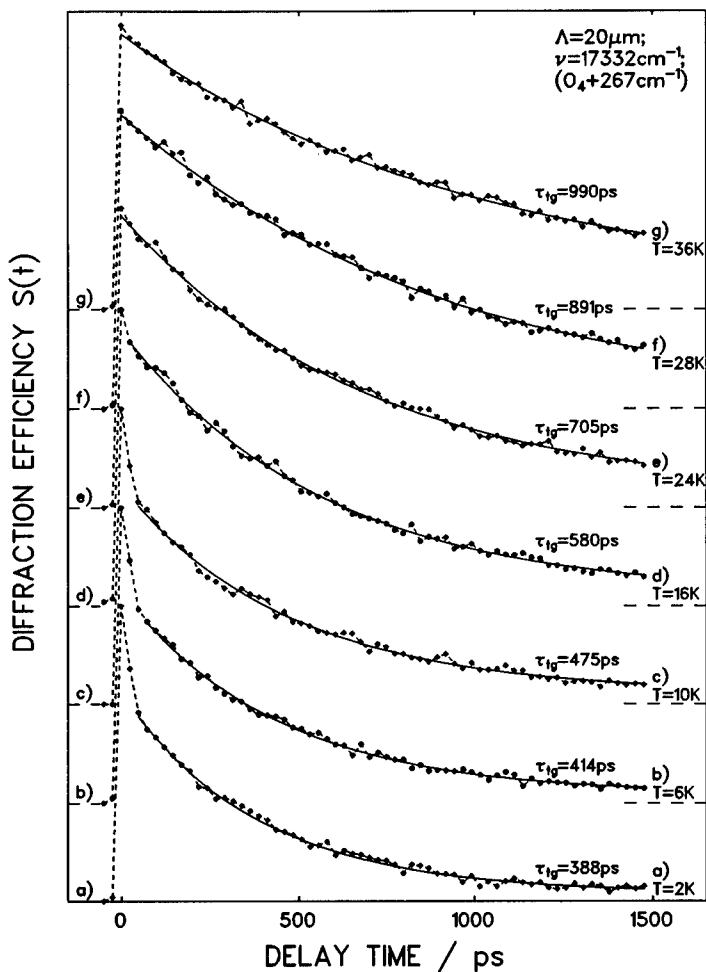


FIGURE 3 Transient grating decay curves plotted as a function of temperature varied from 2 to 36 K for $c_G = 2.1 \times 10^{-3}$ mol/mol and $\Lambda = 20 \mu\text{m}$; the transient gratings were excited into the first vibronic transition of O_4 .

40 K, grating decay time τ_{ig} grows dramatically as illustrated in Figure 3 for a sample of concentration $c_G = 2.1 \times 10^{-3}$ mol/mol. The experimental data and exponential fits are indicated by dots and solid lines, respectively. The drastic increase of τ_{ig} from 388 ps at 2 K to 990 ps at 36 K is certainly a consequence of temperature-inhibited dipole-dipole interactions between the pentacene guests, which implies that the singlet excitation energy transfer occurs between degenerate O_4 sites. Figure 4 represents the dependence of the grating decay rate, k_{ig} , on concentration at 2 K (circles), 10 K (squares) and 20 K (stars). At low concentrations k_{ig} reaches the theoretical limit for infinitely dilute samples of twice the fluorescence rate $1/\tau_F$ (i.e., $k_{ig} = 2/\tau_F$). The increase as a function of guest concentration is nearly linear as illustrated by the solid lines in Figure 4 and the slope of these lines decreases with rising temperature. The linear

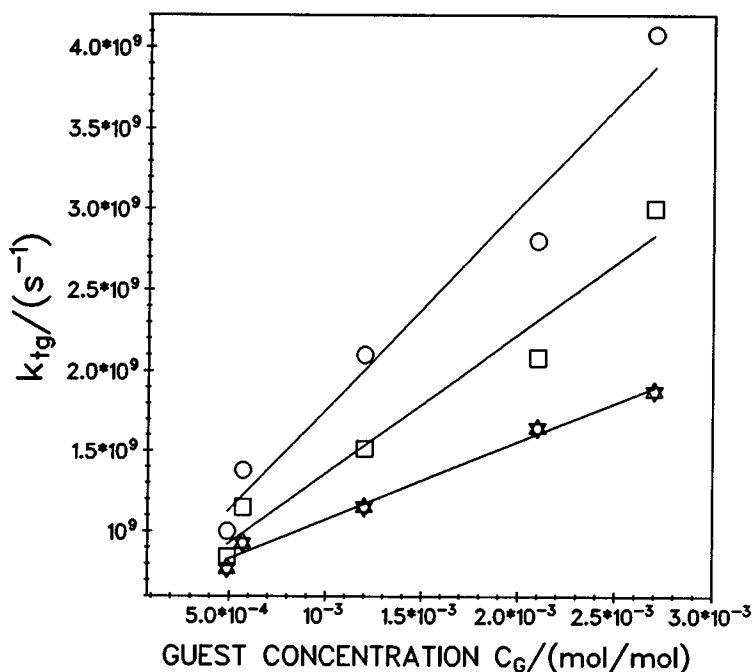


FIGURE 4 Transient grating decay rate k_{tg} as a function of the guest concentration c_G obtained from data recorded after excitation into the pure electronic origin of O_4 at 2 K (circles), 10 K (squares) and 20 K (stars); the solid lines represents the a linear fit to the experimental data.

dependence on guest concentration is interesting, since naive expectations would predict that energy transfer is proportional to the square of the relevant coupling matrix element. The $1/r^3$ distance scaling of both dipole-dipole coupling and guest concentration suggests that the rate of energy transfer depends on the square of the concentration. Fluctuations of the local guest concentrations combined with concomitant correlations of the site energies (see below) might account for the observed behavior, but a quantitative analysis of these effects will be presented elsewhere. The temperature dependence of k_{tg} , for three different guest concentrations, is plotted in Figure 5. These temperature dependences were found to be well described by $k_{tg} = 2(k_F + k_{ET}^\circ/T^{1/2})$, assuming that the guest-to-guest energy transfer is characterized by the rate $k_{ET} = k_{ET}^\circ/T^{1/2}$. The best fits to the experimental data in Figure 5 (solid lines) were obtained by adjusting the value of the constant k_{ET}° : $k_{ET}^\circ = 2.1 \cdot 10^9 \text{ s}^{-1} \text{ K}^{1/2}$ ($c_G = 4.9 \times 10^{-4} \text{ mol/mol}$), $k_{ET}^\circ = 4.1 \cdot 10^9 \text{ s}^{-1} \text{ K}^{1/2}$ ($c_G = 1.2 \times 10^{-3} \text{ mol/mol}$), $k_{ET}^\circ = 7.5 \cdot 10^9 \text{ s}^{-1} \text{ K}^{1/2}$ ($c_G = 2.7 \times 10^{-3} \text{ mol/mol}$). The temperature dependence of $k_{ET} \sim k_{ET}^\circ/T^{1/2}$, as being characteristic for scatterings of coherent excitons by acoustic phonons,¹⁷ suggests that the observed excitation energy transfer occurs among degenerate O_4 sites and exhibits quasi-excitonic dynamics. At temperatures below 20 K inhomogeneous broadening dominates the linewidth of 0-0 transitions in the spectra of high-concentration samples and ΔE exceeds dipolar coupling for guest-to-guest distances of over about 10 Å. We are thus forced to assume that the crystal consists of

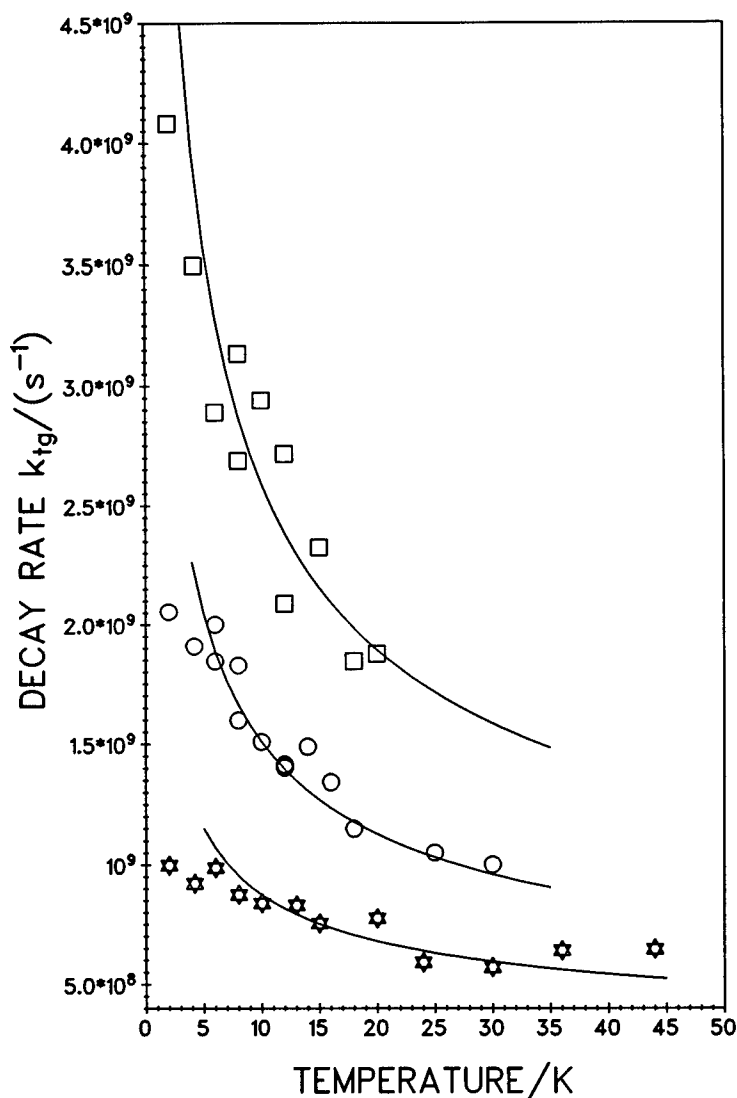


FIGURE 5 The transient grating decay rate k_{tg} as a function of temperature for different guest concentrations: $c_G = 4.9 \times 10^{-4}$ mol/mol (stars), $c_G = 1.2 \times 10^{-3}$ mol/mol (circles) and $c_G = 2.7 \times 10^{-3}$ mol/mol (squares); the experimental data were fitted to $k_{tg} = 2(k_F + k_{ET}/T^{1/2})$ (solid lines).

clusters of guest molecules with local concentrations exceeding the average value of about 1 pentacene/(50 Å)³ in the highest-concentration samples and that some correlation in the site energies exists within these clusters. It is the energy transfer within these clusters that is expressed in the observed response of the samples. The decay of the grating is then entirely determined by population decay, which naturally explains the absence of any dependence on the grating constant. Depletion of excited-state

population in the O_4 sites is due to excitation transfer to lower-energy guest sites (O_3, O_2, O_1). Independent support for this picture comes from measurements of *cw* excited fluorescence spectra, where the emission intensities from the lower-energy sites in high-concentration samples by far exceed the corresponding intensities measured in low-concentration samples under identical excitation conditions.^{15,18}

Accounting for both temperature and concentration dependence, the experimental decay curves are rationalized by invoking, within clusters, efficient delocalization of the excitation energy over quasi-resonant O_4 sites (i.e., quasi-excitonic transport) and less efficient off-resonant transfer to lower-energy guest sites (O_1, O_2, O_3). This implies that the transport topology of singlet excitation energy is determined by the local distributions of pentacene guests in the crystal. A singlet excitation will visit other molecules in a given cluster at very high frequency, while energy transfer between clusters is an unlikely event. In terms of this argumentations, resonant energy transport in pentacene doped *p*-terphenyl crystals will be limited to distances much smaller than microns and involve only a small fraction of guest sites before the excitation becomes trapped.

ACKNOWLEDGEMENTS

This research has been supported by the Deutsche Forschungsgemeinschaft (Az.: Schm 270/7-1,2,3,4,5) and by Der Ministerium für Wissenschaft und Forschung des Landes Nordrhein-Westfalen (Az.IV A 5-106 008 92), and by grants under the EC SCIENCE (SC1*-CT92-0767) and the French-German PROCOPE (Az.: 92240) programs. We would like to thank Prof. Dr. V. M. Agranovich for many valuable and stimulating discussions.

REFERENCES

1. H. C. Wolf, *Adv. Atom. Mol. Physics*, **3**, 119 (1967).
2. R. C. Powell and Z. G. Soos, *J. Lumin.*, **11**, 1 (1975).
3. R. Silbey, *Ann. Rev. Phys. Chem.*, **27**, 203 (1976).
4. V. M. Kenkre, *Springer Tracts in Modern Physics*, Vol. **94**, (Springer-Verlag, Berlin, 1982).
5. V. M. Agranovich and M. D. Galanin, *Electronic Excitation Energy Transfer in Condensed Matter* (North Holland, Amsterdam, 1982).
6. R. Silbey, *Spectroscopy and Excitation Dynamics of Condensed Molecular Systems*, Vol. **2**, eds. V. M. Agranovich and R. M. Hochstrasser p. 1 (North Holland, Amsterdam, 1983).
7. R. Kopelman, *Spectroscopy and Excitation Dynamics of Condensed Molecular Systems*, Vol. **2**, eds. V. M. Agranovich and R. M. Hochstrasser p. 139 (North Holland, Amsterdam, 1983).
8. M. D. Fayer, *Ann. Rev. Phys. Chem.*, **33**, 663 (1982).
9. D. A. Wiersma, *Adv. Chem. Phys.*, **47**, 421 (1981).
10. J. Fünfschilling, I. Zschokke-Gränacher and D. F. Williams, *J. Chem. Phys.*, **75**, 3669 (1981).
11. J. Friedrich and D. Haarer, *Angew. Chem. Int. Ed.*, **23**, 113 (1984).
12. J. B. W. Morsink, B. Kruizinga and D. A. Wiersma, *Chem. Phys. Lett.*, **76**, 218 (1980).
13. Y. Yoshikuni, A. Nakamura, S. Shionoya and M. Aihara, *J. Phys. Soc. Jpn.*, **51**, 2604 (1982).
14. R. J. Gulotty, C. A. Walsh, F. G. Patterson, W. L. Wilson and M. D. Fayer, *Chem. Phys. Lett.*, **125**, 507 (1986).
15. A. Krüger, PhD thesis, Heinrich-Heine-Universität, Düsseldorf, (1994).
16. H. de Vries and D. A. Wiersma, *J. Chem. Phys.*, **70**, 5807 (1979).
17. V. M. Agranovich and Y. V. Konobeev, *Sov. Phys. Sol. State*, **5**, 999 (1963).
18. A. Krüger, C. Kryschi and H. P. Trommsdorff, *y. Phys. Chem.*, in print.

Light Induced Conductivity in N-Methyl-1,10-Phenantroline-TCNQ RIS

Z. STRYŁA, J. KOWALAK, M. LUDWICZAK, J. J. LANGER*
and A. RAJCHEL*

*Adam Mickiewicz University, Institute of Physics, Quantum Electronics Laboratory, *Organic Semiconductor Laboratory, Faculty of Chemistry, Grunwaldzka 6, 60-780 Poznań, Poland*

Received 31 January 1994; accepted March 1994

INTRODUCTION

9,10-Phenantroline and its N-methyl derivative are aromatic donors of planar structure and large π -electron system which are able to interact with TCNQ (a well known strong electron acceptor molecule) forming a charge-transfer (CT) complex or a radical-ion salt (RIS), respectively [Fig. 1]. Both the complex and the salt have actually been obtained in our Laboratory with the aid of a commonly known synthetic procedure.^{1,2} 1,10-NMP-TCNQ₂ is a highly-conducting material ($\sigma = 75$ S/cm along the main crystal axis) crystallizing as needles of high electrical and optical anisotropy.

The crystals are extremely long (more than 10 mm) and thin (usually 10^{-2} – 10^{-1} mm), branched and knotted. A careful crystallization gave us well shaped needles suitable for our studies (see picture).

The ESR spectrum measured at X band shows a strong singlet line ($g = 2.0029$) which corresponds to these usually found in the case of TCNQ radical-ion salts.

The FTIR spectrum of 1,10-NMP-TCNQ₂ is typical for highly conducting TCNQ based RIS: it consists of a strong and very broad absorption with maximum around 4000 cm^{-1} (CT₂ band which corresponds to the electron transfer between TCNQ⁻ and TCNQ⁰) and broad absorption bands at lower wave numbers (e.g., about 1350 cm^{-1} and 1100 cm^{-1}) assigned to highly symmetrical vibration modes activated due to electron-phonon interactions. Other intramolecular vibration modes are much weaker or can be observed as so called Evans holes (e.g., C=N stretching at 2215 cm^{-1}).

EXPERIMENTAL SETUP

The sample was placed on ceramic substrate, with lithographically deposited gold electrodes, and sealed to the electrodes with silver-base conductive glue [Fig. 2]. In some cases the gold electrodes were vacuum deposited on the ends of the crystal. The electrodes on the substrate were soldered to the BNC connectors in a brass block

N-methyl-1,10-phenantroline
7,7,8,8-tetracyanoquinodimethane

Radical-Ion Salt

1,10-NMP - TCNQ₂

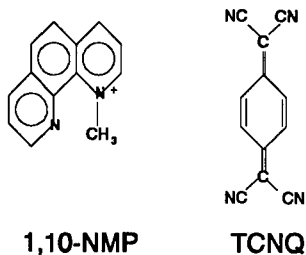


FIGURE 1

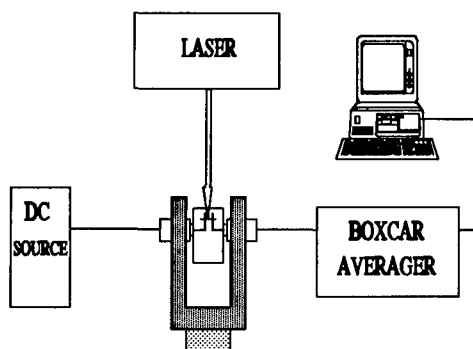


FIGURE 2 Experimental setup.

providing reliable electrical contacts and easy mechanical mounting to the 3-way stage. The 1,10-NMP-TCNQ₂ crystals are very sensitive to mechanical and electrical destruction, so this stable ceramic substrate provided the necessary protection. The distance between the electrodes was about 3 mm.

The nitrogen laser light was focused using the cylindric lens of 5 cm focal length whereas a spherical lens of the same focal length was used to focus the dye laser beam. The energy of the nitrogen laser pulse applied to the crystal was about 200 μ J and that of the dye laser about 40 μ J. The pulse repetition rate was 20 Hz. Adjustment was provided by moving the sample on the 3-way stage. It was very important to set the sample properly relative to the focus of the lens to achieve uniform illumination of the sample and to avoid its overheating or even destruction.

The signals obtained were registered by the BCI-280 boxcar integrator coupled to the computer data acquisition system. The sample was dc-biased using the voltage of 2–10 V.

RESULTS

The transient response [Fig. 3 & Fig. 4] of the crystal has been examined for laser wavelength range 337–760 nm (photon energy 3.65–1.63 eV) which covers the TCNQ absorption band, charge transfer band and the gap between them as well. No evident dependence of the measured signals on the excitation wavelength was found. It suggests that the observed effect is not purely of the photoelectric nature.

A characteristic property of 1,10-NMP-TCNQ₂ crystals is their high natural electric conductivity. The resistance of the sample was typically of 10 kΩ. Applying the formula given by Margulis and Laval [2] to the case of a conducting crystal one obtains that the current switched into a load of impedance Z_0 is:

$$i(t) = \frac{V_{APP}}{Z_0 + \left(\frac{1}{Z_s} + \frac{1}{Z_i \exp(t/\tau)} \right)^{-1}}$$

where

- V_{APP} is the dc bias,
- Z_s static impedance of the sample,
- Z_i the change of the impedance of the crystal immediately after the laser pulse,
- τ the decay constant of the light-generated electric carriers. It can be seen that for a certain combination of the impedances and decay constant the current can show the effect of saturation.

Such a saturation [Fig. 5] occurred in our experiment after exposing the crystal to prolonged illumination. Simultaneously the decay constant increased during the

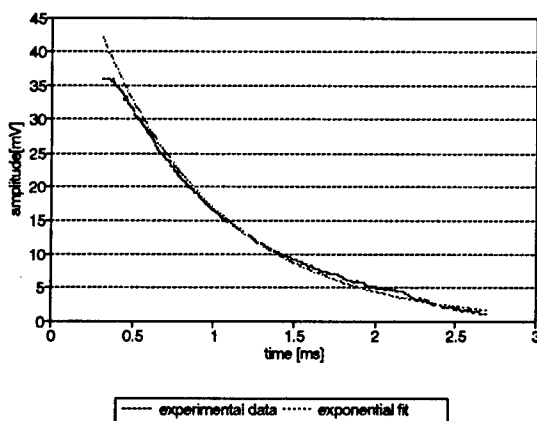


FIGURE 3

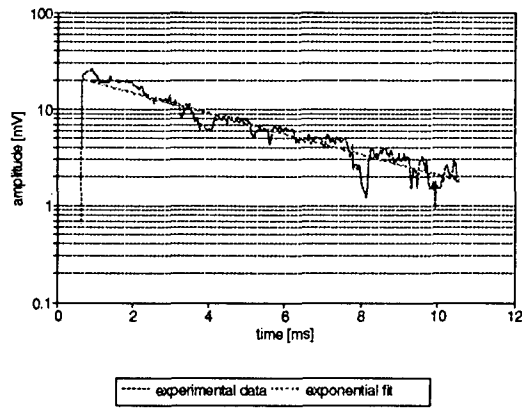


FIGURE 4

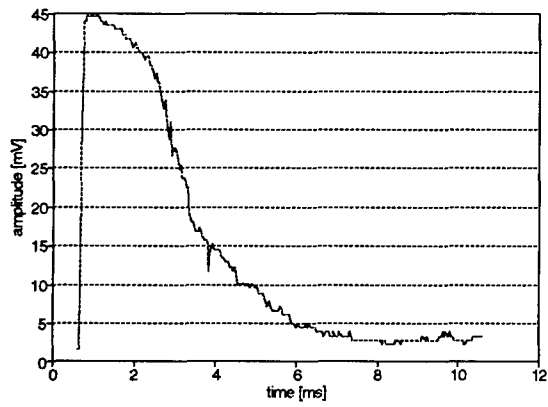


FIGURE 5

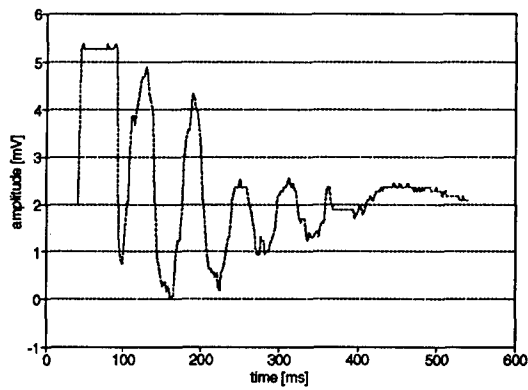


FIGURE 6

experiment from the value of 7.5 ms up to 4.0 ms. Such behaviour suggests that the structure of the sample changes upon exposing to several thousands of laser pulses. In the critical case, just before the destruction of the crystal, the electrical response shows [Fig. 6] a "strange" oscillatory character. It can be explained by acoustic vibration of the crystal just before destruction.

CONCLUSION

Examination of the influence of photon energy on transient response of the sample leads to the conclusion that the observed signals are not of purely photoelectric character. One of the possible reasons can be thermal generation of charge carriers.

The obtained data show the effect of ageing of the sample during the experiment. The decay time increased from about 7.50 ms to 4.0 ms while exposing the sample to the light. This may be caused either by thermal or light induced defecting of the structure.

ACKNOWLEDGMENT

We would like to thank COST D4 project for financial support.

REFERENCES

1. Preliminary report has been presented during the conference Materiały Molekularne '93 (Molecular Materials '93), Świeradów Zdrój Poland, 1993, J. J. Langer and A. Rajchel, Nowe przewodniki organiczne na bazie 1,10-fenantroliny (New organic conductors with 1,10-fenanthroline).
2. L. R. Melby, R. J. Harder, W. R. Hertler, R. E. Benson and W. E. Mochel, *J. Am. Chem. Soc.*, **84**, 3374 (1962).
3. W. Margulis S. Lavel, *Appl. Phys. Lett.*, **40**, 829 (1982).

Demonstration of Enhanced Cerenkov-Radiative SHG with Chirped Nonlinear Optical Susceptibility in Organic Polymer Waveguide

HEIHACHI SATO, HIDEHISA NOZAWA, YUJI AZUMAI* and IWAO SEO**
*Department of Electrical Engineering, National Defense Academy,
Yokosuka 239, Japan, *R&D Corps, Japan Air Self-Defense Force,
Gifu 504, Japan, **Mitsubishi Petrochemical Co. Ltd., Ibaraki 300-03, Japan*

Received 12 January 1994; accepted 6 March 1994

Introducing a chirping configuration (just like a frequency modulation) into the periodic nonlinear optical susceptibility (NLO $\chi^{(2)}$) in a slab waveguide, the Cerenkovian second-harmonic generation (SHG) scheme newly proposed has been experimentally demonstrated, together with some theoretical background. Using the NLO $\chi^{(2)}$ chirping having the average period $20\ \mu\text{m}$ and the chirping period $200\ \mu\text{m}$ to be the chirping index ~ 9 into vinylidene cyanide/vinyl acetate (VDCN/VAc) copolymer, an enhanced SHG is obtained by the factor of ~ 4 in comparison with a uniform periodic scheme, being consistent with the numerical estimates. Additional SHG enhancement is also preliminarily confirmed with a channel waveguide.

INTRODUCTION

In order to obtain efficient second-harmonic generation (SHG), it is of quite importance to produce phase-matching between the fundamental and SH waves within a nonlinear optical (NLO) material. It is, however, not possible to achieve phase-matching by angular setting in organic polymers, usually adopted with inorganic crystals. Thus, powerful schemes such as quasi phase-matching (QPM) and the Cerenkov-radiative phase-matching have often been used for both inorganic and organic materials. Since these techniques are fairly suitable to organic materials, we have applied both techniques to vinylidene cyanide/vinyl acetate (VDCN/VAc) copolymers, verifying significant enhanced SHG.^{1,2} The Cerenkov-radiative scheme is especially promising because of broader tolerance in the thickness of a guiding layer, except for slightly smaller efficiency than that of the QPM scheme. In the Cerenkov scheme a uniformly distributed NLO susceptibility $\chi^{(2)}$ is usually used either in the guiding layer of a slab waveguide or in both the guiding and cladding layers.² However, we have proposed a new enhanced Cerenkovian SHG by inducing a periodic NLO $\chi^{(2)}$ corrugation in the slab waveguide, and have firstly demonstrated its effectiveness with the above organic copolymer.³ Furthermore, we have recently proposed a novel Cerenkovian scheme by which the SHG power can be additionally enhanced with inducing a sinusoidal chirping just like a frequency modulation (FM) into the uniform periodic $\chi^{(2)}$ corrugation, together with numerical estimates.^{4,5} In the present paper we shall thus experimentally demonstrate the chirping effect of a periodic NLO $\chi^{(2)}$

structure on the Cerenkovian SHG power with VDCN/VAc copolymer in the slab waveguide, together with some theoretical background. Preliminary experiments with channel waveguide will also be described.

THEORETICAL BACKGROUND

In the Cerenkovian scheme proposed we assume that the NLO $\chi^{(2)}$ corrugation is sinusoidally modulated along the beam-traveling (y) direction as depicted in Figure 1:

$$\chi^{(2)}(y) = \chi_0^{(2)} [1 + \cos(\beta_{so}y + \phi_m \sin \beta_m y)], \quad (1)$$

where $\chi_0^{(2)}$ is the peak value, β_{so} and β_m are, respectively, the average and modulation phase-constants with the average and modulation periods, i.e., Λ_{so} and Λ_m , and ϕ_m is the modulation (or chirping) index given by $\Delta\beta_s/\beta_m$ ($\Delta\beta_s$: the deviation of phase constant). This can be approximated in the form:

$$\chi^{(2)}(y) \simeq \chi_0^{(2)} \left[1 + \frac{1}{2} \sum_{p=-(\phi_m+1)}^{\phi_m+1} J_p(\phi_m) \{ \exp[i(\beta_{so} + p\beta_m)y] + \exp[-i(\beta_{so} + p\beta_m)y] \} \right], \quad (2)$$

where J_p is the Bessel function of the first kind of order p , and the summation range over $-(\phi_m+1) \sim (\phi_m+1)$ has been well-known to be good approximation.⁶

For experimental correspondence we consider an asymmetric slab waveguide so as to satisfy the Cerenkovian scheme to emit the SHG power towards the upper cladding layer. Then, under the Cerenkov-radiative phase-matching conditions between the

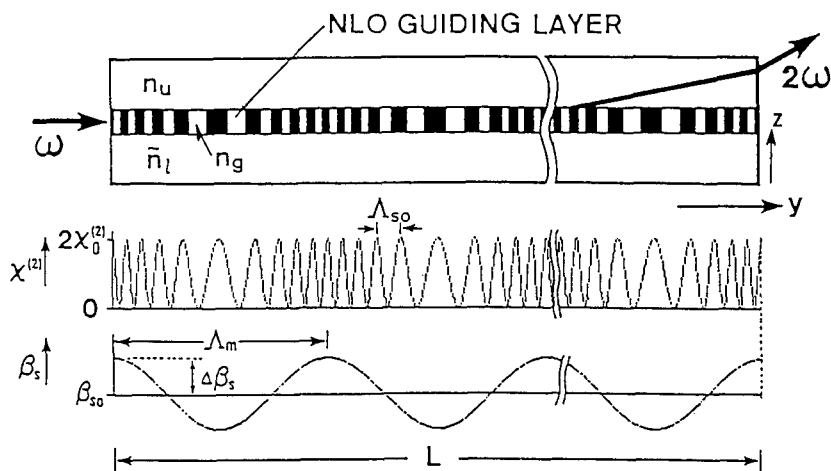


FIGURE 1 Theoretical model of the chirped NLO $\chi^{(2)}$ corrugation for the Cerenkov-radiative SHG scheme.

phase constants of the fundamental and SH waves, β_ω and $\beta_{2\omega}$, as shown in Figure 2:

$$\beta_{2\omega} = 2\beta_\omega, \quad (3a)$$

$$\beta_{2\omega} (\triangleq \beta_{2\omega,p}^\pm) = 2\beta_\omega \pm (\beta_{so} + p\beta_m); p = -(\phi_m + 1) \sim (\phi_m + 1), \quad (3b)$$

the SHG power $P_{2\omega}(L)$ emits over the interaction length L towards many Cerenkov-radiation angles θ_c and θ_c^\pm as⁵

$$\begin{aligned} P_{2\omega}(L) = & \frac{L}{4\omega\mu_0} \{ \beta_{2\omega} |\tilde{A}_{u,2\omega}|^2 \tan \theta_c \\ & + \sum_{p=-(\phi_m+1)}^{\phi_m+1} [\beta_{2\omega,p}^+ |\tilde{A}_{u,2\omega,p}^+|^2 \tan \theta_{c,p}^+ + \beta_{2\omega,p}^- |\tilde{A}_{u,2\omega,p}^-|^2 \tan \theta_{c,p}^-] \\ & + \sum_{p=-(\phi_m+1)}^{\phi_m+1} \{ \text{Re} \{ \tilde{A}_{u,2\omega} \tilde{A}_{u,2\omega,p}^{+*} \exp [i(\beta_{2\omega,p}^+ - \beta_{2\omega})L] \\ & \times (\beta_{2\omega,p}^+ + \beta_{2\omega}) \tan \theta_{c,p}^+ \} \\ & + \text{Re} \{ \tilde{A}_{u,2\omega}^* \tilde{A}_{u,2\omega,p}^- \exp [i(\beta_{2\omega} - \beta_{2\omega,p}^-)L] (\beta_{2\omega,p}^- + \beta_{2\omega}) \tan \theta_{c,p}^- \} \\ & + \sum_{q=-(\phi_m+1)}^{\phi_m+1} \text{Re} \{ \tilde{A}_{u,2\omega,p}^{+*} \tilde{A}_{u,2\omega,q}^- \exp [i(\beta_{2\omega,p}^+ - \beta_{2\omega,q}^-)L] \\ & \times (\beta_{2\omega,p}^+ + \beta_{2\omega,q}^-) \tan \theta_{c,p,q}^+ \} \} \}, \quad (4) \end{aligned}$$

where $\tilde{A}_{u,2\omega}$ is the complex amplitude of SH wave in the upper layer, which involves

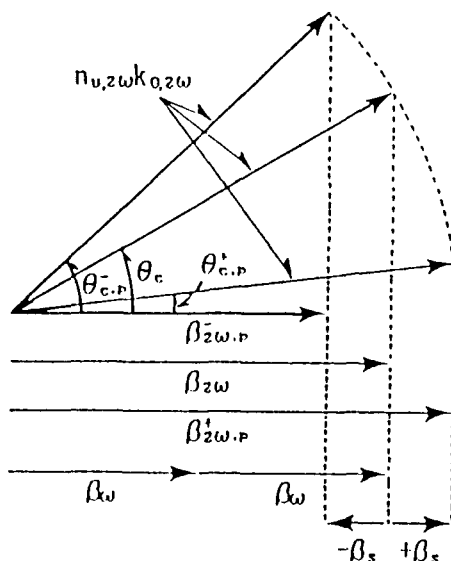


FIGURE 2 Relationship to the Cerenkovian phase-matching between β_ω , and $\beta_{2\omega}$ and $\beta_{2\omega,p}^\pm$ in the chirped Cerenkovian scheme.

NLO $\chi^{(2)}$, the asterisk implies the complex conjugate, and θ_c and θ_c^\pm are, respectively, given by

$$\theta_c = \cos^{-1} \left(\frac{\beta_{2\omega}}{k_{0,2\omega} n_{u,2\omega}} \right), \quad (5a)$$

$$\theta_{c,p}^\pm = \cos^{-1} \left(\frac{\beta_{2\omega,p}^\pm}{k_{0,2\omega} n_{u,2\omega}} \right); p = -(\phi_m + 1) \sim (\phi_m + 1). \quad (5b)$$

Here, $k_{0,2\omega}$ is the wave number in vacuum and $n_{u,2\omega}$ is the refractive index of the upper layer. Theoretical analysis about this scheme will be reported elsewhere in detail later.

As a limiting case of $\beta_{so} = \beta_m = 0$ we have the uniform NLO $\chi^{(2)}$ structure as

$$\chi^{(2)}(y) = 2\chi_0^{(2)} \quad (6)$$

with a single Cerenkov-radiation angle θ_c :

$$\theta_c = \cos^{-1} \left(\frac{\beta_{2\omega}}{k_{0,2\omega} n_{u,2\omega}} \right). \quad (7)$$

The corresponding SHG power $P_{2\omega}(L)$ becomes

$$P_{2\omega}(L) = \frac{L}{4\omega\mu_0} \beta_{2\omega} |\tilde{A}_{u,2\omega}|^2 \tan \theta_c. \quad (8)$$

On the other hand, the uniform periodic NLO $\chi^{(2)}$ corrugation corresponds to the case of $\beta_m = 0$ to yield:

$$\chi^{(2)}(y) = \chi_0^{(2)} (1 + \cos \beta_{so} y). \quad (9)$$

Thus, the SHG power is given by

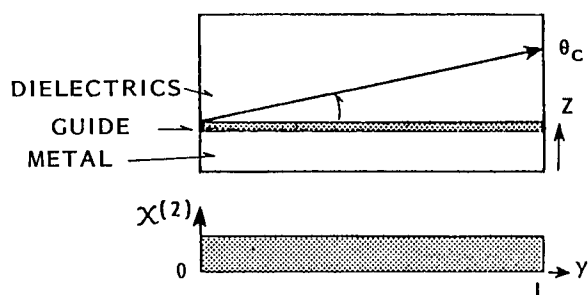
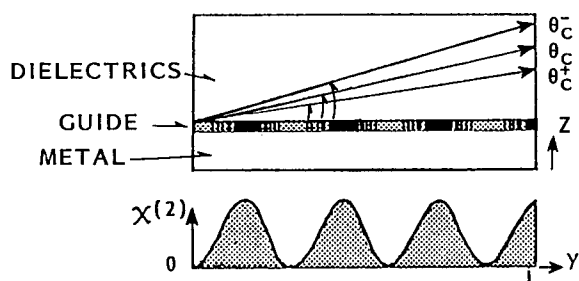
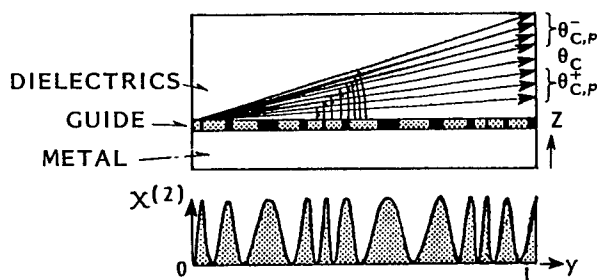
$$\begin{aligned} P_{2\omega}(L) = & \frac{L}{4\omega\mu_0} \{ \beta_{2\omega} |\tilde{A}_{u,2\omega}|^2 \tan \theta_c \\ & + \beta_{2\omega}^+ |\tilde{A}_{u,2\omega}^+|^2 \tan \theta_c^+ + \beta_{2\omega}^- |\tilde{A}_{u,2\omega}^-|^2 \tan \theta_c^- \\ & + \text{Re}[\tilde{A}_{u,2\omega} \tilde{A}_{u,2\omega}^{+*} \exp(i\beta_s L)] (\beta_{2\omega}^+ + \beta_{2\omega}) \tan \theta_c^+ \\ & + \text{Re}[\tilde{A}_{u,2\omega}^* \tilde{A}_{u,2\omega}^- \exp(i\beta_s L)] (\beta_{2\omega} + \beta_{2\omega}^-) \tan \theta_c \\ & + \text{Re}[\tilde{A}_{u,2\omega}^{+*} \tilde{A}_{u,2\omega}^- \exp(i2\beta_s L)] (\beta_{2\omega}^+ + \beta_{2\omega}^-) \tan \theta_c^+ \} \end{aligned} \quad (10)$$

with three Cerenkov-radiation angles as

$$\theta_c = \cos^{-1} \left(\frac{\beta_{2\omega}}{k_{0,2\omega} n_{u,2\omega}} \right), \quad (11a)$$

$$\theta_c^\pm = \cos^{-1} \left(\frac{\beta_{2\omega}^\pm}{k_{0,2\omega} n_{u,2\omega}} \right). \quad (11b)$$

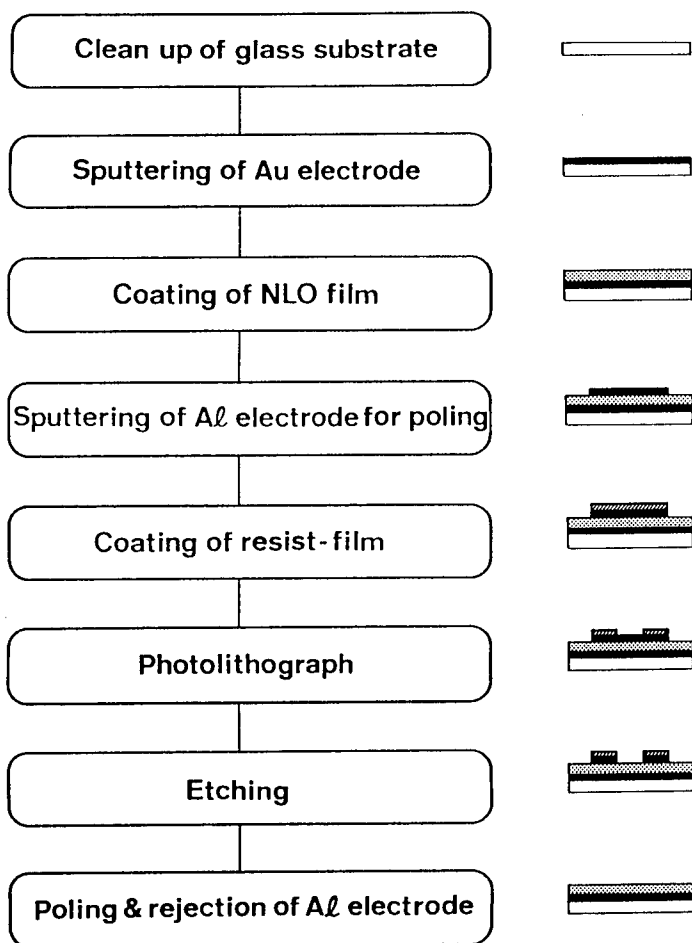
The situations of the three typical Cerenkovian SHG schemes are comparatively illustrated in Figure 3.

(a) Uniform NLO $\chi^{(2)}$ structure(b) Periodic NLO $\chi^{(2)}$ structure(c) Chirped NLO $\chi^{(2)}$ structureFIGURE 3 Qualitative situations of three Cerenkovian SHG schemes with different NLO $\chi^{(2)}$ structures.

EXPERIMENTS

Preparation of Chirped $\chi^{(2)}$ Corrugation

The main flow-chart for processing the chirped NLO $\chi^{(2)}$ film is illustrated in Figure 4. First, Au film was uniformly sputtered onto glass (BK-7) substrate cleaned up as one side of electrode for poling. Then, NLO material (VDCN/VAc) was spin-coated to be

FIGURE 4 Fabrication process of chirped periodic NLO $\chi^{(2)}$ film.

$\sim 1 \mu\text{m}$ thickness, depending on coating time, spinning speed and ambient humidity. In order to induce the chirping effect into the NLO $\chi^{(2)}$ corrugation, two metallic masks were prepared. The mask patterns of the electrode used for both the chirped and periodic $\chi^{(2)}$ corrugations are shown in Figure 5(a) and (b) respectively. Since our numerical estimates indicate that the optimum chirping-index (or modulation index) ϕ_m exists near $\phi_m \simeq 7$, insensitive to the film thickness of the guiding layer,⁴ we have chosen the average corrugation period Λ_{so} of $20 \mu\text{m}$ and the chirping period Λ_m of $200 \mu\text{m}$ (the total length of 2 mm) so as to be close to the optimum index above. Setting these masks over the NLO film, aluminum (Al) was then evaporated as the other side of poling electrode, and a resist-film was coated over it. Now, photolithographic process was performed and its photo-exposed portion was etched. After applying the poling field of 1 MV/cm between the Al and Au electrodes for 15 minutes near the glass-transition temperature T_g of the NLO material, i.e., 180°C , it was then gradually cooled

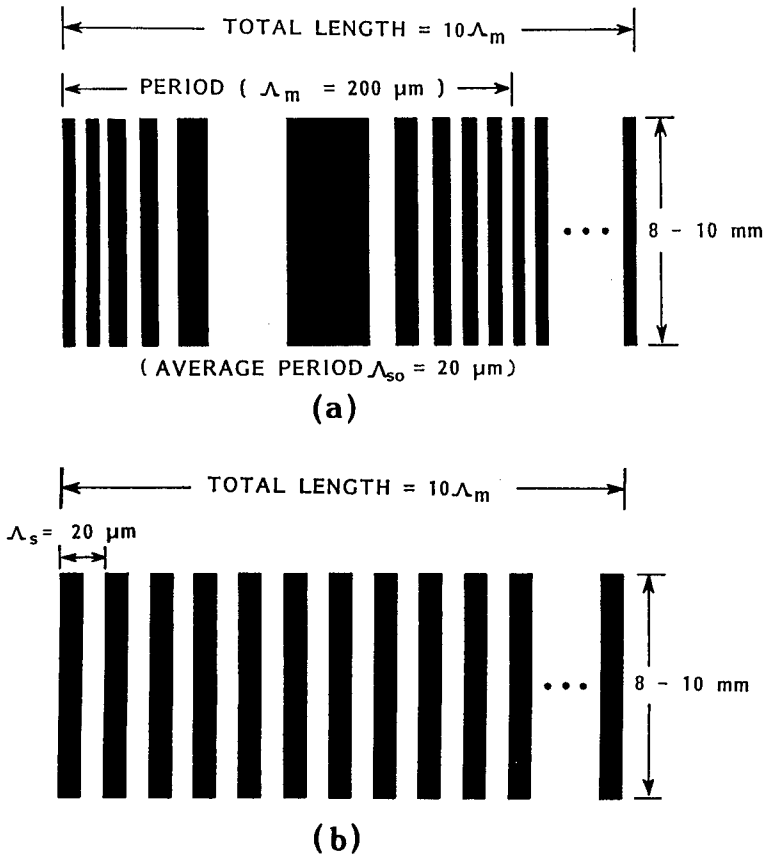


FIGURE 5 Mask patterns of the electrodes for poling: (a) chirped periodic and (b) uniform periodic structures.

down to room temperature to freeze the chirped NLO $\chi^{(2)}$ corrugation. In parallel, the uniform (or nonchirped) periodic NLO $\chi^{(2)}$ structure with the average period $\Lambda_{so} = 20 \mu\text{m}$ has also been prepared with the mask pattern (see Fig. 5 (b)) for comparison. Specifications of the electrode patterns used for poling are summarized in Table 1.

Setup

The experimental setup is schematically depicted in Figure 6. A pulsed Nd:YAG $1.06 \mu\text{m}$ laser (NEC:SL129) was used as the fundamental wave source. This beam was prism-coupled into the asymmetric slab waveguide, in which the VDCN/VAC copolymer film having the chirped NLO $\chi^{(2)}$ corrugation was sandwiched by a fused silica and Au evaporated BK-7 substrate. The Cerenkov-radiative SHG power was detected by the photomultiplier (Toshiba:PM 55) mounted on a linear translator for spatial scanning along the z direction. The fundamental waveform was also monitored

TABLE 1
Specifications of mask patterns for poling.

	Nonchirped	Chirped
Period Λ_z or Average Period Λ_{zo}	$\Lambda_z = 20 \text{ \& } 60 \text{ }\mu\text{m}$	$\Lambda_{zo} = 20 \text{ }\mu\text{m}$
Chirping Period Λ_m	—	200 μm
Modulation Index ϕ_m	—	~ 9
Total Length L	$\sim 2 \text{ mm}$	2 mm

through a beam splitter (B.S.) on CRT, together with the SHG waveform. Since the VDCN/VAc copolymer has an absorption peak near 200 nm, and has some property to decrease its refractive index and lose its NLO susceptibility by absorbing the UV radiation, we have also preliminarily examined enhancement of the SHG power in the channel waveguide made by irradiating the ArF 193 nm laser source.

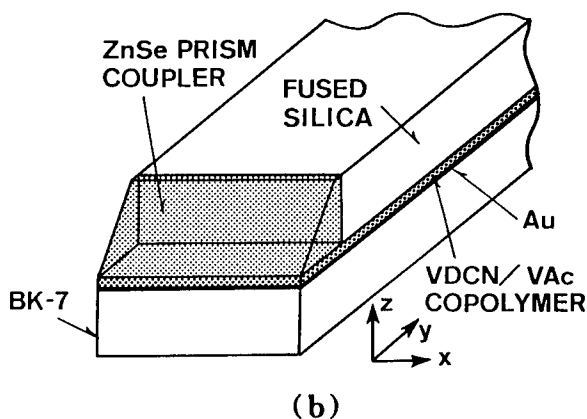
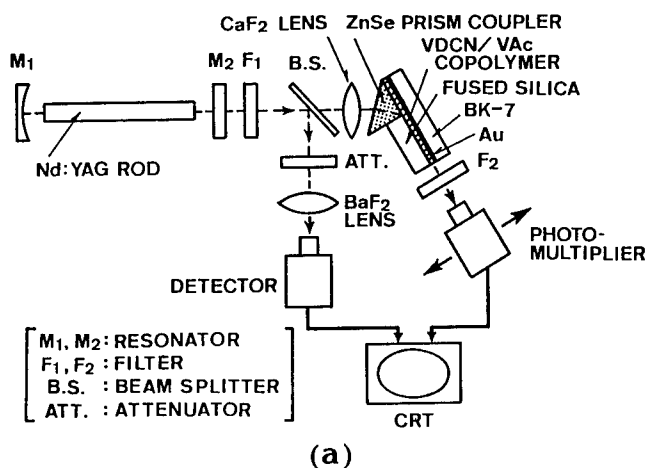


FIGURE 6 Experimental schematic diagram: (a) setup and (b) close-up of NLO slab-guide.

Results

The typical Cerenkovian SHG waveforms observed in the slab-guide is shown in Figure 7, in comparison with those in the channel-guide with the chirped NLO $\chi^{(2)}$ corrugation and in the slab-guide with the uniform NLO $\chi^{(2)}$ corrugation. We can see the reasonable reduction of the pulse-width because of the dependence of the SHG power on the square of the fundamental power. In Figure 8 (a) and (b) the SHG powers $P_{2\omega}$ are illustrated as a function of the square of the fundamental power P_{ω}^2 , showing a good linear dependence for each scheme. From these dependences it is well recognized that the slope efficiency has been significantly improved with introducing the chirping into the NLO $\chi^{(2)}$ corrugation even in the slab-guide. From the preliminary experiments we can also well expect an additional enhancement of the conversion efficiency in the channel-guide with the same NLO $\chi^{(2)}$ configuration as in the slab-guide (Fig. 8(b)). In comparison with the uniform periodic $\chi^{(2)}$ scheme, the enhancement factor of 3.7 and 17 were, respectively, obtained in the slab- and channel-guides.

DISCUSSION AND CONCLUSION

In our previous paper it has been numerically estimated that the SHG power will be periodically enhanced as a function of the chirping (or modulation) index ϕ_m , especially

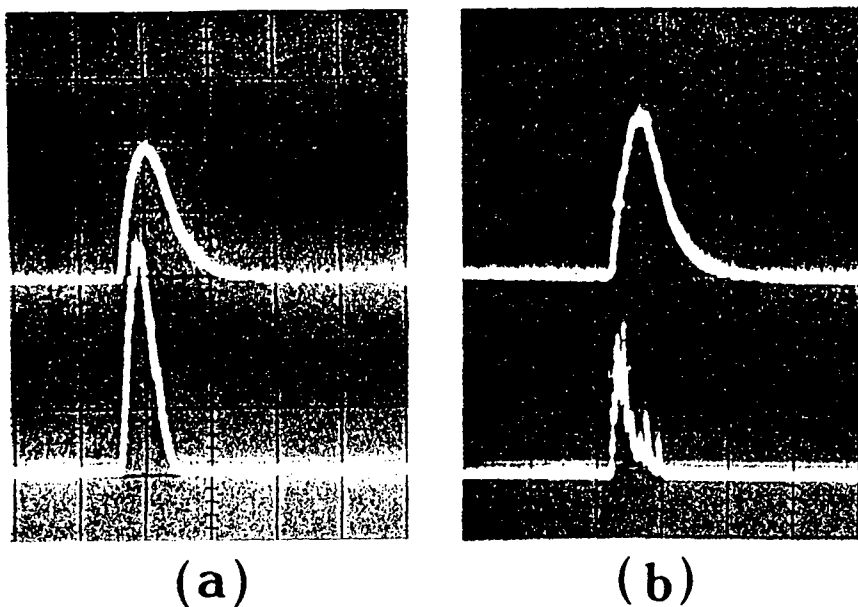


FIGURE 7 Observed SH waveforms with (a) chirped NLO $\chi^{(2)}$ ($\Lambda_{so} = 20 \mu\text{m}$) and (b) uniform NLO $\chi^{(2)}$ ($\Lambda_s = 20 \mu\text{m}$) corrugations, where the upper and lower traces are, respectively, the fundamental and SH waveforms with the vertical scales of 5 mV/div. and 100 mV/div., together with the same horizontal scale of 100 μs /div.

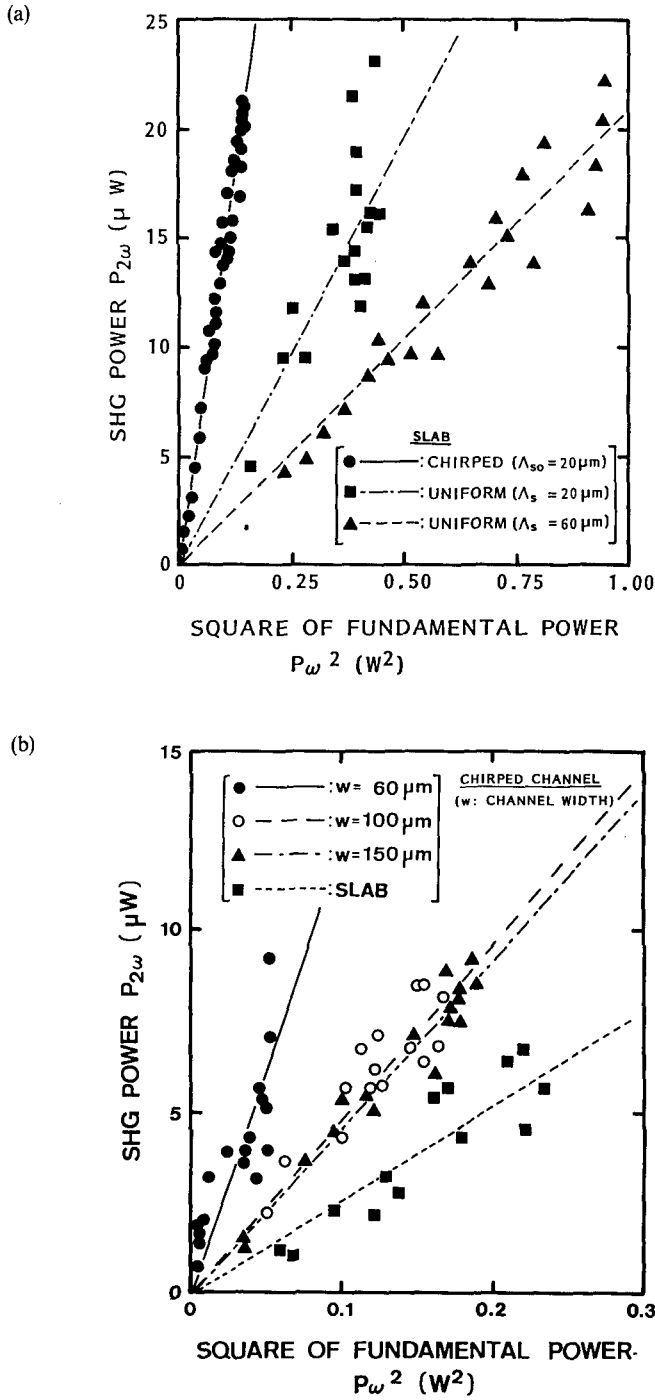


FIGURE 8 Linear dependence of $P_{2\omega}$ on P_{ω}^2 for various NLO $\chi^{(2)}$ schemes: (a) chirped slab-guide and (b) chirped channel-guide.

obtaining the maximum SHG power at $\phi_m \simeq 7$, while the optimum thickness d of the guiding (NLO) layer is $\sim 1.1 \mu\text{m}$, being insensitive to d .⁴ Thus, the electrode pattern for providing the chirped NLO $\chi^{(2)}$ corrugation was designed so as to be close to the above ϕ_m value, and actually corresponds to $\phi_m \simeq 9$ with the average corrugation period Λ_{so} of $20 \mu\text{m}$ and the chirping period Λ_m of $200 \mu\text{m}$. In Figure 9 the numerical calculation of the relative SHG power with the refractive indices corresponding to the experimental setup is shown as a function of the NLO film thickness d for a few different chirped and nonchirped periodic structures,⁵ where the NLO $\chi^{(2)}$ is assumed to be sinusoidally chirped along the y -direction (beam-traveling direction), i.e., $\chi^{(2)}(y) = \chi_0^{(2)} [1 + \cos(\beta_{so} y + \phi_m \sin \beta_m y)]$ in the theoretical treatment.

By using the electrode patterns as mentioned in preparation of chirped $\chi^{(2)}$ corrugation, we have previously recognized that the poled NLO $\chi^{(2)}$ corrugation tends to be close to the sinusoidal profile due to the fringing effect, even though the square-shaped electric field is applied to the electrodes. The experimentally obtained enhancement factors (E.F.) were respectively, 3.9, 1 and 0.52 for the chirped ($\Lambda_{so} = 20 \mu\text{m}$), the uniform ($\Lambda_s = 20 \mu\text{m}$) and the uniform ($\Lambda_s = 60 \mu\text{m}$) $\chi^{(2)}$ corrugation schemes, whereas the theoretical E.F. values of the corresponding schemes based on both the sinusoidally chirped and uniform corrugations assumed were, respectively, 4.7, 1 and 0.50 at the respective NLO film thicknesses as emphasized with the circles in Figure 9. The fact that the enhancement factors obtained in the experiments are consistent well with the numerical estimates to the sinusoidal chirping implies exactly as they are expected in good approximation. The reason of significant improvement of the SHG power in the channel waveguide can be attributed to increase of the field confinement along the spatial (x) direction.

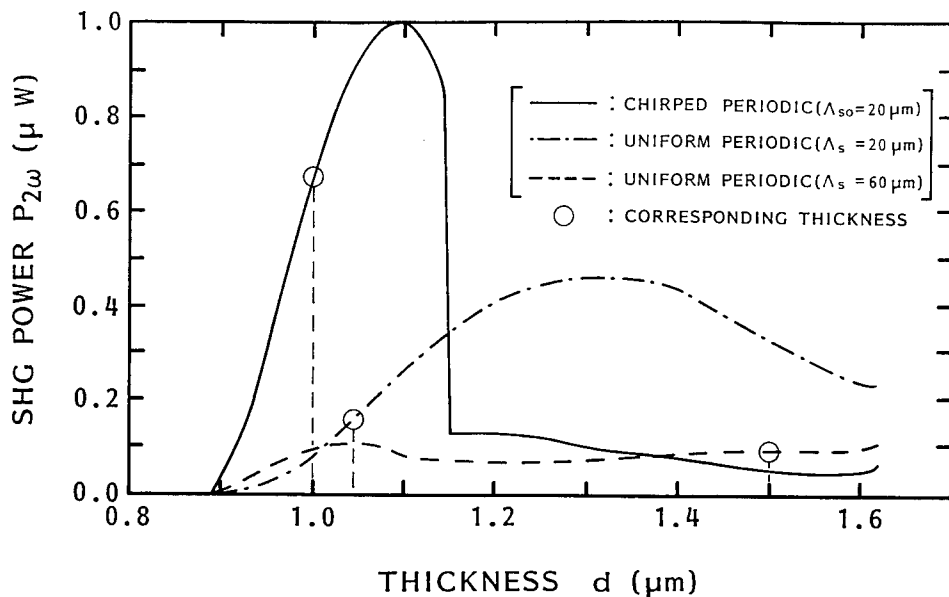


FIGURE 9 Numerical calculations of the relative SHG power as a function of the NLO film thickness.⁴

Introducing the sinusoidal chirping into the periodic NLO $\chi^{(2)}$ corrugation in the slab waveguide, the effective SHG enhancement was experimentally demonstrated in the Cerenkov-radiative scheme by choosing both the chirping (or modulation) index ϕ_m and the NLO film thickness of the guiding layer d appropriately. Fabricating the chirped NLO $\chi^{(2)}$ corrugation onto the VDCN/VAc film ($d = 1.0 \sim 1.05 \mu\text{m}$) by the method of contact electrode so as to be $\phi_m \simeq 9$, the enhanced SHG power was successfully obtained by the factor of ~ 4 with the asymmetric slab-guide, being in good agreement with the numerical estimates. Significant improvement of the SHG power was also preliminarily verified in the experiments with the channel waveguide having the same chirped NLO $\chi^{(2)}$ configuration.

REFERENCES

1. Y. Azumai, M. Kishimoto and H. Sato, *Jpn. J. Appl. Phys.*, **31**, (Part 1), 1358 (1993).
2. Y. Azumai, I. Seo and H. Sato, *IEEE J. Quantum Electron.*, **28**, 231 (1992).
3. H. Sato and Y. Azumai, *J. Opt. Soc. Am. B*, **10**, 894 (1993).
4. Y. Azumai and H. Sato, in Technical Digest of Conference on Lasers and Electro-Optics (Optical Society of America, Washington, 1993), p. 270.
5. H. Sato, H. Nozawa and Y. Azumai, *Opt. Lett.*, **19**, 93 (1994).
6. H. Taub and D. L. Schilling, *Principles of Communication Systems* (McGraw-Hill, New York, 1971), p. 123.

Second-Harmonic Generation by Counterpropagating Beams in Organic Thin Films

A. OTOMO¹, Ch. BOSSHARD¹, S. MITTLER-NEHER¹, G. I. STEGEMAN¹,
M. KÜPFER², M. FLÖRSHEIMER², P. GÜNTHER², W. H. G. HORSTHUIS³
and G. R. MÖHLMANN³

¹*Center for Research in Electro-Optics and Lasers, University of Central Florida, Orlando, Florida 32826, USA,* ²*Nonlinear Optics Laboratory, Institute of Quantum Electronics, Swiss Federal Institute of Technology, ETH Hönggerberg, CH-8093 Zürich, Switzerland,* ³*AKZO Research Laboratories, Corporate Research, Applied Physics Department, Arnhem, The Netherlands*

Received 12 January 1994; accepted 21 March 1994

We demonstrate efficient surface emitting second-harmonic generation due to mixing of counter propagating waves for the first time in organic thin films. We describe experiments performed in plane parallel poled low loss channel waveguides of 4-dimethylamino-4'-nitrostilbene (DANS) side-chain polymers and planar Langmuir-Blodgett film waveguides of 2-docosylamino-5-nitropyridine (DCANP).

INTRODUCTION

Since the first demonstration of second-harmonic generation due to mixing of counter-propagating beams several applications such as spectrometers and pico second signal processing have been proposed or demonstrated.^{1–5} Recently the work in this field has concentrated on GaAs based waveguide structures^{5–10} where the conversion efficiency was improved dramatically by using a form of quasi-phase-matching in multilayered structures. On the other hand, large nonlinear optical coefficients make organic materials an attractive alternative to semiconductor devices. Furthermore the configuration allows to work at second-harmonic wavelengths on resonance ($\omega_0 \approx 2\omega$) since the emitted second-harmonic wave travels less than one micron through absorbing material. Note that, for efficient surface emission, the film is required to have large in-plane diagonal nonlinear optical tensor elements d_{ii} which can be obtained by different approaches (see below).

In this work we report the first observation of the effect of surface emitting second-harmonic generation (SHG) due to mixing of counterpropagating waves in organic waveguides. Our experiments were performed in films of 4-dimethylamino-4'-nitrostilbene (DANS) side-chain polymers and Langmuir-Blodgett (LB) films of 2-docosylamino-5-nitropyridine (DCANP).

COUNTERPROPAGATING SECOND-HARMONIC GENERATION

The mixing of counter propagating guided waves to generate a second-harmonic wave normal to the surface was initially demonstrated in Ti in-diffused LiNbO₃ waveguides over a decade ago.¹ Figure 1 shows the schematic diagram of a typical set-up. Two oppositely propagating guided waves can be written as

$$E_{\pm}^{\omega} = \frac{1}{2} [\varepsilon_{\pm}(x) e^{i(\omega t \mp \beta^{\omega} z)} + \text{c.c.}] \quad (1)$$

where $\varepsilon_{\pm}(x)$ describes the transverse guided wave field distributions, β^{ω} is the propagation constant of the fundamental guided waves, and the \pm signs denote the propagation directions along the $+z$ and $-z$ directions, respectively. These oppositely propagating guided waves create a second harmonic polarization of the form

$$P^{2\omega} = \frac{1}{2} \varepsilon_0 d_{22} [\varepsilon_+(x) \varepsilon_-(x) e^{i2\omega t} + \varepsilon_+(x) \varepsilon_-^*(x) e^{-i2\beta^{\omega} z} + \text{c.c.}] \quad (2)$$

Unlike the case of the usual co-propagating second-harmonic generation, the induced second-harmonic polarization does not have a propagation term along the z -axis. Fields generated by the polarization can propagate only along the $\pm x$ -axis in slab waveguides. This surface emitting configuration has the advantage that the wavevector matching condition parallel to the surface, $\Delta\beta_z = \beta_{+z}^{\omega} + \beta_{-z}^{\omega} - \beta_z^{2\omega} = 0$, is always satisfied under any circumstances. The other unusual property is the spatial shape of the SHG pulses: The resulting SHG pulse shape in the z -direction is the convolution of the fundamental pulse shapes. Hence we can determine the convolution pulse shape by measuring the SHG pulse energy distribution along the z -direction with a CCD array. Several applications of these properties have previously been demonstrated, including picosecond signal processing² and picosecond optical transient digitizers.³ Furthermore this device can be used for real time spectrometers⁴ because the sum frequency fields generated by different input frequency components propagate with unique and different angles from the normal to the film surface. The device potential of this phenomenon for e.g., ultrafast signal processing and wavelength division demultiplexing has attracted considerable attention.⁵

The intensity for second-harmonic generation by counterpropagating beams can be described by $I(2\omega) = A^{NL} I_+(\omega) I_-(\omega)$ where $I_{\pm}(\omega)$ are the line intensities (in W/m) of

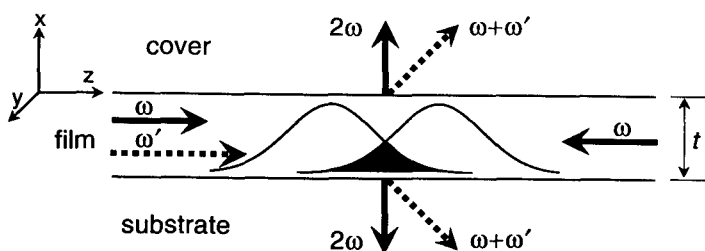


FIGURE 1 Schematic diagram of second-harmonic generation due to counterpropagating beams.

the fundamental beams and A^{NL} is the nonlinear cross section.¹ We have

$$A^{NL} = \epsilon_0 \omega k_0^{(2\omega)} n_c^{(2\omega)} |C|^4 |S(\infty)|^2 \quad (3)$$

where

$$S(\infty) = \int_{-\infty}^{\infty} \frac{d_{22}(x') f_y(x')^2 \exp[ik_0^{(2\omega)} n_f^{(2\omega)} x']}{n_f^{(2\omega)}} dx' \quad (4)$$

is the superposition integral, $k_0^{(2\omega)} = 2\omega/c$, $n_c^{(2\omega)}$ is the refractive index, and $n_f^{(2\omega)}$ is the complex refractive index of the film. $f_y(x')$ is the guided mode profile and C is the normalization constant of the guided mode. The magnitude of the integral oscillates with increasing sample thickness t . Optimum conversion efficiencies are obtained for film thicknesses which are separated by $\lambda/(2n^{2\omega})$. Therefore a precise thickness control is needed to obtain large A^{NL} . With polymers as well as with LB films desired waveguide thicknesses for optimized conversion efficiencies can easily be fabricated.

MATERIAL DESCRIPTION AND SAMPLE PREPARATION

Plane-Parallel Poling of DANS

DANS side-chain polymers¹¹ are one of the most highly developed poled polymers for applications to electro-optic switching devices. Their relatively high glass transition temperature provides long term stability of the poled state at room temperature and large poling field strengths provide nonlinear coefficients d_{22} as high as 120 pm/V at a near-resonant second-harmonic wavelength ($\lambda = 1.064 \mu\text{m}$). Furthermore, structures with lateral confinement can be made by photobleaching which reduces the film index outside the channel region.¹² This allowed us to fabricate low loss channel waveguides.¹³

A schematic cross section of the DANS polymer waveguide fabricated is shown in Figure 2. DANS side-chain polymer films were made by spin coating onto fused silica substrates which had two coupling gratings ion-milled into the glass surface, one at each end, and aluminum poling electrodes on the glass surface. The spacing of the grating was $0.5 \mu\text{m}$ and the spacing between the poling electrodes was $20 \mu\text{m}$. The film thickness of $0.83 \mu\text{m}$ was determined from calibrated data on the spinning rate and the solid concentration in the spinning solution. A $4 \mu\text{m}$ wide channel waveguide with parabolic tapered mode couplers on both sides¹³ was constructed by photobleaching. In this process the film is exposed through a mask to collimated light from a Hg-Arc lamp ($\lambda = 436 \text{ nm}$) for 2 hours. The effective device length was 1 cm. A $15 \mu\text{m}$ thick cover layer of an inactive cross linked polymer was spin coated on top of the DANS polymer in order to prevent discharge through the air during poling and to create a better guided mode profile for efficient surface emitting SHG.

Since a large lateral component (in-plane, along the y -axis in Fig. 2) of the second-order nonlinearity is required for efficient conversion, plane parallel poling was performed at just below the glass transition temperature of $T_g = 142^\circ\text{C}$ where the DANS molecules are rotationally mobile in the host matrix. Previously reported parallel poling was not as successful as plane normal poling because charge injection

can obstruct efficient alignment along the plane-parallel direction.¹⁴ We monitored the current flow into one electrode while a constant poling voltage was applied. A small current (a few tens μA) was observed with consequent electrode damage due to the charge injection when a glass slide was used as a substrate. In the case of a fused silica substrate, no current was observed using a pico-ampere meter (KEITHLEY model 485) with an applied high voltage of 4000 V. In the absence of charge injection, a thick cover layer becomes crucial for parallel poling in order to eliminate arcing through the air. After 30 minutes of poling, the temperature was decreased slowly ($< 1^\circ\text{C}/\text{min.}$) under the applied high voltage and the voltage was turned off at room temperature.

Fabrication of LB Films of DCANP

The linear and nonlinear optical properties of DCANP are well established and both Cerenkov type and phase-matched second-harmonic generation using modal conversion in waveguide configuration have been reported.^{15–19} The LB film fabrication procedure of DCANP induces a preferred alignment of the molecules along the dipping direction. This leads to a net dipole moment within the substrate plane and to a Y-type “herringbone”-like structure (Fig. 3). Therefore no poling is necessary to induce the desired molecular orientation and the films are stable over years.

Commercially available $\text{TiO}_2/\text{SiO}_2$ waveguides (substrate glass AF45) from ASI AG (Zurich, Switzerland) were used into which gratings with a spacing of $1\ \mu\text{m}$ were fabricated by ion milling. The coupling gratings were separated by $5.5\ \text{mm}$ thus defining

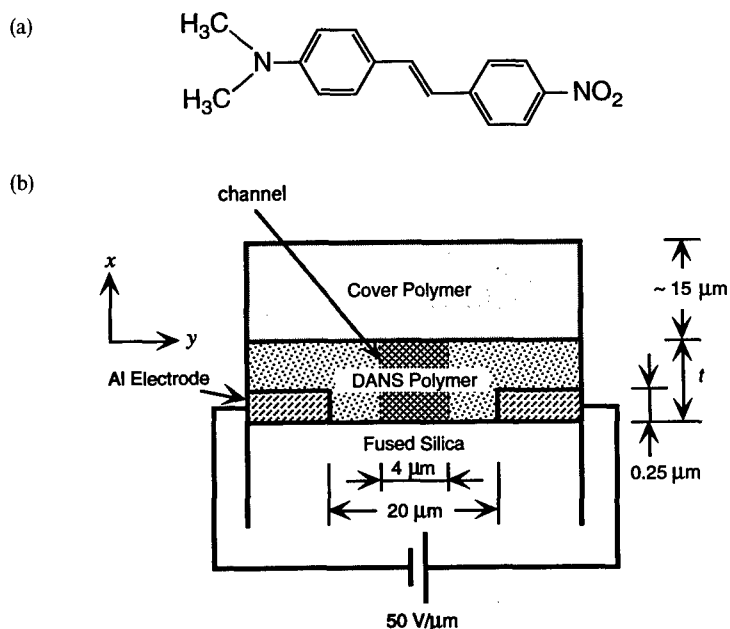


FIGURE 2 (a) Structure of 4-dimethylamino-4'-nitrostilbene (DANS) molecules. (b) Schematic cross section of a parallel poled sample.

the interaction length of the device. Subsequently the surface was cleaned and the film was deposited. The exact preparation procedure is described in Reference 17. For our experiment a sample with a linear layer thickness of $t_{\text{LIN}} = 145 \text{ nm}$ and a LB film thickness of $t_{\text{LB}} = 230 \text{ nm}$ (corresponding to 104 monolayers) was used.

EXPERIMENTAL RESULTS

Surface-Emitting Second-Harmonic Generation in DANS

The nonlinear optical susceptibility d_{22} was measured at $\lambda = 1.064 \mu\text{m}$ by the Maker-fringe technique with a quartz reference ($d_{11} = 0.4 \text{ pm/V}$). Values of 26 pm/V and 120 pm/V were obtained for poling fields of $50 \text{ V}/\mu\text{m}$ and $200 \text{ V}/\mu\text{m}$, showing the expected linear dependence of d_{22} with the poling field.

For the counterpropagation experiments 100 ps pulses from a Q -switched (500 Hz) and mode-locked (76 MHz) Nd:YAG laser (Quantronix 416) were split in half and then coupled into both sides of the waveguide (poled with $50 \text{ V}/\mu\text{m}$) to excite TE_0 modes. The overlap in the waveguide was optimized by changing the optical delay in one arm. The coupling efficiency of the grating couplers was determined by measuring the transmission change, and the total coupling efficiency into the channel waveguide was estimated as 10% for each of the two couplers, including the tapered mode transition loss.¹³ The SHG power was detected in the direction normal to the surfaces by a photomultiplier tube through lenses. Since the generated light had a large divergence angle along the y -axis, the collected power by the lens was only 30% of the total generated power including reflection losses. The measured SHG power was 17 mW for 32 W of input power which yields $0.64 \text{ GW}/\text{cm}^2$ of peak intensity in the channel waveguide. The nonlinear cross section was evaluated as $8.5 \times 10^{-9} \text{ W}^{-1}$ by assuming a Gaussian shape for the pulses in the pulse train. The SHG signal radiated perpendicular to the surface was clearly visible under normal room light conditions.²⁰

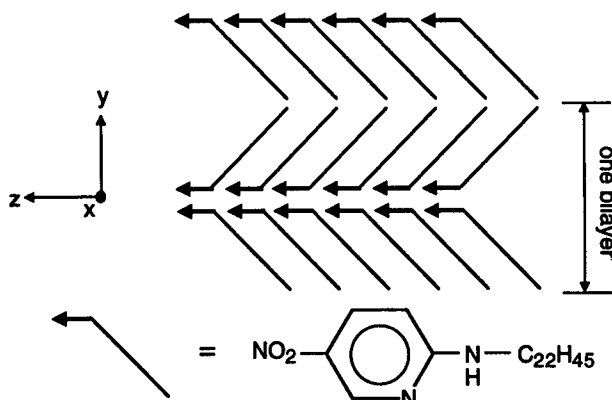


FIGURE 3 Orientation of the DCANP molecules in the LB film. The dipping procedure induces the non-centrosymmetric Y-type structure. The arrows indicate the direction of the dipoles.

The thickness dependence of the magnitude of the nonlinear cross section A^{NL} was calculated for the DANS side chain polymer and is shown in Figure 4. The measured value of the nonlinear coefficient d_{22} for a poling field of 50 V/ μm was used, and absorption and multiple reflection were included in the calculation. The calculated value of $1.45 \times 10^{-8} \text{ W}^{-1}$ at a thickness of 0.83 μm agrees with the measured value. The maximum efficiency would be obtained at a film thickness of 0.47 μm with $A^{NL} = 5.0 \times 10^{-8} \text{ W}^{-1}$. A simple extrapolation to a poling field of 200 V/ μm (assuming that $d_{22} \sim E_{\text{poling}}$) gives $A^{NL} = 8 \times 10^{-7} \text{ W}^{-1}$, a much higher value than the one from a single layer of GaAs.

Surface-Emitting Second-Harmonic Generation in DCANP

The nonlinear optical coefficients of DCANP have already been determined in Reference 16. Due to the coordinate system defined in Figure 1 the largest nonlinear coefficient d_{33} of DCANP is here denoted as d_{22} . The experimental set-up for the counterpropagation measurement was identical to the one for DANS. The fundamental beams were focussed on the grating using cylindrical lenses in order to optimize the coupling. Coupling efficiencies of 11% and 8% were estimated. The peak power of the

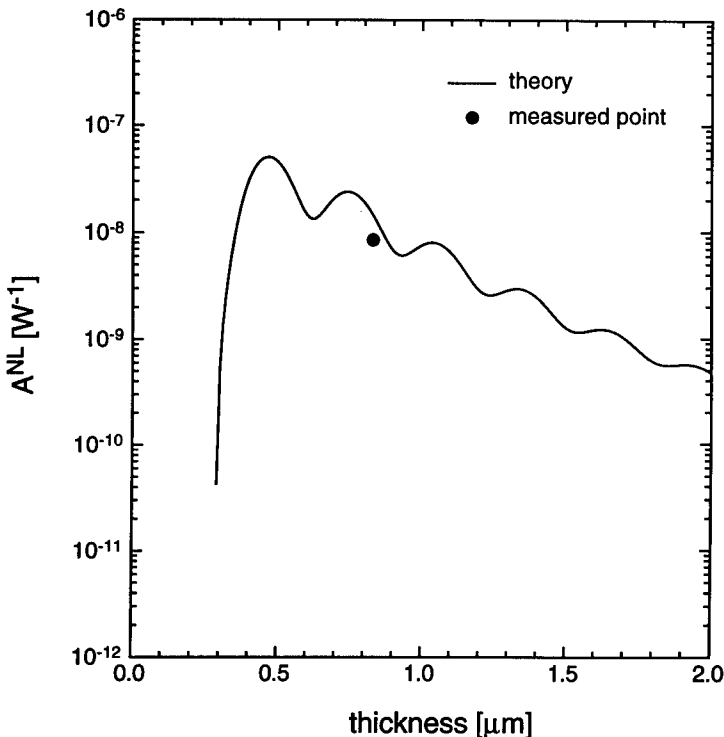


FIGURE 4 Thickness dependence of the nonlinear cross section for DANS side-chain polymer channel waveguides with a cladding refractive index of 1.55 and a fused silica substrate.

fundamental in the waveguide was 74 W (average power of 70 μ W) yielding a peak line intensity of 3.46 kW/m. The generated second-harmonic light could be observed perpendicular to the sample surface. As in the case of DANS it could easily be detected by eye in room light condition. The measured second-harmonic power showed the expected quadratic behavior on the intensity of the fundamental. We measured a maximum average power of $P_{av}^{2\omega} = 6$ nW corresponding to a peak power $P_p^{2\omega}$ of 12.6 mW.²¹ The full divergence angle of the green light was of the order of 0.036rad. Therefore it could be expected that all the light generated was incident on our detector.

From P^w and $P^{2\omega}$ the nonlinear cross section A^{NL} could be calculated. Our measured value of $1.3 \cdot 10^{-8} \text{ W}^{-1}$ is in good agreement with the theoretical value of $A^{NL} = 1.4 \cdot 10^{-8} \text{ W}^{-1}$ in Figure 5 which shows the theoretical non-linear cross section versus thickness for 3- and 4-layer geometries of DCANP and also the measured point. The substrate is either a high-index glass (AF45) or pyrex. For the 4-layer case an optically inactive $\text{TiO}_2/\text{SiO}_2$ film was used. The following parameters were utilized for the calculation: wavelength $\lambda = 1064$ nm, nonlinear optical coefficient $d_{22} = 7.8$ pm/V, thickness of linear $\text{TiO}_2/\text{SiO}_2$ layer $t_{\text{LIN}} = 145$ nm, refractive indices at frequency ω : $n_{\text{LIN}} = 1.75$, $n_s = 1.516$ (or $n_s = 1.4667$ for pyrex), $n_{\text{DCANP}} = 1.573$, refractive indices at frequency 2ω : $n_{\text{LIN}} = 1.85$, $n_s = 1.531$ (or $n_s = 1.4743$ for pyrex), $n_{\text{DCANP}} = 1.624$.

DISCUSSION AND CONCLUSIONS

Let us first discuss DANS. Extending the device to multiple layer films with alternate films of different glass transition temperature should lead to even larger signals due to optimized quasi-phase-matched structures with oppositely directed d_{eff} in quarter wavelength (at ω) thick layers. Also, since the 2ω signal traverses less than one micron of the DANS polymer, resonance enhanced values of d_{eff} can be used in the laser diode wavelength range of 800–850 nm.

In LB films the superposition integral can be optimized by constructing LB layers with periodically reversed nonlinearities and optimized layer thicknesses. This has already successfully been applied to DCANP LB films for optimizing Cerenkov-type and mode-to-mode frequency conversion.^{22,23} For the counterpropagation configuration described here this can lead to an increase in A^{NL} of about one order of magnitude. A projection of the ultimate signal limit has been presented in Reference 21: Values of $P(2\omega)/P^2(\omega)$ up to 200% W^{-1} are feasible for a 1 cm long guide and a channel width of 1 μm .

We used the 4-layer structures mainly for two reasons. First, the attenuation losses of the waveguide can be strongly decreased for LB films as has been demonstrated in Reference 18. Second, fewer layers of DCANP molecules have to be deposited to obtain similar nonlinear cross sections as for usual 3-layer structures (Fig. 5). This is clear since optimum conversion efficiencies are obtained for film thicknesses which are separated by $\lambda/(2n^2\omega)$. This means that generally the first peak in A^{NL} is not accessible since the corresponding thickness is below the cut-off of the waveguide. In 4-layer structures, however, the first peak can be used. Obviously, this always holds true for symmetric

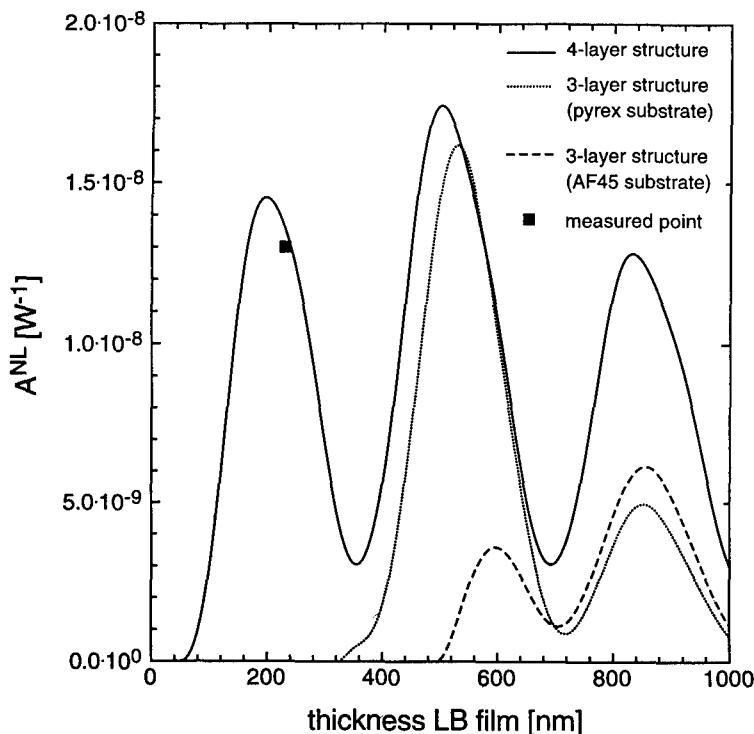


FIGURE 5 Nonlinear cross section vs thickness for 3- and 4-layer waveguide geometries of DCANP.

3-layer waveguides. Note, however, that this first peak not always leads to the highest conversion efficiencies since the confinement of the electric fields may still be small.

Note that in the case of LB films several film thicknesses optimized for different wavelengths can easily be fabricated onto one single substrate by adjusting the number of dipping cycles and the substrate coverage.

In conclusion we have demonstrated efficient second-harmonic generation due to mixing of counterpropagating beam in organic waveguides for the first time. We have measured large nonlinear cross sections both for single films of DANS and DCANP. In the case of DCANP a 4-layer structure (linear/nonlinear) provided an advantageous trade-off between loss and conversion efficiency. The signals measured here are already sufficient for many projected applications.

ACKNOWLEDGEMENTS

We thank J. Ross for fabricating the coupling gratings and U. Stalder for preparing the LB films. The authors acknowledge the support of the Air Force Office of Scientific Research (AFOSR-91-0339).

REFERENCES

1. R. Normandin and G. I. Stegeman, *Opt. Lett.*, **4**, 58 (1979).
2. R. Normandin and G. I. Stegeman, *Appl. Phys. Lett.*, **36**, 253 (1980).
3. R. Normandin and G. I. Stegeman, *Appl. Phys. Lett.*, **40**, 759 (1982).
4. G. I. Stegeman, J. J. Burke and C. T. Seaton, "Nonlinear Integrated Optics", in "Optical Engineering: Integrated Optical Circuits and Components", edited by L. D. Hutcheson, (Marcel Dekker, New York, 1987), Vol. 13.
5. R. Normandin, S. Letourneau, F. Chatenoud and R. L. Williams, *J. Quantum Electron.*, **QE-27**, 1520 (1991); H. Dai, S. Janz, R. Normandin, R. L. Williams and M. Dion, *Electron. Lett.*, **28**, 1540 (1992).
6. D. Vakhshoori and S. Wang, *Appl. Phys. Lett.*, **53**, 347 (1988).
7. D. Vakhshoori, J. Walker, S. Dijaili, S. Wang and J. S. Smith, *Appl. Phys. Lett.*, **55**, 1164 (1989).
8. R. Normandin, R. L. Williams and F. Chatenoud, *Electron. Lett.*, **26**, 2088 (1990).
9. D. Vakhshoori, R. J. Fischer, M. Hong, D. L. Sivco, G. J. Zydzik, G. N. S. Chu and A. Y. Cho, *Appl. Phys. Lett.*, **59**, 896 (1991).
10. R. Normandin, H. Dai, S. Janz, A. Delage, J. Brown and F. Chatenoud, *Appl. Phys. Lett.*, **62**, 118 (1993).
11. G. R. Möhlmann, W. H. G. Horsthuis, C. P. J. M. van der Vorst, A. McDonach, M. Copeland, C. Duchet, P. Fabre, M. B. J. Diemeer, E. S. Trommel, F. M. M. Suyten, P. Van Daele, E. Van Tomme and R. Baets, in *Nonlinear Optical Properties of Organic Materials II*, SPIE **1147**, 245 (1989).
12. M. D. J. Diemeer, F. M. Suyten, E. S. Trommel, A. McDonach, J. M. Copeland, L. W. Jenneskens and W. H. G. Horsthuis, *Electron. Lett.*, **26**, 379 (1990).
13. A. Otomo, S. Mittler-Neher, G. I. Stegeman, W. H. G. Horsthuis and G. R. Möhlmann, *Electron. Lett.*, **29**, 129 (1993).
14. S. Yitzchaik, G. Berkovic and V. Krongauz, *J. Appl. Phys.*, **70**, 3949 (1991).
15. G. Decher, B. Tieke, Ch. Bosshard and P. Günter, *J. Chem. Soc. Chem. Commun.*, **1988**, 933 (1988); G. Decher, B. Tieke, Ch. Bosshard and P. Günter, *Ferroelectrics*, **91**, 193 (1989).
16. Ch. Bosshard, M. Küpfer, P. Günter, C. Pasquier, S. Zahir and M. Seifert, *Appl. Phys. Lett.*, **56**, 1204 (1990).
17. Ch. Bosshard, M. Flörsheimer, M. Küpfer and P. Günter, *Opt. Commun.*, **85**, 247 (1991).
18. M. Flörsheimer, M. Küpfer, Ch. Bosshard, H. Looser and P. Günter, *Adv. Mat.*, **1992**, 795 (1992).
19. Ch. Bosshard, M. Küpfer, M. Flörsheimer and P. Günter, *Mol. Cryst. Liq. Sci. Technol.-Sec. B: Nonlinear Optics*, **3**, 215 (1992).
20. A. Otomo, S. Mittler-Neher, Ch. Bosshard, G. I. Stegeman, W. H. G. Horsthuis and G. R. Möhlmann, *Appl. Phys. Lett.*, **63**, 3405 (1993).
21. Ch. Bosshard, A. Otomo, G. I. Stegeman, M. Küpfer, M. Flörsheimer and P. Günter, *Appl. Phys. Lett.*, **64**, 2076 (1994).
22. N. Asai, H. Tamada, I. Fujiwara and J. Seto, *J. Appl. Phys.*, **72**(10), 4521 (1992).
23. M. Küpfer, M. Flörsheimer, Ch. Bosshard and P. Günter, *Electron. Lett.*, **29**, 2033 (1993).

Phase-Matched Second-Harmonic Generation by Mode Conversion in a $\chi^{(2)}$ -Inverted Waveguide Structure

M. KÜPFER, M. FLÖRSHEIMER^a, Ch. BOSSHARD and P. GÜNTER
*Nonlinear Optics Laboratory, Institute of Quantum Electronics,
Swiss Federal Institute of Technology, ETH Hönggerberg,
CH-8093 Zürich, Switzerland*

Received 12 January 1994; accepted 17 February 1994

Guided-wave frequency-doubling in $\chi^{(2)}$ -inverted 2-docosylamino-5-nitropyridine (DCANP) Langmuir-Blodgett (LB) film waveguides is reported. The nonlinear optically active part of these waveguides consists of two DCANP layers with opposite sign of the nonlinear optical coefficient d_{33} , leading to a large improvement of the overlap integral as compared to conventional waveguides. In first experiments conversion efficiencies up to $1\% \text{ W}^{-1} \text{ cm}^{-2}$ have been obtained.

INTRODUCTION

Thin film optical waveguides are well suited for nonlinear optical applications because they provide strong beam confinement over long propagation distances, leading to high conversion efficiencies in nonlinear optical processes even at the power levels of laser diodes. Second-harmonic generation (SHG) using optical waveguides has been demonstrated in a variety of materials and configurations.^{1–5} In order to obtain high frequency-doubling conversion efficiencies two conditions must be fulfilled simultaneously. The phases of the interacting modes have to be matched and the overlap integral must be optimized.

Recently we have applied a four-layer waveguide configuration to optimize the overlap integral.⁶ The guiding part of that waveguide consists of a linear and a nonlinear optical film. A Langmuir-Blodgett (LB) film of 2-docosylamino-5-nitropyridine (DCANP) has been used as nonlinear layer. A disadvantage of the method used in Ref. 6 is that due to the linear layer only part of the power of the fundamental mode in the waveguide can be used for frequency-doubling. Therefore the SHG conversion efficiency is reduced. In this paper we report on a waveguide configuration where the linear layer is replaced by a second nonlinear optical DCANP LB film with opposite sign of the nonlinear optical susceptibility d_{33} . It will be shown that this leads to a large improvement of the overlap integral and therefore to a much higher SHG conversion efficiency. Independently of us Asai *et al.*, also used a $\chi^{(2)}$ -inverted DCANP waveguide structure for frequency-doubling by the Cerenkov-type configuration.⁷

^a Present address: Physical Institute, University of Münster, D-48149 Münster.

DCANP LANGMUIR-BLODGETT FILMS

The linear and nonlinear optical properties of DCANP are well known and phase-matched SHG in different waveguide configurations has already been reported.^{6,8-10} The LB film fabrication of DCANP leads to a net dipole moment along the dipping direction. This offers the advantage of using the largest nonlinear optical coefficient d_{33} ($d_{33} = 7.8$ pm/V at $\lambda = 1064$ nm) by exciting TE modes in the waveguide.

SECOND-HARMONIC GENERATION IN DCANP WAVEGUIDES

In the non-depleted wave approximation the efficiency η for frequency-doubling by conversion of a guided fundamental mode into a guided second-harmonic mode is given by

$$\eta = \frac{P^{2\omega}}{P^\omega} = \frac{\omega^2 \epsilon_0^2}{4} \frac{P^\omega}{bt} |S|^2 L^2 \sin^2 \left(\frac{2\pi L}{\lambda} (N_{\text{eff}}^{2\omega} - N_{\text{eff}}^\omega) \right) \quad (1)$$

P^ω : power of fundamental wave, L : waveguide interaction length, b : beam width, t : waveguide thickness, N_{eff}^ω , $N_{\text{eff}}^{2\omega}$: effective refractive index at the fundamental and second-harmonic frequency, respectively, λ = wavelength of the fundamental mode, ϵ_0 : vacuum permittivity. S is the overlap integral given by:

$$S = \sqrt{t} \int_0^t d_{33}(y) (E_z^{n,\omega}(y))^2 E_z^{m,2\omega}(y) dy \quad (2)$$

m, n : mode numbers, E_z : z-component of the electric field.

In order to obtain high conversion efficiencies two conditions must be fulfilled:

- i) the phases of the interacting beams have to be matched, i.e., $N_{\text{eff}}^\omega = N_{\text{eff}}^{2\omega}$ and
- ii) the overlap integral S must be optimized.

The phase-matching condition can be fulfilled by a proper choice of the waveguide thickness using modal dispersion given by the mode equation (for TE-modes):

$$t = \frac{\lambda}{2\sqrt{n_s^2 - N_{\text{eff}}^2}} \left[m + \frac{1}{\pi} \left\{ \arctan \sqrt{\frac{N_{\text{eff}}^2 - n_c^2}{n_s^2 - N_{\text{eff}}^2}} \right\} + \arctan \sqrt{\frac{N_{\text{eff}}^2 - n_c^2}{n_s^2 - N_{\text{eff}}^2}} \right] \quad (3)$$

t is the waveguide thickness, N_{eff} is the effective refractive index, n_s and n_c are the refractive indices of the substrate and the cover (air), respectively.

Figure 1 shows as an example the modal dispersion of various TE-modes for $\lambda = 1064$ nm and $\lambda = 532$ nm, respectively. At the marked intersection points the phase-matching condition is fulfilled. In Table 1 the waveguide thicknesses for phase-matching are summarized for the fundamental wavelengths $\lambda = 1318$ nm, $\lambda = 1064$ nm and $\lambda = 926$ nm, respectively.

Due to the tight film thickness control of the LB method (thickness control within 5 nm) phase-matching can easily be achieved by this technique.

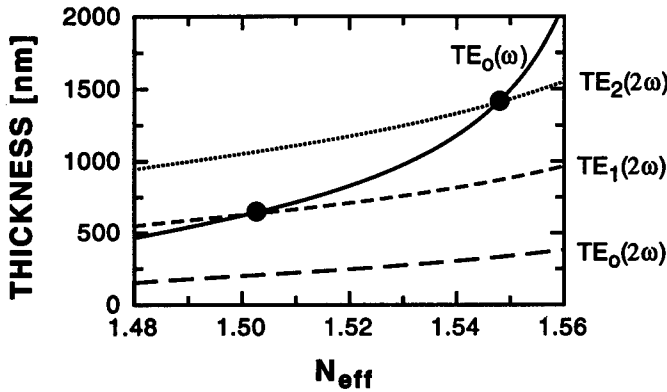


FIGURE 1 Phase-matching conditions for DCANP waveguides on a pyrex substrate ($TE_0 \rightarrow TE_1$, $TE_0 \rightarrow TE_2$). Fundamental wavelength $\lambda = 1064$ nm.

However, even in the case of phase-matched SHG the frequency-doubling efficiency is small unless the overlap integral S is optimized. If the product of the field distributions changes sign across the waveguide the value of S is strongly reduced. Therefore in the case of a 3-layer waveguide the overlap integral is small unless all the interacting modes have the same mode number (Fig. 2(c)). In the 3-layer DCANP waveguide (substrate-DCANP-air), however, efficient conversion of a fundamental mode to a second-harmonic mode with equal mode number is not possible because the phase-matching condition cannot be fulfilled for this case.

Recently we introduced a four-layer optical waveguide consisting of both nonlinear and linear materials.⁶ The linear material is used as a part of the guiding layer in order to reduce destructive interference effects in the overlap integral. A disadvantage of the method used in Reference 6 is that due to the linear layer only part of the power of the fundamental mode in the waveguide can be used for SHG.

We now introduce an improvement of the method described in Reference 6. Figure 2(c) shows the transverse electric field distribution of a fundamental TE_0 and a second-harmonic TE_1 mode (which are phase-matched) in a 3-layer (substrate-DCANP-air) waveguide. The overlap integral S is small because the product of the electric field distributions changes sign across the waveguide (dotted line in Fig. 2(c)).

TABLE 1
Phase-matching conditions for DCANP waveguides ($TE_0 \rightarrow TE_1$, $TE_0 \rightarrow TE_2$).

Wavelength[nm]	Mode at ω	Mode at 2ω	Thickness[nm]	n_3	N_{eff}
1318	TE_0	TE_1	1080 ± 65	1.569	1.519 ± 0.006
1318	TE_0	TE_2	2340 ± 190	1.569	1.555 ± 0.004
1064	TE_0	TE_1	635 ± 20	1.574	1.502 ± 0.004
1064	TE_0	TE_2	1420 ± 84	1.574	1.548 ± 0.003
926	TE_0	TE_1	391 ± 10	1.587	1.473 ± 0.003
926	TE_0	TE_2	850 ± 23	1.587	1.532 ± 0.003

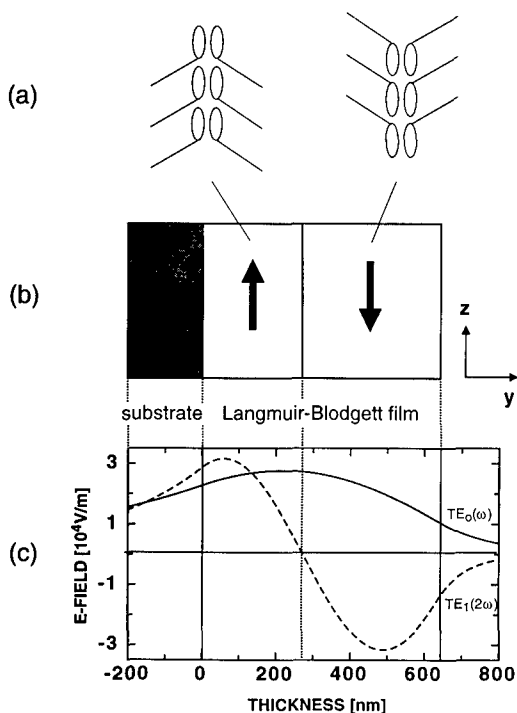


FIGURE 2 (a) orientation of the DCANP molecules in the LB films (schematic), (b) waveguide configuration consisting of a substrate (pyrex) and the two DCANP LB films with opposite sign of the nonlinear optical susceptibility d_{33} , (c) transverse electric field distribution of a fundamental TE_0 and a second-harmonic TE_1 mode in a 3-layer (substrate-DCANP-air) waveguide. Fundamental wavelength $\lambda = 1064$ nm.

According to equation (2), however, the sign change of the integrand of S can be avoided by inversion of the sign of the nonlinear optical susceptibility d_{33} at the dotted line in Figure 2(c). The guiding layer of this new waveguide structure therefore consists of two DCANP LB films with opposite sign of d_{33} . Figure 2(a) schematically shows the different orientations of the DCANP molecules in the two LB films. As can be seen the polar axes (charge-transfer axes) of the molecules are pointing in opposite directions, leading to the sign change of d_{33} .

Using the LB technique the fabrication of such a d_{33} -inverted waveguide structure is very easy. After the deposition of the first DCANP film the sample is rotated by 180° around an axis perpendicular to the substrate plane. Afterwards the second DCANP LB film is deposited.

EXPERIMENTAL RESULTS

Phase-matched conversion of a fundamental TE_0 -mode into a second-harmonic TE_1 -mode in a d_{33} -inverted DCANP waveguide on a pyrex substrate has been

TABLE 2

Overlap integral S , SHG efficiency η_{theor} and SHG efficiency η_{meas} for several waveguide configurations (beam width: 250 μm , attenuation losses are neglected in the calculation of η_{theor}).

$\lambda[\text{nm}]$	Configuration	Modes	$S[\text{V}^{1/2}\text{A}^{-3/2}\text{m}]$	$\eta_{\text{theor}}[\% \text{W}^{-1}\text{cm}^{-2}]$	$\eta_{\text{meas}}[\% \text{W}^{-1}\text{cm}^{-2}]$
1064	3-layer	$\text{TE}_0\text{--TE}_1$	$4 \cdot 10^{-9}$	0.2	—
1064	3-layer	$\text{TE}_0\text{--TE}_2$	$8 \cdot 10^{-9}$	0.6	—
926	4-layer	$\text{TE}_0\text{--TE}_1$	$16 \cdot 10^{-9}$	9	0.5
1064	d_{33} -inverted	$\text{TE}_0\text{--TE}_1$	$48 \cdot 10^{-9}$	9	1
1064	d_{33} -inverted	$\text{TE}_0\text{--TE}_2$	$92 \cdot 10^{-9}$	15	—

demonstrated for the following set of parameters: fundamental wavelength $\lambda = 1064$ nm, thicknesses of the DCANP LB layers: 274 nm and 361 nm, respectively (see Fig. 2). The refractive indices are: $n_{\text{pyrex}}(\omega) = 1.467$, $n_{\text{pyrex}}(2\omega) = 1.474$, $n_{\text{DCANP}}(\omega) = 1.574$ and $n_{\text{DCANP}}(2\omega) = 1.625$. The corresponding effective refractive indices are $N_{\text{eff}}^\omega = N_{\text{eff}}^{2\omega} = 1.502$.

Using equation (2) we calculated the overlap integral for this d_{33} -inverted structure obtaining a value of $S = 48 \cdot 10^{-9} \text{ V}^{1/2} \text{A}^{-3/2} \text{m}$. In the case of the conventional 3-layer (substrate-DCANP-air) waveguide the corresponding overlap integral has a value of only $4.4 \cdot 10^{-9} \text{ V}^{1/2} \text{A}^{-3/2} \text{m}$. Hence the calculated frequency-doubling efficiency in the d_{33} -inverted configuration is more than 100 times larger than in the 3-layer waveguide. Our measurements were carried out using a Q -switched Nd:YAG laser (BMI 501 DNS: wavelength $\lambda = 1064$ nm, pulse width: 25 ns, repetition rate $f = 30$ Hz). Coupling into the waveguides was performed with gratings (coupling efficiencies of about 3%). The second-harmonic light was decoupled through the edge of the sample and was detected with a photomultiplier.

In our preliminary measurements we obtain SHG efficiencies $\eta_{\text{conv}}^{\text{means}} = P^{2\omega}/P^\omega$ (P^ω : power inside of the film) for the conversion of a fundamental TE_0 -mode into a second-harmonic TE_1 -mode of up to $2.4 \cdot 10^{-2}$ ($P^\omega = 240$ W, nonlinear optical coefficient $d_{33} = 7.8$ pm/V, beam width: 0.25 mm, interaction length: 1 mm) yielding a normalized conversion efficiency of $\eta_{\text{norm}} = 1\% \text{ W}^{-1} \text{cm}^{-2}$. This corresponds reasonably to the calculated conversion efficiency $\eta_{\text{calc}} = 5\% \text{ W}^{-1} \text{cm}^{-2}$ if one considers the attenuation of the modes that was neglected in the theory.

Table 2 shows a comparison of the overlap integral S and the calculated SHG efficiency η_{theor} for several waveguide configurations (beam width: 250 μm , attenuation losses are neglected).

CONCLUSION

We have demonstrated phase-matched second-harmonic generation by mode conversion in a new waveguide structure fabricated by the Langmuir-Blodgett (LB) technique. The nonlinear optical active part of the waveguide consists of two 2-docosylamino-5-nitropyridine (DCANP) LB layers with opposite sign of the nonlinear optical coefficient d_{33} . It has been shown that the overlap integral and thus the SHG conversion efficiency in this configuration is much larger than for a conventional

waveguide. In our first experiments maximum conversion efficiencies up to 1% $\text{W}^{-1}\text{cm}^{-2}$ were obtained. This new waveguide configuration is therefore very useful to improve frequency-doubling efficiencies.

ACKNOWLEDGEMENT

The authors would like to thank U. Stalder for LB film preparation and J. Ross and G. Stegeman (CREOL, Florida) for the fabrication of the gratings. This work was partly supported by the Swiss National Foundation (NFP 24: *Chemistry and Physics of Surfaces*).

REFERENCES

1. G. I. Stegeman and C. T. Seaton, *J. Appl. Phys.*, **58**, R57 (1985).
2. K. D. Singer, J. E. Sohn and S. L. Lalama, *Appl. Phys. Lett.*, **49**, 248 (1986).
3. M. G. Roelofs, W. Bindloss, A. Suna, J. D. Lee and J. D. Bierlein, *Advanced Solid-State Lasers and Compact Blue-Green Lasers Technical Digest*, Vol. **2**, 485 (1993).
4. D. Fluck, P. Günter, M. Fleuster and C. Buchal, *Advanced Solid-State Lasers and Compact Blue-Green Lasers Technical Digest*, Vol. **2**, 473 (1993).
5. K. Yamamoto, K. Miuuchi, Y. Kitaoka and M. Kato., *Appl. Phys. Lett.*, **62**, 2599 (1993).
6. M. Flörshheimer, M. Küpfer, Ch. Bosshard, H. Looser and P. Günter, *Adv. Mater.*, **4**, 795 (1992).
7. N. Asai, H. Tamada, I. Fujiwara and J. Seto, *J. Appl. Phys.*, **72**, 4521 (1992).
8. Ch. Bosshard, M. Küpfer, P. Günter, C. Pasquier, S. Zahir and M. Seifert, *Appl. Phys. Lett.*, **56**, 1204 (1990).
9. Ch. Bosshard, M. Flörshheimer, M. Küpfer and P. Günter, *Opt. Commun.*, **85**, 247 (1991).
10. Ch. Bosshard, M. Küpfer, M. Flörshheimer and P. Günter, *Mol. Cryst. Liq. Sci. Technol.-Sec. B: Nonlinear Optics*, **3**, 215 (1992).

Experimental Investigation of Second Harmonic Generation from Organic Waveguides Deposited on Diffraction Gratings

J.-L. COUTAZ¹, G. BLAU², J.-F. ROUX², R. REINISCH², F. KAJZAR³,
P. RAIMOND³, P. ROBIN⁴, E. CHASTAING⁴ and P. LE BARNY⁴

¹LAHC, Université de Savoie, F-73 376 LE BOURGET DU LAC CEDEX, France, ²LEMO-ENSERG, URA-833 CNRS, BP 257, F-38016 GRENOBLE CEDEX 1, France, ³DEIN/SPE, CEN Saclay, F-91 191 GIF SUR YVETTE CEDEX, France, ⁴LCR, Thomson-CSF, Domaine de Corbeville, F-91 404 ORSAY CEDEX, France

Received 30 January 1994; accepted 23 February 1994

We study second harmonic generation from organic waveguides deposited on metallic diffraction gratings. Depending on the experimental conditions, we observe maxima or minima in the second harmonic reflectivity curve when guided modes at pump frequency are excited. These results show the importance of the diffraction process and of the absorption at the second harmonic frequency. We detect also two-photon absorption induced luminescence, which is coupled into the waveguide and diffracted by the grating.

INTRODUCTION

Second harmonic (SH) generation in nonlinear waveguides is one of the ways to produce compact blue light sources. As compared to a bulk device, the guiding structure presents many advantages such as high guided pump power density over long distances, modal propagation and easy fabrication. This geometry is well adapted to the organic materials, which can be deposited in thin films and exhibit large nonlinear coefficients.

However, there still remain some technical difficulties in using organic waveguide structures for SH generation. The first one is the access problem: for the usual butt coupling of the laser beam in the organic layer, the face of the waveguide extremities should be as sharp and clean as possible in order to reduce the input losses. This can be difficult to achieve with spin-coated polymer films. Another way of injecting the pump light in the layer consists of employing a coupler, like a prism or a grating. The grating is more compact than the prism, and it can be fabricated by lithography during the whole fabrication process of the wafer. The second key problem of waveguide SH generation is how to obtain phase-matching between the guided waves at ω and 2ω . Nowadays, among many others, the most common method is the quasiphase-matching one, which requires a periodic value of the nonlinear susceptibility all along the waveguide. Such a technique is commonly applied to crystals like LiNbO_3 ,¹ but less to organic waveguides² because of technological difficulties resulting from the periodical poling process of the

nonlinear layer. It is also possible to compensate for the mismatch of the light velocities at ω and 2ω by a grating etched at the surface of the waveguide: the difference between the wavevectors at ω and 2ω should be equal to a multiple of the wavevector associated to the grating. This idea was first proposed by Somekh and Yariv,³ in the case of structures similar to distributed feedback laser cavities. It should be noted that such a phasematching can be achieved between the fundamental modes both at ω and 2ω .

Considering the potentiality of the gratings as optical couplers and as tools to achieve phase-matching, it appears to us interesting to study these devices, with regard to the influence of several parameters like absorption at 2ω and grating diffraction on the SH generation. These preliminary studies are necessary before starting experiments on grating-assisted phasematched SH generation, which requires long propagation lengths. It is in this framework that we present here some experimental results of SH generation from planar organic waveguides deposited over silvered diffraction gratings. In addition, we present results on the generation of luminescence light induced by two-photon absorption in the organic material, which is resonantly enhanced in the waveguide.

EXPERIMENTAL SET UP

The studied structure is shown in Figure 1. The grating is fabricated⁴ by photolithography and reactive ion etching of the substrate, which can be either a wafer of fused silica or of glass. The groove profile is rectangular. We use a full set of gratings, with periodicities ranging from 0.5 up to 2 μm , and groove depths from 0.03 up to 0.2 μm . A 0.2 μm silver layer is evaporated onto the grating. Then a film of polymer is spin coated over the device. The upper surface of the organic film is generally flat. The organic material is poled by a corona discharge, using the silver film as lower electrode.

We are using two types of nonlinear polymers. The first one is a chromophore of 1-dicyanovinyl-4-diethylamino benzene (DCVDAB) in methyl-methacrylate. It is synthesised by CEA and the chromophore concentration is 15%. The second one is a copolymer of methylmethacrylate and 4 (N-methacryloyloxy propyl N-methyl-amino) 4' cyanobiphenyl (PLBP 80) from Thomson-CSF. Both materials exhibit a $d_{33}(2\omega)$ coefficient of about 10 pm/V. As shown in Figure 2, PLBP 80 is transparent over the whole visible spectrum, while DCVDAB presents its strongest absorption at 430 nm.

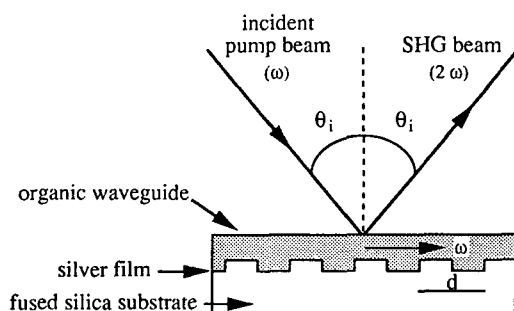


FIGURE 1 Geometry of the studied grating coupler.

The devices are illuminated by a *Q*-switched laser, which is either a Nd:YAG laser ($\lambda = 1.064 \mu\text{m}$) or a Ti:Sa laser ($\lambda = 0.72\text{--}0.86 \mu\text{m}$) pumped by the SH light of the Nd:YAG laser. The pulse duration is 10 ns and the repetition rate is 10 Hz. A part of the pump beam feeds a reference way, in which 2ω light is produced by a KDP or a quartz crystal. The signals from the grating device and the reference are detected by photomultiplier tubes through spectrometers, in front of which colored glass filters stop the remaining pump light. Both signals are processed by a boxcar and a computer which delivers the ratio of both signals, averaged over 30 laser shots. The highest pump power density at the sample location is about 0.1 MW/cm^2 ; for most of the measurements presented here, this value is strongly reduced. At this level of power, we neither observe destruction of the organic layer nor reduction of the SH signal due to photochemical breaking of the chromophores, even when the SH wavelength falls in the absorption band of the polymer.

EFFECT OF COUPLING THE PUMP LIGHT IN THE WAVEGUIDE

The grating is illuminated by the pump beam at the incidence θ_i . The pump light is coupled in the waveguide when the component of the incident wavevector parallel to the mean grating surface is equal to the guided wavevector plus m times the wavevector associated to the grating, where m is an integer. This condition can be reduced to the following relation:

$$\sin \theta_i + \frac{m\lambda}{d} = n_{\text{eff}} \quad (1)$$

where n_{eff} is the effective index of a guided mode, λ is the pump wavelength and d is the grating periodicity. When equation (1) is fulfilled, a resonance at pump frequency occurs, and most of the pump light energy is coupled in the waveguide. Because of the

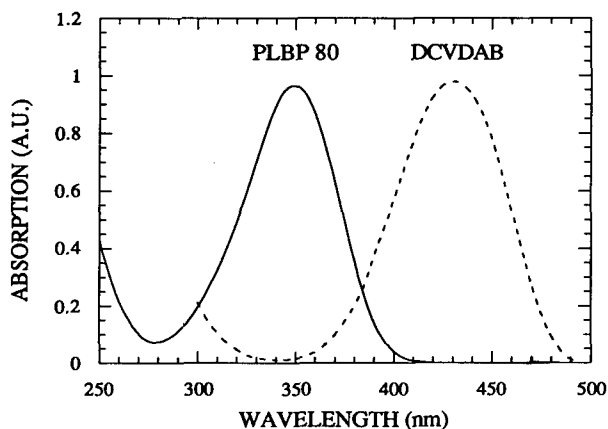


FIGURE 2 Absorption of the polymers versus wavelength. The maxima of absorption of the two curves have been normalized to 1.

optical losses of the polymer film and of the silver layer, a part of the energy is absorbed, which leads to a minimum in the reflected beam. This corresponds to the well-known M-line, whose angular position is mainly determined by the real part of the effective index of the mode. The coupling of the pump light gives a maximum of pump power in the waveguide, leading to an increased value of the nonlinear polarization in the guiding layer. Therefore, we expect that the 2ω diffracted and detected light, for which the nonlinear polarization is the source term, exhibits a peak intensity for the coupling angle.

Such an expected result is seen on Figure 3, where we plot the linear reflexion coefficient and the SH generated signal versus the angle of incidence. In this experiment, the pump wavelength at 844 nm falls out of the absorption band of the PLBP 80 waveguide material. The thickness of the waveguide is $0.92\ \mu\text{m}$ and the periodicity of the grating is $d = 0.7\ \mu\text{m}$. The deep minimum of the reflectivity at 18.3° corresponds to the excitation of the TM_0 mode at the pump wavelength. At the same incidence, the SH signal shows a strong peak. As compared to the off-resonance signal, the enhancement is more than 100. Let us notice that, as expected, the angular width of the SH signal is smaller than that of the linear reflectivity. Similar SH enhancements were already reported for bare silver gratings, which allow the excitation of surface plasmons at pump frequency.^{5,6}

However, when the pump wavelength is tuned towards a smaller value, the angular spectrum of the SH signal exhibits a very different behaviour. This is seen in Figure 4 where, for the same device, we see a minimum of the SH signal for the coupling angle of the mode TM_0 at the 740 nm pump wavelength. This unexpected behaviour was already reported for a polyurethane waveguide deposited on a sinusoidal silver grating (7). It is tempting to relate this phenomenon to the absorption of the SH light, since in the present work, as well as in the case of Reference 7, decreasing the pump wavelength locates the SH wavelength closer to the maximum of the polymer absorption range.

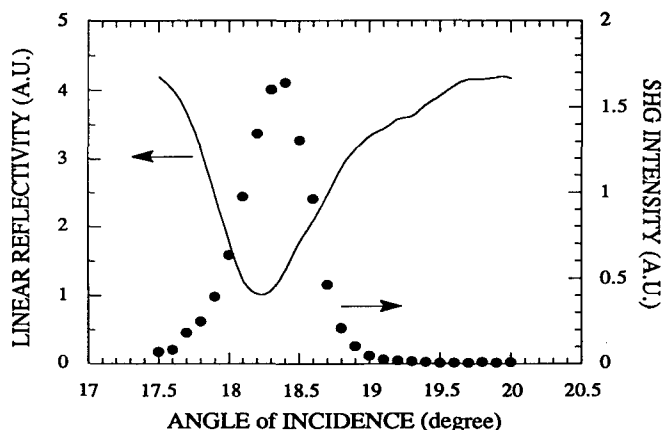


FIGURE 3 Linear reflectivity (continuous curve) and SH intensity (full circles) of the device versus the angle of incidence. The SH intensity is measured in the specular direction. The organic material is PLBP 80, the layer thickness is $0.92\ \mu\text{m}$. The pump wavelength is 844 nm (TM polarization), the grating periodicity is $0.7\ \mu\text{m}$.

This hypothesis has been checked by tuning the pump wavelength in such way that the SH wavelength sweeps the absorption peak of the polymer. It is also expected to observe the influence of the increase of the $d_{33}(2\omega)$ nonlinear coefficient (in the absorption band at 2ω) on the SH generation.⁸ We use a $1\text{ }\mu\text{m}$ thick waveguide made of DCVDAB deposited over a $1.5\text{ }\mu\text{m}$ periodicity grating. We explore the wavelength domain 720–860 nm, which corresponds to an increase of the absorption at 2ω , as we are now located on the short wavelength side of the absorption band at 2ω . But, when changing the pump wavelength, one has also to vary the incident angle in order to couple the light in the waveguide, because of the changing term λ/d (diffraction of the grating) and the mode dispersion in equation (1). The excitation angle of the mode is plotted versus the wavelength in Figure 5. We see the position of the different co- and contra-propagating modes (surface plasmon, TM_0 , TM_1 , TM_2), excited by different orders of diffraction of the grating (different values of m in equation (1)). The SH experiment is performed following the dispersion curve of the TM_0 mode excited by the +1 order of diffraction. For each wavelength, we record the SH signal angular dependence, and we determine the enhancement as being the ratio of the SH signals at the resonance angle and out of resonance. When the enhancement value is greater than 1, this corresponds to an increase of the SH signal leading to a peak in the angular spectrum. On the other hand, if the enhancement is less than 1, a dip is seen in the angular spectrum, as in Figure 4. The enhancement value is then plotted versus the pump wavelength in Figure 6. In the same figure, we also report the optical density of the polymer film at half the pump frequency. We see that the enhancement decreases when the absorption at 2ω increases. This enhancement curve seems to confirm the hypothesis of the existence of the minima in the SH spectrum due to absorption at 2ω . In addition, we observe in Figure 6 irregularities in the shape of the enhancement curve, occurring at wavelengths corresponding to the crossing points of the modal linear dispersion curves (see Fig. 5). At these peculiar points, the grating diffraction induces a

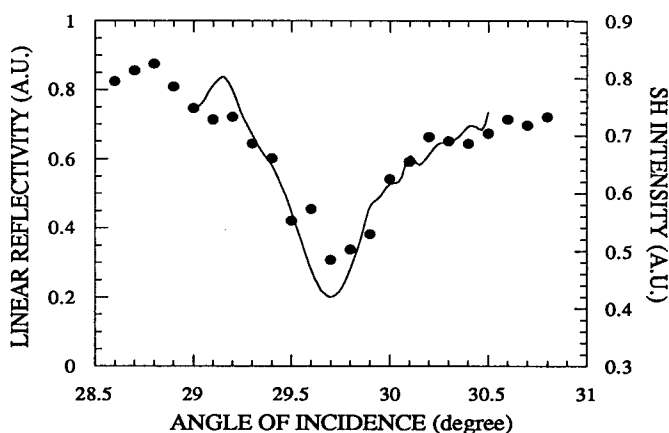


FIGURE 4 Linear reflectivity (continuous curve) and SH intensity (full circles) of the device versus the angle of incidence. The experimental conditions are the same as for Figure 3, except the pump wavelength which is now 740 nm.

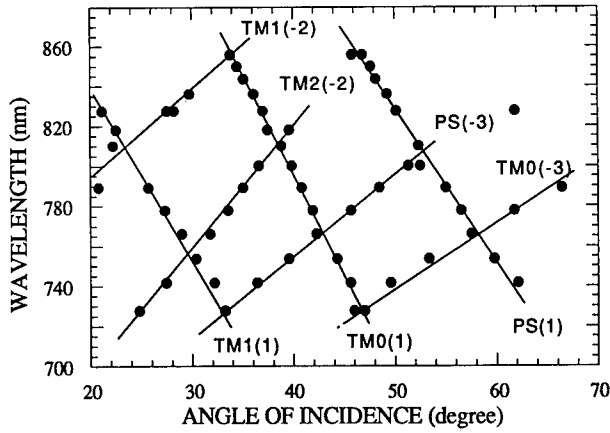


FIGURE 5 Experimental dispersion curves of the DCVDAB waveguide (thickness $1\text{ }\mu\text{m}$) on the $1.5\text{ }\mu\text{m}$ periodicity grating. The angular position of the observed M-lines is plotted versus the wavelength. The notation $\text{TM}_p(m)$ indicates the p mode of the guide excited by the order of diffraction m . Negative values of m correspond to contra-propagative guided modes.

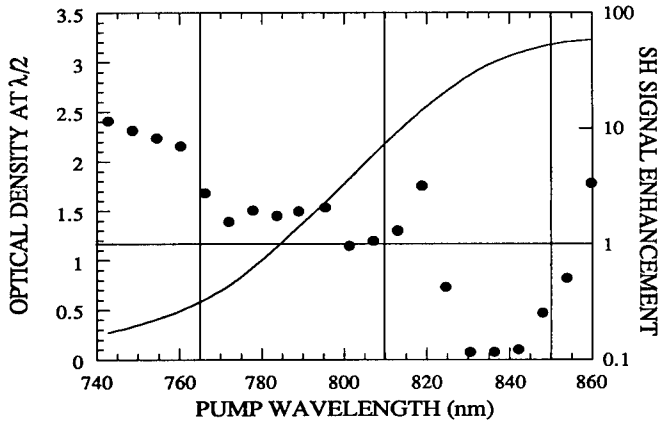


FIGURE 6 SH enhancement (full circles) and optical density (continuous line) at $\lambda/2$ versus the pump wavelength. The device is the same as for Figure 5. The enhancement is defined as the ratio of the SH signals at the angular resonance and out of resonance. The positions of the crossing points deduced from Figure 5 is shown by the vertical lines.

linear coupling between different contra-propagating modes. These wavelengths, deduced from Figure 5, are indicated by vertical lines in Figure 6. This enhancement curve shape leads us to conclude that the linear diffraction plays also a major role in the studied phenomenon, because the crossing of the dispersion curves is a pure diffractive effect independant of the material absorption. At least, the results of this experiment show that the expected higher value of $d_{33}(2\omega)$ in the absorption band at 2ω does not result, in the present experimental geometry, in an enhancement of the measured SH signals.

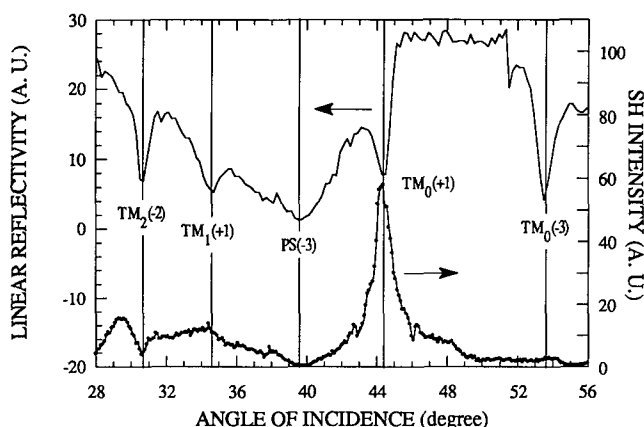


FIGURE 7 Linear reflectivity and SH intensity of the same device (see Fig. 5) versus the angle of incidence. The vertical lines corresponds to the M-line angular positions deduced from Figure 5.

The role of the diffraction in the SH generation from the grating coupler is also revealed by the following experiment. We measure, with the same device, the SH signal for the whole attainable angular range, i.e., from 30 up to 60°. This is done at the pump wavelength of 754.5 nm, for which the SH wavelength is not at the center of the absorption band. The linear reflectivity and the SH signal are plotted versus the angle of incidence on Figure 7. The vertical lines indicate the position of the M-lines deduced from Figure 5. For some of the modes, we observe a peak at 2ω (for example TM_0 excited in the +1 order of diffraction); for some others, we see a dip instead of a peak (for example TM_2 excited in the -2 order of diffraction); finally, for the remaining modes, we observe no special behaviour of the SH signal (as for TM_0 excited in the -3 order of diffraction).

All the reported curves (Figs. 2, 3, 5 and 6) demonstrate that the SH generation from a nonlinear waveguide deposited over a metallic grating depends strongly on both the absorption at 2ω and on the diffraction process. A theoretical analysis, which allows us to distinguish the influence of absorption from that of the diffraction on the resonant SH generation, is in progress.

NONLINEAR EXCITATION OF GUIDED MODES AT 2ω

Another type of coupling can be observed in such experiment. The linear reflectivity curve exhibits no M-line structure as we are far from any angular resonance at ω . Therefore, only a small part of the incident power is refracted into the polymer film, without any guiding effect. This pump beam produces SH light in the film, which is characterized by a longitudinal wavevector equal to twice that of the incident pump beam. When this 2ω longitudinal wavevector is equal to the effective wavevector of a guided mode at 2ω , the generated SH light is coupled to this mode and then outcoupled by the grating. This leads to an increase of the diffracted SH signal, as seen in Figure 8.

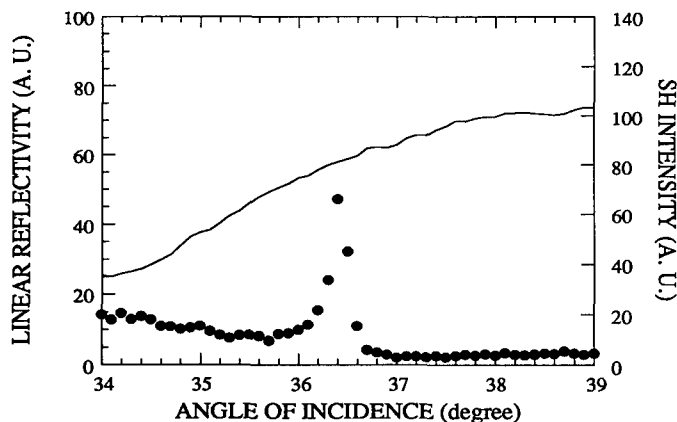


FIGURE 8 Linear reflectivity (continuous curve) and SH intensity (full circles) of the same device (see Fig. 5) versus the angle of incidence. The pump wavelength is now $1.064\ \mu\text{m}$. Excitation of guided modes at pump frequency does not occur in the experimental angular range. The peak of the SH intensity corresponds to the nonlinear excitation of the TM_1 mode at 2ω .

These experimental data have been recorded at a pump wavelength of $1.06\ \mu\text{m}$ with the DCVDAB material, for which the SH wavelength is far from the absorption range. Such a type of nonlinear coupling was already reported for SH generation with gratings etched in a GaAs-Al substrate.⁹

TWO-PHOTON ABSORPTION INDUCED LUMINESCENCE

It is known that organic materials may present relatively high two-photon absorption giving rise to an induced luminescence, when the SH frequency is at half the band gap of the material.¹⁰ Such a phenomenon is observed with the PLPB 80 layer (thickness $0.92\ \mu\text{m}$) deposited over a metallic grating (period $d = 0.5\ \mu\text{m}$). In the present case, the two-photon absorption induces a luminescence signal, ranging from 400 up to 550 nm with a maximum at 440 nm. We have checked¹¹ that this luminescence signal is actually due to two-photon absorption and not to the absorption of the SH light generated in the polymer film: indeed, with *s*-polarized pump light, a weak SH light is generated in the polymer, but we still observe a strong luminescence signal. Moreover, the luminescence intensity varies as the square of the pump light intensity.

At the low level of power we are working with, the luminescence is spontaneous, giving rise to an incoherent light pattern, which is radiated over the whole space. A part of this light couples to the modes of the polymer film, and is then diffracted by the grating. The direction θ_{det} of the diffracted beam at the luminescence wavelength λ_{lum} is given by the following relation:

$$n_{\text{eff}}^p(\lambda_{\text{lum}}) + \frac{q\lambda_{\text{lum}}}{d} = \sin \theta_{\text{det}}(\lambda_{\text{lum}}) \quad (2)$$

where q is an integer and n_{eff}^p is the effective index of the mode p of the waveguide.

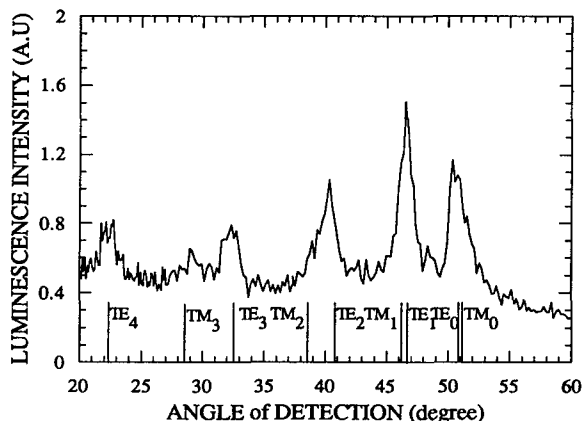


FIGURE 9 Luminescence at 450 nm versus the angle of detection. The device is the same as for Figure 3, but the pump wavelength is now 740 nm and the grating periodicity is 0.5 μm . The angle of incidence (29.6°) permits the coupling of the pump light to the TM_0 mode of the guide. The polarization of the detected luminescence is not selected.

Relation 2 can be verified in two experiments: either we set the angle of detection fixed and we tune the detected wavelength, or we fix the detected wavelength while the detector is rotated around the grating. Only the results of the last procedure are presented here. When relation 2 is fulfilled, we should detect a peak in the angular spectrum of the luminescence corresponding to $\theta_{\text{det}}(\lambda_{\text{lum}})$. This is verified in Figure 9 where we plot the luminescence signal recorded at 450 nm versus the detection angle. The incident angle is set to 29.6° , in such a way that the TM_0 mode is excited at 740 nm. We observe a background which corresponds to the incoherent radiated luminescence. Peaks are detected in the directions of the diffracted guided modes: the positions of the diffracted modes, deduced from a linear experiment, are indicated by vertical lines in Figure 9.

Therefore, we are looking at a two-resonance phenomenon: both the pump light and the luminescence are resonantly coupled in the waveguide. Such a double resonance effect has already been observed in other nonlinear experiments, like Surface Enhanced Raman Scattering.¹² It allows us to detect the two-photon absorption induced luminescence of small amount of material.

However, such a phenomenon can reduce the efficiency of frequency doublers working at wavelengths close to half the band gap. On the other hand, it is known that the nonlinear coefficients are increased in this range of frequency.⁸ Therefore a compromise between the value of the nonlinearity and the two-photon absorption should be found to optimize such devices. Moreover, this kind of experiment may also lead to new waveguide laser configuration.¹³

CONCLUSION

SH generation in organic waveguides using grating couplers is a complex phenomenon involving many different effects. Among all these effects, our experimental results show

that diffraction and two-photon absorption play a major role. Indeed, depending on the experimental conditions, one can observe either a large enhancement of the SH signal or a strong decrease with the same device. Therefore, the realization of an efficient frequency doubler is related to the understanding of these basic effects. The required theoretical analysis of the SH generation from periodically corrugated waveguides is now in progress. This will help us to find the optimized geometrical parameters of the device.

REFERENCES

1. J. Webjöm, F. Laurell and G. Arvidsson, *IEEE J. Lightwave Technol.*, **7**, 1597 (1989).
2. G. Khanarian, R. A. Norwood, D. Hass, B. Feuer and D. Karim, *Appl. Phys. Lett.*, **57**, 977 (1990).
3. S. Somekh and A. Yariv, *Appl. Phys. Lett.*, **21**, 140 (1972).
4. The gratings are fabricated by CSEM, case postale 41, CH-2007 Neuchâtel, Switzerland.
5. J. L. Coutaz, M. Nevière, R. Reinisch and E. Pic, *Phys. Rev. B*, **32**, 2227 (1985).
6. J. C. Quail and H. J. Simon, *J. Opt. Soc. Amer. B*, **5**, 325 (1988).
7. M. Kull, J. L. Coutaz and R. Meyrueix, *Opt. Lett.*, **16**, 1930 (1991).
8. C. C. Teng and A. F. Garito, *Phys. Rev. B*, **28**, 6766 (1983).
9. Z. Chen, D. Cui, H. Lu and Y. Zhou, *Opt. Lett.*, **8**, 563 (1983).
10. G. S. He, J. Zieba, J. T. Bradshaw, M. R. Kazmierczak and P. N. Prasad, *Opt. Commun.*, **104**, 102 (1993).
11. J. F. Roux, J. L. Coutaz, P. le Barny, E. Chastaing and P. Robin, "Two-photon absorption induced luminescence and second harmonic generation in organic waveguides" in *Organic Thin Films for Photonic Applications Technical Digest*, 1993, Vol. **17** (Optical Society of America, Washington, D.C., 1993) pp. 165–168.
12. N. Primeau, J. L. Coutaz and L. Abello, *J. Appl. Phys.*, **73**, 5158 (1993).
13. A. Mukherjee, *Appl. Phys. Lett.*, **62**, 3423 (1993).

Electromagnetic Analysis of Nonlinear Couplers: Application to Nonlinear m-Line Techniques

R. REINISCH and G. VITRANT

*Laboratoire d'Electromagnétisme Microondes et Optoélectronique,
ENSERG, 23 ave des Martyrs, BP 257, 38016 Grenoble Cedex, France*

Received 8 February 1994; accepted 17 February 1994

A unified theory of Kerr-type optical resonators is presented with an emphasis placed on Kerr-type grating couplers. The so-called nonlinear m-line is shown to be one of many phenomena exhibited by such nonlinear devices. A spatio-temporal set of equations are derived which fully describe the nonlinear m-line effect. By comparing with the corresponding results, the nonlinear m-line technique yields not only the real part of χ^3 but also the imaginary part of χ^3 . Thus the nonlinear m-line spectroscopy appears as a powerful tool for the characterisation of the χ^3 -properties of nonlinear thin films, in general, and of organic guiding layers in particular.

INTRODUCTION

One of the characteristics of organic materials is that they lend themselves easily to the realisation of thin films by spin-coating. This feature, in addition to their attractive nonlinearity (short response time (ps or less), high nonlinearity not only for χ^3 but also for χ^2), makes organics good candidates for guided wave nonlinear optics.

There are, at least, two ways to excite guided waves:

- * but-coupling: this technic is difficult to implement since these materials are not easy to cleave,
- * distributed couplers : prism or grating couplers (Fig. 1).

It is in this last type of devices which we will be interested since they are well adapted to organics and we concentrate on χ^3 -media.

In fact, as we show, these couplers belong to a much wider class of devices which we call nonlinear optical resonators: the χ^3 -Fabry-Pérot is another example of such resonators. In those χ^3 -optical resonators, the nonlinear medium exhibits an intensity dependent index of refraction: self-focusing or self-defocusing. The different types of responses of χ^3 -resonators are accounted for by an involved spatio-temporal analysis.^{1,2}

When observed in the far-field, the output signal may show a dip³ (Fig. 2) which is the signature of the resonant excitation of a normal mode of the coupler. This is the so-called m-line. Also the shape of this line is intensity dependent³ (Fig. 2) leading, in this way, to a nonlinear m-line. From these χ^3 -induced modifications, it is possible to deduce not only the real part of χ^3 but also its imaginary part related to the two photon

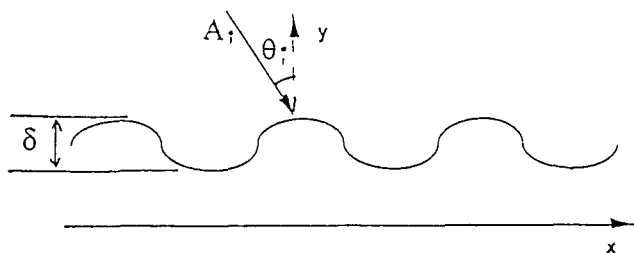


FIGURE 1 A grating coupler with the notations: y and x are respectively the transverse and the longitudinal coordinates.

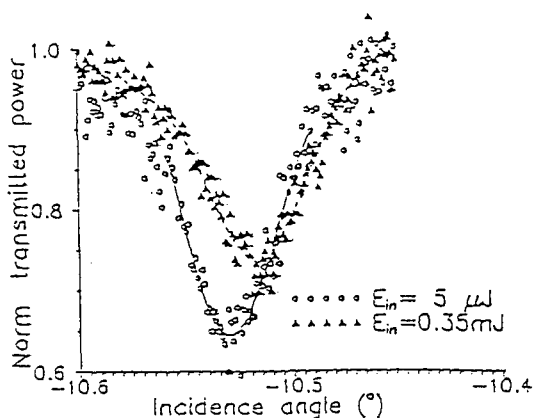


FIGURE 2 Linear and nonlinear m-line(after Ref. 3).

absorption. Moreover, "classical" or "exotic" bistable loops (Fig. 3) has been predicted^{4,5} and observed.⁶ The space-time dependence of the output of nonlinear Fabry-Pérot filled with CS_2 and illuminated by a ps laser pulse has been studied⁷ from an experimental and theoretical point of view (Fig. 4). This very brief list of results shows the wealth of responses exhibited by χ^3 -resonators. One could also add: self-pulsing, chaos...

It is the aim of this paper to present a unified theory of χ^3 -resonators. Section II is devoted to the theoretical study of these resonators. The m-line, linear and nonlinear, is considered in Section III along with some experimental results which will be dealt with in more detail in another paper⁸ of this issue.

NONLINEAR OPTICAL RESONATORS

General Considerations

Prism couplers, grating couplers or Fabry-Pérot allows the resonant excitation of:

- * guided modes for prism or grating couplers,
- * Airy resonances for a Fabry-Pérot

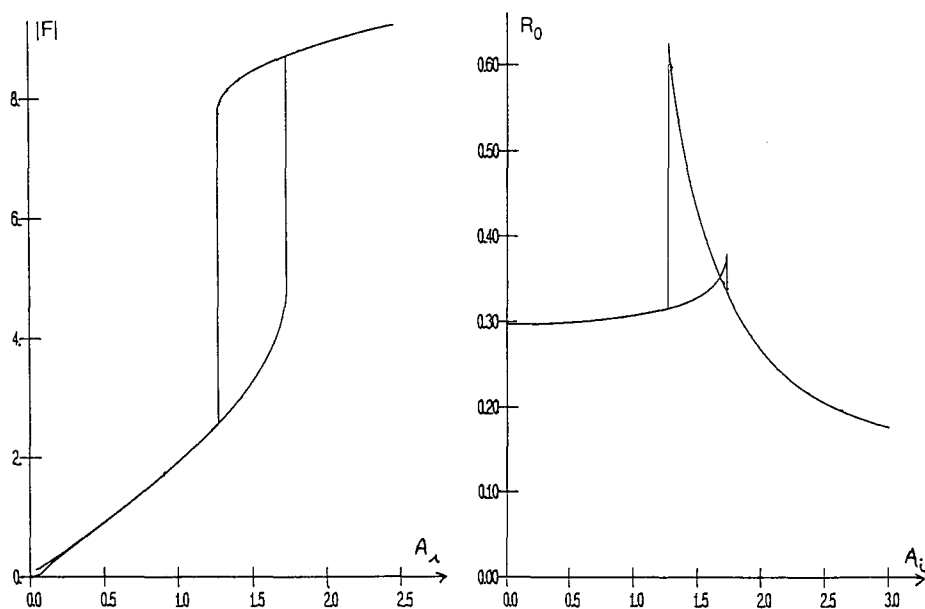


FIGURE 3 (a): Absolute value of the guided wave amplitude, F , as a function of the amplitude of the incident plane wave(after Ref. 5), (b): Zero order reflectivity, R_0 , as a function of the amplitude of the incident plane wave(after Ref. 5).



FIGURE 4 Observed spatio-temporal response under normal incidence (a) and under oblique incidence(12°) (b) of Fabry-Pérot filled with CS_2 (after Ref. 7).

leading to an angular dependence of the guided wave or transmitted intensity corresponding to Figure 5.

These resonators are usually used in the immediate vicinity of an electromagnetic resonance: of the order of a few times the width at half-maximum of the resonance curve. Thus only one mode is involved: forward and/or backward depending on the device and on the angle of incidence.⁹⁻¹¹ This has the following important consequences:

- a) the transverse (along y) field map of the nonlinear resonator corresponds to the one determined in the linear regime,
- b) according to point a), the transverse field map of the nonlinear coupler is known,

- c) thus it is no longer necessary, when dealing with the nonlinear device to integrate along the coordinate y .

Accordingly, the coupled-mode formalism^{12,13} is particularly well-suited for the study of nonlinear optical resonators. This formalism shows that the curve Figure 5 is a lorentzian. In the case of χ^3 -grating couplers, the rigorous theory of diffraction in linear optics¹⁴ is also required. It is seen that, in the stationary plane wave case, things become rather "simple". It is this simplicity that allows an extensive spatio-temporal study of these χ^3 -resonators. Let us see this in more detail.

First of all, it is necessary to identify the successive steps of the coupled-mode analysis:

- 1) define the unperturbed structure: the latter is obtained without the pump beam i. e., it corresponds to a linear leaky resonator,
- 2) find its normal modes. They are associated to complex poles β_p even in the absence of dielectric losses,
- 3) specify the source terms. They have a double origin: one comes from the in-coupling of the incident beam, the other is due to the existence of the χ^3 nonlinear polarization,
- 4) write down the equation of evolution of the normal mode amplitude. This is achieved according to the general results of the coupled-mode formalism.

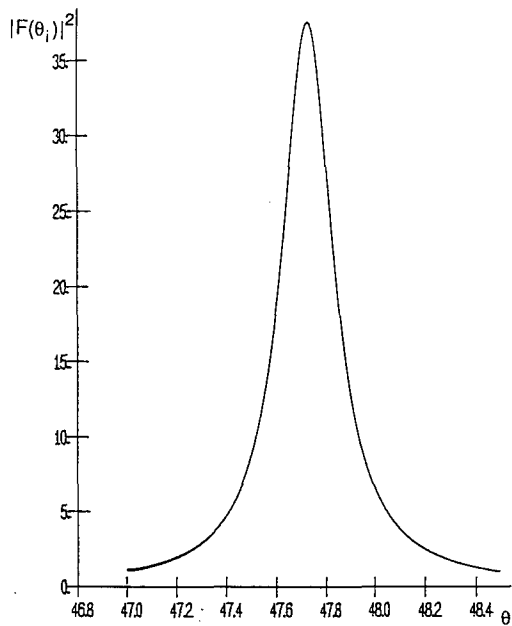


FIGURE 5 A typical resonance curve: for example $|F(\theta_i)|^2$.

Kerr-Type Resonators

The reduced set of spatio-temporal equations For the sake of generality, we consider a non-instantaneous, non-local Kerr-type nonlinearity. In this case, the total electric field amplitude, F , of the resonantly excited guided wave in the case of prism or grating couplers or transmitted wave for Fabry-Pérot obeys the following set of spatio-temporal equations written in reduced units:^{2,15}

$$i \frac{\partial F(x, t)}{\partial t} + \frac{\partial^2 F(x, t)}{\partial x^2} + 2i\alpha_0 \frac{\partial F(x, t)}{\partial x} - \eta[\Delta - U(x, t)]F + iF = iS(x, t) \quad (1a)$$

$$L^2 \frac{\partial^2 U(x, t)}{\partial x^2} - \tau \frac{\partial U(x, t)}{\partial t} = U(x, t) - |F(x, t)|^2 \quad (1b)$$

where:^{2,15}

S : input beam,

α_0 : angle of incidence

Δ : detuning

$\eta = \pm 1$ whether the nonlinear medium is self-focusing or self-defocusing,

U : nonlinear term,

L : diffusion length,

τ : nonlinear response time.

The space x and time t variables are rescaled respectively to the width of the resonance curve and to the resonator build-up time.

It can be immediately checked that in the limit $L = 0$ and $\tau = 0$, equations 1 yield the usual spatio-temporal modal equation.

The validity of eqs. 1 relies on the possibility of isolating a single resonance and of remaining "close" to it. Thus, as long as reduced quantities are used, eqs. 1 apply whatever the geometry of the Kerr-type resonator may be (Fig. 6: prism coupler with

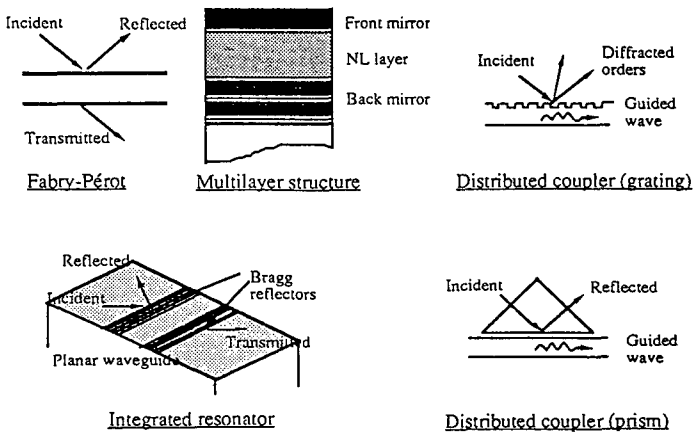


FIGURE 6 Optical resonators for which the modal theory applies.

guided mode resonances, Fabry-Pérot with Airy resonances). In other words, the solution F of eqs. 1 gives the response of all the optical resonators corresponding the same set of reduced parameters. Thus it is no longer necessary to specify the geometry of the Kerr-type resonator provided it is the quantity F which is of interest.

Of course, the relation between F and the electromagnetic field radiated outside the resonator does depend on the geometry of the device. This relation is easy to get when dealing with flat boundary devices such as Fabry-Pérot, prism couplers or multilayer structures like nonlinear interference filters. In the case of χ^3 -grating couplers, the analysis is not so straightforward since one has to go from the amplitude of the resonantly excited evanescent diffracted order to that of the radiated diffracted orders.⁵ It is the object of the next section to consider this point.

The radiated diffracted orders of a Kerr-type grating coupler The procedure is as follows: we consider first, the linear plane wave case. Then we deal with the nonlinear plane wave situation. The last step corresponds to a finite width beam incident on a χ^3 -grating coupler.

a) *Linear plane wave case* Let

$$D_n = \{B_n, T_n\}$$

be the amplitude of the n th radiated diffracted order in reflection (B_n) or transmission (T_n). According to Reference 14, there exists a scattering matrix $[S]$ such that:

$$D_n = S_n A_i \quad (2a)$$

with¹⁴

$$S_n = c_n \frac{\beta - \beta_{z,n}}{\beta - \beta_p} \quad (2b)$$

$\beta_{z,n}$: complex zero of the n th radiated diffracted order. The quantity $\beta_{z,n}$ is different whether one is interested in the n th diffracted order in reflection or in transmission.

c_n : factor independent of the angle of incidence which depends on the groove depth of the grating.

$$\beta = k_0 \sin \theta_i + q \left(\frac{2\pi}{d} \right)$$

q : integer

d : periodicity of the grating

θ_i : angle of incidence

From eqs. 2, we derive:

$$D_n = c_n A_i + c_n \frac{\beta_p - \beta_{z,n}}{\beta - \beta_p} A_i \quad (3)$$

since^{12,13}

$$F = \frac{t_p}{\beta - \beta_p} A_i$$

equation 3 can be rewritten as:

$$D_n = c_n A_i + g_n F \quad (4)$$

with

$$g_n = c_n \frac{\beta_p - \beta_{z,n}}{t_p}$$

This relation shows that there exists no coupling terms between the radiated diffracted orders: the amplitude D_n results from the off-resonant contribution of the incident plane wave and from the contribution of the leaky resonantly excited guided wave.

b) Nonlinear plane wave case According to the fact that the transverse field map is not modified by the Kerr nonlinearity, it follows that c_n , t_p and g_n are the same in the linear and in the nonlinear cases. Thus eq. 4 becomes for χ^3 -grating couplers:

$$D_n^{NL} = c_n A_i + g_n F^{NL} \quad (5a)$$

where now:^{12,13}

$$F^{NL} = \frac{t_p}{\beta - \beta_p^{NL}} A_i \quad (5b)$$

with

$$\beta_p^{NL} = \beta_p + \xi_p |F^{NL}|^2 \quad (5c)$$

According to eqs. 5:

$$D_n^{NL} = c_n \frac{\beta - \beta_{z,n}^{NL}}{\beta - \beta_p^{NL}} A_i \quad (6a)$$

with

$$\beta_{z,n}^{NL} = \beta_{z,n} + \xi_{z,n} |F^{NL}|^2 \quad (6b)$$

Equations 5c and 6b show that the nonlinear zero has the same nonlinear dependence than the nonlinear pole. It is this feature which yields the butterfly loops⁵ (Fig. 3b).

c) Finite width incident beam in the nonlinear case Equation 5a allows determining the field map along x when illuminating a Kerr-type grating coupler by a finite width incident beam. Indeed, the coefficients c_n and g_n can be considered as independent of θ_i over the width of the resonance curve. Thus a Fourier transform of eq. 5a yields the desired result:

$$\mathcal{D}_n^{NL}(x) = c_n \mathcal{A}_i(x) + g_n \mathcal{F}^{NL}(x) \quad (7a)$$

where

$\mathcal{D}_n^{NL}(x)$: reflected or transmitted field spatial distribution of any radiated diffracted order n ,

$\mathcal{F}_n^{NL}(x)$: x -dependent guided wave amplitude,

$\mathcal{A}_i(x)$: spatial amplitude distribution of the incident beam.

Besides, it has been shown¹⁶ that $\mathcal{F}_n^{NL}(x)$ obeys the following equation:

$$i\left(\frac{\partial \beta'_p}{\partial \omega}\right) \frac{\partial \mathcal{F}_n^{NL}(x, t)}{\partial t} + i \frac{\partial \mathcal{F}_n^{NL}(x, t)}{\partial x} + (\beta_p - \beta + U) \mathcal{F}_n^{NL}(x, t) = -t_p \mathcal{A}_i(x, t) \quad (7b)$$

β'_p : real part of the pole β_p

The determination of the unknown coefficients c_n , t_p and g_n together with the complex zero and the pole is achieved using the plane wave rigorous theory of diffraction in linear optics.¹⁴ The quantity ξ_p , related to the overlap integral, is obtained using the standard methods of coupled mode analysis.^{12,13} It is worth noticing that proceeding along these lines, the groove depth of the grating is rigorously taken into account.¹⁴

Figure 7 is the theoretical counterpart⁷ of Figure 4a and b. As can be seen, the nonlinear set eqs. 7 account well for the observed effect.

LINEAR AND NONLINEAR m-LINES

Let us consider briefly the linear m-lines their main features.

Linear m-Lines

The electromagnetic field corresponding to a diffracted order can be written as:

$$\mathcal{D}_n(x, y) = \int_{-\infty}^{+\infty} D_n(\beta) e^{j\vec{k} \cdot \vec{r}} d\beta \quad (8)$$

The far-field pattern is obtained from an asymptotic evaluation of eq. 8 using the steepest descent method.¹⁷ This leads to:

$$\mathcal{D}_n(\theta) \propto c_n A_i(\theta) \frac{\beta - \beta_{zn}}{\beta - \beta_p} \quad (9)$$

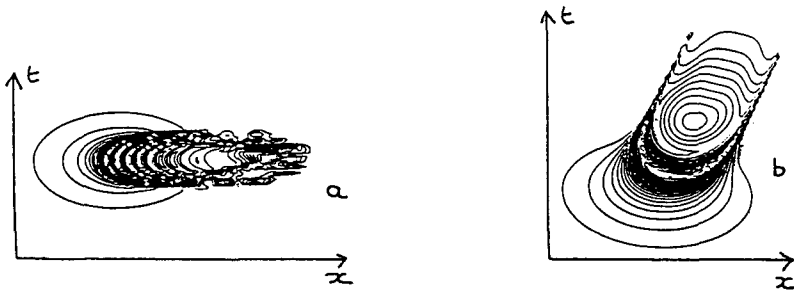


FIGURE 7 Calculated spatio-temporal response under normal incidence (a) and under oblique incidence (12°) (b) of Fabry-Pérot filled with CS₂ (compare with Fig. 4), (after Ref. 7).

Resonance occurs when:

$$\beta = \text{Re}[\beta_p] \quad (\text{Re: real part of})$$

The feature of the associated m-line may be different whether prism couplers or grating couplers are considered.

In the case of:

- a) a prism coupler with lossy media, the m-line is dark. As is well-known, there even exists an optimum value of the gap for which β_z is real. In that case, optimization is achieved for an incidence θ_i which fulfils:

$$k_0 \sin \theta_i = \beta_z \quad (10)$$

For the value of θ_i deduced from eq. 10:

$$|\mathcal{D}(\theta_{i,\text{res}})| = 0$$

and the corresponding m-line is black.

When the media are lossless:

$$\beta_z = \bar{\beta}_p$$

and according to eq. 9:

$$|\mathcal{D}(\theta)| \propto |c A_i(\theta)|$$

Thus no m-line is observed in the far-field.

- b) a grating coupler, the m-line may be either dark (even black) or bright depending on the location of the zero in the complex plane¹⁸ (Fig. 8).

Although not usually dealt with, the question of the distance at which the m-line is observed is important¹⁹ as we show now.

The field pattern, derived from eq. 8, is represented on Figures 9, which correspond respectively to a lossless prism coupler (Fig. 9a) and to a lossless grating coupler (Fig. 9b), for different distances to the optical resonator. It is seen on these figures that

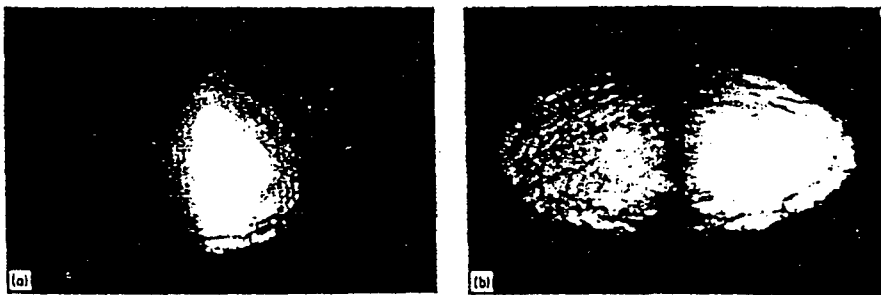


FIGURE 8 Far-field pattern of a grating coupler(after ref. 18), (a) the reflected beam, (b) the transmitted beam.

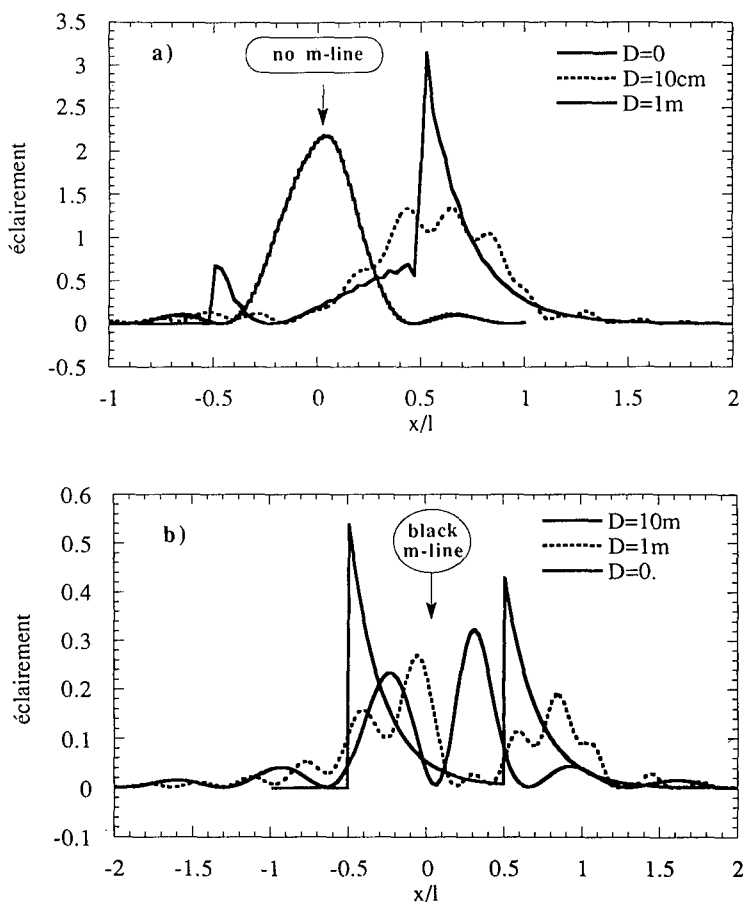


FIGURE 9 Field-pattern(after Ref. 19) of, (a) the reflected beam of a lossless prism coupler, (b) the transmitted beam of a lossless grating coupler, (the incident beam is a box beam, D is the distance to coupler).

the far-field region (the Fraunhofer zone) may be located more than one meter from the coupler.

Hence the importance of a far-field criterium which can be expressed as:

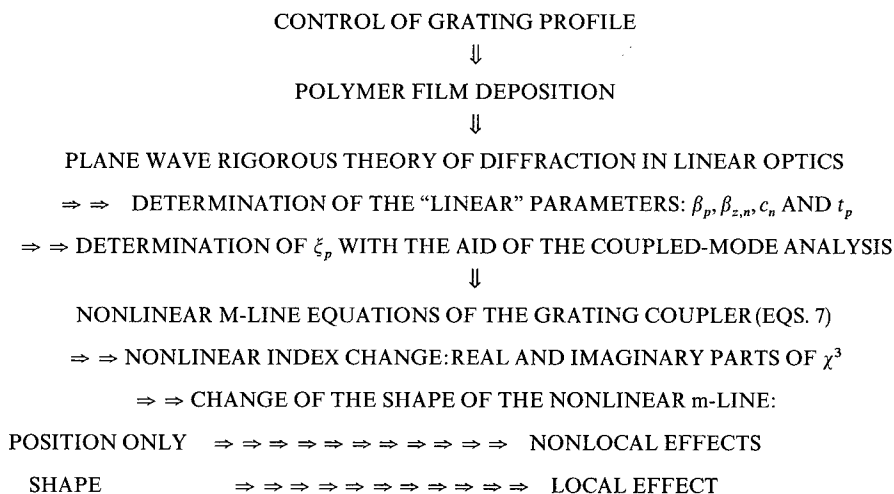
$$r > r_{\min} = \frac{2[x_0 + \ell_c]^2}{\lambda} \quad (11)$$

where x_0 and ℓ_c denote respectively the width of the incident beam and the coupling length (λ is the wavelength). Equation 11 shows a result which could have been easily anticipated namely that the thinner the angular width, $\Delta\theta$, of the resonance curve, i.e., the larger the coupling length, the greater the minimum value, r_{\min} , of the distance r beyond which one enters the far-field zone. For example, when $\Delta\theta \cong 10^{-2}$, r_{\min} is of the order of several meter.

Nonlinear m-Lines

The nonlinear m-line problem is fully described by the set of eqs. 7 together with the material equation obeyed by the nonlinear term U . In the following, we concentrate on Kerr-type grating couplers.

It is interesting to establish the flow chart describing a nonlinear m-line experiment. This flow chart may be put under the following form:



Nonlinear m-line experiments have been performed with a guiding layer of functionalized polymer obtained by free radical polymerization of a 1:1 mixture of methyl methacrylate and 4'-(*N*-ethyl-*N*-(methacryloxyethyl)amino)-4-nitroazobenzene obtained by esterification with methacrylic acid of commercially available (Aldrich) Disperse Red #1. This film has been spin-coated on a lamellar grating. The m-line, which is associated to the resonant excitation of a TE mode, has been recorded for two values of the input power:

* low intensity: linear regime,

* high intensity: nonlinear regime.

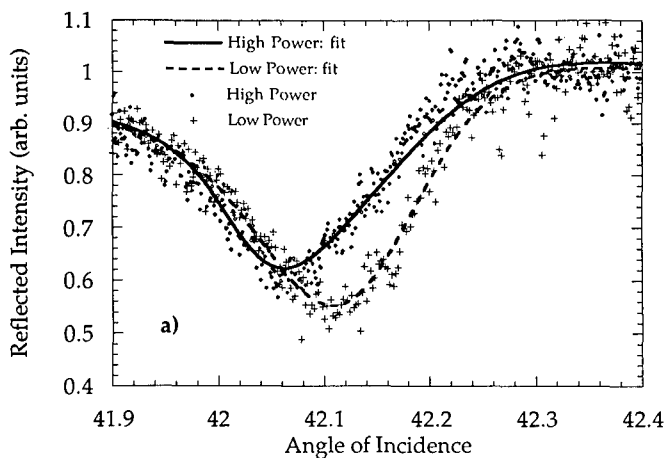
This has been done with nanosecond pulses and a train of picosecond pulses.⁸ The working wavelength is 1.318 μm , rather than 1.06 μm , in order to avoid a molecular conformational change (cis-trans transformation) induced by two photon absorption. The linear and nonlinear m-lines are shown in Figures 10.

The curves, dashed and full lines, correspond to the fit based on the use of the nonlinear m-line eqs. 7. In both, the nanosecond and the picosecond regimes, the agreement, between theory and experiment, is seen to be very good. From this fit, it has been found that the nonlinearity n_2 is:

$$n_2 = (-4 + i0.5)10^{-20} \text{ m}^2 \text{ V}^{-2}$$

The low value of the imaginary part of n_2 is a check of the low contribution of photon absorption.

(a)



(b)

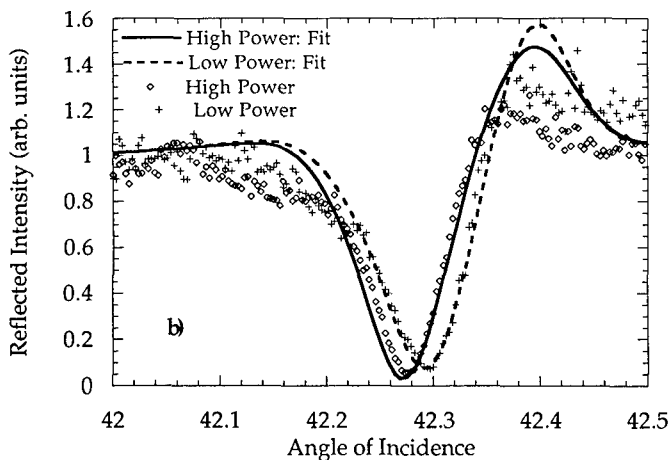


FIGURE 10 Nonlinear shift of the m-line at high input energy. The organic thin film is made with a polymer functionalized with Disperse Red #1 (PMMA-DR1), pump wavelength: 1.318 μm , repetition rate: 10 Hz, (a) Pulse duration: 50 ns, (b) Train of ps-pulses, total duration of the illumination: 3 ns.

Nearly the same value of n_2 has been determined in the nanosecond and picosecond regime. In addition, the nonlinear m-line is not only shifted with respect to the linear one but also its shape is different. Accordingly this nonlinearity is not of thermal origin and can be considered as a fast local one.

CONCLUSION

It is seen that nonlinear grating couplers constitute a powerful spectroscopic tool for the investigation of the linear and nonlinear parameters of organic thin films. The modification of the nonlinear m-line does not give access directly to n_2 but to the

product of the Kerr-nonlinearity by the electromagnetic field inside the guiding layer. Hence the need of an accurate spatio-temporal theory of the response of Kerr-type grating couplers to derive the value of n_2 . This nonlinear m-line technique yields not only the value of the real part of n_2 but also that of its imaginary part. Even low two photon absorption can be exhibited demonstrating the sensitivity and the interest of the nonlinear m-line spectroscopy.

The analysis takes full advantage of the fact that these Kerr-type grating couplers are used in the immediate vicinity of an isolated electromagnetic resonance. As a result, the geometry of the resonator is no longer the important parameter: the key point is the existence of a resonance curve which can be approximated by a lorentzian. Thus the theory presented in this paper can be viewed as a unified one since it applies to a variety of devices which belong to the class of Kerr-type optical resonators. Moreover, this theory not only accounts for the nonlinear m-line effect but also for other phenomena such as: optical bistability including butterfly loops, space-time deformation of the response of χ^3 -Fabry-Pérot, self-pulsing, chaos

REFERENCES

1. G. Vitrant, "Third order nonlinear integrated optical resonators", in Guided Wave Nonlinear Optics, Eds. D. B. Ostrowsky and R. Reinisch, NATO ASI Series E, Kluwer Academic Publishers 1992.
2. G. Vitrant and R. Reinisch, "Nonlinear optical resonators and integrated devices" in Studies in Classical and Quantum Nonlinear Optics, Ed. O. Keller, Nova Science Publishers, N. Y. 1993.
3. M. B. Marques, G. Assasto, G. I. Stegeman, G. R. Möhlmann, E. W. P. Erdhuisen and W. H. G. Horsthuis, *Appl. Phys. Lett.*, **58**, 2613 (1991).
4. P. Vincent, H. Akhouayri and M. Nevière, *J. Soc. Opt. Am. B*, **8**, 1149 (1991).
5. R. Reinisch, M. Nevière, P. Vincent and G. Vitrant, *Opt. Comm.*, **91**, 51 (1992).
6. V. Brigueot, J. Kramer and W. Lukosz, *J. de Phys. Colloque*, C2 49, (suppl. 6), 325 (1988).
7. G. Vitrant, M. Haelterman, G. Martinelli, A. Barthélémy and C. Froehly European Conference on Optics, Optical Systems and Applications, *Inst. Phys. Ser.*, N° 115, Section 3, Roma(1), 1990.
8. G. Vitrant *et al.*, This issue.
9. M. Haelterman, G. Vitrant and R. Reinisch, *J. Soc. Opt. Am. B*, **7**, 1309 (1990).
10. G. Vitrant, M. Haelterman and R. Reinisch *J. Soc. Opt. Am. B*, **7**, 1319 (1990).
11. R. Reinisch, G. Vitrant and M. Haelterman *Phys. Rev. B*, **44**, 7870 (1991).
12. "Theory of dielectric waveguides" in Integrated Optics, H. Kogelnik, ed. T. Tamir, Springer-Verlag(New-York, 1975).
13. "Théorie des guides d'ondes électromagnétiques" C. Vassalo, Tomes 1et 2(CNET-ENST, Eyrolles, Paris, 1985).
14. "Electromagnetic theory of gratings", ed. R. Petit, Springer-Verlag (New-York, 1980).
15. J. Danckaert and G. Vitrant, *Opt. Comm.*, **104**, 196 (1993).
16. G. Vitrant, R. Reinisch and F. Kajzar, ACS/OSA "Topical Meeting Organic Thin Films for Photonic Applications", Toronto(C)6-8/10/1993.
17. G. Arfken, Mathematical Methods for Physicists, Academic, N. Y. 1970.
18. G. A. Golubenko, A. S. Svakhin, V. A. Sychugov, A. V. Tischenko, E. Popov and S. Mahev, *Optical and Quantum Electronics*, **18**, 123 (1986).
19. G. Vitrant, R. Reinisch and J. L. Coutaz, *Journées Nationales d'optique Guidée*, Marseille (F), 26-27/5/93.

Electro-Optic Measurements of Poled Polymeric Films

J. D. SWALEN and J. I. THACKARA

IBM Almaden Research Center, 650 Harry Road, San Jose, CA 95120

Received 12 January 1994; accepted 25 February 1994

Second order optical nonlinearities of poled polymeric films containing optically nonlinear chromophores can be measured either by second harmonic generation in a Maker fringe experiment or by the change in refractive index induced by an electric field in an electro-optic experiment. Theoretically the results of these two types of experiments are related, but experimentally, this has been observed to be only approximately true because of frequent occurrence of some resonance enhancement at the second harmonic wavelength. Electro-optic experiments at wavelengths having little or no absorption lead, in our opinion, to a more reliable way to measure the optical nonlinearity of these poled polymeric thin film structures. This is especially important for modulation and switching applications. Some common methods, which we have used for the determination of the electro-optic coefficient, are attenuated total reflection (ATR), ellipsometric reflection, Mach-Zehnder interferometry and the modulation index in an electro-optic phase modulator. Fabry-Pérot cavity transmission or reflection has been applied by others. A comparison of these experimental methods will be given.

INTRODUCTION

Organic polymers have recently been shown to exhibit improved optical linear and nonlinear properties, and in many cases they exceed the known inorganic and organic crystals. For these reasons and because of their ease of preparation, these polymers are being actively studied for potential optoelectronics applications, such as electro-optic modulation and switching. For example, in the past few years a number of conferences and symposia have been held on this topic.^{1–3} Much of the excitement in the field stems from their high nonlinearity, which is almost exclusively electronic in nature. There is little contribution from phonons, that is, ionic or molecular motions. Responses in the tens of gigahertz frequency range have been observed.^{4–6} In addition, these materials possess large bandwidths and low dielectric constants, that is, the dielectric constants are only slightly larger than the square of the refractive index. This means that the optical and microwave signals propagate at nearly the same velocity, resulting in a long interaction length.

Current research has been directed towards designing and synthesizing new thermally stable polymers with chromophores attached. Not only must the chromophores exhibit exceptionally high optical nonlinearity, but also they must possess comparable thermal stability to that of the polymer backbone. Some recent success has been achieved in this area with some high temperature polymers of the polyimide type⁷ and with some new chromophores.⁸ The optical transparency at the desired operating wavelength and the interactions between the various layers of a multilayer device are also important properties which must be optimized. Since many of the proposed

devices operate at the infrared wavelengths for optical communications (1.32 μm or 1.55 μm), optical absorption and waveguide loss from either the chromophore or the polymer are usually negligible. Exceptions, however, have been observed where, for example, in *p*-nitroaminotolane, the electronic absorption band extended out to $\sim 1 \mu\text{m}$ and made the films unacceptable at wavelengths shorter than that.⁹ Absorption in the 1–2 μm range is caused mainly by the overtones of the C—H stretch vibrational bands.¹⁰ Fortunately, there are windows at both 1.32 μm and 1.55 μm wavelengths, making it unnecessary to synthesize and use deuterated or fluorinated polymers for many applications. Optical transparency can, therefore, be quite good in these films. Scattering, either in the bulk by inhomogeneities or at the surface by roughness, can cause most of the loss. This can be partially controlled by improved processing conditions. Low optical losses are important for any optical channel waveguide devices with path lengths of several millimeters to a few centimeters. Losses by any source must be less than a few dB/cm for a practical device.

When a new NLO polymer is acquired, customarily the first experiment performed is that of second harmonic generation by the Maker fringe technique, where the film is measured as a function of rotation angle with respect to the laser beam from a Nd:YAG or Nd:YLF laser. With thin polymeric films of the order of 1 to 2 μm thick, the first fringe is barely reached and therefore the accuracy is somewhat limited. Jerphagnon and Kurtz¹¹ derived expressions for the second harmonic signal as a function of angle for films of finite thickness and Gadret *et al.*,¹² slightly modified these expressions to be applicable to ultrathin films. These preliminary measurements can then give an approximate magnitude of the optical nonlinearity and also optimize the poling temperature. Poling should be done close to the glass transition temperature, T_g , where the polymer becomes rubbery. Too far below T_g the molecules orient too slowly and poling can take an inordinate amount of time. Too high above T_g the polymer becomes too electrically conducting for the film to hold a poling field of any magnitude. This situation is, in most cases probably, caused by impurities in the film which become mobile.

The relationship between the second order nonlinear molecular polarizability and the macroscopic polarizability is¹³

$$\chi^{(2)} = 2d = Nf_{2\omega}(f_{\omega})^2 \beta \Theta \quad (1)$$

where N is the number of molecules, the f 's are the local field factors, β is the molecular polarizability, and Θ is the order parameter. For d_{33} , $\Theta = \langle \cos^3 \theta \rangle$ and for d_{31} , $\Theta = \frac{1}{2} \langle \sin^2 \theta \cos \theta \rangle$. The angle θ is the angle between the nonlinear optical axis of the molecules and the direction of the poling field. The order parameter depends on the degree of poling alignment.

The electro-optic coefficient is defined as

$$r = \frac{2}{n^3} \times \frac{\Delta n}{\Delta E} \quad (2)$$

and an approximate relationship between d and r is

$$d = -\frac{n^4}{4} \times r. \quad (3)$$

Note that we have suppressed the subscripts on d and r . For these second order phenomena, there are two fields and the direction of the polarizability. We define the direction "3" to be perpendicular to the surface, that is in the poling direction, while directions "1" and "2" are in the plane of the film. Singer *et al.*,¹⁴ have given a more detailed relation between the second harmonic coefficient and the electro-optic coefficient.

$$\frac{d_{33}(-2\omega'; \omega', \omega')}{r_{33}(-\omega; \omega, 0)} = -\frac{n_{\omega}^4 \beta(-2\omega'; \omega', \omega') f_3^{2\omega'} (f_3^{\omega'})^2}{4 \beta(-\omega; \omega, 0) (f_3^{\omega})^2 f_3^0}, \quad (4)$$

$$\frac{d_{31}(-2\omega'; \omega', \omega')}{r_{13}(-\omega; \omega, 0)} = -\frac{n_{\omega}^4 \beta(-2\omega'; \omega', \omega') f_3^{2\omega'} f_3^{\omega'} f_1^{\omega'}}{4 \beta(-\omega; \omega, 0) f_1^{\omega} f_3^{\omega} f_3^0}, \quad (5)$$

where β are the hyperpolarizabilities of the chromophore and

$$\frac{\beta(-2\omega'; \omega', \omega')}{\beta(-\omega; \omega, 0)} = \frac{3\omega_0^2 [\omega_0^2 - \omega^2]^2}{[\omega_0^2 - 4\omega'^2][\omega_0^2 - \omega'^2][3\omega_0^2 - \omega^2]}. \quad (6)$$

Here ω_0 is the circular frequency at the absorption maximum and the local field factors, f^k , are

$$f^0 = \frac{\epsilon(0)[n_{\omega'}^2 + 2]}{n_{\omega'}^2 + 2\epsilon(0)}, \quad (7)$$

$$f^{2\omega'} = \frac{n^2(2\omega') + 2}{3}, \quad (8)$$

$$f^{\omega'} = \frac{n^2(\omega') + 2}{3}, \quad (9)$$

and

$$f^{\omega} = \frac{n^2(\omega) + 2}{3}. \quad (10)$$

Although these expressions are quite good approximations, when absorption occurs close to the second harmonic wavelength significant deviations result. A resonance enhancement is observed and the d values are higher than the corresponding wavelength corrected r values.¹⁵ Recently Eich and colleagues¹⁶ have introduced absorption into the expressions of Jerphagnon and Kurtz to correct for this problem. Gadret *et al.*,¹² have also given additional expressions including absorption.

Although much of the effort has been on measuring the second harmonic signal from new materials by the Maker fringe technique in order to evaluate their optical nonlinearity, the present anticipated use is in electro-optic modulators and switches. Hence, in order to characterize these materials for applications, it is most important to measure the electro-optic coefficients directly and to estimate how large they can be. M. L. Dumont, Y. Levy and D. Morichère¹⁷ reviewed a few years ago of a number of methods. The field has, however, been fast moving and new methods have been proposed and tested. We will give an up to date account of various methods which we feel are becoming the most widely used. These are the attenuated total reflection method (ATR),^{15,17-22} an ellipsometric technique,^{15,17,23-28} a Mach-Zehnder

interferometer,^{15,17,29-33} Fabry-Pérot cavity,³⁴⁻³⁸ and a modulation technique in an electro-optic phase modulator.^{9,39} These techniques will be reviewed and compared.

ATTENUATED TOTAL REFLECTION (ATR)

In the ATR technique a laser beam can excite both the surface plasmon mode and the waveguide modes at the base of a prism face coated with a layered structure. Note that the surface plasmon mode is only observed with TM polarized radiation. The experimental arrangement is shown schematically in Figure 1a. As a function of angle, the various modes are excited in the NLO polymer layer and the extracted energy from the beam leads to sharp dips in the reflectivity curve. A common configuration is prism/gold/NLO polymer/ITO/quartz. Depending on the type of measurement, the gold layer can be either evaporated directly on the prism or on the top of the NLO layer. With a computer program, based on the Fresnel reflection formula of a multilayered system^{40,41} and by fitting theoretical and experimental curves, the linear optical parameters, index ($n + i\kappa$) and thickness of each layer can be adjusted to give accurate values for these parameters. As the NLO layer is considered to be a uniaxial medium, both polarizations of the light, transverse electric (TE) and transverse magnetic (TM), are required to determine separately n_o and n_e . Note that with axes labelling of 1, 2 and 3, $n_1 = n_2 = n_o$ and $n_3 = n_e$. For a calculation of the electro-optic coefficient, r , one measures the waveguide modes and their shifts in coupling angles with applied voltage. This is done by applying a low frequency voltage $V \cos \omega t$ ($\omega \simeq 1$ kHz) to the electrodes and detecting the modulated signal with a lock-in-amplifier tuned to ω . If one observes an inversion in sign of the modulated signals, it can be concluded that electro-mechanical effects (piezoelectric) contribute to the electro-optic effects.^{17,19,20} In many cases, common NLO polymers show little or no piezoelectric effects. Only in polymers like poly(vinylidene fluoride), which can exhibit some pyroelectric, piezoelectric or electrostrictive effects, does one see this inversion effect. Normally, any contribution from changes in thickness from electro-mechanical effects can be neglected. Changes in overall thickness can, however, occur if significant modulation voltages are applied to the two electrodes.

For TE (or s) polarization and for each mode of order m , we can relate the change in reflectivity R to a change in refractive index.

$$\Delta R_s = \frac{\partial R_s}{\partial n_o} \Delta n_o \quad (11)$$

For TM (or p) polarization we have a similar expression

$$\Delta R_p = \frac{\partial R_p}{\partial n_o} \Delta n_o + \frac{\partial R_p}{\partial n_e} \Delta n_e \quad (12)$$

The partial derivatives of R with respect to the index are calculated numerically from the Fresnel equations.^{35,36} The variations in index are then determined by these derivatives and the experimental modulation curves (see references for some examples) with equations 11 and 12. By this procedure, the modulation curves are fit for all the

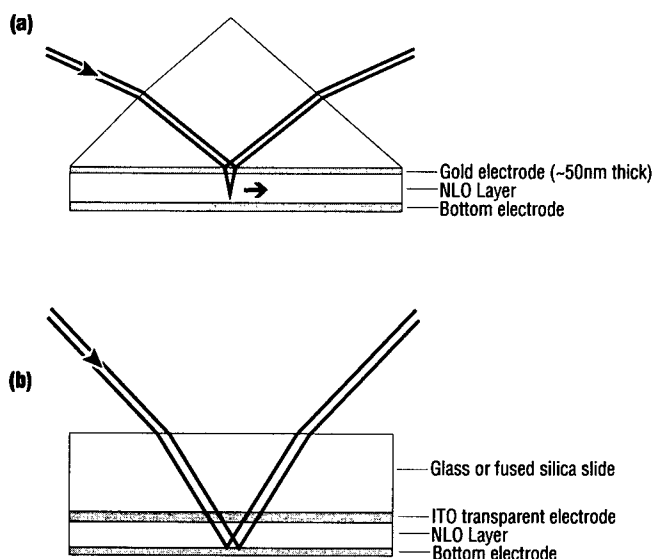


FIGURE 1 Experimental arrangements for reflectivity measurements. (a) ATR arrangement for either TE or TM waveguide modes and the surface plasmon mode (TM polarization). (b) ellipsometric arrangement with the polarization at 45° or Fabry P  rot modes at TE or TM polarizations. Here the ITO layer is replaced by a metallic thin film for better reflectivity.

waveguide modes and lead to a determination of r_{33} and r_{13} by Eq. (2) with the known applied voltage.

The surface plasmon mode can also be used, but since its linewidth is larger than the waveguide modes, the accuracy is not quite as good. Also as mentioned, it is limited to TM modes only.

In a related method by Horsthius and Krijnen,⁴² the electro-optic coefficient changes the index of refraction and hence prism coupling angles to the various guided modes. By measuring the change in angle one can calculate the electro-optic coefficient quite accurately. The only problem, as with other waveguide techniques, is that buffer layers must be above and below the guiding layer to prevent loss from the optical field encountering the electrodes. This will add more processing steps.

ELLIPSOMETRY

Recently, a very simple adaptation of the ellipsometry technique has been developed for measuring the electro-optic coefficients of NLO polymers deposited in thin films.²³ This technique has been proposed independently by Teng and Man²⁴ and Schildkraut.²⁵ One measures the change in phase of reflected light from the bottom of a quartz substrate. The sample (quartz/ITO/NLO polymer/gold) is located between two crossed polarizers. A HeNe laser beam at 633 nm, linearly polarized at 45° with respect to the plane of incidence is reflected from this multilayered structure, as shown schematically in Figure 1b. A Soleil-Babinet compensator enables one to vary the

phase mismatch between the TE and the TM components. Similar to the ATR measurements, a low frequency voltage is applied to the two electrodes and the modulation signal is detected by a lock-in-amplifier.

The analysis of the experiment is as follows: The intensity of the reflected light is

$$I = |r_s + r_p|^2$$

If we define the complex reflectivity, r , as

$$r_s = \rho_s e^{i\delta_s} \quad \text{and} \quad r_p = \rho_p e^{i(\delta_p + \pi)}$$

then

$$I = \rho_s^2 + \rho_p^2 - 2\rho_s\rho_p\cos(\delta_s - \delta_p) \quad (13)$$

Now if we define ϕ as

$$\phi = \delta_s - \delta_p + \psi_{SB},$$

where ψ_{SB} is the phase shift introduced by the Soleil-Babinet compensator, so that

$$I = \rho_s^2 + \rho_p^2 - 2\rho_s\rho_p\cos\phi \quad (14)$$

$\phi = \pi/2$ or $\phi = 3\pi/2$ corresponds to the points of half the maximum intensity and at the maximum change in intensity. When the electric field is imposed, all the parameters change (denoted by primes).

$$I' = \rho_s'^2 + \rho_p'^2 - 2\rho_s'\rho_p'\cos\phi' \quad (15)$$

Since

$$\psi_{SB} = \frac{\pi}{2} - (\delta_s - \delta_p)$$

then

$$\phi' = (\delta_s' - \delta_p') + \frac{\pi}{2} - (\delta_s - \delta_p) \equiv \Delta + \frac{\pi}{2} \quad (16)$$

Combining all these results and normalizing them to maximum intensity $(\rho_s + \rho_p)^2$, the change in intensity by the application of a modulating field can be written:¹⁵

$$\frac{\Delta I'}{I_{\text{MAX}}} = \frac{1}{(\rho_s + \rho_p)^2} \left\{ \rho_s'^2 + \rho_p'^2 - 2\rho_s'\rho_p'\cos\left(\Delta + \frac{\pi}{2}\right) - (\rho_s^2 + \rho_p^2) \right\} \quad (17)$$

In the case of no absorption the ρ 's are only slightly modified and all are approximately equal. The main effect is from the phase changes, $\delta_s \rightarrow \delta_s'$ and $\delta_p \rightarrow \delta_p'$. This expression then reduces to those of Teng and Man²⁴ and Schildkraut.²⁵ Any imaginary components in the indices of refraction require the inclusion of the changes in ρ . Clays and Schildkraut²⁶ showed that with absorption at a fixed angle that signals at $\pi/2$ and $3\pi/2$ are not equal, as would be the case with no absorption. Morichere *et al.*¹⁵ showed further that with an angular scan the signals at $\pi/2$ and $3\pi/2$ vary seemingly independently and in rather wild fashion. This points out the fact that for absorbing materials, (the case for many NLO polymers with absorption bands extending into the red and infrared regions of the spectrum), an angular scan of the modulation signal is recommended in order to determine accurately the electro-optic coefficients.

A related technique used by Nahata *et al.*,^{43,44} also measures the phase shift, but here a light beam polarized at 45° to the principal axis of the electro-optic material is passed through a Senarmont compensator and the modulating voltage is applied to coplanar electrodes. As a consequence, the electric field has components parallel and perpendicular to the plane of the substrate. Although the perpendicular component is small and can be neglected, the field varies across the gap and is compensated by an average field factor.

MACH-ZEHNDER METHOD

A number of investigators have used a Mach-Zehnder arrangement to determine the electro-optic coefficient. Crystals have been placed between electrodes in one arm of an interferometer.²⁹⁻³⁰ Also, an NLO polymeric film has been placed perpendicular to the beam in one arm.³¹ This gave a determination of only r_{13} . Now if the sample is rotated with respect to the polarization direction, then both components can be calculated. As a function of this angle α , we have the relation:¹⁵

$$n_{\text{eff}}^3 r_{\text{eff}} = n_0^3 r_{13} + (n_e^3 r_{33} - n_0^3 r_{13}) \sin^2 \alpha \quad (18)$$

From the intercept, we can obtain r_{13} . Knowing this and an independent measure of n_0 and n_e , we can calculate r_{33} from the slope of n_{eff} vs. $\sin^2 \alpha$.

Other experiments have involved placing the NLO polymeric film in an optical waveguide configuration with prism coupling in one arm of the interferometer.^{32,33} Now both components can be determined by coupling either to TE or TM modes. Also the indices of refraction and thickness can be determined by solving the eigenvalue equation for the modes. Here again the main problem is making a layered structure with buffer layers. Also one must have good guiding properties of the film.³³

FABRY-PÉROT METHOD

Another approach has been to make Fabry-Pérot etalons for operation either in transmission^{34,35} or reflection.³⁶⁻³⁸ Here with the angle of incidence at, say, 45°, the polarization is set to either the TE or TM modes, that is, the polarization is either perpendicular to the plane of incidence or parallel to the plane, not at 45° as in the case of ellipsometry. The configuration for transmission is two thin gold electrodes (each about 20 to 40 nm thick) on each side of the NLO polymeric film. The arrangement is similar to that shown in Figure 1b. For reflection, the bottom electrode is made thicker. As with the other techniques, a low frequency modulation is applied and the signal is measured with a lock-in-amplifier.

HETERODYNE MEASUREMENTS

The electro-optic coefficient can also be calculated conveniently in a completed device by measuring the sidebands on the optical carrier generated by a single frequency rf

signal applied to the modulating electrode. The heterodyne arrangement is shown schematically in Figure 2. The half-wave plate and prism angle are adjusted for optimum coupling to either the TE_0 or TM_0 mode. Several TE and TM modes can be supported by films in the thickness range of $2\ \mu\text{m}$. Usually, little or no intermode coupling is observed. For heterodyne detection, the local oscillator is frequency shifted by an acousto-optic modulator. If this were not done and the local oscillator were at the carrier frequency, the two sidebands, which are 180° out of phase, would be at the same frequency and mixing would lead to a cancellation of any signal.

This type of measurement technique has also been used effectively to measure poling transient effects in organic NLO films.⁴⁵ The high sensitivity inherent to heterodyne detection allows accurate device characterization by using only a small fraction of the drive voltage needed to produce a π phase shift. The electric fields in the phase modulated (or signal) and local oscillator beams are:^{46,47}

$$E_s = E_o e^{i(\omega_c t + M \sin \omega_m t)} = E_o e^{i\omega_c t} + \frac{ME_o}{2} (e^{i(\omega_c + \omega_m)t} - e^{i(\omega_c - \omega_m)t}) \quad (19a)$$

$$E_{lo} = E_a e^{i(\omega_c + \omega_a)t} \quad (19b)$$

where E_o and E_a are the field amplitudes, ω_c , ω_m and ω_a are the angular frequencies of the carrier, the rf modulation, and the acousto-optic frequency shift, respectively, and M is the amplitude, or modulation index, of the induced phase modulation. For a waveguide modulator in which the optical mode extends beyond the electro-optic core into the passive buffer layers, the modulation index is related to the change in the core index by

$$M = \frac{\pi \Delta n_{\text{eff}} L}{\lambda} = \frac{\pi \Delta n_c^{\text{TM}} L}{\lambda \Phi_m}, \quad (20)$$

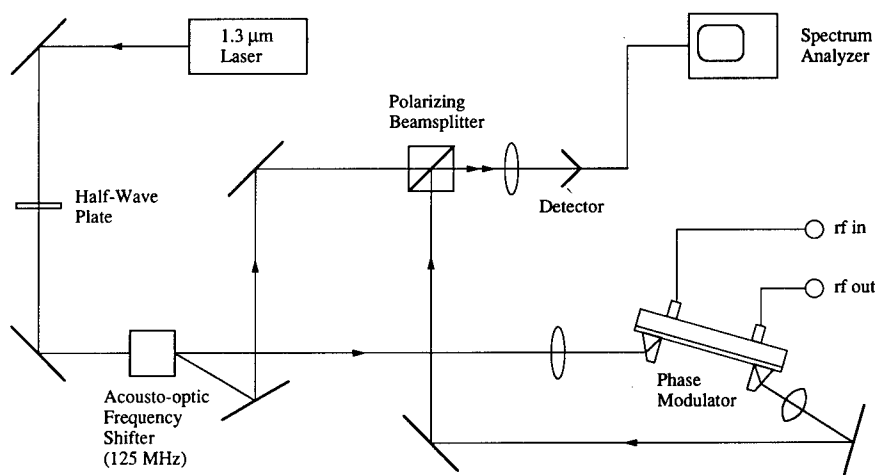


FIGURE 2 Experimental arrangement for the heterodyne measurements.

where λ is the carrier wavelength, n_{eff} is the effective index for the guided mode in the multilayer structure, n_c^{TM} is the TM refractive index for the poled polymer layer, L is the length of the active region, and Φ_m is the ratio of the change in the core index to that of n_{eff} . The modulation index can now be expressed in terms of the device parameters by using eq. 2:

$$M = \frac{\pi L \Delta E_c (n_c^{\text{TM}})^3 r_{33}}{2 \lambda \Phi_m} = \frac{\pi \sqrt{2} L V_s (n_c^{\text{TM}})^3 r_{33}}{\lambda t_c \Phi_m} \left[1 + \frac{2 \varepsilon_c t_b}{\varepsilon_b t_c} \right]^{-1}, \quad (21)$$

where V_s is the rms applied voltage, t_c and ε_c are the thickness and dielectric constant of the NLO polymer in the poled region, t_b and ε_b are the thickness and dielectric constant of each buffer (assumed to be the same) in the poled region, and r_{33} is the electro-optic coefficient. The modulation index for the TE mode is obtained from eq. (21) by replacing n_c^{TM} with the corresponding n_c^{TE} and replacing the electro-optic coefficient, r_{33} , by r_{13} . The determinations of n_c and ε_c are difficult in modulators poled with both lower and upper buffer layers present. The value of $\varepsilon_c/\varepsilon_b$ can be estimated with the assumption that the ratio of dielectric constants for most polymeric materials at frequencies above a few hundred kHz is nearly equal to the ratio of the squares of the refractive indices.

At the detector, the total intensity is given by

$$|E_s + E_{io}|^2 = 2E_o E_a \cos(\omega_a t) - ME_o E_a \sin(\omega_a - \omega_m)t + ME_o E_a \sin(\omega_a + \omega_m)t, \quad (22)$$

neglecting terms of order M^2 or higher. The detected signal generated by a phase modulator driven at 5 MHz is shown in Figure 3. The ratio of the optical powers in the central beat at ν_a and the side peaks at $\nu_a \pm \nu_m$ is $M/2$, and therefore the ratio of the

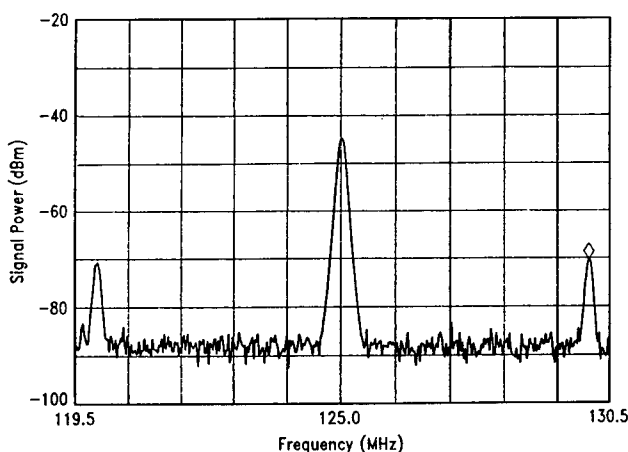


FIGURE 3 The carrier signal at 125 MHz with the sidebands ± 5 MHz. The sidebands are ~ 26 dBm down from the carrier. Note: 0 dBm = 1 milliwatt.

electrical powers is $M^2/4$. Expressed in terms of the difference, Δ , between the electrical power in the central peak to that of the side peaks measured in dB:

$$M = 2 \times 10^{-\frac{\Delta}{20}} \quad (23)$$

The electro-optic coefficient r_{33} can then be written as

$$r_{33} = \frac{\sqrt{2}\lambda t_c 10^{-\frac{\Delta}{20}}}{\pi L V_s (n_c^{\text{TM}})^3} \left[1 + \frac{2\varepsilon_c t_b}{\varepsilon_b t_c} \right] \Phi_m \quad (24)$$

By using this heterodyne technique, electro-optic measurements can be easily carried out with drive voltages of $1 V_{\text{rms}}$ or less, and at moderate frequencies. For example, a frequency of 2 MHz is high enough to avoid any contribution to the electro-optic signal from chromophore motional effects (the frequency responses of all modulators we have tested were found to be flat over the measured range from 10 kHz to 2 MHz), while still being low enough to allow precise determination of the modulating voltage. The drive voltage should be limited to levels that ensure the validity of the assumption that $M^2 \ll M$.

CONCLUSIONS

We have described a number of methods to determine the electro-optic coefficient, r . They all can give essentially the same results. For the ellipsometric, Mach-Zehnder and Fabry-Pérot methods, the indices and the thickness of the film structures must be known and must be determined by other experiments. The ATR technique, on the other hand, is a method giving both the indices and thickness, as well as the electro-optic coefficients. In particular, both indices, being anisotropic from poling, can be determined.

The waveguided mode configurations require multilayered structures and as such are more complicated to assemble. The main problem with the multilayer structures of waveguides and buffer layers is that the dielectric constant and thickness of each must be known to apportion the electric field across each layer, in particular, to know the field in the NLO layer. This will require other experiments to determine these values. The index of the metallic layer can be taken from the literature. This might introduce some slight error into the determination of r but it should not be large.

The modulation voltage required for the heterodyne technique is only $\sim 1 \text{ kV/cm}$, while all the other methods discussed require something between 10 and 100 kV/cm, usually around 30 kV/cm. This is a distinct advantage for the heterodyne technique because higher voltages could cause some problems, such as sample degradation, movement of trapped charges and electrostriction. The waveguide and ATR techniques not only give both components of the electro-optic coefficient, r , but also the thickness and indices of refraction of each layer. Because of poling, most films exhibit an anisotropy. Also the two electro-optic coefficients, r_{33} and r_{13} , are determined separately. The ratio, r_{33}/r_{13} , theoretically should be 3. This follows from the Langevin

functions:^{48,49}

$$\Theta = \langle \cos^3 \theta \rangle = L_3 \approx \frac{u}{5}$$

and

$$\Theta = \frac{1}{2} \langle \sin^2 \theta \cos \theta \rangle = \frac{1}{2} (L_1 - L_3) \approx \frac{1}{2} \left(\frac{u}{3} - \frac{u}{5} \right) = \frac{u}{15},$$

where $u = \mu E/kT$. In some experiments, the ratio has been found to be larger than three and closer to four. This had been explained²¹ as a result of incomplete rotational freedom. This could be consistent with our materials which are side-chain polymers in which the chromophores have difficulty executing rotations in all directions. Also, under conditions of high poling, that is $u > 1$, the ratio from the Langevin function^{44,49} is greater than 3. On the other hand, in a number of experiments, like ellipsometry, where only one component can be measured, the ratio is assumed to be 3.

We feel each of the methods presented here can be used to evaluate new polymeric electro-optic materials. For electro-optic device applications, however, we recommend measuring the electro-optic coefficient directly in a device, because the actual performance of a material must be evaluated under its operating conditions.

ACKNOWLEDGEMENTS

We thank G. C. Bjorklund for his support and help and C. A. Walsh for her comments on the manuscript. This research was partially supported by a NIST-ATP contract and a NATO contract CRG 910169.

REFERENCES

1. *Progress in Nonlinear Optics: Organic and Polymeric Materials*, Washington State University, Pullman, WA, July 16-17, 1992, Chair: Mark G. Kuzyk.
2. *Nonlinear Optical Properties of Organic Materials VI*, G. Möhlmann (chair/editor) *Proc. SPIE* **2025** (1993).
3. *Polymer Thin Films for Photonic Applications* Optical Society of America-American Chemical Society Joint Meeting, Toronto, Canada, Oct. 6-8, 1993, Chair: Gary Bjorklund.
4. D. G. Garton, S. L. Kwiatkowski, G. F. Lipscomb and R. S. Lytel, *Appl. Phys. Lett.*, **58**, 1730 (1991).
5. C. C. Teng, *Appl. Phys. Lett.*, **60**, 1538 (1992).
6. O. Solgaard, F. Ho, J. I. Thackara and D. M. Bloom, *Appl. Phys. Lett.*, **61**, 2500 (1992).
7. R. D. Miller, private communication.
8. C. R. Moylan, R. J. Twieg, V. T. Lee, S. A. Swanson, K. M. Betterton and R. D. Miller, *J. Amer. Chem. Soc.* (accepted).
9. J. D. Swalen, G. C. Bjorklund, W. Fleming, R. Hung, M. Jurich, V. Y. Lee, R. D. Miller, W. E. Moerner, D. Y. Morichère, A. Skumanich and B. A. Smith, *Proc. SPIE*, **1775**, 369 (1992).
10. A. Skumanich, M. Jurich and J. D. Swalen, *Appl. Phys. Lett.*, **62**, 446 (1993).
11. J. Jerphagnon and S. K. Kurtz, *J. Appl. Phys.*, **41**, 1667 (1970).
12. G. Gadret, F. Kajzar and P. Raimond, *Proc. SPIE*, **1560**, 226 (1991).
13. D. J. Williams "Nonlinear Optical Properties of Guest-Host Polymer Structures," *Nonlinear Optical Properties of Organic Molecules and Crystals*, D. S. Chemla and J. Zyss, Eds., Academic Press, Orlando Vol. 1, pp. 405-435 (1987).
14. K. D. Singer, S. L. Lalama, J. E. Sohn and R. D. Small, "Electro-Optic Organic Materials," *Nonlinear Optical Properties of Organic Molecules and Crystals*, D. S. Chemla and J. Zyss, Eds., Academic Press, Orlando, Vol. 1, pp. 437-468 (1987).
15. D. Morichère, P.-A. Chollet, W. Fleming, M. Jurich, B. A. Smith and J. D. Swalen, *J. Opt. Soc. Amer. B*, **10**, 1894 (1993).
16. M. Eich, private communication.

17. M. L. Dumont, Y. Levy and D. Morichère, "Electrooptic organic waveguides: optical characterization," in *Organic Molecules for Nonlinear Optics and Photonics*, J. Messier, F. Kajzar and P. Prasad (editors), NATO ASI Series, Kluwer Academic Publishers, pp. 461-480 (1991).
18. J. C. Loulergue, M. L. Dumont, Y. Levy, P. Robin, J. P. Pocolle and M. Papuchon *Thin Solid Films*, **160**, 399 (1988).
19. V. Dentan, Y. Levy, M. Dumont, P. Robin and E. Chastaing, *Opt. Commun.*, **69**, 379 (1989).
20. D. Morichère, M. Dumont, Y. Levy, G. Gadret and F. Kajzar, *Proc. SPIE*, **1560**, 214 (1991).
21. S. Herminghaus, B. A. Smith and J. D. Swalen, *J. Opt. Soc. Amer. B*, **8**, 2311 (1991).
22. C. B. Rider, J. S. Schildkraut and M. Scozzafava, *J. Appl. Phys.*, **70**, 29 (1991).
23. D. Haas, H. Yoon, H. -T. Man, G. Cross, S. Mann and N. Parsons, *Proc. SPIE*, **1147**, 222 (1989).
24. C. C. Teng and H. -T. Man, *Appl. Phys. Lett.*, **56**, 1735 (1990).
25. J. S. Schildkraut, *Appl. Optics*, **29**, 2839 (1990).
26. K. Clays and J. S. Schildkraut, *J. Opt. Soc. Amer. B*, **9**, 2274 (1992).
27. Y. Levy, M. Dumont, E. Chastaing, P. Robin, P.-A. Chollet, G. Gadret and F. Kajzar, *Nonlin. Opt.*, **4**, 1 (1993).
28. P. Röhl, B. Andress and J. Nordmann, *Appl. Phys. Lett.*, **59**, 2793 (1991).
29. M. Sigelle and R. Hierle, *J. Appl. Phys.*, **52**, 4199 (1981).
30. S. Ducharme, J. Feinberg and R. R. Neurgaonkar, *IEEE J. Quantum Electronics*, **QE-23**, 2116 (1987).
31. K. D. Singer, M. G. Kuzyk, W. R. Holland, J. E. Sohn, S. J. Lalama, R. B. Comizzoli, H. E. Katz and M. L. Schilling, *Appl. Phys. Lett.*, **53**, 1800 (1988).
32. D. J. Williams, private communication.
33. L. M. Hayden, G. F. Sauter, F. R. Ore, P. L. Pasillas, J. M. Hoover, G. A. Lindsay and R. A. Henry, *J. Appl. Phys.*, **68**, 456 (1990).
34. H. Uchiki and T. Kobayashi, *J. Appl. Phys.*, **64**, 2625 (1988).
35. R. Meyrueix, J. P. Lecomte and G. Tapolsky, *Nonlin. Opt.*, **1**, 201 (1991).
36. K. C. A. Eldering, A. Knoesen and S. T. Kowel, *J. Appl. Phys.*, **69**, 3676 (1991).
37. D. Yankelevich, A. Knoesen, C. A. Eldering and S. T. Kowel, *Proc. SPIE*, **1560**, 406 (1991).
38. D. Yankelevich, A. Knoesen, C. A. Eldering and S. T. Kowel, *J. Appl. Phys.*, **69**, 3676 (1991).
39. J. I. Thackara, M. Jurich and J. D. Swalen, *J. Opt. Soc. Amer. B*, **11**, 835 (1994).
40. O. S. Heavens, *Optical Properties of Thin Solid Films* (Dover Publications, New York, 1965) pp. 46-74.
41. J. F. Rabolt and J. D. Swalen, "Structure and Orientation in Thin Films: Raman Studies with Integrated Optical Techniques," in *Spectroscopy of Surfaces, Advances in Spectroscopy*, **16**, R. J. H. Clark and R. E. Hester (editors), (J. Wiley & Sons Ltd., Chichester, 1988) pp. 1-36.
42. W. H. G. Horsthuis and G. J. M. Krijnen, *Appl. Phys. Lett.*, **55**, 616 (1989).
43. A. Nahata, C. Wu and J. T. Yardley, *IEEE Trans. Instrum. Meas.*, **41**, 128 (1987).
44. A. Nahata, J. Shan, J. T. Yardley and C. Wu, *J. Opt. Soc. Amer. B*, **9**, 1552 (1993).
45. J. F. Valley, J. W. Wu and C. L. Valencia, *J. Appl. Phys.*, **57**, 1084 (1990).
46. B. A. Smith, M. Jurich, W. E. Moerner, W. Fleming, J. D. Swalen, G. C. Bjorklund and W. Volksen, *Proc. SPIE*, **2025**, 499 (1993).
47. J. I. Thackara, G. C. Bjorklund, W. W. Fleming, M. C. Jurich, B. A. Smith and J. D. Swalen, *Proc. SPIE*, **2025**, 564 (1993).
48. K. D. Singer, M. G. Kuzyk and J. E. Sohn, *J. Opt. Soc. Am. B*, **4**, 968 (1987).
49. R. H. Page, M. C. Jurich, B. Beck, A. Sen, R. J. Twieg, J. D. Swalen, G. C. Bjorklund and C. G. Willson, *J. Opt. Soc. Amer. B*, **7**, 1239 (1990).

Development and Application of Organic Electro-Optic Modulators

L. R. DALTON, C. XU, A. W. HARPER, R. GHOSH, B. WU,
Z. LIANG, R. MONTGOMERY and A. K.-Y. JEN*

*Loker Hydrocarbon Research Institute, University of Southern California,
Los Angeles, CA 90089-1661, *EniChem America Inc., Research
and Development Center, Cornwall Road, Monmouth Junction,
NJ 08852*

Received 1 March 1994; accepted 16 March 1994

An overview of the status of development of prototype electro-optic modulators is presented together with a progress report of work being carried out at the University of Southern California. Fabrication of high frequency (1 MHz to 100 GHz) electro-optic modulators requires not only the development of materials with large optical nonlinearity but also materials capable of being processed into low loss, buried channel, nonlinear optical waveguides which can be impedance matched and secured by mechanically stable coupling to fiber optic transmission lines. Moreover, organic polymeric materials must then be interfaced to metal drive electrodes and accompanying semiconductor electronic circuitry. The various steps of synthesis and processing necessary to achieve an integrated polymer/semiconductor device are discussed with emphasis on the latest research advances in each area. Particular emphasis is given to the utilization of ultrastructure synthesis schemes which permit realization of thermally-stable, noncentrosymmetric lattices.

PREPARATION OF STABILIZED NONCENTROSYMMETRIC LATTICES INCORPORATING LARGE β CHROMOPHORES

With the exception of octopolar chromophores,¹ organic second order nonlinear optical materials have been prepared from dipolar chromophores of the general form, (electron donor)-(π electron connective segment)-(electron acceptor). The relationship of first hyperpolarizability, β , to structure is becoming reasonably well understood even within the framework of simplified theoretical models.² However, device requirements demand not only an adequate β value but also good thermal stability to withstand the temperatures encountered in fabrication of integrated organic/inorganic devices and in the operation and storage of these devices. Thus, trade-off is often made between optimizing optical nonlinearity and thermal stability, e.g., heteroaromatic moieties are being used with increasing frequency as replacements for polyene segments as the connective element in dipolar chromophores.^{2,3} Once an adequate chromophore has been synthesized, it must be incorporated into a noncentrosymmetric arrangement in a macroscopic lattice.

Three general approaches have been used to achieve this objective; namely, (1) exploitation of molecular self-assembly—most notably, crystal growth or incorporation into inclusion compounds; (2) sequential synthesis exploiting Van der Waals, ionic, or

covalent interactions, and (3) utilization of external force, e.g., induction of molecular order by electric field poling.

Molecular self-assembly is, of course, chromophore specific and natural formation of noncentrosymmetric lattices is quite rare due to dipolar repulsion between chromophores.⁴ Moreover, coupling of organic crystals to fiber optic transmission lines and interface of organic crystals to drive electrodes in electro-optic modulators poses difficulties. This comment, of course, also applies to inorganic crystals such as lithium niobate. Thus, while crystal growth continues to hold promise for frequency doubling applications, this approach currently is not the method of choice for preparation of materials for electro-optic modulation applications.

A variety of sequential synthesis methods have been adapted to the preparation of noncentrosymmetric lattices. These include Langmuir-Blodgett methods,⁴ Merrifield-type stepwise covalent coupling reactions,⁴⁻⁶ stepwise ionic coupling reactions,^{4,7} and modified molecular beam epitaxy methods.^{4,8} Sequential synthesis methods afford the advantage of permitting the preparation of thin films of precisely controlled dimensions which can be quite useful in phase-matched second harmonic generation. However, fabrication of films of thicknesses on the order of 1 micron becomes quite labor intensive. Thus, while sequential methods afford the possibility of very high order and the preparation of intricate and highly defined structures,^{4,5,6} such methods cannot currently be viewed as the method of choice for fabricating prototype electro-optic modulators. The current method of choice for the fabrication of noncentrosymmetric lattices used in electro-optic modulators appears to be electric-field poling.

Electric-field poling can be applied quite generally to dipolar chromophores existing as components of polymer composites, as pendants covalently coupled to polymer backbones, or as covalently-incorporated components of polymer backbones.⁴ Utilization of composites has the advantage of convenience as commercially available chromophores and host polymers can frequently be employed without chemical modification. The disadvantages of composite materials include finite solubility of the nonlinear optical chromophore in the host polymer, phase separation and chromophore aggregation, poor coupling of the chromophore dynamics to that of the host polymer leading to relaxation of poling-induced order, sublimation of chromophores at high processing temperatures, and dissolution of chromophores with application of cladding layers. Composites appear most promising when the host polymer exhibits a high glass transition temperature, T_g .

Attachment of chromophores as pendants to flexible chain polymer backbones or incorporation of chromophores as components of the polymer backbone leads to improvement in chromophore loading and in the stability of poling-induced order relative to composite materials; however, realization of stability at temperatures above ambient requires further lattice hardening reactions.

In the following, we discuss three general schemes for achieving lattice hardening (T_g elevation) subsequent to inducing noncentrosymmetric order by electric field poling. These include (1) use of end-functionalized chromophores to carry out a two-step synthesis.⁹ In the first step (polymerization reaction), a processible precursor polymer is synthesized, spin cast into an optical quality film, heated and poled. The second step consists of an addition or condensation reaction to produce a heavily-crosslinked (hardened) matrix. (2) The second approach exploits the well-known

imidization reaction to achieve lattice hardening.^{4,10,11} (3) The third procedure uses multi-functional chromophores to achieve a tightly coupled three-dimensional lattice. This approach can be viewed as analogous to sol-gel processing of glasses¹² or as a modification of the first procedure where steps one and two are not clearly separated.

A schematic representation of the first procedure is shown in Figure 1. Practical examples are given in Figures 2, 3 and 4; representative thermal stabilities are given in Figures 5 and 6. Note that although we are interested in electro-optic modulation in this communication, second harmonic generation is used to assess the thermal stability of the second order optical nonlinearity in materials being developed for modulator applications. This detection scheme is chosen simply for its convenience. Details of the synthesis of the monomers and polymers are reported elsewhere.^{9,13} The temporal stability data shown in Figures 5 and 6 clearly indicates the effectiveness of heavy crosslinking in enhancing the stability of nonlinear optical activity at elevated temperatures. We have also found it useful to employ a dynamic assay of the thermostability of nonlinear optical activity. In Figure 7, we show a schematic representation of the experimental arrangement used to effect such measurements; and in Figure 8, we show representative data. Comparison of data such as shown in Figure 8 with thermal gravimetric analysis data is useful in understanding the roles of both lattice (polymer)

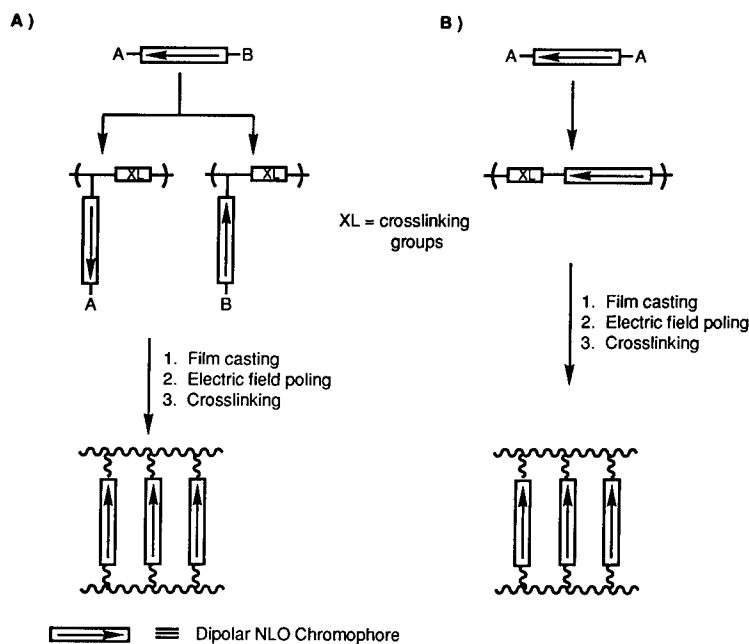


FIGURE 1 General methodologies for preparing crosslinked matrices using endfunctionalized chromophores are shown. In Figure 1A, the intermediate processible polymer contains the chromophore as a pendant and crosslinking involves the A or B functionalities at the free ends of the chromophores. In Figure 1B, the intermediate processible polymer contains the chromophore as an integral component of the backbone and crosslinking involves the XL moiety on adjacent chains. The functionalities A and B are capable of undergoing either condensation or addition reactions.

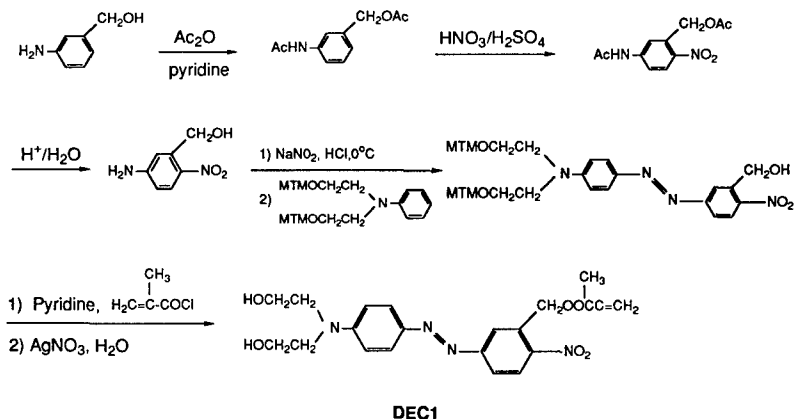


FIGURE 2 Synthesis of a disperse red derivatized double-end crosslinkable chromophore is shown. This chromophore has been used with the pendant approach of Figure 1A.

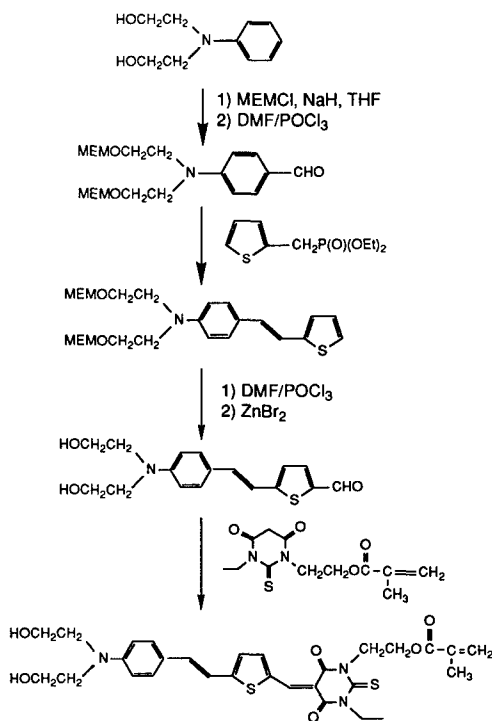


FIGURE 3 Synthesis of a high β , double-end crosslinkable chromophore is shown. This chromophore has been used with the pendant approach of Figure 1A.

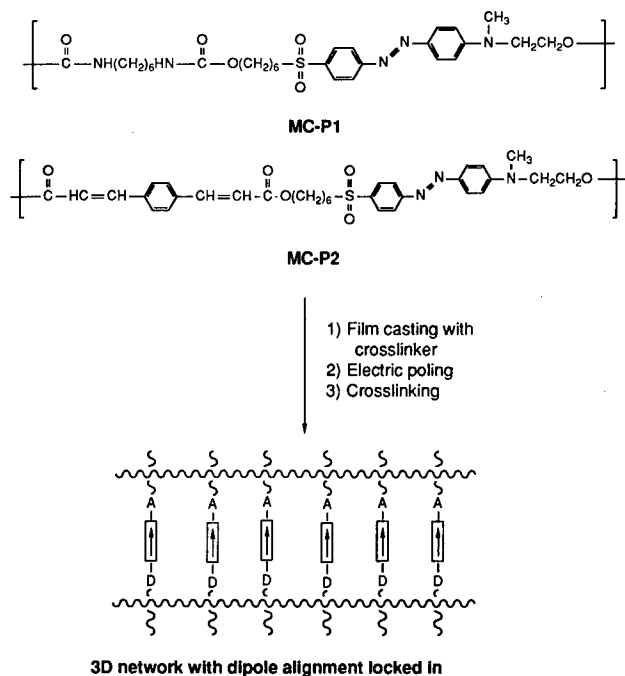


FIGURE 4 Polymers containing double-end functionalized chromophores as components of the polymer backbone are shown. This corresponds to the scheme shown in Figure 1B.

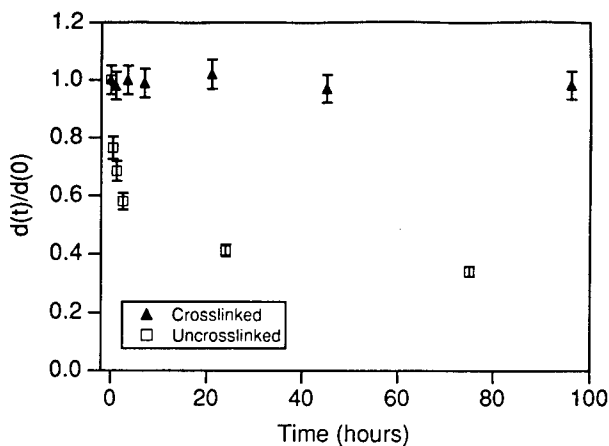


FIGURE 5 The temporal stabilities of two samples, prepared using the chromophore of Figure 2, and maintained at 100°C are shown. The solid triangles are for a sample which has not been crosslinked; thus, these data correspond to a pendant polymer. The open squares are for the sample material which has been crosslinked. Note that second harmonic generation is used to assess the temporal stability of optical nonlinearity.

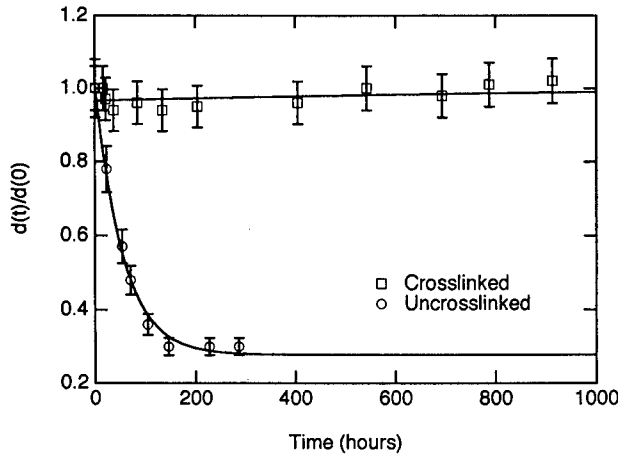


FIGURE 6 The temporal stabilities of two samples prepared according to Figure 4 are shown. Again a dramatic improvement in the temporal stability of optical nonlinearity is observed upon crosslinking.

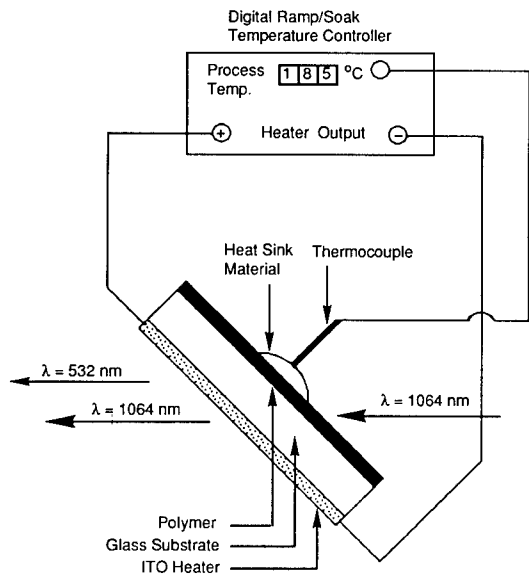


FIGURE 7 A schematic diagram of the thermal ramping setup used to assess the thermal stability (referred to as the “dynamic” stability) of optical nonlinearity (i.e., second harmonic generation) is shown.

dynamics and lattice decomposition in loss of optical nonlinearity at elevated temperatures. Detailed analysis of dynamic NLO data such as shown in Figure 8 is also useful in accessing the effectiveness of lattice hardening reactions. A step trace which does not reflect complete loss of NLO activity (such as shown in Fig. 9) can be indicative of incomplete lattice crosslinking. The step nature of the curve reflects the existence of

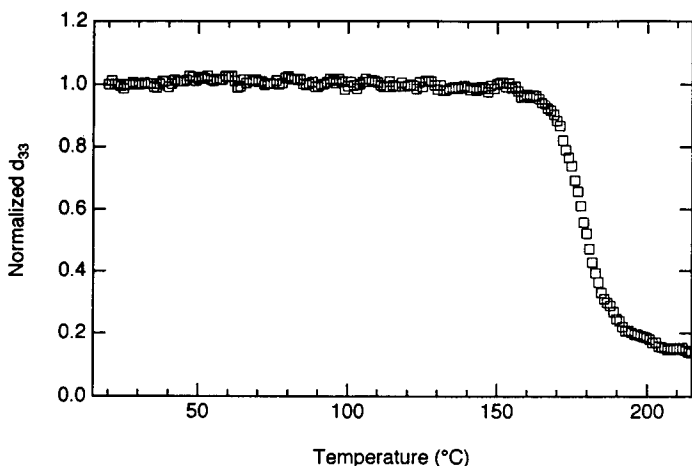


FIGURE 8 The "dynamic" thermal stability obtained using the apparatus of Figure 7 is shown for a crosslinked polymer prepared from the NLO chromophore shown in Figure 2.

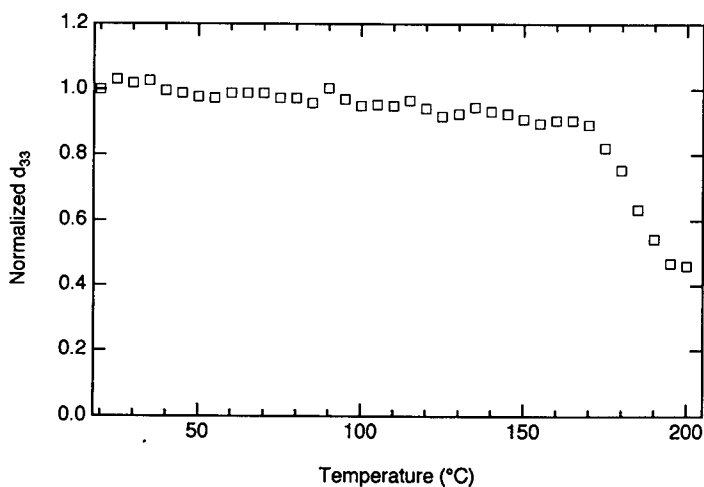


FIGURE 9 The "dynamic" thermal stability for a crosslinked polymer prepared from the DEC4 chromophore (shown in Figure 10) is given. Note the retention of substantial optical nonlinearity even after the breakpoint temperature which illustrates heterogeneity of crosslink density in the lattice.

regions of the lattice with different crosslinking densities. The progress of lattice hardening can be investigated by repeating dynamic measurements on samples exposed to different reaction conditions. Such studies, together with pressure-dependence studies to assess the dependence of free volume upon crosslinking, should in the future prove useful in both optimizing lattice hardening protocols and in assessing the limits of this approach for enhancing thermal stability of NLO lattices. As might be expected,

an empirical relationship can be established between dynamic and static assays of thermal stability; long term stability is routinely observed for temperatures 30°C or more below the temperature at which loss of NLO activity is first observed in the dynamic assays.

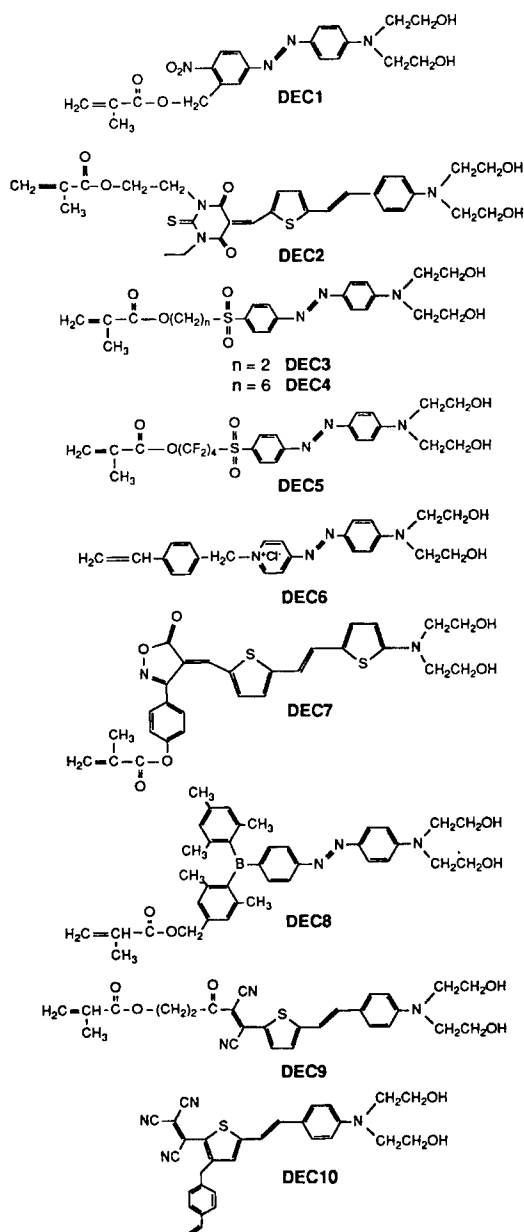


FIGURE 10 Representative double-end crosslinkable chromophores are shown.

Representative chromophores used with procedure 1 are listed in Figure 10. Some general comments can be made concerning the current state-of-the-art for this approach. Currently, stability for periods of several thousand hours at temperatures in the range 90 to 150°C are realized with this approach. This is by no means the ultimate stability possible with this approach since complete lattice hardening has not likely been realized and the polymers currently used contain extended flexible chain segments. Reduction of the extent of flexible chain segments should permit long term stability at higher temperatures to be realized; however, this improvement may be at the price of some reduction in poling efficiency. Employing azobenzene chromophores, we have achieved thermally stable r_{33} values in the range 7–13 pm/V (using a sulfonyl acceptor)¹⁴ and 17 pm/V (using a nitro group acceptor). Waveguides with optical losses, at 1.3 micron wavelength, on the order of 0.1 dB/cm have been fabricated from these materials. With high β chromophores, thermally-stable electro-optic coefficient values of 30 pm/V have been achieved although it should be noted that these values do not reflect the optimization of poling protocols for these materials.

Two general synthetic approaches have been employed to achieve modified polyimide lattices containing covalently incorporated chromophores. These schemes are illustrated in Figures 11 and 12 and representative data on the thermal stability of NLO activity are shown in Figures 13 and 14. The behavior observed for these modified polyimide systems is similar to that observed for the lattices prepared by procedure 1. Electro-optic coefficients are slightly less and the thermal stability is slightly superior

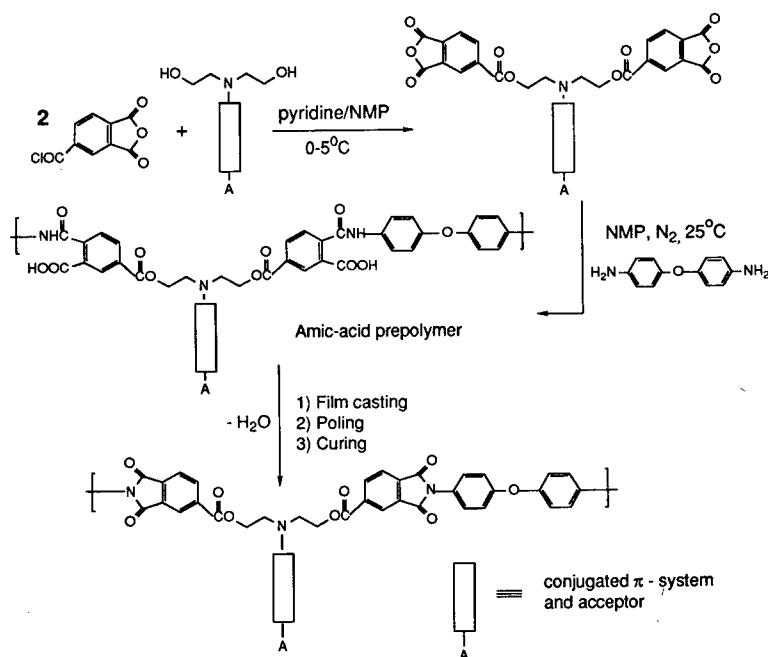


FIGURE 11 A scheme which has been employed to incorporate a variety of NLO chromophores into polyimide lattices is shown.

(long term stability has been observed to temperatures as high as 175°C). The processing protocol is similar between procedures 1 and 2 in that in both cases a processible precursor (to the final hardened polymer) polymer is prepared. In procedure 2, the processible material is a polyamic acid. A problem with the imidization step

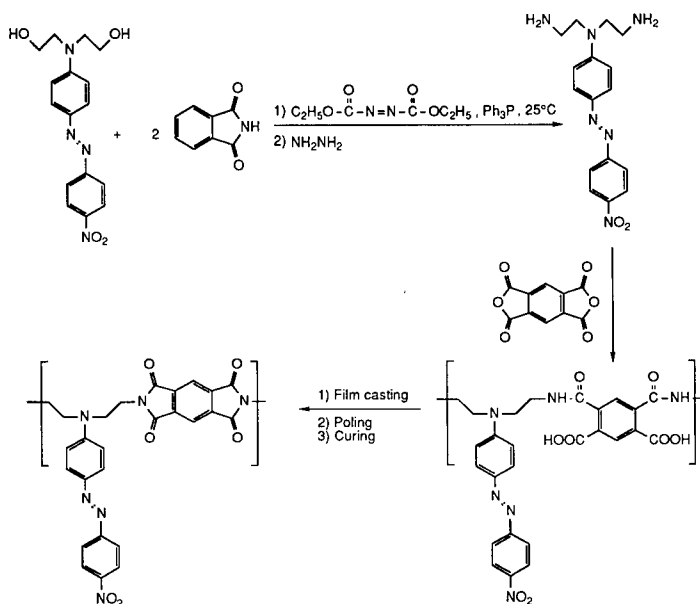


FIGURE 12 A second scheme for incorporation of NLO chromophores into polyimides is shown. This scheme has resulted in exceptionally high chromophore loading.

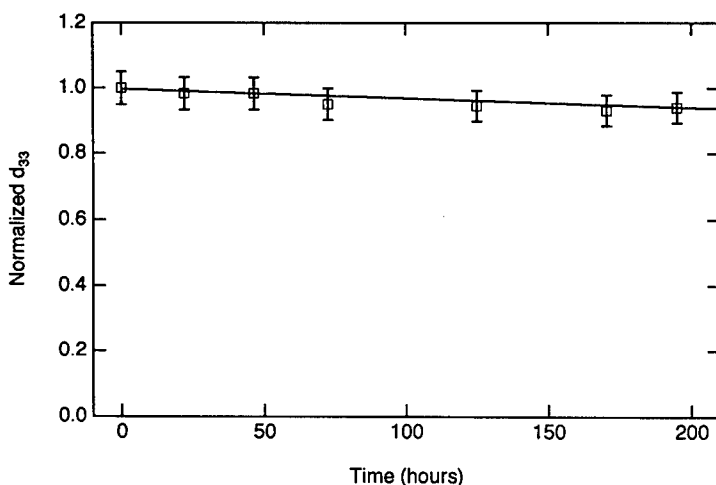


FIGURE 13 The temporal stability at 90°C of NLO activity of a chromophore containing polyimide prepared according to the scheme of Figure 11 is shown.

is that quite high temperatures are required for complete imidization. If these temperatures are not achieved in the hardening step, then lattice condensation may occur during thermal aging at elevated temperatures. We typically observed this phenomena as a slow loss of optical nonlinearity with aging. Another feature of modified polyimides worth noting is that, depending upon the exact nature of the structure, it may be difficult to achieve films of high optical quality. This is likely due to the fact that spin casting options (e.g., choice of solvent) are more limited for modified polyamic acids than for the precursor polymers of procedure 1.

Two different schemes following procedure 3 are illustrated in Figures 15 and 16 and representative thermal stability data are shown in Figures 17, 18 and 19. Again, in the broader sense, comparable thermal stability and optical nonlinearities are observed for this approach as for procedures 1 and 2. At a closer level of comparison the magnitudes of the electro-optic coefficients and the thermal stability of nonlinear optical activity are not quite as good with this approach; this observation likely reflects the fact that the poling and lattice hardening steps are not cleanly separated and the latter interferes with the former. Moreover, complete lattice hardening is realized only at elevated temperatures so that temporal stability studies often reveal a slow evolution of optical nonlinearity. Of course, an advantage of procedure 3 is that it permits modified sol-gel glasses to be prepared which may be of potential utility for interfacing with fiber optic transmission lines.

At this point in time no absolute preference can be argued for one of the above three procedures although prototype devices have largely been fabricated employing procedures 1 and 2. Clearly, more effort is required to optimize and evaluate each of the approaches. On the positive side, it is already clear that any of the above approaches can fulfill the thermal requirements of electro-optic modulator applications.

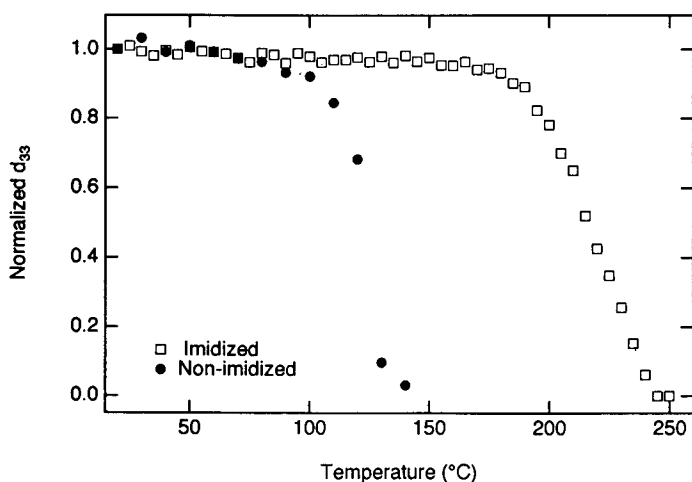
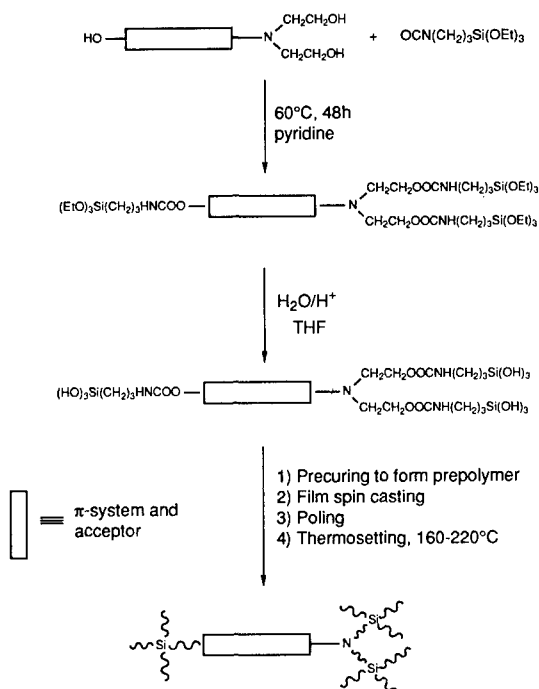


FIGURE 14 The "dynamic" thermal stability of NLO activity of the chromophore of Figure 13 is shown. The heating rate is 10°C/min.



3D network with dipole alignment locked in

FIGURE 15 A generalized sol-gel synthesis scheme incorporating second order NLO chromophores is shown.

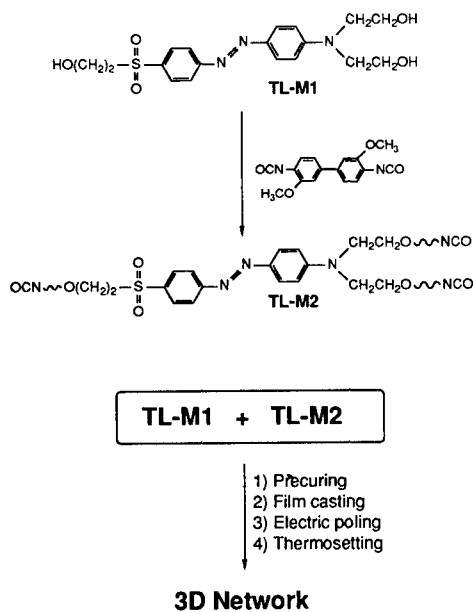


FIGURE 16 A thermosetting organic system, analogous to the sol-gel scheme of Figure 15, is shown.

PREPARATION OF BURIED CHANNEL NONLINEAR OPTICAL WAVEGUIDES

Four different procedures have been utilized for the fabrication of buried channel nonlinear optical waveguides.⁴ These include (1) photochemical processing,^{4,14,15} (2) reactive ion etching (RIE),¹⁴ (3) laser etching,⁴ and (4) spatially selective poling.⁴

A variety of photochemical processes can lead to reduction in index of refraction necessary to prepare a channel waveguide structure. These include trans-to-cis isomerizations (such as encountered with azobenzene chromophores), ring opening reactions, interconversion between charge transfer conformations, etc. Most of the

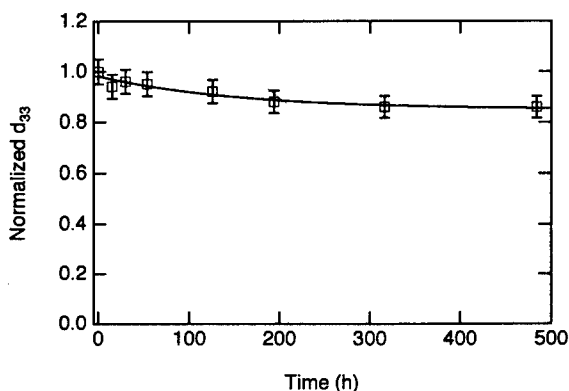


FIGURE 17 The temporal stability of the nonlinear optical activity of the material prepared according to the sol-gel scheme of Figure 15 is shown. The sample was maintained at 100°C for these measurements. Note the gradual loss of nonlinear optical activity with time.

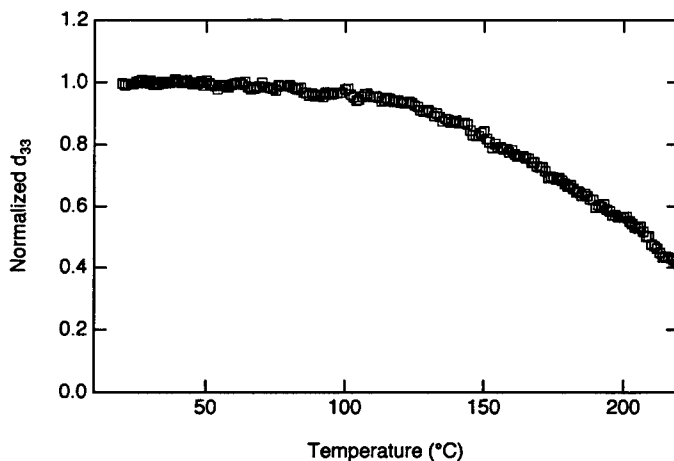


FIGURE 18 The "dynamic" thermal stability of the material prepared according to the procedure of Figure 15 is shown. Note the gradual loss of optical nonlinearity with thermal ramping in contrast to the observations for the materials prepared according to procedures 1 and 2.

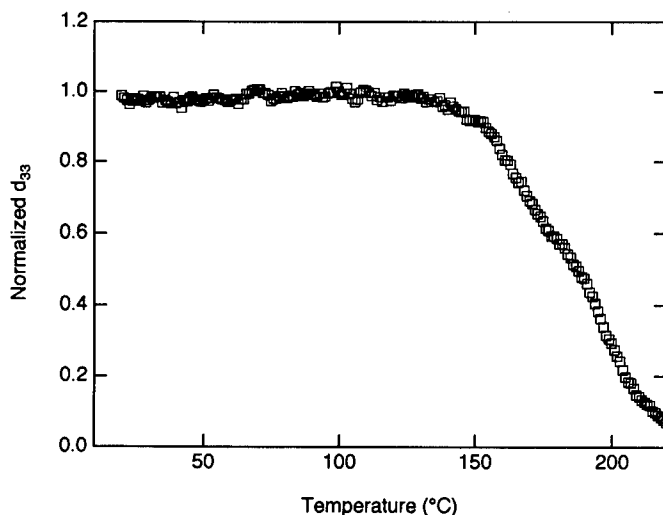


FIGURE 19 The "dynamic" thermal stability of a material prepared according to the procedure of Figure 16 is shown.

photochemical processing reported in the literature, including the work carried out at USC, has focused upon trans-to-cis isomerization.^{4,14,15} Note that the actual mechanism of index change observed for azobenzenes is more complex than simple trans-to-cis isomerization and likely involves rapid relaxation back to the trans conformation but in such a manner that the net effect is that of molecular reorientation.

Photochemical processing can be used to fabricate a buried channel waveguide directly without deposition of a cladding layer. The procedure involves two step, two color processing with change of the mask between steps. The development of a buried channel by this procedure depends upon the fact that the penetration of the radiation into the sample will depend upon radiation wavelength. The first step involves use of a mask (Karl Suss MJB3 mask aligner) to protect a channel of high index, nonlinear optical material from the top of the film to the bottom. Radiation at a wavelength characterized by low absorption (hence good penetration through the film) is used to reduce the index of refraction of the material around the protected region. The low absorption must, of course, be offset by a long exposure time to achieve effective bleaching. Following this step, the mask is removed and the unbleached region is exposed to radiation of a wavelength corresponding to the absorption maximum (or near the maximum). Electromagnetic radiation of such a wavelength has a shallow penetration depth so, for a short exposure time, bleaches only the uppermost region creating a buried channel of unbleached, nonlinear optical material. Moving from the bottom to the top of the material, one finds (1) the lower cladding layer, (2) the unbleached, high index, nonlinear optically active channel surrounded by bleached regions, and (3) the bleached, low index upper layer. This process is illustrated in Figures 20 and 21.

The second method that we have employed to fabricate buried channel waveguides is reactive ion etching and the general scheme is outlined in Figure 22. An oxygen plasma

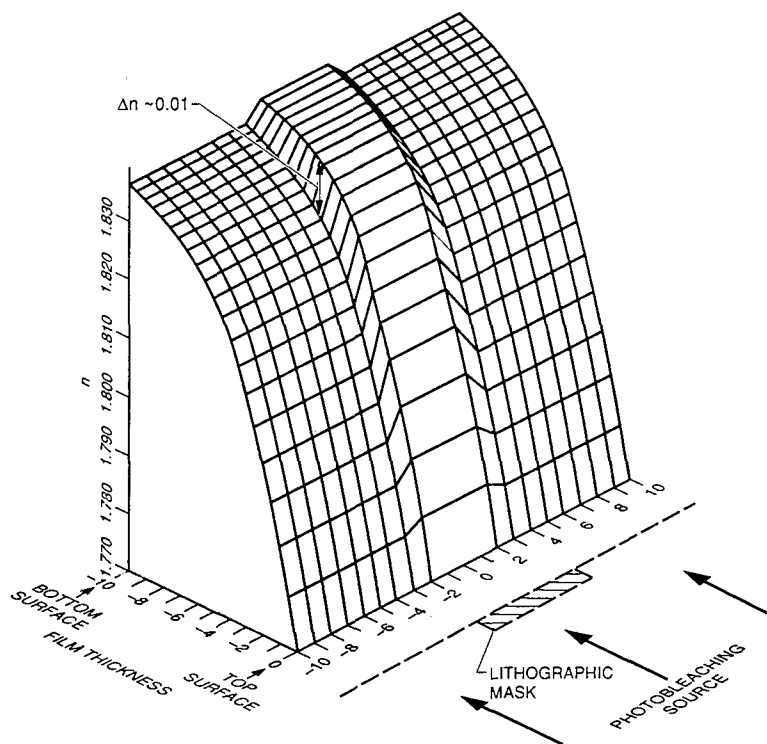


FIGURE 20 A cross-section of the refractive index in a film resulting from photobleaching at two wavelengths using a lithographic mask is shown.

is known to react with most organic polymers. This method does not change the refractive index but rather the shape of the thin films as indicated in Figure 22. Most waveguides prepared with RIE have a ridge cross section so the waveguide area is protected and the surrounding area is exposed to an oxygen plasma. In our experiments, we typically coat a layer of photoresist (Shipley 1400-17) directly onto the surface of a poled polymer film so that an etch mask can be defined to protect the desired waveguide region. We use a mask aligner and a laser patterned photomask in our photolithographic process. The etch mask is obtained after development and rinse with deionized water. The structure was then etched in a Plasma Technology model DP80M RIE apparatus employing 200 millitorr oxygen pressure and 100 watts radio-frequency power. For a typical azobenzene containing polymer such as discussed above, the initial etch rate was approximately sixty angstroms/second while the etch rate of the photoresist was on the order of approximately twenty angstroms/second. In Figure 23, we show a typical Y-branch of an integrated Mach-Zehnder interferometer prepared by RIE. An advantage of the RIE method is that it is compatible with silicon v-groove technology for the pigtail of the nonlinear optical channel to fiber optic transmission lines. Moreover, the RIE method can be more generally applied than photochemical processing in that it does not require the presence of a photoactive species.

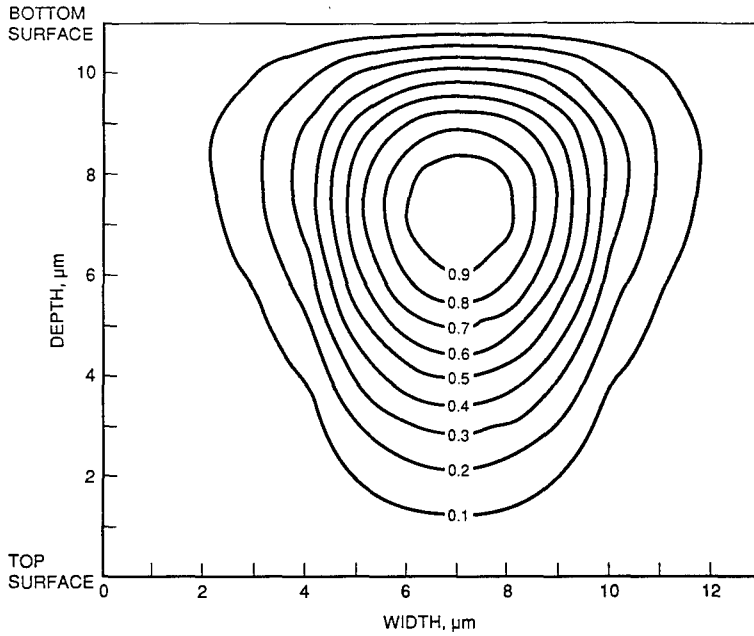


FIGURE 21 A contour plot of the single guided mode supported by the photobleached index profile is shown.

Buried Channel Waveguide Fabrication

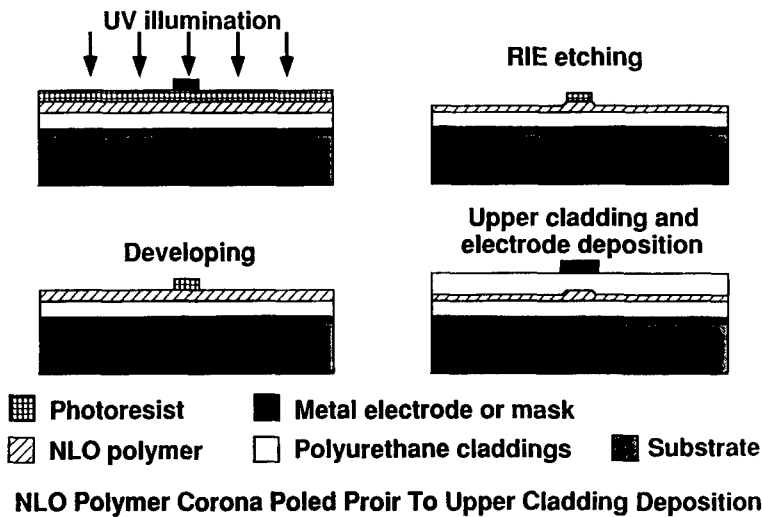


FIGURE 22 The steps involved in producing a buried channel waveguide by reactive ion etching are shown.

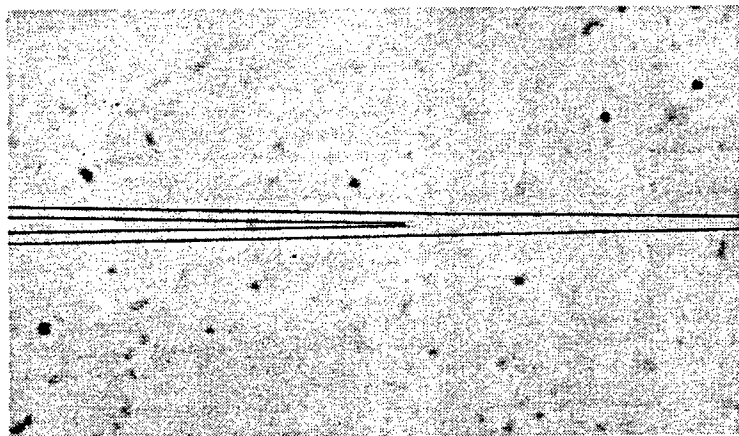


FIGURE 23 A Y-branch defined by RIE in a polymer film fabricated from chromophore DEC4 of Figure 10 is shown. The magnification of the optical microscope is times 200.

Finally, we note that RIE avoids the problem of unwanted photochemical aging of structures with exposure to environmental radiation during the lifetime of the device. However, we emphasize that it is clearly possible to use more than one technique in processing a material for nonlinear optical applications and it is possible to encapsulate materials to avoid environmental radiation; thus, a discussion of the advantages of one method versus another is somewhat misleading.

Of course, index of refraction variations and the dimensions of the buried channel structure define mode propagation characteristics of the waveguide. Single mode propagation is desired in many devices such as integrated Mach-Zehnder interferometers. Since the indices of the films are fixed and not easily varied, we choose two parameters, film thickness and etching depth, to control modal characteristics. From the standpoint of optical fiber coupling, we desire to maximize the waveguide cross section to reduce coupling losses. Thus, we first calculate the maximum film thickness using the effective index method, to determine the maximum waveguide width at a given etch depth and maximum film thickness for single mode operation. Two typical structures, based upon representative materials discussed in preceding sections, are shown in Figure 24.

Laser etching is analogous to RIE but uses laser ablation to define the ridge or channel. Care must be taken in this process to insure that the active region temperature does not exceed the depoling temperature of the polymer or alternately the polymer must be poled after the laser etch process.

Spatially selective poling produces a birefringence of aligned poled material.⁴ This approach suffers from the disadvantage of limiting poling configuration so that corona and in-plane configurations are not conveniently used. The result is often some reduction in poling efficiency.

Although some experimentation has been carried out for all four procedures, our greatest success and hence focus has involved photochemical and reactive ion etching protocols.

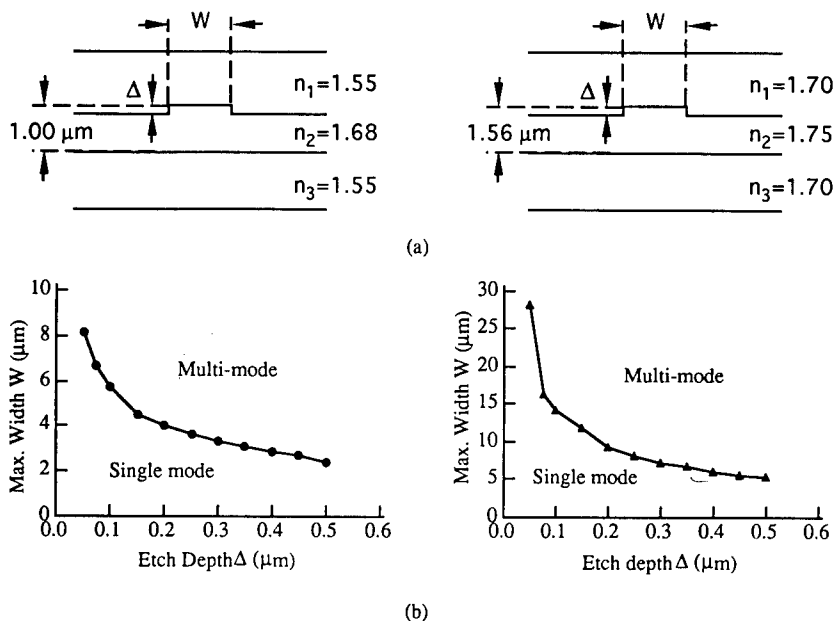


FIGURE 24 Conditions for single and multi-mode operation defined in terms of waveguide dimensions are given for two polymers. Data on the left hand side of the figure are for a modified polyurethane polymer covalently incorporating an azobenzene chromophore while the data on the right hand side of the figure are for a modified polyimide polymer covalently incorporating an azobenzene chromophore.

COUPLING TO FIBER OPTIC TRANSMISSIONS LINES, ELECTRONIC-OPTICAL CIRCUIT INTEGRATION, AND PROTOTYPE DEVICE EVALUATION

A schematic representation of a representative electro-optic modulator and associated test bed is shown in Figure 25. It is clear that once a buried channel nonlinear optical waveguide has been fabricated these components must be integrated with the remaining optical and electronic circuitry.

Optical integration has been accomplished either by prism coupling or by pigtailling to fiber optic transmission lines. Prism coupling is convenient and has been the most commonly used approach. However, this mode of coupling is not commercially viable and is of utility only for prototype device demonstration. Commercial applications of electro-optic modulators require a compact, efficient, and mechanically stable coupling to commercially available fiber optic transmission lines. Pigtailling to fiber optic lines appears to be a critical area for the development of practical electro-optic modulators. We have chosen to effect pigtailling by exploiting silicon v-groove technology. Two coupling schemes which we have pursued are shown in Figure 26. A meaningful evaluation of the ultimate coupling efficiency which can be realized by this approach cannot be given at this time. Indeed, a great deal remains to be done to optimize coupling efficiency, e.g., photochemical tuning of indices of refraction to achieve

Experiment Setup

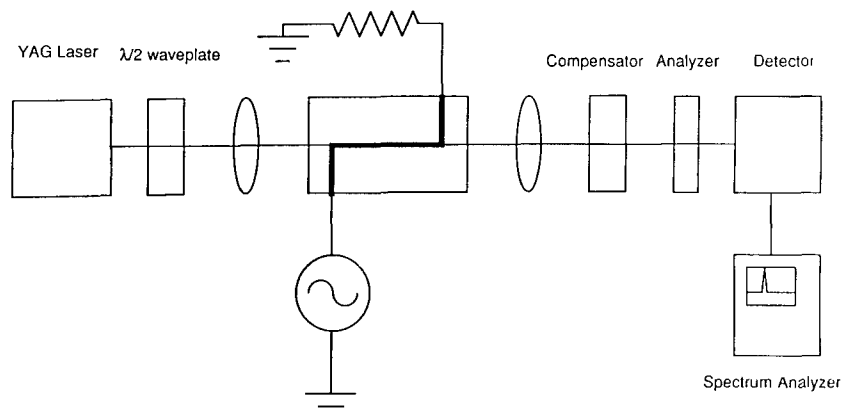
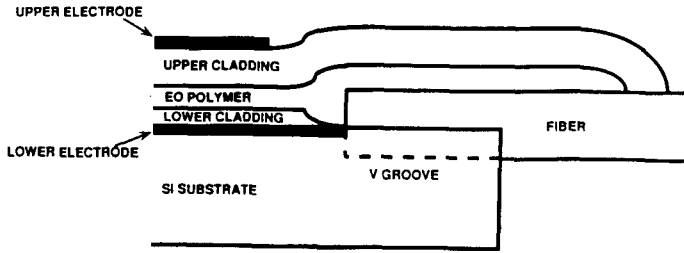


FIGURE 25 A schematic representation of an electro-optic modulator and associated test bed is shown.

optimum coupling. However, this technique works sufficiently well at this time to permit construction and evaluation of prototype devices.

Deposition of metal electrodes and optimization of the coupling of radiofrequency (microwave, millimeter wave) radiation into the nonlinear optical waveguides is again a process which can be reasonably well accomplished with current materials but is an area where improvements can be realized by improved electrode design, by development of improved materials, and by development of creative processing techniques.

A brief comment regarding electrode design is appropriate. Most electro-optic modulators have been fabricated employing a Mach-Zehnder design which effects an amplitude modulation of an optical beam.^{4,16-21} We have also fabricated prototype modulators employing the z-line electrode design^{4,14} shown in Figure 27. This modulator can be used either as a phase or a birefringence amplitude modulator. If the input is either a pure TE or a pure TM mode, the device acts as a phase modulator. If the input beam excites both TE and TM modes, the birefringence of the waveguide is changed by the applied voltage and the output polarization changes according to the modulation field. The analyzer shown in Figure 27 converts the polarization modulation into an amplitude modulation. Representative modulation signals are shown in Figures 28 and 29. These signals were detected using an InGaAs p-i-n photodetector (Fermionics FD80S) and monitored by a Hewlett-Packard HP8652A spectrum analyzer. Although these signals were obtained using thick cladding layers (total device thickness approximately 15 microns) and the modulator uses only 2/3 of the available r_{33} nonlinearity, a halfwave V_{π} voltage of 35 volts was obtained using a 15 mm electrode (this corresponds to an electro-optic coefficient of 12 pm/V which was expected for the azobenzene incorporated polymer used). This design has also recently been explored by other groups.^{22,23}



A. ETCHED POLYMER LOWER CLADDING - STRIP LINE

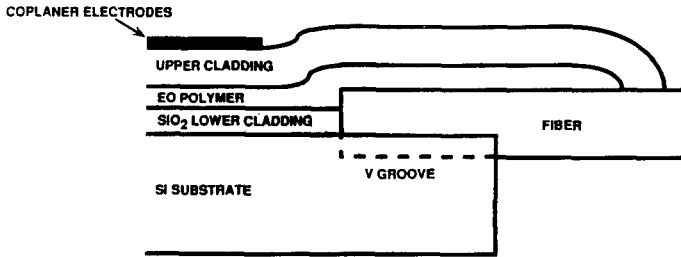
B. ETCHED SiO_2 LOWER CLADDING - COPLANAR ELECTRODES TRANSMISSION LINE

FIGURE 26 Two schemes for pigtailing nonlinear optical waveguides to fiber optic transmission lines are schematically illustrated.

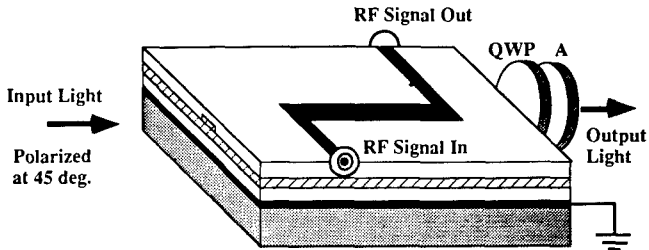
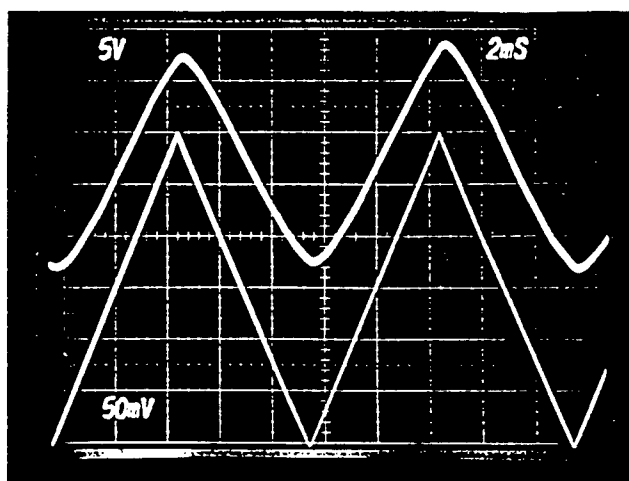
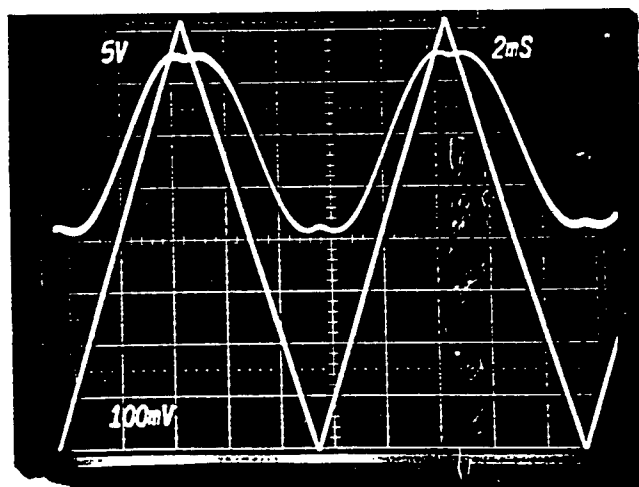


FIGURE 27 A birefringent electro-optic modulator and input-coupling are shown.

For the sake of completeness, it is appropriate to review the fabrication of the modulator used to obtain the data shown in Figures 28 and 29. The nonlinear optical material is an azobenzene containing polyurethane processed according to procedure 3. Fused quartz slides (ESCO products, Inc.) were used as substrate materials. A layer of

Modulation Signal

 V_{π} MeasurementFIGURE 28 Low frequency modulation and V_{π} measurement are shown.

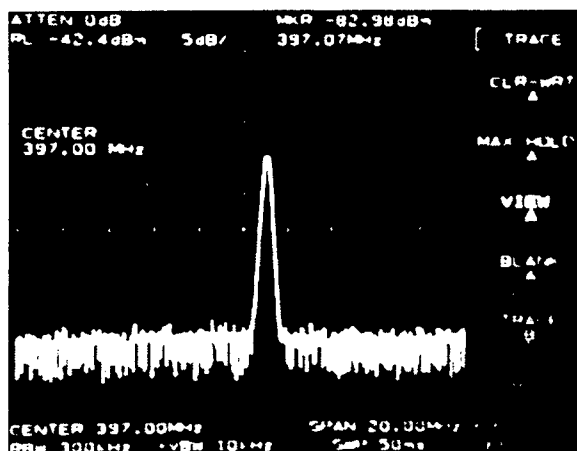


FIGURE 29 A spectrum analyzer scan detecting 400 MHz modulator is shown.

gold (approximately 0.5 micron thick) was sputtered using an argon plasma sputtering system. The lower and upper polymer claddings were cast from commercial polyurethane (Epoxylite 9653-1). The lower cladding was first spin-cast on the gold coated substrate then was baked at 90°C for several hours. The NLO material was dissolved in dioxane and was spin cast into approximately one micron films using a spin speed of approximately 1000 rpm. The film was then heated and poled using a corona discharge set-up with needle to plane distance of approximately 2 cm. A 5.5 KV voltage was applied. The temperature was raised to approximately 160°C and the hardening reaction initiated. The NLO waveguide was then defined by RIE as discussed above. The top cladding layer was spun on top of the etched surface and was cured at room temperature. The upper electrode with dimensions of 15 mm length and 30 microns width was defined photolithographically and was plated to 5 micron thickness to reduce DC resistance.

Both Mach-Zehnder and z-line designs have been evaluated to frequencies approaching 40 GHz and require V_{π} voltages in the range 10–50 volts (depending on the chromophore used, cladding layer thickness, processing conditions, electrode design, etc.). Performance at wavelengths from 0.83 to 1.3 microns has been evaluated. Commercial application will require further improvement in V_{π} , namely, reduction of required drive voltages to digital voltage levels. A critical area of focus for the realistic achievement of modulation at frequencies above 50 GHz is electrode design as losses at electrodes appear to be the limiting factor in the frequency range 50–100 GHz.

It is appropriate to mention one signal transduction application which has quite different requirements than those mentioned above. This is the use of organic electro-optic modulators for photonic detection of radar (electromagnetic) wavefronts. Such modulators are particularly appropriate when a Luneburg lens is employed to amplify (focus) the wavefront. Luneburg lenses are typically constructed of polystyrene so there is no impedance matching problem for organic electro-optic modulators in contrast to the serious impedance matching problem which is faced with lithium niobate

modulators. Moreover, since metal electrodes are not required, many of the thermal processing requirements for organic nonlinear optical materials are greatly relaxed.

CONCLUSIONS

Electro-optic coefficients in the range of several hundred picometers per volt have been realized for several organic crystals⁴; however, such materials are not suitable for development of electro-optic modulators. High β chromophores competitive with the chromophores of the aforementioned crystals, have recently been developed^{2,3} and are being incorporated into processible polymers. Several limitations are inherent to the poled polymer approach including (1) chromophore loading and (2) poling efficiency. Compared to the value of $\chi^{(2)}$ which could be achieved for a perfectly aligned, pure chromophore lattice, at least a factor of two in magnitude of macroscopic optical nonlinearity will be lost due to finite chromophore loading (incorporation in the polymer matrix) and a factor of two will be lost due to finite poling efficiency. Thus, a total reduction of a factor of at least four is expected. In practice, the situation is even worse than this projection and currently observed electro-optic coefficients lie in the range of 30 pm/V. Preliminary results from our laboratory and from other laboratories suggest that this value will be increased by approximately a factor of two in the coming year. Further increase beyond that value will be difficult without new chromophores or techniques for improving loading and noncentrosymmetric alignment. However, 60 pm/V is a very useful number and will certainly make organic modulators competitive with inorganic materials.

It is clear that all of the necessary processing technologies required to realize prototype and commercial electro-optic modulator device packages are now being explored. These procedures include development of buried channel nonlinear optical waveguides, pigtailling to fiber optic transmission lines, and integration with associated electrical circuitry. It is clear that these processing technologies are far from optimized but even in the current primitive state of development prototype devices can be fabricated which operate effectively to 40 GHz with drive voltages in the range 10–50 volts. Clearly, performance will be enhanced in the near future with refinement in the incorporation and processing of high β chromophores. High frequency performance is limited by losses at metal electrodes and electrode design and fabrication must be given increased attention to effectively increase the bandwidth of devices to 100 GHz.

Although transduction of electrical into optical signals for long range transport over fiber optics lines appears to be the dominant application of organic electro-optic modulators, other applications can be anticipated as well. For example, organic electro-optic modulators afford distinct advantages for use in photonic detection of radar signals.

As a final comment, we would note that this communication is an overview of the many activities required to produce practical electro-optic modulators. It is written from the perspective of work carried out at USC. No effort has been made to effect a review of the enormous amount of work that has been carried out by others. Indeed, we assume that much of that work will be appropriately reviewed in this volume. Moreover, no attempt has been made to go into a detailed discussion of each activity

necessary for the production of prototype waveguides. Detailed discussions are deferred to other publications.

ACKNOWLEDGEMENTS

We particularly thank Professor William Steier without whose support and assistance the present work would not be possible. We also thank Professor Harold Fetterman for millimeter wave measurements. We gratefully acknowledge collaboration with Drs. Seth Marder and Joseph Perry on the incorporation of high β chromophores into hardened polymer lattices. This research was supported by the National Science Foundation under Grant DMR-91-07806 and by the Air Force Office of Scientific Research under contracts F49620-91-0054 and F49620-91-0270. This work also benefited from the resources of the National Center for Integrated Photonic Technology.

REFERENCES

1. C. Zyss, *J. Chem. Phys.*, **98**, 6583 (1993); *Nonlinear Optics*, **1**, 3 (1991).
2. S. R. Marder, D. N. Beratan and L.-T. Cheng, *Science*, **252**, 103 (1991); S. Gilmour, A. K.-Y. Jen, S. R. Marder, A. J. Neissink, J. W. Perry, J. Skinkhoj and J. M. Cai, in *Materials Research Society Symposium Proceedings*, Vol. **328**, *Electrical, Optical and Magnetic Properties of Organic Solid State Materials*, eds., A. F. Garito, A. K.-Y. Jen, C. Y.-C. Lee and L. R. Dalton (Materials Research Society, Pittsburgh, 1994) p. 485; G. Bourhill, L.-T. Cheng, G. Lee, S. R. Marder, J. W. Perry, M. J. Perry, and B. G. Tiemann, in *Materials Research Society Symposium Proceedings*, Vol. **328**, *Electrical, Optical and Magnetic Properties of Organic Solid State Materials*, eds., A. F. Garito, A. K.-Y. Jen, C. Y.-C. Lee, and L. R. Dalton (Materials Research Society, Pittsburgh, 1994) p. 625.
3. V. P. Rao, K. Y. Wong, A. K.-Y. Jen and R. M. Mininni, *Proc. SPIE*, **2025**, 156 (1993).
4. L. R. Dalton, L. S. Sapochak, M. Chen and L. P. Yu, in *Molecular Electronics and Molecular Electronic Devices*, Vol. **2**, ed., K. Sienicki (CRC Press, Boca Raton, 1993) pp. 125-208.
5. S. Yitzchaik, A. K. Kakkar, S. B. Roscoe, T. J. Marks, P. M. Lundquist, W. Ling and G. K. Wong, in *Materials Research Society Symposium Proceedings*, Vol. **328**, *Electrical, Optical and Magnetic Properties of Organic Solid State Materials*, eds., A. F. Garito, A. K.-Y. Jen, C. Y.-C. Lee and L. R. Dalton (Materials Research Society, Pittsburgh, 1994) p. 27.
6. L. R. Dalton, C. Xu, B. Wu and A. W. Harper, in *Frontiers of Polymer Research*, eds. P. N. Prasad and J. Nigam (Plenum, New York, 1993).
7. H. E. Katz, S. F. Shane, W. L. Wilson, M. L. Schilling and S. B. Ungashe, in *Materials Research Society Symposium Proceedings*, Vol. **328**, *Electrical, Optical and Magnetic Properties of Organic Solid State Materials*, eds., A. F. Garito, A. K.-Y. Jen, C. Y.-C. Lee and L. R. Dalton (Materials Research Society, Pittsburgh, 1994) p. 361.
8. S. R. Forrest, P. E. Burrows, E. I. Haskal and Y. Zhang, in *Materials Research Society Symposium Proceedings*, Vol. **328**, *Electrical, Optical and Magnetic Properties of Organic Solid State Materials*, eds., A. F. Garito, A. K.-Y. Jen, C. Y.-C. Lee, and L. R. Dalton (Materials Research Society, Pittsburgh, 1994) p. 37.
9. C. Xu, B. Wu, L. R. Dalton, Y. Shi, P. M. Ranon, S. Kalluri and W. H. Steier, in *Materials Research Society Symposium Proceedings*, Vol. **328**, *Electrical, Optical and Magnetic Properties of Organic Solid State Materials*, eds., A. F. Garito, A. K.-Y. Jen, C. Y.-C. Lee and L. R. Dalton (Materials Research Society, Pittsburgh, 1994) p. 461; C. Xu, B. Wu, O. Todorowa, L. R. Dalton, Y. Shi, P. M. Ranon and W. H. Steier, *Macromolecules*, **26**, 5303 (1992).
10. M. A. Hubbard, T. J. Marks, J. Yang and G. K. Wong, *Chem. Mater.*, **4**, 965 (1992).
11. M. W. Becker, L. S. Sapochak, L. R. Dalton, Y. Shi, W. H. Steier and A. K. Jen, *Chemistry of Materials*, in press.
12. K. J. Shea and D. A. Loy, *Chem. Mater.*, **1**, 572 (1989); K. J. Shea, O. Webster, and D. A. Loy, *Proc. Mat. Res. Soc. Sym.*, **180**, 975 (1990); K. J. Shea, D. A. Loy and J. H. Small, *Chem. Mater.*, **4**, 255 (1992); K. J. Shea, D. A. Loy, and O. Webster, *J. Amer. Chem. Soc.*, **114**, 6700 (1992).
13. C. Xu, B. Wu, M. W. Becker, L. R. Dalton, P. M. Ranon, Y. Shi and W. H. Steier, *Chem. Mater.*, **5**, 1439 (1993).
14. W. H. Steier, Y. Shi, P. M. Ranon, C. Xu, B. Wu, L. R. Dalton, W. Wang, D. Chen and H. Fetterman, *Proc. SPIE*, **2025**, 535 (1993).

15. Y. Shi, W. H. Steier, L. P. Yu, M. Chen and L. R. Dalton, *Proc. SPIE*, **1559**, 118 (1991); Y. Shi, W. H. Steier, L. P. Yu, M. Chen and L. R. Dalton, *Appl. Phys. Lett.*, **59**, 2935 (1991); W. H. Steier, Y. Shi, L. P. Yu, M. Chen and L. R. Dalton, *Proc. SPIE*, **1775**, 379 (1992).
16. D. Gorton, S. Kwiatowski, G. F. Lipscomb, and R. Lytel, *Appl. Phys. Lett.*, **58**, 1730 (1991).
17. C. C. Teng, *Appl. Phys. Lett.*, **58**, 1538 (1992); T. Findakly and C. C. Teng, *Proc. SPIE*, **2025**, 526 (1993).
18. K. W. Beeson, P. M. Ferm, K. A. Horn, C. W. Knapp, M. J. McFarland, A. Nahata, J. Shan, C. Wu and J. T. Yardley, *Proc. SPIE*, **2025**, 488 (1993).
19. T. A. Tumolillo, Jr. and P. R. Ashley, *Proc. SPIE*, **2025**, 506 (1993).
20. W. H. G. Horsthuis, M. M. K. Koerkamp, J.-L. P. Heideman, H. W. Mertens and B. H. Hams, *Proc. SPIE*, **2025**, 516 (1993).
21. A. Brauer, L. Erdmann, T. Gase, P. Dannberg, W. Karthe and Ch. Wachter, *Proc. SPIE*, **2025**, 547 (1993).
22. J.-C. Dubois, P. Robin and V. Dentan, *Proc. SPIE*, **2025**, 467 (1993).
23. B. A. Smith, M. Jurich, W. E. Moerner and W. Volksen, *Proc. SPIE*, **2025**, 499 (1993); J. J. Thackara, G. C. Bjorklund, W. Fleming, M. Jurich, B. A. Smith and J. D. Swalen, *Proc. SPIE*, **2025**, 564 (1993).

Photomechanical Effects in Polymer Optical Fibers

M. G. KUZYSK, D. J. WELKER and S. ZHOU

*Department of Physics, Washington State University, Pullman,
Washington 99164–2814 December 13, 1993*

Received 7 January 1994; accepted 8 January 1994

Motivated by the well known observation in intensity dependent refractive index measurements that refractive index changes are often accompanied by density and length changes, we have demonstrated photomechanical effects in polymer optical fibers and have investigated the possibility of making all-optical devices that have a mechanical function. We report on the demonstration of two separate devices: An all-optical position stabilizer and digital positioner; and an ultrafast all-optical positioner.

INTRODUCTION

Most third-order susceptibility measurements of the intensity dependent refractive index change employ methods in which light induces a phase change in itself or another beam. Because the optical phase difference between the input and output face of a sample is given by:

$$\phi = \frac{2\pi nl}{\lambda}, \quad (1)$$

where n is the refractive index of the material, l the sample thickness, and λ the wavelength of the light beam. A phase change can result from either a length change or a refractive index change:

$$\Delta\phi = \frac{2\pi}{\lambda}(l\Delta n + n\Delta l). \quad (2)$$

In many intensity dependent refractive index measurements, it is assumed that the thickness-induced phase change is small relative to the phase change due to the refractive index change. In cases where the length changes are large, such effects are usually considered a nuisance that needs to be eliminated. In this contribution, we study photomechanical effects in multimode polymer optical fibers and show how light-induced length changes can be used to build all-optical photomechanical devices.

PHOTOMECHANICAL MECHANISMS

While every mechanism that leads to a refractive index change will also lead to a length change, for purposes of illustration, we only discuss two such mechanisms: optical heating¹ and electrostriction.² It is typical for the magnitude of the refractive index

change to be largest when the response time is the slowest.³ The same is true for photomechanical effects. The thermal response is slow (≈ 100 ms) but large while the electrostrictive effects are fast (< 1 ns) but small. We discuss each mechanism below.

Optical Heating

The optical heating mechanism is a three step process. A beam of light that propagates in a waveguide is partially absorbed by the material, the energy is converted into heat, and the material expands or contracts according to the temperature change. The magnitude of the length change depends on the power of the laser beam, the optical absorption coefficient of the material, the thermal expansion coefficient, the heat capacity, the mass of the sample, and its thermal conductivity.

Electrostriction

It is well known that an electric field gradient exerts pressure on a dielectric.² In an isotropic medium, an electric field will induce a dipole moment. If the electric field is non-uniform, the dipole will feel a net force. Because the direction of the force is along the field gradient, polarizable molecules tend to be attracted to regions of high fields. Because light is composed of an oscillating electric field, molecules will also be attracted to regions of high field strength.

In our studies, we use multimode poly(methyl methacrylate) (PMMA) polymer optical fiber. In a neat PMMA fiber waveguide in air, the light is confined to the polymer region while the evanescent field is found in the surrounding air. By necessity, the surface of the waveguide experiences a large intensity gradient. As such, there is a net inward force on the polymer surface. Furthermore, because the light intensity falls off over a distance comparable to the wavelength of light, the electric field gradient can be large. The inward force on the fiber waist will result in an increase in fiber length if its volume remains fixed during the deformation. Specifically, the equilibrium strain along the fiber axis (\hat{z}) is:⁴

$$u_{zz} = \frac{16\pi\sigma\chi^{(1)}}{\epsilon n c} P, \quad (3)$$

where P is the beam power density, c the speed of light, n the refractive index of the waveguide, ϵ is Young's modulus of PMMA, $\chi^{(1)}$ the linear susceptibility of the guide, and σ is Poisson's ratio.

EXPERIMENTS, RESULTS AND DISCUSSION

Both the stabilizer/digital positioner and the fast actuator experiment are described below.

Stabilizer and Digital Positioner

Figure 1 shows a photograph of the self stabilizing positioner. The apparatus measures about 70 cm in height. Figure 2 shows a close-up side view and schematic of the device.

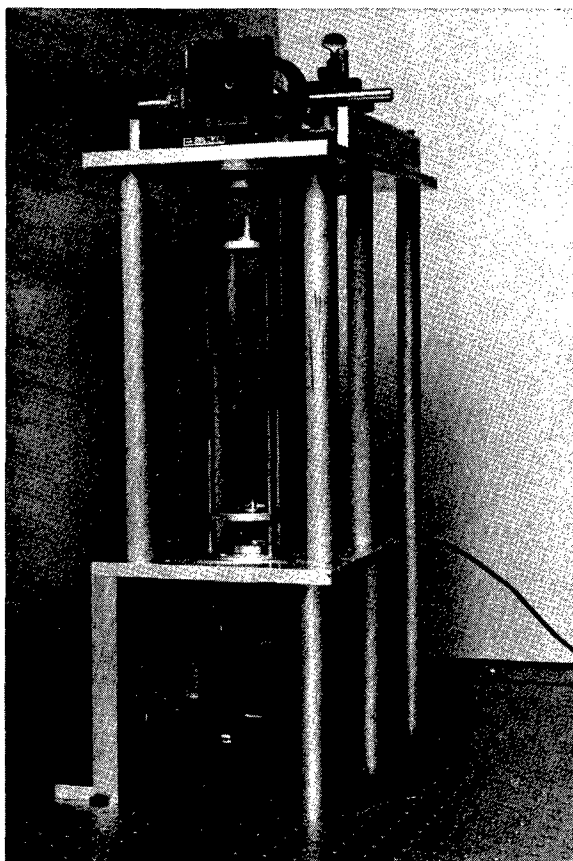


FIGURE 1 Photograph of the photomechanical stabilization experiment.

The schematic of the apparatus is intentionally not drawn to scale so that a close up of the relevant parts of the experiment can be conveniently displayed.

A 647.1 nm Krypton laser beam is launched into a Michelson interferometer. The light that passes through the beam splitter of the interferometer illuminates a stationary mirror while the reflected beam is directed to a mirror that is suspended by the hanging polymer optical fiber. The output of the interferometer is directed around the evacuated chamber and through an aperture into the hanging fiber. The upper fiber end is mounted from a platform that sits on three legs. The other end of the fiber is attached to the hanging mirror with a fixture that is attached with three fishing lines to a sliding ring that is fixed to the three legs lines with set screws. The fishing lines prevent the mirror from swaying or twisting but otherwise allow the mirror to move freely in the vertical direction provided that the displacement is small compared to the 2–3 cm length of the fishing lines. Given that typical displacements are on the order of microns, this condition is well obeyed.

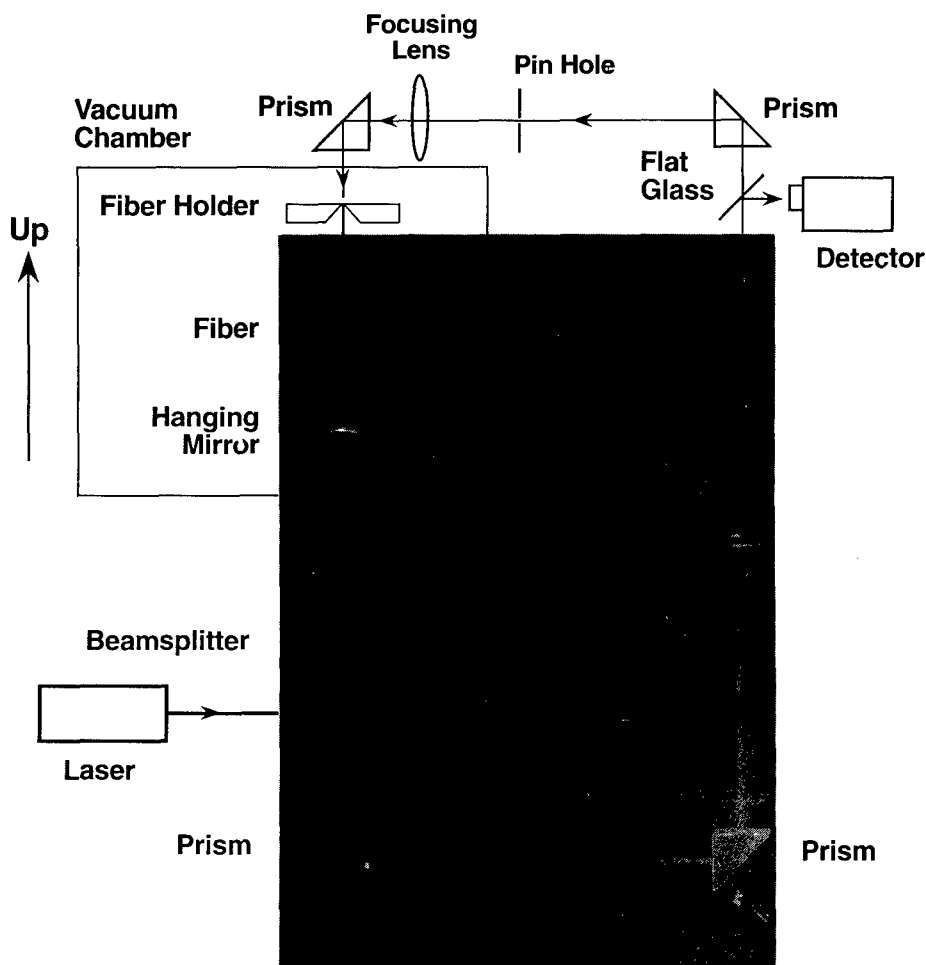


FIGURE 2 Hybrid schematic of the photomechanical stabilization experiment.

To understand the feedback mechanism, it is useful to first consider the interferometer apparatus without feedback. Assuming that the fixed mirror is rigid, the output intensity of the interferometer is a sinusoidal function of the fiber length. Figure 3 shows the calculated intensity dependence. The length of the fiber, on the other hand, is proportional to its temperature. The line in Figure 3 represents the length's dependence on temperature. If the output of the interferometer is directed into the hanging fiber, its length will be a linear function of the interferometer output. The optical feedback therefore connects the output intensity of the interferometer to the temperature which is related to the fiber length. It is straightforward to show that the equilibrium fiber length condition is determined from the intersection between the two functions as represented by dark squares in Figure 3. Note that for a positive thermal expansion coefficient, the intersection points in regions where the interferometer

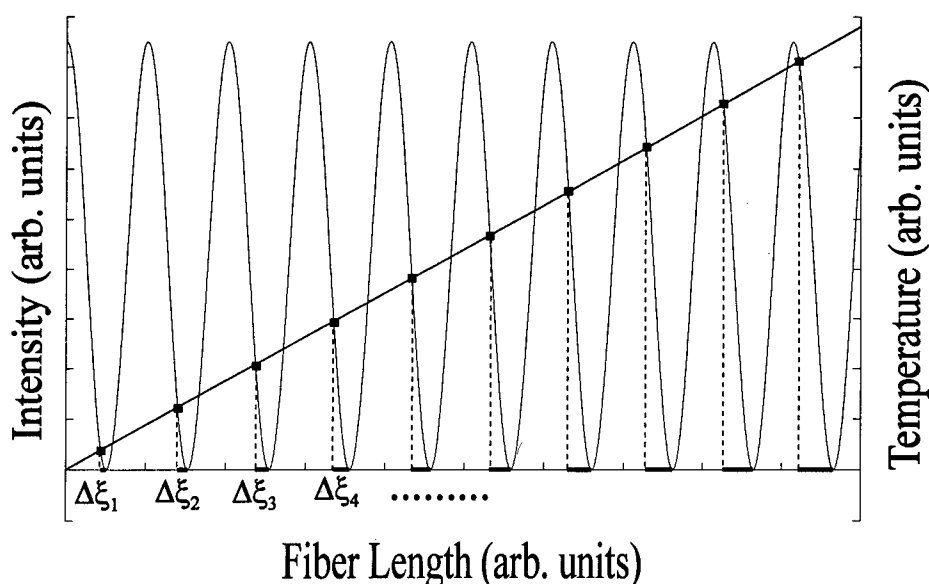


FIGURE 3 Calculated intensity out of the interferometer as a function of fiber length and fiber length as a function of temperature.

output has positive slope are unstable. Because the collection of equilibrium points is discrete and adjacent points are approximately evenly spaced, the stabilizer can be digitally stepped as described below.

If the system is prepared so that it occupies one of these equilibrium states, any small perturbation in the fiber length will be corrected. We call this effect active stabilization. If the perturbation is large enough to bring the interferometer output past the zero-intensity point, the fiber length will settle to the next equilibrium point. The solid lines ($\Delta\xi_n$) on the fiber length axis label the region between stable points and the critical point past which the interferometer jumps to the next higher stable point. When the feedback is turned off by closing the shutter, however, the stabilization effect is lost and the fiber relaxes to its original length.

Figure 4 shows the intensity leaving the interferometer as a function of time. When the shutter is closed, the interferometer drifts over a period of several minutes. When the feedback loop is turned on by opening the shutter, the fiber length stabilizes at the first equilibrium point. From the magnified insert, the turn-on time is estimated to be about 200 ms. Note that while this is a stable point, it is so close to the zero-intensity point in the sinusoidal curve that a small perturbation will increase the fiber length to its next equilibrium state (i.e., $\Delta\xi$ is small). Indeed, such a spontaneous jump is observed in Figure 4.

Figure 5 is a continuation of Figure 4 and shows the time dependence of the interferometer output beginning at the second equilibrium point. The arrows show times at which the interferometer is mechanically agitated by bumping the apparatus. Note that it is easy to get the system to jump through the first couple of steps. Once the system reaches state $n=6$, it becomes impossible to agitate the system with enough force to bump it up to $n=7$. We can uniquely determine that the system was in state

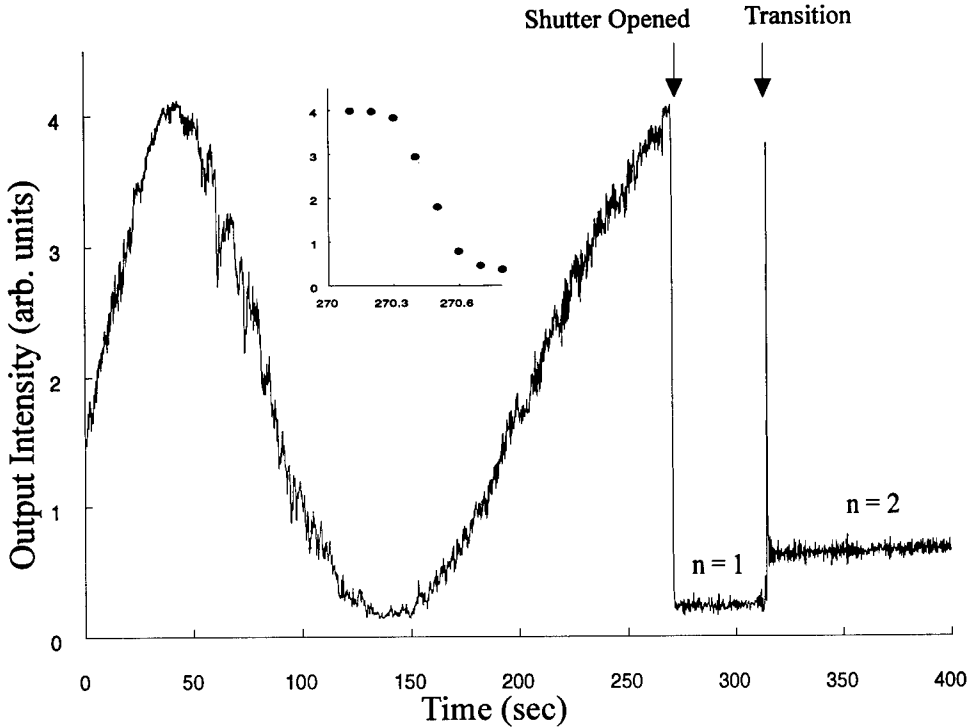


FIGURE 4 Light intensity leaving the interferometer as a function of time.

$n = 6$ by turning off the feedback and counting the number of fringes that have passed (as shown in the latter part of Figure 5). The reason for the high level of stability at $n = 6$ can be understood by investigating the two parameters that determine the strength of stabilization for state n : the distance to the next minimum intensity $\Delta\xi_n$ and the slope dI/dl . When the equilibrium intensity is far away from the next intensity minimum, large fluctuations in the fiber length are required to push the system to the next equilibrium point. In regions where the slope is large, the stabilization effect is the largest. Figure 6 shows a plot of each of these parameters as determined from Figure 3. ξ grows with fiber length while the slope peaks at point $N/2$. It is not surprising that we found it impossible to step the interferometer past $n = 6$ given that $N \approx 10$ for our system. We note that once the system settles to this point, it is always found to remain at the stable point for the duration of the experiment (usually about 10 minutes). There is no reason to believe that the system should not stay there indefinitely.

The latter time portion of Figure 5 can be used to determine the thermal relaxation rate. The intensity of the light leaving the interferometer is a function of Δl (the difference between the ambient fiber length and elevated temperature length) and is of the form:

$$I = I_{\max} \cos^2 \left(\frac{2\pi\Delta l}{\lambda} + \delta \right), \quad (4)$$

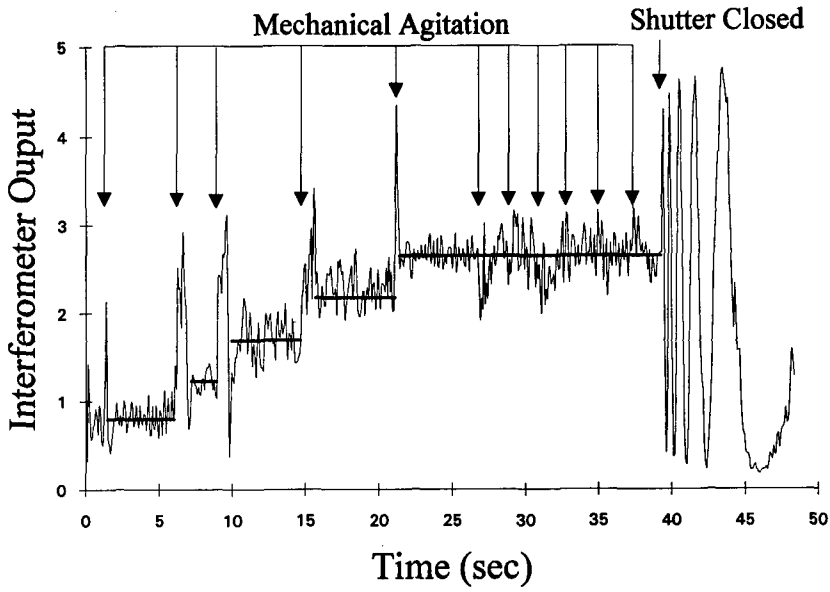


FIGURE 5 Light intensity leaving the interferometer as a function of time starting at the second equilibrium point.

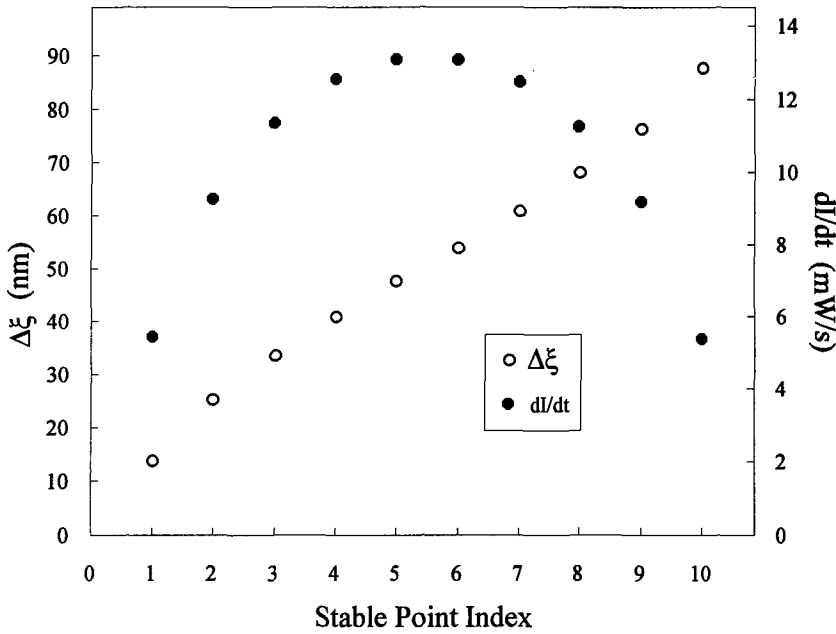


FIGURE 6 ξ and dI/dt as a function of equilibrium point index n .

where δ is the ambient phase difference between the two arms of the interferometer and λ the wavelength of the light source. If the fiber length is at one of the equilibrium points and is extended by an amount Δl_0 from its dark length, the fiber length will relax exponentially as a function of time after the feedback shutter is closed according to:

$$\Delta l = \Delta l_0 \exp\left[\frac{-t}{\tau_c}\right], \quad (5)$$

where τ_c is the characteristic cooling time. A log plot of the fiber length versus time after the shutter blocks the feedback beam should give a straight line whose slope is the decay rate (inverse relaxation time). The length can be determined from Equation (4) and is given by:

$$\Delta l = \frac{\lambda}{2\pi} \cos^{-1} \left[\left(\frac{I}{I_{\max}} \right)^{1/2} \right] - \frac{\lambda\delta}{2\pi}. \quad (6)$$

Figure 7 shows the log plot of the length change as a function of time as determined from Equation (6). Note that the zero of the time axis was selected such that $\delta = 0$. Also, the multiple valuedness of the arc cosine function and the two branches of the square root were taken into account when constructing Figure 7.

From the slope of the line in Figure 7, we determine the thermal cooling time constant to be about $\tau_c = 2$ s. Note that this is much longer than the turn-on time for stabilization. This asymmetry is reasonable given that energy can be pumped into the system more quickly than it can be dissipated. The stabilization process is therefore also asymmetric. Changes in the fiber length that use photothermal heating result in much quicker stabilization than those that rely on cooling. The stabilization process, however, does not seem to be strongly affected by this asymmetry. We note that the cooling rate can be substantially increased if the thermal conductivity of the fiber or surrounding medium is increased.

Fast Actuator

Figure 8 shows the fast actuator apparatus. The laser source is a 5 ns Continuum Sure-light laser. A KDP crystal generates a small amount of second harmonic. The fundamental is directed to the hanging fiber and acts as the pump while the second harmonic is used to probe the length change. The polarization of the probe is rotated 45° to the table and a polarizing beam splitter separates the two orthogonal polarizations. One of the pulses is delayed by about 8 ns and is recombined with the first pulse. The pulse pair is sent to an interferometer. One of the interferometer mirrors is held by the hanging fiber. With the pump pulse turned off, the interferometer is tuned and balanced so that both probe pulses have equal amplitude when leaving the interferometer.

After the interferometer is so calibrated, the pump pulse is turned on and timed so that it arrives in the fiber just after the first probe pulse hits the mirror and just before the second pulse arrive. Figure 9 shows the timing of the pulses.

Figure 10 shows the probe pulse pairs with and without pumping. With no pump, the two pulses have the same amplitude. With the pump on, the later pulse has a larger

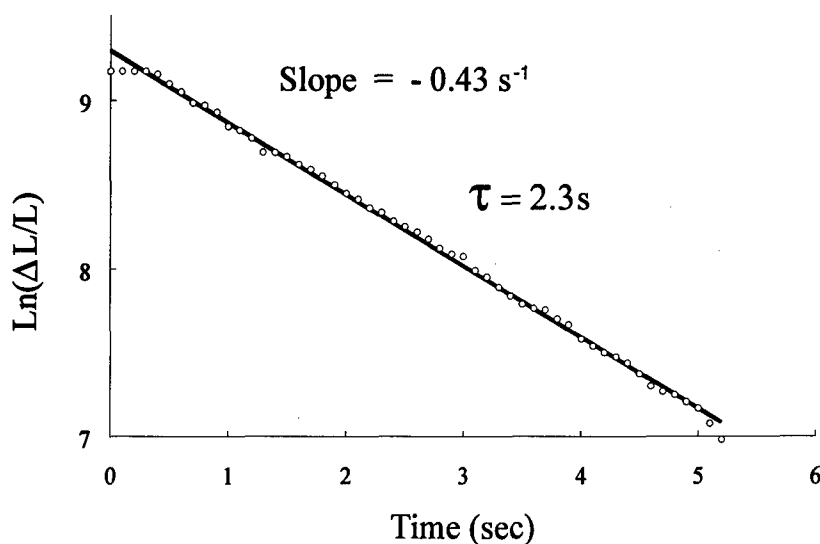


FIGURE 7 Log plot of the fiber length as a function of time after the feedback shutter is closed.

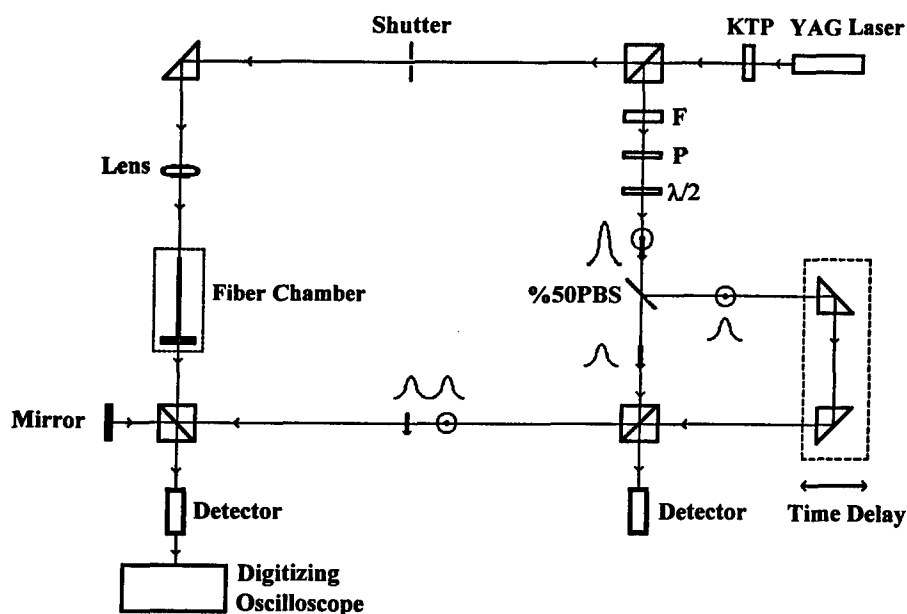


FIGURE 8 Fast pump-probe photomechanical actuator experiment.

amplitude. We can estimate the length change from the difference between the two pulse amplitudes. We find that the mirror's position changes by about 5 nm over a time interval of 4 ns. While the pump pulse is on, this corresponds to an acceleration of about $6 \times 10^8 \text{ m/s}^2$.

Timing of the probe and pumping pulses

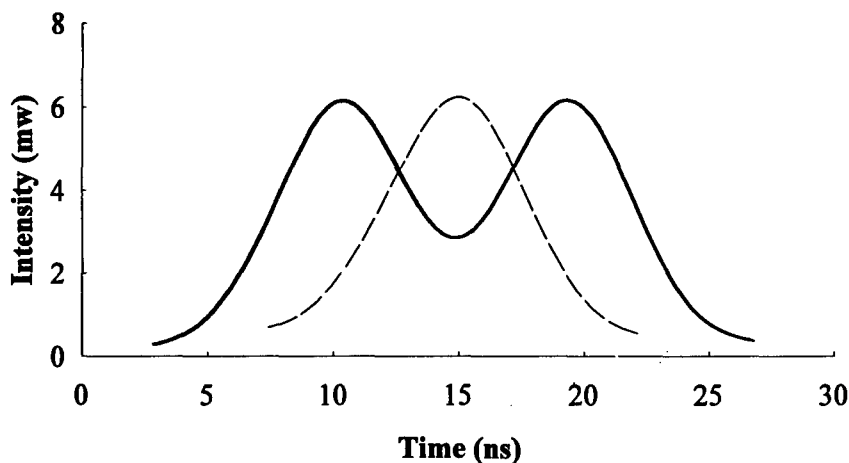


FIGURE 9 Timing of the pump and probe pulses.

Oscilloscope trace of the probe pulses leaving the interferometer

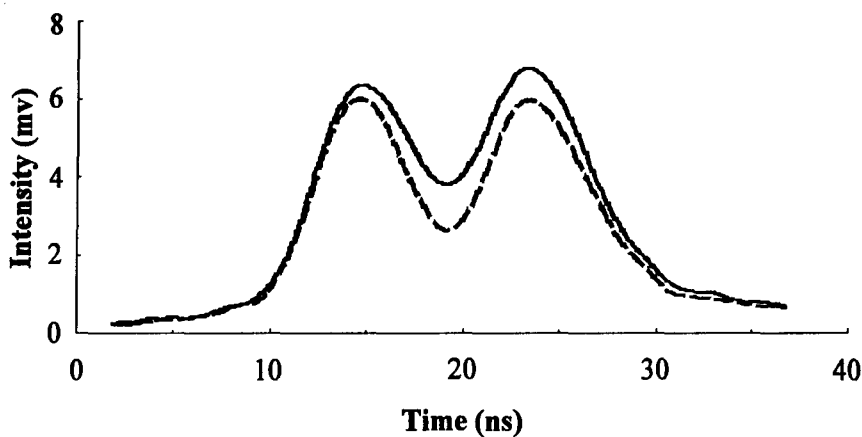


FIGURE 10 Probe pulse pair with and without pump.

A closer inspection of Figure 10 shows that both probe pulses are affected by the pump. Because the leading edge of the pump beam overlaps the first pulse, it is also affected. A pump-probe experiment with variable delay in the second probe pulse is planned to study the temporal response of the photomechanical response to more definitively determine the mechanisms.

CONCLUSION

We have demonstrated an all-optical circuit using the photothermal mechanism that can be used to stabilize a mirror in an interferometer and show that this configuration can be used to make a digital positioner. We have also demonstrated a fast photo-mechanical actuator based on the photostrictive effect that can change the position of an 8 g mirror in 4 ns. A digital positioner with optical stepper and temporal dependent studies of the fast electrostrictive mechanism are planned.

ACKNOWLEDGEMENTS

We thank Mr. Montgomery from LeCroy for setting up a demonstration 9360 oscilloscope that was used for some of the data acquisition. This investigation was supported by the Army Research Office.

REFERENCES

1. J. R. Kenemuth, C. B. Hogge and P. V. Avizonis, *Appl. Phys. Lett.*, **17**, 220 (1970).
2. C. J. F. Bottcher, *Theory of Dielectric Polarization*, Vol. I, 2nd Ed., p.318, Elsevier, New York (1973).
3. R. W. Boyd, *Nonlinear Optics*, p. 163 Academic Press, New York (1992).
4. M. G. Kuzyk, "All-Optical Materials and Devices," in *Science and Technology of Organic Thin Films for Waveguiding*. Nonlinear Optics, F. Kajzar and J. D. Swalen, Eds., Gordon and Breach, in Press.

Electro-Optic Polymer Waveguide Arrays in Digital Systems

G. F. LIPSCOMB, R. LYTEL and A. J. TICKNOR

Akzo Electronic Products Inc. Redwood City, CA 94065

Received 28 March 1994; accepted 4 April 1994

Electro-optic(EO) polymer waveguide modulators may be used in parallel external modulation arrays supplied by branching structures providing fanout from a CW laser for a variety of digital data communications applications. This paper highlights some of the benefits of using EO polymer modulators in arrays for point-to-point digital data communications.

INTRODUCTION

Electro-Optic (EO) polymer materials have emerged in recent years as serious candidates for use in integrated optic components.^{1,2,3,4} In this paper we describe the potential application of EO polymer active waveguide devices to parallel optical interconnects. EO polymers are particularly attractive for highly parallel optical data links due to the high levels of optical integration that can potentially be achieved only with EO polymers.⁵ We begin with a brief introduction comparing EO polymers with inorganic materials for integrated optics. Particular emphasis is placed on the fabrication flexibility inherent in EO polymers that may enable highly integrated photonic components. Next, current developments in optical interconnection for datacom are summarized. In order to illustrate the potential application of EO polymers to parallel optical interconnects, a specific example of an eight line optical interconnect is developed. The power consumption for an array of external modulators is compared to that for an array of laser diodes. Lastly, some of the factors that need to be considered in the design of EO polymer based modulator arrays for datacom applications are discussed in some detail.

A comparison of the figures-of-merit for the three leading electro-optic (EO) integrated optic materials is given in Table 1. This table is not meant to be exhaustive, but merely to illustrate some of the considerations that go into device design. Such figures-of-merit are useful tools, provided their limitations are also recognized. For example, the traditional parameter of comparison for electro-optic materials has been the electro-optic coefficient, r . The current best electro-optic polymers now approach lithium niobate with an electro-optic coefficient of $r = 30 \times 10^{-12}$ meters/V = 30 pm/V, and are far more active than gallium arsenide (GaAs). However, as has been widely recognized, the index change for an applied voltage is proportional to n^3r rather than to r . Since the index of refraction is smaller in EO polymers, their n^3r figure-of-merit falls to half that of lithium niobate and remains twice that of GaAs.

TABLE 1
Comparison of Active Electro-Optic Waveguide Technologies.

FIGURE-OF-MERIT	GaAs	LiNbO ₃	EO Polymers
EO coefficient r (pm/V)	1.5	31	30
Dielectric constant ϵ	10	28	3.5
Refractive index n	3.5	2.2	1.6
n^3r (pm/V)	64	248	123
Voltage-length product (V-cm)	1	5	10
n^3r/ϵ (pm/V)	6.4	8.7	31
Space-BW product (GHz-cm)	10	10	120
Loss(dB/cm @ $\lambda = 1.3$ mm)	2	0.2	0.5

Another important figure of merit for integrated optic devices is the voltage-length product. This figure of merit takes into account certain geometrical factors that are too involved to describe here, in addition to the n^3r factor. The voltage length product gives the length required for a device to operate at a given voltage. Lithium niobate devices typically have a voltage length product of 5 V-cm, as compared to 10 V-cm for the best EO polymer devices. In other words an EO polymer device must in general be about twice as long as lithium niobate device to operate at the same voltage. The large index of refraction of GaAs, however, enables small waveguide geometries, and results in voltage length products as low as 1 V-cm. These waveguide geometries are not well matched to optical fiber, and the large index results in unwanted back reflections, making it difficult to realize a significant advantage with GaAs.

The conclusion of this discussion is that from a stand point of electro-optic modulation in integrated optic devices, EO polymers are now competitive with lithium niobate and GaAs devices. Furthermore, EO polymers are now in the early childhood phase of development, while GaAs and lithium niobate are quite mature technologies. The electro-optic coefficients of GaAs and lithium niobate are not going to change. In contrast, several laboratories have now reported organic chromophores with intrinsic nonlinearities between one and two orders of magnitude larger than that of the standard chromophore DANS^{6,7} which was used in the majority of published EO polymer devices.^{8,9} It seems very likely that an improvement of a factor of 3 to 10 in the electro-optic coefficient can be realized in the next few years, giving EO polymers a decided advantage in modulating power.

When the device bandwidth is considered, however, the potential advantages of EO polymers are significant. For devices with a lumped element electrode design the figure-of-merit incorporating bandwidth is n^3r/ϵ . This figure-of-merit takes into account the capacitance of the lumped electrode structure, and shows that an EO polymer device would run 3.5 times faster than a comparable lithium niobate device and 5 times faster than a GaAs device. Most high speed devices, however, use travelling wave electrode designs. In this case the device bandwidth is limited by the velocity mismatch between the rf wave in the electrode and the optical wave in the waveguide. The figure-of-merit in this case is the length-bandwidth product. Due to electronic origin of the electro-optic effect in EO polymers, the optical and electrical group velocities are very well matched, leading to a length-bandwidth product of over 120 GHz-cm, more than an order of magnitude larger than that of lithium niobate or GaAs.

If all of the other device parameters can be made equal, EO polymers would be the material of choice for very high speed integrated optic devices.

The most important ultimate advantages of EO polymers, however, are not listed in Table 1. The fabrication simplicity and flexibility of polymer materials potentially make possible complex and powerful integrated optic systems at reasonable cost. Using standard semiconductor fabrication processes, multi-layer structures of EO polymers can be fabricated in large areas and with high device packing densities. In fact, the same processes that resulted in the dramatic evolution of electronic integrated circuits will apply to EO polymer integrated optic circuits. EO polymers are first deposited quickly and economically into multi-layer structures by standard spin coating techniques. The active area is limited only by the wafer sizes currently supported by standard processing equipment, currently ≥ 8 in. Next, waveguides are fabricated using any of several standard techniques listed in Figure 1. Lastly, metal electrodes are deposited and patterned, again using standard processes from the semiconductor industry.

Of equal importance to the economies of scale achieved by processing large area wafers and the corresponding increase in level of integration, are the potential benefits in packaging and assembly that arise from building on a silicon substrate. The silicon substrate on which the polymer devices are fabricated can be micro machined to enable auto-alignment of optical fibers, receiver arrays and can support other active integrated circuits. The ultimate expression of EO polymer technology may be in complex hybrid assemblies, such as that shown in Figure 2, which contain

CHANGE CORE/CLADDING INDEX

- POLING
- PHOTBLEACHING
- PHOTOCHEMISTRY
- IN- & OUT-DIFFUSION

MACHINE CORE OR CLAD

- LASER ABLATION
- PLASMA ETCH
- ION ETCH
- MOLDING

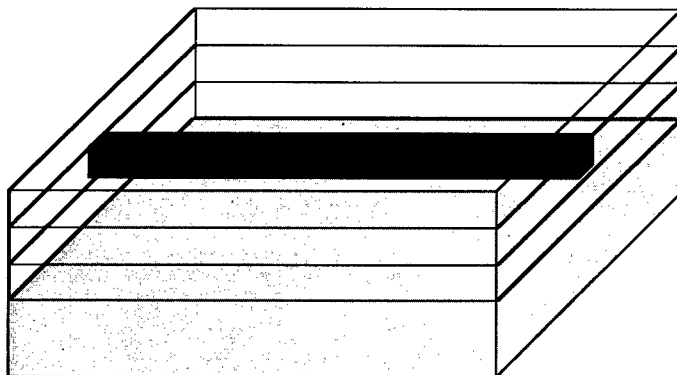


FIGURE 1 Methods of Waveguide Formation in Planar Electro-Optic Polymer.

electronic and photonic functionality combined on a single silicon motherboard. The parallel optical datalinks described in the remainder of this paper are designed to take advantage of the higher levels of optical integration that are achievable with EO polymers.

A summary of the current performance achieved in EO polymer integrated optic devices, and a projection of the performance that will be achieved within the next year are presented in Table 2. An example of a current EO polymer Mach-Zehnder modulator with a half wave voltage of 6 V is given in Figure 3. The subject of the thermal stability of EO polymers is critical to their ultimate success. To meet processing and packaging methodologies of standard electronic components, new EO polymer materials with extremely high thermal stability are under development in various groups around the world.¹⁰ These materials do not yet equal the EO performance of current lower temperature materials but are expected to achieve comparable performance in the future. Meanwhile, there are numerous applications of EO polymers which do not require thermal stability at 350°C, but instead, demand stability and reliability in device performance at temperatures up to 80°C. Such applications include digital data communication links. This paper addresses application of EO polymers to such systems.

CONNECTORS FOR DATA COMMUNICATIONS

IBM (Rochester, MN) has developed¹¹ a fiber-optic card for use in its workstations (RS6000 series) that is available in 1994 to select users for evaluation and will be

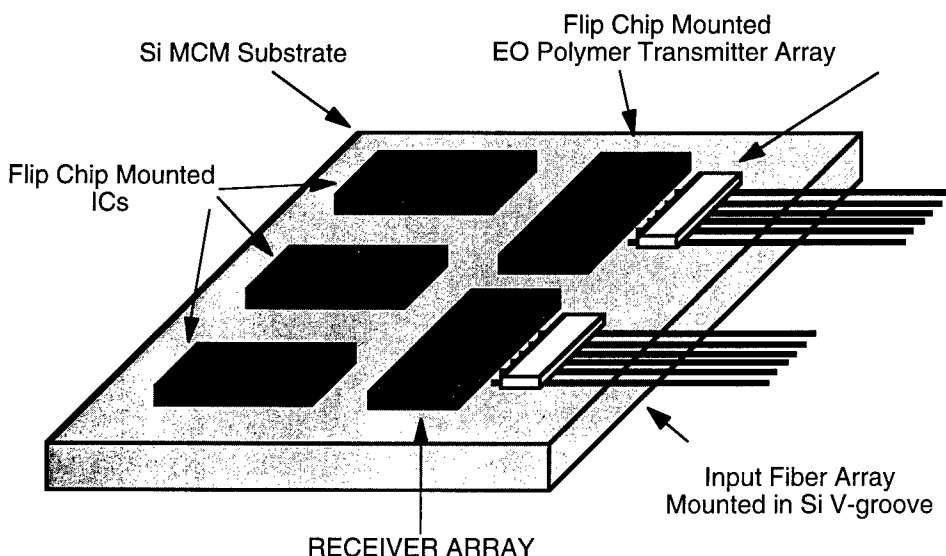


FIGURE 2 Integrated Hybrid Processor Employing Flip-Chip Mounted Electro-Optic Polymer Modulator Arrays.

TABLE 2
Current and Projected Performance of Electro-Optic Polymer Waveguides.

CURRENT PERFORMANCE	
• Half-wave voltage	6 V
• Total loss in channel	1–2 dB/cm @ 1.3 μm
• $V_{\pi}L$	10–15 V-cm
• Dielectric constant	3.5
• Sustained operating temp.	70°C
PROJECTED PERFORMANCE	
• Half-wave voltage	3.3 V
• Total loss in channel	0.4 dB/cm @ 1.3 μm
• $V_{\pi}L$	5 V-cm
• Dielectric constant	3.5
• Sustained operating temp.	100°C

manufactured and distributed to the general marketplace in late 1994 or early 1995. The card is an FDDI link for distances up to several hundred meters and transmits serialized information over a graded-index multimode (MM) fiber at frequencies up to 1062 Mb/sec. The card uses electronic multiplexing and 8B/10B coding (FDDI standard) for error correction. The signal to be transmitted modulates a compact disk laser directly, which is then coupled to the MM fiber. A receiver is also mounted on the card

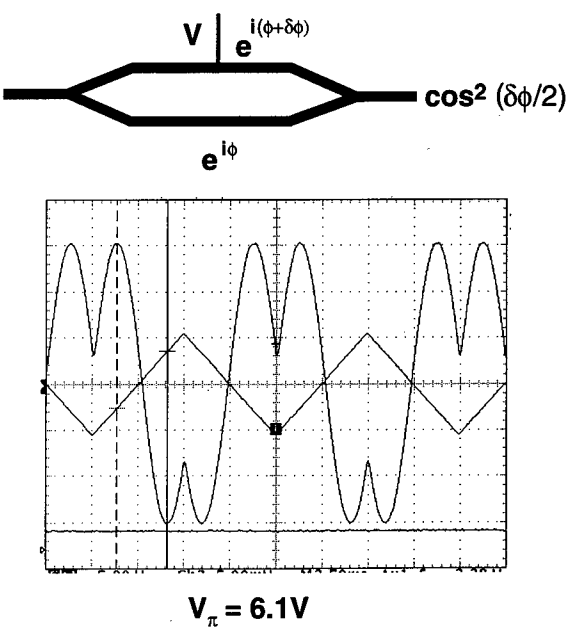


FIGURE 3 Electro-Optic Polymer Modulator With a Half Wave Voltage of $V_{\pi} = 6.1 V$.

and consists of demux, error correction, and clock recovery chips, plus a Silicon PIN diode. The entire two way link maintains a bit error rate (BER) of 10^{-12} or less and is projected to cost under \$300 to the consumer next year when it is released. This is a remarkable development for data communications in local area networks, such as interoffice workstation communications. Future systems will require either higher performance components (laser, driver chips, receiver, mux/demux chips, etc.) or a shift to a parallel interface, whereby signals are transferred in parallel, perhaps with a clock signal.

Figure 4 illustrates such an interface. A package containing a laser or modulator array, driver circuits, and a fiber-attach array assembly is addressed by N electrical digital input signals at some frequency, f , and the output is a parallel array of optical signals with N signal channels and perhaps additional channels for clock, synchronization, or data.

The design of a parallel fiber-optic transmitter may be accomplished by using directly modulated lasers coupled to fiber arrays or may also be accomplished by utilizing an integrated optic modulator array comprised of a CW laser input, a $1 - N$ fanout section, and an array of external modulators, as shown for $N = 5$ in Figure 5. External modulation has been thoroughly examined from a systems standpoint by a number of authors for CATV.¹² Here, it is shown how such an approach for datacom may be especially beneficial if realized using EO polymer modulators.

Consider first the potential benefit of using a single EO polymer modulator as an external modulator for a CW laser. Assuming a push-pull lumped electrode configuration, a driver circuit sees a load comprised of a capacitance C of approximately 310 fF and resistance R of approximately 56Ω . Thus, the modulator is charged by a 3 volt source in about 50 psec ($RC \sim 17.4$ psec) with a peak current of 5 mA @ 1 GHz and a much lower average current in this short time interval. The amount of output light is then determined by the input power to the integrated optic device from the CW laser and the loss in the waveguides. Thus, 5 mA of peak current applied by a driver over 17 psec can modulate any amount of light, without the chirp associated with direct modulation of semiconductor lasers. This is the main advantage of external modulation.

Consider next an array of modulators compared to an array of directly modulated lasers. First, consider external modulators. The total power dissipated in driving the modulator is $0.5 CV^2 f \sim 1.4$ mW at 1 GHz, independent of the optical power launched

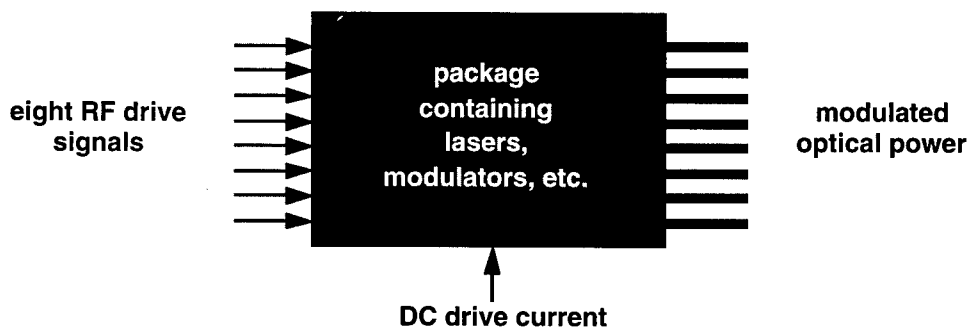


FIGURE 4 Parallel Connector Model.

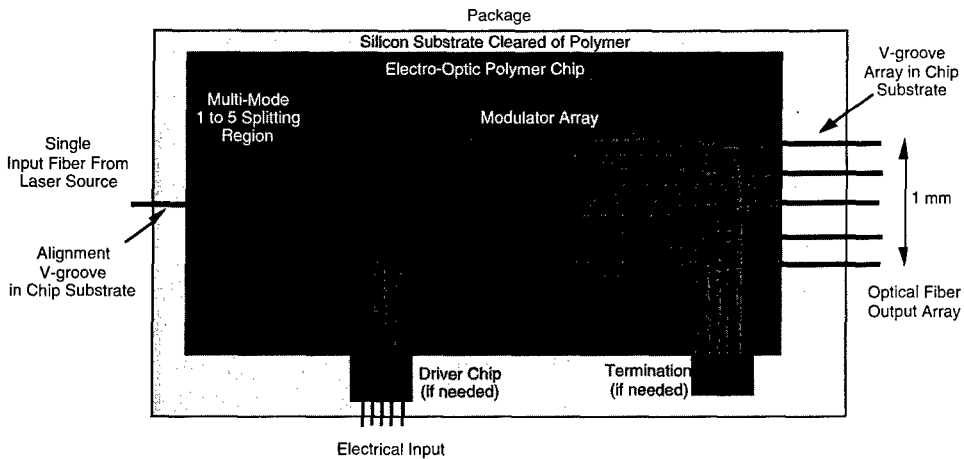


FIGURE 5 Five Channel Modulator Array Chip.

into the output fiber. The total RF power dissipated in the connector is then 11.2 mW. Additional power (DC) is dissipated in driving the CW laser. Assuming a total waveguide length of 4 cm (fanout plus modulator), a 0 dBm output optical power into each output fiber requires 10.23 dBm launched into the input end of the splitter, assuming a waveguide loss of 0.3 dB/cm. Assuming a 3 dB coupling loss and a 20% wallplug efficiency, this requires a DC electrical input to the laser of 105 mW. It is emphasized that this is DC, not RF power. Doubling the output optical power per channel simply drives up the required DC electrical power, without changing the RF drive power provided by the driver circuits transmitting the digital information. Table 3 summarizes these results. Also shown in the Table are the corresponding numbers for directly-modulated lasers, assuming 18 mA of bias current and an average of 14 mA of RF drive current to produce a 0 dBm optical output power at 1 GHz (typical numbers for a 1.3 μm laser such as that used in the Ortel 1510 A laser module). Assuming a 50 Ω impedance, the values derived for directly modulated lasers are shown in Table 3.

TABLE 3
Eight Line Parallel Interconnect Summary.

Power Dissipation in Connector @ Optical Power/Channel			
Method	- 3 dBm	0 dBm	3 dBm
Direct Modulation			
• RF power	20 mW	80 mW	320 mW
• DC power	128 mW	128 mW	128 mW
External Modulation			
• RF power	11.2 mW	11.2 mW	11.2 mW
• DC power*	53 mW	105 mW	210 mW

* can be mounted external to modulator array and pigtailed into connector.

The key conclusion is that externally modulated arrays have lower total RF drive power requirements at all output optical powers launched into the fibers and lower overall power requirements for optical output powers less than about 3 dBm (where the fanout loss begins to dominate power dissipation for the external modulator example). In other words, external modulation provides options for better driver design and thermal management for parallel datacom links in nearly all practical applications. This conclusion is based upon power dissipation and becomes even stronger when the effects of chirp, noise, and crosstalk are included.

As discussed below, EO polymer modulators may contain $50\ \Omega$ microstrip electrodes, rather than pure capacitive loads, even at modest frequencies. Nonetheless, the potential benefits of utilizing an array of modulators with a single CW laser over an array of lasers remain and become more significant at even higher frequencies.

The analysis above assumes lumped electrodes for the modulators. The best EO polymer waveguide technology has $V_\pi L \sim 10\text{--}15\text{ V}\cdot\text{cm}$. Consequently, modulation electrodes capable of supplying half-wave of modulation will typically have $L \sim 2\text{--}3\text{ cm}$. At $L = 2\text{ cm}$, the propagation delay time is $t_{pd} \sim 120\text{ psec}$. Transmission lines are necessary whenever the driver's electrical rise time $t_r < 2.5 t_{pd}$, or $t_r < 300\text{ psec}$. In a good digital system, the rise time is typically $0.1/f$, where f is the (external bus) clock frequency. For an analog signal at frequency f , the "rise time" is roughly $1/4f$. Consequently, for the current waveguides, microstrips will be required whenever $f > 333\text{ MHz}$ for digital systems and $f > 833\text{ MHz}$ for analog systems. The breakpoint for conversion of wire to fiber lies roughly in the same range of frequencies. Therefore, EO polymer modulators fabricated using current materials will likely require microstrips for applications where customers are interested in shifting from wire to fiber. Improved EO polymer materials with considerably larger electro-optic coefficients may enable short enough devices such that high impedance lumped element electrodes can be utilized.

The $V_\pi L$ product can be cut in half by building push-pull devices but the electrode structures are more complicated and would still have to be microstrips for many applications. One other way out is to include an on-chip amplifier to supply $V \gg 5\text{ volts}$ to the device. For example, suppose we supply 20 V at 1 GHz. The electrode length is then 5 mm and $t_{pd} \sim 30\text{ psec}$. The rise time is $t_r \sim 100\text{ psec}$ and a lumped electrode may be satisfactory. The power dissipated in driving the capacitance ($C \sim 1\text{ pF}$, including wire-bond) is $p \sim 0.5 CV^2 f \sim 200\text{ mW}$, a fairly hefty driver. Still, for certain applications, e.g., a CATV modulator, the transmitter could probably be designed to provide this power and, for this application, latency is not a problem. It should be clear that this approach will not scale to frequencies much higher than 1 GHz, and cannot be used in applications such as datacom, where skew, latency, and driver power dissipation are key factors to minimize. Moreover, even in CATV, the modulator is just a part of the entire transmitter circuit which must consist also of a CW laser, linearization circuitry, and stabilization circuitry. A transmitter containing a modulator that dissipates 200 mW in an IC driver and also contains a 200 mW (electrical) laser driver, plus circuitry, is not a cost-effective solution. Some CATV applications require more launched power into the fiber than can be achieved with high frequency DFB lasers. However, lowering the modulator drive voltage back to 5 V or even 1 V makes the EO polymer external modulator more attractive than the directly modulated laser, but

then we're back to building microstrips. Thus, near term application of EO polymer modulators requires microstrip design.

CONCLUSIONS

EO polymer modulators appear to have the potential for practical application in parallel, highly integrated, data communication networks. This application requires materials with EO coefficients of order 30 pm/V (to provide low $V_{\pi}L$ products, with $L < 2-3$ cm), and thermal stability to 80°C. Current generation EO polymer based devices probably require both high speed electrodes and drift stabilization for datacom, just as they do for CATV and telecom, even in moderate-rate digital signaling systems. Subsequent generation electro-optic polymers with greatly enhanced electro-optic coefficients may simplify device design over the frequency ranges currently of interest.

REFERENCES

1. R. S. Lytel, G. F. Lipscomb, J. T. Kenney and E. S. Binkley, "Electro-Optic Polymer Materials and Devices For Optical Interconnect Applications", *Proc. SPIE*, **1215**, 252 (1990).
2. K. D. Singer, J. E. Sohn and M. G. Kuzyk, "Orientationally Ordered Electro-optic Materials", in *Nonlinear Optical and Electro-active Polymers*, P. N. Prasad and D. R. Ulrich, ed., Plenum Press, New York (1988), p. 189.
3. D. G. Girtan, S. Kwiatkowski, G. F. Lipscomb and R. Lytel, "20 GHz Electro-optic Polymer Mach-Zehnder Modulator", *Appl. Phys. Lett.*, **58**, 1730 (1991).
4. C. C. Teng, "Traveling-wave Polymeric Optical Intensity Modulator with More Than 40 GHz of 3 dB Electrical Bandwidth", *Appl. Phys. Lett.*, **60**, 1538 (1992).
5. "Large Scale Integration of Electro-optic Polymer Waveguides", R. Lytel, G. F. Lipscomb, J. T. Kenney and E. S. Binkley, in *Polymers for Lightwave and Integrated Optics: Technology and Applications*, L. A. Hornak, editor (Marcel Dekker, New York) 1992, Chapter 16, pp. 433-473.
6. V. Pushkara Rao, K. Y. Wong, Alex K.-Y. Jen and R. M. Mininni, "Optimization of Second-Order Nonlinear Optical Properties of Push-Pull Conjugated Chromophores using Heteroaromatics", *Proc. SPIE*, **2025**, 156 (1993).
7. G. Bourhill, C. B. Gorman, S. R. Marder, J. W. Perry, J. Skindhoj and B. G. Teimann, "Optimization of the First and Second Order Hyperpolarizabilities of Organic Dyes", American Chemical Society/Optical Society of America Topical Meeting: Organic Thin Films for Photonic Applications, Toronto, Canada, October 6-8, 1993.
8. G. R. Mohlmann, W. H. Horsthuis and C. P. van der Vorst, "Recent Developments in Optically Nonlinear Polymers and Related Electro-optic Devices", *Proc. SPIE*, **1177**, 67 (1989) and G. R. Mohlmann *et al.*, *Proc. SPIE*, Vol. **1337**, 215 (1990).
9. T. E. Van Eck, A. J. Ticknor, R. S. Lytel and G. F. Lipscomb, "Complementary Optical Tap Fabricated in an Electro-optic Polymer Waveguide", *Appl. Phys. Lett.*, **58**, 1588 (1991).
10. J. F. Valley, J. W. Wu, S. Ermer, M. Stiller, E. S. Binkley, J. T. Kenney, G. F. Lipscomb and R. Lytel, "Thermoplasticity and Parallel-plate Poling of Electro-optic Polyimide Host Thin Films", *Appl. Phys. Lett.*, **60**, 160 (1992); G. R. Mohlmann ed., *Proc. SPIE*, **2025** (1993).
11. R. L. Soderstrom, S. J. Baumgartner, B. L. Beukema, T. R. Block and D. L. Karst, "CD Laser Optical Links for Workstations and Midrange Computers", *Proc. 43rd Electronic Components and Technology Conference (IEEE 1993)*, p. 505.
12. M. Nazarathy, J. Berger, A. J. Ley, I. M. Levi and Y. Kagan, "Progress in Externally Modulated AM CATV Transmission Systems", *J. Lightwave Tech.*, **11**, 82 (1993).

Design and Fabrication of Electro-Optic Polymer Waveguides

J. LIANG, R. LEVENSON, J. ZYSS,^a D. BOSC and F. FOLL^b

^aFRANCE TELECOM/CNET/PAB, 196 Rue Henri Ravera,
BP 107 F-92225 BAGNEUX (France), ^bFRANCE TELECOM/CNET/LAB/
FCI/PIH, Route de Trégastel, BP40, 22300 Lannion (France)

Received 23 March 1994; accepted 25 March 1994

INTRODUCTION

Poled functionalized electro-optic polymers provide an interesting alternative to bulk materials such as lithium niobate for a range of application encompassing electrooptic modulators, switches, or directional couplers. Their ability to be spin-coated on semiconductor substrates and their compatibility with such processing techniques as photolithography or reactive ion etching, now classically used in III-V semiconductor-based optoelectronics, provide a great potential towards their integration in optronic circuits.

We report here the stripe structure of a nonlinear polymer waveguide buried between passive polymer buffers of lower refractive index deposited on top of a semiconductor substrate (see Fig. 1).

By the Effective Index Method, the cut-off diagram can be plotted for such a guiding structure. (see Fig. 2). It exhibits that a $1 \times 2 \mu\text{m}$ section guide will be unimodal at $1.32 \mu\text{m}$. The lateral confinement of the TEOO mode is plotted Figure 3.

SIMULATION

The light propagation in this polymer waveguide is simulated by BPM-CNET (ALCOR)^{1–4} (a software developed by CNET FRANCE TELECOM), based on the Beam Propagation Method (BPM). A S-bend waveguide and a Y junction are shown respectively in Figure 4a and Figure 4b.

Photolithography masks which include a series of S-bends with different angles (from 1° to 26°) and a series of Y junctions have been first fabricated.

TECHNOLOGY

The fabrication process of polymer waveguides is summed-up in Figure 5. The different steps are: spin-coating, photolithography, and reactive ion etching techniques. [patent n°9114662].

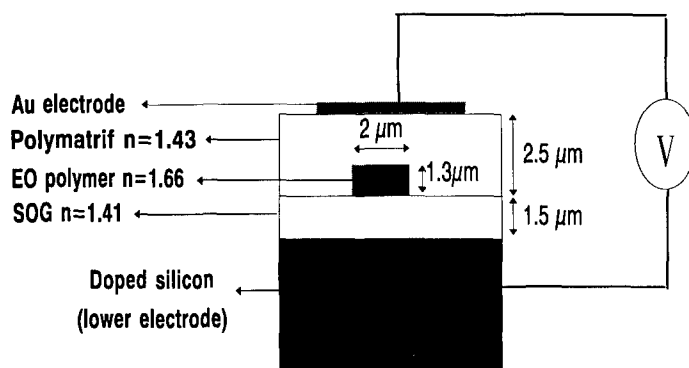


FIGURE 1 Strip structure of a nonlinear polymer waveguide.

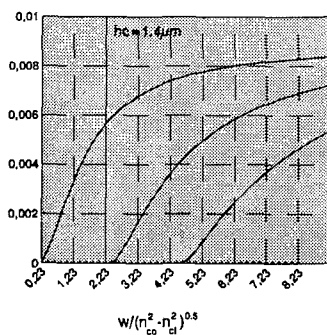
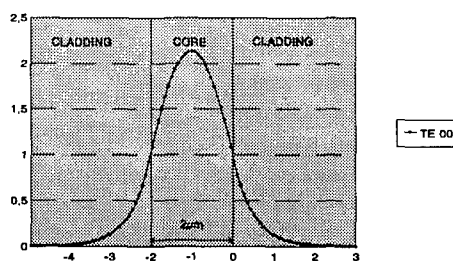
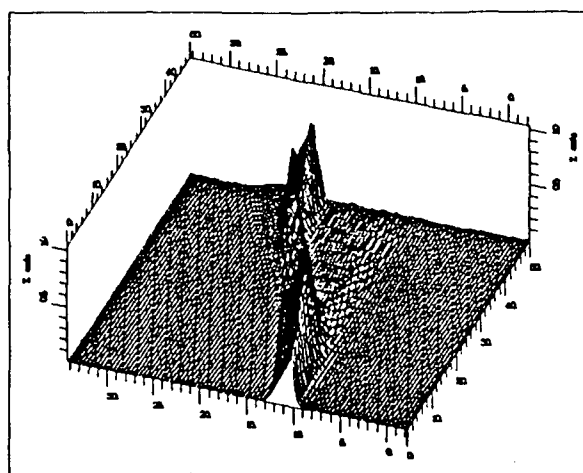


FIGURE 2 Cut of diagram of a MMA-DR1 strip.

FIGURE 3 Lateral confinement of TE_{00} mode waveguide.FIGURE 4a Propagation in a S-bend with a curvature radius of $100\ \mu\text{m}$.

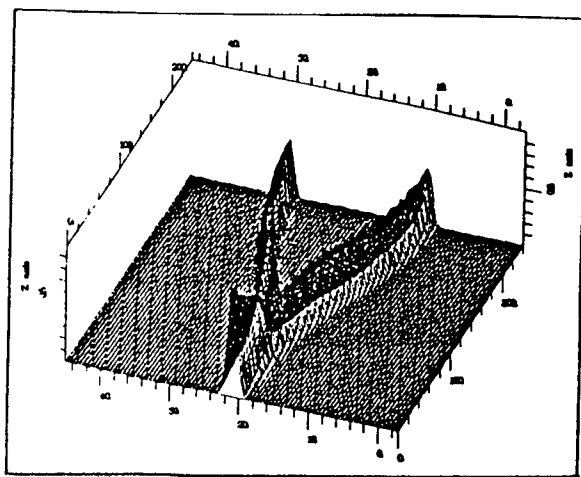
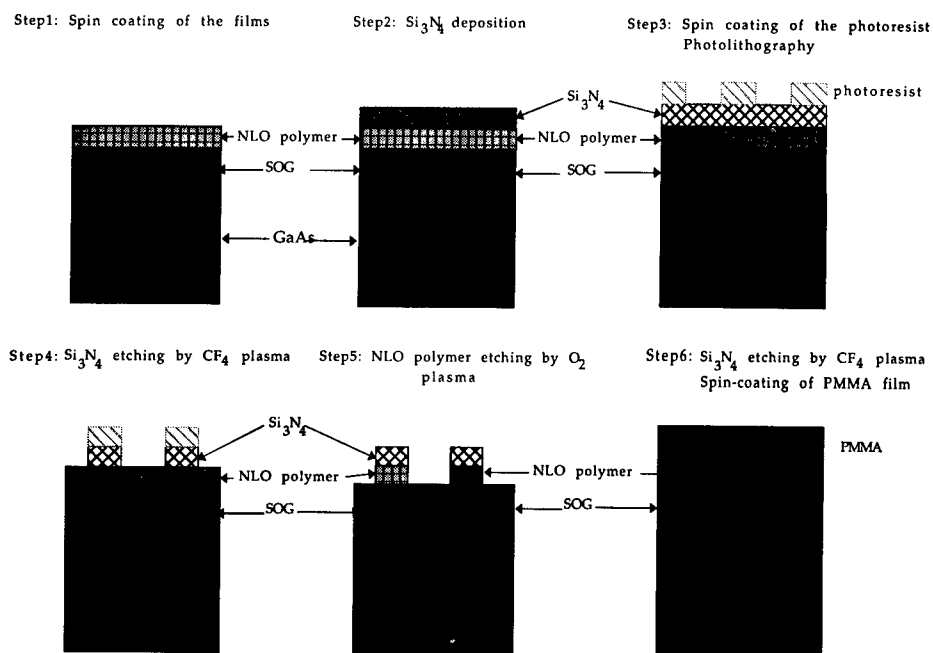
FIGURE 4b Propagation in a Y junction with a curvature radius of 200 μm .

FIGURE 5 Fabrication process of polymer waveguides.

As shown on the electron beam microscope photograph of the polymeric core ridge of the structure the sides of the guide are quite smooth. Therefore the propagation losses in such an optical waveguide were measured by the cut-back method at less than 1 db/cm.

PASSIVE FUNCTIONS

The propagation loss of 9 S-bend structures has been measured. The loss is inferred from comparison between the output signal of a S-bend waveguide and a straightline waveguide, the ratio of the two signals outgoing evidencing the losses due to the curvature radius of the waveguide with results presented in Figure 7.

The experimental results are in good agreement with the simulation . The curvature radius of S-bends is a function of the angle given by: $R = e/(2 \theta)^2$.Where e is the distance between input and outputs of the S-bend waveguide.

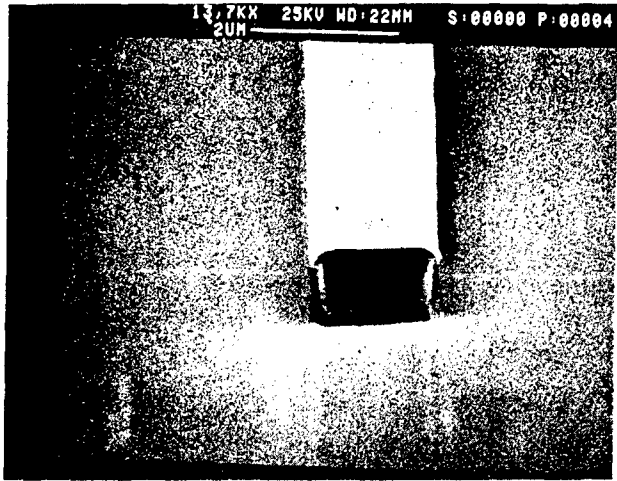


FIGURE 6 Electron Beam Microscope photograph of the core ridge of the polymer.

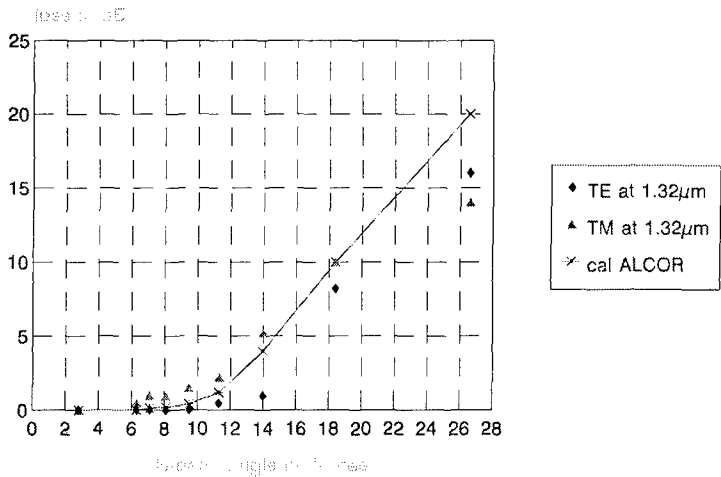


FIGURE 7 Propagation loss of S-bends as a function of angles.

Figure 7 shows that the propagation loss is negligible when the angle is less than 10° corresponding to a curvature radius of $100\text{ }\mu\text{m}$. This value is one order of magnitude smaller than that of LiNbO_3 in which the typical S-bend angle is about 1° . A polymer integrated device may thus have a much smaller size. Firstly, the waveguide width is about $2\text{ }\mu\text{m}$ instead of $10\text{ }\mu\text{m}$ in $\text{LiNbO}_3^{(5)}$ and the gap between parallel waveguides is $10\text{--}20\text{ }\mu\text{m}$ instead of $100\text{--}200\text{ }\mu\text{m}$. Secondly, the transition length of a low loss S-bend is shorter, $100\text{--}200\text{ }\mu\text{m}$ instead of $1\text{--}2\text{ mm}$. The combination of these two advantages opens new perspectives to polymer in optronic devices. It permits the design of new integrated optics devices achievable in polymer but out of reach for LiNbO_3 . The latter technology is limited by crystal growth and the small refractive index step as from titane in-diffusion.

Based on this technology, 1 to 4 asymmetric and symmetric junctions have been achieved (see respectively Fig. 8a and 8b). For that application the bottom buffer layer is Spin On Glass (a planarization resin commercialized by Allied Chemical), the strip guide is polystyrene and the top buffer layer is Teflon AF.

ELECTROOPTIC DEVICES

The non linearity of an active polymer (side chain MMA-DR1) has been demonstrated in phase and amplitude modulators. (Respectively in linear strip waveguides and integrated Mach-Zehnder geometry.) For that application the bottom buffer layer is SOG and the top buffer layer is pure PMMA.

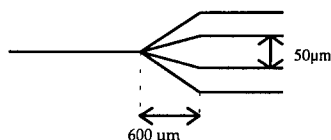
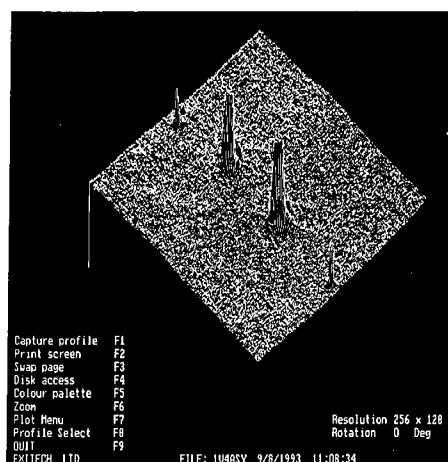


FIGURE 8a Asymmetric 1 to 4 junction.

The best figures obtained so far at $1.06\ \mu\text{m}$ are the half-wavelength voltage $V_\pi = 25\ \text{V}$ for the phase modulator inserted between crossed polarizers and $V_\pi = 16\ \text{V}$ for the Mach-Zehnder modulator working in TM polarization (Fig. 9).

A phase modulator was realized with a cross-link polymer Red-acid Magly (CNET patent N°9310572). In the first demonstration, we have measured the half-wavelength voltage V_π of 30 and 45 V respectively at $1.06\ \mu\text{m}$ and at $1.32\ \mu\text{m}$. This polymer is stable at 85°C for more than several weeks.

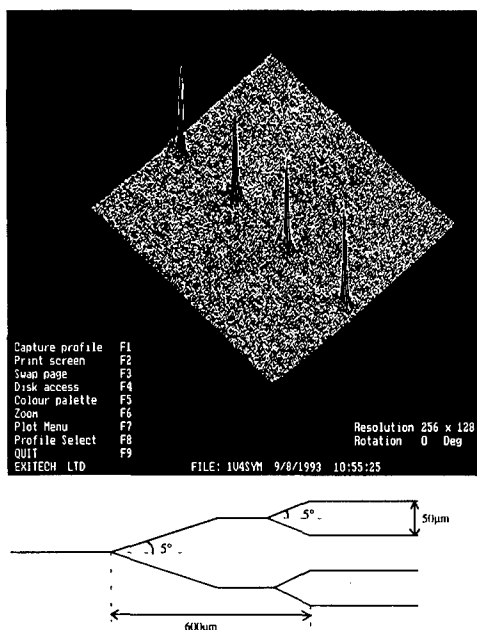


FIGURE 8b Symetric junction.

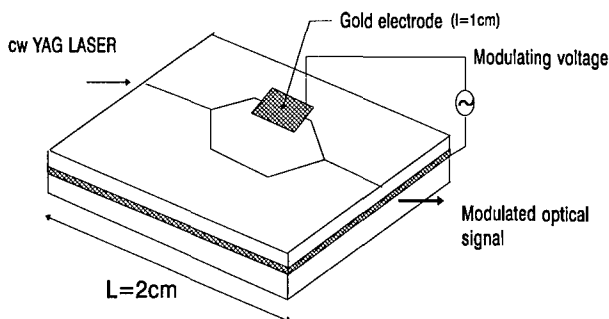


FIGURE 9 Structure of an integrated Mach-Zehnder interferometer.

These values should be decreased by an optimization of the poling conditions of the multilayer as it corresponds to a r_{33} of about 6.5 pm/V in the side chain MMA-DRI and 4 pm/V in the cross-link Magly whereas the best r_{33} measured for the same polymers in thin film geometry is 13 pm/V and 10 pm/V.

REFERENCES

1. BPM-CNET(ALCOR) software developed and distributed by France Telecom/CNET.
2. M. Filoche, PhD Thesis, 6 March 1991, Université de Paris Sud.
3. G. Hervé-Gruyer. *Electronic letters*, VOL. 26, n°17, pp. 1338–1339, August 1992.
4. G. Hervé-Gruyer, M. Filoche, F. Ghirardi. ECIO 93. NEUCHATEL April 1993.
5. *Guided-wave optoelectronics*. T. Tamir. Springer Verlag. 1990.

Polymers in New Electrooptic Components

JEAN-CLAUDE DUBOIS

*Thomson-CSF, Laboratoire Central de Recherches, 91404 ORSAY,
Cédex, France*

Received 4 March 1994; accepted 25 March 1994

This paper describes the properties and applications of some recent polymers in the field of electrooptic components. In the first part of this paper we describe the synthesis and properties of polysilanes. We have used these polysilanes after doping in association with a liquid crystal cell for the realisation of a spatial light modulator. We describe the good results obtained in the field of pattern recognition with this device. The second part describes the properties of ferroelectric copolymers (PVDF-TrFE) specially their pyroelectric properties. We describe the realisation and performances of an IR pyroelectric sensor using these copolymers of polyvinylidene fluoride-ethylene trifluoride, a new component which can be used in an IR camera for civil applications.

INTRODUCTION

Polymers can be used in optics and optoelectronics as “active” materials in different components. They combine the possibility of easy processing with an infinite potential of functionalization. They have been used for long as passive materials for components in electronics and electrooptics. They can be conductors or semiconductors, ferroelectrics, mesomorphous and can exhibit interesting properties such as photoconductivity, piezo, pyroelectricity or non linear optical properties. As a consequence they are now used for merging active components in the field of electrooptics such as displays, sensors or modulators for optical signal treatment.

Poly(methyl phenyl) silane show after doping interesting photo-conductive properties, in association with a nematic liquid crystal cell. This polymer has been used for realisation of a spatial light modulator allowing pattern recognition.

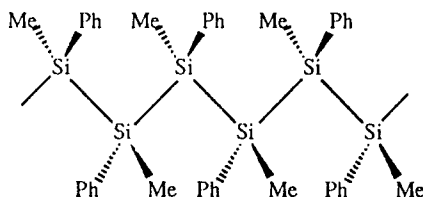
Other polymer derivatives of polyvinylidene fluoride are ferroelectric and pyroelectric and have been used for realisation of new IR detector for the first time in association with silicon components.

POLYSILANES AND SPATIAL LIGHT MODULATOR

A first example is the association of a photoconductive polymer and a liquid crystal cell to form a component for pattern recognition called “spatial light modulator” (SLM). SLM's based on the photoconductor-liquid crystal structure have been widely investigated.^{1,2} One of the main goals is to achieve high resolution which requires the photoconductor to have a low thickness and a high source-level resistivity.

The Polymeric Photoconductor

Polymeric photoconductors are interesting candidates since they are easily processable if they are soluble.³ Classical photoconducting polymers are doped TNF polyvinyl carbazole. Recently, polysilanes have been synthesized. However a dopant is necessary to enhance the sensitivity for visible wavelengths since the polysilane only absorbs in the 300–400 nm region. The polysilane is the polyphenyl methyl silane:



This compound³ is synthesised by polycondensation of the dichloromethyl phenyl silane in the presence of sodium using ultrasonic stirring. We have obtained a T_g of 120°C and a molecular weight $M \approx 10^5$. The polysilane is photosensitized by 10–30% of substituted phtalocyanine. Figure 1 shows the compared absorption spectra of the phtalocyanine and of the complex of the polysilane and the phtalocyanine.

The photoconductivity of a material can be represented as follows:

$$\sigma = \sigma_0 + \beta \cdot I$$

σ : conductivity under illumination

σ_0 : conductivity in the dark

β : sensitivity

I : illumination intensity

Different substitutants of the phtalocyanine have been tried and their sensitivity measured. The best sensitivity as a dopant in the polysilane is obtained with the

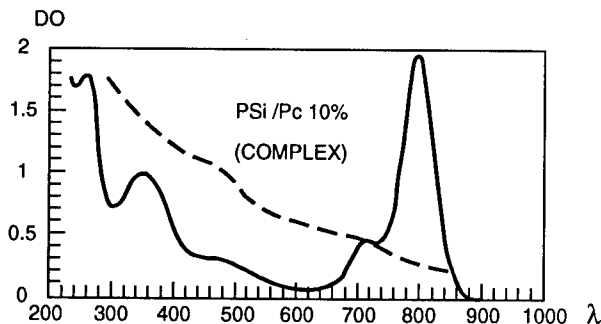


FIGURE 1 Absorption spectra of the phtalocyanine and the complex Psi phtalocyanine ($C = 0,22 \cdot 10^{-5} \text{ mol/C} - \text{CHCl}_3$).

compound $H_2P_C(S_{-I}P_R)_{16}$, where H_2P_C is the non metallated phthalocyanine. The sensitivity β is in the order of $10 \times 10^{-11} \cdot \Omega^{-1} \text{ cm} \cdot \text{W}^{-1}$.

The Liquid Crystal Cell

The liquid crystal cell associated with the photoconductor is represented in Figure 2. The nematic liquid crystal is sandwiched between two ITO electrodes with the polysilane on one side. The planar orientation of the liquid crystal is obtained using a polyimide polymer. The liquid crystal is a Merck 3651 chosen for its low dielectric anisotropy and its high resistivity ($\rho > 10^{12} \Omega \cdot \text{cm}$). The sensitivity is 2 mW/cm^2 at 514 nm and the resolution is up to 100 lp/mm .

The writing beam projects the hologram (Fourier transform) of an unknown pattern S and of a reference set R through a writing lens. The interferences of R and S are written by a writing beam (Doubled frequency yag laser— $\lambda = 532 \text{ nm}$) (Fig. 3).

The interferences are transferred to the liquid crystal and read by a plane wave ($\lambda = 633 \text{ nm}$). The reverse Fourier transform is obtained by a second lens and allow to

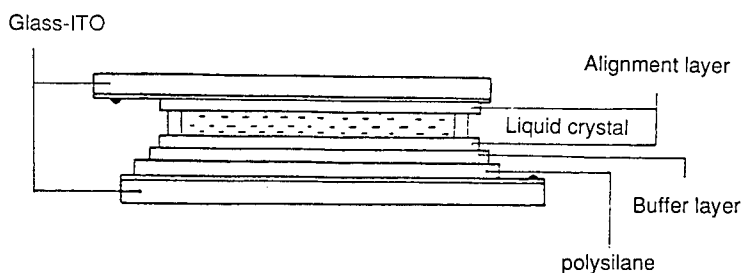


FIGURE 2 Psi/liquid crystal spatial light modulator.

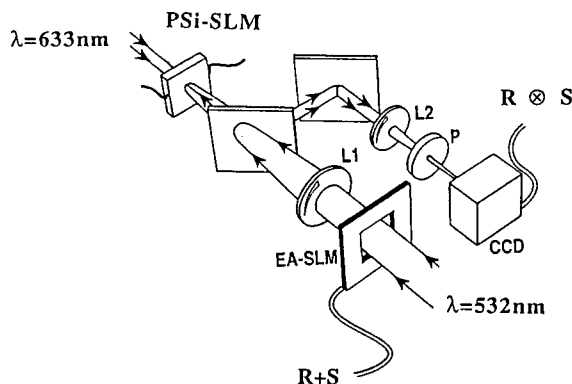


FIGURE 3 Principle of the optical correlator using the PSI-SLM (polysilane-spatial light modulator).

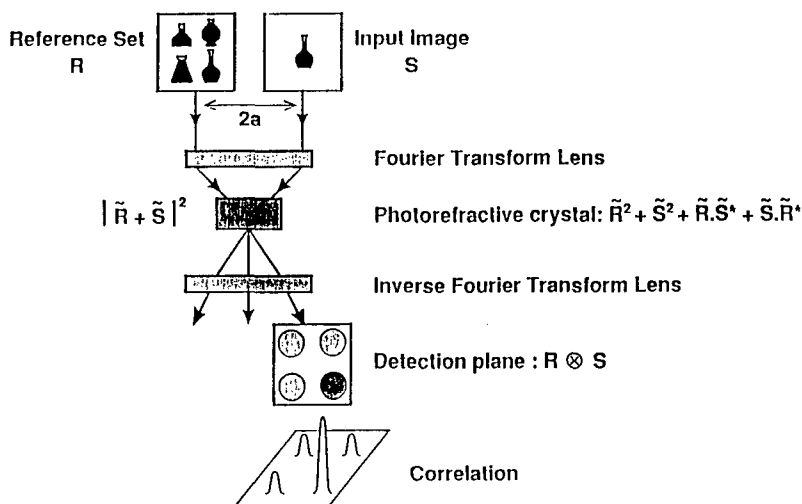


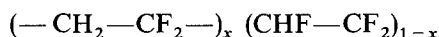
FIGURE 4 Optical architecture for a multichannel joint transform correlator. The input intensity distribution consisting of the reference set of object R and the unknown object S is Fourier transformed. The interference between R and S is recorded in an updatable photorefractive crystal. Upon inverse Fourier transform, the output plane contains the correlation product $R(x,y) \otimes S(x,y)$.

obtain the correlation function $R \times S$, when the unknown object is identical to one object of the set. A spatial resolution of less than $10 \mu\text{m}$ can be obtained for a diffraction yield of 5% (Fig. 4).

The SLM allow pattern recognition with good accuracy of unknown object among a set of known objects.

FERROELECTRIC POLYMERS AND IR IMAGING

Copolymers of the vinylidene difluoride and the trifluoroethylene show interesting ferroelectric and pyroelectric properties:⁷



They are soluble in solvent such as *n*-methyl pyrrolidone so they can be spun coated in thin layers on substrates such as silicon. They can crystallise directly in the β phase which is the ferroelectric phase, depending on the concentration of the co-monomers.

The phase diagram Figure 5 shows the existence of the ferroelectric phase versus the proportions of co-monomer vinylidene difluoride with trifluoroethylene. The ferroelectric phase exists at about 50% of VF_2 . However the most interesting copolymer is around 70% of VF_2 . For $x = 0.75$, the Curie temperature is around 125°C . These copolymers are manufactured by Penwalt-Atochem, Kureha and Piezotech. In order to obtain the ferroelectric properties it is necessary to polarise the β non centrosymmetric phase. The applied electric field is in the range of $100 \text{ V}/\mu\text{m}$. For $\text{P}(\text{VDF}_{75}/\text{TrFE}_{25})$ it gives a remanent polarization $P_r = 0.09 \text{ C}/\text{m}^2$.

These copolymers show a typical ferroelectric behaviour as shown on the Figure 6:

These ferroelectric copolymers are also pyroelectric. This means that a capacitor formed with the polymer will get a charge proportional to the temperature increase of the material. The measurement of the voltage of the capacitor or of the charge on the electrodes allows the temperature rise of the capacitor and thus the incident IR flux to be determined (Fig. 7).

The pyroelectric coefficient is:

$$P_y(C/m^2/K) = \frac{\Delta P}{\Delta T}$$

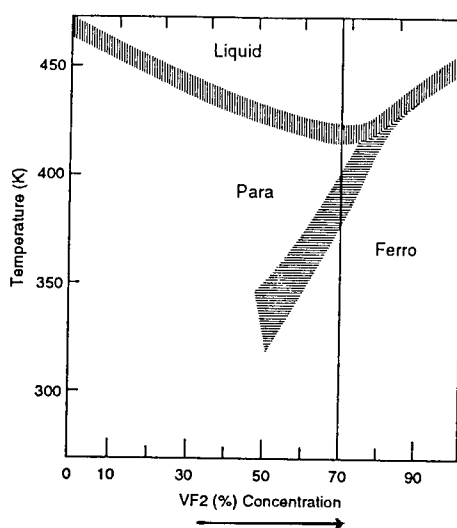


FIGURE 5 Phase diagram of P(VDF-TrFF) copolymers.

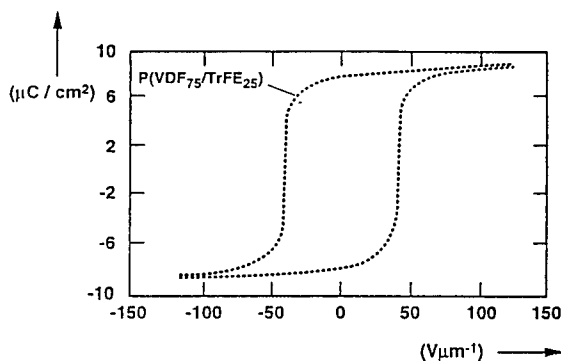


FIGURE 6 Hysteresis cycle of polarisation P versus the electric field E for the P(VDF_{0.75}-TrFE_{0.25}) copolymer.

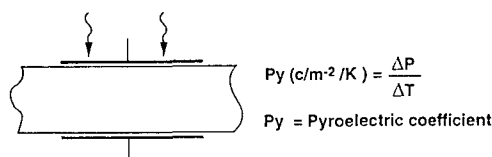


FIGURE 7 Pyroelectricity: principle of the pyroelectricity detection.

This coefficient depends on two factors: the variation of spontaneous polarisation in the crystalline phase (major effect) and the thermal dilatation of the polymers. These two factors are significant in determining the signal to noise ratio of the pyroelectric capacitor – multiplexor couple. Among the different materials which have been studied only the copolymer is directly compatible with the semiconductor fabrication process because it is soluble. The copolymer also shows a low thermal diffusion and the best merit factor (in voltage) as seen on the following table:

Pyroelectric materials	Nature	TC	P_y $\text{Cm}^{-2} \text{K}^{-1}$	ϵ_r	DT $10^{-7} \text{m}^2/\text{s}$	Voltage merit factor P_y/ϵ_r
TGS	crystal	49	3.5	50	2.6	7
PZT	ceramic	> 300	3.5	300	6	1.2
PVDF ₂ -TrFE	polymers	125	0.4	7	0.2	5.7

where:

- the pyroelectric coefficient P_y gives the intrinsic detectivity,
- the ϵ_r dielectric permittivity
- thermal diffusion Dt : ratio of the calorific capacity to the thermal conductivity,
- merit factor in voltage defined as P_y/ϵ_r ,

Thomson-TCS and LCR have realized an IR detector (8–14 μm range) associating this copolymer with a silicon CCD matrix.^{7,8,5}

IR detection in the 8–14 μm band is realized today essentially by semiconductors working at 77°K which need expensive and bulky cooling systems. The realization of sensors working at room temperature using integrated silicon circuit manufacturing technology opens up the possibility of manufacturing IR sensors with characteristics similar to the sensors working in the visible range.

One of the advantages of the pyroelectric detector concerns its use at room temperature, as semiconductor detectors work at low temperature. The other concerns its potential low cost. The principle of the Thomson polymer IR sensor^{5,8} is represented by Figure 8 and Figure 9. The P(VF₂-TrFE) copolymer constitutes the pyroelectric layer (5–10 μm), the insulation layer is a polyimide (10 μm). The upper electrode is also the infrared absorber and is made in aluminium or gold black. The lower level is the CCD level which constitutes the second electrode. The polarization of the polymer is realised by application of 100 V/ μm between the two electrodes of the pyroelectric capacitor.

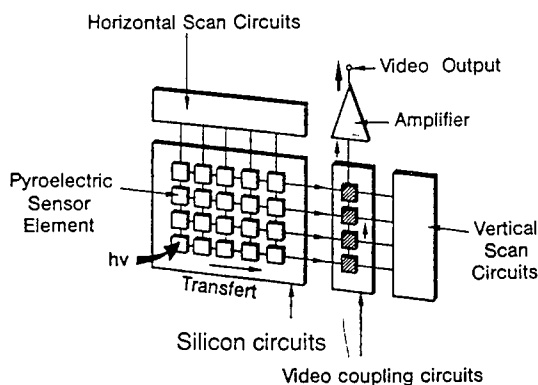


FIGURE 8 Three layers models for IR-pyroelectric CCD detector.

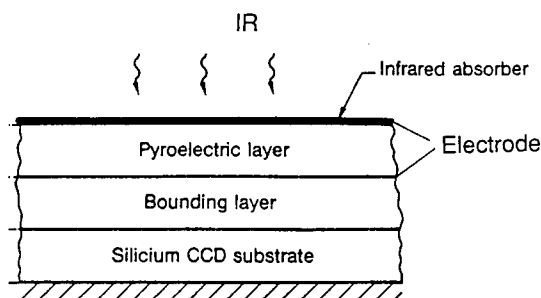


FIGURE 9 Configuration of pyroelectric IR-CCD sensor.

The matrix array detector has 128×128 pixels of $80 \times 80 \mu\text{m}^2$ surface area. The NETD (Noise Equivalent Temperature Detection) is 0.64 K at 40 Hz for an $f/1$ aperture.

The detector has been characterized at room temperature using an IR germanium optics. The following table summarizes the performance of this detector.

pixel number	128 × 128
pixel size	$80 \times 80 \mu\text{m}^2$
Curie temperature	125°C
spectral range	8–14 μm
sensitivity	11 mV/K
NETD($f/1$, $\tau_r = 0.7$, 40 Hz)	0.64 K

Applications

Applications of this component can be found with realisation of a low cost camera. This camera have different potential applications in different domains such as:

- security (night vision), research in sea for coastguards,
- vision through smoke (for firemen, research of persons during fire)
- anticollision car systems: the fog is transparent in the 8–12 microns IR band and stopped cars can be detected, specially on highways, in order to avoid serial accidents.

CONCLUSION

Polymers such as ferroelectric polymers can be used as “active” materials in components for electrooptics. The association of these polymers with silicon have conducted to the manufacture of an IR matrix array sensor 128×128 with NEDT of 0.64 K potentially low cost component. Moreover such component is now commercially available at TCS. Others polymers show many potentialities in optical signal treatment and we have shown that polymeric photoconductors can be used in an SLM for pattern recognition with the advantage of resolution and simplicity.

ACKNOWLEDGEMENT

We thank P. Le Barny, P. Robin, M. Lagarde, J. P. Huignard, P. Joffre, H. Rajbenbach, P. Dautriche, P. Pourquier who have done this work. One part of this work (SLM) has been down under ESPRIT contract 2284.

REFERENCES

1. P. Aubourg, J. P. Huignard, M. Hareng and R. A. Mullen, *Appl. Optics*, **21**, 3706 (1982).
2. H. Rajbenbach, S. Bann, P. Refregier, P. Joffre, J. P. Huignard, H. S. Buchkremer, A. S. Jensen, R. Rasmussen, K. H. Brenner and G. Lohman, *Appl. Optics*, **31**, 5666 (1992).
3. M. Lagarde, T. MY. Moisan and J. C. Dubois, *Molecular Engineering*, 1:221–239 (Kluwer Acad.) (1991).
4. J. C. Dubois, P. Le Barny, P. Robin, V. Lemoine and H. Rajbenbach, *Liquid Crystals*, vol. **14**, n°1, 197–213 (1993).
5. J. C. Dubois and coll., *Proceedings SPIE 93, Sand Diego*, vol. **2025**/467.
6. R.W. Whatmore, *Ferroelectrics*, vol. **118**, 241–59 (1991).
7. P. Robin, H. Facoetti, D. Broussoux, G. Vieux, J. L. Ricaud, *Revue Technique Thomson-CSF*, vol. **22**, n° 1, Mars 1990.
8. P. Dautriche, P. Pourquier, *Opto 93*, Paris.
9. France-Japan Joint Forum (*JFJF'93*), Tokyo 1993.

Molecular Engineering of Organic Materials for Efficient Spatial Light Modulation

JEAN-MICHEL NUNZI and FABRICE CHARRA

*Commissariat à l'Energie Atomique, Leti/Technologies Avancées,
DEIN-SPE, Groupe Composants Organiques, Centre d'Etudes de Saclay,
F91191 Gif-sur-Yvette, France, Tel: 33(1) 69 08 68 12, Fax: 33(1) 69 08 76 79,
E-mail: nunzi@roitelet.saclay.cea.fr*

Received 25 February 1994; accepted 15 March 1994

Third order nonlinear optical materials are evaluated with respect to their free-wave optical modulation properties. The optically addressed spatial light modulator is identified as a key device for beam handling. It can be characterized in terms of pixel density, exposure sensitivity and switching time. Third order nonlinear optical materials are attractive in order to improve on pixel density and switching speed. Their major advantage with respect to more classical spatial light modulation materials is in their molecular nature which permits the achievement of high pixel densities in thin films. Figures of merit appropriate to the comparison of third-order nonlinear optical materials are derived. Speed limitations of high density all-optical processing devices are deduced. Photochromic processes relevant to spatial light modulation with organics are proposed. The high pixel density permitted using organic thin-films is experimentally demonstrated using real-time holography.

INTRODUCTION

Since more than a decade, significant work has been performed with an aim at characterizing and optimizing organic materials with respect to optical processing applications. It is the tremendous work performed on third order nonlinear optical characterization of organics.^{1,2} However, except for spectroscopy, photophysics and nonlinear optical science, such characterization is useless to applications unless target performances are identified and figures of merit defined. The usual question is indeed what is $\chi^{(3)}$ for? And the answer begins with what is the identified application? This question has been addressed at large with respect to waveguide optical modulation by Stegeman.^{3,4} However, since the very recent discovery of cascading effects in phase-matched second order materials,^{5,6} the answer has always been that the actual figure of merit $\chi^{(3)}/\alpha$ is too low for practical devices to emerge in this particular field of optical communications.

On another hand, in the field of image and beam processing, there is great need for devices in which a spatial light-intensity profile (image) can be recorded and transformed into a transmission or a phase retardation profile (Fig. 1). A solution in order to process a still increasing volume of information issued from sensors and data banks is indeed to treat it in parallel. And as information is often available as optical images, a simple idea is to pre-process or to compress it prior to acquisition. This is performed using correlation or novelty filtering techniques and a key device in this respect is the

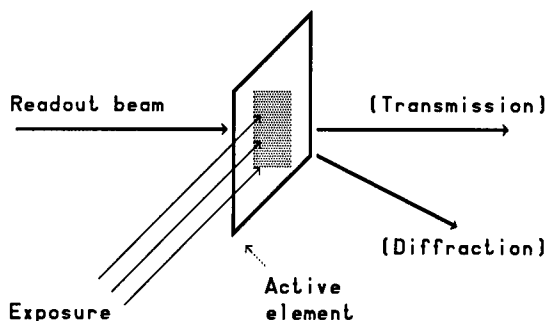


FIGURE 1 Typical SLM geometries. The dashed region represents the induced index or absorption profile. Signal can be either analyzed in transmission or in diffraction if exposure is an interference (correlation, holography).

optically addressed spatial light modulator (SLM).⁷ A special class of such devices is for instance the incoherent to coherent optical converter.⁸ It permits the achievement of input functions in optical image processors based on holographic and Fourier optics.⁹ The most widely used type of SLM is simply the silver-halide photographic recording plate.¹⁰ Its principle is that a real image is recorded under incoherent illumination on a photographic film, the developed slide then modulates a coherent beam for optical processing of the image. The drawback of silver-halide photography is the delay, close to one minute, between exposure and processing. One common wish with optical processing is indeed to perform real-time operations. Different techniques, with commercially available devices, already permit the realization of real-time spatial light modulators. However a potential target promised by optical processing with typical pixel densities of $1 \mu\text{m}^{-2}$, beam surfaces of 1 cm^2 treated at 100 MHz rates, offering an equivalent of 10^{16} operations per second, is far from being realized with commercial SLMs. It is the reason for considering in this paper some material requirements aimed at optimizing an SLM, with emphasis on the possibilities offered by third-order nonlinear optical $\chi^{(3)}$ materials. We shall derive figures of merit appropriate to the comparison of nonlinear optical materials and give the physical speed limitations of high density all-optical processing devices. We shall propose some relevant photochromic processes and demonstrate the ultimate high pixel density which can be achieved using organic thin-films in the case of a real-time holography trial performed with the well known photochromic dye spiropyran.

MATERIALS REQUIREMENTS

As in photographic techniques, two functions characterize SLM: the exposure or recording and the readout. In usual (commercial) real-time SLMs, recording is performed using a photoconductor in order to switch optically the voltage applied across an electro-optic material which then modulates the readout beam.⁷ This is the

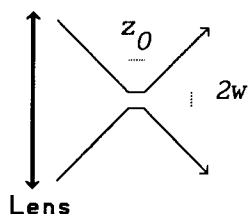


FIGURE 2 Addressing capability of a lens. It sets the thickness limitation ($t \leq z_0$) of the active layer. z_0 is the Rayleigh length and w the waist at focus for a Gaussian beam.

case in photoconductor – liquid-crystal light valves.^{11,12} In photorefractive and in self electro-optic devices,^{13,14} both functions are performed in the same material. Basically, SLMs may be characterized by their spatial resolution (Ab in cycle/mm), exposure sensitivity per pixel (W in pJ/px) where the pixel is defined as the smallest resolution element, and switching time (τ in sec). Properties of typical representatives of SLMs are given in Table 1, together with the target figure of an optimized SLM.¹⁶

In order to fully exploit the parallel addressing capabilities of light, an optimized SLM should have a spatial resolution limited by diffraction ($Ab \approx \lambda^{-1} \approx 10^3$ cycle/mm). This determines the maximum thickness of the device. Consider the waist at the focal point of a lens (Fig. 2): its radius w is connected to the Rayleigh length z_0 by $z_0 = \pi w^2 / \lambda$, where λ is the optical wavelength. If device thickness is larger than z_0 , addressed waists will overlap in the active layer. Resolution is thus optimized when device thickness is $t \leq \lambda$ (Tab. 1).

The ultimate speed of charge-transfer SLMs is limited by carrier drift and capacitance.^{11–14} In order to achieve high speed performances in the MHz to GHz range (Tab. 1), a recognized route is the use of materials with large third-order nonlinear optical properties such as quantum confined semiconductor heterostructures¹⁵ or organic semiconducting polymers.¹⁷ Those materials are characterized by a susceptibility $\chi^{(3)}$ describing the complex index change $\delta n = 2n_2 I$ induced on a read beam by a write (pump) beam of intensity I :

$$\delta n = \frac{3\chi^{(3)} I}{2\epsilon_0 c n^2}. \quad (1)$$

TABLE 1
Typical performances of spatial light modulators.

OASLM	Ab (cycle/mm)	W(pJ/px)	τ (sec)	ref.
Nematic liquid crystal	60	5	0.01	11
Ferro. liquid crystal	100	0.2	10^{-4}	12
Photorefractive crystal	300	100	0.1	13
Self Electro-Optic	12	180	10^{-6}	14
Quantum well etalons	100	100	10^{-8}	15
Silver halide films	10^3	10^{-2}	100	10
Optimized target	10^3	1	$10^{-5} - 10^{-9}$	16

The complex phase retardation variation induced inside the material is

$$\delta\varphi = \delta\varphi' + i\delta\varphi'' = 2\pi(\delta n' + i\delta n'')\frac{t}{\lambda}. \quad (2)$$

In order to achieve a contrast ratio of 10 for the device transmission $T = \exp(-2\delta\varphi'')$ in Figure 1, the imaginary part of the phase retardation must reach $\delta\varphi'' \approx 1.2$. For interference configurations (Fig. 1) the same $\delta\varphi'$ value is large enough to reach the limiting 34% diffraction efficiency $\eta \approx |\delta\varphi/2|^2$ of thin phase gratings.¹⁸ As $t/\lambda \approx 1$, the required index change necessary for efficient modulation in thin films is $\delta n \approx 0.2$.

For $\chi^{(3)}$ materials to be efficient in SLM, the write process also needs to be optimized. With the elements given in Table 1, a realistic switching energy is $W \approx 1$ pJ/px. With $1\mu\text{m}^2$ pixels, this corresponds to an average energy consumption $I\tau \approx 100\mu\text{J}/\text{cm}^2$. Using equation (1), this sizes the magnitude of the optical nonlinearity for efficient thin-film spatial light modulation:

$$\frac{\chi^{(3)}}{\tau} = \frac{2\epsilon_0 n^2 c \delta n}{3I\tau} \geq 10^{-3} \text{ m}^2 \text{ V}^{-2} \text{ s}^{-1}. \quad (3)$$

The nonlinearity is also alternatively expressed in terms of nonlinear index n_2 ^{3,4} and its useful range is: $n_2/\tau \geq 0.1 \text{ m}^2/\text{J}$. For a switching time of 1 ns, it corresponds to $\chi^{(3)} \geq 10^{-4} \text{ esu}$ ($1 \text{ m}^2 \text{ V}^{-2} = 7.2 \times 10^7 \text{ esu}$). Such a magnitude can be achieved only if the optical-field frequencies are close to resonance with real transitions.

In order to evaluate the optical modulation potentialities of nonlinear materials, we must estimate the magnitude of resonant nonlinearities in terms of elementary material parameters. We consider an assembly of non-interacting molecules described by real transitions within a four-level system (Fig. 3). Molecules in the ground state g are excited in resonance using a recording beam at frequency ω_e . Immediately after excitation, molecules in state e undergo ultrafast internal conversion to a metastable state e' , with a time constant τ_i which is down to 100 fsec for Franck-Condon nuclear relaxation¹⁹ and in the 100 psec range for efficient inter-system crossing to the triplet manifold.²⁰ The excited state e' has a lifetime τ . The induced absorption from the excited state e' to the final state f is probed in resonance using a readout beam at frequency ω_t (Fig. 3). For a homogeneous isotropic assembly of one-dimensional

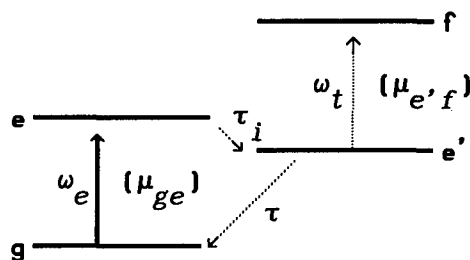


FIGURE 3 Real transitions involved into the resonant nonlinear optical response of a single isolated molecule. g , e , e' and f are the relevant molecular states, ω are optical frequencies and μ are dipole matrix elements.

(rod-shaped) molecules with density N , the resonant part of the relevant third-order nonlinear optical susceptibility can be written:

$$\chi^{(3)} = \text{Im}(\chi_{(\omega_e)}^{(1)})\tau \left(\frac{|\mu_{e'f}|^2}{\omega_{f'e'} - \omega_t - i\gamma_{f'e'}} - \frac{2|\mu_{ge}|^2}{\omega_{eg} - \omega_t - i\gamma_{eg}} \right) / 10\hbar^2 \quad (4)$$

where μ_{ij} are the transition dipole matrix elements and γ_{ij} the transverse relaxation rates between states i and j . The positive term in equation 4 gives the photochromic contribution to the resonant $\chi^{(3)}$ (it involves excited state transitions and replaces the usual two photon term²¹) and the negative term gives the saturable absorption contribution (the factor 2 may be omitted for bleaching). The linear susceptibility of the material is $\chi^{(1)}(\omega_e) = N|\mu_{ge}|^2/3\hbar\epsilon_0(\omega_{eg} - \omega_e - i\gamma_{eg})$. It is related to the absorption of the sample at wavelength λ by $\alpha = 2\pi \text{Im}(\chi^{(1)})/n\lambda$. The refractive index of organic materials is $n \approx 1.5$ ($n \approx 3.5$ in GaAs). The intrinsic element of comparison between nonlinear optical materials is thus the well known figure:¹⁷

$$\frac{\chi^{(3)}}{\alpha\tau} \approx \frac{3\epsilon_0 n^2 \lambda^2 \Delta\sigma}{40\pi^2 \hbar} \quad (5)$$

This represents the net optical switching efficiency per absorbed photon. It is also the switching efficiency per excited molecule and it is proportional to the average molecular absorption cross-section variation between ground and excited states $\Delta\sigma$ ($\sigma = \alpha/N$). Using equation (3) and taking $\alpha \approx 10^7 \text{ m}^{-1}$ for efficient thin-film absorption, a good figure of merit is: $\chi^{(3)}/\alpha\tau \geq 10^{-10} \text{ m}^3 \text{ V}^{-2} \text{ s}^{-1}$. It is satisfied when $\Delta\sigma \geq 2 \times 10^{-15} \text{ cm}^2$. Such value is among the highest cross sections available with the most efficient organic dyes.²² Table 2 gives a comparative evaluation of materials useful for SLM under resonant excitation. Switching efficiencies span over 6 orders of magnitude, however not all materials can support large pixel density SLMs because they cannot satisfy the thin-film condition.

TABLE 2
Switching efficiencies of resonant nonlinear optical materials obtained from saturable absorption and (sa) and photochromic (pc) experiments.

Material	$\chi^{(3)}/\alpha\tau (10^{-10} \text{ m}^3 \text{ V}^{-2} \text{ s}^{-1})$	Ref.
Cs vapor	1 (sa)	23
C ₆₀	0.03 (pc)	24
Au colloid	0.4	25
CdS _{1-x} Se _x glass	0.5 (sa)	26
PTS crystal	1 (sa)	27
9740 Kodak dye	2 (sa)	28
AsGa bulk ($n^2 \approx 12$)	30 (sa)	29
AsGa MQW ($n^2 \approx 12$)	300 (sa)	30
Thermal effect	0.1	4
cis-trans isomery	0.01 (pc)	31
Bacteriorhodopsin	0.05 (pc)	32
Spirooxazine	0.005 (pc)	33
Fulgides	0.0002 (pc)	34
Eosin Y	0.1 (sa)	35
α 6-thiophene	1 (pc)	8

SPEED LIMITATIONS OF SPATIAL LIGHT MODULATION

It is often considered that organics are promising materials for Tera- to Peta-Hertz optical modulation. However this is possible only with a low duty cycle³⁶ or eventually with the low parallelism of guided wave optics.³ It is indeed simple to conclude that owing to the resonant behaviour of the nonlinearity (eqn.3) imposed by the small thickness requirement, power dissipation $P = W/\tau$ will reach the GW/cm^2 for picosecond switching times. Figure 4 gives power dissipation of a high density SLM with respect to working frequency for different switching energies. If for practical considerations, one limits the maximum permissible power dissipation to $1 \text{ KW}/\text{cm}^2$, the maximum working frequency of an optimized material will not exceed the 10 MHz range with as low as $1 \text{ pJ}/\mu\text{m}^2$ switching energy. In order to increase switching rate, switching energy must be reduced. This can be performed using amplification techniques such as microchannel plates,⁷ optical microresonators¹⁵ or chemical processing,¹⁰ but the drawbacks are either a dramatic pixel density or acceptance angle reduction, or a processing speed reduction, as in the living-eye vision. Temptatives of replacement of the photoconductor by a photochromic molecule in order to activate the phase transition in liquid crystal SLMs have been made.³⁷ Such ideas offer promising amplification perspectives in order to overcome the 10 MHz parallel processing frequency limitation.

PHOTOCHROMIC PROCESSES

Excited state absorption of dye molecules has been proposed for optical modulation by Ebbesen in 1985.³⁸ The fully resonant nonlinearities which can be described by the simplified scheme in Figure 3 are often referred to as photochromism in the literature.³⁹ Few parameters are necessary in order to characterize photochromism in terms of

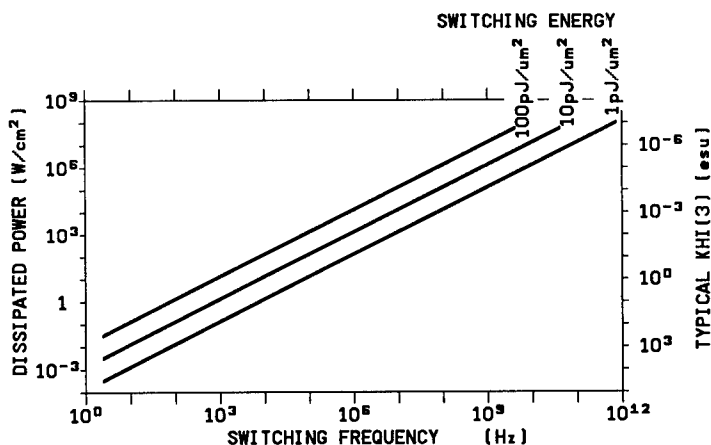


FIGURE 4 Power dissipation requirements for ultrafast high-resolution spatial light modulation. Typical $\chi^{(3)}$ size for $1 \text{ pJ}/\mu\text{m}^2$ switching energy is given in esu on left scale ($1 \text{ esu} = 7.2 \times 10^7 \text{ m}^2/\text{V}^2$).

switching efficiency. Large nonlinearities within acceptable switching times and thicknesses are obtained in resonance with fully spin and parity allowed transitions. The efficiency to populate an excited state e' depends on the quantum efficiency ϕ of conversion of the absorbed photons. Transitions are characterized by their oscillator strengths $f = 2m_e \mu_{ij}^2 \omega_{ij} / e^2 \hbar$. They are close to unity in most organic dyes.²² Cross-sections of real (inhomogeneously broadened) absorptions are proportional to the inverse line-width Γ^{-1} (hwhm) of the absorption profile. The magnitude of the switching efficiency (eqn. 5) can then be written as $\chi^{(3)} / \alpha \tau = A \phi f \omega_i / \Gamma_{e'f}$ with $A = n c e^2 / 20 m_e \hbar \omega_e \omega_i^2$. For visible (2 eV) to infrared (1 eV) optical conversion, $A = 7.8 \times 10^{-13} \text{ m}^3 \text{ V}^{-2} \text{ s}^{-1}$. The figure of merit which characterizes efficient photochromic effects is thus

$$\mathcal{F} = \frac{\phi f \omega_i}{\Gamma_{e'f}} \geq 10^2 \quad (6)$$

We see that the largest \mathcal{F} values are obtained with narrow excited state transitions. This is the effect of *spectral concentration*¹⁶ that we recently discovered for the $S_1 \rightarrow S_n$ singlet excited state transitions in thiophene oligomers.⁴⁰ *Spectral concentration* within the $T_1 \rightarrow T_n$ triplet excited states also makes α -6T thiophene thin-films potentially attractive SLM materials.⁸ Molecular engineering rules of the effect have recently been proposed¹⁶ and are currently being demonstrated.⁴¹

In order to cover the different frequency domains necessary for image processing using organic materials, different photochromic processes are possible. Examples are the ring opening reactions of which spiropyran is a classical representative⁴² for Hz rate operations, the trans to cis isomerization⁴³ occurring for instance in azo-benzenes for KHz rate operations, and the intersystem crossing to triplet states⁴⁴ for MHz rate operations (with oxygen and at room temperature). Those processes are sketched in Figure 5. The major drawback when increasing the switching or memorization time τ is that the longer τ is, the most efficient unwanted side relaxation pathways are. This reduces quantum efficiency ϕ of absorbed photon conversion which should ideally be equal to 1 for optimized modulation.

THE ULTIMATE PIXEL DENSITY OF ORGANIC THIN FILMS

In order to demonstrate the possibility of ultimate pixel density in organic photochromic thin-films, we performed a real-time holography experiment under large F/1 aperture angle conditions. The holographic exposure source was a continuous argon-ion laser delivering 2 W at the green 514 nm wavelength. It was splitted into two unequal parts, 40% of which, with 800 mW intensity was sent on the holographic plate as a 7 cm² reference beam and the other 60% part was illuminating the observed object and scattered on to the plate. This object, a metallic tool, had a typical 5 cm size and was located at 5 cm from the holographic plate. This plate was made with 10 weight % nitro-BIPS spiropyran (Fig. 5) doped into a PMMA matrix. A 1 μm thickness film was spin-coated from a MIBK solution onto a 5 cm diameter RG 610 Schott-glass filter. Such colored filter was used in order to block the 514 nm light and to permit real-time visualization of the holographic readout using the 633 nm red light of a He-Ne laser.

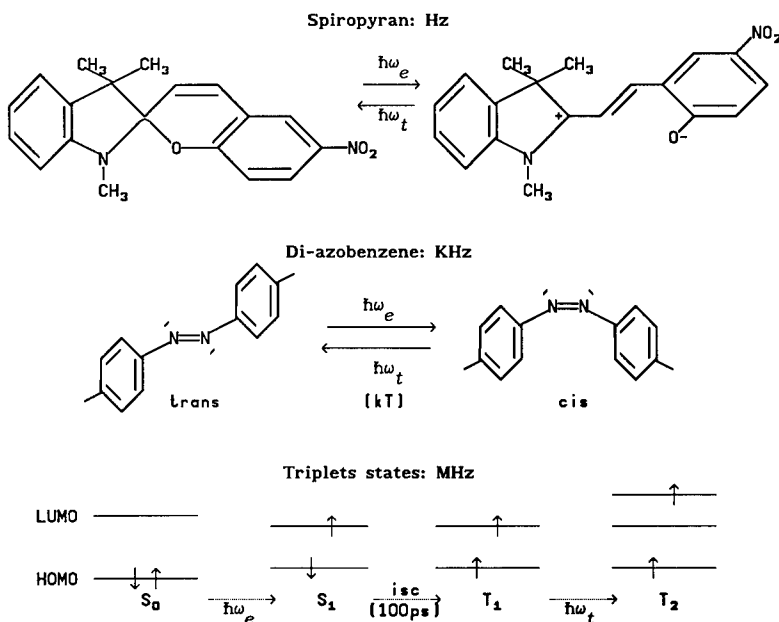


FIGURE 5 Transient molecular photochromic processes usable for SLM in the Hz, KHz and MHz frequency ranges.

Figure 6 is a picture of the experiment. The ultimate pixel density performance is demonstrated by the large $\approx 45^\circ$ viewing angle with which the hologram is recorded. It corresponds to $a \approx 1 \mu\text{m}$ pixel size (fringe pitch). Real time holography can be visualized because readout is performed with a different wavelength than exposure. This is only possible with thin-film holograms which have noncritical Bragg conditions. In this experiment, the spiropyran film was initially colored in the blue open form using a UV lamp. The photochromic reaction for holographic exposure was the backward closure reaction in Figure 5. Its efficiency is lowered by a factor of ten with respect to the opening reaction.³³ This made the spiropyran SLM work at 0.2 Hz rate with $\approx 6 \text{ nJ}/\mu\text{m}^2$ switching energy, an efficiency as low as for fulgides in Table 2.

CONCLUSION

The realization of organic SLMs using thin films in which optical modulation is achieved on a molecular scale opens the door to devices processing large densities of parallel information (images). As organic materials have an ultrafast response time and typical room temperature triplet relaxation times in the μs range, their resonant third order optical nonlinearity opens the door to optical image processing above MHz frequency rates. With their processing ease and chemical tailoring capability, organic materials can play a significant role in the field of image and optical beam handling. A molecular engineering strategy is being currently developed for the optimization of photochromic nonlinear optical materials for spatial light modulation.



FIGURE 6 View of the real-time holography experiment performed with a spiropyran thin-film deposited on a red glass disk (on right of the picture). The observed object, a metallic tool in the center of the picture, is illuminated with the expanded green beam of an argon-ion laser. Readout was performed with a He-Ne laser whose output is visible on the left-most part of the figure. The reconstructed holographic image is visible in red colour behind the holographic film.

ACKNOWLEDGEMENTS

This work was supported by the *Direction des Recherches, Etudes et Techniques*.

REFERENCES

1. J. Messier, F. Kajzar, P. Prasad and D. Ulrich, Nonlinear Optical effects in organic polymers, *NATO ASI Series E*, Vol. 162, Kluwer (Dordrecht, 1991).
2. J. Messier, F. Kajzar and P. Prasad, Organic molecules for nonlinear optics and photonics, *NATO ASI Series E*, Vol. 194, Kluwer, p. 359 (Dordrecht, 1991).
3. G. I. Stegeman *et al.*, in Organic materials for Nonlinear Optics, R. A. Hann and D. Bloor (eds.), Special publication of the Royal Society of Chemistry, p. 369 (London, 1989).
4. G. I. Stegeman, in Organic materials for Nonlinear Optics II, R. A. Hann and D. Bloor (eds.), Special publication of the Royal Society of Chemistry, p. 311 (London, 1991).
5. G. I. Stegeman, M. Sheik-Bahae, E. van Stryland and G. Assanto, *Opt. Lett.*, **18**, 13 (1993).
6. D. Y. Kim, W. E. Torruellas, J. Kang, C. Bosshard, G. I. Stegeman, P. Vidakovic, J. Zyss, W. E. Moerner, R. Twieg and G. Bjorklund, Second order cascading as the origin of large third order effects in organic single crystal core fibers, *submitted to Opt. Lett.* (1994).
7. C. Warde and A. D. Fisher, in Optical signal processing, J. L. Horner (ed.), *Academic*, p. 477 (New York, 1987).
8. D. Fichou, J. M. Nunzi, F. Charra and N. Pfeffer, *Adv. Mater.*, **6**, 64 (1994).
9. A. Vanderlugt, Optical signal processing, Wiley (New York, 1992).
10. K. Biedermann, in Holographic recording materials, H. M. Smith (ed.), Springer, p. 21 (Berlin, 1977).
11. J. Grinberg, A. Jacobson, W. Bleha, L. Miller, L. Fraas, D. Boswell and G. Myer, *Opt. Eng.*, **14**, 217 (1975).

12. K. Johnson, *Physics World*, **5**(9), 37 (1992).
13. J. W. Yu, D. Psaltis, A. Marrakchi, A. R. Tanguay Jr. and R. V. Johnson, in *Photorefractive materials and their applications II*, P. Gunter and J. P. Huignard (eds.), Springer, p. 275 (Berlin, 1989).
14. G. Livescu, D. A. B. Miller, J. E. Henry, A. C. Gossard and J. H. English, *Opt. Lett.*, **13**, 297 (1988).
15. B. G. Sfez, E. V. K. Rao, Y. I. Nissim and J. L. Oudar, *Appl. Phys. Lett.*, **60**, 607 (1992).
16. J. M. Nunzi, F. Charra and N. Pfeffer, *Journal de Physique III*, **3**, 1401 (1993).
17. F. Kajzar, J. Messier, J. M. Nunzi and P. Raimond, in *Polymers for Lightwave and Integrated Optics: Technology and Applications*, L. A. Hornak (Ed.), Marcel Dekker, p. 595 (New York, 1992).
18. H. M. Smith, in *Holographic recording materials*, H. M. Smith (ed.), Springer, p. 1 (Berlin, 1977).
19. J. M. Nunzi, C. Hirlimann and J. F. Morhange, *Chem. Phys. Lett.*, **221**, 199 (1994).
20. J. M. Nunzi, N. Pfeffer, F. Charra and D. Fichou, *Chem. Phys. Lett.*, **215**, 114 (1993).
21. N. Pfeffer, P. Raimond, F. Charra and J. M. Nunzi, *Chem. Phys. Lett.*, **201**, 357 (1993).
22. J. Fabian and H. Hartmann, *Light absorption in organic colorants*, Springer, (Berlin, 1980).
23. M. Oria, D. Bloch, M. Fichet and M. Ducloy, *Opt. Lett.*, **14**, 1082 (1989).
24. D. K. Palit, A. V. Sapre, J. P. Mittal and C. N. R. Rao, *Chem. Phys. Lett.*, **195**, 1 (1992).
25. F. Hache, D. Richard, C. Flytzanis and U. Kreibig, *Appl. Phys. A*, **47**, 347 (1988).
26. P. Roussignol, D. Ricard and C. Flytzanis, *Appl. Phys. A*, **44**, 285 (1987).
27. B. I. Greene, J. F. Mueller, J. Orenstein, D. H. Rapkine, S. Schmitt-Rink and M. Thakur, *Phys. Rev. Lett.*, **61**, 325 (1988).
28. W. Koechner, in *Solid-state laser engineering*, Springer, p. 465 (Berlin, 1976).
29. J. L. Oudar, in *Nonlinear optics, materials and devices*, C. Flytzanis and J. L. Oudar (eds.), Springer, p. 91 (Berlin, 1986).
30. D. S. Chemla, in *Nonlinear optics, materials and devices*, C. Flytzanis and J. L. Oudar (eds.), Springer, p. 65 (Berlin, 1986).
31. R. A. Lessard, J. J. A. Couture and P. Galarneau, in *Nonlinear Optical effects in organic polymers*, J. Messier, F. Kajzar, P. Prasad and D. Ulrich, *NATO ASI Series E*, Vol. **162**, Kluwer, p. 343 (Dordrecht, 1991).
32. R. Thoma, N. Hampp, C. Bräuchle and D. Oesterhelt, *Opt. Lett.*, **16**, 651 (1991).
33. V. Weiss, A. A. Friesem and V. A. Krongauz, *Opt. Lett.*, **18**, 1089 (1993).
34. C. J. G. Kirkby and I. Bennion, *IEE Proceed.*, **133**, 98 (1986).
35. S. Speiser, in *Nonlinear optical properties of organic materials IV*, K. D. Singer (ed.), *SPIE proc.*, **1560**, 434 (1990).
36. P. D. Foote, G. M. Proudley, G. S. Beddard, G. G. McFadyen, G. D. Reid, L. M. Connors, M. Bell, T. J. Hall and K. Powell, *Appl. Opt.*, **32**, 174 (1993).
37. T. Moriyama, J. Kajita, Y. Takanisi, K. Ishikawa, H. Takezoe and A. Fukuda, *Jpn. J. Appl. Phys.*, **32**, L598 (1993).
38. T. W. Ebbesen, *Appl. Opt.*, **25**, 2193 (1986).
39. R. Dessauer and J. P. Paris, in *Advances in Photochemistry*, Vol. **1**, Interscience, p. 275 (New York, 1963).
40. F. Charra, D. Fichou, J. M. Nunzi and N. Pfeffer, *Chem. Phys. Lett.*, **192**, 566 (1992).
41. F. Charra, T. P. Nguyen, J. M. Nunzi, N. Pfeffer and V. H. Tran, *Picosecond light-induced dichroism in thin films of phenylene-vinylene oligomers*, *ICONO 1 proceedings, to be published in Nonlinear Opt.* (1994).
42. R. Guglielmetti, in *Photochromism: molecules and systems*, H. Durr and H. Bouas-Laurent, Elsevier, p. 314 (Amsterdam, 1990).
43. F. Wilkinson, in *Organic molecular photophysics*, J. B. Birks (ed.), Wiley, Vol. **2**, p. 95 (New York, 1975).
44. D. L. Ross and J. Blanc, in *Photochromism*, G. H. Brown (ed.), *Techniques of chemistry III*, Wiley, p. 471 (New York, 1971).

Transient Photochromism of Oligothiophenes and its Use to Design an Incoherent-to-Coherent Optical Converter

DENIS FICHO^a, JEAN-MICHEL NUNZI^b, FABRICE CHARRA^b and NICOLA PFEFFER^b

^aLaboratoire des Matériaux Moléculaires- CNRS, UPR 241, 2, rue Henry Dunant- 94320 Thiais, France, ^bService de Physique Electronique, CEA, LETI- Département d'Electronique et d'Instrumentation Nucléaire, Saclay, 91191-Gif-sur-Yvette, France

Received 17 February 1994; accepted 14 March 1994

Conjugated oligomers of thiophene have recently become a new class of molecular semiconductors with potential applications in microelectronics. We show here that these compounds are also attractive third-order nonlinear optical materials with potential applications in optical signal processing. We report on the picosecond photoinduced dichroism of thiophene oligomers α -nT ($n = 2 - 6$) in solution and thin film. Spectral concentration in the excited state is identified as the key phenomenon to design a prototype incoherent-to-coherent optical converter (ICOC). Vacuum deposited thin films of the model sexithiophene α -6T meet the material requirements to achieve 1 pJ/pixel exposure sensitivity in the MHz frequency range.

INTRODUCTION

Conjugated thiophene oligomers attract a considerable interest since three years because they form a new class of organic semiconductors with exceptional charge transport properties and potential applications in MIS devices such as thin film transistors.¹ These pseudo-polyenes also have well-defined linear² and third order nonlinear³ optical properties that have been much less investigated but could also have potential applications in optical signal processing.

Spatial light modulators (SLMs) are two-dimensional input devices aimed at fully utilizing the potential speed and parallelism capabilities of light and can be considered as the building blocks of image and beam processors.⁴ In conventional real-time optically-addressed SLMs, the active recording material can be a liquid crystal, a photorefractive crystal, a multi quantum well semiconductor or a silver halide film. The comparative performances of various OASLMs based on such materials have recently been discussed by Nunzi *et al.*⁵ The basic requirements for an optimized OASLM are 1) a uniform response throughout their transverse surface, 2) a pixel size as small as possible in order to reach the resolution limits of optics ($D < 1 \mu\text{m}^2$), 3) a reduced thickness to avoid optical aberrations ($E < D^2/\lambda \approx 1 \mu\text{m}$), 4) a short response time t_r , and an adjustable lifetime τ allowing "real time" processing, 5) a good write sensitivity ($W \approx 1 \text{ pJ/pixel}$) and finally 6) the write (λ_w) and read (λ_r) spectral tunabilities. But up to now, none of the materials used meet all the requirements necessary for optimizing the

SLM performances, in particular spatial resolution which remains limited to $\approx 100 \mu\text{m}^2$, exposure sensitivity per pixel (typically 10 pJ/pixel) and switching times ($t_r > 1 \mu\text{s}$) because of collective effects in liquid crystals and polarization effects in photorefractives and MQW. In the quest for new materials with high spatial light modulation efficiencies, organics have both advantages of developing instantaneous molecular effects and being easily processible as large area homogeneous thin films.

To this respect, photochromic materials have been intensively studied in view of a number of optical signal processing applications. At the exception of the well-known silver halides which undergo self-darkening when irradiated in the UV-visible, most of the photochromic materials are organic compounds. Organic photochromism usually results from photoinduced isomerism (cis-trans) or molecular re-arrangement (ring closure-opening). In this article, we investigate the transient photochromism of thiophene oligomers and show that these compounds can be the key materials of an ultrafast incoherent-to-coherent optical converter (ICOC), a particular class of optically-addressed SLMs.

MATERIALS

The synthesis of unsubstituted α -*n*T oligothiophenes have already been extensively described according to various routes.⁶ Homocoupling of shorter oligomers via organo-metallic intermediates is the most widely used method.

Solutions of α -*n*T are prepared in dichloromethane. For optical measurements, the solutions are placed in polarimetric-quality fused-quartz cells of thickness 1 mm. The optical densities (OD) of the α -3T, α -4T and α -5T solutions are 1.0 at their respective excitation wavelengths (355 nm for α -3T; 396 nm for α -4T and α -5T). The OD of the α -2T solution is 0.4 at the minimum available excitation wavelength and that of the α -6T one close to saturation is 0.33 at 396 nm.

Thin solid films of α -6T are easily prepared by vapor deposition heating a small quantity of purified powder (melting point = 305°C) in a tungsten boat under reduced pressure (10^{-4} Pa). Typical deposition rates are in the range 1–4 nm/sec up to thicknesses in the range 100–300 nm. This procedure affords homogeneous, stable and highly crystalline α -6T thin films. The high optical quality of our samples is due to the extremely small size of the crystallites (30–100 nm). The linear refractive index of the α -6T thin films ($n = 1.965$ at 632.8 nm) has been measured in the transparency region by excitation of evanescent optical waves with a He-Ne laser using the conventional Kretschman configuration.⁷ In contrast to poly(3-alkylthiophenes) films, whose high porosity generally results in low refractive indices, the high refractive index of α -6T thin films can be ascribed to the combined effects of a long π -conjugated system (electronic factors) and high film crystallinity and density (morphology factors).

TRANSIENT PHOTOINDUCED DICHROÏSM

Kerr Ellipsometry Technique

Photoinduced dichroism in α -*n*T solutions and thin films is measured using a modified Kerr ellipsometry technique based on the anisotropy induced by a linearly polarized

optical pump in the initially isotropic material.⁸ Briefly, it consists in the analysis of the polarization state of a probe beam transmitted by the sample after action of the pump beam. Incoming pump and probe are linearly polarized and their polarization directions make an angle of 45°. This method permits an accurate and sensitive measurement of both the birefringence and dichroism induced by the pump.

Dichroism is represented by the imaginary part of the complex phase retardation ϕ which is related to the variation of absorption coefficient at the probe frequency ω_s by:

$$\text{Im}(\phi) = \frac{1}{4l[\Delta\alpha_{\parallel}(\omega_s) - \Delta\alpha_{\perp}(\omega_s)]} \quad (1)$$

where \parallel and \perp denote the probe polarization parallel and perpendicular to the pump polarization and l is the optical path length in the sample. The variation of the difference (1) with ω_s reflects the differential spectral properties of the optically excited molecules.

The source is a Nd³⁺:YAG laser delivering 33 ps pulses at 1064 nm with a repetition rate of 10 Hz. Three excitation wavelengths are derived from this source at 532, 396 and 355 nm. The maximum pump intensity is 40 MW/cm² at 355 nm and 8 MW/cm² at 396 nm. The probe is a weakly chirped continuum generated by focussing the 1064 nm beam in a 5 cm long deuterated-water cell and is detected in the 420–910 nm range.

Measurements in Solutions

The spectra of induced dichroism in α -*n*T solutions ($n = 2$ to 6) are given in Figure 1. The main feature is a sharp peak for α -3T, α -5T and α -6T at increasing wavelengths, while it is slightly broader for α -2T and α -4T. A similar size dependent behavior has also been observed by Chosrovian *et al.*, but with broader spectra.⁹ Our narrow spectra strongly contrast with the smooth and broad photoinduced absorption spectra of polythiophenes and other conjugated polymers. Since these sharp PA peaks are

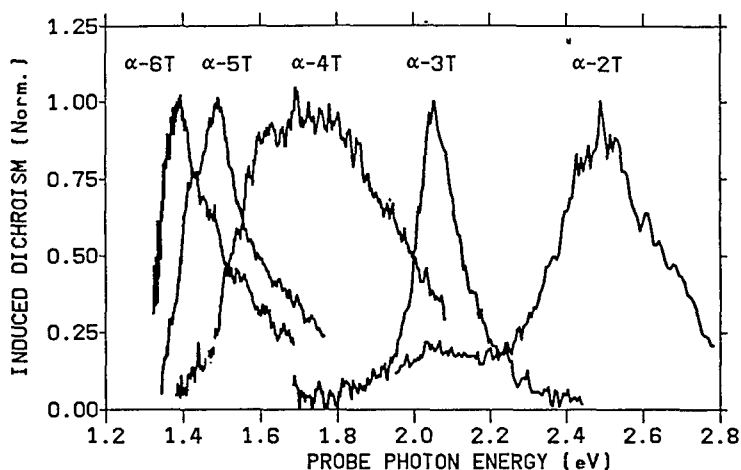


FIGURE 1 Photoinduced dichroism spectra of oligothiophenes α -*n*T ($n = 2-6$) in dichloromethane.

TABLE 1
Characteristics of linear and photoinduced absorption in oligothiophenes
 α -nT ($n = 2-6$).

Oligomer	λ_{\max} (nm)	ϵ ($10^{-4} \text{ M}^{-1} \text{ cm}^{-1}$)	λ_{PA} (nm)	ϵ_{PA} ($10^{-4} \text{ M}^{-1} \text{ cm}^{-1}$)
T	243	0.156		
α -2T	302	1.247	498	9
α -3T	355	2.505	603	25
α -4T	391	4.550	720	28
α -5T	410	5.520	836	39
α -6T	432	≈ 6	≈ 890	≈ 50

produced by excitation in the broader fundamental absorption band, we call this phenomenon *spectral concentration*.

The efficiency of the process is given in Table 1 in terms of extinction coefficient per absorbed pump photon. As a rule, these spectra are independent of the excitation wavelength. The signal is proportional to the absorbed pump energy, showing that it results from a one-photon absorption process. The rise time is lower than 10 ps and the lifetime of induced anisotropy increases with the oligomer size (18 ps for α -3T and 65 ps for α -5T in dichloromethane).

The dynamics of the induced dichroism also reveals interesting features (Fig. 2). The nanosecond-lived absorption of α -3T at 460 nm has already been observed¹⁰ and can be assigned to the triplet state absorption ($T_1 \rightarrow T_n$). On the other hand, the picosecond transient peak of α -3T at 600 nm is of different origin. Its line shape and chain length dependence are reminiscent of those of the corresponding radical cations α -nT⁺ as prepared by chemical doping.¹¹ But owing to its short lifetime and evolution towards the triplet state it should rather be attributed to the lowest singlet state absorption ($S_1 \rightarrow S_n$). The maximum photoinduced absorption is almost independent on the

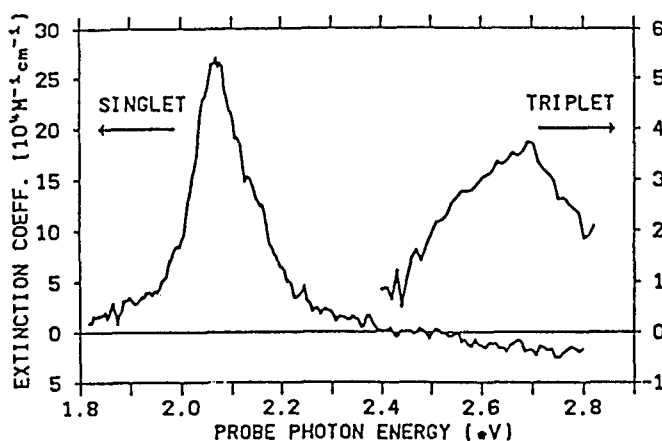


FIGURE 2 Photoinduced absorption of α -3T in a highly viscous solvent at zero (S_1 absorption) and 660 ps (T_1 absorption) probe delay.

solvent polarity (methanol, dichloromethane or cyclohexane) which is another argument in favor of a nonpolar species as its origin. Furthermore, as for the $\alpha\text{-}n\text{T}^+$ radical cations, the maximum absorption wavelength fits a linear $1/n$ progression with the oligomer length n from the trimer to the hexamer (Fig. 3). But the constant 0.2 eV energy difference between both curves again rules out the possibility for the induced dichroism to originate from the respective $\alpha\text{-}n\text{T}^+$ radical cations.

Measurements in Thin Films

Spectral concentration is also observed in the solid state as exemplified here with $\alpha\text{-}6\text{T}$ thin films. The linear absorption spectrum of an $\alpha\text{-}6\text{T}$ thin film is represented in Figure 4 (dashed curve) showing the broad and structured $\pi\text{-}\pi^*$ transition peaking at 398 nm ($\alpha = 2.6 \times 10^6 \text{ cm}^{-1}$) with three equally-spaced ($\Delta E = 0.194 \text{ eV}$) vibronic sidebands. The vibronic contributions, which are not observed in solution, are characteristic of the quasi-planar and rigid-rod conformation of $\alpha\text{-}6\text{T}$ in the solid state.^{2a} The left spectrum (solid line) represents the photoinduced dichroism in the transparency region 670 ps after excitation at 532 nm (2.33 eV). At a zero time delay, excitation at three different wavelengths (355, 395 and 532 nm) always results in the same photoinduced transient spectrum showing that photoexcitation in the absorption band homogeneously generates the same excited state. It peaks at 790 nm (1.57 eV) instead of 890 nm (1.39 eV) for the $S_1 \rightarrow S_n$ transition observed in solution and has an extremely narrow half-intensity width of 0.1 eV as compared to that of the linear absorption of the film (FWHM $\approx 1.0 \text{ eV}$).

The dynamics of photoinduced dichroism in a $\alpha\text{-}6\text{T}$ film after excitation at 2.33 eV by a 50 MW/cm^2 light pulse of 33 ps is shown in Figure 5. The rise time is shorter than 10

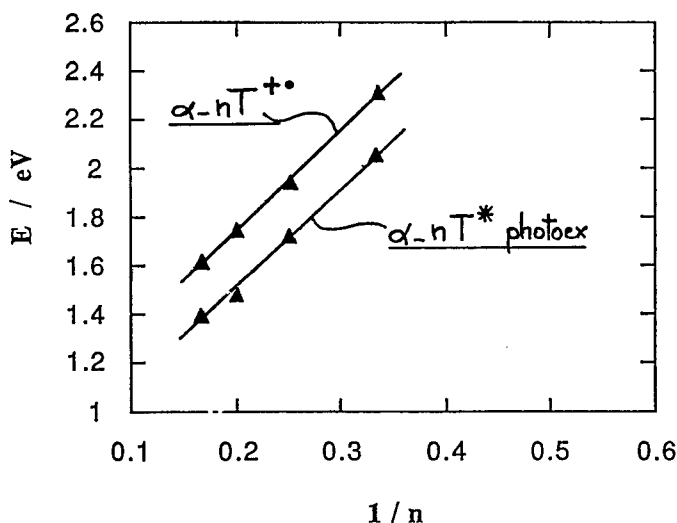


FIGURE 3 Linear $1/n$ progression of the photoexcited ($\alpha\text{-}n\text{T}^*$) and radical cations ($\alpha\text{-}n\text{T}^+$) maximum absorption wavelengths with the oligomer length n .

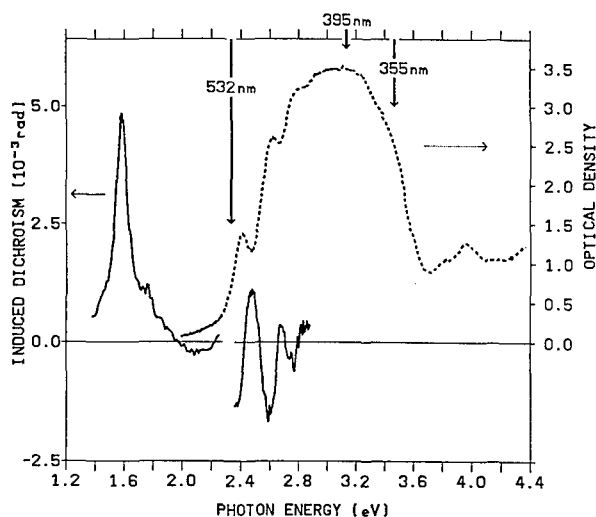


FIGURE 4 Photoinduced dichroism (full line on the left) in an α -6T film (thickness 320 nm) excited at 532 nm after a 670 ps probe delay. The dashed curve on the right represents the linear absorption of the film.

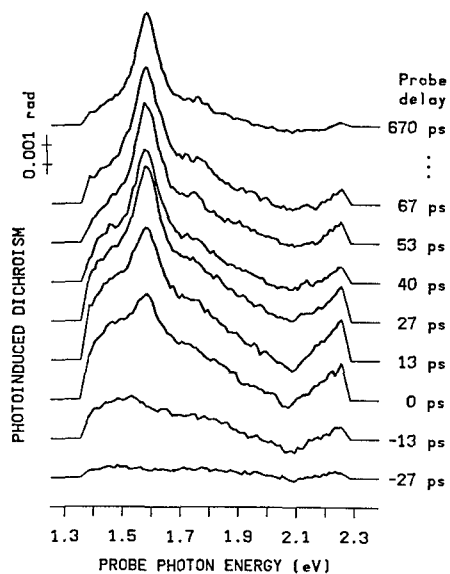


FIGURE 5 Time-resolved spectra of photoinduced dichroism in an α -6T film excited at 532 nm by a 50 MW/cm^2 laser pulse of 33 ps.

ps which is our detection limit. A structureless spectrum extending from 1.35 to 2.1 eV and peaking at about 1.55 eV develops during the first 30–40 ps. Due to its short lifetime ($\tau = 40$ ps) and by analogy with what is observed in solution, it can be attributed to the absorption of the lowest singlet excited state S_1 . Then, this first spectrum rapidly

interconverts into a sharper one peaking at the same energy but with a much longer lifetime ($\tau = 5$ ns). We attribute it to absorption by the T_1 triplet state after S_1 relaxation via intersystem crossing (ISC), in agreement with observations on α -3T.¹⁰ The absence of simultaneous absorption in the 0.8 eV near infrared region excludes the possibility to attribute this photogenerated state to the α -6T⁺ radical cation.¹¹

The probe-wavelength dependence of the real (birefringence) and imaginary (dichroism) parts of the complex phase retardations induced in a α -6T film are displayed in Figure 6. It shows that modulation of both phase and amplitude are obtained. The induced optical density at 790 nm is $\delta DO \approx 10^{-2}$ and results of an excitation energy close to 1 mJ/cm². The results evidence the Kramers-Kronig relation between birefringence and dichroism.

From a molecular point of view, spectral concentration may result from a greater contribution of the quinoid-like electronic configuration (Fig. 7) inducing an homogenization of the excited state of the molecule. Molecular engineering rules leading to spectral concentration are discussed elsewhere⁵ and consist in identifying the physico-chemical parameters that allow the oscillator strength to be confined in a narrow spectral region close to $kT = 0.025$ eV. Three of them seem essential: (1) damping of vibronic side bands, (2) conservation of the oscillator strength, and (3) homogeneity of the molecule.

AN α -6T BASED INCOHERENT-TO-COHERENT OPTICAL CONVERTER

In respect to its short response time (< 10 ps), α -6T could be used to design an ultrafast photochromic incoherent-to-coherent optical converter (ICOC).¹³ The typical optical arrangement of a prototype ICOC using α -6T as the modulating material is represented in Figure 8. The device itself consists in an α -6T thin film vacuum-deposited on an SiO₂ substrate. A continuous white light source illuminates an object whose image is

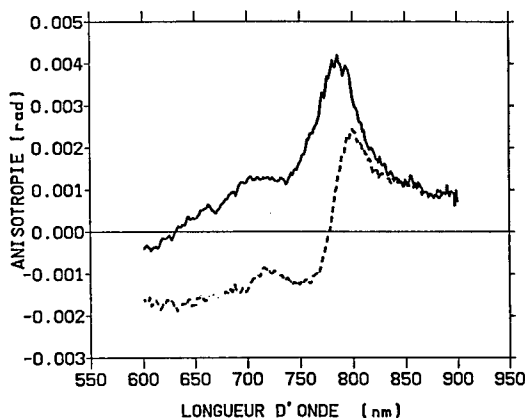


FIGURE 6 Birefringence (dashed line) and dichroism (full line) induced in an α -6T film after excitation at 532 nm and a 500 ps probe delay.

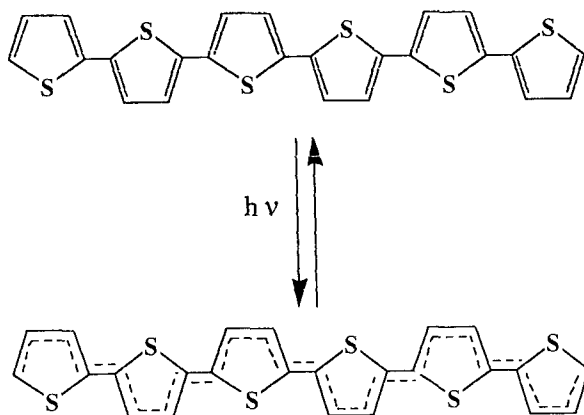


FIGURE 7 Reduction of bond alternance in the quinoïd-like electronic structure of α -6T in its photo-excited state.

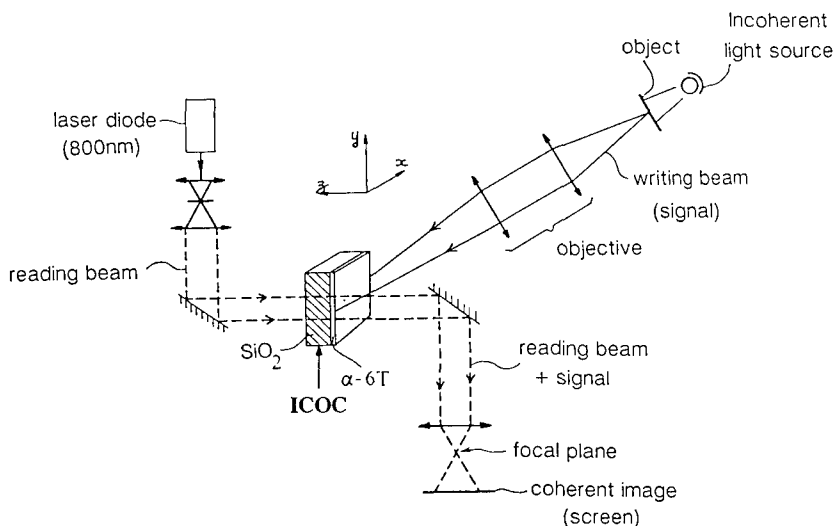


FIGURE 8 Experimental setup of an α -6T based incoherent-to-coherent optical converter (ICOC).

formed on the surface of the device by mean of an objective. This incoherent writing beam carrying the signal reaches the α -6T film by the x - y front face. The coherent reading beam is produced by a laser diode ($\lambda = 800$ nm) and successively passes through a spatial filter and a collimation lens before reaching the back x - y face of the ICOC, i.e., the SiO_2 substrate. The laser diode has been selected because its wavelength matches that of the photoinduced absorption of the α -6T film ($\lambda_{\text{max}} = 790$ nm).

The simultaneous excitation of α -6T by the writing and reading beams finally results in a coherent beam carrying the signal initially contained in the incoherent beam. The

coherent image of the illuminated object can then be deflected by a mirror, focussed by a lens on an holographic filter and the correlation result can be displayed on a screen. Such coherent holographic filtering also permits an amplification of the photochromic contrast.

Since the lifetime of the T_1 state responsible of the transient photochromism is $\tau \approx 5$ ns under room conditions, it is in principle possible to use the α -6T based ICOC to process images with frequencies up to 200 MHz. However, such a modulation rate requests a 200 kW/cm^2 continuous white light illumination. This is by far too large and it is better either to dissolve α -6T in an outgazed polymer matrix into which triplet lifetimes can be increased up to microseconds at room temperature or to use pulsed white light exposure. At 1 MHz frequency, exposure energy is reduced to the acceptable value of 1 kW/cm^2 . The readout frequency can also be adjusted by selecting the appropriate oligomer length n because of the size dependence of photoinduced absorption.

CONCLUSION

As compared with other ICOC materials such as photorefractive crystals,¹⁴ liquid crystal light valves¹⁵ and semiconductor heterostructures,¹⁶ α -6T films can improve the speed and spatial resolution of image processing by two orders of magnitude while having the same exposure sensitivity. These performances together with spectral tunability by selecting the appropriate oligomer size make sexithiophene α -6T and other one-dimensional conjugated α -oligothiophenes the "archetype" photochromic materials for ultrafast incoherent-to-coherent optical conversion.

REFERENCES

- (a) X. Peng, G. Horowitz, D. Fichou and F. Garnier, *Appl. Phys. Lett.*, **57**, 2013 (1990),
(b) F. Garnier, G. Horowitz, X. Z. Peng and D. Fichou, *Adv. Mater.*, **2**, 592 (1990),
(c) H. Akimichi, K. Waragai, S. Hotta, H. Kano and H. Sakaki, *Appl. Phys. Lett.*, **58**, 1500 (1991),
(d) P. Ostoja, S. Guerri, S. Rossini, M. Servidori, C. Taliani and R. Zamboni, *Synth. Met.*, **54**, 447 (1993).
- (a) D. Fichou, G. Horowitz, B. Xu and F. Garnier, *Synth. Met.*, **48**, 167 (1992),
(b) N. Periasamy, R. Danieli, G. Ruani, R. Zamboni and C. Taliani, *Phys. Rev. Lett.*, **68**, 919 (1992),
(c) S. Hotta and K. Waragai, *J. Phys. Chem.*, **97**, 7427 (1993).
- (a) D. Fichou, F. Garnier, F. Charra, F. Kajzar and J. Messier, in *Organic Materials for Nonlinear Optics*, eds. R. Hahn and D. Bloor, Royal Society of Chemistry, London (1989), p. 176,
(b) H. Thienpont, G. L. J. A. Rikken, E. W. Meijer, W. ten Hoeve and H. Wynberg, *Phys. Rev. Lett.*, **6**, 2141 (1990),
(c) G. Marowsky, R. Steinhoff, L. F. Chi, J. Hutter and G. Wagnière, *Phys. Rev. B*, **38**, 6274 (1988).
- (a) A. Vanderlugt, *Optical Signal Processing* (Wiley, New-York 1992),
(b) C. Warde and A. D. Fischer, in *Optical Signal Processing*, ed. J. L. Horner (Academic Press, Inc., 1987), p. 477.
- J.-M. Nunzi, F. Charra and N. Pfeffer, *J. Phys. III France*, **3**, 1401 (1993).
- J. Nakayama, T. Konishi and M. Hoshino, *Heterocycles*, **27**, 1731 (1988).
- H. Knobloch, D. Fichou, W. Knoll and H. Sasabe, *Adv. Mater.*, **5**, 570 (1993).
- N. Pfeffer, F. Charra and J.-M. Nunzi, *Opt. Letters*, **16**, 1987 (1991).
- (a) F. Charra, D. Fichou, J.-M. Nunzi and N. Pfeffer, *Chem. Phys. Lett.*, **192**, 566 (1992),
(b) H. Chosrovian, S. Rentsch, D. Grebner, D. U. Dahm, E. Birkner and H. Naarmann, *Synth. Met.*, **52**, 213 (1992),
(c) D. V. Lap, D. Grebner, S. Rentsch and H. Naarmann, *Chem. Phys. Lett.*, **211**, 135 (1993).
- C. H. Evans and J. C. Scaiano, *J. Am. Chem. Soc.*, **112**, 2694 (1990).
- D. Fichou, B. Xu, G. Horowitz and F. Garnier, *Synth. Met.*, **39**, 243 (1990).

12. J.-M. Nunzi, N. Pfeffer, F. Charra and D. Fichou, *Chem. Phys. Lett.*, **215**, 114 (1993).
13. D. Fichou, J.-M. Nunzi, F. Charra and N. Pfeffer, *Adv. Mater.*, **6**, 64 (1994).
14. J. W. Yu, D. Psaltis, A. Marrakchi, A. R. Jr. Tanguay and R. V. Johnson in *The Photorefractive incoherent to coherent optical converter, Photorefractive materials and their applications II*, eds. P. Gunter and J.-P. Huignard (Springer, Berlin, 1989), p. 275.
15. T. Moriyama, J. Kajita, Y. Takanishi, K. Ishikawa, H. Takezoe and A. Fukuda, *Jpn. J. Appl. Phys.*, **32**, L589 (1993).
16. B. G. Sfez, E. V. K. Rao, Y. I. Nissim and J.-L. Oudar, *Appl. Phys. Lett.*, **60**, 607 (1992).

NOTES FOR CONTRIBUTORS TO NONLINEAR OPTICS

MANUSCRIPTS

Papers should be typed with double spacing and wide (3 cm) margins on good quality paper, and submitted in triplicate to any of the editors, or via a member of the Editorial Advisory Board. Submission of a paper to *Nonlinear Optics* will be taken to imply that it represents original work not previously published, that it is not being considered elsewhere for publication, and that if accepted for publication it will not be published elsewhere in the same form, in any language, without the consent of editors and publisher.

Language: English language is preferred, but French or German papers will be accepted if an English summary of 200–300 words is also supplied.

Abstract: Each paper requires an abstract of 100–150 words summarizing the significant coverage and findings. Non-English papers should have a similar abstract in the language, but must also contain an English-language abstract of 200–300 words.

It is a condition of acceptance by the editor of a typescript for publication that the publishers acquire automatically the copyright in the typescript throughout the world.

FIGURES

All figures should be numbered with consecutive arabic numbers, have descriptive captions, and be mentioned in the text. Keep figures separate from the text, but indicate an approximate position for each in the margin.

Preparation: Figures submitted must be of a high enough standard for direct reproduction. Line drawings should be prepared in black (India) ink on white paper or on tracing cloth, with all lettering and symbols included. Alternatively, good sharp photoprints ("glossies") are acceptable. Photographs intended for half-tone reproduction must be good glossy original prints, of maximum contrast. Clearly label each figure with author's name and figure number; indicate "top" where this is not obvious. Redrawing or retouching of unusable figures will be charged to authors.

Size: Figures should be planned so that they reduce to 11 cm column width. The preferred width of line drawings is 15 to 22 cm with capital lettering 4 mm high, for reduction by one-half. Photographs for halftone reproduction should be about twice the desired size.

Color Plates: Whenever the use of color is an integral part of the research, or where the work is generated in color, the journal will publish the color illustrations without charge to the authors. Reprints in color will carry a surcharge. Please write to the Editor for details.

EQUATIONS AND FORMULAE

Mathematical: Mathematical equations should preferably be typewritten, with subscripts and superscripts clearly shown. It is helpful to identify unusual or ambiguous symbols in the margin when they first occur. To simplify typesetting, please use: (1) the "exp" form of complex exponential functions; (2) fractional exponents instead of root signs; and (3) the solidus (/) to simplify fractions — e.g. $\exp x^{1/2}$.

Chemical: Ring formulae, and other complex chemical matter, are extremely difficult to typeset. Please, therefore, supply reproducible artwork for equations containing such chemistry. Long reaction sequences should be designated as "Schemes" and treated like figures; i.e. keep artwork separate from the text, indicate in the margin an appropriate position, and supply a separate list of scheme captions. Where necessary, individual chemical formulae can be identified with bold arabic numbers. Chemical equations referred to in the text should be indicated with arabic numbers set over to the right, and in parentheses.

Marking: Where chemistry is straightforward and can be set (e.g. single-line formulae), please help the typesetter by distinguishing between, e.g. double bonds and equal signs and single bonds and hyphens, where there is ambiguity. The printer finds it extremely difficult to identify which symbols should be set in roman (upright) or italic or bold type, especially where the paper contains both mathematics and chemistry. Therefore, please underline all mathematical symbols to be set italic and put a wavy line under bold symbols. Other letters not marked will be set in roman type.

TABLES

Number tables consecutively with roman numerals, and give each a clear descriptive caption at the top. Avoid the use of vertical rules in tables. Indicate in the margin where the printer should place tables.

REFERENCES AND NOTES

References and notes are indicated in the text by consecutive superior arabic numbers (without parentheses). The full list should be collected and typed at the end of the paper in numerical order. Listed references should be complete in all details, but excluding article titles in journals. Authors' initials should precede their names; journal title abbreviations should conform to *Chemical Abstracts* style. Examples:

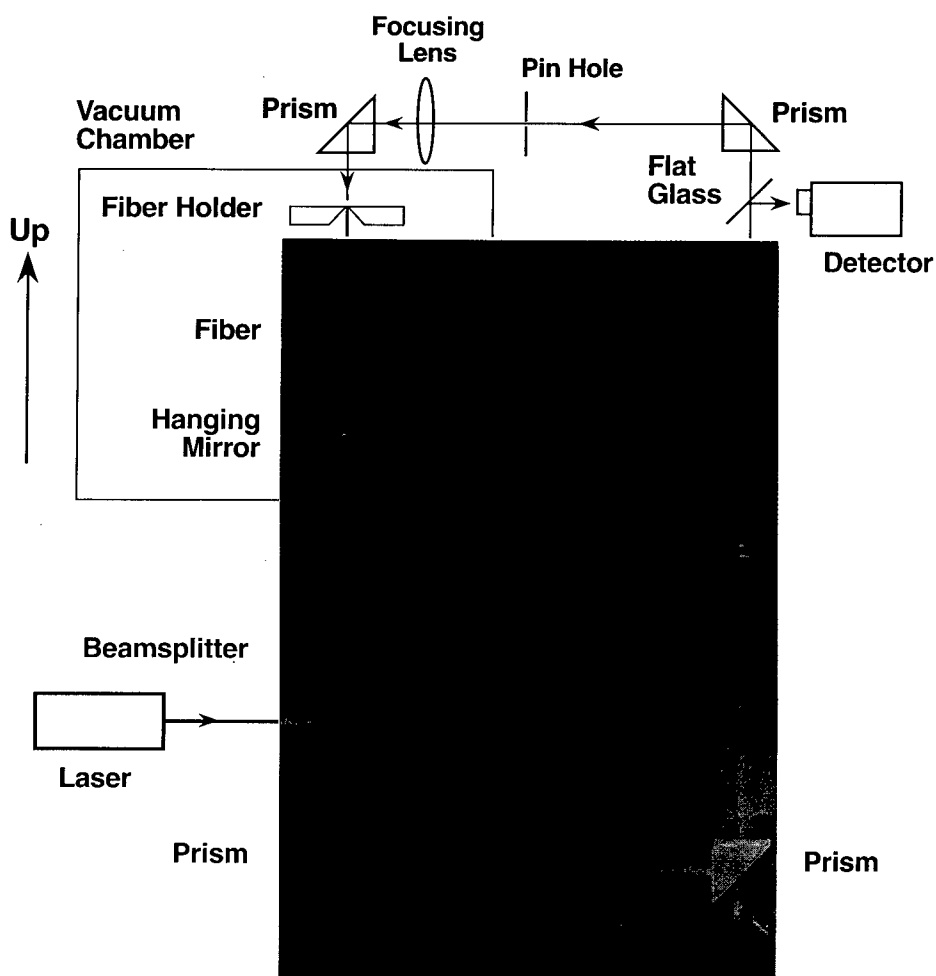
1. A. B. Smith and C. D. Jones, *J. Appl. Phys.* **34**, 296 (1965).
2. R. B. Brown, *Molecular Spectroscopy* (Gordon and Breach, New York, 1970), 3rd ed., Chap. 6. pp. 95–106.

PROOFS

Authors will receive page proofs (including figures) by airmail for correction, which must be returned to the printer within 48 hours of receipt. Please ensure that a full postal address is given on the first page of the typescript, so that proofs are not delayed in the post. Authors' alterations in excess of 10% of the original composition cost will be charged to authors. **Reprints:** 25 free reprints will be provided to the first-named author of each paper. Additional reprints may be ordered by completing the appropriate form sent with proofs.

PAGE CHARGES

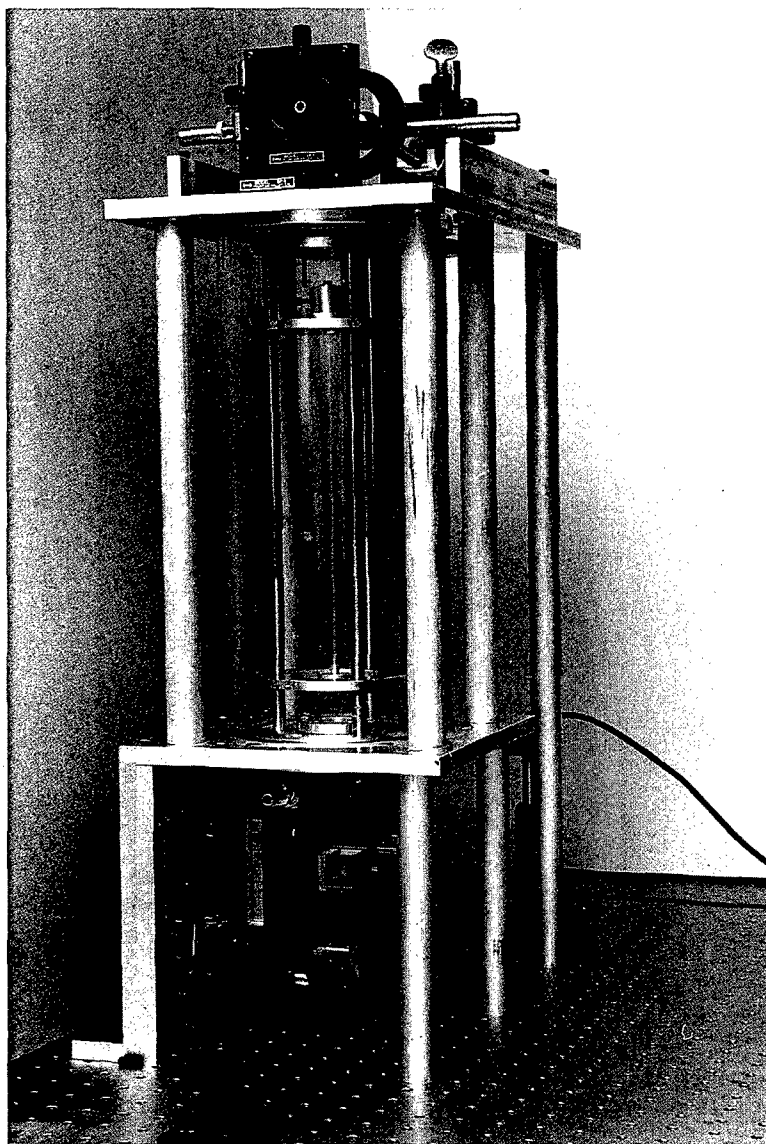
There are no page charges to individuals or to institutions.



COLOUR PLATE I

See Kuzyk et al., Fig. 1

Photograph of the photomechanical stabilization experiment.



COLOUR PLATE II

See Kuzyk et al., Fig. 2

Hybrid schematic of the photomechanical stabilization experiment.



COLOUR PLATE III

See Nunzi et al., Fig. 6

View of the real-time holography experiment performed with a spiropyran thin-film deposited on a red glass disk (on right of the picture). The observed object, a metallic tool in the center of the picture, is illuminated with the expanded green beam of an argon ion laser. Readout was performed with a He-Ne laser whose output is visible on the left-most part of the figure. The reconstructed holographic image is visible in red colour behind the holographic film.

continued from inside front cover

Orders may be placed with your usual supplier or with International Publishers Distributor at one of the addresses shown below. Journal subscriptions are sold on a per volume basis only; single issues of the current volume are not available separately. Claims for nonreceipt of issues will be honored free of charge if made within three months of publication of the issue. Subscriptions are available for microform editions; details will be furnished upon request.

All issues are dispatched by airmail throughout the world.

Subscription Rates

Base list subscription price per volume: ECU 107.00 (US \$129.00)*. This price is available only to individuals whose library subscribes to the journal OR who warrant that the journal is for their own use and provide a home address for mailing. Orders must be sent directly to the Publisher and payment must be made by personal check or credit card.

Separate rates apply to academic and corporate/government institutions, and may also include photocopy license and postage and handling charges.

*ECU (European Currency Unit) is the worldwide base list currency rate; payment can be made by draft drawn on ECU currency in the amount shown or in local currency at the current conversion rate. The US Dollar rate is based upon the ECU rate and applies to North American subscribers only. Subscribers from other territories should contact their agents or the Publisher. All prices are subject to change without notice.

Publication Schedule Information: To ensure your collection is up-to-date, please call the following number for information about the latest issue published:

USA (201) 643-7500 - Dial extension 290 - Enter the ISSN followed by # key.

Note: If you have a rotary phone, please call our Customer Service at the numbers listed below.

Orders and enquiries should be placed through International Publishers Distributor in care of one of the addresses below:

Postfach, 4004
Basel, Switzerland
Telephone: (41-61) 261-01-38
Fax: (41-61) 261-01-73

820 Town Center Drive
Langhorne, PA 19047, USA
Telephone: (215) 750-2642
Fax: (215) 750-6343

Kent Ridge, PO Box 1180
Singapore 9111
Republic of Singapore
Telephone: 741-6933
Fax: 741-6922

Yohan Western Publications Distribution Agency
3-14-9 Okubo, Shinjuku-ku
Tokyo 169, Japan
Telephone: (03) 3208-0186
Fax: (03) 3208-5308

Photocopy License

This publication and each of the articles contained herein are protected by copyright. If the subscription price paid by the subscriber includes a fee for a Photocopy License, then the subscriber is permitted to make multiple photocopies of single articles for the internal study or research purposes of the subscriber. The Photocopy License is not available to individuals or to certain other subscribers. The Photocopy License does not permit copying for any other purpose, such as copying for distribution to any third party (whether by sale, loan, gift or otherwise); as agent (express or implied) of any third party; for purposes of advertising or promotion; or to create collective or derivative works. All requests for permission to copy beyond the scope of the Photocopy License must be made to the Publisher. No copyright licensing organization in any territory has authority to grant such permission on the Publisher's behalf. Any unauthorized reproduction, transmission or storage may result in civil or criminal liability.

Rights and Permissions/Reprints of Individual Articles

Permission to reproduce and/or translate material contained in this journal must be obtained in writing from the Publisher. Copies of individual articles may be obtained from SCAN, the Publisher's own document delivery service. For either service, please write or fax to: International Publishers Distributor at one of the addresses listed above.

Voluntary Page Charges

The United States National Science Foundation has extended the allowance of page charge funds for payments to journals regardless of the publisher's commercial status. Previously this was reserved for only nonprofit society-sponsored journals. Voluntary page charge payments are now accepted for this journal, and authors may elect to pay any amount up to a maximum of \$25.00 per page. Payments will be refunded in the form of a voucher at 100% value of total payment. This voucher can be used by the author or the author's university library for any product or service offered by the Publisher, and thereby can be used to supplement library funding.

Negative Page Charges

The principal author of each article will receive a voucher for his contribution in the amount of ECU 15.00 (US \$20.00, Yen 3,000), which can also be used to purchase the Publisher's products directly or through university libraries, thereby reducing costs of publications to those authors supporting the journal.

Distributed by International Publishers Distributor.

Printed in Malaysia.

June 1995